



## City Research Online

### City, University of London Institutional Repository

---

**Citation:** Marchi, A. (2009). Internal flow and spray characteristics of an outwards opening pintle-type gasoline-injector. (Unpublished Doctoral thesis, City University London)

This is the accepted version of the paper.

This version of the publication may differ from the final published version.

---

**Permanent repository link:** <https://openaccess.city.ac.uk/id/eprint/19617/>

**Link to published version:**

**Copyright:** City Research Online aims to make research outputs of City, University of London available to a wider audience. Copyright and Moral Rights remain with the author(s) and/or copyright holders. URLs from City Research Online may be freely distributed and linked to.

**Reuse:** Copies of full items can be used for personal research or study, educational, or not-for-profit purposes without prior permission or charge. Provided that the authors, title and full bibliographic details are credited, a hyperlink and/or URL is given for the original metadata page and the content is not changed in any way.





**CITY UNIVERSITY  
LONDON**

**The University for Business  
and the Professions**

# **Internal flow and spray characteristics of an outwards opening pintle-type gasoline-injector**

**Dipl. Andrea Marchi**

**School of Engineering and Mathematical Sciences**

**This thesis is submitted for the fulfilment of the requirements for the  
Degree of Doctor of Philosophy**

*"La scienza ci ha promesso la verità. Non ci ha promesso pace e felicità"*

*(Gustave Le Bon)*

**December 2009**

**THE FOLLOWING HAVE BEEN REDACTED AT THE  
REQUEST OF THE UNIVERSITY**

**PAGE 48 FIG 1-7 P49 FIG 1.9A AND 1.9B, P51 FIG 1.13,  
P59 FIG 1.16, P60 FIG 1.17, P66 FIG 1.21A, P349 FIG 7.1  
AND P350 FIG 7.2 .**

---

*"La scienza ci ha promesso la verità. Non ci ha promesso pace e felicità"*  
(Gustave Le Bon)

---

# *List of Contents*

<i>List of Contents</i>	3
<i>List of tables</i>	9
<i>List of figures</i>	10
<i>Acknowledgement</i>	20
<i>Declaration</i>	21
<i>Abstract</i>	22
<i>Nomenclature</i>	24
<b>Chapter 1. Introduction</b>	26
1.1. MOTIVATION	26
1.2. INTRODUCTION	28
1.3. PRE EMISSION PERIOD	28
1.4. EARLY FUEL METERING SYSTEMS	30
1.4.1. Carburetor	30
1.4.2. Fuel Injection	34
1.4.3. Alternative Injector Schemes:	39
1.4.3.1. Throttle body injection	39
1.4.3.2. Continuous Injection	39
1.4.3.3. Central Port Injection (CPI)	40
1.4.3.4. Multipoint fuel Injection (MPFI)	40
1.5. EMISSIONS IN INTERNAL COMBUSTION ENGINES	41
1.6. DIRECT INJECTION	45
1.6.1. Background history and diffusion of direct injection technology	45
1.6.2. From DISC to DISI Engines	47
1.6.3. Gasoline Direct Injection versus Port Fuel injection	52
1.6.4. Strategies and approaches to achieving Stratified charge	57
1.7. TYPES OF DISI INJECTORS	61
1.7.1. Swirl Injector	63
1.7.2. Multihole Injector	65
1.7.3. Outward opening Injector (pintle-type Injector)	66
1.8. OBJECTIVES OF THE INVESTIGATION	68
1.9. THESIS OUTLINE	70
<b>Chapter 2. Literature Review</b>	71
2.1. INTRODUCTION	71

---

2.2. INTERNAL FLOW CHARACTERISATION IN LARGE-SCALE MODELS	72
2.3. SPRAY FLOW CHARACTERISATION IN REAL SIZE MODELS	79
2.4. SPRAY RECIRCULATION AND AIR ENTRAINMENT	89
2.5. INVESTIGATION IN OPTICAL ENGINE	93
2.6. PINTLE-TYPE INJECTOR	96
2.7. MISCELLANEOUS ON DISI CONCEPT	100
2.8. LITERATURE REVIEW SUMMARY	102
<b>Chapter 3. Large-scale Model</b>	<b>108</b>
3.1. INTRODUCTION	108
3.2. EXPERIMENTAL TECHNIQUES	108
3.2.1. Mie-scattering	108
3.2.2. LDV (Laser Doppler Velocimetry)	109
3.3. DESCRIPTION OF THE TEST RIG AND OF THE EXPERIMENTAL SET UP	110
3.3.1. Injectors under investigation	113
3.3.2. Flat window for in-nozzle visualisation.	114
3.3.3. Spray visualisation	115
3.4. NON CAVITATING MODEL: RESULTS AND DISCUSSION	118
3.4.1. Near-nozzle flow visualisation	119
3.4.2. In-nozzle flow visualisation	120
3.4.3. LDV measurements	123
3.4.4. Nozzle exit frequency	124
3.4.5. Flow filaments formation characteristics at the nozzle exit	126
3.4.6. Liquid film flapping	129
3.5. INWARD SEAL BAND (CAVITATING MODEL): RESULTS AND DISCUSSION	130
3.5.1. Flow operating conditions	130
3.5.2. In-nozzle flow	132
3.5.3. Injection into air, air entrainment	134
3.5.4. Angle analysis	140
3.5.5. String structure analysis	142
3.5.6. Cavitation	151
3.6. REAL SIZE SPRAY CORRELATION	162
3.6.1. Inward Seal Band - needle position	162
3.6.2. Inward Seal Band - Fuel mass rate	164
3.6.3. Inward Seal Band – string analysis	166
3.7. SUMMARY	173
<b>Chapter 4. Spray Characterization under atmospheric and high pressure conditions</b>	

	176
<b>4.1. INTRODUCTION</b>	<b>176</b>
4.1.1. Atomisation	177
4.1.2. Disintegration of liquid sheets	177
4.1.3. Drop size distribution	178
4.1.4. Typical Droplet sizes	179
<b>4.2. EXPERIMENTAL TECHNIQUES AND EQUIPMENT DESCRIPTION</b>	<b>180</b>
<b>4.3. TEST RIG STRATEGIES</b>	<b>181</b>
4.3.1. PIV Experimental set up	182
4.3.2. PDA Measurements under Atmospheric Condition: Experimental set up	184
4.3.3. String Identification	190
4.3.4. Results and discussion	192
4.3.4.1. First phase structure. Bulky leap at leading edge of the spray	194
4.3.4.2. Second phase structure: Fish bone structure	199
4.3.4.3. Third phase structure: unstable string structure	203
4.3.4.4. Analysis of droplet diameter distribution	212
4.3.4.5. Secondary breakup and Weber number analysis	215
4.3.4.6. Average Mean Diameter distribution along the axial direction.	217
4.3.4.7. Velocity distribution summary	220
4.3.4.8. Spray Recirculation	224
4.3.4.9. 2D Mie scattering	226
4.3.4.10. Particle Imaging Velocimetry of the spray recirculation area	229
4.3.4.11. Particle Imaging Velocimetry of the near nozzle area	235
4.3.4.12. Comparison of air entrainment velocity field for different injection pressure	238
4.3.5. Parametric investigation	242
4.3.5.1. Varying the injection pressure	242
4.3.5.2. Varying the injection duration	245
4.3.5.3. PDA Measurements in constant volume chamber: - Experimental Set-up	247
4.3.5.4. Spray imaging in constant volume chamber	247
4.3.5.5. PDA measurement in the constant volume chamber - Introduction	251
4.3.5.6. Effect of Backpressure at $P_i = 200$ bar	251
4.3.5.7. Effect of Backpressure at $P_i = 100$ bar	252
4.3.5.8. Effect of Injection Pressure	253
4.3.5.9. Effect of Chamber Temperature at 200 bar injection pressure	256
<b>4.4. SUMMARY</b>	<b>257</b>

---

<b>Chapter 5. Spray characteristics in the Optical Engine</b>	<b>263</b>
<b>5.1. INTRODUCTION</b>	<b>263</b>
<b>5.2. EXPERIMENTAL SET UP</b>	<b>263</b>
<b>5.2.1. Integral Mie scattering</b>	<b>266</b>
<b>5.3. SIGNAL CONTROL SET-UP</b>	<b>268</b>
<b>5.4. TEST CELL LAY OUT</b>	<b>270</b>
<b>5.5. EXPERIMENTAL STRATEGY</b>	<b>273</b>
<b>5.5.1. Spray Angle Analysis</b>	<b>278</b>
<b>5.6. SINGLE INJECTION: RESULT AND DISCUSSION</b>	<b>280</b>
<b>5.6.1. Injector comparison</b>	<b>281</b>
<b>5.6.1.1. Backpressure: ambient condition</b>	<b>281</b>
<b>5.6.1.2. Backpressure: 10.9bar</b>	<b>283</b>
<b>5.6.1.3. Backpressure: 16.6bar</b>	<b>285</b>
<b>5.6.2. Backpressure: 16.6bar, Minimum needle Lift: bit position 0000.</b>	<b>286</b>
<b>5.6.3. Influence of Spark Plug and Engine speed</b>	<b>288</b>
<b>5.6.3.1. Injector prototype: Positive step Inward Seal Band (+ISB). Minimum needle lift: bit position 1111</b>	<b>288</b>
<b>5.6.4. Injector prototype: Positive step Inward Seal Band (+ISB). Minimum needle lift: bit position 0000</b>	<b>290</b>
<b>5.6.5. Influence of Backpressure.</b>	<b>292</b>
<b>5.6.5.1. Injector prototype: Standard Seal band (SSB) Injection pressure: 200bar</b>	<b>292</b>
<b>5.6.5.2. Injector prototype: Inward Seal Band (+ISB) Injection pressure: 200bar</b>	<b>294</b>
<b>5.6.5.3. Injector prototype: Inward Seal Band (-ISB) Injection pressure: 200bar</b>	<b>295</b>
<b>5.6.5.4. Injector prototype: Inward Seal band (+ISB), Injection pressure: 100bar</b>	<b>297</b>
<b>5.6.5.5. Injector prototype: Inward Seal band (-ISB), Injection pressure: 100bar</b>	<b>298</b>
<b>5.6.6. Influence of Rail Pressure</b>	<b>299</b>
<b>5.6.6.1. Comparison at ambient pressure: -ISB 100bar; +ISB 100bar / 200bar.</b>	<b>300</b>
<b>5.6.6.2. Comparison at 16.6bar backpressure: -ISB 100bar; +ISB 100bar / 200bar.</b>	<b>301</b>
<b>5.6.7. Influence of Needle Lift.</b>	<b>302</b>
<b>5.6.7.1. Injector prototype: Standard Seal Band (SSB).</b>	<b>303</b>



---

5.6.7.2. Injector prototype: positive step Inward Seal Band (+ISB).	304
5.6.7.3. Injector prototype: negative step Inward Seal Band (-ISB).	306
5.6.7.4. Influence of Needle Lift: angle analysis summary	308
5.7. DOUBLE INJECTION: RESULT AND DISCUSSION	309
5.7.1. Comparison of Reference.	310
5.7.2. Comparison between EOI1 and EOI2.	311
5.7.3. Comparison of EOI1, EOI2 and Lift.	312
5.7.4. Injector Comparison.	314
5.8. SUMMARY OF RESULTS	315
5.8.1. Influence on Spray Angle of SSB. Spark Plug, RPM, Double Injection.	315
5.8.2. Influence on Spray Angle of ISB (negative step). Spark Plug, RPM, Double Injection.	316
5.8.3. Influence on Spray Angle of ISB (positive step). Spark Plug, RPM, Double Injection.	317
5.8.4. Influence of RPM on Spray Angle. Injector Comparison.	317
5.8.5. Influence of Backpressure on Spray Angle. Injector Comparison (Single Injection).	318
5.8.6. Influence of Backpressure on Spray Angle. Injector Comparison (Second Injection).	319
5.8.7. Influence of Injection pressure on Spray Angle. Injector Comparison (Single Injection, 1000rpm).	319
5.8.8. Influence of Needle Lift on Spray Angle. Injector Comparison (Single Injection, 1000rpm).	320
5.8.9. Influence of Needle Lift on Spray Angle. Injector Comp. (Second Injection, 1000rpm).	321
5.8.10. Visualisation of Spray Recirculation in the optical engine	322
5.8.10.1. Effect of Engine speed on the spray recirculation	327
5.8.10.2. Effect of backpressure on the spray recirculation	329
5.9. SUMMARY	332
Chapter 6. Conclusion and recommendations for future work	337
6.1. LARGE-SCALE MODEL	337
6.2. REAL SIZE INJECTOR	340
6.2.1. Spray Characteristics	340
6.2.2. Spray Recirculation and Air Entrainment	341
6.2.3. Parametric Studies	342
6.3. REAL SIZE INJECTOR IN THE OPTICAL ENGINE	343
6.4. SPRAY RECIRCULATION IN THE HYDRA ENGINE	344



---

<b>6.5. RECOMMENDATION FOR FURTHER WORK</b>	<b>345</b>
<b>6.5.1. Large-scale Injector Model</b>	<b>345</b>
<b>6.5.2. Spray Characterisation of the Real Size Injector.</b>	<b>346</b>
<b>6.5.3. Optical Engine.</b>	<b>347</b>
<b>6.5.4. Optical Engine: Spray Recirculation</b>	<b>347</b>
<b>Appendix A</b>	<b>349</b>
<b>7.1. MEASUREMENT TECHNIQUES AND ERROR ANALYSIS</b>	<b>349</b>
<b>7.1. PHASE-DOPPLER ANEMOMETRY –MEASURING PRINCLIPLES</b>	<b>349</b>
<b>7.2. PDA/LDA ERROR ANALYSIS [104, 109]</b>	<b>354</b>
<b>7.2.1. Error and Uncertainties</b>	<b>355</b>
<b>7.2.2. PDA, size accuracy</b>	<b>358</b>
<b>7.3. PARTICLE IMAGING VELOCIMETRY - MEASUREMENT PRINCIPLE</b>	<b>359</b>
<b>7.4. PIV ERROR ANALYSIS [111]</b>	<b>365</b>
<b>7.4.1. Particle image diameter</b>	<b>365</b>
<b>7.4.2. Particle image shift</b>	<b>366</b>
<b>7.4.3. Effect of Particle Image Density</b>	<b>367</b>
<b>References</b>	<b>370</b>

---

## *List of tables*

Table 1-1 Engine emissions standards for heavy-Duty diesel and petrol engines.....	43
Table 1-2 Engine emissions regulations for Euro III (2000) and Euro IV (2005).....	43
Table 1-3 Advantages of GD-I systems Vs PFI systems [19] .....	56
Table 1-4 Disadvantages of GD-I systems Vs PFI systems [19].....	56
Table 1-5 Requirements of GDI injector not present in the PFI. ....	56
Table 1-6 Comparison among swirl, multihole and outward opening atomisers [22].	63
Table 2-1 Internal flow characterisation in large-scale models .....	79
Table 2-2 Spray flow characterisation in Real size models .....	89
Table 2-3 Spray recirculation and air entrainment.....	92
Table 2-4 Investigation in optical engine.....	95
Table 2-5 Pintle-type Injector .....	100
Table 2-6 Miscellaneous on DISI concept.....	101
Table 3-1 Flow model operating conditions and its corresponding values for the real size nozzle .....	119
Table 3-2 Flow test conditions and their corresponding values for the real size nozzle. .....	131
Table 3-3 Air bubble penetration into the nozzle for different operating conditions. The difference between narrow and wide angle is about equal the valve lift ....	139
Table 3-4 Flow tests conditions for cavitation.....	152
Table 5-1 Operating parameters and Engine set up. ....	275
Table 5-2 Operating conditions under which the images were obtained for single injection investigation. (First set of results).....	276
Table 5-3 Injector ranking for different parameter variation. (1,2,3 injector prototype ranking. ++,+,- very positive, positive, negative) .....	322
Table 5-4 Test conditions for spray recirculation visualisation (for all cases full lift 1001). ....	324

---

## *List of figures*

Figure 1-1 Carburetor: schematic [ <a href="http://en.wikipedia.org/wiki/Carburetor">http://en.wikipedia.org/wiki/Carburetor</a> ].	31
Figure 1-2 Carburetor working principles [ <a href="http://en.wikipedia.org/wiki/Carburetor">http://en.wikipedia.org/wiki/Carburetor</a> ].	32
Figure 1-3 Fuel Injector scheme [ <a href="http://en.wikipedia.org/wiki/Fuel_injection">http://en.wikipedia.org/wiki/Fuel_injection</a> ].	34
Figure 1-4 Throttle body injection	39
Figure 1-5 Particle emissions for different concepts (updated on 2000) [6, 7].	44
Figure 1-6 Mercedes-Benz 300SL	45
Figure 1-7 First gasoline direct-injection application (Daimler-Benz DB 601-1933).	48
Figure 1-8 Mercedes 300SL system configuration	48
Figure 1-9 (a) The Mercedes 300SL gasoline direct-injection engine. (b) The Mercedes 300SL "Gull wing"	49
Figure 1-10 MAN FM combustion system	50
Figure 1-11 Texaco TCCS Combustion system.	50
Figure 1-12 The FORD PROCO combustion system	51
Figure 1-13 Cut-away view of the Mitsubishi GDI system	51
Figure 1-14 Mitsubishi GDI combustion system	52
Figure 1-15 Spray-guided, Wall-guided and Air-guided combustion systems [22]	58
Figure 1-16 Representation of the 1st generation "wall-guided" configuration	59
Figure 1-17 Representation of the 2nd generation "spray-guided" configuration.	60
Figure 1-18 Averaged Fuel economy improvement of spray-guided systems[22].	61
Figure 1-19 (a) Schematic of Siemens Inward Seal Band piezo injector, (b) Schematic of piezoelectrically actuated DI injector	62
Figure 1-20 (a) schematic of a swirl injector, (b) Swirl spray structure	64
Figure 1-21 (a) Model of a multihole injector, (b) Spray of 6-hole injector.	66
Figure 1-22 (a) Model of an outward opening nozzle injector (b) hollow cone spray under atmospheric pressure produced by an outward opening nozzle.	67
Figure 3-1 Schematic of the flow diagram showing the pumps, pipelines and valves used to control the flow admitted to the injector.	110
Figure 3-2 Schematic diagram shows the main components of the large-scale model.	111
Figure 3-3 Schematic of the nozzle exit showing convergent-divergent region at the valve seat.	111
Figure 3-4 Upper cartridge flow passages	112
Figure 3-5 (a) Schematic diagram of the injector assembly mounted onto the rig; (b) the rig assembly.	112
Figure 3-6 Comparison of three enlarged models: Comparison of three enlarged models: (a) and (b) non-cavitating model; (c) cavitating model.	113
Figure 3-7 Injector model: (a) with lower chamber; (b) without the lower chamber.	114
Figure 3-8 Schematic diagram of the flow passage between needle and cartridge of the cavitating nozzle; the arrangement of the flat window is shown.	115
Figure 3-9 The overall test cell set up showing the camera and image processor position in relation to the injector assembly.	116
Figure 3-10: Schematic diagram of spark light, camera and PC set up, and their connections.	117
Figure 3-11 Different image magnifications for nozzle flow and overall spray.	117
Figure 3-12 Geometry of the needle and its seat	119
Figure 3-13 Flow imaging: Thick strings downstream of the nozzle exit originated from the pairs of counter rotating vortices.	120
Figure 3-14 Schematic representation of the camera locations for flow visualisation	

between the square-section needle guide and the valve seat for both (a) front and (b) side jet water flows. ....	121
Figure 3-15 Images showing the flow between the square-section needle guide and the valve seat for both (a) side and (b) front jet water flows: needle lift=0.57 mm and flow rate 1.7 l/s. ....	122
Figure 3-16: Schematic of the flow pattern between the valve seat and the square-section needle guide .....	123
Figure3-17 LDV measurement locations inside and outside the nozzle.....	123
Figure 3-18 Control volume locations for LDV tangential velocity measurements..	124
Figure 3-19 Tangential velocity measurements within the liquid jet at the nozzle exit. ....	124
Figure 3-20 Dominant frequencies of the flow at two vertical locations, $Q=0.71/s$ , lift=0.93mm. ....	125
Figure 3-21 Dominant frequencies of the flow at two different vertical locations, $Q=0.71/s$ , lift= 0.93mm.....	125
Figure 3-22 Variation of dominant frequency with (a) flow rates and (b) Reynolds numbers. ....	126
Figure 3-23 Images showing the stings on the surface of the liquid film close to the nozzle exit. ....	126
Figure 3-24 Image of spray from a real size injector at 0.1 ms after the start of injection at injection pressure of 200 bar and atmospheric backpressure.....	127
Figure3-25 Area of visualization .....	128
Figure3-26 Images showing the filaments in the gap between the needle and its seat for different flow rates, injection velocities and needle lifts.....	128
Figure 3-27 Variation of string spacing as a function of injection velocity and needle lift. ....	129
Figure 3-28: Images of string-type spray structure: (a) Effect of flow rate at the full needle lift, 0.93mm, and (b) effect of the needle lift at a flow rate of 1.8 l/s. ...	131
Figure 3-29 Presence of gas bubble inside the nozzle flow passage near the exit at a needle lift of 0.57 mm and flow rate of 0.98 l/s.....	132
Figure 3-30 Real time images of air entrainment evolution into the nozzle flow passage for a needle lift of 0.93mm and a flow rate is 1.2 l/s; the time interval between each image is 0.55 ms. ....	133
Figure 3-31: A simple model for air traps attached on (a) the needle causing a wide spray deflection and (b) the cartridge causing a narrow spray deflection.....	135
Figure 3-32 High-speed video images for comparison between the shadows of the air bubbles from the narrow and wide cone angles. ....	136
Figure 3-33 Real time images of air entrainment evolution into the nozzle flow passage for a needle lift of 0.55mm and a flow rate is 1.8 l/s; and Injection pressure 2.16 bar. ....	137
Figure 3-34 Bubble height as projected in a plane parallel to the injector axis. Schematic .....	139
Figure 3-35 Effect of needle lift on the cone angle for narrow angle case. ....	140
Figure 3-36 Variation of narrow spray half cone angle as a function of flow rate for two valve lifts.....	141
Figure 3-37 Variation of wide spray half cone angle as a function of flow rate for two valve lifts. ....	141
Figure 3-38: Full size and magnified images of string structure of real size injector. ....	142
Figure 3-39 Full size and magnified images of string structure of large-scale injector .....	142

Figure 3-40: Correlation between the strings and the in-nozzle air bubble in the large-scale model.....	143
Figure 3-41 Visual differences in the strings structure observed in the images for the (a) wide and (b) narrow cone angle at a needle lift of 0.57mm and a flow rate of 1 l/s.....	144
Figure 3-42 Image of corrugated liquid spray strings when there is no air bubble present in the nozzle at the full needle lift and a flow rate of 1.61 l/s. ....	145
Figure 3-43 Effect of flow rate on surface quality at full needle lift for flow rates of (a) 1.35l/s with air bubble (string structure) and (b) 1.8l/s without air bubble (smooth or corrugated structure).....	145
Figure 3-44 Effect of the valve lift on surface quality at a flow rate of 1.8 l/s at valve lift 0.57mm (a) and full lift 0.93mm (b).....	146
Figure 3-45 Spray structure map.....	147
Figure 3-46 Overall snapshots of surface type transition from smooth (or corrugated) to string type (rough).....	147
Figure 3-47 Variation of string spacing as a function of Reynolds number at a valve lift of 0.57mm. ....	148
Figure 3-48 Variation of string spacing as a function of the needle lift at a constant velocity of 8.4m/s.....	149
Figure 3-49 Variation of string spacing as a function of Reynolds number at a constant velocity for different needle lifts. ....	149
Figure 3-50 Comparison of spray surface quality obtained for cavitating and non-cavitating nozzle models. ....	150
Figure 3-51 Image of a cavitating jet spray emerging from the nozzle at $L=0.4$ mm, $Q=1.12$ l/s and $CN=1.3$ . ....	152
Figure 3-52 Images of cavitation development inside nozzle seat at $L=0.3$ mm, $Q=0.8$ l/s, $CN=3.12$ and a framing rate of 18000 fps.....	154
Figure 3-53 Close up Comparison between the air bubbles entrainment and cavitation structure. (image width 6mm).....	155
Figure 3-54 Images of cavitation development inside nozzle seat at $L=0.4$ mm, $Q=1.60$ l/s, $CN=2.1$ and a time step of 80 $\mu$ s (25000 fps). ....	156
Figure 3-55 Schematic representations of air entrainment and cavitation.....	157
Figure 3-56 Image of spray and in-nozzle flow at a valve lift of 0.57mm, a flow rate of 2.6 l/s and a CN of 1.6 (image width 6mm). ....	158
Figure 3-57 Real time images at 30kfps of air entrainment and cavitation evolution into the nozzle flow passage for a needle lift of 0.55mm, a flow rate is 1.2l/s and cavitation number of 0.47. (image width 7mm).....	161
Figure 3-58 Injector control panel .....	162
Figure 3-59 Magnified image of the needle lift. (Image width 1.13mm) .....	163
Figure 3-60 Variation of needle lift as a function of time for different switch positions. ....	163
Figure 3-61 Variation of needle lift as a function of switch position calculated from image cross correlation. ....	164
Figure 3-62 Variation of real size injector mass rate as a function of injection pressure for different needle lift set up.....	165
Figure 3-63 Averaged flow velocity variation through the nozzle with injection pressures.....	165
Figure 3-64 Variation of needle lift as a function of injection velocity: comparison of (a) CFD simulation [78] for injection pressure 160bar and (b) experimental tests at different injection pressures. ....	166
Figure 3-65 Real size spray magnification at injection pressure of 200bar and needle	

lift energy level “1001” ( $\sim 30\mu\text{m}$ ). (image width 3.5mm).....	167
Figure 3-66 Polar transformation of Figure 3-65 in order to obtain a vertical representation of the string structure.....	168
Figure 3-67 Averaged pixel grey level distribution of Figure 3-66.....	169
Figure 3-68 Strings number along the whole spray circumference as a function of injection pressure for different needle lift set up. ....	169
Figure 3-69 Variation of strings number as a function of injection velocity for different needle lift set up. ....	170
Figure 3-70 Real size injector: Total strings number versus Reynolds number for different needle lifts. ....	171
Figure 3-71 Large-scale injector: Total strings number versus Reynolds number at constant lift of 0.57mm corresponding to 0.025mm lift in the real size injector (0100). ....	172
Figure 3-72 Variation of the strings number as a function of needle lift for different injection pressures. ....	172
Figure 4-1 Experimental set up for variable and ambient backpressure PDA measurement .....	181
Figure 4-2 Schematic of experimental setup of the high-speed PIV system with incorporated Injector system.....	183
Figure 4-3 Test rig for ambient condition PIV measurement .....	184
Figure 4-4 Purposed design setup to minimize attenuation of laser beams and scattered light to allow full spray measurements inside the central region of the spray thickness. ....	185
Figure 4-5 Experimental set-up schematic of fuel injection system and optical devices. ....	185
Figure 4-6 Test rig arrangement with 3-D traverse for ambient condition PDA measurement .....	186
Figure 4-7 Injector holder built and installed into the test rig.....	187
Figure 4-8 Screen print out of the PDA software while acquiring data.....	188
Figure 4-9 The development of a temporal graph.....	189
Figure 4-10 Development of a spatial graph.....	189
Figure 4-11 PDA Coordinate system .....	190
Figure 4-12 Visualisation of control volume with respect of the string position.....	191
Figure 4-13 Laser beams converging in the vertical edge of the spray during PDA measurement .....	192
Figure 4-14 Front view of the spray turned 45°. The white spot is the reflected laser light of the control volume. The ticks along the yellow line represent the measurement locations. ....	193
Figure 4-15 Three phases of the spray structure at 3.5mm from the nozzle exit.....	194
Figure 4-16 Camera, mirror and injector layout for the spray visualisation of emerging flow .....	195
Figure 4-17 Emerging spray at start of injection: $P_i=200\text{bar}$ , Needle lift = $29\mu\text{m}$ (1001) . ....	195
Figure 4-18 Spray structure at start of injection: $P_i=200\text{bar}$ , Needle lift = $29\mu\text{m}$ (1001) at 15, 25, 35 $\mu\text{s}$ ASOI. ....	196
Figure 4-19 Leap between strings (particular of Figure 4-18 at 25 $\mu\text{s}$ ASOI).....	197
Figure 4-20 Velocity and droplet diameter vs. time at $z=4.24\text{mm}$ from the tip and on the external surface of the jet. It shows the presence of highly spread velocity and big droplet size when the jet tip passes through control volume.....	198
Figure 4-21 Spatial velocity distributions at the start of the injection across the tip of the spray. ....	198

Figure 4-22 Temporal droplet velocity and size distribution on the outer surface of the spray. Schematic representation of wakes behind the spray rim. ....	199
Figure 4-23 Magnified visualisation of the spray structure at 0.36 ms ASOI: fish bone structure. The red spot represent the CV location at $z=3.54\text{mm}$ ( $z'=2.5\text{mm}$ ). The white spot is the CV (the actual image of the CV) at a location of $z=14.14\text{mm}$ ( $z'=10\text{mm}$ ). ....	200
Figure 4-24 Temporal variation of droplets mean velocity and AMD diameter at the string centre for $z=3.54\text{mm}$ ( $z'=2.5\text{mm}$ ) and $z=14.14\text{mm}$ ( $z'=10\text{mm}$ ) from injector nozzle. The magenta line corresponds to the time of the snap shot of Figure 4-23. ....	201
Figure 4-25 Velocity and droplet size distribution on the outer surface of the spray. ....	202
Figure 4-26 Scheme showing the velocity distribution through the spray thickness after the leading edge ....	202
Figure 4-27 X distribution of Mean droplet velocity and size at 0.46ms ASOI, immediately after the spray leading edge.....	202
Figure 4-28 Magnified image of the spray structure at 0.53 ms: unstable string structure. The red spot represent the CV location at $z'=3.54$ ( $z=2.5\text{mm}$ ).....	204
Figure 4-29 Temporal velocity and droplet size distribution at the spray centre ( $x=-0.4\text{mm}$ ) at standard condition.....	205
Figure 4-30 Temporal velocity and droplet size distribution at the inner edge of the spray ( $x=0.3\text{mm}$ ) at standard condition .....	205
Figure 4-31 Camera and injector layout for the spray visualisation of inner spray surface. ....	206
Figure 4-32 High-speed video of inner spray surface. Standard conditions: Injection duration 1ms, Pi 200bar, Needle lift (1001).....	206
Figure 4-33 Vector velocity distribution for standard condition from 0.2ms to 0.84ms ASOI .....	208
Figure 4-34 Mean Velocity and SMD distribution from $z=3.0\text{mm}$ to $11.2\text{mm}$ . SMD distribution in the outer cloud with flat velocity profile. ....	209
Figure 4-35 (c) Velocity and AMD distribution along the Y coordinate at $z=28.28\text{mm}$ . ....	211
Figure 4-36 Velocity and AMD distribution for standard condition from 0.24ms to 1.00ms ASOI.....	214
Figure 4-37 Temporal distribution of Weber number for two different vertical locations ( $z=3.54$ and $z=14.14$ )......	215
Figure 4-38 Weber Number distribution along the axial location .....	216
Figure 4-39 Time range considered in the droplet size statistical analysis which excludes the leading and trailing edge of the spray. ....	217
Figure 4-40 Probability density function of droplet diameters at the centre of the string for different $z$ locations .....	219
Figure 4-41 Statistical values of mean droplet diameter, modal diameter and Standard Deviation in the string centre as a function of axial locations. ....	220
Figure 4-42 velocity distribution summary.....	223
Figure 4-43 (b) recirculation (-ve velocity) $X=-1\text{mm}$ , $Y=0\text{mm}$ , $Z=3.54\text{mm}$ .....	225
Figure 4-44 Schematic presentation of recirculation zones at the inner and outer edges of the spray.....	226
Figure 4-45 Camera and injector layout for the 2D Mie scattering visualisation. ....	227
Figure 4-46 Comparison between 2D and 3D Mie scattering.....	227
Figure 4-47 2D Mie scattering: High-speed video of spray recirculation Pi=200bar, 1ms Inj. Duration, Bit pos.1001 .....	229

Figure 4-48 Recirculation velocity field of spray injected in atmospheric condition with injection pressure of 200bar and needle set to 1001 bit position. ....	234
Figure 4-49 Vectorial composition: Relative field + Sliding velocity = absolute rotating field.....	235
Figure 4-50 Air entrainment velocity field around spray when injected into air at ambient condition with injection pressure of 200bar and needle set to 1001 bit position.....	237
Figure 4-51 LDV Set up for air entrainment investigation.....	239
Figure 4-52 LDV assessment of the seeding dispersion velocity during idle.....	240
Figure 4-53 LDV air motion and spray droplet areas in the normal velocity component ( $V_y$ ).....	240
Figure 4-54 Air entrainment investigations: PIV velocity field, LDV normal velocity component. (The green dots in the PIV images represent the CV position for the LDV experiments).....	241
Figure 4-55 Temporal variation of mean droplet velocity for different injection pressures.....	243
Figure 4-56 Temporal variation of mean droplet diameter for different injection pressures.....	244
Figure 4-57 Temporal variation of mean droplet velocity for different injection durations.....	245
Figure 4-58 Temporal variation of mean droplet diameter for different injection durations.....	246
Figure 4-59 Experimental set-up of constant volume chamber and fuel injection system.....	247
Figure 4-60 Vertical images of spray penetration at different back-pressures, 200 bar injection pressure and 0.33 ms injection duration: (a) 0.075 ms ASOI; (b) 0.150 ms ASOI.....	249
Figure 4-61 Horizontal images of spray penetration at different back-pressures, 200 bar injection pressure and 0.33 ms injection duration: (a) 0.075 ms ASOI; (b) 0.150 ms ASOI.....	249
Figure 4-62 Effect of backpressure on the vertical penetration of the spray. ....	250
Figure 4-63 Horizontal images of spray penetration at 100ms after SOI, ambient back-pressure and 0.33ms injection duration: (a) 200bar Injection pressure; (b) 100bar injection pressure. ....	250
Figure 4-64 PDA measurement at different Pb: Temporal variation of droplet mean velocity and diameter at $P_i = 200$ bar, $T = 160$ °C, $z=2.5$ mm (upper row) and $z=10$ mm (lower row). ....	252
Figure 4-65 PDA measurement at different Pb: Temporal variation of droplet mean velocity and diameter at $P_i = 100$ bar, $T = 160$ °C, $z=2.5$ mm (upper row) and $z=10$ mm (lower row). ....	253
Figure 4-66 PDA measurement at different injection pressures: Temporal variation of droplet mean velocity and diameter at $P_b = 1$ bar, $T = 160$ °C, $z=2.5$ mm (upper row) and $z=10$ mm (lower row). ....	254
Figure 4-67 PDA in constant volume chamber; measurement locations and coordinate system.....	255
Figure 4-68 PDA measurement at different injection pressures: Spatial variation of droplet mean velocity and diameter at $P_b = 1$ bar, $T = 25$ °C; (a) $z=2.5$ mm, (b) $z=10$ mm. Coloured symbols are for $P_i=100$ bar and the black symbols for $P_i=200$ bar.....	256
Figure 4-69 PDA measurement at different chamber temperature: Temporal variation of droplet mean velocity and diameter at $P_b = 1$ bar, $P_i = 200$ bar, $z=2.5$ mm	



(upper row) and $z=10\text{mm}$ (lower row).....	257
Figure 5-1 First model optical engine with limited quartz window.....	264
Figure 5-2 Second model optical engine with full quartz liner.....	264
Figure 5-3: Second model optical engine: (a) full stroke quartz liner (b) and 45 degree mirror situated in the cavity at the bottom of the piston. ....	265
Figure 5-4 Flame deck configuration for first model Hydra engine. ....	265
Figure 5-5 Flame deck configuration for second model Hydra engine. ....	265
Figure 5-6 Fast CCD camera in front of the engine cylinder.....	266
Figure 5-7 Flash light device on the left of the engine. ....	266
Figure 5-8 Mie scattering Set up in the optical engine: (a) Vertical view set up (b) Horizontal view set up. ....	267
Figure 5-9 Available Positions of the optical fibres around the liner. ....	268
Figure 5-10 Control SCECU box.....	269
Figure 5-11 Square signal set for double injection. ....	269
Figure 5-12 Synchronization System for Double Injection. ....	269
Figure 5-13 Test cell lay out and system and signal arrangement. ....	270
Figure 5-14 Optical engine test cell lay out. ....	271
Figure 5-15 Dyno used to drive the optical engine.....	271
Figure 5-16 Supercharger with turning vane .....	272
Figure 5-17 Plenum chamber.....	272
Figure 5-18 Common rail system with pressure gauge on top of the optical engine.....	272
Figure 5-19 Right hand side view of optical engine. ....	272
Figure 5-20 Engine temperature and pressure display unit.....	273
Figure 5-21 Engine and signal control unit.....	273
Figure 5-22 Injector geometries: Inward Seal Band positive step (+ISB) , Inward Seal Band negative step (-ISB) and Standard Seal Band No step (SSB).....	274
Figure 5-23 Test conditions for double injection investigation. (case No – injection No) .....	276
Figure 5-24 Synchronization System for Double Injection. ....	277
Figure 5-25 Image Processing procedure.....	278
Figure 5-26 Spray angle for each image cycle.....	278
Figure 5-27 Histograms for left side angle, right side angle and overall angle. ....	279
Figure 5-28 Statistical spray angle value for a set of 64 images.....	279
Figure 5-29 Reference comparison (case 1 vs Case 25) of single shot, mean and RMS spray images for same operating condition.....	280
Figure 5-30 Angle comparison for the same operating condition. (Case 1 and Case 25) .....	281
Figure 5-31 Image comparison for three different injector prototypes. Bit position 1111, 1000rpm, $P_b=1.1\text{bar}$ , $P_i=200\text{bar}$ . ....	282
Figure 5-32 Angle comparison for three different injector prototypes. Bit position 1111, 1000rpm, $P_b=1.1\text{bar}$ , $P_i=200\text{bar}$ . ....	283
Figure 5-33 Image comparison for the three different injector prototypes. Bit position 1111, 1000rpm, $P_b=10.9\text{bar}$ , $P_i=200\text{bar}$ . ....	284
Figure 5-34 Angle comparison for the three different injector prototypes. Bit position 1111, 1000rpm, $P_b=10.9\text{bar}$ , $P_i=200\text{bar}$ . ....	284
Figure 5-35 Image comparison for the three different injector prototypes. Bit position 1111, 1000rpm, $P_b=16.6\text{bar}$ , $P_i=200\text{bar}$ . ....	285
Figure 5-36 Angle comparison for three different injector prototypes. Bit position 1111, 1000rpm, $P_b=16.6\text{bar}$ , $P_i=200\text{bar}$ . ....	286
Figure 5-37 Image comparison for three different injector prototypes. Bit position 0000, 1000rpm, $P_b=16.6\text{bar}$ , $P_i=200\text{bar}$ . ....	287

Figure 5-38 Angle comparison for three different injector prototypes. Bit position 0000, 1000rpm, Pb=16.6bar, Pi=200bar. ....	288
Figure 5-39 Spray comparisons for different speed and spark plug presence: +ISB, Bit pos. 1111, Pb=16.6bar, Pi=200bar. ....	289
Figure 5-40 Angle comparisons for different speed and spark plug presence: +ISB, Bit pos. 1111, Pb=16.6bar, Pi=200bar. ....	290
Figure 5-41 Spray comparisons for different speed and spark plug presence: +ISB, Bit pos. 0000, Pb=16.6bar, Pi=200bar. ....	291
Figure 5-42 Angle comparisons for different speed and spark plug presence: +ISB, Bit pos. 0000, Pb=16.6bar, Pi=200bar' ....	291
Figure 5-43 Spray comparisons for different backpressures: SSB, Bit pos. 1111, 1000rpm, Pi=200bar. ....	293
Figure 5-44 Angle comparisons for different backpressures: SSB, Bit pos. 1111, 1000rpm, Pi=200bar. ....	293
Figure 5-45 Spray comparisons for different backpressures: +ISB, Bit pos. 1111, 1000rpm, Pi=200bar. ....	294
Figure 5-46 Angle comparison for different backpressures: +ISB, Bit pos. 1111, 1000rpm, Pi=200bar. ....	295
Figure 5-47 Spray comparisons for different backpressures: -ISB, Bit pos. 1111, 1000rpm, Pi=200bar. ....	296
Figure 5-48 Angle comparisons for different backpressures: -ISB, Bit pos 1111, 1000rpm, Pi=200bar. ....	296
Figure 5-49 Spray comparisons for different backpressures: +ISB, Bit pos 1111, 1000rpm, Pi=100bar. ....	297
Figure 5-50 Angle comparisons for different backpressures: +ISB, Bit pos 1111, 1000rpm, Pi=100bar. ....	298
Figure 5-51 Spray comparisons for different backpressures: -ISB, Bit pos 1111, 1000rpm, Pi=100bar. ....	299
Figure 5-52 Angle comparisons for different backpressures: -ISB, Bit pos 1111, 1000rpm, Pi=100bar. ....	299
Figure 5-53 Spray comparisons for different Injection pressures and Injector prototypes: Bit pos 1111, 1000rpm, Pb=1.1bar. ....	300
Figure 5-54 Angle comparisons for different Injection pressures and Injector prototypes: Bit pos 1111, 1000rpm, Pb=1.1bar. ....	301
Figure 5-55 Spray comparisons for different Injection pressures and Injector prototypes: Bit pos 1111, 1000rpm, Pb=16.6bar. ....	302
Figure 5-56 Angle comparisons for different Injection pressures and Injector prototypes: Bit pos 1111, 1000rpm, Pb=16.6bar. ....	302
Figure 5-57 Spray comparisons for different needle lifts: SSB, 1111, 1000rpm, Pi=200bar, Pb=16.6bar. ....	304
Figure 5-58 Angle comparisons for different needle lifts: SSB, 1111, 1000rpm, Pi=200bar, Pb=16.6bar. ....	304
Figure 5-59 Spray comparisons for different needle lifts: +ISB, 1111, 1000rp Pi=200bar, Pb=16.6bar. ....	305
Figure 5-60 Angle comparisons for different needle lifts: +ISB, 1111, 1000rpm, Pi=200bar, Pb=16.6bar. ....	306
Figure 5-61 Spray comparisons for different needle lifts: -ISB, 1111, 1000rpm, Pi=200bar, Pb=16.6bar. ....	307
Figure 5-62 Angle comparisons for different needle lifts: -ISB, 1111, 1000rpm, Pi=200bar, Pb=16.6bar. ....	307
Figure 5-63 Angle comparisons for different needle lifts for the three injector	

prototypes: 1000rpm, $P_i=200\text{bar}$ , $P_b=16.6\text{bar}$ .....	308
Figure 5-64 Penetration comparison at full and low lift for ISB injectors.....	309
Figure 5-65 Reference comparison (Case 1, Case 1-2, Case 25-2) at same operating conditions. ....	310
Figure 5-66 Angle Comparisons for same operating conditions (Case 1, Case 1-2, Case 25-2) . ....	311
Figure 5-67 Spray comparisons for double injection (first and second injection) and single injection. +ISB, 1111, 1000rpm, $P_i=200\text{bar}$ , $P_b=16.6\text{bar}$ .....	312
Figure 5-68 Angle comparisons for double injection (first and second injection) and single injection. +ISB, 1111, 1000rpm, $P_i=200\text{bar}$ , $P_b=16.6\text{bar}$ .....	312
Figure 5-69 Spray comparisons for different EOI and lifts.+ISB, 1000rpm, $P_i=200\text{bar}$ , $P_b=16.6\text{bar}$ .....	313
Figure 5-70 Angle comparisons for different EOI and lifts. +ISB, 1000rpm, $P_i=200\text{bar}$ , $P_b=16.6\text{bar}$ .....	313
Figure 5-71 Spray comparisons for different EOI and lifts. -ISB, 1000rpm, $P_i=200\text{bar}$ , $P_b=16.6\text{bar}$ .....	314
Figure 5-72 Angle comparisons for different EOI and lifts. -ISB, 1000rpm, $P_i=200\text{bar}$ , $P_b=16.6\text{bar}$ .....	315
Figure 5-73 Angle comparisons for different speed and spark plug presence: $P_i=200\text{bar}$ , $P_b=16.6\text{bar}$ , Bit pos. 1111, SSB.....	316
Figure 5-74 Angle comparisons for different speed and spark plug presence: $P_i=200\text{bar}$ , $P_b=16.6\text{bar}$ , Bit pos. 1111, -ISB. ....	316
Figure 5-75 Angle comparison for different speed and spark plug presence: $P_i=200\text{bar}$ , $P_b=16.6\text{bar}$ , Bit pos. 1111, +ISB.....	317
Figure 5-76 Angle comparison for different speeds and injector prototypes: $P_i=200\text{bar}$ , $P_b=16.6\text{bar}$ , Bit pos. 1111, single injection. ....	317
Figure 5-77 Angle comparison for different backpressures: $P_i=200\text{bar}$ , Bit pos. 1111, single injection), 1000rpm. ....	318
Figure 5-78 Angle comparison for different backpressures: $P_i=200\text{bar}$ , Bit pos. 1111, double injection (2nd inj.), 1000rpm.....	319
Figure 5-79 Angle comparison for different needle lifts: $P_i=200\text{bar}$ , $P_b=16.6\text{bar}$ , 1000rpm, double injection (2nd inj.). ....	319
Figure 5-80 Angle comparison for different needle lifts: $P_i=200\text{bar}$ , $P_b=16.6\text{bar}$ , 2000rpm, single injection.....	320
Figure 5-81 Angle comparison for different needle lifts: $P_i=200\text{bar}$ , $P_b=16.6\text{bar}$ , 1000rpm, double injection (2nd inj.). ....	321
Figure 5-82 Mie scattering images: High-speed video of spray injected under ambient condition at 2.1ms ASOI, $P_i=200\text{bar}$ , 1ms Inj. Duration, Bit pos.1001. ....	323
Figure 5-83 Recirculation velocity field of spray (using PIV) injected in ambient condition at 1.93ms ASOI Injection pressure of 200bar and needle set to 1001 bit position.....	323
Figure 5-84 Mie scattering images of spray recirculation. N/A 70 BTDC, 1000rpm, $P_b=2.7\text{bar}$ , injection duration $T_i=1.0\text{ ms}$ , $P_i=200\text{bar}$ , Needle lift set up. Bit. 1001 .....	325
Figure 5-85 Mie scattering images of spray recirculation. N/A 70 BTDC, 1000rpm, $P_b=2.7\text{bar}$ , injection duration $T_i=1.0\text{ ms}$ , $P_i=200\text{bar}$ , Needle lift set up. Bit pos 1001.....	326
Figure 5-86 Mie scattering images of spray recirculation. N/A 120 BTDC, 1000rpm, $P_b=1\text{bar}$ , injection duration $T_i=1.0\text{ ms}$ , $P_i=200\text{bar}$ , Needle lift set up. Bit pos 1001.....	327
Figure 5-87 Mie scattering images of spray recirculation. N/A 120 BTDC, 2000rpm,	

Pb=1bar, injection duration $T_i=1.0$ ms, $P_i=200$ bar, Needle lift set up. Bit pos 1001.....	328
Figure 5-88 Mie scattering images of spray recirculation. N/A 120 BTDC, 1000rpm, Pb=1 bar, injection duration $T_i=0.6$ ms, $P_i=200$ bar, Needle lift set p. Bit 1001.329	
Figure 5-89 2D Mie scattering images of spray recirculation. N/A 70 BTDC, 1000rpm, Pb=2.7bar, injection duration $T_i=0.6$ ms, $P_i=200$ bar, Needle lift set up. Bit pos.1001. ....	330
Figure 5-90 Mie scattering images of spray recirculation. SC 70 BTDC, 1000rpm, Pb=4bar, injection duration $T_i=0.6$ ms, $P_i=200$ bar, Needle lift set up. Bit. ....	331
Figure 7- 1 Schematic of the measurements principle of PDA (Source: Dantec Dynamics). ....	349
Figure 7- 2 Scattered light from a spherical particle (Source: Dantec Dynamics). ...	350
Figure 7- 3 Doppler Velocity measurement principle.....	351
Figure 7- 4 Particle diameter measurement principle. ....	352
Figure 7- 5 Schematic of the Dantec 2D PDA system.....	353
Figure 7- 6 Overview of PIV measurement principle and data processing [108].....	360
Figure 7- 7 (a) Representation of the particle-laden flow on the CCD chip; (b) and discretisation of image domain into interrogation areas. ....	363
Figure 7- 8 Schematic of imaging transfer function for one image pair.....	364
Figure 7- 9 Cross-correlation, correlation array and peak search [110] .....	364
Figure 7- 10 Measurement uncertainty (RMS random error) in digital cross correlation PIV evaluation with respect to varying particle image diameter for single exposure/double frame PIV imaging. ....	366
Figure 7- 11 Monte Carlo simulation results for the measurement uncertainty in digital PIV cross correlation PIV evaluation as a function of particle image displacement.....	367
Figure 7- 12 Simulation results showing the difference between actual and measured displacement as a function of the particle image displacement. Bias correction removes the displacement bias.....	368
Figure 7- 13 Measurement uncertainty for single exposure/double frame PIV as a function of particle image shift for various particle image densities NI.....	369

---

## *Acknowledgement*

All the work described in this thesis has been conducted at the Research Centre for Energy and the Environment, School of Engineering and Mathematical Sciences of City University.

I would like to thank my Supervisor Dr.J. M. Nouri for his meaningful help and contribution to this work and for his human support during my entire doctorate.

I gratefully acknowledge Professor C. Arcoumanis for his professional supervision and for giving me the opportunity to undertake this Project.

A special “thank” to Dr Y. Yan for her precious help and guidance and to all the Member of the Labs for their technical support.

I would also like to thank all my colleagues for sharing hilarious moments together and for their professional contribution.

Finally, I would like to thank the technical staff, Mr Tom Fleming, Jim Ford and Dr. Gunawardana Wahalathanthriga; who have done an exceptional job to construct and set up the experimental rigs.

Additionally, I would like to acknowledge Siemens VDO Automotive and BMW for their financial support and for their contribution to my research program.

---

## *Declaration*

I hereby declare that the presented work in this thesis is my own or was developed in a joint effort with other members of the research group as it is stated and referenced in the text accordingly.

I grant powers of discretion to the University Librarian to allow this thesis to be copied in whole or in part without further reference to me. This permission covers only single copies made for study purposes, subject to normal conditions of acknowledgement.

London, \_\_\_\_\_

(Andrea Marchi)

\_\_\_\_\_

---

## *Abstract*

The focus of the present study was on the spray characterization of an outwards opening pintle-type injector to be used for spray-guided direct injection spark-ignition (DISI) engines. This spray-guided approach requires excellent spray performance and stability over a wide range of operating conditions. To achieve these goals it is necessary to have a good understanding of the internal nozzle flow and its link with the spray characteristics. In particular, the knowledge of the in-nozzle two-phase flow structure (air entrainment and cavitation), the spray development (spray angle, penetration and recirculation zones) and droplets velocity and size distribution is essential. Therefore, this study was planned and carried out in three main phases:

The first phase of the investigation was focused on a comprehensive study of the internal flow of the injector in order to understand not well-clarified flow/spray phenomena such as the longitudinal string formation and the spray-to-spray variation (flapping) which play a very important role in the behaviour of the overall spray-guided DISI system. To overcome the problems related to the small dimension of the injector and its optical accessibility, an enlarged transparent model about 23 times the real size injector was manufactured. Quantitative flow analysis performed with the Laser Doppler Velocimetry (LDV) technique was matched with 3D Mie scattering visualization to provide full information about the internal flow behaviour and allow correlation of the flow upstream and downstream of the nozzle exit.

The flow between the needle guide and the nozzle seat in the enlarged injector consisted of four liquid jets and four pairs of unstable counter rotating vortices which were found to be responsible for the tangential oscillation of the flow downstream of the nozzle exit. The emerging hollow cone spray exhibited a string type structure similar to that of the real size injector with the string spacing depending on the flow velocity. The origin of these strings has been attributed to the formation of a two-phase flow inside the nozzle due to flow separation just upstream of the nozzle exit giving rise to air entrainment in the form of small bubbles. The presence of these bubbles in the nozzle outlet was correlated with the exiting flow and the formation of large longitudinal strings. The initiation and development of cavitation at the nozzle seat was also identified and was found to enhance the spray breakup and droplet atomisation.

The second part of the investigation was focused on the spray characterization of the real size injector by 3D Mie scattering visualization and a parametric study of the

---

velocity field and droplet size by Phase Doppler Anemometry (PDA), Particle Image Velocimetry (PIV) and LDV measurements. The post processed data have characterised the string-to-string velocity a droplet size distribution as a function of injection and backpressure, injection duration, chamber temperature and pintle needle lift. An alternative arrangement set up made it possible to overcome problems associated with the signal attenuation due to the high spray density and also allow characterisation of the internal and external spray recirculations where ignition takes place. By introducing very low velocity atomized water mist against the spray, the velocity field of the air entrainment around the nozzle exit of the injector was measured and showed the flow development during the spray injection process which may influence the string instability and contribute to the primary droplet break up phenomenon. Validation of the results concerning recirculation and air entrainment was obtained by a PIV investigation.

The performance of three prototype pintle-type injectors having different nozzle exit designs was investigated and, in particular, the interaction of the spray with the in-cylinder flow was observed by mounting the injectors in an optical engine and visualizing the effects of the injection and engine parameters on the spray stability, spray angle variation and spray flow recirculation. Overall, the classification of the three prototypes has shown that the Inward Seal Band positive step design produced the most robust spray angle which is ideally suited for stratified fuel mixture formation in spray-guided configurations for DISI engines which offer promise for outstanding efficiency and reduced CO<sub>2</sub> emissions, approaching the levels of passenger car diesels.



# *Nomenclature*

## Abbreviations

<b>2-D</b>	Two dimensional
<b>3-D</b>	Three dimensional
<b>AMD</b>	Arithmetic mean diameter
<b>ASOI</b>	After Start of Injection
<b>B/W</b>	Black and Wait
<b>BDC</b>	Bottom-dead-centre
<b>BTDC</b>	Before top-dead-centre
<b>CA</b>	Crank angle
<b>CCD</b>	charge-coupled device
<b>CFD</b>	Computational fluid dynamics
<b>CI</b>	Compression-ignition
<b>CIDI</b>	Compression-ignition direct-injection
<b>CO/CO<sub>2</sub></b>	Carbon monoxide/dioxide
<b>CV</b>	Control Volume
<b>Dbl Inj</b>	Double Injection
<b>DFI</b>	Digital Fuel Injection
<b>DI</b>	Direct-injection
<b>DISI</b>	Direct-injection spark-ignition
<b>ECU</b>	Electronic control unit
<b>EFI</b>	Electronic Fuel Injector
<b>EGR</b>	Exhaust gas recirculation
<b>EOI</b>	End of injection
<b>EU</b>	European Union
<b>fps</b>	Frame per second
<b>GDi</b>	Gasoline Direct injection
<b>GHG</b>	Green-house gases
<b>HC</b>	Hydro carbon
<b>HMI</b>	Hydrargyrum medium-arc iodide lamp bulb
<b>HSDV</b>	High-speed digital video
<b>ISB</b>	Inward Seal Band
<b>LDA</b>	Laser Doppler Anemometry
<b>LDV</b>	Laser Doppler Velocimetry
<b>LIEF</b>	Laser induced Exciplex fluorescence
<b>LIF</b>	Laser induced fluorescence
<b>MAP</b>	Manifold Absolute Pressure
<b>Mie</b>	Based on Lorenz-Mie theory
<b>MMD</b>	mean droplet diameter
<b>N/A</b>	Naturally aspirated
<b>NO<sub>x</sub></b>	Nitrogen oxides
<b>OBD</b>	On-Board Device
<b>OCP</b>	Orbital Combustion Process
<b>PDA</b>	Phase Doppler Anemometry
<b>pdf</b>	Probability density function
<b>PFI</b>	Port-fuel injection
<b>PIV</b>	Particle Image Velocimetry
<b>PM</b>	Particulate Matter

---

<b>PROCOM</b>	programmed combustion
<b>RMS</b>	Root mean square
<b>RPM</b>	Revolutions per minute
<b>S</b>	String spacing
<b>SC</b>	Super Charged
<b>SI</b>	Spark-ignition
<b>SMD</b>	Sauter mean diameter
<b>SOI</b>	Start of injection
<b>SSB</b>	Standard Seal Band
<b>STD</b>	Standard Deviation
<b>TCCS</b>	Texaco Controlled Combustion System
<b>TDC</b>	Top-dead-centre
<b>TPS</b>	Throttle Position Sensor
<b>TWC</b>	Three-way catalyst
<b>UBHC</b>	Unburnt Hydrocarbon
<b>YAG</b>	Yttrium Aluminium Granat

### Symbols

<b>CN</b>	Cavitation number
<b>D</b>	Injection hole diameter / Droplet diameter
<b>h</b>	Plank's constant
<b>I</b>	Light intensity
<b>We</b>	Weber Number
<b>D<sub>32</sub></b>	Sauter mean Diameter
<b>p</b>	Pressure
<b>P<sub>back</sub>, P<sub>b</sub></b>	Chamber pressure
<b>P<sub>inj</sub>, p<sub>i</sub></b>	Injection pressure
<b>Re</b>	Reynolds number
<b>T</b>	Temperature
<b>U, V</b>	Velocity
<b>V<sub>0</sub></b>	Maximum spray front velocity
<b>P<sub>u</sub></b>	Pressure upstream
<b>P<sub>d</sub></b>	Pressure downstream
<b>ρ<sub>f</sub></b>	Density fuel
<b>μ<sub>f</sub></b>	Dynamic viscosity fuel
<b>P<sub>v</sub></b>	Vapor Pressure
<b>P<sub>A</sub></b>	Aerodynamic pressure
<b>P<sub>σ</sub></b>	Surface Tension
<b>P<sub>i</sub></b>	Internal pressure
<b>N<sub>1</sub></b>	Number of Droplet
<b>D<sub>1</sub></b>	Individual droplet diameter
<b>z'</b>	Axial position
<b>z</b>	projection of z' on the jet trajectory
<b>Q</b>	Water flow rate
<b>L</b>	Valve lift

---

# Chapter 1.

## *Introduction*

### **1.1.MOTIVATION**

This study covers the experimental work carried out at City University in collaboration with Siemens and BMW AG during a period of 3 years in which it was studied the in-nozzle flow and spray characteristics of the Siemens pintle-type injector expected to be used by BMW AG for its 3rd generation spray-guided DISI engines. The topic became the focus of many car manufacturer and related industries research activities which involved many research centres and Universities all around the world in the effort of developing more efficient and environmentally friendly propulsion systems. At the current situation, the direct injection spark-ignition (DISI) engines are probably among the top solutions to achieve a significant improvement in terms of fuel efficiency and power output without radically moving away from the internal combustion technology. Such a result was achieved by controlling the amount of injected fuel at part load and directing the ignitable mixture around the spark plug area. Half of the last century improvements in stratified charge technology were necessary to move to the next step in fuel injection. While this technology had been in use for many years in diesel applications, the continued dependence on expensive (and somewhat imprecise) mechanical injection systems prevented its wide spread use in gasoline-powered passenger cars. One notable exception to this was the 1955 Mercedes Benz 300 SL which used a very effective, though extremely costly, mechanical gasoline injection system. After a long path of investigation on the direct injection system started in the beginning of the century, finally the technology was mature to develop a reliable DISI engine. Many other solutions have been object of studies in the past decade but still the optimum stratified charge at part load has not been achieved completely. In the earliest DISI models, the stratification was achieved by wall guiding the injected fuel, redirecting the mixture by piston impingement. However, it was seen that the fuel film produced by the impingement was producing liquid film with an increase of unburned HC and emissions. As the target of most of the automotive companies are strictly ruled by environmental laws it was fundamental that alternative solutions have to be developed.

In the latest decades the Kyoto Protocol stated that the industrialized countries have to

---

reduce their collective emissions of greenhouse gases by 5.2% compared to the year 1990 (note that, compared to the emission levels that would be expected by 2010 without the Protocol, this target represents a 29% cut)[1]. The goal is to lower overall emissions of six greenhouse gases - carbon dioxide, methane, nitrous oxide, sulphur hexafluoride, HFCs, and PFCs - calculated as an average over the five-year period of 2008-12. National targets range from 8% reductions for the European Union and some others to 7% for the US and 6% for Japan and permitted increases of 8% for Australia and 10% for Iceland. The next step in the improvement of DISI technologies would benefit the fuel consumption and in addition would decrease considerably the emission in the sphere of a more and more worrisome and important issues like the level of petroleum reserves, and the reduction of CO<sub>2</sub> as one of the greenhouse gases contributing to the global warming [Kyoto Protocol, [1, 2]

The recent developments on the direct-injection systems put a strong effort in the achievement of the stratified fuel charge by spray-guided mode which gives relevant benefits in terms of efficiency, power output and above all gas emissions[2]. The spray-guided injection removes the fuel film formation that was causing problems in the previous DISI generation, and it provides the fuel mixture cloud uniquely by the characteristics of the spray which it produces the necessary fuel atomisation and it places the stoichiometric cloud around the ignitable area. The task covered by the injector thus becomes more demanding and complex and it requires specific technical characteristics that are still under investigation in most of the direct injection projects. The purpose of this investigation is to give a contribution in understanding relevant issues regarding the spray-guided technology for pintle-type injector leading toward the completion and optimisation of a more efficient and clean combustion technology. The pintle-type injector used in the present study is a new injector designed by Siemens based on new concept of nozzle geometry and needle opening and it needs to be characterized in terms of stability, spray shape, atomisation and more generally in the flow dynamics that rules its behavior under different parametric conditions. In order to observe the complete behaviour of the injector the study was undertaken in three stages: at first, it was analyzed the internal nozzle characteristic by observing the flow behaviour in a large-scale transparent model. It followed the analysis of the spray in the real size injector tested in a constant volume chamber first and then in an optical engine later.

---

## 1.2. INTRODUCTION

Taking a brief look at the history of internal combustion engines it can be seen how engines evolved rapidly through time from the first internal combustion engines such as the steam-powered and coal powered engines to the recently and most commonly used spark-ignition and compression-ignition engines, then finally, to the latest engines powered by electricity, hydrogen cells and other fuels [1]. These achievements have been obtained after years and years of experimentation, trials and testing, from scientists and engineers. These engines will continue to be developed as our knowledge and understanding of engine processes has increased, as new technologies have become available, as the demand for more efficient engines has arose and as the enormous constraints imposed by stringent emission regulations has called for radical changes in the automotive productions throughout the world. The industries designing, developing and producing internal combustion engines play a significant role in the fields of power, propulsion and energy. In recent years the growing awareness of environmental issues has seen an explosive growth in engine research and development as the need to conserve limited fossil energy resources and the issues of pollution, fuel cost, and market competitiveness have become increasingly important. The strict requirements to lower pollutant emissions alone has caused a significant shake up in the automotive industry as leading companies such as Mitsubishi, Ricardo, Toyota, Mercedes and BMW alone have poured enormous amounts of money in researching new engines that will meet today's Euro 5 and tomorrow's emission regulations. European Union plans to adapt a low carbon energy system that starts from its member states to commit themselves to lower their vehicle fleets' CO<sub>2</sub> emissions to a maximum average of 120g/km by 2012 as set by the European Automobile Manufacturers Association (ACEA) [2]. To achieve such targets in terms of emission a big effort has been put on the development of more efficient injection systems. The success of its development is mainly due to the high contribution of the electronic technology which permitted a more effective and flexible control of metering issues.

## 1.3. PRE EMISSION PERIOD

History of pre emission periods of IC engines has been given in many literatures and a full history is given in Wikipedia [[http://en.wikipedia.org/wiki/Fuel\\_injection](http://en.wikipedia.org/wiki/Fuel_injection)]; here a

---

brief history of the events is provided. The first experiments about fuel injection were carried out by Frederick William Lanchester by the Forward gas Engine Company Birmingham in the 1889. Until the 1920s fuel injection was employed commercially in Diesel engines and during World War II it was adapted for use in petrol-powered aircraft. Direct injection was employed for the first time in some notable design like the Daimler-Benz DB 603 and later on the version of the Wright R-3350 used in the B-29 Superfortress.

The very first commercialised direct injection system mechanically controlled was developed by Bosh and introduced in 1955 on Mercedes-Benz 300SL.

This new injection system, a first in any gasoline-powered car allowed a top speed of 260 Km/h depending on gear ratio, making the 300SL the fastest production car of its time.

Another mechanical fuel injection design was introduced by Chevrolet in 1957 and was developed by General motor' Rochester division for its 283 V8 engine. In this model, the intake air was directed across a "spoon shaped" plunger, which was displacing proportionally to the air volume. The plunger is connected to the metering system and it mechanically dispensed fuel to the cylinders through distribution tubes. In the 300SL design, Mercedes adopted six individual plungers to delivery fuel to each of six cylinders.

In the 1960s, other injection systems mechanically controlled such as Hilborn were occasionally used on modified American V8 engines mainly in racing applications like oval racing, drag racing and road racing. However, these racing prototype system were not suitable for utilitarian streetcar use. In the 1957, Electrojector was one of the first electronic injection system developed by Bendix Corporation. AMC introduced a special edition Ramble rebel with a 288 horsepower engine (5400cc), optionally equipped with Electrojector. This was suppose to be the first electronic production of electronic fuel injector (EFI) but several teething problems caused the release of this model only in few cars so equipped and all retrofitted with-4 barrel carburettors before they were first commercialized. In the 1958, Chrysler offered Electrojector (DeSoto Adventurer) arguably the first commercialized production car equipped with throttle body and Electronic fuel injection system, but the early electronic components were too slow to keep up with the demands of "on the fly" engine control. The patent of the Electrojector system was then sold to Bosh which developed a new system called D-Jetronic and commercialized on the VW 1600TL in the 1967. This injector

---

system was adopted by Mercedes-Benz, VW, Porsche, Saab, Citroën, and Volvo; it consists in a speed/density system which uses engine speed and intake manifold air density to calculate "air mass" flow rate and thus fuel requirements. The system used mainly discrete electronics, analog, and electro-mechanical pressure sensor. In the 1974, the K-Jetronic and L-Jetronic systems superseded the D-Jetronic (apart from several cars such as Volvo164 which continued with the D-Jetronic and Cadillac which adopted a similar copy of D-Jetronic) which first appeared on the 1974 in the Porsche 914. The working principle of such a design differs from the D-Jetronic equipped with a mechanical air flow meter which gives an output signal proportional to the air volume. To calculate the air mass, the flow meters required additional sensors to evaluate the atmospheric pressure and temperature. L-Jetronic was distributed in large-scale on the European market of that period and a short time later also in few Japanese models.

## **1.4. EARLY FUEL METERING SYSTEMS**

Since the earliest spark-ignition engines prototypes, the fuel metering systems went through a long process of modifications and development which enhanced significantly the engines performance.

Before the advent of the largely diffuse electronic fuel injector (EFI) the carburetors was the primary method to meter fuel. Nevertheless, widespread variety of injection systems have been developed since the earliest models of spark-ignition engines.

### **1.4.1. Carburetor**

A good history of the development of this device is given in Wikipedia [<http://en.wikipedia.org/wiki/Carburetor>.] and here a brief review is provided. Carburetors were employed in the earliest gasoline engine to blend fuel and air to be introduced in the combustion chamber. It was designed by Hungarian scientist Donat Banki and Janos Csonka in 1893 and successfully developed by Frederick William Lanchester and his brother who incorporated the complete version in a 1000-mile tour in the 1900 contributing to an important step forward in automotive engineering.

For specialised automobiles such those designed for stock car racing and small engines, carburetors are still employed mainly due to its economical convenience, and also the majority of motorcycles are still carbureted even though since 2005 the new models are gradually being introduced with fuel injection. The majority of carbureted engines use a single carburetor, only few exceptions employ multiple carburetors. The



earliest carburetors were designed according to an updraft drawing which allowed the air to be drawn in from the bottom of the carburetor and exiting through the top. The advantage of such a design consisted in preventing the engine from being flooded by fuel droplets falling out of the carburetor instead of into the intake manifold. It gives also the possibility to be matched with an oil bath air cleaner, which was employed when yet the paper air filter did not exist. Since the 1930s, downdraft carburetors were the most diffuse type in United States whereas in Europe, for reason of free space in the engine bay, the side craft model substituted the downdraft. Few small propeller-driven aircraft engines still utilize the updraft type, however the latest design have used a more modern device as for example the CV Bing model.

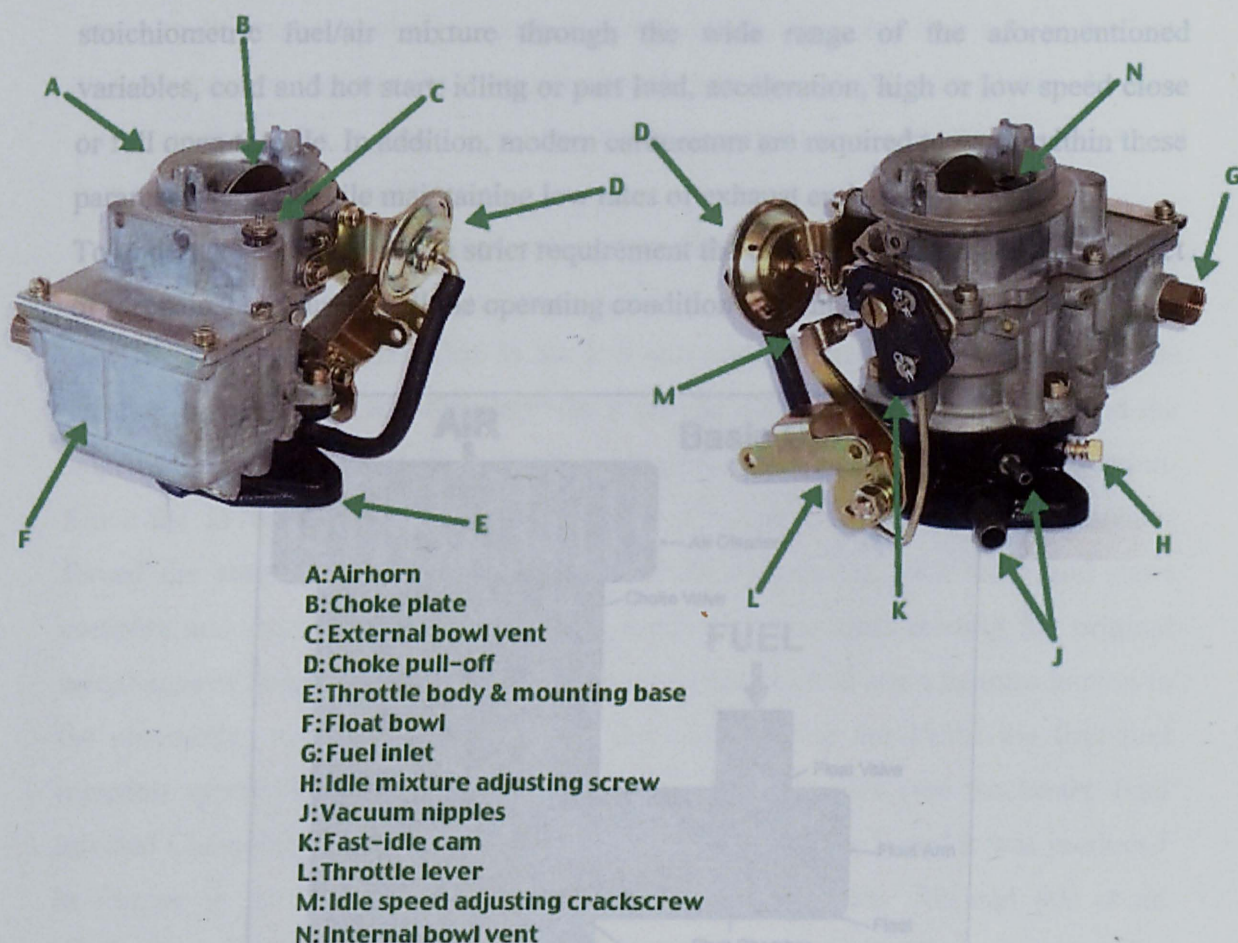


Figure 1-1 Carburetor: schematic [<http://en.wikipedia.org/wiki/Carburetor.>]

The working principle of the carburetor is based on the law of Bernoulli which uses the increase of air velocity to create a drop of pressure. The throttle valve does not directly control the fuel amount but only the mechanism which meter the mixture



being inhaled into the engine. The speed of the flow therefore determines the fuel ratio drawn into the air stream.

The main tasks of a carburetor are the followings:

- Meter the airflow of the engine
- Deliver a stoichiometric air fuel ratio in a range adjusted according external factors (such as atmospheric pressure and temperature)
- Prepare a fine and even mixture between fuel and air

Because of the deviation from the ideal fluid behaviour of air and gasoline then the viscosity, drag forces and flow momentum are actually quite distant from the actual values and vary significantly according the engine working conditions and the ambient parameters. Despite these deviations, the carburetor must provide the stoichiometric fuel/air mixture through the wide range of the aforementioned variables, cold and hot start, idling or part load, acceleration, high or low speed close or full open throttle. In addition, modern carburetors are required to work within these parameter ranges while maintaining low rates of exhaust emissions.

To undertake correctly such a strict requirement the carburetors contain a complex set of mechanism to support all the operating condition and engine modes.

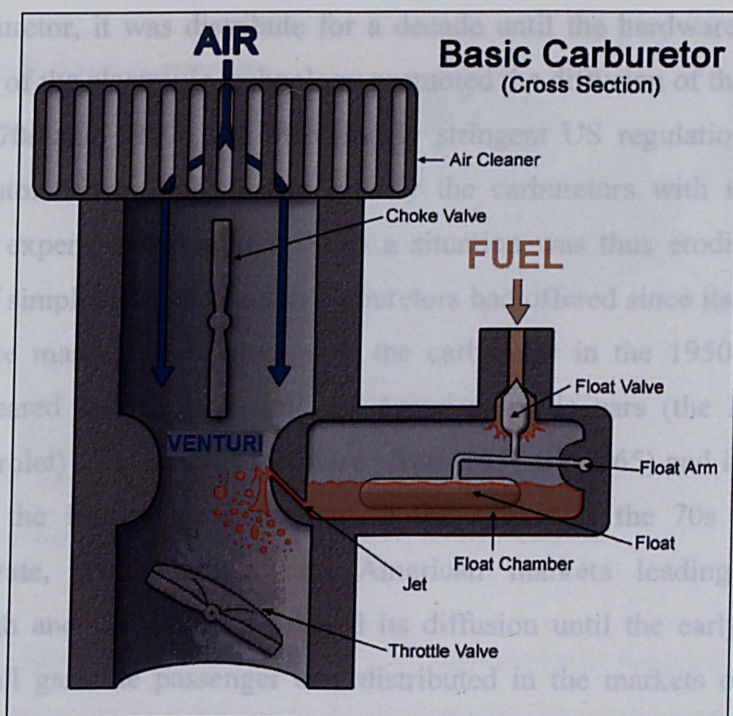


Figure 1-2 Carburetor working principles [<http://en.wikipedia.org/wiki/Carburetor.>]

---

A carburetor is composed of a pipe (throat or barrel) through which the air passes to the cylinder manifold. The throat presents a Venturi shape with a narrow section in the middle where the airflow increases in speed. The throttle valve is located below the Venturi and is a rotating disc, which allows the airflow passes trough according is opening angle that can vary from  $0^\circ$ , for close throttle, to  $90^\circ$ , for wide-open throttle (WOP). Controlling the airflow through the carburetor throat and thus the Fuel/air ratio it regulates the engine power and the speed. Through calibrated bores at the Venturi location, fuel is sucked by the pressure drop produced by the airflow passage. As the throttle varies the opening angle and consequently the air velocity increases the fuel flow responds to the variation of pressure drop adjusting by means of the calibrated orifices, referred to as jets, in the fuel path of Figure 1-2. The minute air pressure difference emulsify (premix fuel with air) the fuel, and then acts as the force to push the mixture from the carburetor nozzle into the induction air stream. As more air enters the intake, a greater pressure drop is generated, and a bigger amount of fuel is metered into the cylinders.

In the 1980s, a new device that could adapt the base mixture according the signal response from a gas Oxygen sensor placed in the exhaust was introduced in the American-market vehicles. Due to the low cost and the practical adaptability to the existing carburetor, it was distribute for a decade until the hardware prices and the improvement of the electronic technology promoted the diffusion of the fuel injection. Since the 1970s and 1980s, the increasingly stringent US regulation on emissions forced the automotive companies to modify the carburetors with more and more complex and expensive equipment. Such a situation was thus eroding the original advantages of simplicity and cost that carburetors had offered since its introduction in the automotive market. In contrast with the carburetor in the 1950s the first fuel injection appeared for the first time on American-made cars (the Rochester Fuel Injected Chevrolet) Corvette, manufactured from 1957 till 1965) and it was produced in Europe in the 1960s and distributed in the market in the 70s and 80s at an accelerating rate, with German and American markets leading whereas the Commonwealth and UK markets delayed its diffusion until the early 1990s. Since then, almost all gasoline passenger cars distributed in the markets of US, Europe, Japan, Australia were equipped with electronic fuel injection (EFI).



### 1.4.2. Fuel Injection

The characteristics of a fuel injector can vary considerably for the different systems still having the common task of supplying fuel for the combustion process [3]. However, the differences on the designs can play a significant role in the optimization of the injector performance such as:

- Power output
- Fuel consumption
- Emissions performance
- Possibility to employ alternative fuels
- Cost
- Maintenance cost
- Diagnostic capability
- Range of environmental operation

Unfortunately, not all these targets are achievable simultaneously since most of them are in conflict with each other. The optimization of these criteria requires a tough goal and the recent digital EFI systems can fulfil its objectives much more competitively than a carburetor.

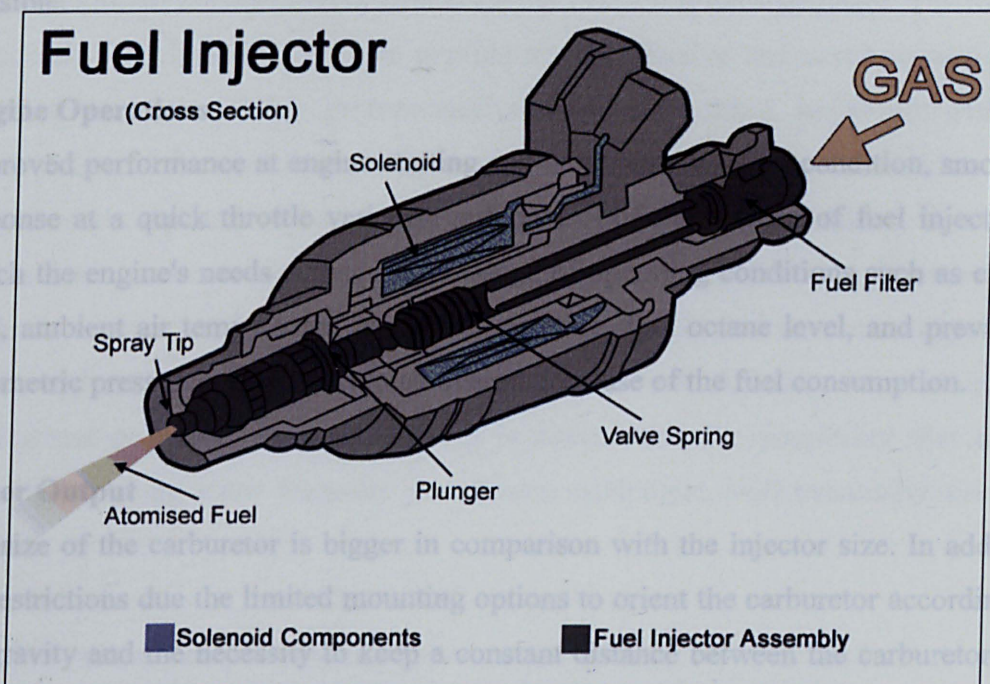


Figure 1-3 Fuel Injector scheme [[http://en.wikipedia.org/wiki/Fuel\\_injection](http://en.wikipedia.org/wiki/Fuel_injection)]

---

In order to achieve the desired engine performance of driveability, efficiency, and of emission, the air/fuel ratio in an engine must be accurately controlled in a wide range of operating condition [2, 4]. The recent EFI system has the ability to meter the injected fuel very precisely and their accuracy is even increased when they are matched with an Exhaust Gas Oxygen Sensor (EGO Sensor). The distribution of digital fuel control in a closed loop, based on feedback from an EGO, sensor certainly marked the superiority of EFI in the comparison with the carburetor.

The two main improvements are:

1. The amount of fuel distributed in the several cylinders can be equally metered resulting in a significantly improving on the cylinder-to-cylinder fuel distribution of the engine
2. The engine response time to a sudden throttle change is very short

The effects of the aforementioned improvements lead to the following benefits:

### **Exhaust Emissions reduction**

Significantly reduced feed gas emissions (which are the combustion products) and in the final tailpipe (combustion gas rate 99.9%) the feed gas are properly conditioned according to a stoichiometric condition in order to make the catalyst as effective as possible.

### **Engine Operations**

Improved performance at engine starting and at extreme weather condition, smoother response at a quick throttle variation and control of the amount of fuel injected to match the engine's needs across a wide range of operating conditions such as engine load, ambient air temperature, engine temperature, fuel octane level, and prevailing barometric pressure which leads to an overall decrease of the fuel consumption.

### **Power Output**

The size of the carburetor is bigger in comparison with the injector size. In addition the restrictions due the limited mounting options to orient the carburetor according to the gravity and the necessity to keep a constant distance between the carburetor and each cylinder which can otherwise impose a restriction to the airflow into the engine. In contrast, the EFI system allows a high level of freedom in the intake system improving the air's path and thus the volumetric efficiency. A less significant reason

---

of pressure loss in the carburetor also occurs when the airstream flows into the narrow cross section of the Venturi duct that is no longer present in the EFI system.

In general, the benefit in terms of increased efficiency in a fuel injection system is much more significant than the carburetor due to the better atomisation which offers a more homogeneous fuel mixture. The improvement in the cylinder-to-cylinder fuel distribution produces a decrease in fuel consumption for the same power output. This concept can be explained by the mechanism of fuel supply and its effect in an unbalance cylinder-to-cylinder fuel distribution. In a non ideal case, where the power output is asymmetrical with respect to air/fuel ratio (which is even worse in the case of carbureted engine), some cylinders receive excess fuel as a side effect of ensuring that all cylinders receive *sufficient* fuel. The extra fuel burned in the rich cylinders does not affect the power nearly as much as burning too little fuel in a lean cylinder. However, in general the calibration is set to deliver extra fuel to lean cylinders or less fuel to the richer cylinders to provide stoichiometric air/fuel ratio to all cylinders. In this way, the net power output improves with all the cylinders at an optimised power. Another benefit of EFI is associated with a better fuel atomisation in the intake; constant-choke carburetors give poor atomisation at low air speed, needing particular design such as sequential twin-barrel.

The evolution of the injection system since the 1980s is quite significant. The modern Electronic Fuel Injection Systems provide a cost effective and accurate method of metering fuel. Subjective performance and emission have improved with the development of the modern digital control. For this reason, by now the EFI systems have almost completely replaced the carburetor in the automotive market.

EFI is more and more economically convenient and reliable through widespread usage. In contrast, carburetors are becoming less available and thus more expensive. As the reliability has improved, the EFI systems are diffusing even in marine applications and according this trend it is conceivable the possibility that all SI engines, including snow throwers and garden equipment, will eventually use EFI systems.

### **Injection system components and function**

The process of metering which determines the amount of fuel delivered into the engine was controlled in all early injection systems mechanically. Nowadays, almost all the current systems are electronically controlled and they use an electronic

---

solenoid to actuate the needle lift and so the injection event. The injected fuel mass is calculated by the engine control unit (ECU) which can be hardware based or recently also software based. The fuel is injected directly into the intake air stream and for a certain opening time an external pump is generally coupled to the fuel injection system controlled by the ECU to provide the right pressure to inject the mapped amount of fuel. The engine sensors (throttle position, lambda, engine speed, thermocouples, pressure sensors, etc.) acquire the parameters needed by the ECU to calculate by mean of mapped functions the amount of fuel to be injected and therefore the injector opening time. The optimum fuel amount depends on running conditions such as engine and ambient temperatures and pressure, torque, engine speed and exhaust gas composition. The pintle of the fuel injector is closed during idle phase and as soon as electricity flows through the solenoid, a force is applied to the needle which opens it to allow the injection. Alternatively, the needle may be actuated by piezo bodies which react to a voltage by changing their volumes producing the pintle displacement. The amount of fuel injected depends on the injector opening time which is proportional to the pulse width. The number of the injections may be controlled sequentially on each individual cylinder injection event, or according a batch fire system which supplies the pulses to groups of injectors. In the batch fire injection the ECU calculates the overall fuel quantity required by groups of cylinders and deliver a correspondent train of pulses to deliver that amount. In a sequential system, the amount of fuel is customised for each individual cycle. The fuel for each induction event, cylinder and injector is calculated separately and a different pulse width is introduced based on that specific fuel requirement. To perform these calculations, it is necessary to know the mass of air (engine breathes) during each cycle which is proportional to the intake manifold's air temperature/pressure, depending on the throttle angle. One of the targets of an optimized injection is to achieve a complete combustion in which all the carbon and hydrogen combined with the oxygen present in the air charge are fully reacted chemically. Such a condition can only be achieved if the fuel and air are present in a stoichiometric ratio, and the ECU uses this information to obtain such a ratio in real time.

Since this ratio for gasoline is 14.64:1, the mass of fuel is equal 14.64 times the mass of air. Once the fuel mass is known the pulse width is calculated and sent to the injector driver to actuate the needle lift. In several particular conditions such as cold start or heavy load, the air-to-fuel ratio can range from 10:1 to 18:1 (for gasoline).

---

The pulse width is calculated taking into consideration the pressure drop upstream and downstream of the injector. If for example the injector pressure increases and /or the backpressure decreases, a smaller pulse width will supply the same fuel mass.

Alternatively, a pressure regulator will provide a fix pressure drop through the injector leaving the injector opening the only parameter defining the fuel amount. Fuel injector are available in a wide spread range of size and spray characteristics and compensation for these and other factors are mapped in to the ECU's software.

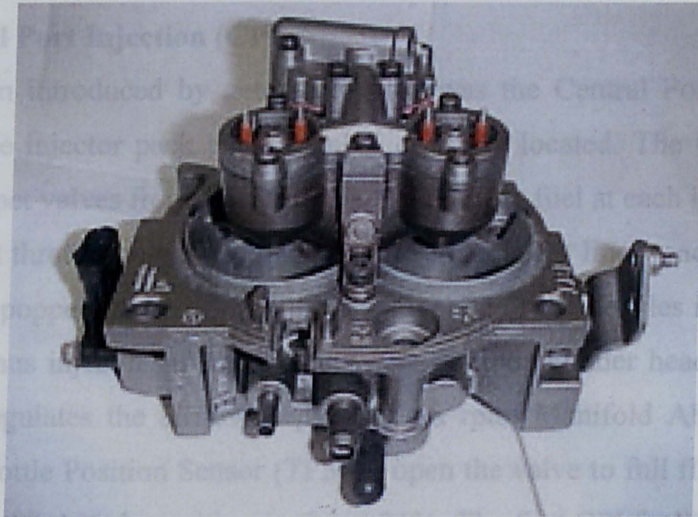


---

### 1.4.3. Alternative Injector Schemes

#### 1.4.3.1. Throttle body injection

As a transient device from the carburetor to Port Fuel Injection, general Motors and Ford introduced an injector system injecting in the throttle body in the same position where the carburetor introduced fuel. The air-fuel mixture flows through the intake runner like in a normal carburetor.



**Figure 1-4 Throttle body injection**

The main advantage of the TBI systems was the low cost, which permitted the adoption of many components still used in the carburetor system such as fuel line routing, intake manifold and air cleaner. This prevented the car companies from redesign further components until the next generation of fuel injection system known as EFI took over in the automotive market. TBI was employed in heavy-duty trucks and on passenger cars during the middle 80's until the 1995.

#### 1.4.3.2. Continuous Injection

In 1974, the system Bosch-K-Jetronic was introduced in the car market and used for many years by Ferrari, Lamborghini, Mercedes-Benz, Ford, Volkswagen, Porsche, Volvo, Saab and Audi. It consisted in a system constantly spraying from the injectors rather than releasing a pulse during the intake strokes. Gasoline comes from the fuel tank to a fuel distributor which is a large control valve separating the tank from the single fuel injectors and each of them supplies fuel into smaller pipes, one for each



---

injector. The intake air must pass through a control vane located beneath the fuel distributor. According to the angle of air vane the system supplies fuel to the injectors, which are simply actuated by a spring loaded check valve with nozzle. The valve opens as soon as the pump pressurised the fuel at a pressure higher than the counter spring force. The variant to the K-Jetronic system was called KE-Jetronic with electronic trim instead of the mechanical pressure control that enabled the use of a catalytic converter.

#### **1.4.3.3. Central Port Injection (CPI)**

Another system introduced by general Motors was the Central Port Fuel Injection (CPFI) with the injector pack and assembly centrally located. The CPI system uses tubes with poppet valves from a central injector to spray fuel at each intake port rather than the central throttle-body. When the pressure inside the lines reaches the opening pressure of the poppet valves (43 psi), fuel sprays out of the nozzles into the engine's intake ports. Thus injecting in each intake port, on the cylinder heads, the manifold tuning valve regulates the airflow depending on rpm, Manifold Absolute Pressure (MAP) and Throttle Position Sensor (TPS) to open the valve to full flow and help the breathing when the throttle position is above 36%. The first CPI fuel injection intakes 1992-93 had this valve controlling the full flow of the air in the fuel injection intake, excluding the Cyclone and Typhoon models. This type of injection is a batch fire, speed density, fuel injection which also refers to as "Central Multi-point Fuel Injection" (CMFI). However, fuel is continuously injected to all ports simultaneously, which is less than optimal besides this system presents a high failure rate.

#### **1.4.3.4. Multipoint fuel Injection (MPFI)**

The Multi-Point Fuel Injection system differs from the central port injection system from the injection position which is located into the intake port just upstream of the cylinder's intake valve rather than within an intake manifold like the CPI system. MPFI can be sequential, batched or Simultaneous. In the first case, the injection is timed and synchronized with each cylinder intake stroke whereas in the Batched design, the injected fuel does not have any synchronization and is injected into the cylinder in groups without precise synchronisation to any particular cylinder's intake stroke. Finally, in the Simultaneous design, the fuel is injected at the same time to all the cylinders.

---

From the 1970s to the early 90, several Toyota's and other Japanese cars employed a multipoint L-Jetronic system manufactured under licence by DENSO which uses a vane-type Air Flow Meter (AFM).

## **1.5. EMISSIONS IN INTERNAL COMBUSTION ENGINES**

In the 1975, the Californian State (California's Air Resources Board, CARB) issued new stringent emission rules and regulations, which required a dramatic reduction of exhaust gases. It included three components of regulation: (1) emissions regulation, (2) zero-emissions vehicles mandate, which requires approximately 40% of all vehicles sold in the state to certify to the zero-emissions vehicles standards, and (3) CO<sub>2</sub> regulations. The only feasible solution to achieve a satisfying emission reduction was the development of the catalytic converter. Only recently, General Motor has developed the automotive exhaust catalyst and rushed this new technology into production.

The emissions of an engine play a key defining part in any engine concept. Emissions in today's world are one of the main drivers of the automotive industry's funding and development of engines. In fact, it has almost become an obsession with the industry, as it is a key step for the success of any new engine. All engines at present undergo intense scrutinising in terms of emissions before they enter the market. It has become the main policy for many countries to reduce emissions, which are included in many current regulation standards. (Kyoto, EURO1-6, ACEA, etc.).

The emissions that play the biggest role in internal combustion engines are Hydrocarbons (HC), nitrogen oxides (NO<sub>x</sub>), Carbon monoxide (CO) and Particulate matter (PM). Many other emissions are formed in the chamber but they consist of very small quantity and thus do not play a significant role in the emission regulation.

In DISI engines the main sources of UBHC during stratified and homogeneous-charge operation is produced during flame quenching on the cylinder walls from the unburned mixture in the crevices escaping combustion and from fuel wall wetting due to the overly rich region formed on the piston wall. Another source of hydrocarbon formation is also associated to a substantial temperature drop of the exhaust gas around the EVO period, which significantly degrades the conversion efficiency of the catalyst system.

---

HC formation does not only occur during hot operating modes but it is also an effect of cold starting. However, SIDI engine has been proven to show less HC during cold starting than the PFI engine. In fact, in the PFI engines, the initial fuel is injected onto the intake valve and port wall where the fuel mass entering the cylinder is not necessarily what is being metered by the injector on that cycle. Whereas SIDI engines utilize a stoichiometric or lean mixture during cold starting thus reducing cold-enrichment and acceleration-enrichment compensation, which in turn reduces HC emissions.

The CO and NO<sub>x</sub> formations are dependant on the gas temperature and on the level of excess air. The temperature in SIDI engines operating with stratified charge remains high within the reaction zone due to the presence of a stoichiometric or slightly rich mixture in the core region of this stratified charge; therefore, NO<sub>x</sub> is not avoidable because there is combustion of near stoichiometric mixtures which produce high temperature zones. PM will definitely be formed if high temperature and rich mixtures co-exist and for DISI engines the conditions of PM formation is unavoidable, especially at high load conditions. Particulates in DI injection engines are produced at a lesser degree than a traditional diesel engine but are of much smaller size, and therefore more dangerous to human health as it becomes readily airborne and enters into the body undeterred. This is why the industry has introduced additives in the mixture to reduce particulates as they tend to auto burn at lower temperatures. Over the past two decades, the attempt to reduce engine out emissions has been the main agenda for the automotive industry and countries alike. Therefore, these countries and the related industries formed bodies to regulate and measure these emissions, such as the European Emissions Regulations, Kyoto Convention, Environmental Protection Agency (EPA), European Automobile Manufacturers' Association (ACEA) and various other bodies around the world. This in turn leads us to the latest European Emissions Regulations for passenger cars, light and heavy commercial vehicles for Euro III and Euro IV (Tables 1.1 & 1.2) [1, 5]:

Euro III, IV and V Emission Standards for Heavy-Duty Diesel and Petrol Engines						
Tier	Effective date	CO g/kWh	NMHC g/kWh	CH <sub>4</sub> g/kWh <sup>1</sup>	NO <sub>x</sub> g/kWh	PM <sup>2</sup>
Euro III	1999 (EEVs)	3.0	0.40	0.65	2.0	0.02
	2000	5.45	0.78	1.6	5.0	0.16 0.21 <sup>3</sup>
Euro IV	2005	4.0	0.55	1.1	3.5	0.03
Euro V	2008	4.0	0.55	1.1	2.0	0.03

**Table 1-1 Engine emissions standards for heavy-Duty diesel and petrol engines.**

Figure 1-5 Particle emissions for different concepts (updated on 2000) [6, 7]

Euro III (2000) and Euro IV (2005) Emission Standards For Passenger Cars and Light Commercial Vehicles								
Effective date, MY	Category/class	Ref. mass	Fuel type	CO g/km	HC g/km	NO <sub>x</sub> g/km	HC+NO <sub>x</sub> g/km	PM <sup>1</sup> g/km
2000	M <sup>2</sup>	All <sup>2</sup>	Petrol Diesel	2.3 0.64	0.20 —	0.15 0.50	— 0.56	— 0.050
	N <sup>3</sup> /1	≤1,305 kg	Petrol Diesel	2.3 0.64	0.20 —	0.15 0.50	— 0.56	— 0.050
	N <sup>3</sup> /2	>1,305≤1,760 kg	Petrol Diesel	4.17 0.80	0.25 —	0.18 0.65	— 0.72	— 0.070
	N <sup>3</sup> /3	>1,760 kg	Petrol Diesel	5.22 0.95	0.29 —	0.21 0.78	— 0.86	— 0.100
2005	M <sup>2</sup>	All <sup>2</sup>	Petrol Diesel	1.0 0.50	0.10 —	0.08 0.25	— 0.30	— 0.025
	N <sup>3</sup> /1	≤1,305 kg	Petrol Diesel	1.0 0.50	0.10 —	0.08 0.25	— 0.30	— 0.025
	N <sup>3</sup> /2	>1,305≤1,760 kg	Petrol Diesel	1.81 0.63	0.13 —	0.10 0.33	— 0.39	— 0.040
	N <sup>3</sup> /3	>1,760 kg	Petrol Diesel	2.27 0.74	0.16 —	0.11 0.39	— 0.46	— 0.06

**Table 1-2 Engine emissions regulations for Euro III (2000) and Euro IV (2005)**

The particulate emission of a Diesel engine is very high compared to those of gasoline engines. With the introduction of the GDi engine this values varies from the gasoline standards as during the stratified mode operation with rich AFR, particulate emissions can increase.

A test on the rolling road shows that the mass of particulate emissions in a SIDI engine is higher than a Multi-Point Injection (MPI) engine but much lower than modern diesel engine and it meets the future stringent US ULEV levels (0.01 g/mile)



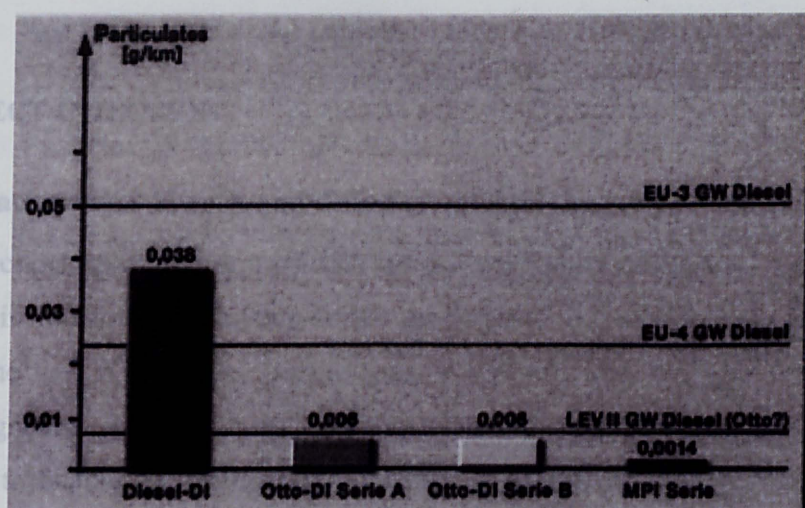


Figure 1-5 Particle emissions for different concepts (updated on 2000) [6, 7]

Fulfilling the actual regulations on gas emission is strictly essential for the future engine design. In order to justify the manufacturing investments the investigation purpose must have the potential to achieve future emission levels. Currently the fuel efficiency potential of a SIDI cannot be achieved under European and US boundary conditions. In this situation of tension between lowest fuel consumption and lowest emission, the different DI concepts have their specific points of weakness and strength. Several approaches have been compared to conventional MPI engines. The combustion systems for both stoichiometric and lean concepts are the core element for good fuel efficiency and low emissions. For instance, particulate emissions have to be avoided in both concepts with careful combustion development and to achieve this it is necessary to develop different combustion methods over a short period.

For stoichiometric concept, SIDI technology does not produce high fuel economy improvement, but can be employed with conventional aftertreatment technology, which in turn helps to keep low the emission level. Double or multiple injections give a new flexibility during start or warm up phases contributing to improve emission behaviour.

For lean operation, it is possible to achieve the highest fuel economy potential but the required aftertreatment technology needs special fuel quality and a specific on-board device (OBD) system. The percentage of short term and mid term content of sulphur on the US market brings several obstacles.

However, the relevant progress in the storage catalysts development during the last years causes optimism as long as it will be shortly determined where and when will be available extra sulphur fuel. [6]



## 1.6. DIRECT INJECTION

### 1.6.1. Background history and diffusion of direct injection technology

Direct-injection spark-ignition (DISI) is an alternative injection system to PFI employed in the four-stroke, two-stroke gasoline or biobutanol engines. Instead of injecting the fuel in the intake port or throttle body like the Port injection the fuel is injected right into each cylinder. The main improvement of the GDI system is the possibility to enable the formation of an ultra lean burn mode (stratified charge) to improve the fuel efficiency and emission levels at part load.

As aforementioned in the pre-emission period the technology of the direct injection was first applied in the gasoline-powered car Mercedes-Benz 300SL with Bosch fuel injectors placed into the bores used by the spark plugs in previous six-cylinder engines. However, with the early technology of that period the DISI system resulted expensive and the development of less expensive indirect injection systems froze further DISI engine development.



Mercedes-Benz 300SL	
Manufacturer	Mercedes-Benz
Also called	Mercedes Benz 300 SLR 2-door coupe
Production	1952-1963
Predecessor	none
Successor	Mercedes-Benz 230SL
Class	sports car
Body style	2 door coupé, roadster
Engine	Mercedes 2995cc, SOHC
Transmission	4-speed MANUAL
Wheelbase	2400 mm (94.5 in)
Length	4520 mm (178 in)
Width	1790 mm (70.5 in)
Height	1300 mm (51.1 in)
Curb weight	1093 kg (2351 lb)

Figure 1-6 Mercedes-Benz 300SL

---

Only forty years later, gasoline direct-injection was reintroduced in the market by Mitsubishi Motors in the Galant/Legnum's 4G93[8] which was the first GDI engine released by Japanese companies. The same GDI engine was subsequently distributed in Europe in 1997 in the Mitsubishi Carisma[9], however the high sulphur concentration in the European fuel caused problem of emissions and fuel efficiency[10]. Mitsubishi applied this GDI technology widely, distributing over a million of direct-injection engines in four families by 2001[11], Hyundai Motors and PSA Peugeot Citroën both licensed Mitsubishi's GDI technology, the former using the first GDI V8[12]. In 2000, Daimler Chrysler produced a special engine distributed only in countries with low sulphur fuel.

Since then, other companies developed gasoline direct injection technology but GDI (with capitalised "I") remains a trade mark of Mitsubishi Motors[13].

Further improvement on GDi technology was brought forward by Volkswagen/Audi in the 2001, which led the trend with their direct-injection engine under a different trademark FSI (Fuel Stratified Injection). BMW introduced a low-pressure injector GDi system in a V12 engine, which due to its poor fuel atomisation could not enter in lean-burn mode. In the 2006 a second GDi version was introduced by BMW with a high precision injection system on the update N52 straight-6 which surpassed many other direct injection system with a wider envelope of lean burn time resulting in an overall improved efficiency [14]. In the 2002, General Motors planned to produce a full range of GDi engines but till now only two engine models have been introduced. The first was made in the 2004, which was a version of the 2.2 L Ecotec adopted in the Opel Vectra followed in the 2005 by the 2.0L Ecotec with VVT technology mounted in Pontac Solstice GXP.

The first engine sold in America for a mainstream vehicle was produced by Isuzu in the 2004. The main innovation of Isuzu GDi system was given by the cooling effect produced by the in-cylinder injection, which allowed a higher compression ratio (10.3 versus the previous ratio of 9.1).

Toyota's 2GR-FSE V6 released in the 2006 a combined injection system with direct and indirect injection, which uses a traditional injector in the port and a new direct injection per cylinder.

In the 2006, Mazda referred to its GDi system as Direct Injection Spark-ignition (DISI) and was mounted in Mazdaspeed 3 and in Mazdaspeed 6 / Mazda 6 MPS, the CX-7 sport-ute engines.

---

In the 2002, Colorado State University sponsored EnviroFit, a non-profit corporation to develop a direct injection retrofit kits for two-stroke motorcycles in an environmental project finalized to reduce the pollution in Southeast Asia. The technology used in this GDi kit uses a patent developed by Orbital Corporation Limited of Australia and is based on a mixed injection of compress air and fuel. The injection of compress air in the cylinder promotes the fuel break up thus improving the combustion efficiency. The kits were so installed in millions of two-stroke motorcycles taxi (big sidecars) and the Philippines EnviroFit claim a reduction in fuel consumption of the 35 percent, in particular, 76 percent of carbon monoxide reduction, 26 percent carbon dioxide reduction and 89 percent hydrocarbon emissions. Orbital's OCP GDi Kits was also employed in Tohatsu's TLDI DFI outboard engines, Mercury's Optimax DFI outboard engines in Bombardier's SeaDoo personal watercraft and in the mscooter by Piaggio, Aprilia, Kymco and Peugeot. Research and development of OCP system applied in four stroke engines is currently in progress

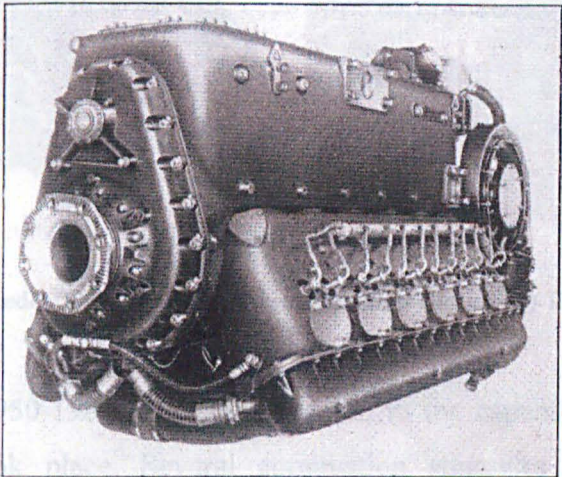
### **1.6.2. From DISC to DISI Engines**

DISI engines are essentially the evolution of the Direct Injection Stratified Charge (DISC) gasoline engines, a concept of the early 20th century, enabling technologies such as the high pressure, common rail, gasoline injection system and advanced computer control. In a way similar to the diesel quality control, also the power output of the DISC engines is controlled by varying the amount of fuel injected into the cylinder. The air induction is not significantly throttled, thus the negative work associated with the pumping loop of the cycle is dramatically reduced [15]. The principal target of DISI concept is fuel efficiency improvement, which is mainly achieved by the possibility to inject in different modes according the engine operating conditions. More specifically as direct injection enables extreme lean combustion mode it is possible to minimize charging losses during part load operation. This characteristic gives DISI the outstanding base as the most effective contribution for a fuel economy idea.

From a historical perspective, dual stratified chamber was the subject of research by British, German, French, Russian, American, and other developers in the early 20th century. It used two separate chambers with a rich air/fuel ratio in one (usually a small pre-chamber containing the spark plug) and a very lean mixture in the other (or main) combustion chamber. In most such engines, a relatively homogeneous gasoline-air

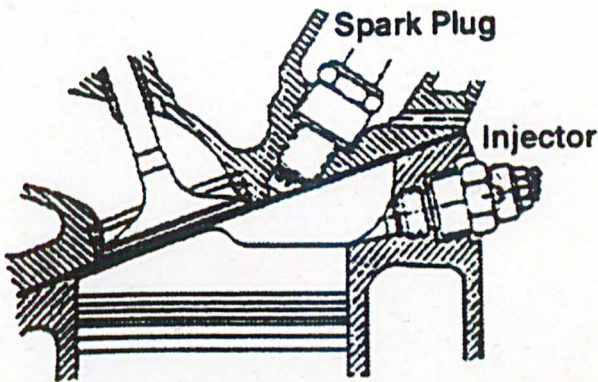


mixture is fed into both chambers; the flame from the fuel-rich pre-chamber ensures ignition and complete combustion of all of the lean mixture in the main chamber [16]. The first application of gasoline direct-injection was the *Daimler-Benz DB 60*, a German aircraft engine built during World War II. It was a liquid-cooled inverted V12 which powered the *Messerschmitt BF 109*. This was a 33.9 litre engine (Figure 1-7), with two spark plugs, 4-valves per cylinder using direct fuel injection and a single stage supercharger.



**Figure 1-7 First gasoline direct-injection application (Daimler-Benz DB 601-1933)**

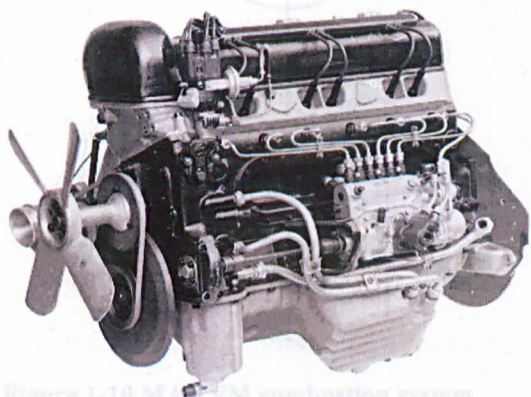
The first attempt in automotive applications was made in the 1952 by Mercedes with the 300SL (Figure 1-8). The 300SL racing sports car featured innovative technology such as the world's first automotive four-stroke gasoline engine with direct mechanical fuel injection and it won the famed Le Mans 24-hour race in its debut season. In 1954, the company entered the car into production series.



**Figure 1-8 Mercedes 300SL system configuration**

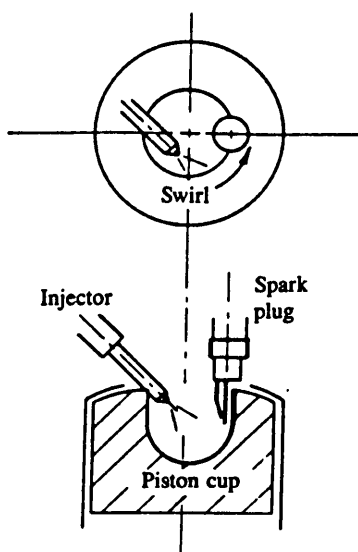


This engine, 3-litre inline 6 cylinder design, used early direct injection during the induction stroke to achieve homogeneous air fuel mixture. However, utilising a low-pressure mechanical fuel injection system, its high fuel consumption and the cost forced the company to stop its production 3 years later.

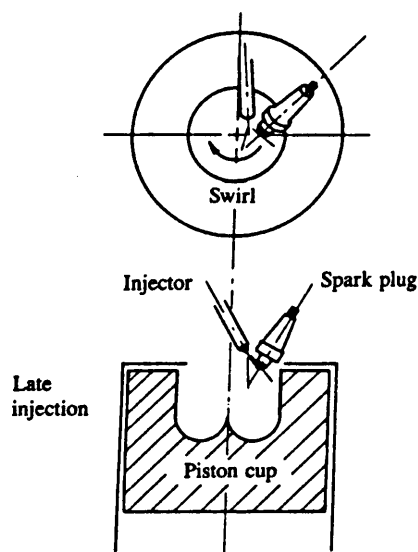


**Figure 1-9 (a) The Mercedes 300SL gasoline direct-injection engine. (b) The Mercedes 300SL “Gull wing”**

During the period 1950-1980, extensive research in the capabilities of DISC spark-ignition engines took place. Several combustion strategies were proposed and implemented by various companies and researchers, including the Texaco Controlled Combustion System (TCCS) in 1951 (Figure 1-11), the MAN FM (Maschinenfabrik Augsburg-Nürnberg A. G) (Figure 1-10), GM DISC (General Motors Direct Injection Stratified Charge) and the Ford Programmed Combustion Control system (PROCO) in 1968 (Figure 1-12). Most of these earlier systems were based upon engines having two valves per cylinder and incorporating a bowl in piston combustion chamber. Late injection operation was achieved by employing mechanical pump-line-nozzle fuel injection systems for engine applications[16].



**Figure 1-10 MAN FM combustion system**



**Figure 1-11 Texaco TCCS Combustion system**

In these systems, unthrottled operation was obtained over most of the load range and low BSFC values were achieved, making DISC engines competitive against the indirect-injection diesel engine of that era. A major drawback was the lack of control on the injection duration on the late injection mode at part load which was maintained even at full load due to limitations of the mechanical (non-electronic) fuel injection system. This resulted in smoke limited combustion for air/fuel ratios richer than approximately 20:1[17].

The necessity of using diesel fuel injection equipment coupled with the need for a turbocharger to provide adequate power output, resulted to an engine that exhibited performance characteristics similar to those of a diesel engine, but showed poor emission at part-load with high unburned hydrocarbon (HC).



with four valves per cylinder and a compression ratio of 12:1 (Figure 1-8). This engine enabled reverse tumble using a variable valve timing system to achieve stratified charge which adopt late injection strategy for part load operation and early injection for full load operation.

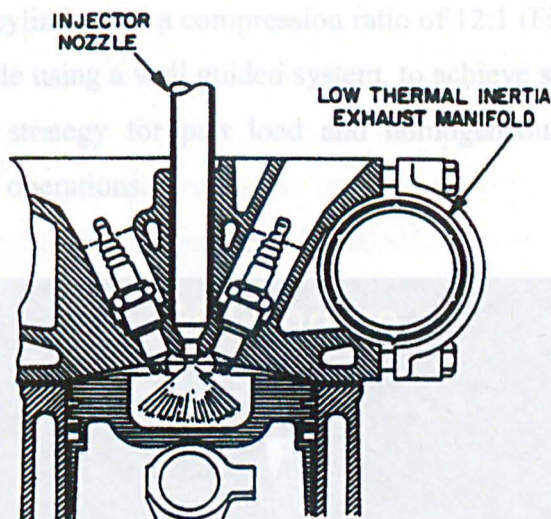


Figure 1-12 The FORD PROCO combustion system

The PROCO combustion system was a DISC alternative design which utilised a centrally located injector to provide a hollow cone spray with injection occurring early in the compression stroke. Even in such a system, the control of HC emissions was extremely difficult at light load operation (Figure 1-12) and the combination of relatively poor air utilisation with the use of mechanical fuel injection equipment limited in speed range resulted in an engine with low specific power. Research continued in the late 70s, on the development of two stroke direct gasoline injection engines, employing air assisted atomisers.

Many of the problems associated with the DISC engines at part load, their mixture preparation and combustion control strategies, emissions characteristics and deposit formation mechanisms. The main difference between port fuel injected (PFI) and DISC engines lies in the mixture preparation strategy. In the DISC engine fuel is injected into the intake port, and the fuel is drawn into the combustion chamber by the intake flow. This is in contrast to the PFI engine where the fuel is injected directly into the combustion chamber. The direct injection system allows for better control of the fuel-air mixture, leading to improved combustion efficiency and reduced emissions.

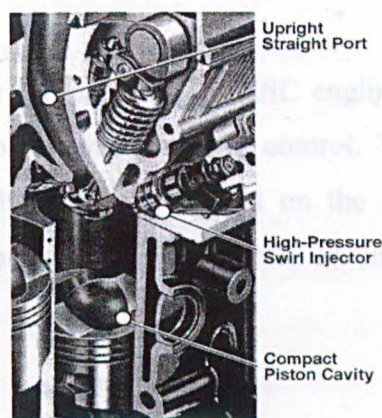
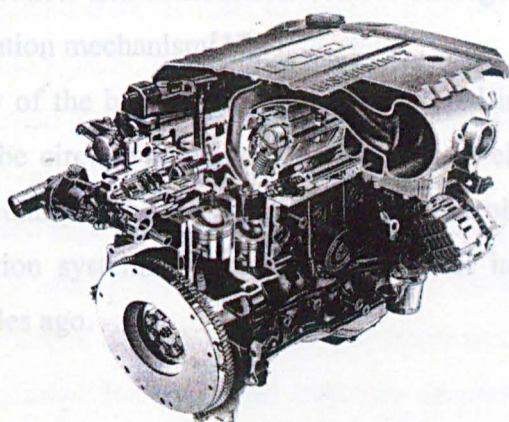


Figure 1-13 Cut-away view of the Mitsubishi GDI system

The main difference between port fuel injected (PFI) and DISC engines lies in the mixture preparation strategy. In the DISC engine fuel is injected into the intake port, and the fuel is drawn into the combustion chamber by the intake flow. This is in contrast to the PFI engine where the fuel is injected directly into the combustion chamber. The direct injection system allows for better control of the fuel-air mixture, leading to improved combustion efficiency and reduced emissions.

In 1996 competition among automotive industry was intensified, with Mitsubishi being the world's first car maker to commercialise a 1.8 lt, 4 cylinder GDI engine,



with four valves per cylinder and a compression ratio of 12:1 (Figure1-8). This engine enabled reverse tumble using a wall guided system, to achieve stratified charge which adopt late injection strategy for part load and homogeneous charge using early injection for full load operations.

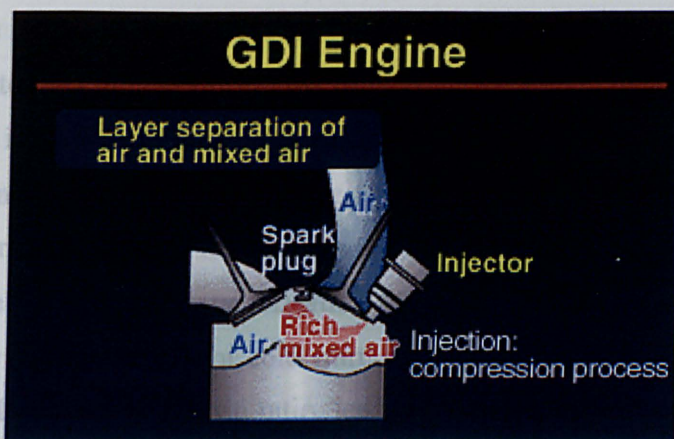


Figure 1-14 Mitsubishi GDI combustion system

New technologies and computer control strategies, such as laser techniques and CFD (computational fluid dynamics), are currently being invoked by a number of automotive companies to re-examine the extent to which the potential benefits of DISI engines can be accomplished in production engines. The targets in the development of DISI engines are to exceed the fuel economy of diesels at part load, their mixture preparation and combustion control strategies, emissions characteristics and deposit formation mechanism[17].

Many of the basic limitations encountered in the earlier work on DISC engines can now be circumvented due to advances in electronics and computer control. This is particularly true for the significant control limitations that existed on the direct-injection systems, in particular, the fuel injectors and pump controls around two decades ago.

### 1.6.3. Gasoline Direct Injection versus Port Fuel injection

The main difference between port fuel injected (PFI) and DISI engines lies in the mixture preparation strategies. In the PFI engines fuel is injected into the intake port of each cylinder, and there is an associated time lag between the injection event and the induction of the mixture into the cylinder. Most of the current automotive PFI

---

engines worldwide perform timed fuel injection on the back of the intake valve occurring before the opening event. 20% of the PFI engines adopt an injector mounted on the cylinder head upstream of the intake valve, while the remaining 80% of the PFI applications mount a single injector on the intake manifold near the cylinder head [17]. The former configuration presents the drawback of a transient film of liquid fuel formation in the intake valve area during cranking and cold start. Some portion of this film is drawn into the cylinder during the induction event and consequently the fuel is metered rather inaccurately from the pool created in the film, which acts as a capacitor, and not from the injector itself, causing a fuel delivery delay and an associated metering error due to the partial vaporization of the spray. This effect, coupled with the relatively poor vaporisation from the cold puddle of fuel, creates the need for a larger supply of fuel for cold start, which exceeds significantly the amount of fuel required for a stoichiometric ratio, leading to unstable burn on the first 4 to 10 cycles of a cold start and to a significant increase in the unburned hydrocarbons (UHC) emissions. On the other hand, injecting fuel directly into the cylinder does not only avoid fuel wall-wetting formation in the ports but it also enhances the control of the metered fuel by reducing transport time. DISI engines can be started cold using a stoichiometric or even slightly lean mixture. This gives DISI engine a significant HC emission reduction potential, especially during cold start and warm up. However, this is very much dependent on the quality of spray delivered from the fuel system. The fuel pump and fuel rail pressure need to be able to generate quickly high pressures during cold start, in order to achieve high level of atomisation. With common rail high pressure system, the actual mass of fuel entering the cylinder can be more accurately controlled giving potential for leaner combustion, less (cycle or cylinder) air/fuel ratio variations and reduced BSFC.

It is well established that direct injection of gasoline with insignificant enrichment can provide starts on the first cranking cycle, exhibiting significant reductions in hydrocarbon spikes during load transients. The difference in the minimum fuel requirement for cold start becomes greater as the ambient temperature decreases. However, injecting directly into the cylinder reduces the time available for evaporation and mixing, which leads to the requirement for high-level fuel spray atomisation. This is achieved by adopting an injection pressure of the order of 100 to 200bar which is substantially higher than the injection pressure of 6bar operated on the PFI system. The significant increase in atomisation and fuel vaporisation rate

---

produced by the high injection pressure consents to achieve stable combustion at cold start during the first or second injection cycle without the need to supply fuel excess and therefore giving the potential to achieve a level of HC emissions similar to that at steady operating conditions. The evaporation of the finely atomized fuel injected directly into the cylinder, also contributes in the increase of volumetric efficiency, by substantially cooling the inducted charge of air in the cylinder. A penalising limitation of the PFI engine is the throttling operation that is required for basic load control. Although throttling is a reliable and well-established load control mechanism in the PFI engine, it also represents a substantial thermodynamic loss associated with it. The thermodynamic loss is associated with the negative pumping loop and results in thermal efficiency degradation particularly at low levels of engine load. In the DISI stratified charge mode, the engine load is controlled by varying the amount of fuel injected into the cylinder reducing considerably or abolishing the throttling operation with its associated pumping losses and therefore enhancing the thermodynamic efficiency of the engine.

Another potential advantage of the DISI engine is the option of inserting fuel cut-off on deceleration providing additional improvements in fuel economy and HC emissions. In the PFI engine, which operates from an established fuel film in the intake port, fuel cut-off during deceleration is not a viable option, as it reduces or even eliminates the liquid fuel film in the port. If this happens, the reestablishment of the film would origin a transient event lasting several engine cycles, which can result in lean mixtures in the combustion chamber that may lead to a misfire or backfire[17]. The advantages of the PFI engines over the DISI engines are limited and focus on the fact that their intake system acts as a prevaporising chamber. In direct-injection engines, the mixture preparation time is reduced dramatically, especially in stratified mode, resulting in a high atomisation requirement aiming to droplet size small enough to enable a fast evaporation in the limited time between injection and ignition. Fuel droplets that do not vaporize are very likely to burn with diffusion and exit the engine as HC and PM emissions. Also, when injecting fuel directly in the cylinder, an unintended fuel impingement may occur, on the piston crown and/or the cylinder wall, contributing to increase the level of HC and particulate emissions and also to increase the level of cylinder bore wear[17].

Some other advantages of PFI engines are the use of a low-pressure fuel system and the feasibility of using three way catalysts (TWC) providing higher exhaust

---

temperatures for improved catalyst efficiency. Generally, NO<sub>x</sub> formation is favoured by the increased in-cylinder temperature, especially in the maximum reaction zone [18]. PFI engines exhibit their NO<sub>x</sub> emission peak when burning leaner than stoichiometric (air fuel ratio 1.25 times higher than stoichiometric) and as the air fuel ratio increases the maximum reaction zone temperature reduces with consequent decrease of NO<sub>x</sub> formation. However, DISI engines operating with stratified charge produce a high reaction zone temperature due to the stoichiometric or slightly rich mixture in the stratified charge region. Due to the cooling effect of the in-cylinder vaporisation and to the intrinsic characteristic of the stratified charge, DISI engines are usually more robust against knocking enabling higher compression ratios with consequent increase in thermal efficiency but also in peak temperatures and therefore NO<sub>x</sub> formation [17]. Finally, the high local NO<sub>x</sub> production under part load operation in DISI engines results in infeasibility of utilising three way catalysts to full advantage. Operating the DISI engine under overall lean conditions does reduce the engine NO<sub>x</sub> emissions, but this cannot achieve the minimum 90% reduction level that can be attained using TWC [17]. The excessive HC emissions at part load also represent an important research task for DISI engines development.

In spite of these concerns and difficulties, the DISI engine offers a horizon for future applications that expands beyond that of a well developed PFI engine. The current high technology PFI engine, although highly evolved has nearly reached the limit of its potential. For the same reasons that port fuel injection gradually displaced carburetors and throttle body injectors, a DISI combustion configuration will dominate and gradually displace the PFI applications.



---

### **Advantages GDI**

- No transient film so less misfire, less UBHC emission in the cranking period and during load variation
- Better delivery control
- Fuel cut-off during deceleration
- Small fuel transport time
- Potential for leaner combustion
- Less cylinder to cylinder variation in the air fuel ratio
- Lower operating BSFC values (brake specific fuel consumption)
- The higher pressure produce a better atomisation, less gasoline required in the starting
- Inlet unthrottled so absence of pumping work and therefore improved fuel economy: (25% potential improvement)
  1. less pumping loss
  2. Volumetric efficiency increasing
  3. less heat losses
  4. higher compression ratio
  5. lower octane requirement

**Table 1-3 Advantages of GD-I systems Vs PFI systems [19]**

### **Disadvantages GDI**

- Presence of variable fuel films in the chamber (piston) and consequently UBHC increasing (for piston guided combustion concept)
- Short vaporization time which results in a low participation in burning diffusion and consequently high UBHC at the exhausts.
- High full-load UBHC, part-load NO<sub>x</sub> (due to stratified operation), soot formation full-load particulate, deposit formation in the injector
- No use of three way catalysis due to the lean composition of the exhaust gas at part load operation
- Increased electrical power and voltage required
- Problem of lubrication in the pumping system
- Elevated fuel system pressure and fuel pump parasitic loss
- Difficulty in controlling the stratified charge

**Table 1-4 Disadvantages of GD-I systems Vs PFI systems [19].**

### **Requirements of GDI injector not present in PFI systems**

- Significant enhancement of atomisation spray.
- More emphasis in spray penetration control, sac volume spray control
- Enhanced resistance to deposits formations
- Smaller flow variability under high pressure gradients
- Combustion sealing capability
- Avoidance of needle bounce that create unwanted secondary spray( uncontrolled atomisation or anatomised ligaments. and loss in metering

**Table 1-5 Requirements of GDI injector not present in the PFI.**

---

#### 1.6.4. Strategies and approaches to achieving Stratified charge

Many different approaches have been developed over the years, for DISI combustion systems. These comprise of a wide range of combinations of in-cylinder charge motion (swirl, tumble and squish), chamber and piston geometry and spark plug and injector position. Spray structure/shape, mean droplet size, spray penetration and fuel delivery rate must be matched with air-flow field, piston bowl geometry, and spark location. The injection strategy is also one of the main parameter and its optimisation play an important role in the operation of the DISI concept. For instance, in order to improve warm up operation Mitsubishi made the late injection during the expansion stroke in order to increase the temperature of the exhaust and improve the catalysis operation during cold starting.

One of the goal in DISI engine optimisation is to provide operation in both homogeneous and stratified mode as well as a smooth transition between them[20]. To improve the transition between low and high load, Toyota introduced two stage injections; early injection and late injection during intake stroke and compression stroke respectively.

The methods of stratified charge preparation have seen the evolution of different injection strategy generations. Wall-guided and air-guided were the strategies employed in the first generation DISI engine whereas spray-guided is currently adopted by the second Generation DISI engines (Figure 1-15). For wall guided DISI injection, as their name imply, the charge stratification is achieved by spray impingement on the piston surface, whereas the air guided take advantage of the charged flow field velocity and the spray dynamics to redirect the stoichiometric plume toward the spark [17, 18]. The two modes of the first generation concept provided the best solution for mass production and robustness in terms of component and manufacturing tolerances. On the other hand, they are inherently limited from a thermodynamic point of view since the stratified mixture formation is directly linked to the piston motion. Additionally under homogeneous operation, quenching is also increased due to the higher surface to volume ratio of the combustion chamber (piston bowl) which is required for the stratified operation. Furthermore, the stratified operating range is limited by smoke emission due to the formation of liquid film on the piston surface. From this issue the second generation DI systems are addressing their effort to overcome this problems whilst still achieving an advantageous cost-benefit ratio [21].

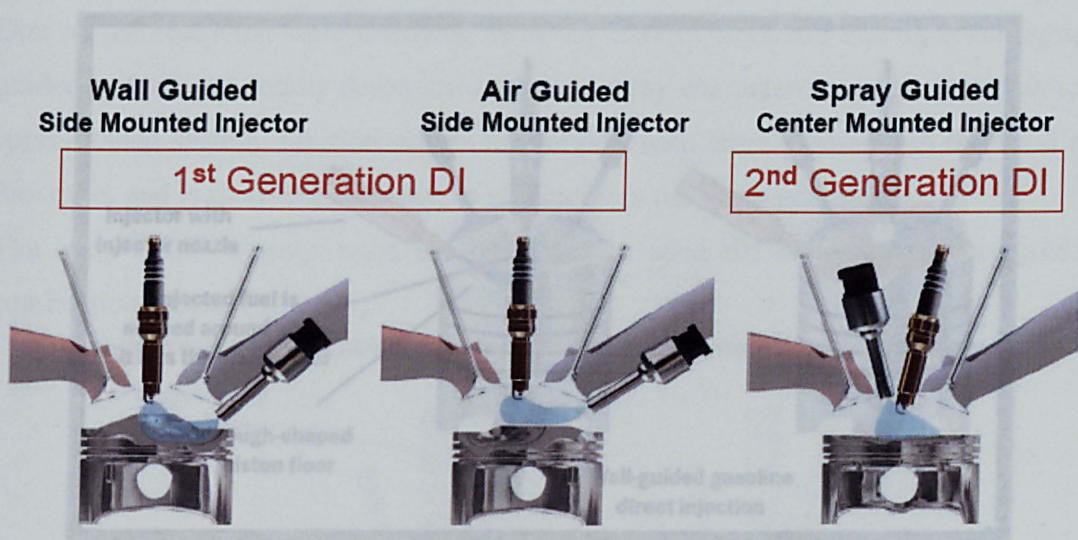
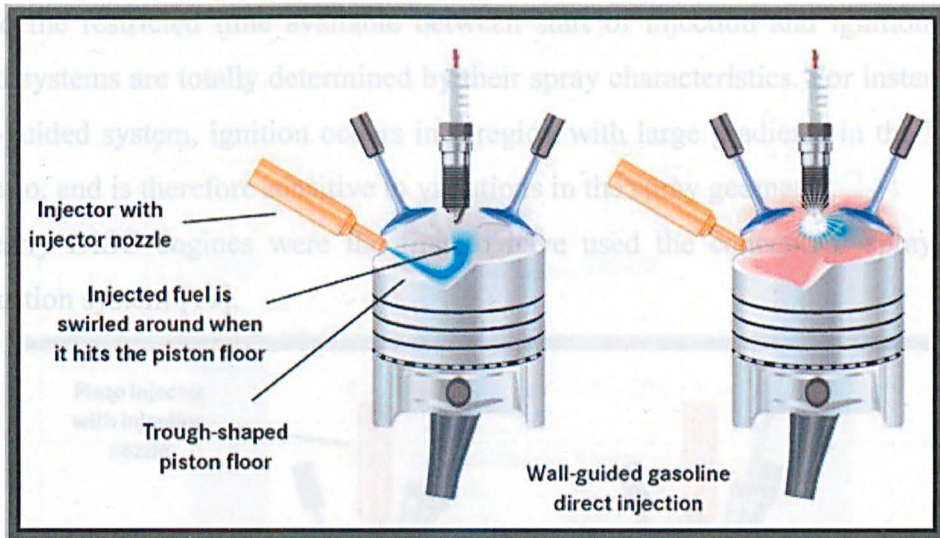


Figure 1-15 Spray-guided, Wall-guided and Air-guided combustion systems [22]

**Wall-guided systems:** this type of configuration (1<sup>st</sup> generation) is associated with the “wide spaced” gap between the injector and the spark plug. The concept uses spray impingement on a piston cavity in order to achieve stratified mixture. The injector is mounted at a greater distance from the spark plug, compared to spray-guided systems, and more time is given to the mixture to be formed and well atomised at the expense of some loss in combustion stability.

A well designed piston cavity can offer a high efficient air entrainment in the cylinder resulting in a system being more robust and less dependent on spray characteristics. The main concerns to achieve stratified combustion in this type of systems are the piston bowl design and the balance of tumble and swirl in the cylinder. On the other hand, the spray impingement on the walls increases soot formation and wall wetting, which leads to increased HC emissions. The efficiency at high cylinder pressure is influenced by combustion phasing, heat release rate and wall heat losses. The combination of these aspects combined with high charge motion and high surface-to-volume ratio, increases considerably wall heat losses and is detrimental for the overall combustion efficiency. However, Wall-guided wide spaced systems have been first used successfully by Mitsubishi on their first production GDI engines (Figure 1-16). The idea was then extended, adopting reverse tumble to create stratified charge near the spark gap [23].





**Figure 1-16 Representation of the 1st generation "wall-guided" configuration**

**Air-guided systems:** This type of configuration is also associated with the “wide spaced” and the 1<sup>st</sup> generation of injection strategy. It relies on the coupling of the fuel spray with air tumble motion to create stratified charge and redirect it toward the spark plug. A wide spacing configuration is used, as in wall-guided systems, but no assistance is required from wall surface. Any concerns associated with wall wetting and HC increase, are thus avoided. However, the disadvantage of this system consists of its dependency on the in-cylinder air flow which may cause unstable combustion at part load when air flow is weak.

Although a piston cavity is not essential to air-guided systems, a well designed piston will help homogeneous combustion. Other concerns for an effective air guided system are the spray characteristics and the cylinder geometry which must promote tumble formation but still avoiding spray impingement.

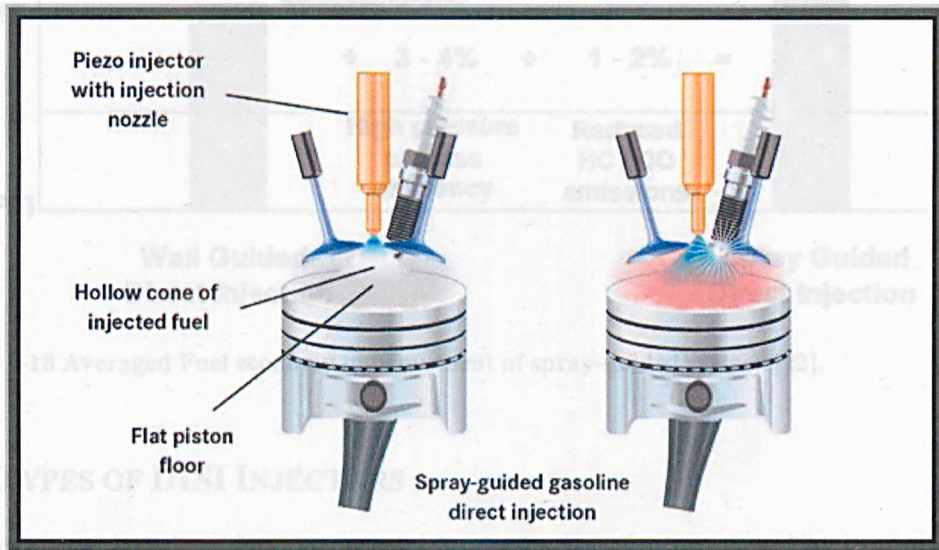
**Spray-guided systems:** Stratified lean combustion is achieved by spray-guided strategy by mean of a narrow spaced configuration, with the spray boundary and the spark gap operating within a very small distance. The mixture is not affected by cylinder charge motions or piston cavity design and is controlled mainly by the spray dynamics.

However, the requirement for very close spacing of the injector and spark plug results in a reduction of the intake valves sizes. The vicinity of the injector to the spark plug may also result in misfiring due to the very short interval between them or even soot formation due to the possible impingement of the spray on the spark plug or valves.



Due to the restricted time available between start of injection and ignition, spray-guided systems are totally determined by their spray characteristics. For instance, in a spray-guided system, ignition occurs in a region with large gradients in the local air fuel ratio, and is therefore sensitive to variations in the spray geometry.

The early DISC engines were the first to have used the concept of spray-guided combustion system [17].



**Figure 1-17 Representation of the 2nd generation "spray-guided" configuration.**

Currently, further improvement need to be concentrated on high pressure cycle efficiency, reduction of exhaust emissions and on the extension of the stratified operation range. Air-guided concept presents an enhancement of these aspects but still does not achieve the level of the spray-guided which offers a higher potential of improvement. With this concept the need of piston bowl and air flow motion becomes secondary thus the systems become easily adaptable to the traditional PFI design parts with current port design and flat piston. On the other hand, the mixture formation quality relies on the spray characteristics which increase considerably the need of higher injector performance and cost. The spray must present strong characteristic of stability against operating variables such as ambient backpressure, ambient temperature, engine speed, internal flow motion and a high level of droplet atomisation. Furthermore, the close position of the injector to the spark plug causes problem of deposit formation which add the requirement to the injector to be robust against fouling formation. Another problem related with the close-spacing configuration is due to the increased valve size constrain which causes packaging problems in the pent-roof shaped combustion chamber designs.



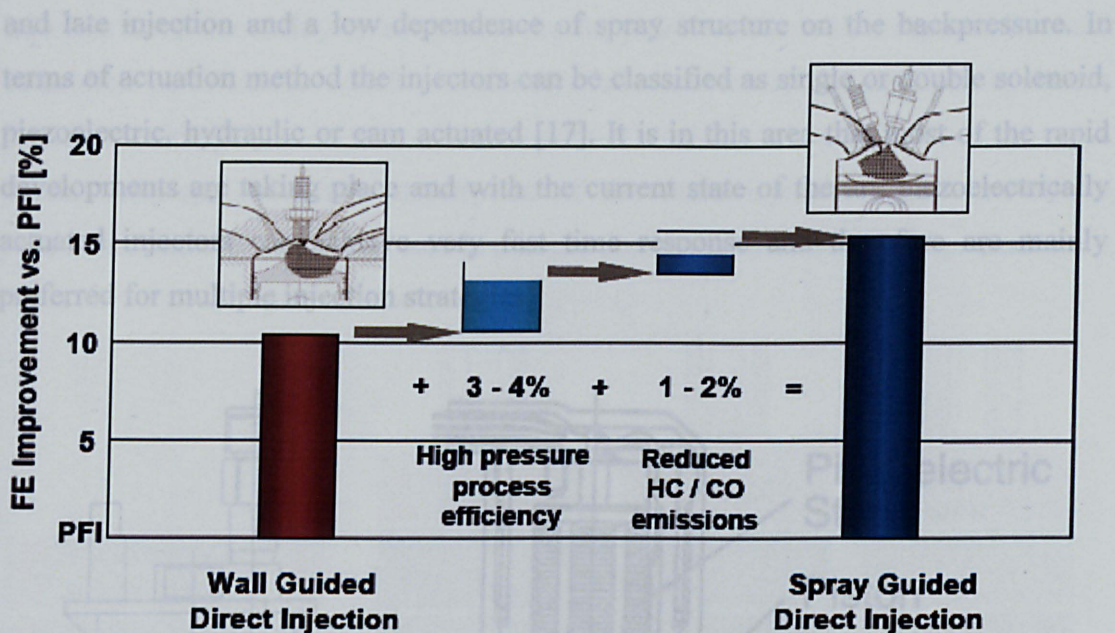


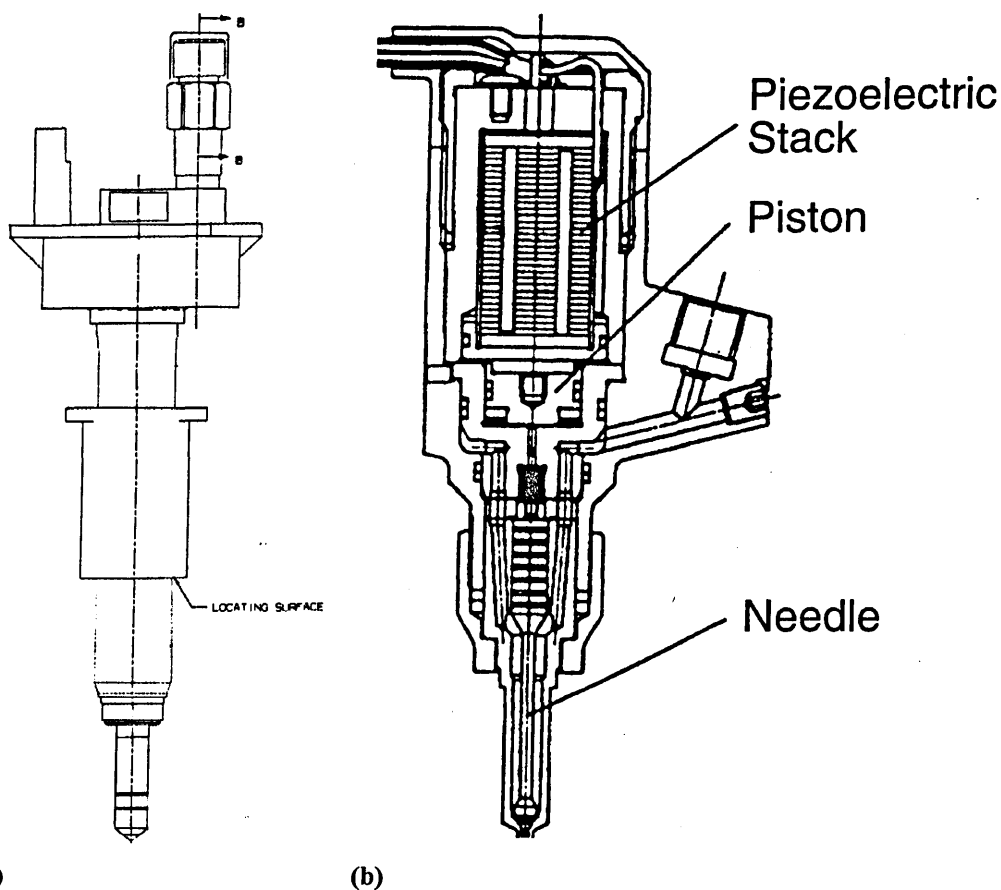
Figure 1-18 Averaged Fuel economy improvement of spray-guided systems[22].

### 1.7. TYPES OF DISI INJECTORS

Injectors can be classified by actuation method and more specifically by several parameters such as nozzle and spray configuration, atomisation method, or pintle opening. Many combinations of these characteristics have been attempted by swirl-type atomiser, the most widely used in DISI applications, with an inwardly opening pintle. Swirl injectors are used to enhance atomisation, due to the additional rotational momentum applied to the fuel which promotes the secondary break up of the spray. Also Multi-hole nozzles, like those used in diesel engines, have been developed by several manufacturers for DISI applications and are characterised by enhanced air utilization for early injection improving thus the flame propagation, however the small size of the holes and their external position were creating problems of carbon deposits and penetration control in early injection.

Significant research is taking place on outwardly opening injectors which exhibit certain advantages versus the inwardly opening ones. Due to their geometry, these injectors are effectively more robust to deposit formation and seal very firmly ensuring minimal leakage. The outwardly opening injectors have no sac volume, which is associated with fuel residuals. These injectors offer a better control over the spray angle and penetration, which is also one of the topics of this investigation. Furthermore, the hollow cone spray produced by this type of injectors presents a better air utilization than the multi-hole with good control on penetration during early

and late injection and a low dependence of spray structure on the backpressure. In terms of actuation method the injectors can be classified as single or double solenoid, piezoelectric, hydraulic or cam actuated [17]. It is in this area that most of the rapid developments are taking place and with the current state of the art, piezoelectrically actuated injectors can achieve very fast time response and therefore are mainly preferred for multiple injection strategies.



**Figure 1-19 (a) Schematic of Siemens Inward Seal Band piezo injector, (b) Schematic of piezoelectrically actuated DI injector**

**Piezoelectrically Actuated Injector:** Piezoelectric injectors used in DISI engines, contain crystals with non-uniform charge distribution within the crystal lattice. When exposed to an electric field, this charge distribution shifts rapidly and the crystal changes its shape. The pintle of the DISI injector is actuated by the rapid change of the lattice dimensions of a stack of crystals, when voltage is applied. This results in rapid actuation response of the needle providing an opening time which is more than one order of magnitude faster than typical solenoid systems. In this way, atomisation level is improved and furthermore the injector's dynamic range is enhanced. Piezo



injectors have the ability to use much shorter pulse widths with a repeatable, well-controlled performance which are characteristics necessary for multiple injections implementation [17].

In the following section a description of the main injector types currently in production and their important role in mixture preparation will be briefly presented.

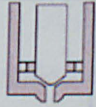

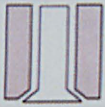
			
	Swirl	Multihole	Outward opening
Flexibility of spray pattern	+	++	0
Backpressure influence	-	+	+
Costs	0	+	--
Robustness against deposits	0	-	+
Atomisation quality	+	-	0
Sac volume presence	-	-	++
Penetration control	+	-	++

Figure 1-30 (a) schematic of a swirl injector, (b) swirl spray structure

Table 1-6 Comparison among swirl, multihole and outward opening atomisers [22].

Further changes in atomisation level are caused also by altering the swirl ratio which in addition affects the penetration curve. By keeping constant the atomisation level and increasing the spray swirl-ratio the required injection pressure decreases

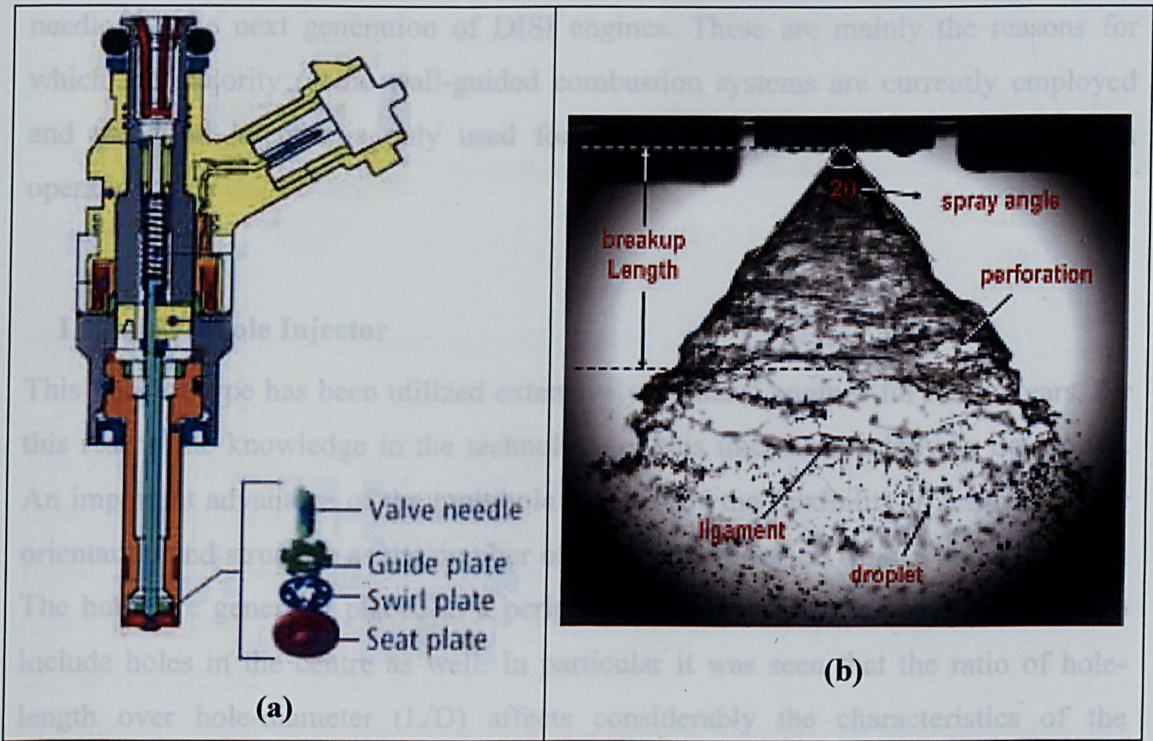
### 1.7.1. Swirl Injector

The most diffuse DISI injector type currently used by most of the automotive companies is the pressure single-hole swirl injector with inwardly opening needle. The main characteristic on the atomisation strategy of a swirl injector consist of turning pressure energy of the liquid in angular momentum. The fuel under pressure coming from the common rail enters in a conical swirl chamber through tangential slots with either cylindrical or conical cross section. From a single discharge hole the liquid emerges as an annular cylindrical sheet spreading radially outwards and forming a hollow cone spray.

The swirl injector presents flexibility on the discharge directions which means that according the required air utilization in the chamber and the spark plug position the



nozzle can be designed with either axial or slightly off-axis spray direction. In general the use of an offset axle injector reduce the performance of the injector (penetration, atomisation...etc) and in order to overcome this inconvenient it is necessary to increase the injection pressure [17]. Furthermore, skewing the injection axis can be associated with asymmetrical wall impingement on the piston which forms uneven thickness and consequently different time of evaporation with increasing of UBHC.



**Figure 1-20 (a) schematic of a swirl injector, (b) Swirl spray structure**

Further changes in atomisation level are caused also by altering the swirl ratio which in addition affects the penetration curve. By keeping constant the atomisation level and increasing the spray swirl-ratio the required injection pressure decreases promoting the air entrainment in the vortex.

The axial velocity decreases with the distance from the injector due to the drag effect of the air opposing to the axial motion, whereas the swirl velocity remains almost constant since the near field environment swirls together with the droplets.

The conical spray produced by a swirl atomizer under ambient backpressure is composed by a very fine mist of droplet within the spray having a relatively low penetration, thus ideal for the early injection strategy. On the other hand, it was observed a strong dependency of the spray angle on the air density and therefore on backpressure which is crucial for late injection operation. In general, the increase in

---

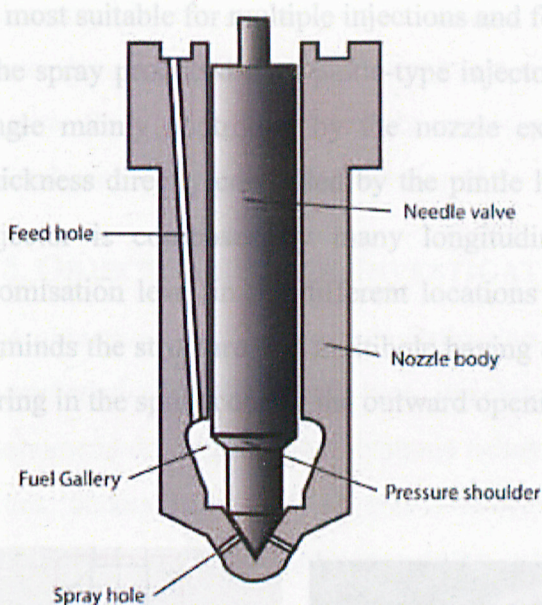
backpressure intensifies the polar field gradient of the density transforming the hollow cone structure into a compact solid plume. The penetration and velocity of the spray reduce monotonically with cylinder pressure increase and ultimately the spray collapses. Furthermore, the poor atomisation encountered at the early injection stages, known as pre-spray, has led manufacturers towards the development of alternative injector types such as the close cap slit, the multi-hole type and the outwards opening needle for the next generation of DISI engines. These are mainly the reasons for which the majority of the wall-guided combustion systems are currently employed and the swirl injector is only used for homogeneous strategy at early injection operation.

### **1.7.2. Multihole Injector**

This injector type has been utilized extensively in diesel engines for many years, for this reason the knowledge in the technology of this injector is relatively developed. An important advantage of the multihole is given by the flexibility in terms of spray orientation and structure as the number of holes can be varied from 5 up to 12 holes. The holes are generally placed in a peripheral location with the extra possibility to include holes in the centre as well. In particular it was seen that the ratio of hole-length over hole-diameter ( $L/D$ ) affects considerably the characteristics of the emerging spray jet in terms of air entrainment, atomisation quality and penetration length.

The nozzle of the multihole atomizer produces thus a series of thin jets with average cone angle of approximately  $10^\circ$ . Each jet presents a remarkable spray stability and cycle-to-cycle repeatability with penetration dependent only on the room condition [17, 24, 25]. All these advantages make the multihole a good candidate for the spray-guided application. On the other hand, for a rail pressure of 100bar multihole injector presents a poorer atomisation quality than the swirl atomizer which improves at a satisfying level by increasing the injection pressure. However beyond a certain pressure ( $\sim 200$ bar) the spray over penetrate leading to excessive wall impingement.





**Figure 1-21 (a) Model of a multihole injector, (b) Spray of 6-hole injector**

The inward opening design of this injector implies also the presence of an initial liquid mass trapped in the external open volume of the nozzle (sac volume). Since this initial fuel, trapped in the sac volume, emerges from the nozzle with very low injection pressure then the atomisation will be very poor and thus a significant amount of fuel entering the cylinder as large liquid droplets.

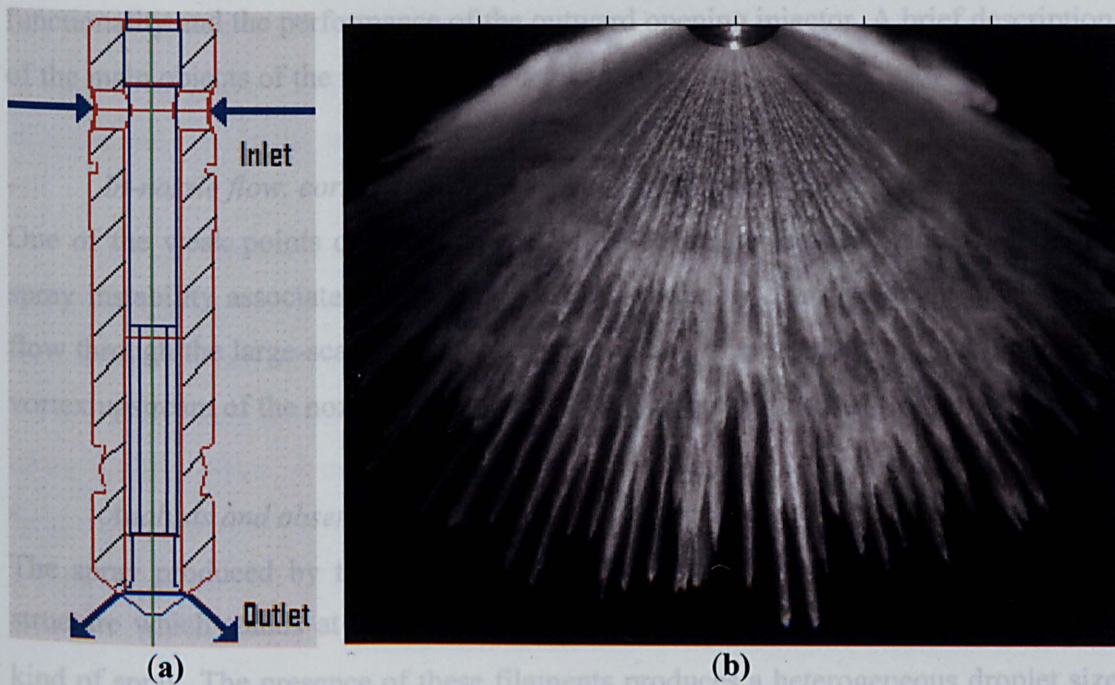
In addition, unlike swirl and outward opening type injector, the multihole atomizer presents the problem of nozzle contamination by high temperature carbon soot due to its relatively small hole diameter (range of 0.07-0.14mm). For this reason the design and the layout of this injector inside the cylinder has to be optimised not only for the best air utilization but also to limit the average tip temperature.

### **1.7.3. Outward opening Injector (pintle-type Injector)**

The outward opening injector represents the solution to many restrictions encountered in the swirl and multihole atomiser. A comparative analysis of this injector with the aforementioned atomizers has arisen many positive qualities which attracted the interest of several automotive companies in the competition for the DI sprays guided Technology. The injector used in this study belongs to the category of outward opening atomizers and it was recently distributed in the market by Siemens Automotive VDO. It is known also as piezo injector due the nature of its actuation system which provides an extremely fast opening and closing operation (0.2 ms) and



is most suitable for multiple injections and for stratify mode at very late injection. The spray produced by a pintle-type injector has the shape of a hollow cone with an angle mainly controlled by the nozzle exit geometry and the initial liquid sheet thickness directly controlled by the pintle lift. The spray structure of the pintle-type injector is composed by many longitudinal filaments presenting a non-uniform atomisation level in the different locations of the string cross-section. Such a spray reminds the structure of a multihole having a number of jets as large as the number of string in the spray cone of the outward opening injector.



**Figure 1-22 (a) Model of an outward opening nozzle injector (b) hollow cone spray under atmospheric pressure produced by an outward opening nozzle.**

One of the main advantages of this atomizer is the absence of the stagnant liquid mass lying externally in the sac volume generated by most inward opening atomizers. The outward opening injector offers a design flexibility to allow spray angle and droplet size to be controlled independently so that it is possible to have a comparable atomisation quality for different cone angles and same injection pressure [17]. In addition the design without micrometric holes presents the advantage to be very robust against soot deposition which makes the outward opening atomizer resistant to high temperature peaks. Nevertheless, a problem strongly penalizing this injector is

---

represented by the cycle-to-cycle variation (flapping) of the spray shape which may cause the displacement of the ignitable mixture from the spark plug resulting in misfire. Such a problem becomes severe when this injector is to be used in spray-guided concept as it has been developed.

## 1.8. OBJECTIVES OF THE INVESTIGATION

The objectives of the current investigation focused on the observation of the spray characteristics of the pintle-type injector primarily aiming to observe the main phenomena driving the flow dynamic behaviour of the spray and ultimately to have a better understanding of several practical aspects directly implicated with the functionality and the performance of the outward opening injector. A brief description of the main objects of the investigation is given as follow:

- *In-nozzle flow, correlation between internal flow and spray structure:*

One of the weak points of the spray performance of the Siemens pintle-type is the spray instability associated with spray-to-spray variation. By visualizing the internal flow through the large-scale model it was possible to identify the correlation between vortex upstream of the nozzle and tangential oscillation of the emerging spray.

- *Analysis and observation of the string structure*

The spray produced by the pintle-type injector is characterised by a typical string structure which stands at the base of the atomisation and break up process for this kind of spray. The presence of these filaments produces a heterogeneous droplet size distribution through the string cross section. The string characteristics and their dependence from the operating parameters were observed according a statistical analysis.

- *Analysis and observation of the multi-phase flow (cavitation and air entrainment) in the nozzle exit*

The presence of a second phase was observed in the nozzle passage caused by air entrainment and/or cavitation. This gas phase was found to be responsible for the spray angle variation and string formation. As aforementioned, string structure has been for long time object of investigation and hereby it was possible to speculate a model which may contribute to a trustworthy explanation of such behaviour.



---

- *Velocity field distribution and parametric study*

To characterise the air utilization, spray development and to gather information on the actual spray displacements it was necessary to determine the velocity field. A detailed scan of the string cross section was performed in different condition of temperature, needle lift, injection pressure and backpressure.

- *Droplet size distribution and parametric study*

The droplet size distribution covers a role of primary importance in the mixture formation since the fuel vaporisation strictly depends on the surface-volume ratio. For this reason it was studied the droplet size dependence from the operative parameters in order to establish droplet break up occurrence and the size distribution with respect of space and time in the same condition of the velocity scan.

- *Spray recirculation*

In the outward opening injector the ignitable mixture is formed primarily in the spray recirculation which takes place on the surface of the hollow cone and it develops as the spray penetrate into chamber. The vortex evolution covers a main role in the study of the ignition phase. A measure of the spray recirculation was thus assessed in the far field of the injector by mean of Phase Doppler Anemometry (PDA) and Particulate Image Velocimetry (PIV).

- *Air entrainment in the spray near-nozzle field*

From CFD calculation, it seems that the air entrainment has an important role in the spray stability and in the secondary break up. In the case of the outward opening injector, several studies claim the air entrainment to have a role on the phenomenon of string formation. To have a better understanding the air velocity characteristics in the near field of the injector was measured.

- *Spray behaviour operating in a optical engine*

Finally, a visualization of spray structure in actual condition was carried out inside of an optical engine supplied by BMW. The spray stability in terms of cone angle and spray recirculation was observed through 2D and integral Mie scattering.

---

## 1.9.THESIS OUTLINE

The current thesis comprises of six chapters subdivided according the experimental phases carried out along the course of the investigation. At the beginning of the main chapters, the experimental set up is described followed by the results and analysis.

Chapter 1 presents a paragraph summarizing the motivation and the objectives of this thesis followed by an introductive description of the fuel metering systems from the carburetor until the current DISI system. The brief explanation comprises drawbacks, benefits and targets of the new direct injection systems including the descriptions of the DI injector currently under investigation.

Chapter 2 contains a table with the description of the literature reviews and findings about gasoline direct injection. More specifically, it reports the review of literature about investigation on enlarged models, spray characterisation and publications on the pintle-type and air entrainment. Every paper or document reported includes the list of Authors, the description of experimental set up, Technique and the main conclusions.

Chapter 3 reports the results observed on the large-scale model of the pintle-type injector. The first part describes the internal flow behaviour and its correlation with the flow characteristics in the nozzle exit, in the second part the phenomena regarding the presence of gas phase in the nozzle exit is analysed and its correlation with string formation and spray angle behaviour is discussed.

After a qualitative investigation on the scaled model, chapter 4 describes the PDA results and Mie scattering images obtained in the parametric study on the real size injector tested in a constant volume chamber under different operating conditions. The velocity of the near and far field of the spray and air entrainment is analysed by mean of different techniques and where possible correlated with the previously observed scaled model.

Chapter 5 shows the actual behaviour of the spray in the optical engine analysing the angle statistic and spray recirculation in a parametric study.

Chapter6 concludes the thesis with the summary of the major findings of the results described through chapter 3 to 5. Recommendations for further work in the area of experimental research on the pintle-type injector are also given in Chapter 6.

Chapter 7 reports the bibliography of the references of publication and documentation cited throughout the thesis.

---

## Chapter 2.

### *Literature Review*

#### 2.1. INTRODUCTION

This chapter provides a collection of the literature review concerning the state of art on the direct-injection technology. As the research on the Piezo Injector started just recently and is still at the beginning of its development, it was not possible to find a relevant amount of material on this specific prototype. However, the techniques of investigation used in the characterisation of other atomisers provided useful information on the understanding of similar flow mechanisms. Other publications, listed in tables 2.1 to 2.7, show experimental methodologies used in the investigation of the pintle-type injector and it was found to be very useful in terms of comparison and as outline of the techniques employed in this project.

The paper collection was subdivided in six sections retracing the experimental stages of the thesis:

- *Internal flow characterisation in large-scale models.* This table collects a list of papers which describes the results visualized in scaled model of different type of injector.
- *Spray flow characterisation in Real size models.* It was the second phase of the investigation and the papers listed in the second table described mainly results focusing on the spray characteristics generated from different type of real size injectors tested in constants volume chamber in terms of spray structure, fuel droplets size/velocity distribution and fuel vapour structure.
- *Spray recirculation and air entrainment* The literature review collected in this section presents the results of several studies on the air interaction with the spray and the spray recirculation on the far spray field.
- *Investigation in optical engine.* As the final stage of this investigation is concerned about the study and characterisation of the Spray under real condition then this section presents the papers related to spray investigation in optical engines.
- *pintle-type Injector.* This type of injector was recently introduced in the direct-injection gasoline engines. For this reason the state of the art and the review of literature on this injector is limited. Thus, this section provides most of the currently available literature/information on the pintle-type Piezo Injector.

- *Miscellaneous on DISI concept.* Finally the last group of papers describes general characteristics of the DISI technology.

The tabular format provides an easily readable list which summarises the papers related with the present investigation. The columns of the tables are subdivided for Authors and year of publication , Experimental Set-up and equipment, experimental techniques or processing procedures and in the last column the major conclusions and findings of the investigation.

## 2.2. INTERNAL FLOW CHARACTERISATION IN LARGE-SCALE MODELS

Authors and Year	Experimental Set-up	Techniques	Major Findings
J. M. Nouri, N. Mitroglou, Y. Yan and C. Arcoumanis (2007) [7]	Steady state flow test rig with large-scale model injector (Multihole six-hole mini sac type nozzle)	<ul style="list-style-type: none"> <li>• Mie Scattering</li> </ul>	<ul style="list-style-type: none"> <li>• The visualisation revealed that the flow into the nozzle holes is originated either from the incoming annular flow above the six injection holes or from the deflected annular flow in-between two adjacent injection holes.</li> <li>• This seemed to be the cause for the formation of vortices in the sac volume between the needle face and the two adjacent injection holes.</li> <li>• Needle strings appeared first in the multi-hole gasoline injector prior to any cavitation hole structures.</li> <li>• Onset cavitation starts for cavitation number approaching 0.7 to 0.9 and presents a well developed structure for CN higher than 1 when needle string start to disappear.</li> <li>• Following the disappearance of the needle strings, another type of string known as 'vortex string'.</li> </ul>
Nouri, J.M., Abo-Serie, E., Marchi, A., Mitroglou, N. Arcoumanis, C. (2005) [26]	Steady state flow test rig with large-scale model injector (outward opening gasoline direct injector)	<ul style="list-style-type: none"> <li>• Imaging of internal nozzle flow patterns and cavitation structures with CCD and high-speed video cameras</li> <li>• Laser Doppler Velocimetry</li> </ul>	<ul style="list-style-type: none"> <li>• Four jet-like flows were identified internally and upstream the valve seat due to the design configuration of the needle.</li> <li>• In the mixing chamber of the four jet-like flows just upstream the valve seat, four pairs of counter-rotating vortices were identified with highly unstable patterns</li> <li>• The aforementioned instability can be seen downstream the valve seat on the spray itself</li> <li>• Confirmed the existence of cavitation initiated on the valve seat.</li> </ul>

Matsumura E., Tomita T., Takeda K., Furuno S., Senda J., (2003)[27]	Enlarged model of a slit nozzle. Argon ion laser CCD and high speed video camera	<ul style="list-style-type: none"> <li>• Mie Scattering</li> </ul>	<ul style="list-style-type: none"> <li>• Unsteady flow forms were developed due to periodic vortices generated in the sac.</li> <li>• The smaller the disturbances in the seal, such as injection pressure, needle lift and seal shape, the smaller the scale vortex in the sac.</li> <li>• Sac flow fluctuation and variation had a large effect on flow in the slit nozzle.</li> <li>• Spray angle was found dependent upon the vortex in the sac. A small vortex resulted in reduced spray angle, stronger penetration and fine atomisation.</li> <li>• Spherical seal was found to suppress the scale of the vortex within the sac and promote penetration as well as atomisation.</li> </ul>
I.S. Carvalho a, M.V. Heitoyr b, D. Santos (2002) [28]	The 2-D liquid film generator consists of: (i) an inner liquid flow, with an exit thickness of $t_l=0.7$ mm, and an aspect ratio of $L/t_l = 114$ , that is, 80 mm wide; and, (ii) two co-current air flows, with a thickness $t_g=7$ mm, which are passed along both sides of the liquid .lm to produce a shear force at the air-liquid interface.	Back light and laser light sheet illumination, to visualise the instability amplitudes, which leads to the liquid film disintegration and the spray formation; strobe light illumination, for the quantification of either breakup lengths and frequencies, a laser attenuation technique for frequency measurements	<ul style="list-style-type: none"> <li>• The disintegration of the liquid sheet is associated with a periodic process, which is mainly dependent on the absolute air velocity and the air-liquid momentum ratio.</li> <li>• An extended analysis of the non-dimensional breakup lengths and breakup frequencies showed the importance of the air-to-liquid momentum ratio group, MR, as the parameter that allows to correlate the present results.</li> </ul>



Roth et al. (2002) [29]	Steady-state and quasi transient flow test rig with large-scale model injector (transparent 6-hole conical mini-sac and VCO type nozzle)	<ul style="list-style-type: none"> <li>• Refractive index matching technique</li> <li>• Laser Doppler Velocimetry measurements in mini-sac nozzle</li> <li>• Imaging of cavitation structures in both nozzle types with high-speed digital video</li> </ul>	<ul style="list-style-type: none"> <li>• Vortex flow inside nozzle tip volume is prerequisite for string cavitation</li> <li>• Cavitation strings in the nozzle tip volume can induce hole cavitation</li> <li>• Strong helical flow and 'needle strings' inside injection hole of VCO nozzle identified</li> <li>• Cavitation initiation at side corners of hole inlet possible</li> <li>• Higher needle lift results in more stable cavitation flow structures for both nozzle types</li> <li>• No appreciable liquid movement identified in lower nozzle tip volume</li> <li>• Non-cavitating flow conditions result in reduced recirculation zones close to the injection hole entrance for higher needle lifts</li> <li>• Turbulence levels increase in lower part of injection hole with increasing cavitation numbers at moderate flow rates</li> <li>• At moderate as well as increased flow rates the normalized RMS are higher at low needle lifts compared to those at high needle lifts due to bottleneck effect</li> <li>• Increasing cavitation and Reynolds numbers result in higher turbulent kinetic energy in the injection hole bulk flow although this increase is less apparent further downstream</li> <li>• Close to the hole exit the averaged TKE decreases asymptotically to the turbulence level of the non-cavitating flow due to cavitation bubble breakup</li> </ul>
----------------------------	--	---	--

Soteriou et al. (2000) [30]	Steady-state flow test rig with transparent 20x scaled up models of plain orifices employing either variable throttling of the injection hole exit or the hole inlet; injection into atmosphere	<ul style="list-style-type: none"> <li>• Refractive index matching technique</li> <li>• Laser light sheet illumination and still imaging of non-cavitating flow (seeded with hollow glass spheres)</li> <li>• Laser Doppler Velocimetry measurements close to hole exit</li> <li>• Spray visualisation and determination of spray angle</li> </ul>	<ul style="list-style-type: none"> <li>• Flow through throttled model orifices and emerging jets/sprays are significantly different compared to those produced by conventional sac or VCO type nozzles</li> <li>• Fan-shaped jets, horseshoe-shaped jets and quasi-normal sprays were observed for decreasing degree of exit throttling; cavitation is suppressed for most of the investigated conditions</li> <li>• In the case of hole entry throttling, hollow non-circular, non-circular, two-jet and rotated non-circular sprays were identified with progressive opening of the hole; cavitation occurred at reduced levels compared to normal nozzles and produced bushy opaque sprays in some cases</li> <li>• Overall, inlet throttling causes spray angles to be significantly wider than with normal orifices, but not as large as with exit throttling</li> <li>• Entry throttling causes the flow velocity to drop appreciable inside the orifice, while exit throttling seems to have a smaller effect on the velocity; thus, for the same degree of throttling, partially open entry throttled holes produce lower spray velocities than partially open exit throttled holes</li> </ul>
David P. Schmidt, C. J. Rutland and M. L. Corradini P. Roosen and O. Genge (1999) [31]	flat nozzle design between two thick quartz glass windows. A steel lamella is placed, creating the contour of the ejection canal after a long, large, inlet flow cross section. The liquid is fed through a hole in one of the quartz windows .The "bore hole" consists of a rectangular-shaped canal	<ul style="list-style-type: none"> <li>• 2D simulation</li> <li>• Mie Scattering</li> </ul>	<ul style="list-style-type: none"> <li>• Photographs revealed that the liquid-vapor interface is smooth near the inlet corner and becomes rough and convoluted near the end of the cavitation region.</li> <li>• The occurrence of cavitation at the inlet corner was found to be similar to that of axisymmetric nozzles. The occurrence of separation at the nozzle exit was found to be a function of Reynolds number for low cavitation numbers and a function of cavitation number for high Reynolds number.</li> </ul>

Afzal et al. (1999) [32]	Steady-state flow test rig with enlarged model injector (transparent 6-hole conical mini-sac and VCO type nozzle)	<ul style="list-style-type: none"> <li>• Refractive index matching technique</li> <li>• Flow rate and pressure measurements</li> <li>• Imaging of cavitation structures with CCD camera</li> <li>• Calculations for non-cavitating conditions</li> </ul>	<ul style="list-style-type: none"> <li>• Initiation and development of cavitation structures inside the injection holes and nozzle volumes were visualized and this revealed different patterns in terms of spatial and temporal development of the cavitation bubbles as a function of needle lift and needle eccentricity</li> <li>• Discharge coefficient decreases asymptotically to its minimum value for increasing cavitation numbers</li> <li>• Over a wide range of nozzle operating conditions significant transient pressure variations (5-10% of the mean) have been recorded for the difference between upstream and downstream pressure</li> <li>• From the various images obtained, comprehensive sketches were drawn summarising the most important observations of the cavitating flow structures in the two nozzles</li> <li>• CFD calculations of velocity flow field, pressure and turbulent kinetic energy distribution for varying needle lift and nozzle geometries</li> </ul>
Yule et al. (1998) [33]	Large-scale axisymmetric models of VCO nozzle orifice (sharp and rounded orifice inlet edge) under transient flow conditions due to fast valve (needle) movement; various working fluids were utilised	<ul style="list-style-type: none"> <li>• High-speed video imaging of developing orifice flow for different injection pressures and atmospheric backpressure</li> <li>• Valve opening rate determination from image data</li> <li>• Pressure measurements and calculation of discharge coefficient</li> </ul>	<ul style="list-style-type: none"> <li>• Interesting aspects of internal flow development occurred during first third of injection duration</li> <li>• Recirculation zone at the orifice inlet contains cavitation bubbles above a certain pressure drop</li> <li>• Movement of the pulsing recirculation zone near the orifice wall towards the orifice exit is believed to cause hydraulic flip above a certain Reynolds number even without occurrence of cavitation</li> <li>• Atomisation occurred more rapidly for the orifice with sharp inlet edge compared to the rounded one under the same pressure conditions</li> </ul>

<p>Soteriou, C. Smith, M. Andrews, R.J (1998) [34]</p>	<p>Steady-state flow test rig with a scaled up plain orifice nozzle; injection with un-submerged and submerged outlet</p>	<ul style="list-style-type: none"> <li>• Refractive index matching technique</li> <li>• Laser light sheet illumination and still imaging of cavitation</li> <li>• Laser Doppler Velocimetry measurements in non-cavitating flow</li> <li>• Pressure measurements</li> </ul>	<ul style="list-style-type: none"> <li>• Downstream, close to orifice inlet, is a strong flow recirculation area and separation of the boundary layer for non-cavitating flow conditions</li> <li>• This separated flow strongly influences the cross-sectional velocity profiles</li> <li>• Formation of hole cavitation structures depends on Reynolds number of flow upstream of orifice: <ul style="list-style-type: none"> <li>→ Laminar flow allows large voids to form</li> <li>→ Turbulent flow encourages formation of small bubbles</li> </ul> </li> <li>• Cavitation within attached boundary layer causes emerging spray to become slightly bushy and increases the spray angle</li> <li>• When plug cavitation extends to orifice outlet the angle and bushiness of spray increases significantly</li> <li>• Flow in cavitating plug is more turbulent than non-cavitating flow which is believed to be a reason for improved spray development</li> </ul>
<p>Arcoumanis et al. (1998) [35]</p>	<p>Steady-state flow test rig with enlarged model injector (transparent 6-hole conical mini-sac type nozzle)</p>	<ul style="list-style-type: none"> <li>• Refractive index matching technique</li> <li>• Laser Doppler Velocimetry</li> <li>• Flow rate measurements</li> <li>• Imaging of cavitation structures with CCD and high-speed camera</li> <li>• Calculations for non-cavitating conditions</li> </ul>	<ul style="list-style-type: none"> <li>• Flow rate shows asymptotic behaviour for needle lifts higher than a value that is still "far" below full lift</li> <li>• Even for symmetric nozzle conditions the individual hole flow rates can vary noticeably due to small differences in hole size, wall roughness and hole inlet shape</li> <li>• CFD calculations of velocity flow field, pressure and turbulent kinetic energy distribution for varying needle lift and nozzle geometries as a parametric study</li> <li>• CFD calculations confirmed that manufacturing tolerances in the geometry of the nozzle from its nominal geometric characteristics result in unequal flow distribution between the injection holes</li> <li>• LDV results from measurements of local mean velocities and RMS values were used to validate CFD calculations; predictions are generally in good agreement with experimental values, but do not capture well the recirculation zone at the hole inlet</li> <li>• Initiation and development of cavitation structures inside the injection hole were visualized and this revealed different patterns in terms of spatial and temporal development of the cavitation bubbles as a function of needle lift and needle eccentricity</li> </ul>

He and Ruiz (1995) [36]	Enlarged two-dimensional channel flow rig with liquid into liquid injection; working fluid is water	<ul style="list-style-type: none"> <li>• Laser Doppler Velocimetry</li> <li>• Flow rate measurements</li> </ul>	<ul style="list-style-type: none"> <li>• Turbulence after cavitation zones was found to be higher than after recirculation zones</li> <li>• Noticeable pressure losses were caused by increased turbulent kinetic energy in case of cavitating flow</li> <li>• Cavitation has strong influence on velocity profiles across the flow area near the channel inlet</li> </ul>
Soteriou et al. (1993) [37]	Steady-state flow rig with large-scale model nozzles; transient injection test rig with various real-size nozzles; injection into liquid and into gas	<ul style="list-style-type: none"> <li>• Mie Imaging</li> <li>• pressure measurements and calculation of nozzle discharge coefficients</li> </ul>	<ul style="list-style-type: none"> <li>• Investigation of large-scale nozzle flow and spray characteristics considered to be a valuable tool when cavitation and Reynolds number are matched simultaneously to those found in real-size flows</li> <li>• Overall, results from investigations in large-scale and real-size nozzles in good agreement</li> <li>• Cavitation in injection holes to be found the predominant mechanism causing spray atomisation</li> <li>• Cavitation encourages separation in the boundary layer of the nozzle hole flow</li> <li>• Higher turbulence levels in nozzle flow can prevent occurrence of hydraulic flip phenomenon</li> <li>• Hydraulic flip is believed to cause unequal sprays from VCO nozzles</li> <li>• VCO nozzles with eccentric needle produce hollow cone sprays</li> <li>• Discharge coefficient only depends on cavitation number and not on Reynolds number</li> <li>• Cavitation characteristics do not change beyond a specific cavitation or Reynolds number and above a certain pressure</li> </ul>
Arcoumanis et al. (1992) [38]	Steady-state flow test rig with enlarged model injector (transparent single-hole nozzle) Refractive index matching	<ul style="list-style-type: none"> <li>• Laser Doppler Velocimetry</li> </ul>	<ul style="list-style-type: none"> <li>• Simulating Diesel fuel with a mixture of hydrocarbons having the same refractive index as the acrylic model nozzle proved to be a useful tool in characterizing the internal flow in Diesel injectors</li> <li>• Three-dimensional components of mean velocities and RMS values measured for <math>Re = 18800</math></li> <li>• The measured flow field provided insight into the dependence of the injector flow on nozzle geometry, needle lift and injection pressure</li> <li>• The results are useful for validating multi-dimensional CFD models</li> </ul>



Laurent Pouvreau [39]	Water at room temperature is pressurized within an accumulator using an air pump. An adjustable heater gives the possibility to study the effect of water temperature. Four types of nozzles are being used.	Integral Mie Scattering	<ul style="list-style-type: none"> <li>Preliminary results show that the jet coming out of a nozzle is highly depending on the internal flow. Though high pressure atomisation is the usual process, low pressure atomisation can be achieved by using a cavitating flow. However, this flow is unstable and as the cavitation extends might lead to the hydraulic flip, where the flow is completely detached from the wall and atomisation does not occur anymore. The coming step will now be an attempt to correlate the proprieties of the jet with the turbulence within the nozzle.</li> </ul>
-----------------------	--	-------------------------	---

**Table 2-1 Internal flow characterisation in large-scale models**

## 2.3. SPRAY FLOW CHARACTERISATION IN REAL SIZE MODELS

Authors and Year	Experimental Set-up	Techniques	Major Findings
Roland Domann, Yannis Hardalupas (2002) [40]	Spray produced by a atomizer, which injected liquid on the centreline of an industrial burner	<ul style="list-style-type: none"> <li>Droplet Sizing</li> <li>Planar Droplet Sizing technique</li> </ul>	<ul style="list-style-type: none"> <li>The results presented in this article confirm that accurate, quantitative information can be obtained from Planar Droplet Sizing if careful image pre-processing is applied, the correct dye concentration is chosen and the calibration is adapted according to the characteristics of the scattered and fluorescence light dependence on droplet diameter.</li> </ul>

Hyeonseok Koh, Kihoon Jung and Youngbin Yoon [41] (2002)	A solid-cone spray was used to obtain the uniform volume distribution. The spray was injected vertically at an atmospheric condition. In order to obtain fluorescence signals, a methanol/water solution containing 30 mg/l fluorescence in dye (Aldrich F245-6, C <sub>20</sub> H <sub>12</sub> O <sub>5</sub> ) was used as a test fluid.	<ul style="list-style-type: none"> <li>• Planar imaging Techniques</li> </ul>	<ul style="list-style-type: none"> <li>• The mass distribution of a solid-cone spray was obtained using laser induced fluorescence signal since the fluorescence signal is proportional to the volume or the mass of spray.</li> <li>• It was found that if the signal was attenuated asymmetrically due to the viewing perspective or the significant non-uniformity of spray pattern, the single-image detection may not give accurate information on the local fuel mass distribution either quantitatively or qualitatively.</li> <li>• The size distribution is also affected by the signal attenuation, because the attenuation coefficient may be dependent upon the wavelength of the signal.</li> </ul>
Z. Dai, G.M. Faeth (2001) [42]	The tests were carried out in a rectangular shock tube with the driven section open to the atmosphere and the side walls windowed to provide optical access. A vibrating capillary tube drop generator, and an electrostatic drop selection system.	<ul style="list-style-type: none"> <li>• Single- and double-pulse shadowgraphy and holography</li> </ul>	<ul style="list-style-type: none"> <li>• With increasing Weber numbers, the multimode breakup regime begins at the end of the bag breakup regime at <math>We = 18</math> and ends at the start of the shear breakup regime at <math>We = 80</math>.</li> <li>• With increasing <math>We</math> in the range <math>18 \pm 80</math>, <math>t/t_*</math> at the onset of breakup decreases from a value of 3.0 to a value of 2.0 at the onset of shear breakup. The end of breakup has values of <math>t/t_* = 4.0</math> and 5.0</li> <li>• Drop deformation and drag properties prior to the onset of breakup appear to be relatively universal for <math>We</math> of <math>13 \pm 150</math></li> </ul>
Nouri J.M., Brehm C, Whitelaw J.H (1999)[43]	Prototype swirl injector In a Constant volume chamber	<ul style="list-style-type: none"> <li>• Mie Scattering</li> <li>• Phase Doppler Anemometry</li> </ul>	<ul style="list-style-type: none"> <li>• It was found that the shape of the spray is almost independent of the injection pressure (30,70 and 100bar). However, the spray penetration was found to increase by increasing the injection pressure.</li> <li>• The maximum droplet velocities were found to increase from 50 m/s to 70 m/s by increasing the injection pressure from 30 bar to 70 bar respectively while the arithmetic as well as the Sauter mean diameters (30 and 60<math>\mu</math>m respectively) were found to be nearly independent of the injection pressure.</li> </ul>

<p>Kashdan J.T., Shrimpton J., Arcoumanis C. (1999)[44]</p>	<p>Constant volume chamber. Single cylinder spray-guided optical engine with flat piston</p>	<ul style="list-style-type: none"> <li>• Spray imaging</li> <li>• Mie scattering</li> <li>• Phase Doppler Anemometry</li> </ul>	<ul style="list-style-type: none"> <li>• High chamber pressure under quiescent conditions was found to suppress both the axial and radial spray penetration of a swirl injector spray. Increasing the pressure from 1 to 5 bar led to a reduced spray penetration by 25% by the end of the injection and decreased cone angle from approximately 60° to 49°.</li> <li>• In-cylinder spray visualisation showed that for central positioning of the injector, (a) During the intake stroke the airflow has relatively little effect on the generated spray structure in terms of spray dispersion, repeatability and symmetry. However the toroidal vortex becomes distorted as a result of a combined air motion induced by the tumble and the secondary flow caused by the downward moving piston.</li> <li>• (b) For the late injection strategy the higher in-cylinder pressures caused significant contraction of the spray which resembled more a solid than a hollow cone type. Spray images revealed that piston impingement occurred with resulting liquid film.</li> <li>• An increase in the chamber pressure from 1bar to 7 bar caused significant reduction in the droplet velocities and resulted in increased mean droplet diameters.</li> </ul>
<p>Abo-Serie E., Arcoumanis C., Gavaises M. (1999)[45]</p>	<p>Constant volume chamber CCD camera</p>	<ul style="list-style-type: none"> <li>• Mie Scattering</li> </ul>	<ul style="list-style-type: none"> <li>• The spray development generated by a high pressure swirl injector was analyzed and four stages were identified. The first two correspond to the period prior to the liquid film formation, in the nozzle hole, while the other two to the period of film development.</li> <li>• A very early asymmetric purely atomised bulk of liquid located at the centre of the injection hole</li> <li>• An asymmetric non-hollow spray</li> <li>• A swirl developing hollow-cone spray with a multi layer structure</li> <li>• A fully developed and well-atomised hollow cone spray with cone angle nearly independent of injection pressure.</li> <li>• High magnification images revealed 2 modes of droplet formation, through ligaments in the direction of injection and through wave crest stripping in the radial direction.</li> </ul>

Adomeit P., Lang O., Pischinger S., (2000)	Spray visualisation CCD camera	<ul style="list-style-type: none"> <li>• Computational Fluid Dynamics</li> <li>• Mie scattering</li> <li>• Phase Doppler Anemometry</li> </ul>	<ul style="list-style-type: none"> <li>• CFD provides valuable information on the spray propagation and mixture formation when validated models of atomisation and spray generation are used.</li> <li>• The validation of the current model was achieved by comparing the calculated results with Schlieren visualization and PDA measurements.</li> <li>• The simulation reveals the importance of the pre-jet on penetration as well as on the overall spray behaviour as it carries a sufficient momentum to induce a secondary recirculation gas flow which strongly contracts the main conical spray.</li> <li>• In-cylinder CFD analysis, for particular air guided engine, shows that the tumble charge motion strongly affects the spray propagation and mixture formation in the stratified operation mode by transporting the fuel vapor cloud towards the spark plug.</li> </ul>
Miyajima A., Okamoto Y., Kadomukai Y., Togashi S., Kashiwaya M., (2000)[46]	High pressure chamber CCD camera	<ul style="list-style-type: none"> <li>• Mie scattering</li> <li>• Computational Fluid Dynamics</li> </ul>	<ul style="list-style-type: none"> <li>• A method of controlling the fuel spray pattern was developed. A swirl type DI fuel injector with L-cut orifice nozzle (L-type) and a taper-cut orifice nozzle (taper type) were designed. The fuel spray patterns of these injectors were measured experimentally for different ambient and fuel pressures and simulated numerically.</li> <li>• Experimentally and numerically it was confirmed that the L-type and the Taper-type nozzles produced inclined spray pattern.</li> <li>• The Spray angle of the L-type nozzle decreased by 0.5° and that of the taper-type by 2.6° degree respectively as ambient pressure increased from 0.1 to 0.6 MPa.</li> <li>• The influence of the fuel pressure was minor for both nozzles.</li> <li>• The spray pattern was found to be controllable by changing the depth of the orifice. The general trend was that by increasing the L/D the cone angle as well as the penetration of both nozzles decreased.</li> <li>• CFD code show that the fuel velocity contours and the air void shapes inside of both orifices are inclined which results in inclined fuel sprays. In addition it could predict the spray angle with reasonable accuracy.</li> </ul>



VanDerWege B., Hochgerb S., (2000)[47]	Modified flat head and piston single cylinder optical engine with square cross section which allows optical access through three quartz windows	<ul style="list-style-type: none"> <li>• Phase Doppler particle analysis (PDPA)</li> </ul>	<ul style="list-style-type: none"> <li>• The spray structure and droplet diameter distribution were observed over a wide range of engine temperatures and sub-atmospheric ambient pressures in a DISI engine.</li> <li>• Droplet mean diameter was found to decrease substantially with increasing fuel temperature and decreasing ambient density.</li> <li>• Under conditions with high potential for vaporization (low pressure, high temperature), an additional droplet size reduction mechanism was observed which was associated with flash boiling or evaporation of the volatile components in the fuel.</li> <li>• A good correlation was found between the spray cone angle expansion and the decrease in the measured droplet diameter under high volatility conditions. This suggests that expansion of the initial cone angle, thinning liquid sheet, may be dominant mechanism leading to increased atomisation.</li> <li>• Spatial and temporal variations in droplet diameter were found to be relatively small compared with changes due to operating conditions while variation in droplet velocity behave as expected (decrease after the end of injection).</li> </ul>
Nouri J.M., Whitelaw J., (2002)[48]	High pressure chamber Intensified CCD Camera Argon-ion laser sheet	<ul style="list-style-type: none"> <li>• Mie scattering</li> <li>• Phase Doppler Anemometry</li> </ul>	<ul style="list-style-type: none"> <li>• The photographic investigation of a prototype swirl injector indicated delay times of 0.225 and 0.2ms due to the opening and closing of the needle of the injector.</li> <li>• The shape of the sprays was nearly independent of injection pressure at all chamber pressures.</li> <li>• The effect of chamber pressure was considerable with large reduction in droplet mean velocity by up to 50%, spray cone angle by 35%, suppression of the droplet velocity fluctuations by 40% , and an increase in the droplet arithmetic Sauter mean diameters by up to 20% with an increase in the chamber pressure from 1 to 12 bar.</li> </ul>

<p>Mitroglou N., Nouri J.M., Arcoumanis C., (2002)[49]</p>	<p>Constant volume chamber Common rail system Six hole multihole injector CCD camera Strobe light</p>	<ul style="list-style-type: none"> <li>• Mie scattering</li> <li>• Phase Doppler Anemometry</li> </ul>	<ul style="list-style-type: none"> <li>• The overall angle of each spray from the injector axis was found to be 40° and almost independent of the injection pressure (120, 200 bar).</li> <li>• The effect of chamber pressure was to reduce the spray tip penetration of each of the six sprays due to the increased drag.</li> <li>• Temporal velocity profiles revealed that the droplet velocities increased sharply at the start of injection to a maximum value, then remained unchanged, during the main part of injection, before decreasing rapidly towards the end of injection.</li> <li>• The spatial velocity profiles were jet-like at all axial locations with the maximum values on the spray axis.</li> <li>• The Sauter mean diameters in the main spray at 10mm plane from the nozzle exit were of the order of 19 and 14µm at injection pressure of 120 and 200 bar respectively under atmospheric chamber pressure.</li> <li>• The effect of injection pressure on the droplet size was small while the increase in chamber pressure resulted in smaller droplet velocities by up to fourfold and larger droplet sizes by up to 40%</li> </ul>
<p>Miyajima A., Okamoto Y., Kadomukai Y., Kashiwaya M., Kubo H., Fujii H., (2003)[50]</p>	<p>High pressure chamber</p>	<ul style="list-style-type: none"> <li>• Mie scattering</li> <li>• Phase Doppler particle analysis</li> </ul>	<ul style="list-style-type: none"> <li>• The spray pattern of swirl type injectors with a V-groove cut orifice nozzle and a U-groove nozzle were investigated experimentally by accounting for the influences of ambient pressure and fuel pressure.</li> <li>• V-groove nozzle produced flat hollow cone spray pattern while U-groove nozzle produced flat solid cone spray pattern.</li> <li>• The spray angle in the flat cross section of the V-groove nozzle decreased by 11° and that of the U-groove nozzle by 1° for an ambient pressure increase of 0.5 MPa while the penetration of both nozzles decreased by 16mm for the same pressure rise.</li> <li>• By increasing the injection pressure from 5 to 12 MPa the spray cone angles of both the V-groove and U-groove decreased less than 3° while penetration increased by approximately 6mm.</li> <li>• Measurements showed that the spray pattern could be controlled by the orifice-depth</li> <li>• SMD increased by, increasing ambient pressure or decreasing injection pressure.</li> </ul>

<p>Tanaka Y., Takano T., Sami H., Sakai K., Osumi N., (2003) [51]</p>	<p>Constant volume chamber CCD camera</p>	<ul style="list-style-type: none"> <li>• Schlieren Shadowgraphy</li> </ul>	<ul style="list-style-type: none"> <li>• The spray behaviour produced by four swirl nozzles with designed cone angle 40°, 60°, 90° and 110° and a slit nozzle with 60° spray angle were studied using a constant volume chamber and three kinds of single component fuels as well as gasoline.</li> <li>• The sprays penetrate at a constant speed for a while after the injection start and the inside of these was found no to be hollow. This indicates that spray does not entrain air and the widening after the injection start is caused by fuel vaporization inside the spray.</li> <li>• The sprays begin to decelerate at a certain time and the deceleration time coincides with the turbulence occurring time, ascertained in the spray behaviour obtained by Shadowgraph images.</li> <li>• A breakup theory was proposed and a non-dimensional equation was introduced which describes the breakup conditions in relation to various parameters such as ambient pressure and temperature, fuel properties, and nozzle specifications.</li> </ul>
<p>Pontoppidan M., Gaviani G., Bella G., De Maio A., (2004)[52]</p>	<p>High pressure flow rig High pressure chamber Firing engine</p>	<ul style="list-style-type: none"> <li>• Spray imaging based on continuous or phase controlled flash illumination</li> <li>• Particle Image Velocimetry</li> <li>• Phase Doppler Anemometry</li> <li>• Computational Fluid Dynamics</li> </ul>	<ul style="list-style-type: none"> <li>• The main objective of the particular study was to isolate the fundamental injector atomizer parameters to optimize within the frame of physical phenomenon of mixture preparation in a high-speed spray-guided wide spacing racing engine operating at homogeneous stoichiometric mode.</li> <li>• The data collected from visualisation measurements, PIV and PDA on various sprays produced by a swirl, a closed cap slit, a multihole, and a colliding jet multihole injector were used as inputs to the CFD optimization code.</li> <li>• A 4 hole multihole injector with the holes located in a linear array with a maximum angular separation of the outer jet axis of 80° was found to give the best results which were also validated during the firing engine tests.</li> <li>• Although the colliding multihole injector had the potential to give the best performance results, as it promotes a secondary break up, it did not give any improvement compared to the multihole injector due to the very limited free path space available in the racing engine around the intake TDC.</li> <li>• The work done showed that it is possible to obtain a potential 2% high-end performance gain with DI-technology compared to PFI-technology.</li> </ul>

Choi J., Lee S., Bae C., (2004)[53]	Wind tunnel used for the simulation of a range of in-cylinder flow conditions. High pressure swirl injector.	<ul style="list-style-type: none"> <li>• Mie scattering</li> <li>• Shadowgraphy</li> <li>• Phase Doppler Anemometry</li> </ul>	<ul style="list-style-type: none"> <li>• High pressure swirl injection characteristics of a GDI injector in a cross-flow up to 15m/s were investigated to study the interaction between flow field and spray.</li> <li>• The sac spray penetration (pre spray) depth varied with injection but the main spray penetration depth and spray width were not affected by the injection pressure or the cross-flow velocity.</li> <li>• Fuel vaporization rate was found to be proportional to cross-flow velocity.</li> <li>• Liquid and vapor fuel were distinguished by Mie scattered images and shadowgraphy.</li> <li>• The PDA velocity measurements showed the existence of vortices with different motion at various cross-flow velocities.</li> <li>• Acceleration of the fuel droplet vaporization by increasing cross-flow velocity was confirmed by PDA.</li> </ul>
Hung L.S., Chmiel M.D., Markle L.E., (2004)[54]	High pressure flow rig Delphi single cylinder spray-guided optical engine with flat piston	<ul style="list-style-type: none"> <li>• Mie scattering</li> <li>• Cylinder head flow bench testing</li> <li>• Particle Image Velocimetry</li> </ul>	<ul style="list-style-type: none"> <li>• The Presence Probability Image (PPI) technique was demonstrated for the evaluation of the macroscopic spray variations of a swirl injector, both at atmospheric as well as in-cylinder engine conditions.</li> <li>• In addition to the standard spray characteristics, such as spray tip penetration and spray cone angle the two-dimensional global spray structure variation was also revealed by using the probability approach. Therefore multiple spray characteristics could be examined simultaneously.</li> <li>• By overlaying an individual spray boundary on the PPI a visualisation of the two-dimensional spray structure variation can be obtained.</li> </ul>
Abe M., Okamoto Y., Kadomukai Y., Tanabe Y., Ishikawa T., (2004)[55]	High pressure chamber CCD camera	<ul style="list-style-type: none"> <li>• Mie scattering</li> </ul>	<ul style="list-style-type: none"> <li>• Two new nozzles with new spray pattern were developed for meeting the needs of the wide spacing and the close spacing spray-guided DISI configurations.</li> <li>• An L-cut orifice nozzle that produces a horseshoe spray pattern was used to create a rich and lean concentration region. The spray shape and the fuel distribution was found to be controllable by configuring the L-cut step walls.</li> <li>• The rich portion within the horseshoe spray fuel distribution is created from the vertical side edge of the L-step while the lean portion is created by the obstruction of the L-step wall</li> </ul>



<p>Kubo. M., Sakakida. A., Iiyama. A., (2001)[56]</p>	<p>Spray visualization of three prototype nozzles, (strong swirl, weak swirl, strong swirl tapered), in a high pressure chamber using laser sheet and two CCD cameras operating with a slight delay produced by a highly accurate delay system.</p>	<ul style="list-style-type: none"> <li>• Particle image Velocimetry (PIV).</li> <li>• Computational Fluid Dynamics</li> </ul>	<ul style="list-style-type: none"> <li>• The developed CFD code for analyzing the flow through the swirl injector can be used to calculate the spray formation process to some extent, from the development of the initial spray to the main spray.</li> <li>• Properties critical to the nozzle design such as the flow coefficient, cone angle and cavity factor can be calculated with relatively good accuracy, at atmospheric as well as backpressure conditions, in comparison with the theoretical formula proposed by Tanasawa.</li> <li>• Increasing the fuel injection pressure promotes better atomisation leading to a smaller mean droplet size and more homogeneous spray distribution. However that effect is reduced under a condition of high backpressure. The mechanism of atomisation is closely related to the spray flow velocity distribution during fuel injection.</li> <li>• The reason why a nozzle with a tapered tip produces a spray shape that is laterally asymmetrical is the flow rate distribution toward the circumference of the nozzle hope exit.</li> </ul>
<p>Seoksu Moon, Jaejoon Choi, Essam Abo Serie and Choongsik Bae (2005) [57]</p>	<p>Wind tunnel with optical access allowed by an acrylic transparent window. The injectors tested were a slit injector and a swirl injector The Injectors were heated by circulating water inside an injector adapter.</p>	<ul style="list-style-type: none"> <li>• 2d Mie Scattering and Shadowgraphy</li> <li>• Phase Doppler Anemometry</li> </ul>	<ul style="list-style-type: none"> <li>• Injector temperature showed an influence not only on the macroscopic structure but also on the droplet diameter distribution within the free spray.</li> <li>• Increasing the injector temperature decreases the spray penetration and increases the spray width for slit injector. However when using the swirl injector the reverse trend was observed. A reduction in diameter was found when the injector temperature increases for both injector.</li> </ul>
<p>Eriko Matumura, Tomojiro Sugimoto, Mutsumumi Kanda (2006) [58]</p>	<p>10 and 2.2 times enlarged Slit Injector .To visualize the fuel flow within the sac, a polyamide resin tracer was mixed into the compressed fuel</p>	<ul style="list-style-type: none"> <li>• 2D Mie scattering</li> <li>• 3D Mie scattering shadowgraphy</li> <li>• Phase Doppler Anemometry</li> </ul>	<ul style="list-style-type: none"> <li>• The vortices that form within the sac continuously propagate in a periodic manner within the sac.</li> <li>• The streamline of fuel that flows from the sac to the slit is influenced by the continuous vortices within the sac.</li> <li>• The smaller the scale of vortices that form within the sac, the thinner the liquid film region at the edge of the slit and the larger the cavitation region in the central portion of the slit.</li> </ul>

Yan-jun Wang, Jian-Xin, Shi-Jin, Xiao-Hu Lei and Xin-Liang An (2005) [59]	Swirl spray in a High Pressure chamber	<ul style="list-style-type: none"> <li>• Computational Fluid Dynamics (KIVA program)</li> <li>• Mie scattering</li> </ul>	<ul style="list-style-type: none"> <li>• Spray penetration increases with injection pressure while the impact of injection pressure on the main cone are little comparatively; higher surrounding pressure leads to the shorter penetration distance.</li> <li>• There is an optimal injection timing which result in better injection performance and more homogeneous charge. Too early injection result in piston impingement and too late injection results in cylinder impingement.</li> <li>• The second injection timing can be optimised to form a reasonable mixture concentration distribution in the spark-ignition timing and rich mixture at the periphery of the spark plug which can benefit the stable ignition and quick combustion</li> <li>• Different mass ratio between first and second injection have significant effect on engine performance.</li> <li>• By the optimization of the fuel injection parameters a simple TSGDI combustion system can achieve a fuel consumption 15%-24% lower than PFI</li> </ul>
Anand H., Corey E. Weaver and Eric W. Curtis, Terrence F. Alger, Carl L. Anderson, Duane L. Abata (2006) [60]	Constant volume chamber with ambient temperature kept at 20 °C. and Optical motored engine, Pressure swirl hollow cone injector	<ul style="list-style-type: none"> <li>• Mie scattering</li> </ul>	<ul style="list-style-type: none"> <li>• The cone angle typically enlarged as the MAP decreased</li> <li>• The profile of the cone angle as a function of time after SOF resembled a logarithmic function with an asymptote of 45-50deg</li> <li>• Counteracting effects on the cone angle: as the fuel pressure increased the effect of reducing MAP (increased cone angle) was amplified. As the fuel pressure increased, the spray developed vortices along its edges which had a narrow effect on the cone angle</li> <li>• Sufficient space is required on either side of the spray for vortices to fully develop.</li> <li>• The penetration increases slightly as the MAP decreases.</li> <li>• The frequency of injection was not a significant factor in spray development.</li> </ul>

Anand H. Gandhi, Corey E. Weaver, Eric W. Curtis, Terrence F. Alger, Carl L. Anderson, Duane L. Abata (2006) [61]	Constant volume chamber with ambient temperature kept at 20 °C. Pressure swirl hollow cone injector	<ul style="list-style-type: none"> <li>• Phase Doppler Particle Anemometry</li> </ul>	<ul style="list-style-type: none"> <li>• Counteracting effects on cone angle due to MAP and fuel pressure. As the fuel pressure increased, the effect of reducing MAP was amplified.</li> <li>• The spray velocity was generally constant between 0 – 7.5mm from the injector axis regardless of MAP or fuel pressure. The velocity versus pressure difference across the fuel injector profile resembled a logarithmic function for all MAP values</li> <li>• The SMD typically increased as the radial distance increased from the injector axis</li> <li>• As the pressure difference across the fuel injector increased, the SMD decreased in a profile resembling exponential decay at each position considered.</li> <li>• As the MAP decreased, the SMD generally decreased and the velocity typically increased. The SMD and velocity profile were generally inversely related.</li> </ul>
---	---	---	--

**Table 2-2 Spray flow characterisation in Real size models**

## 2.4. SPRAY RECIRCULATION AND AIR ENTRAINMENT

Authors and Year	Experimental Set-up	Techniques	Major Findings
G.E.Cossali, A.Gerla and A.Coghe, G.Brunello (1996) [62]	Spray injected vertically into a confined quiescent atmosphere and the air entrainment was measured by evaluating the velocity component normal to a cylindrical geometric surface	<ul style="list-style-type: none"> <li>• Laser Doppler Anemometry</li> </ul>	<ul style="list-style-type: none"> <li>• Most of the gas is entrained during the main injection period, after the passage of the spray head.</li> <li>• The non dimensional entrainment air averaged over a time interval corresponding to the main injection period clearly depends on the axial distance and both gas density and temperature</li> <li>• The gas temperature affects the air entrainment directly in fact the gas temperature the mass flow rate increases at constant density</li> <li>• the non dimensional entrainment rate increases with the nozzle distance</li> </ul>

Andriani, R. Coghe, A. Cossali, G.(1996) [63]	Gas or liquid Fuel were injected in a close cylindrical chamber with variable internal pressure and temperature	<ul style="list-style-type: none"> <li>• Constant temperature thermometer</li> <li>• Laser Doppler Anemometry</li> </ul>	<ul style="list-style-type: none"> <li>• A transient period: caused by the passage of the jet head vortex and characterized by a strong similarity between jets and sprays when appropriate dimensionless variables were introduced. The jet head vortex was found to move almost at almost constant velocity <math>V_t</math></li> <li>• A quasi-steady period: this was reached quickly after the passage of the head vortex, when the gas entrainment begins and the nondimensional entrainment rate depends on the nozzle distance for both jet and diesel sprays.</li> </ul>
Cossali, G. E. Coghe, A. Brunello, G (1993)[64]	Close cylindrical chamber and a standard Diesel injector mounted with nozzle flush with the inner wall of the cylinder head, and injecting vertically downward along the chamber axis. To simulate the fuel impingement was used an adjustable plate	<ul style="list-style-type: none"> <li>• laser Doppler Anemometer</li> </ul>	<ul style="list-style-type: none"> <li>• The presence of the wall affects the entrainment by increasing the entrained mass flow rate in the region close to the wall during the main injection period. By increasing the wall angle, the entrainment decreases, thus partially compensating the effect of the presence of the wall</li> <li>• The asymmetry of the impingement geometry (tilted wall) produces an asymmetry in the entrainment through different parts of the cylinder surrounding the spray</li> <li>• The entrainment rate was found to be dependent from the experimental geometry and axial coordinate <math>z</math></li> </ul>
Cossali, G. E. Brunello, G. Coghe, A. (1991) [65]	Close cylindrical chamber and a standard Diesel injector mounted with nozzle flush with the inner wall of the cylinder head, and injecting vertically downward along the chamber axis. The injector system was operated in a controlled continuous mode at variable pump speed	<ul style="list-style-type: none"> <li>• laser Doppler Anemometer</li> </ul>	<ul style="list-style-type: none"> <li>• The present study demonstrated the possibility of detailed, space and time resolved measurement of entrainment rates in transient diesel spray.</li> <li>• The radial distribution of the entrainment velocity <math>U</math> was modeled in function of the time and coefficients depending on space, time and injection pressure history.</li> <li>• The entrainment process takes place mainly during the main injection period that, for the present experiment lasts about 80% of the entire injection duration.</li> <li>• The entrained mass flow rate increases with the injected mass flow rate</li> <li>• The entrainment in the near field zone of transient liquid jet appears to be lower than that in steady liquid jets.</li> </ul>
Siebers, D. L. (1999) [66]	Constant volume combustion vessel with a top-hat injection rate profile	Development of a computational model and comparison with the penetration measured in the chamber.	<ul style="list-style-type: none"> <li>• A law correlating the normalize penetration with the time was modeled for a diesel jet. As a consequence of the scaling law it was modeled the relation between the air entrainment flow rate and the fuel mass flow rate.</li> </ul>



J. J. Sutherland, P. E. Sojka and M. W. Plesniak (1999) [67]	Air collected and measured in an inverted graduated cylinder placed in a water bath. cylindrical housing that enclosed a nozzle mounted to a back plate. Effervescent atomizer with porous medium to control the diameter of ligaments Matheson 602 rotameter with a stainless steel float Omega Engineering FL-1503A rotameter and controlled by a needle valve	Air Entrainment into steady two-phase jets where the gas and liquid streams exhibit interphase velocity slip can be modeled using the momentum rate approach of Ricou and Spalding (1961), although their entrainment number value is no longer applicable. The experimentally determined entrainment number for the two-phase jets studied here increases with ALR.	<ul style="list-style-type: none"> <li>• The appropriate experimentally determined entrainment number, E, for ligament-controlled effervescent atomizer produced sprays is <math>0.15 + 0.056</math>. This value of E predicts entrainment to within 40% for sprays considered in this study.</li> <li>• Entrainment depends on the structure of the spray present at the atomizer exit, as shown by a comparison of results from this study with those of Bush (1994).</li> </ul>
S. Krüger and G. Grünefeld (1999) [67]	Measurements performed in a hollow-cone gasoline direct-injection spray operated with 50bar rail pressure in room air. maximum droplet density is about $5106/\text{cm}^3$ in the probe volume.	• 2D laser-Based Flow Tagging	<ul style="list-style-type: none"> <li>• In comparison to well-established techniques, such as PDA and PIV, the present techniques are much less affected by multiple light scattering, beam steering and beam attenuation in optically thick two-phase flows.</li> <li>• The present techniques yield the possibility to study the interactions of dispersed and continuous phase in highly particle-laden, evaporating and non-evaporating gas flows.</li> </ul>
K.D. Driscoll, V. Sick, C. Gray (2003) [68]	All measurements were performed using a pressure-swirl GDI spray (60° cone angle), which was injected into a static test cell (1000 cm <sup>3</sup> test volume) at room temperature and ambient pressure.	• Particle Imaging Velocimetry (PIV)	<ul style="list-style-type: none"> <li>• A new technique was demonstrated for the simultaneous determination of entrained air velocities and fuel velocities in a dense spray. This method allows for unambiguous phase separation and optimal adaptation to best velocity resolution through the adjustment of laser delay times. The ability to achieve simultaneous velocity measurements with 1-mm resolution will assist efforts to model atomisation and mixing in dense sprays.</li> </ul>

Nauwerck, A. Pfeil, J. Velji, A. Spicher, U. Richter, B.(2005) [69]	Pressurized chamber with optical access. The investigated injectors were high pressure hole type injectors with a nominal cone angle of 90°	<ul style="list-style-type: none"> <li>• Laser light sheet visualization.</li> <li>• Phase Doppler Anemometry</li> <li>• Particle Image Velocimetry</li> </ul>	<ul style="list-style-type: none"> <li>• In the beginning, frictional effects predominate, so both spray width and length reduce. At later point of time, due to inertia of the fuel mass a widening of the jet was observed, while its length remained nearly constant. This effect increases with the pressure.</li> <li>• The basic composition of the airflow with torus-like vortex, entrainment flow and centre flow has been investigated. An increase of maximal velocities in the entrainment flow with higher injection pressure was detected.</li> <li>• Droplet dimension does not increase in the same way as the fuel pressure. High gradients of velocities were detected inside the spray. The smallest droplet diameter was detected at the highest fuel pressure. The Sauter mean diameter was about 13µm at 10 MPa and 6 µm at 50MPa.</li> </ul>
Cossali, G. E. (2001) [70]	model for predicting entrainment into full cone non-evaporating steady spray	<ul style="list-style-type: none"> <li>• Computational Fluid Dynamics</li> </ul>	<ul style="list-style-type: none"> <li>• The model developed here allows the prediction of some important features of the gas entrainment mechanism in steady full cone sprays.</li> <li>• The entrained mass flow rate depends on the distance from the nozzle in a way quite different from that found in steady gaseous jets. In the near-field the entrained mass flow rate follows a 3/2-power law, which leads to a 1/2-power law of the normalized entrainment rate, whereas in the far field the linear dependence of the entrained mass flow rate on nozzle distance (as in gas jets) is recovered.</li> <li>• Comparison with available experimental data seems to confirm this dependence on nozzle distance in the near field with acceptable accuracy.</li> <li>• Two new non-dimensional parameters are found to characterize the entrainment process, namely the non-dimensional mean drop diameter <math>d=D</math> and the nondimensional group <math>\mu D = \mu_0</math>. This explains why the experimental results reported in the form of jet entrainment coefficient or normalized entrainment rate (which do not contain such parameters) under different conditions do not show consistency.</li> </ul>

**Table 2-3 Spray recirculation and air entrainment**

## 2.5. INVESTIGATION IN OPTICAL ENGINE

Authors and Year	Experimental Set-up	Techniques	Major Findings
Y Yan, S Gashi, J M Nouri, R D Lockett and C Arcoumanis (2005) [71]	Piezo pintle-type injector installed inside a 4-valve optical engine with pentroof design. The back of the piston was elongated and hollowed to allow for a fixed 45° mirror to be positioned directly under the cylinder axis. The piston crown has a flat design and offers a good optical access to obtain horizontal images.	<ul style="list-style-type: none"> <li>Planar Laser Induced Fluorescence</li> <li>Laser Doppler Velocimetry</li> </ul>	<ul style="list-style-type: none"> <li>The airflow motion around the tip of the spark plug was measured at engine speeds of 1000 and 1500 RPM, with mean and rms values of up to 16 and 7Vp, respectively, during early induction stroke, while the corresponding values towards the late compression stroke were 0.7 and 0.7Vp where a low tumbling motion exists.</li> <li>The mean droplet velocity in the annular spray jet 16 mm from the nozzle exit was found to be high during late compression injection with maximum value of around 73 m/s for both engine speeds. The effect of increasing the in cylinder backpressure caused substantially reduction in droplets mean and rms velocities, for example, a delay in injection from 310° CA to 320° CA reduced the mean and rms by 10.5 and 27%, respectively.</li> <li>Hollow conical spray structure had a tendency of bending inwards against an elevated backpressure; therefore, the design for spark plug location should accommodate the curvature of the spray.</li> <li>Spray structure was not affected by the tumble motion of air during the compression stroke as at these times the tumbling flow velocity was too low compared to that of spray droplets velocity with the highest maximum velocity ratio of 0.048.</li> </ul>
Himes. M., Farrel. P.V. (1999)[72]	Hydra single cylinder, four valve, pent-roof, direct injection optical engine. (close - spacing).	<ul style="list-style-type: none"> <li>Mie Scattering</li> <li>Laser Doppler Velocimetry</li> </ul>	<ul style="list-style-type: none"> <li>At high loads the spray pattern differs considerably from the more symmetric spray observed for lighter loads</li> <li>Comparing three loading conditions, (low, medium, high), it was observed that the swirl motion changes during the compression from counter-clockwise (low load) to clockwise (high load).</li> <li>As the load increased the RMS fluctuations around the injection timings were also increased which is considered in favor to the mixing process.</li> <li>The increased airflow at high load conditions caused convection of the fuel to the region between the intake valves.</li> </ul>

Kakouhou. A., Urushihara. T., Itoh. T., Takagi. Y. (1999)[73]	Four valve single cylinder optical engine with pentroof type chamber, piston crown bowl and swirl control valve. (wide spacing)	<ul style="list-style-type: none"> <li>• Laser Doppler Velocimetry</li> <li>• Particle Image Velocimetry</li> <li>• Laser Induced Fluorescence</li> </ul>	<ul style="list-style-type: none"> <li>• The combined effect of the swirl motion in the cylinder head the cylindrical piston bowl positioned eccentrically to the cylinder central axis forms an upward flow that rises from the piston crown near the cylinder centre area to the cylinder head in the latter half of the compression.</li> <li>• The fuel injected directly into the cylinder initially enters the piston bowl and then transported to the vicinity of the spark plug by the upward flow forming mixture stratification.</li> <li>• The ideal injection timings are determined from the balance between fuel trapping in the piston bowl and fuel film formation on the piston crown.</li> <li>• Too early injection timing results in a fuel spray that is not trapped in the piston bowl and travels towards the exhaust side of the combustion chamber which precludes mixture stratification and causes a large fluctuation in the mixture concentrations in the vicinity of the spark plug thus resulting in unstable combustion.</li> <li>• Too late injection timing results in higher mixture concentration in the vicinity of the spark plug however results in increased liquid film on the piston bowl.</li> </ul>
B.Befrui et al (2002)[74]	Single cylinder optical engine, DISAC combustion system, High pressure swirl injector Investigation of spray structure and an its temporal development3w2	<ul style="list-style-type: none"> <li>• Phase Doppler Anemometry</li> <li>• Planar Laser Induced Fluorescence</li> <li>• Planar Laser Induced Exciplex Fluorescence</li> </ul>	<ul style="list-style-type: none"> <li>• Combustion stability and efficiency over a wide window of injection and spark timings</li> <li>• Significant charge stratification potential</li> <li>• Significant optimisation potential</li> </ul>
Salters, D. et al (1996)[75]	Single cylinder research GDI engine High pressure liquid fuel injector Fuel spray behaviour investigation	<ul style="list-style-type: none"> <li>• High-speed video imaging</li> </ul>	<ul style="list-style-type: none"> <li>• Early spray injection impacted the piston, and was deflected towards the cylinder walls, although significant impaction of the walls was not identified</li> </ul>



Julian T. Kashdan, Jerome Cherel and benoist Thirouard (2006) [76]	Optical engine single cylinder with 4 valve pentroof cylinder head and flat piston geometry. Swirl Injector and Piezo actuated injector.	<ul style="list-style-type: none"> <li>• Laser Induced Fluorescence</li> <li>• Planar OH LIF</li> <li>• Planar Laser Induced Fluorescence</li> </ul>	<ul style="list-style-type: none"> <li>• Under stratified conditions, the structure of the combustion zone is highly wrinkled and inherently inhomogeneous. , this is believed to be due predominantly to local fuel mixture stratification and the presence of high fuel concentration gradients. The flame propagation pathway is ultimately determined by these local fuel mixture inhomogeneities. Furthermore the flame front and burned gases appear to enclose the fresh gases which are locally either too lean or too rich to maintain flame propagation, resulting in bulk quenching. After the end of the primary combustion, it was observed a strong oxidation due either to remaining unburned fuel from the bulk-quenched zones or following evaporation of liquid film on the piston top surface. Under homogeneous charge conditions, the structure of the combustion zone has been significantly different to that observed under stratified operation. The flame consumes the unburned mixture as it expands toward the combustion chamber without leaving pockets of unburned fuel behind. Flame wrinkling appeared to be significantly lower under homogeneous operation whilst the structure of the combustion zone resembled a deformed sphere. Post oxidation was identified possibly caused by re-ignition of unburned or which it flows out from the crevice volumes.</li> </ul>
--	--	--	--

**Table 2-4 Investigation in optical engine**

## 2.6. PINTLE-TYPE INJECTOR

Authors and Year	Experimental Set-up	Techniques	Major Findings
Brad A. VanDerWege, Zhiyu Han, Claudia O. Iyer, Rubén H. Muñoz and Jianwen Yi (2003) [77]	test single-cylinder engine with bore and stroke of 89 and 79.5 mm, respectively. It features a pent-roof Combustion chamber with four valves and a swirl-control valve (SCV) that can partially or totally block one of the two intake ports.	<ul style="list-style-type: none"> <li>• Computational Fluid Dynamics</li> <li>• High-speed video camera</li> </ul>	<ul style="list-style-type: none"> <li>• An 18% fuel consumption reduction over a test cycle compared with a PFI baseline.</li> <li>• An additional 4-7% fuel consumption reduction over a wall-guided DI system. The primary reasons for this are improved combustion efficiency and phasing, which result from the ability to provide an improved fuel-air mixture later in the compression stroke.</li> <li>• Stratified-charge operation up to high loads (about 5 bar BMEP) and speeds (about 4000 rpm). Potential for even higher load unthrottled operation was shown through split injection.</li> <li>• Potential for improved full-load performance due to improved homogeneous mixing. The central injector location and the wide cone angle spray aid the mixing.</li> </ul>
M. Gavaises, S. Tonini and A. Marchi (2006) [78]	Eulerian and lagrangian near-nozzle model and spray model of an Outward Opening Piezo-driven pintle injector	<ul style="list-style-type: none"> <li>• Computational Fluid Dynamics</li> </ul>	<ul style="list-style-type: none"> <li>• The exiting flow has been found to vary considerably around the nozzle periphery, both in terms of actual velocity magnitude but also in flow direction. This, in turn, has been found to affect the dispersion of the injected droplets in the inner and outer recirculation zones formed at the two sides of the developing spray. Those recirculation zones, which are known to result to the so-called 'collapsing' or 'opening', spray types, were found to be affected not only by the internal nozzle flow but also from the outside nozzle shape and the boundary conditions. Finally, evidence was provided for the formation of the 'string' type spray structure produced by such nozzles both from experimental images and multi-phase flow calculations. It has been demonstrated that the formation of strings is due to the liquid separation from the surface of the cartridge, which is due to its expansion in the radial direction.</li> </ul>

Sudhakar Das and Paul G. VanBrocklin (2003) [79]	The existing Taylor Analogy Breakup (TAB) atomisation model in KIVA-3V code was used for atomisation (droplet breakup). The basic structure of the code is for spray originating from an orifice.	<ul style="list-style-type: none"> <li>• Computational Fluid Dynamics</li> </ul>	<ul style="list-style-type: none"> <li>• Based on the simulation study, collapsing spray can be influenced by the following: <ul style="list-style-type: none"> <li>• Seat angle</li> <li>• Streamwise velocity/tangential velocity</li> <li>• Nozzle exit diameter</li> </ul> </li> </ul>
Ch.Schwarz, E. Schunemann, B. Durst, J. Fisher and A. Witt (2006) [80]	Spray test Chamber, optical engine. Multicylinder engine test bench. Combination with Turbo-charging Variable valve cam timing	<ul style="list-style-type: none"> <li>• Mie imaging</li> <li>• Laser Induced Fluorescence</li> <li>• High-speed Videoscapy</li> <li>• 3D Computational Fluid Dynamics calculations of in-cylinder charge motion</li> </ul>	<ul style="list-style-type: none"> <li>• DI specific spark plug and double VANOS variable cam timing is well suited for the combination with innovative supercharger technology which provides highest dynamic performance and response, while at the same time offering additional fuel consumption potential by enhancing stratified operation.</li> </ul>
Stan C., Troeger R., Stanciu A., (2002)[81]	Pressure pulse direct injection system with an outwardly opening poppet valve type injector. Single cylinder four valve four stroke motorcycle engine.	<ul style="list-style-type: none"> <li>• Free spray Mie scattering</li> <li>• Computational Fluid Dynamics</li> <li>• In-cylinder Mie scattering</li> <li>• Pressure analysis</li> <li>• HC, CO emissions analysis</li> </ul>	<ul style="list-style-type: none"> <li>• The development of a gasoline direct injection system for engines with compact combustion chambers requires special attention on the interaction between the movement of piston, valves and the time and space related spray development.</li> <li>• Generally a spray directed on the piston provides the best results for engines with compact combustion chambers where a specific chamber shape is not possible.</li> <li>• CFD simulation is an effective tool for achieving the optimum result in a relatively short time.</li> <li>• The optimum injection start is not always the one providing the minimum interaction between spray and piston.</li> <li>• The optimized set up, central injector with twin lateral spark plugs, show considerable improvement in terms of HC and CO emission behaviour by an average reduction of 14% and 60% within the operating regime compared to the stock arrangement.</li> </ul>

J M Nouri, M A Hamid, Y Yan and C Arcoumanis (2005) [82]	Piezo pintle-type injector installed inside a constant-volume chamber	<ul style="list-style-type: none"> <li>• Phase Doppler Anemometry</li> <li>• Mie scattering</li> </ul>	<ul style="list-style-type: none"> <li>• Spray visualization illustrated that the spray was string structured and that the locations of the strings did not change from one injection to the next. The string structure remained the same in elevated back-pressure from 1 bar to 12 bar. The overall spray cone angle was stable and independent of back-pressure, a significant advantage relative to swirl pressure atomisers. The effect of backpressure was to reduce the spray tip penetration due to the increased drag so that the averaged vertical spray tip velocities.</li> <li>• Detailed PDA measurements were carried out under atmospheric condition with an aid of spray visualization to locate a particular string in the spray cone. The maximum axial mean droplet velocity reached, was 155 m/s at 2.5 mm from injector which was reduced to 140 m/s at <math>z = 10</math> mm. The string spacing was determined from PDA measurements to be around 0.375 and 0.6 mm at <math>z=2.5</math> and 10 mm, respectively. The maximum mean droplet diameter was found to be in the core of the strings with values up to 40 <math>\mu\text{m}</math> at <math>z=2.5</math> mm reducing to 20 <math>\mu\text{m}</math> at <math>z=10</math> mm.</li> </ul>
--	---	--	--

A. Marchi, J. M. Nouri, Y. Yan and C. Arcoumanis (2007) [83]	Large-scale transparent model of pintle-type Injector	<ul style="list-style-type: none"> <li>• Mie Scattering</li> </ul>	<ul style="list-style-type: none"> <li>• Spray visualization of the cavitating nozzle revealed the presence of gas-phase in the near nozzle exit region. This could be either cavitation under conditions where the pressure drop corresponded to a cavitation number of 1.1 and above, or air entrainment into the nozzle due to the liquid flow separating</li> <li>• cavitation and air entrainment were two separate phenomena occurring under different operating conditions</li> <li>• For the case of air entrainment, the emerging spray can have two distinct large and small cone angles</li> <li>• The surface structure of the sprays corresponding to the two cone angles consisted of longitudinal strings due to the profiling effect of the liquid flow around the entrained air pocket;</li> <li>• it is still risky to speculate that air entrainment is the only mechanism responsible for the string-type spray structure since a finer string structure has been observed in a non-cavitating nozzle tested previously</li> <li>• The dynamics of cavitation vapour pockets proved to be much faster than those of the entrained air bubbles</li> <li>• Limited tests at low lifts and very high flow rates, where air entrainment and cavitation bubbles could co-exist, revealed that the main mechanism for the formation of a string-type structure was still the entrainment of air bubbles, but that the presence of enhanced cavitation at high liquid velocities could create a string-type spray structure which was very similar to that of the real size injector.</li> <li>• Overall, the results presented above suggest that, apart from air entrainment, there may be other mechanisms that might either hinder or enhance the formation of string-type spray structures like the balance between dynamic, surface tension and aerodynamic forces due to the induced air recirculation near the nozzle exit.</li> </ul>
--	---	--	---



B.Befrui, G. Corbinelli, D. Robart and W. Reckers [84]	Side illumination is used for imaging of the longitudinal spatial-temporal development of the spray geometry, while the “frontal” illumination is employed to examine the spray circumferential structure.	<ul style="list-style-type: none"> <li>• Mie Scattering</li> <li>• CFD (VOL-LES simulation)</li> </ul>	<ul style="list-style-type: none"> <li>• The jet-string structure formation is primarily a hydrodynamic characteristic of the high pressure conical sheet breakup and is a feature of the injector valve group design</li> <li>• There is a transition in the spray breakup mechanism between the Kelvin-Helmholtz and jet string break up regime</li> <li>• The VOF-LES simulations, for an injector valve group design with “coarse” jet-string spray structure, reveals that the liquid flow detachment (separation) from the nozzle wall, upstream of the nozzle exit, is the primary cause of formation of the “jet-string” flow structure. The fluid dynamic origin of the flow detachment is separate from flow cavitation in the nozzle.</li> <li>• The liquid flow detachment from the nozzle wall engenders “ingestion” of the ambient air into the nozzle that promote the near field irregular circumferential break up of the conical liquid sheet, through irregular growth of Kelvin-Helmholtz waves at the liquid-air interface.</li> </ul>
--	--	--	---

**Table 2-5 Pintle-type Injector**

**2.7. MISCELLANEOUS ON DISI CONCEPT**

Authors and Year	Experimental Set-up and Measurement	Major Findings
Henning Kleeberg ,Dean Tomazic, Oliver Lang ,Knut Habermann (2006) [85]	Test bench with Turbo charged Direct Injected Gasoline Engines: Charge air cooling, electrically assisted supercharger placed upstream of the turbocharger compressor, and possibility of utilizing a series of two differently sized turbochargers. Compressor map, IMEP and torque measurement.	<ul style="list-style-type: none"> <li>• Several methods to decrease the turbo lag effect have been found: <ul style="list-style-type: none"> <li>-variable valve timing</li> <li>-Charge air cooling</li> <li>-Additional air charging</li> </ul> </li> <li>• The investigation on these concepts have shown that high boost levels at low engine speeds can lead to abnormal combustion events like pre-ignition</li> </ul>

Alasdair Cairns, Hugh Blaxill and Graham Irlam (2006) [86]	Turbo charged four cylinder gasoline direct injection research engine. The original pent-roofed engine was of naturally aspirated wall-guided design, with injector located between the two inlet valves	<p>Benefits of EGR in a turbocharged DI gasoline engine:</p> <ul style="list-style-type: none"> <li>• At part load, high amounts of internal and external EGR were used to invoke CAI combustion and achieve up to 10% reduction in CO<sub>2</sub> over the New European Drive Cycle.</li> <li>• Further Fuel saving of 3% were also made at moderate engine output using reduced EGR flow rate in spark-ignition condition</li> <li>• Cooling external EGR helps suppressing knock more than excess of air, with increased charge specific heat capacity, combustion phasing further advanced toward the optimum timing and improved combustion stability over a wide operating range.</li> <li>• The cooled EGR makes tolerable higher compression ratios in boosted downsized engines.</li> </ul>
Philip Price, Richard Stone, Tony Collier, Marcus Davies (2006) [87]	Wall guided DISI optical engine with swirl atomizer, Spray-guided DISI optical engine with multihole atomizer	<ul style="list-style-type: none"> <li>• The PM emissions from the SGDI engine tested were significantly lower than a similar engine with a wall guided combustion system. Unlike wall guided DISI, a significant accumulation mode was not detected, but the number concentration of nucleation mode PM was similar to a PFI engine; and the number concentrations generally similar and less than an order of magnitude more. The improvement is attributed to the higher fuel pressure, reduced impingement of fuel on the combustion chamber surfaces and generally better mixture propagation</li> <li>• PM number was shown to depend on fuel composition; and the highest PM emissions were measured when toluene was used as the fuel.</li> <li>• Advancing the ignition timing increased the number concentration of PM emissions.</li> <li>• For SGDI with toluene a monotonic increase in PM mass concentration over one order of magnitude was measured when sweeping the injection timing from 60 CAD a TDC to 160 CAD a TDC. The same trend was measured when using isooctane, but the increase in PM mass concentration was smaller</li> <li>• Fuel Type had biggest effect on PM emissions followed by air-fuel ratio, injection timing and ignition timing</li> </ul>
Yang J., Aderson R.W., (1998)[88]	Single cylinder direct injection engine. Pressure analysis In-cylinder temperature.	<ul style="list-style-type: none"> <li>• A split injection strategy in the intake and the compression strokes realized both the volumetric efficiency and the knock suppression benefits increasing the full load IMEP by a further 3%</li> <li>• When the first injection contained more than two thirds of the total fuel injected the combustion stability was insensitive to the timing of the second injection</li> <li>• An increase in the second injection fuel ratio relative to the first, dictated the use of the earlier second injection timing of 150° BTDC</li> </ul>

**Table 2-6 Miscellaneous on DISI concept**

---

## 2.8.LITERATURE REVIEW SUMMARY

The primary step on the investigation of the flow characterization of an injector consists of the understanding of the internal behaviour in order to be able to explain and optimise the spray characteristics. Several attempts have been made in real size nozzles by replacing a nozzle portion in quartz thus gaining optical accessibility to a hole [89]. Nevertheless, this approach was causing a deformation of the internal geometry and to the adjacent holes adding unexpected behaviour in the internal flow characteristics. Furthermore, this approach was preventing the observation of the flow behaviour in the sac volume and the simultaneous visualization of the injector holes. To overcome this inconvenient, the whole transparent nozzle was to be manufactured in transparent material like quartz or Perspex to provide an overall 3-D view of the internal behaviour [90].

The high complexity of the set up arrangement and the low optical accessibility due to the very small size of the nozzle, made it difficult to go for real size model for this investigation and the preferred choice was to do the internal observation in a larger scale model for preliminary investigation under steady state flow condition. The simple arrangement set up with lower cost and the high optical accessibility offered by the large-scale used in this investigation provided a large amount of information which gave guideline mechanisms that were kept in consideration in the subsequent study in the real size model.

Few analogies between previous large-scale findings and the current injector model are here summarised. In the experiment from Nouri et. al. [7] on cavitation in the large scale multihole mini-sac type nozzle, onset of cavitation was observed approaching a cavitation number of 0.7 to 0.9. These values are very close to the onset of cavitation observed in the large-scale model of the pintle type injector with an onset cavitation of 0.5 which is slightly lower probably due to the different onset detection technique implied in the two experiments. Similar findings were also observed in the experiments from Matsumura et. al. [27] where the mechanism of vortex were linked to the downstream flow behaviour in a large scale slit nozzle model. It was found that the formation of small vortices forming in the sac had large effect on the flow fluctuation and in the spray angle. Similarly, in the large-scale pintle type model the dependency of downstream flow tangential fluctuation could be linked to the oscillation to the 8 counter rotating vortices occurring upstream in the body of the injector.

---

An important finding is also given by Carvalho et. al. [28] who observed the structure of a flat liquid film in a 2-D liquid film generator. It is interesting to notice that in such a structure no string filament formation could be observed under any operating condition. This outcome proves that the strings formation observed in the conical hollow spray of the pintle type injector are strictly associated to the conical shape of the liquid sheet and the instability originated from the progressively decreasing of the film thickness as it expands with downstream distance.

An important phenomenon associated with the string formation and described in the third chapter is the hydraulic flip, which consists in the flow separation from the nozzle wall occurring at the injector exit.

Evidence of flow separation were identified by Schimdt et. al. [31] and Yule et. al. [33]. In the experiment of Schmidt the nature of the separation was cavitation driven as a function of cavitation number and Reynolds number. In the large-scale pintle type nozzle it was not possible to investigate flow separation in the presence of cavitation, however, its occurrence and development in the absence of cavitation was investigated and its link to the filament formation outside the nozzle was established. The same phenomenon of hydraulic flip was observed in the absence of cavitation by Yule et. al. [33] in a large scale model of a VCO multihole injector and its effect was found to be related to the Reynolds number. Soteriou et. al. [37] has also investigated and analysed the phenomenon of hydraulic flip in VCO nozzles and suggested that they can cause unequal spray from one nozzle to another in the absence of flow cavitation. In the large-scale cavitating model of pintle type injector, the current data showed that the hydraulic flip occurrence was diminishing with Reynolds number but only at high needle lift.

Pouvreau [39] showed how hydraulic flip can be an undesired phenomenon as it enhances spray instability with no clear evidence of any further improvement in atomisation. The angle analysis in the large-scale model reported in Chapter 3 of the current thesis has also revealed the high level of instability associated with hydraulic flip as a function of position of the air trap attachment to the needle wall or injector body inside the nozzle, causing two distinct large and small spray angle modes, respectively.

In the scaled up model of gasoline multihole nozzles, the phenomenon of cavitation and it's effect on the spray characteristics was fully identified [30]. In order to correlate the model with the real injector, geometrical, kinematical and dynamical

---

similarity were respected. However, due to the non-linearity of pressure ratios between the two scales, it was not possible to maintain the same similarity with cavitation number (CN) and the enlarge CN values were in general much smaller than the CN in the real size operating under real conditions. Several general conclusions could be drawn from the reviewed papers in the open literature regarding the effect of cavitation mainly in multihole models. It was established the positive effect of cavitation on the spray atomisation which was related to the decrease of discharge coefficient and the consequent velocity increase in the non cavitating areas ([33], [37]). Those effects were then validated also in the real size pintle-type injector where it was noticed a small decrease of the fuel rate per injection beyond an injection pressure of 160bar thus suggesting a discharge coefficient reduction probably due to an increase of cavitation. In addition to experimental results, further CFD calculation confirmed the presence of cavitation for same operating conditions and also air entrainment was identified in the simulation from the presence of adverse gradient around the nozzle exit [15]. The phenomenon of cavitation was split in two main philosophical opinions between cavitation supporter stating the benefit of cavitation in terms of increased in-nozzle turbulence and spray atomisation and non-cavitation supporters claiming the strong instability and unpredictable nature of the cavitation phenomenon.

In fact, a crucial feature of the pintle type injector consists in the stability and repeatability of the spray characteristics over different operating conditions. Historically many injector showed shape and pattern variation with the backpressure. For instance a contraction of the spray cone is well established for the swirl type injector up to 35% of the cone angle at ambient condition [44, 45, 48]. Kasdhan et. al. [44] also observed a progressive distortion of the toroidal vortex, an increase in mean droplet diameter and a decrease in spray penetration, the last effect mainly occurring for every injector type as affect of the increase drag effect. The multihole shape was found to be very robust against injector pressure however the penetration is highly variable as a function of back pressure so that spray impingement maybe an issue [49].

The angle analysis on the pintle type injector by mean of Mie scattering in the optical engine has revealed a high robustness of its shape under ambient with an angle variability of  $\pm 2^\circ$  for an injector pressure of 200bar. The penetration decreases with the backpressure however the controllable needle lift due to the multiple piezo



---

crystals activation allows high degree of freedom to avoid wall impingement.

The level of atomisation observed by Mitroglou et. al. [49] on a multihole injector reported a variation of order of  $19\mu\text{m}$  and  $14\mu\text{m}$  at injection pressure of 120bar and 200bar respectively under atmospheric back pressure.

The current investigation applied to the pintle type has shown a mean droplet diameter in a range within  $8\mu\text{m}$  an  $14\mu\text{m}$  for the same operating condition described in [49] at 10mm from the injector exit. These results suggest that the atomisation performance of the pintle type is higher than the atomisation of the multihole injector. At the same distance from injector, the PDA parametric analysis performed in the constant volume chamber revealed a growing trend of droplet size as the injection pressure decreased or as the chamber pressure increased. A similar droplet size trend was observed in the PDA experiments of Anand et. al. [60] performed on a swirl hollow cone injector where an increase in injection pressure was associated with an SMD decrease. On the other hand, a decrease in backpressure in the swirl type injector was associated with an SMD decrease and vice versa, i.e. an increasing in backpressure results in larger SMD due to increased drag. However, when increasing the backpressure, droplets evaporation become significant and its effect on SMD size is opposite to that of drag. As the backpressure increases, it reduces the droplets velocity and therefore increased droplets resident time, which leads to enhanced vaporisation. The spray shape of the swirl type is highly sensitive to the chamber pressure and when this increases, the PDA measurement point measure the velocity in a different relative radial position (as the spray cone has contracted) and thus it detects a larger droplet size. In fact, another conclusion from Anand PDA assessment [60] is that SMD typically increases as the radial distance increases from the injector axis.

The studies on the air entrainment and recirculation was largely studied by Cossali et. al. [62-64] and modelled according a scaling law by Siebers et. al. [66].

The flow characteristic of the air entrainment on the spray near nozzle field was observed in this study giving introductory experimental information which could be used for the comparison between the air recirculation from the spray on a single hole of the multihole injector and the air recirculation on the longitudinal filaments (strings) present in the spray structure of the pintle-type injector. In fact, the spray structure formed in the outward opening injector can be associated to those of a Multihole having as many holes as the strings number of the pintle-type. This approach may provide a link for the behaviour of the two injector types giving a better

---

understanding on the air entrainment and recirculation area in the near and far spray field.

LDV measurement performed by Cossali et. al. [65] characterised the air entrainment of a Diesel injector and observed the relation between the growth of injected mass and the growth of the air entrained flow rate. Same result with a different measurement technique was also achieved by Nauwerck et. al. [69] who measured the air entrainment of high pressure hole type injector in a pressurised chamber with optical access by both PIV and LDV techniques. Nauwerck et. al. [69] as Cossali [65] observed an increase of the maximal velocities in the entrainment flow with increasing injection pressure.

The same approach was adopted in the current study where LDV diagnostic confirmed the PIV assessment performed on the air entrainment of the pintle type injector spray. The parametric study revealed a linear law of proportionality between air entrainment velocity and injection pressure in the near-field for a range between 50 to 200bar.

On the optical engine, the review of the literature covers for different engine operating conditions and engine configurations. Previous experiments on the pintle-type shown the robustness of the spray shape against the tumble motion at late injector and engine speed [71]. In the present investigation, the pintle-type injectors showed enhanced behaviour in terms of spray angle, shape and overall spray angle stability. In particular, it was observed for two Inward Seal Band prototypes the influence of several injector parameters which showed a robust behaviour against injection to injection variation. However, in previous performance analysis of similar injector in the optical engine, for different cylinder pressure the hollow cone shape exhibited a variation on its curvature, more specifically the spray was bending inwards against an elevated backpressure [71].

The review of the literature shows adequate experimental investigation on multi-hole and swirl injectors for the gasoline direct-injection engines but the information on pintle-type outward opening injector are limited and sparse.

However the overall performance of the injector under investigation were assessed by Brad et. al. [77] who describes the combustion system concept and an initial assessment of it, performed on a single-cylinder test engine. Their testing result on the Vortex Induced Stratification (which is the mixture formation method for the pintle injector spray type) have indicated that an 18% fuel consumption reduction can be

---

achieved, compared with a baseline PFI engine, over a drive cycle and an additional 4-7% fuel consumption reduction can be achieved over the wall guided strategy. These benefits are shown to arise from improved combustion phasing, reduced unburned hydrocarbon emissions, and an enlarged window of stratified operation [77].

The results presented in subsequent chapters of this thesis and related publications are aimed to improve the literature on these topics, and also to allow further development in gasoline direct-injection engines and eventually establishment of a “cleaner” internal combustion gasoline engine.

---

## **Chapter 3.**

### ***Large-scale Model***

#### **3.1. INTRODUCTION**

The internal flow and the spray structure of a pintle-type injector have been investigated in an enlarged model in this chapter to have a better understanding of many aspects still not well understood like in-nozzle flow structure, longitudinal string formation of spray and its link to in-nozzle flow and spray stability, in particular, spray-to-spray variation (flapping). These phenomena have an important role in the behaviour of the overall spray-guided DISI system and they are still investigated extensively. The use of a transparent enlarged model helped to overcome the difficulties encountered in the observation of the internal flow in a real size injector. Quantitative flow analysis performed with LDV technique was matched with 3D Mie scattering visualisation to give information about the internal behaviour and the correlation of the flow upstream and downstream the nozzle exit.

#### **3.2. EXPERIMENTAL TECHNIQUES**

##### **3.2.1. Mie-scattering**

Mie-scattering is technically a simple method that takes advantage of a high-resolution CCD camera and a simple optical set up. Using laser sheet imaging of the Mie scattered light, cross-sections of the spray can be imaged to reveal the internal structure by observing the scattered light (optical density) from the particles surface area.

One of the most frequently used techniques for the extraction of qualitative information regarding the fuel droplet behaviour of a high-pressure liquid spray inside a transparent model, a constant volume chamber or even an engine's cylinder is the Lorenz-Mie scattering technique. More specifically, Mie scattering is an elastic scattering technique where light of same wavelength to the incident radiation is scattered from particles or droplets, which move with the flow [16, 26]. The light intensity according to Lorenz-Mie theory is a complex function depending upon the droplet diameter, the scattering angle, and the refractive index of the droplet, the

---

polarisation and the wavelength of the incident radiation. Because of several problems, the Mie technique has found limited use as a quantitative technique and is instead more frequently used to visualise spray and even flame structures.

Forward illumination imaging and shadowgraphy techniques are two simple forms of Mie-scattering and they were the methods chosen for this experiment in order to visualise the spray morphology and provide details of the transient structure and temporal development of sprays. These particular methods focus on the overall shape of the spray rather than just the particles. The methods will be discussed further in the processing of experimental data section.

### **3.2.2. LDV (Laser Doppler Velocimetry)**

Laser Doppler Velocimetry (LDV) is a tool for acquire flow velocities. The technique is based on the determination of the velocity of fine tracer particles that follow the fluid flow with virtually no delay. The technique is well established and has been used by many researches in different subject areas, for example, Hockey and Nouri (1996) [91], Arcoumanis et al. (1997 & 1998) [18, 35]. Here a brief introduction is given and the readers are referred to references given below. The velocity is determined for a single point of the flow field. For the evaluation of the whole flow field velocity, the velocity has to be measured at many different points. The spatial resolution is given by the size of the measurement volume, which is defined by the intersection of two laser beams. The beams are produced by splitting one laser beam into two parallel beams, which are focused symmetrically by a lens at its focal point to form the measuring volume. At the measuring volume, the interface of the two beams produces a fringe pattern of bright and dark region. When a tracer particle passes through the fringes in the measuring volume, it will scatter light with a frequency modulation linearly related to the tracer velocity. A photomultiplier with its collecting optics (comprised collimating and focusing lenses, a 100  $\mu\text{m}$  pin hole and a photomultiplier equipped with amplifier) was located in front of the measuring volume collects the scattered light. The signal from photomultiplier was fed into the processor interfaced to a PC and led to time-average values of the mean and RMS velocities.



### 3.3. DESCRIPTION OF THE TEST RIG AND OF THE EXPERIMENTAL SET UP

A large-scale nozzle (23.3:1) has been manufactured from Perspex simulating the outward opening DISI injector as shown in Figure 3-2.

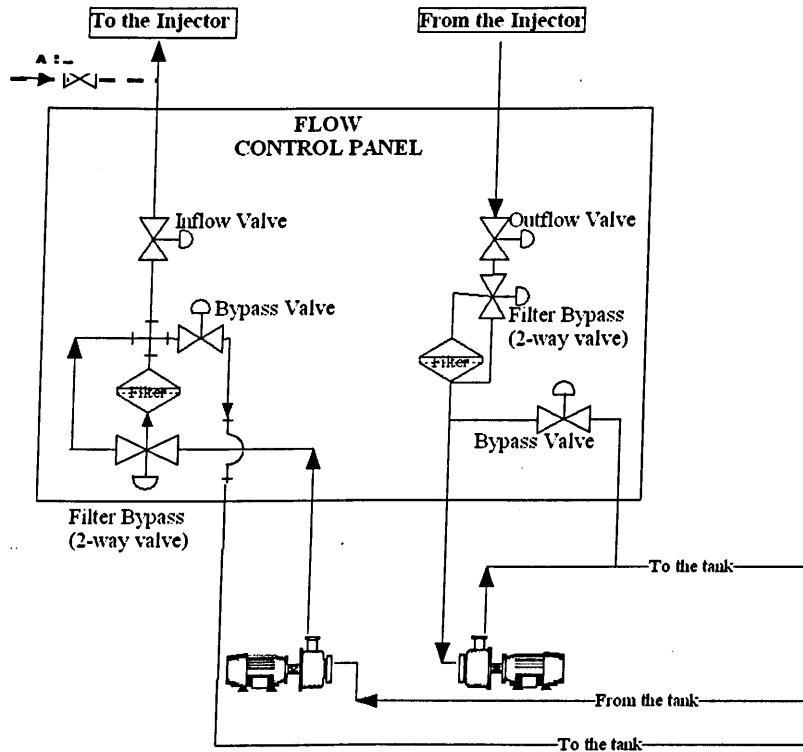
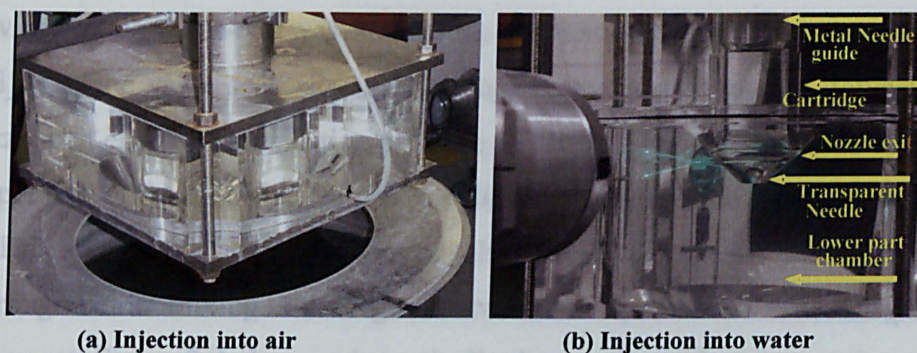


Figure 3-1 Schematic of the flow diagram showing the pumps, pipelines and valves used to control the flow admitted to the injector.

The model was designed based on geometric, kinematic and dynamic similarity. Specifically to preserve the dynamic similarity all operating conditions aimed to achieve Reynolds numbers as for the real injector at the nozzle exit. The flow through the enlarged nozzle injector was operated under steady flow condition by fixing the needle position to different lifts. The water flow passes through the nozzle at a pre-specified lift using two electrical pumps (Figure 3-1). The nozzle internal flow was visualized using a high resolution CCD camera 1280x1024 pixels and to capture the dynamic evolution of the flow a high-speed video camera with acquisition rate up to 180000 frame per second was used.

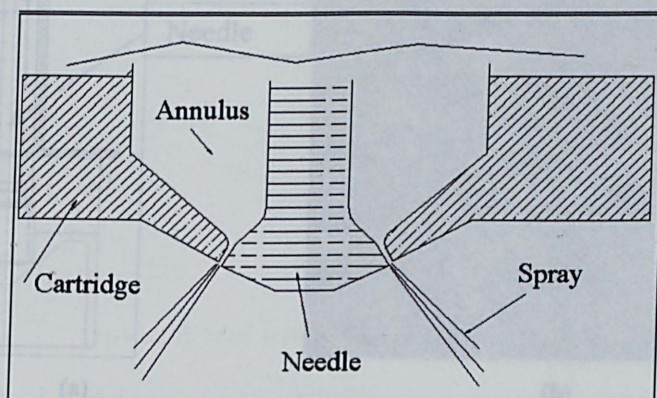


**Figure 3-2** Schematic diagram shows the main components of the large-scale model.

LDV system was also employed to measure the circumferential flow velocities at the nozzle exit as shown in Figure 3-2. It was not possible to measure this flow velocity component at the nozzle exit if the water is injected into air due to the liquid surface shape dynamics that causes the laser beam to be scattered all over. Therefore, the measurements across the main jet were achieved by projecting the laser beam through a closed Perspex chamber filled with water while having the control volume within the water jet. It should be noticed that this flow velocity may not be equal to the free surface velocity (when the water is injected into air) because of the different viscous effect. Nevertheless, the velocity measurements in the vicinity of the nozzle exit is less affected by the external different boundary condition and could provide useful information that helped to understand the internal mechanism of the flow inside the injector.

All the transparent components, nozzle-block, the last section of the needle and lower chamber have been manufactured from acrylic (Perspex), while the rest of the needle and the needle casing (cartridge) were machined from stainless steel.

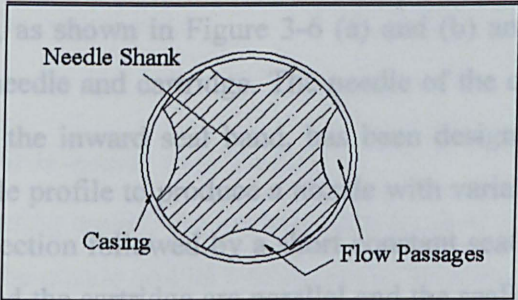
The valve lift was measured and adjusted at the top of the rig by a micrometer and a fine screw thread respectively.



**Figure 3-3** Schematic of the nozzle exit showing convergent-divergent region at the valve seat

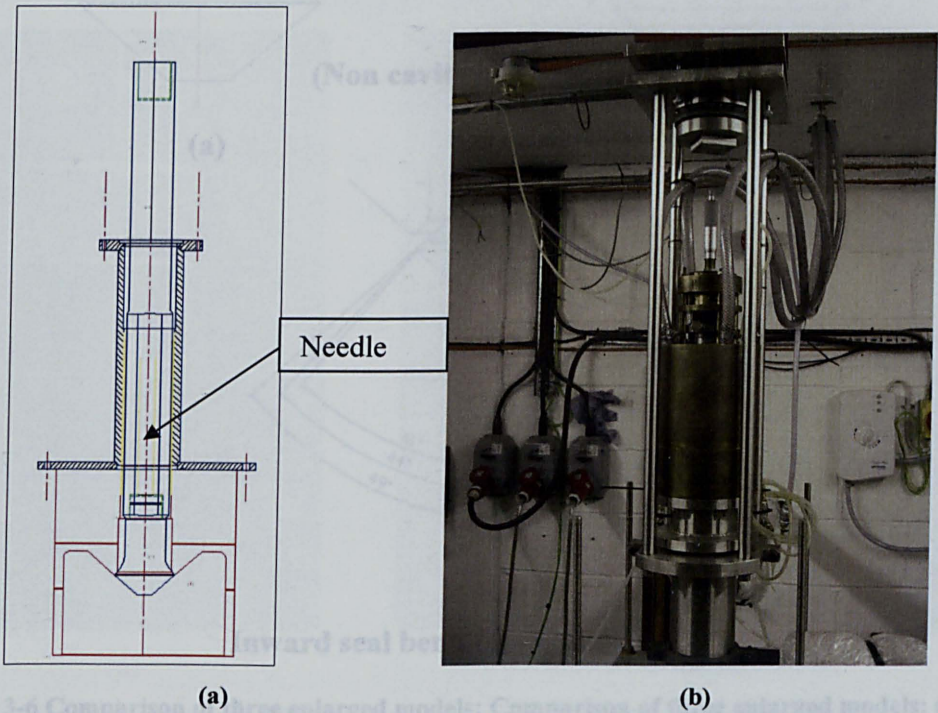


A viewing window cut-out was located on the same horizontal plane, and almost parallel with, the valve seat. Pressure tapings located upstream and downstream of the nozzle exit enabled the injection pressure and backpressure to be measured. The upper part of the cartridge featured a cylindrical bore that encased a square needle guide. This arrangement provided four equally spaced flow passages for the liquid to flow through before mixing in the region between the square-section needle guide and the valve seat. Figure 3-4 shows schematically the needle guide cross-section with the flow passages.



**Figure 3-4 Upper cartridge flow passages**

At the inlet to the model injector, a mixing chamber was installed and water was fed into this chamber through four pipes equally spaced around the chamber (Figure 3-5) to insure thorough mixing and uniform flow into the model injector.



**Figure 3-5 (a) Schematic diagram of the injector assembly mounted onto the rig; (b) the rig assembly.**

### 3.3.1. Injectors under investigation

Two different designs of transparent model injectors were investigated based on their ability to generate cavitation and will be referred to as cavitating model and non-cavitating model. After completing the investigation in the non-cavitating model, further investigation has been performed in the cavitating model with a modified nozzle in order to investigate the effect of cavitation on the spray characteristics. The two types of injector present several geometrical differences. More specifically, the non-cavitating nozzles were designed with a profile following different angles of 80 degree and 90 degree, as shown in Figure 3-6 (a) and (b) and had a parallel nozzle passage between the needle and cartridge. The needle of the cavitating model, which will be referred to as the inward seal band, has been designed differently and it is shaped with triple angle profile to produce a nozzle with variable gap. Its passage has an initial convergent section followed by a short constant seat region where the cone angles of the needle and the cartridge are parallel and the sealing takes place. Finally, the nozzle terminates with a divergent section where the outer edge of the needle is aligned with the cartridge edge.

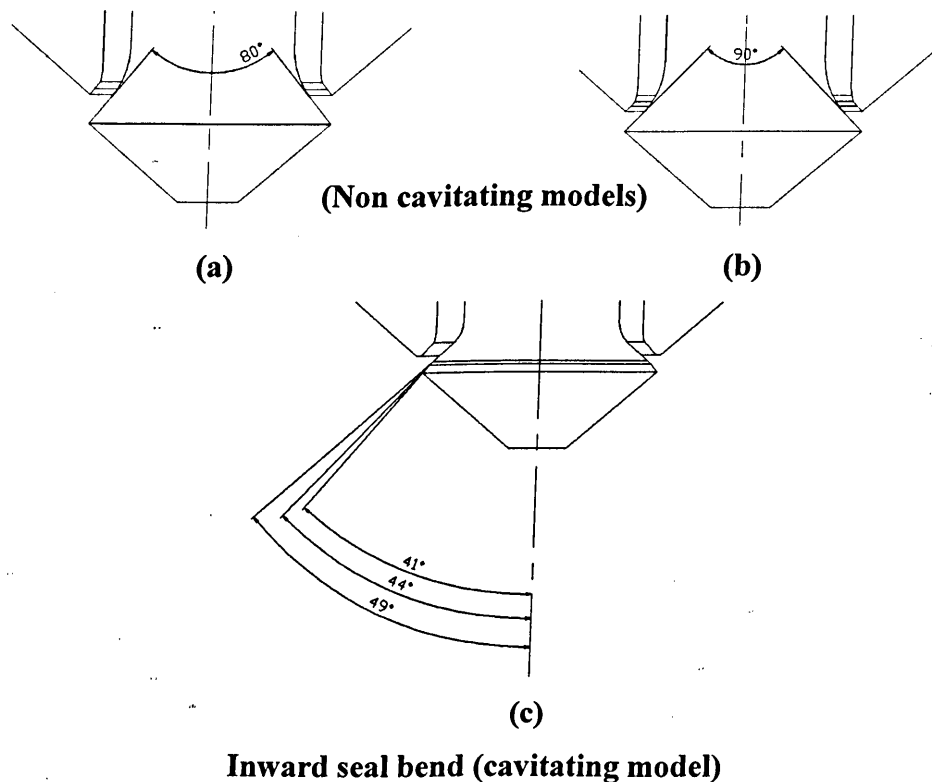


Figure 3-6 Comparison of three enlarged models: Comparison of three enlarged models: (a) and (b) non-cavitating model; (c) cavitating model.



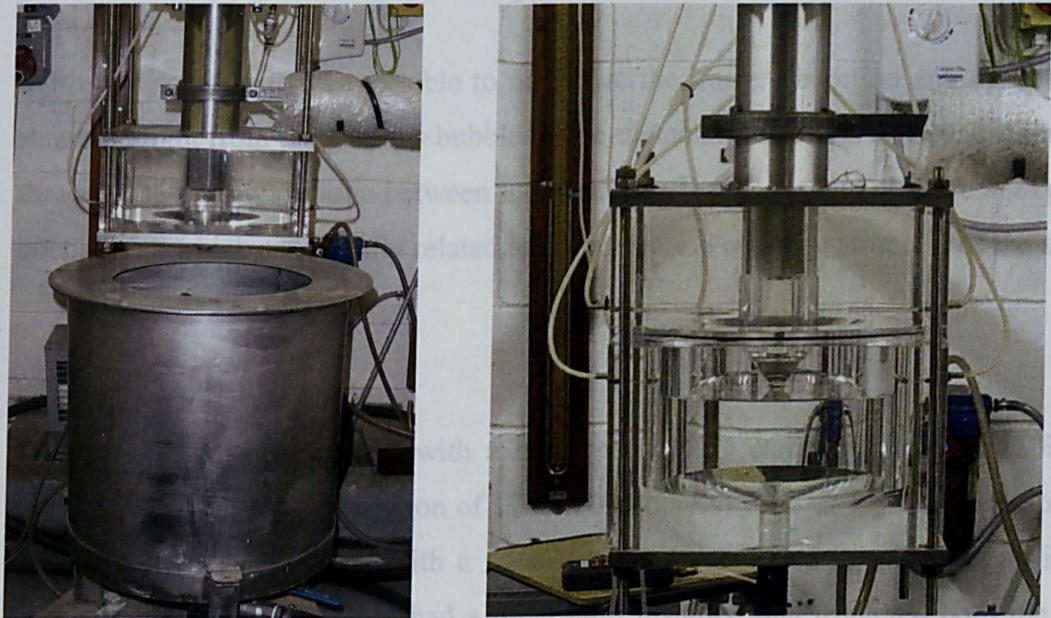
This particular shape designed for the inward seal band type creates a loss of pressure of the flow passing through the narrow section, which consequently under certain conditions (when the liquid pressure goes below its vapour value) makes the liquid to cavitate. Besides the cavitation, it could be observed that such geometry has also additional effects on the spray structure and in particular on the spray angle, which has been the object of further investigations. The new cavitating prototype was composed by a cartridge with conical internal surface. The needle surface was shaped as three subsequent truncated cones with progressively decreasing angle and with the sealing surface being the central cone.

Figure 3-3 Schematic diagram of the flow passage between needle and cartridge of the cavitating

3.3.2. Flat window for in-nozzle visualisation.

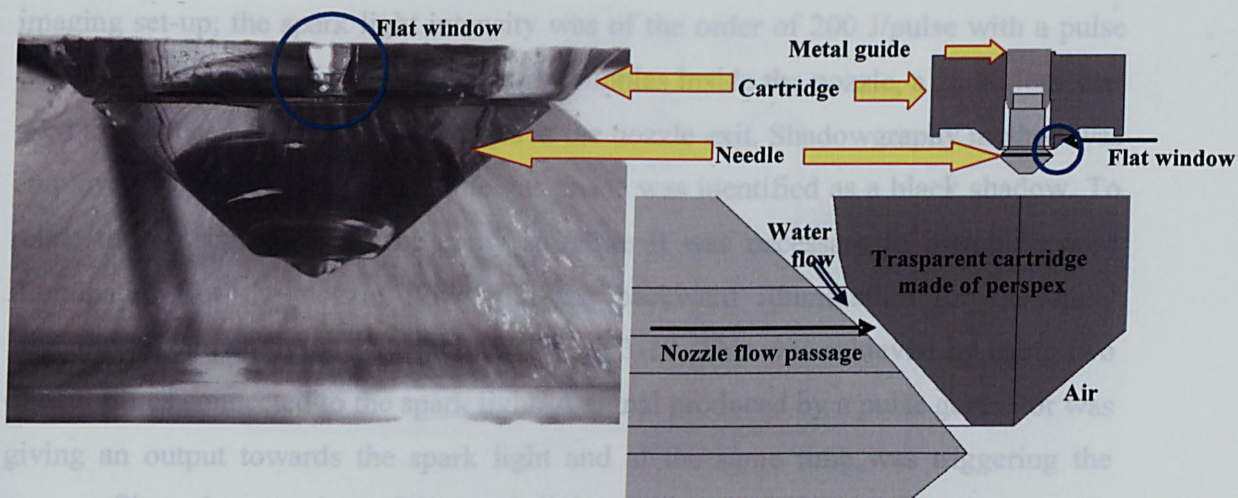
In the large-scale cavitating model, the investigation focused on the observation of the flow behaviour inside the nozzle and its correlation to the spray structure. To visualize these phenomena the rig was set up without lower part chamber. In this way, the injector was spraying inside a barrel (Figure 3-7 (a)); i.e. injection into ambient air. When cavitation was being studied, the injector was arranged with the bottom chamber for injecting liquid into liquid in order to visualize the gas phase without ambiguity of secondary air entrainment (Figure 3-7(b)).

Figure 3-4 Clear view of the nozzle seat region. The window was machined on the outside surface of the cartridge, as shown in



(a) and (b) could be adjusted with lamp illumination and the camera. All internal camera settings could be adjusted with the image acquisition software. The spray was illuminated by a Xenon spark light equipped with two flexible optical fibers which increased the effectiveness of the





**Figure 3-8 Schematic diagram of the flow passage between needle and cartridge of the cavitating nozzle; the arrangement of the flat window is shown.**

The initial visualisation of in-nozzle flow experiments in the large-scale transparent model were presenting several optical problems of image distortion due to the curved and conical profiles of the interface surfaces with large difference in refractive index between fluids and boundaries (Perspex) which caused substantial light reflection and refraction. To overcome this difficulty the cartridge was externally provided with a flat window of 10 mm width and 20 mm long, to insure a clear view of the nozzle seat region. The window was machined on the outside surface of the cartridge, as shown in Figure 3-8.

With this solution it was possible to minimize the image distortion and optimise the scattered light from the gaseous bubble inside the nozzle and thus to visualise the flow through the narrow passage between the needle and cartridge and observe unexpected phenomena which are directly related to the formation of string structure of the spray.

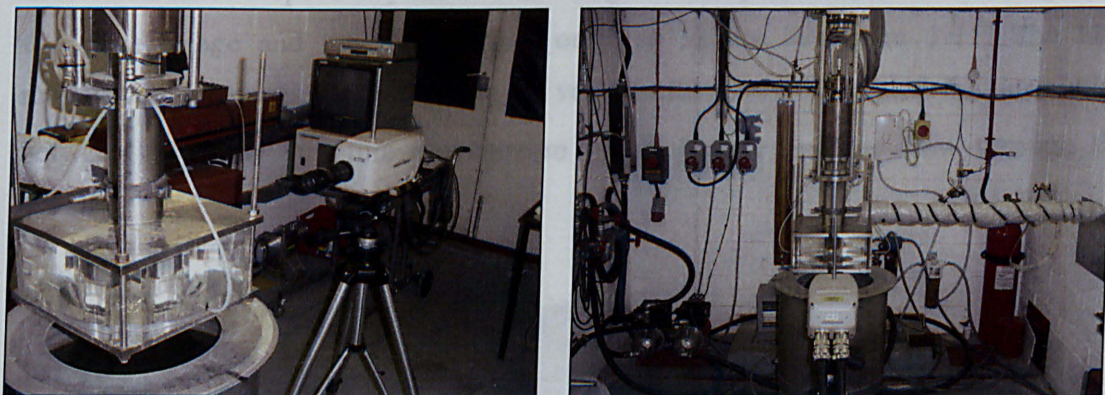
### 3.3.3. Spray visualisation

The images have been taken with a high-speed CCD camera (having a 12bit fast shutter Sensicam and a resolution of 1280x1024 pixels) with an exposure time of 0.7-3 $\mu$ s. The camera was fitted with a zoom lens and connected to a PC via an image acquisition card. The PC also had a timer card installed that triggered both the flash lamp illumination and the camera. All internal camera settings could be adjusted with the image acquisition software. The spray was illuminated by a Xenon spark light equipped with two flexible optical fibbers which increased the effectiveness of the



imaging set-up; the spark light intensity was of the order of 200 J/pulse with a pulse duration of 10 $\mu$ s. To visualise the gaseous bubbles inside the nozzle, a zoom lens was used to produce high-magnified images at the nozzle exit. Shadowgraphy method was employed so that the presence of the gas phase was identified as a black shadow. To relate these occurrences to the spray structure it was necessary to match forward illumination for the nozzle flow with the backward illumination for the spray structure, as shown in the schematic of Figure 3-10. This was achieved by using two optical fibres connected to the spark light. A signal produced by a pulse generator was giving an output towards the spark light and at the same time was triggering the camera. Since the capacitor of the spark light needs 12 seconds to get fully charged, the trigger frequency was set to 0.08 Hz.

In order to understand the dynamic behaviour and the temporal evolution of the flow phenomena inside the nozzle, a high-speed video recorder was used which could capture up to 40000 frames per seconds.

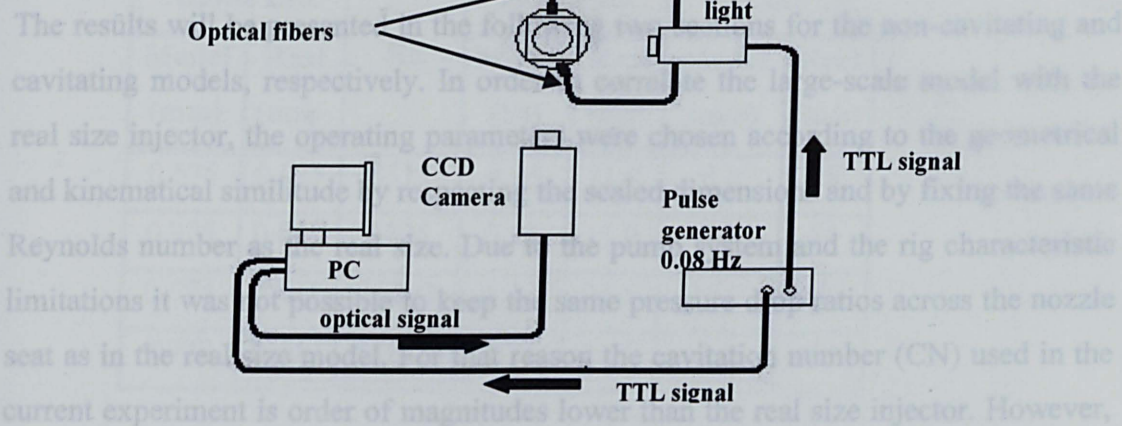


**Figure 3-9** The overall test cell set up showing the camera and image processor position in relation to the injector assembly.

Two 200Watts halogen spotlights have been employed as the constant and continuous light source. The video recorder was triggered by a remote control connected to a data store unit and then the images were transferred to the computer for the image processing. Similar flow conditions were considered as those observed with the Sensicam.

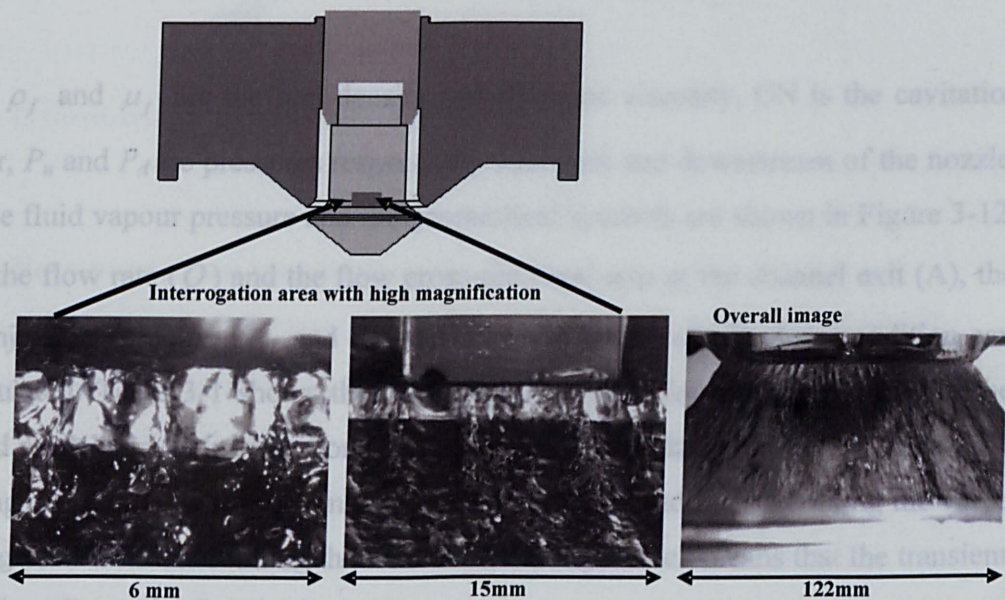


### 3.4. NON CAVITATING MODEL: RESULTS AND DISCUSSION



**Figure 3-10: Schematic diagram of spark light, camera and PC set up, and their connections.**

In order to understand the flow phenomena inside the nozzle, images were taken with different magnifications with both camera and video camera using different zoom lenses assemblies. Three magnifications of spatial resolution 122, 15 and 6 mm were used to visualise respectively the overall image of the spray, nozzle flow and spray in the same image and the nozzle flow only, as shown in Figure 3-11. The high magnification images were found to be very useful as they revealed the correlation between the spray structure downstream of the nozzle and the flow through the nozzle.



**Figure 3-11 Different image magnifications for nozzle flow and overall spray.**

---

### 3.4. NON CAVITATING MODEL: RESULTS AND DISCUSSION

The results will be presented in the following two sections for the non-cavitating and cavitating models, respectively. In order to correlate the large-scale model with the real size injector, the operating parameters were chosen according to the geometrical and kinematical similitude by respecting the scaled dimensions and by fixing the same Reynolds number as the real size. Due to the pump system and the rig characteristic limitations it was not possible to keep the same pressure drop ratios across the nozzle seat as in the real size model. For that reason the cavitation number (CN) used in the current experiment is order of magnitudes lower than the real size injector. However, the qualitative information provided by the large-scale model was useful to speculate several flow mechanisms which may explain the behaviour of the real size injector.

The Reynolds number,  $Re$ , for the following geometry was calculated as follows:

$$Re = \frac{2 \cdot \rho_f \cdot U_{inj} \cdot Lift \cdot \sin \alpha}{\mu_f} \quad (3-1)$$

$$U_{inj} = \frac{\dot{Q}}{A} \quad (3-2)$$

$$CN = \frac{P_u - P_d}{P_d - P_v} \quad (3-3)$$

where  $\rho_f$  and  $\mu_f$  are the fuel density and dynamic viscosity, CN is the cavitation number,  $P_u$  and  $P_d$  are pressures respectively upstream and downstream of the nozzle,  $P_v$  is the fluid vapour pressure and the geometrical symbols are shown in Figure 3-12. Given the flow rate ( $\dot{Q}$ ) and the flow cross-sectional area at the channel exit ( $A$ ), the mean injection velocity,  $U_{inj}$ , and Reynolds number under steady flow condition can be calculated. Table 3-1 shows the operating conditions for three flow rates in the enlarged model and their corresponding values in the real size injector. All these flow operating conditions were performed under steady flow conditions by fixing the valve lift at a given value and running the flow continuously, which means that the transient effect of needle on the flow is absent.



Needle Lift		Re	Flow Rate		Uinj	
Model (mm)	Real (mm)		Model (l/s)	Real (g/s)	Model (m/s)	Real (m/s)
0.575	0.025	6513	0.95	11.9	8.8	88
0.928	0.040	6526	0.95	11.9	5.5	54
0.575	0.025	11793	1.72	21.5	16.0	159
0.928	0.040	11815	1.72	21.5	9.9	99

Table 3-1 Flow model operating conditions and its corresponding values for the real size nozzle

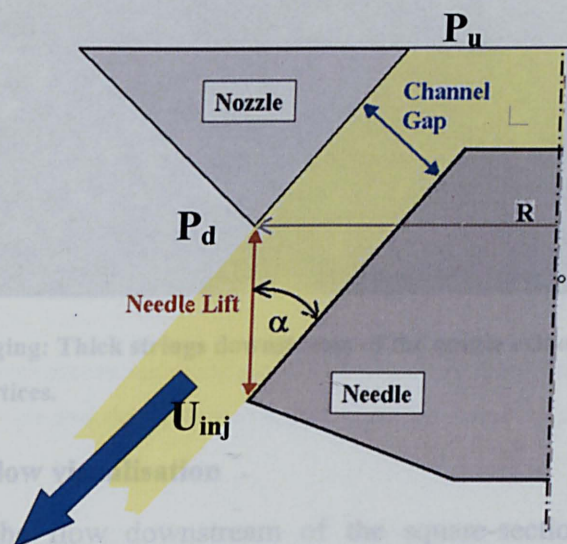


Figure 3-12 Geometry of the needle and its seat

### 3.4.1. Near-nozzle flow visualisation

In order to understand the structure of the liquid film injected from the nozzle, images have been obtained close to the nozzle exit of the non cavitating nozzle of Figure 3-6 (a). The first set of images was obtained for the liquid film outside the nozzle (Figure 3-13). The following structure and behaviour have been observed:

- The conical liquid film was oscillating in the circumferential direction
- The liquid film spray was relatively uniform around the nozzle exit except at four locations where four distinct liquid jets can be seen with thicker strings compared to the rest of the liquid spray, and relatively longer penetration.



---

These four locations correspond to the axis of the square guide locations.

- The liquid film presents a string structure uniformly distributed which is originated at the nozzle exit.
- Liquid film spray cone flaps radially due to aerodynamic mechanism related to spray shape and the tank geometrical conditions.

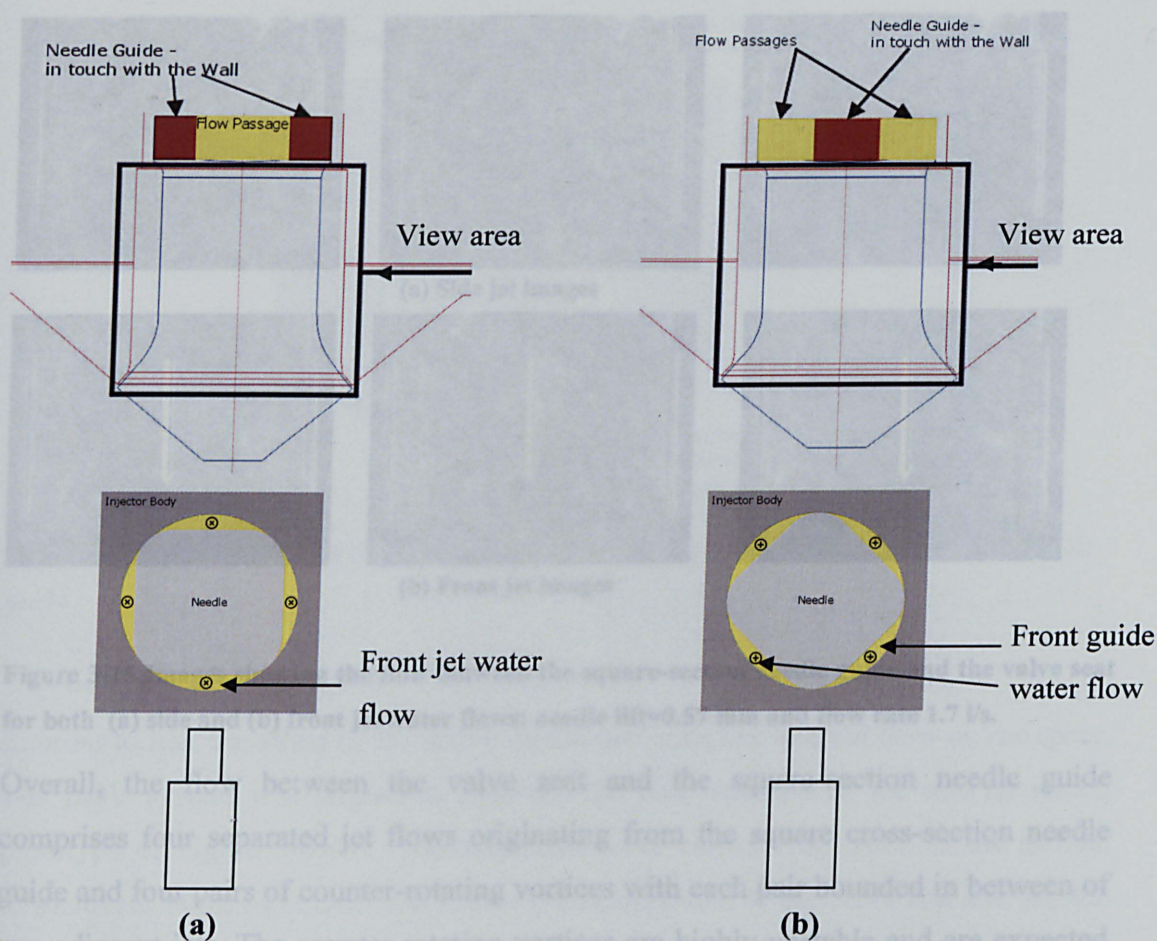


**Figure 3-13 Flow imaging: Thick strings downstream of the nozzle exit originated from the pairs of counter rotating vortices.**

### 3.4.2. In-nozzle flow visualisation

In order to trace the flow downstream of the square-section needle guide and upstream of the valve seat, a small amount of air has been introduced into the main delivery pipe through a needle of the non-cavitating nozzle of Figure 3-6(a). The air forms small air bubbles that follow the water flow streamlines and could be visualised due to the difference in refractive index between air and water. Although special attention has been paid to reduce the air bubble sizes by changing the air needle size and the amount of injected air, it was not possible to have satisfactory small air bubbles at low flow rate. However, images obtained for both low and high flow rates showed similar flow patterns and dynamics. This method was successful to describe the mean flow pattern but not accurate to have any quantification for model validation. In order to collect quantitative data about the flow velocities inside the nozzle 1-D LDV diagnostic was carried out and it will be described in the next paragraph.

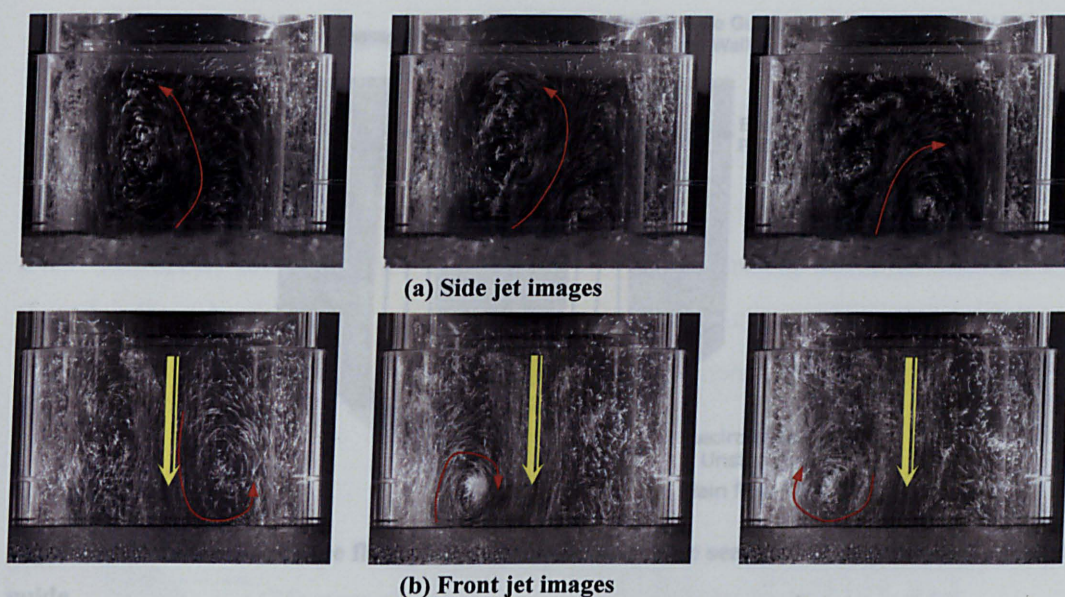




**Figure 3-14 Schematic representation of the camera locations for flow visualisation between the square-section needle guide and the valve seat for both (a) front and (b) side jet water flows.**

The flow is visualised upstream the valve seat using a high resolution CCD camera at random times with the camera facing the jet (front jet view) or the side of two jets (front guide view), as shown in Figure 3-14 (a) and (b). The side jet images revealed the presence of two counter-rotating vortices (re-circulation zones) formed by the interaction of two adjacent jets originating from the square cross-section needle guide. These side jet images can be seen in Figure 3-15 (a) and show clearly the presence of the counter-rotating vortices which are highly unstable and their interaction causes an upward jet that is swinging from left to right. Figure 3-15 (b) shows the front jet images with the main jet in the centre moving down from the guide towards the nozzle seat and two main vortices on either side.



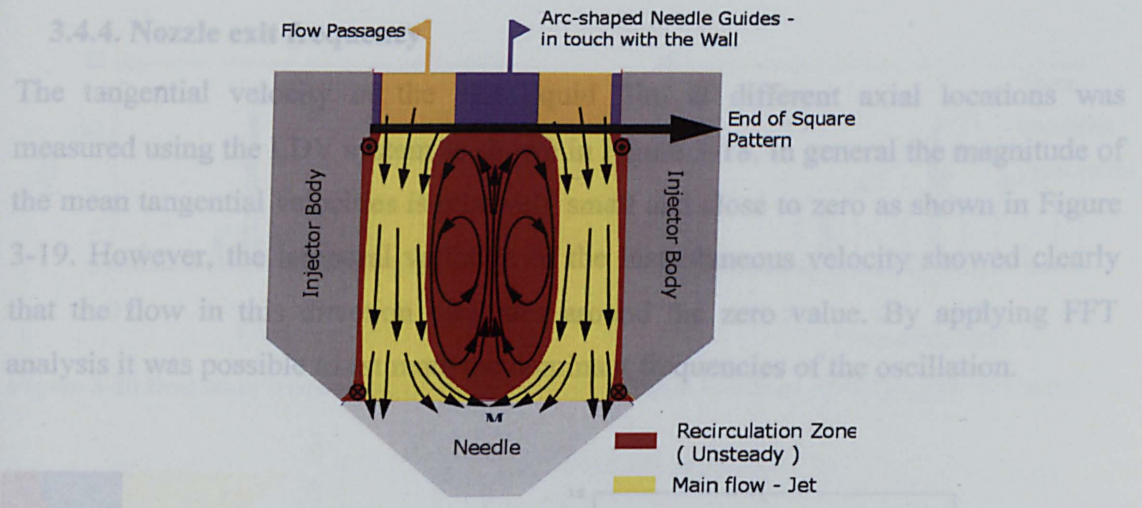


**Figure 3-15 Images showing the flow between the square-section needle guide and the valve seat for both (a) side and (b) front jet water flows: needle lift=0.57 mm and flow rate 1.7 l/s.**

Overall, the flow between the valve seat and the square-section needle guide comprises four separated jet flows originating from the square cross-section needle guide and four pairs of counter-rotating vortices with each pair bounded in between of two adjacent jets. The counter-rotating vortices are highly unstable and are expected to affect the spray stability outside the nozzle. This instability is more evident from video record of the flow, which was presented in the conference presentation ( of ICOLAD 2005 [26]. A schematic description of flow pattern in this region is depicted in Figure 3-16 which shows how the two adjacent jet flows (yellow coloured) meet each other above the valve seat. This meeting point, (M in Figure 3-16) of the two jets is as unstable as the two vortices above it.

The instability is visible in the form of oscillation in both longitudinal (along the axis of injector) and circumferential directions and further observation from the spray showed that the longitudinal mode of oscillation was suppressed as the flow passed through the narrow valve seat. On the other hand, the circumferential flow oscillation was transmitted by the liquid flow through the valve seat into the spray causing a similar oscillation on the spray. Simultaneous recording of liquid spray and internal flow (counter-rotating vortices) showed that both were oscillating with the same frequency. Similar flow pattern and instability were also observed in a wide range of examined flow rates, valve lifts, and it was observed that the change of these parameters has an effect only on the velocity of the liquid and not on the flow scene.

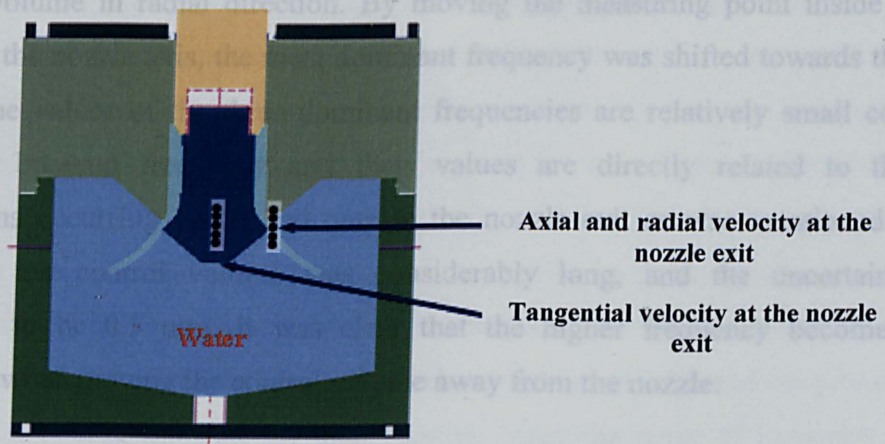




**Figure 3-16: Schematic of the flow pattern between the valve seat and the square-section needle guide**

### 3.4.3. LDV measurements

In order to link the effect of the above mentioned complex internal flow on the spray, 1-D LDV system was aligned to measure the flow velocity in the non cavitating prototype of Figure 3-6 (b). Measurements were carried out inside in the nozzle, downstream of the square-section needle guide, upstream of the valve seat and outside the nozzle across the main jet. The measurements across the main jet were achieved by projecting the laser beam through the closed Perspex chamber filled with water to avoid air-liquid jet interface which causes light path disturbance. Axial, radial and tangential velocities have been measured at different locations as shown in Figure3-17. Different forward scattering angles have been used during the measurements depending on optical accessibility in order to minimise the noise to signal ratio while having a reasonable data rate.

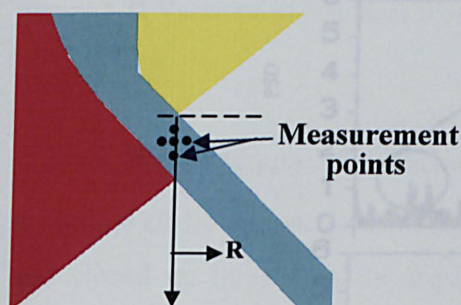


**Figure3-17 LDV measurement locations inside and outside the nozzle**

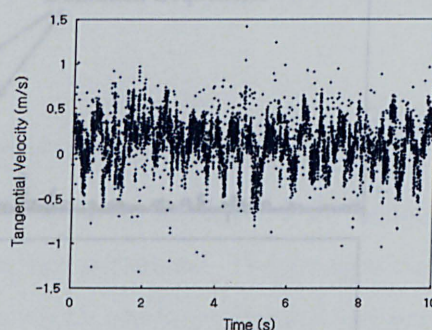


### 3.4.4. Nozzle exit frequency

The tangential velocity of the exit liquid film at different axial locations was measured using the LDV system as shown in Figure 3-18. In general the magnitude of the mean tangential velocities is relatively small and close to zero as shown in Figure 3-19. However, the temporal variation of the instantaneous velocity showed clearly that the flow in this direction oscillates around the zero value. By applying FFT analysis it was possible to estimate the dominant frequencies of the oscillation.



**Figure 3-18** Control volume locations for LDV tangential velocity measurements



**Figure 3-19** Tangential velocity measurements within the liquid jet at the nozzle exit.

The FFT analysis showed that there are three dominant frequencies as shown in Figure 3-20. One of these three frequencies is always the most dominant than the other two. Moving the control volume vertically along the gap of exit nozzle does not affect the most dominant frequency; however, this is not the case when moving the control volume in radial direction. By moving the measuring point inside the gap closer to the nozzle axis, the most dominant frequency was shifted towards the lower value. The values of the three dominant frequencies are relatively small compared with the breakup frequency and their values are directly related to the flow oscillations occurring inside and outside the nozzle exit as was mentioned before. Although the control volume was considerably long, and the uncertainty was estimated to be 0.5 mm, it was clear that the higher frequency becomes more dominant when moving the control volume away from the nozzle.

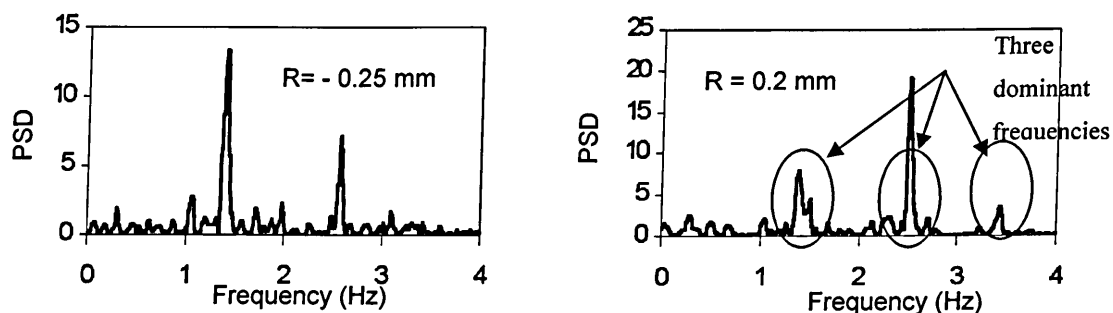


Figure 3-20 Dominant frequencies of the flow at two vertical locations,  $Q=0.7\text{ l/s}$ , lift= 0.93mm.

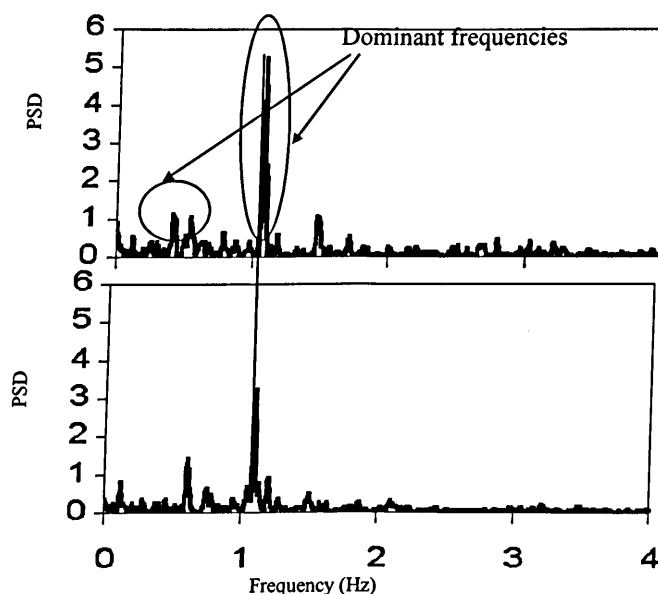


Figure 3-21 Dominant frequencies of the flow at two different vertical locations,  $Q=0.7\text{ l/s}$ , lift= 0.93mm

In order to study the effect of flow rate (or Reynolds number) on the dominant frequencies, the three dominant frequencies were computed and plotted for different flow rates. The results showed a linear relationship between flow rate and frequencies and more specifically the dominant frequencies are directly proportional to flow rates as their extrapolation passes through the origin of the axes (Figure 3-22(a)). Since the flow rate is calculated from injection velocity and needle lift, it was necessary to perform a sensitivity analysis to assess which of these two parameters is more influential and therefore each factor was individually examined. The linear relationship with the frequencies was found for both injection velocity and needle lift and the plot shown in Figure 3-22(b) illustrates clearly this linearity. Since the range of Reynolds number was chosen similar to the typical values of the real size model similar frequencies are theoretically expected to be found in the real size injector.



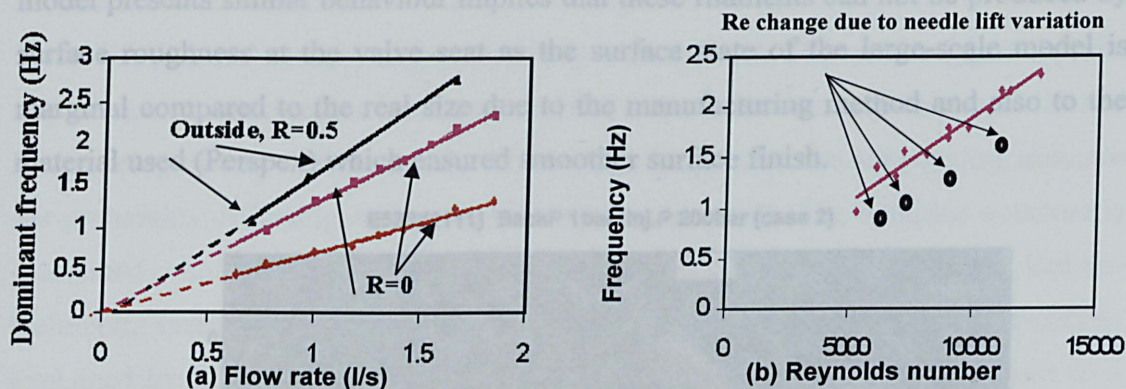


Figure 3-22 Variation of dominant frequency with (a) flow rates and (b) Reynolds numbers.

### 3.4.5. Flow filaments formation characteristics at the nozzle exit

A sample of flow close to the nozzle exit is shown in Figure 3-23 where the overall and closed up images of the liquid film are presented. The images shows a wavy structure on the circumferential direction which produces streamwise interconnecting filaments on the liquid film surface. The existence of these filaments was observed to be dependent on injection velocity so that at very low flow rates the liquid film surface was very smooth with a tulip shape and no evidence of filaments structure. In general, the string structure could be observed in the whole range of flow rates with equivalent Reynolds number as the real size injector. The filament spacing seems to be relatively small in relation to the nozzle diameter, but comparable to the gap of the nozzle and therefore within the atomisation length scale.

Accordingly, it was necessary to put more effort to examine the source of such strings and to identify the factors affecting their size.

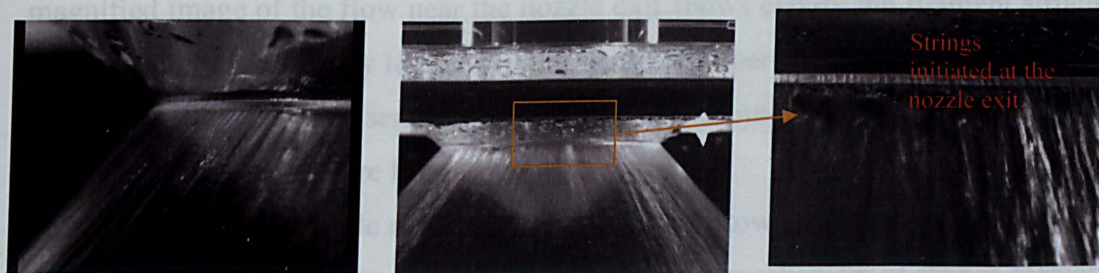
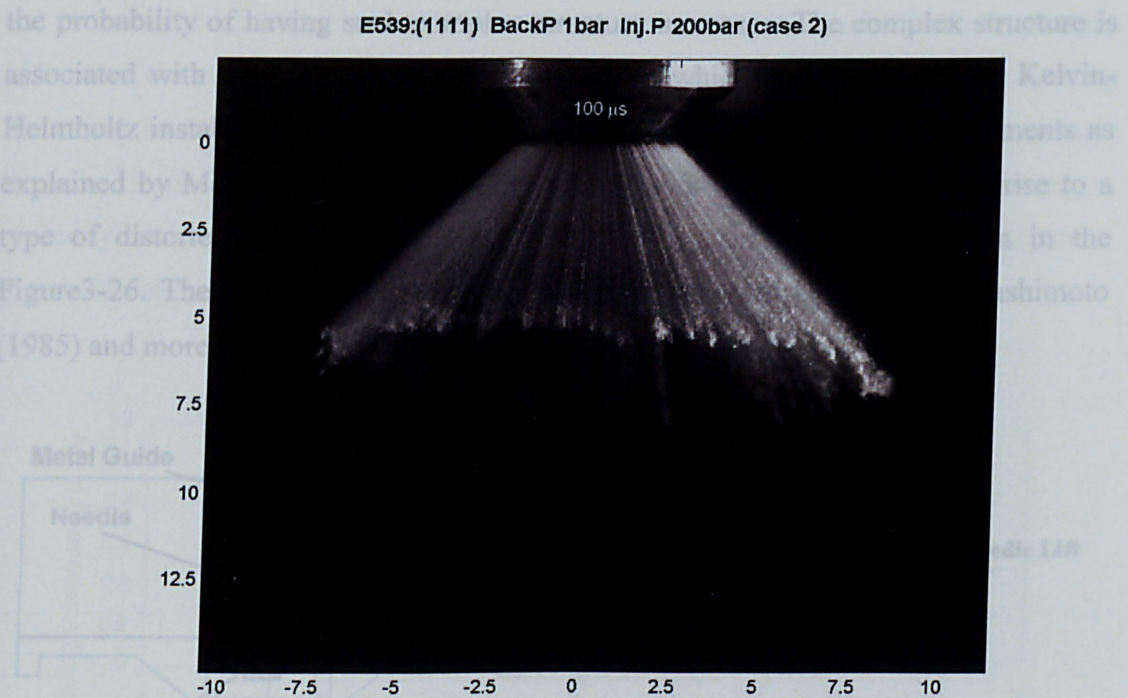


Figure 3-23 Images showing the stings on the surface of the liquid film close to the nozzle exit.

The observation of filaments structure was important since a similar structure was observed in the real size injector as shown in Figure 3-24. The fact that the large-scale



model presents similar behaviour implies that these filaments can not be produced by surface roughness at the valve seat as the surface state of the large-scale model is marginal compared to the real size due to the manufacturing method and also to the material used (Perspex) which ensured smoother surface finish.



**Figure 3-24 Image of spray from a real size injector at 0.1 ms after the start of injection at injection pressure of 200 bar and atmospheric backpressure.**

In order to find the origin of these filaments the camera was focused to visualize the flow at the nozzle exit, in the narrow gap between the needle and its seat. By using back lighting technique and zoom lens to magnify the flow structure, it was possible to visualize clearly the filaments as can be seen in the image of Figure 3-23. The magnified image of the flow near the nozzle exit shows clearly the filament structure, which gives the possibility to identify the strings number over an imaging area 6 mm long. With this set up a series of test were carried out to investigate the effect of injection velocity and valve lift on filaments formation.

Figure3-26 shows a sample of images displaying the flow structure produced by three different flow rates and two needle lifts. Although the mechanism of strings formation seems to be similar for these different operating conditions, the length scale of the whole structure becomes smaller as the liquid flow velocity increases. At higher liquid flow velocity, the string structure is converted into a more complex structure as shown in Figure3-26(c). The comparison of Figure3-26(c) and (f) for two needle lifts



at same flow rate indicates that despite the higher velocity through the nozzle at the lower lift (1.6 times) the string structure is well defined. This may suggest that the appearance of this complex structure is related to the ratio between the needle lift and interspacing distance. If the needle lift becomes larger than the interspacing distance the probability of having such complex structure increases. The complex structure is associated with the formation of spanwise waves which may be caused by Kelvin-Helmholtz instability and superimposed on top of the main streamwise filaments as explained by Mansour and Chigier [20]. The growth of these waves gives rise to a type of distorted waves which looks like a corrugated surface as shown in the Figure3-26. These structures are similar to those presented by Arai and Hashimoto (1985) and more recently by Cavhalho et al.[92].

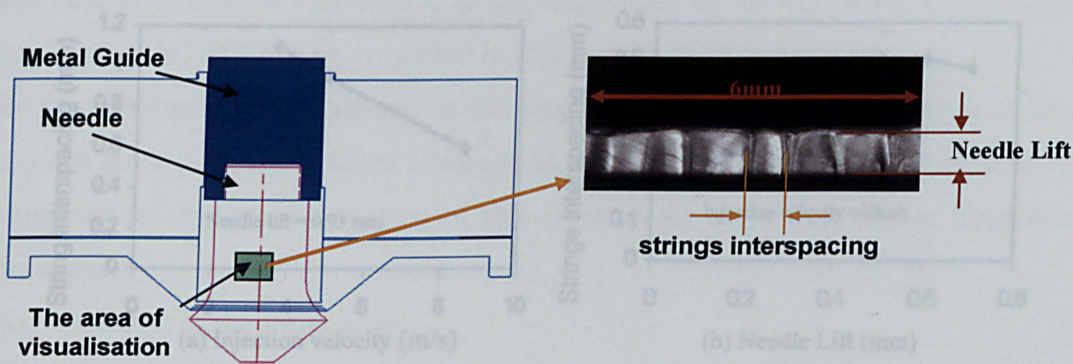


Figure 3-27 Variation of string spacing as a function of injection velocity and needle lift.

Figure3-25 Area of visualization

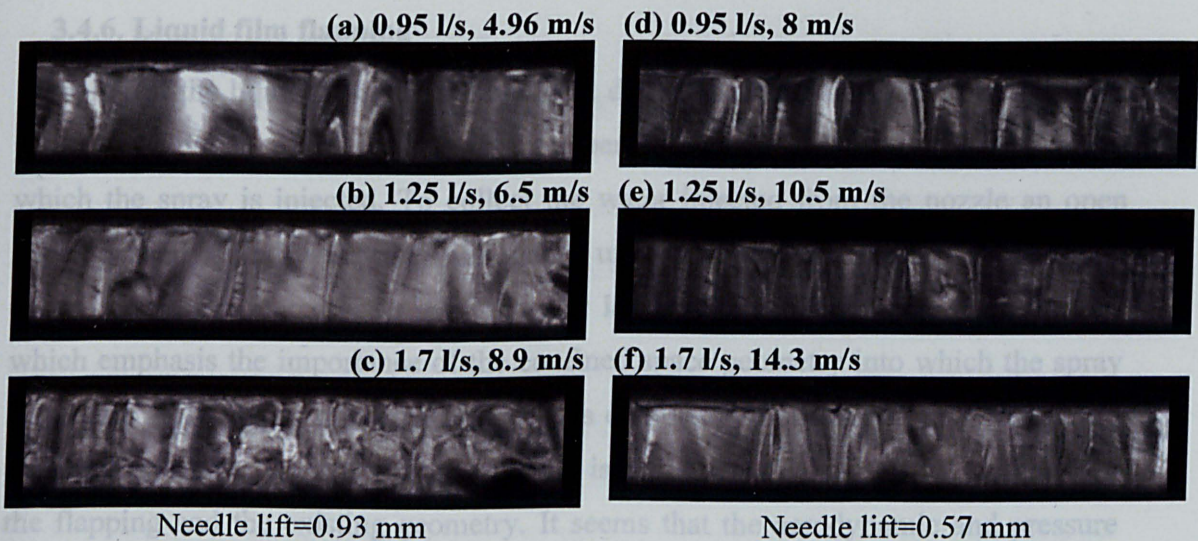


Figure3-26 Images showing the filaments in the gap between the needle and its seat for different flow rates, injection velocities and needle lifts.

The number of strings was counted from 20 images within a field of 6 mm for each operating condition and a mean interspacing distance between two adjacent filaments was calculated and presented in Figure 3-27.

The results show that the average strings interspacing distance decreases linearly with the increase of injection velocity whereas the needle lift was only producing minor effects on the strings number. Thus, it could be stated that the main factor affecting the string interspacing is the injection velocity and therefore the injection pressure. However it must be observed that the rate of reduction at higher injection velocity is probably not the same as for the analysed range in Figure 3-27(a) and there may be a threshold beyond which the velocity has no effect on the string spacing.

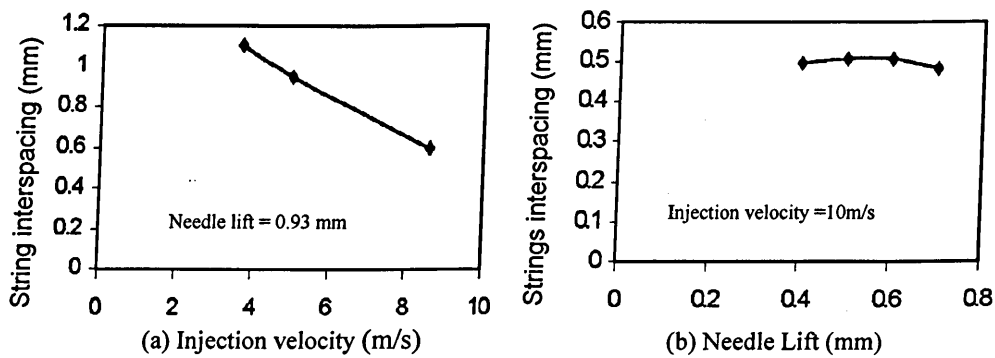


Figure 3-27 Variation of string spacing as a function of injection velocity and needle lift.

### 3.4.6. Liquid film flapping

Flapping of the liquid film was well evident downstream the nozzle and it was more pronounced under certain conditions and depending on the geometry of the space into which the spray is injected. To collect the water injected from the nozzle an open barrel partially filled with water was placed underneath the nozzle exit. It was found that the flapping increases at certain water level and specific operating conditions which emphasis the importance of the confined space geometry into which the spray is injected. Keeping in mind that this tank is completely not geometrically related to the piston cylinder geometry in the engine it is difficult to find a relationship between the flapping and the existing geometry. It seems that the aerodynamic and pressure fluctuations inside the hollow cone structure are playing a major role in spray flapping.

In a simple experiment, the closed liquid surface of the hollow cone film was

---

intentionally opened at one plane allowing the trapped air inside the hollow cone to communicate with the air outside producing a more stable spray with considerable reduction in spray flapping. This approach could be achieved in real size injector, if similar geometrical confinement is encountered (which is quite rare) by blocking the nozzle at one point. However inserting a small part to partially block the nozzle could have drawbacks and may partially deteriorate the atomisation process.

### **3.5. INWARD SEAL BAND (CAVITATING MODEL): RESULTS AND DISCUSSION**

The previous investigation in a non-cavitating model with a parallel nozzle section showed neither cavitation nor air entrainment under any operating conditions. The following results were carried out in the large-scale cavitating model (Inward Seal Band prototype) and will be presented in this session.

The spray behaviour encountered in the large-scale model of the Inward Seal Band has been quite different to those observed in the previous injector models. Due to the complexity of the spray structure of this injector the following effects have been investigated:

- a) Variation of the spray angle
- b) Presence of air pocket inside the nozzle seat
- c) Variation of spray surface
- d) String structure analysis

#### **3.5.1. Flow operating conditions**

The results correspond to different operating conditions of flow rate and needle lift and revealed that cavitation occurred only under certain operating conditions, particularly at high flow rates and very low needle lifts, while for different operating conditions the observed gas phase entrainment into the nozzle from outside had a relevant effect on the spray structure. The results of the air entrainment will be presented first followed by the cavitation results.

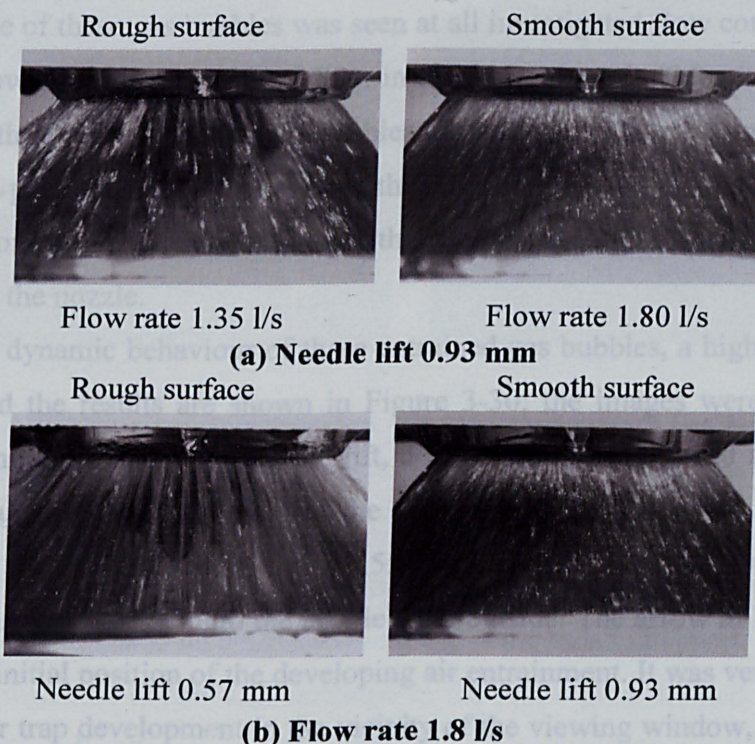
To keep consistency with the previous experiments carried out on the non-cavitating model the same operating conditions have been used also in the tests on the cavitating model. Measurements were made for two valve lifts of 0.575 and 0.928 mm and for each lift three different flow rates (low, medium and high) were used as can be seen in the Table 3-2



Valve lift [mm]		Flow Rate		$U_{inj}$ [m/s]		Re	CN
Model	Real size	Model [l/s]	Real [g/s]	Model	Real size		
0.575	0.025	0.7	8.75	5.9	64.7	5383	0.184
0.575	0.025	1.2	15	10.1	111	9228	0.29
0.575	0.025	1.8	22.5	15.17	166	1384	0.474
0.928	0.04	0.7	8.75	3.67	39.7	5393	0.093
0.928	0.04	1.2	15	6.28	68	9246	0.17
0.928	0.04	1.8	22.5	9.42	102	13868	0.31

**Table 3-2** Flow test conditions and their corresponding values for the real size nozzle.

Preliminary observation of the spray in the new enlarged cavitating model showed a different structure to that observed in the previous non-cavitating injector model. The sample results, presented in Figure 3-28 shows the complex nature of the spray surface for different flow rates and valve lifts which suggests the existence of different spray structure depending on the operating conditions. These different flow dynamic aspects of the cavitating models have been object of the following investigation. First the internal annular nozzle flow behaviour was observed by visualising the flow through the flat window (Figure 3-8) when injected into air, and then the spray structure outside the nozzle exit was observed and correlated to the in-nozzle phenomena.



**Figure 3-28:** Images of string-type spray structure: (a) Effect of flow rate at the full needle lift, 0.93mm, and (b) effect of the needle lift at a flow rate of 1.8 l/s.



### 3.5.2. In-nozzle flow

Preliminary observations under normal operating conditions revealed the presence of gas bubbles inside the nozzle passage and therefore in order to identify the nature of this gas flow closer inspection was needed. For this purpose a series of highly magnified images of the flow in the nozzle seat area were obtained through the designed flat window shown in Figure 3-11 and a sample of them is presented in Figure 3-29 which shows clearly the presence of gaseous bubbles (the black area) just upstream of the nozzle exit.

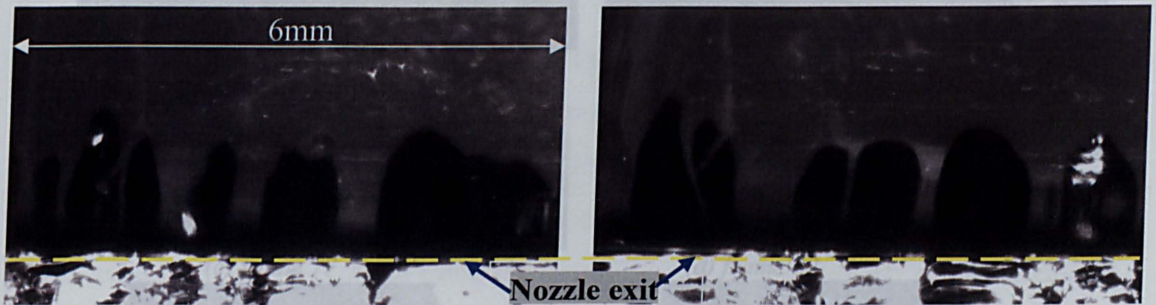


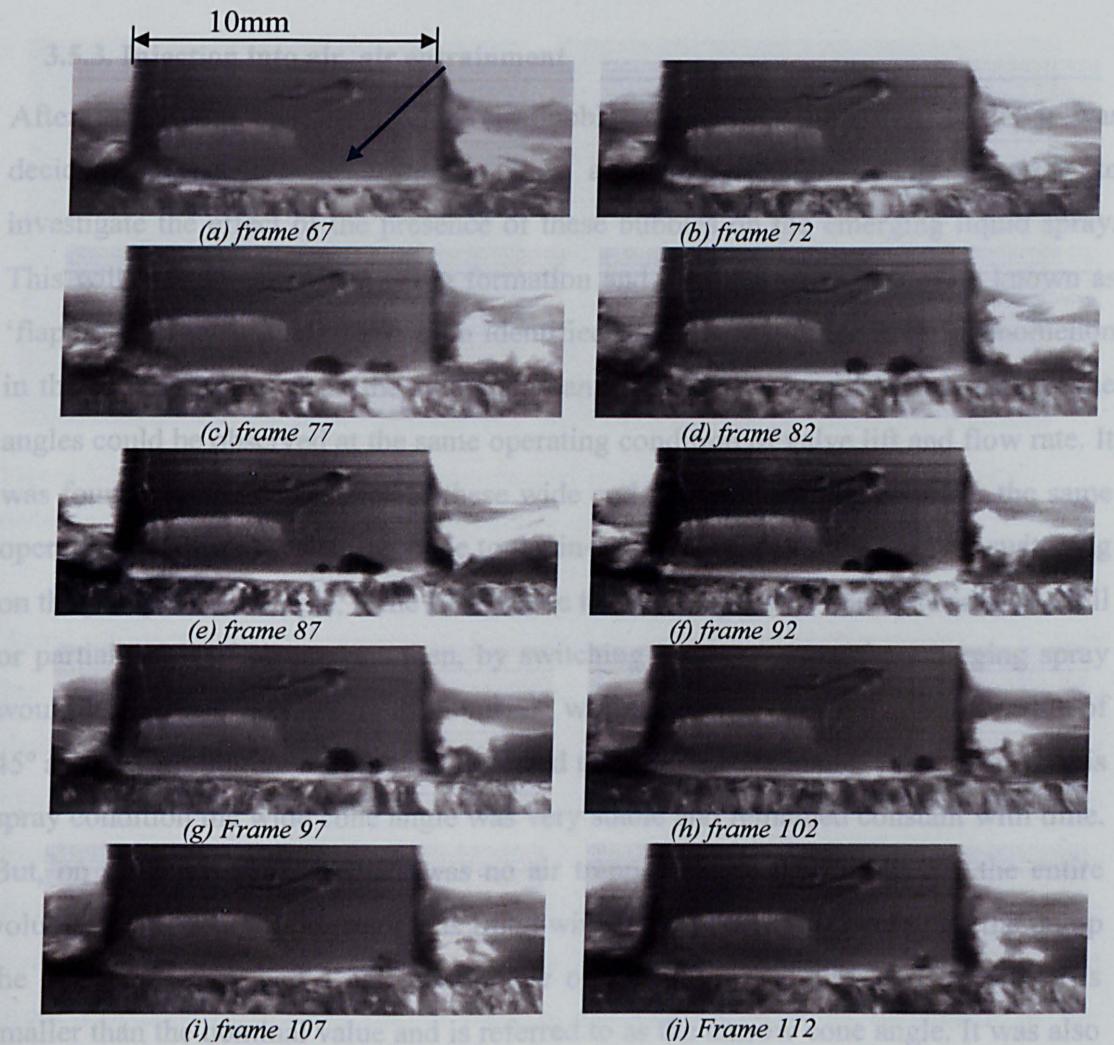
Figure 3-29 Presence of gas bubble inside the nozzle flow passage near the exit at a needle lift of 0.57 mm and flow rate of 0.98 l/s.

The presence of these gas bubbles was seen at all investigated flow conditions even at very low flow rates. It was noticed that, in all cases, these bubbles were attached to the edge of the nozzle exit, with no bubbles detaching and moving upstream into the nozzle flow passage. This implies that their formation does not take place in the narrow section of the nozzle passage and that they were entrained into the seat region from outside the nozzle.

To show the dynamic behaviour of these entrained gas bubbles, a high-speed camera was used and the results are shown in Figure 3-30; the images were related to an operating condition of 0.93mm needle lift, a flow rate of 1.2 l/s, and a frame rate of 9000fps. Figure 3-30(a) to (j) shows the sequence of the real time images of the nozzle flow with a time interval of 0.55 ms which reveal the evolution of air entrainment as air is sucked into the nozzle from outside. The arrow in Figure 3-30(a) indicates the initial position of the developing air entrainment. It was very fortunate to capture the air trap development in the vicinity of the viewing window, since most of the air traps appeared at the window as soon as the flow was starting and were usually circulating around the valve seat area. Nevertheless, the sequence of images in Figure



3-30 clearly demonstrates the formation of the air bubbles taking place at the edge of the nozzle exit. The bubble started to penetrate into the nozzle in Figure 3-30(b) and grew in time so that at 2.2 ms later, Figure 3-30(f), it is at its most developed phase; this gives an estimate of the overall time taken for a typical bubble to be fully developed, which is of the order of 2.78ms.



**Figure 3-30 Real time images of air entrainment evolution into the nozzle flow passage for a needle lift of 0.93mm and a flow rate is 1.2 l/s; the time interval between each image is 0.55 ms.**

The exit flow velocity at this flow condition is 6.2 m/s which gives a mean flow time response of 0.106ms based on  $t=G/U_{inj}$  where  $U_{inj}$  is the mean injection velocity and  $G$  is the gap between the needle and cartridge in the seat region defined by  $G=(\text{needle lift})\cos 45^\circ$ . This indicates that the flow time response at this flow condition is about 26 times faster than that of the bubble development. This suggests that, for the bubble

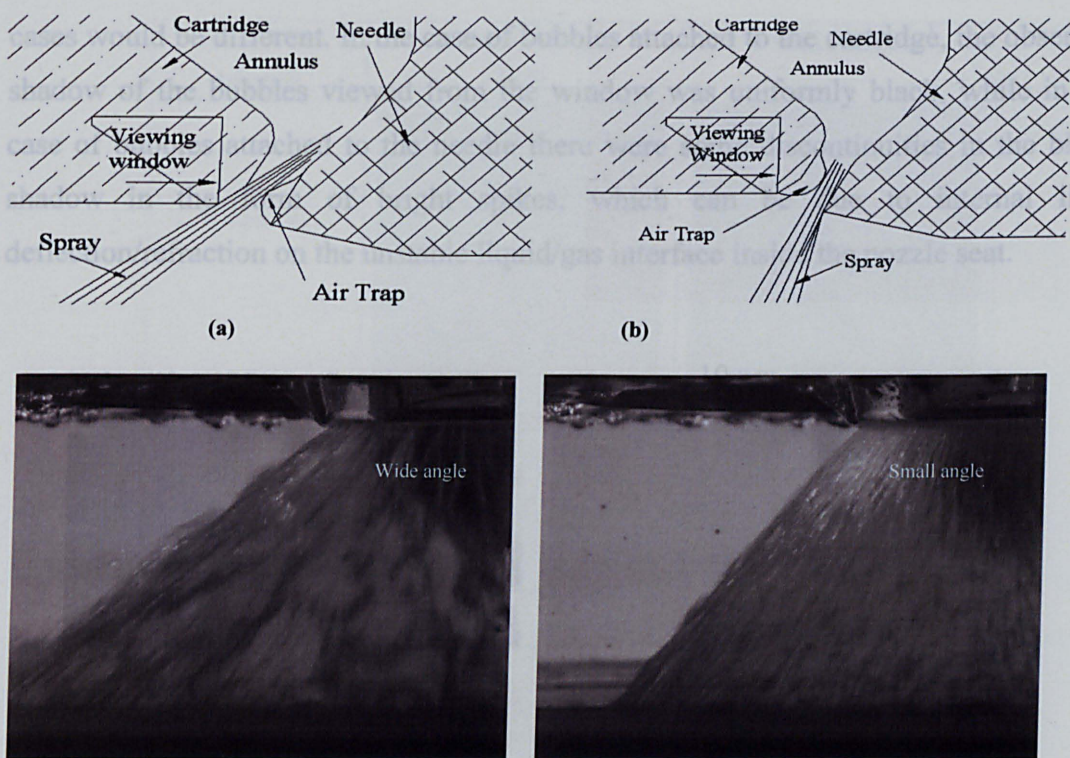
---

to be able to penetrate into the nozzle against such a high liquid jet flow momentum, there should be flow separation of the jet from either the cartridge or needle surfaces close to the exit, with a flow time response comparable to that of the bubble development. The bubble formation on the needle or cartridge surfaces has different implications, mainly on the spray cone angle, and will be discussed later.

### **3.5.3. Injection into air, air entrainment**

After identifying the presence of air bubble entrainment into the nozzle, it was decided to visualise the in-nozzle flow and spray simultaneously in order to investigate the effect of the presence of these bubbles on the emerging liquid spray. This will help to clarify the string formation and also the spray instability known as ‘flapping’. Initial visual observation identified the presence of the latter phenomenon in the form of variation in the spray cone angle so that wide and narrow spray cone angles could be observed at the same operating condition of valve lift and flow rate. It was found that the occurrence of these wide and narrow cone angles under the same operating condition was entirely due to the in-nozzle flow conditions before switching on the pump. For example, if the flow inside the nozzle passage and upstream was full or partially-full of air pockets then, by switching on the pumps, the emerging spray would have a half cone angle of about  $51^\circ$  which is larger than the nominal value of  $45^\circ$  as shown in Figure 3-31(a), and referred to as wide cone angle. Once created, this spray condition the wide cone angle was very stable and remained constant with time. But, on the other hand, if there was no air trapped inside the nozzle, i.e. the entire volume of the in-nozzle injector was filled with water, then by switching on the pump the emerging spray had a half cone angle of around  $41^\circ$ , Figure 3-31(b), which is smaller than the nominal value and is referred to as the narrow cone angle. It was also observed that under certain conditions (small lift and high flow rate), it was very difficult for the flow to maintain this narrow cone angle structure and became unstable in such a way that the spray cone angle was constantly switching between a narrow and a wide angle.





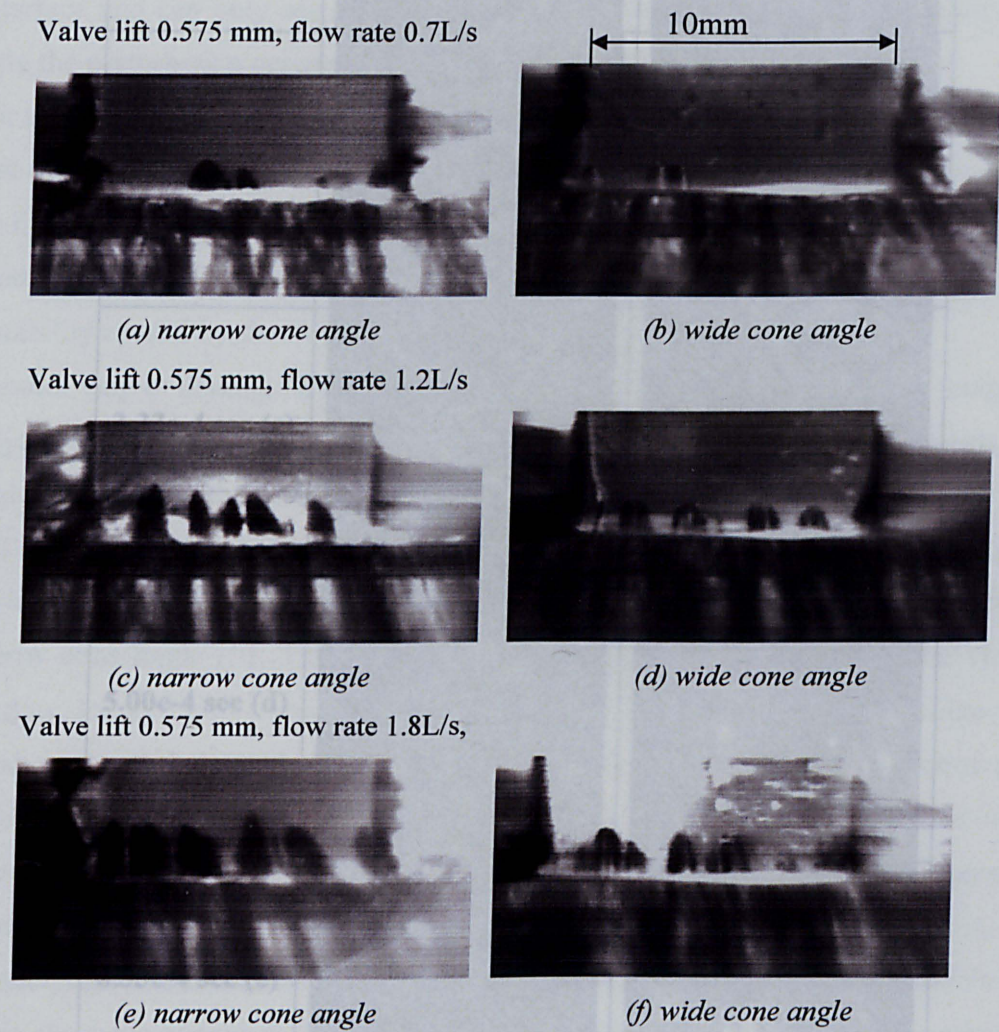
**Figure 3-31: A simple model for air traps attached on (a) the needle causing a wide spray deflection and (b) the cartridge causing a narrow spray deflection.**

Based on the results and discussion presented in the preceding paragraphs, it is clear that the presence of air bubbles entrained into the nozzle is responsible for the observed instability in the spray cone angle. To explain the flow mechanism under which the narrow and wide cone angle can be initiated, a simple flow model is proposed, as presented in Figure 3-31, in which the existence of different spray cone angles are linked to the position of the air bubbles with respect to the cartridge or the needle lift. When pockets of air are entrained into the nozzle then, depending on the location of flow separation, the air bubbles are attached to either the needle or the cartridge surfaces. When the bubbles are attached to the needle then they act as a cushion and deflect the liquid flow outwards, as shown schematically in Figure 3-31(a), therefore producing a wider cone angle. On the other hand, when the bubbles are attached to the cartridge, the flow is deflected inwards and thus a narrower cone angle is formed, Figure 3-31 (b).

There are several ways to identify whether the bubbles are attached to the needle or to the cartridge from the images. First, such distinction can be made from the quality of the bubbles shadow in the recorded images, which is related to the different type of light reflection/refraction, as the light path (for different refractive indices) in the two



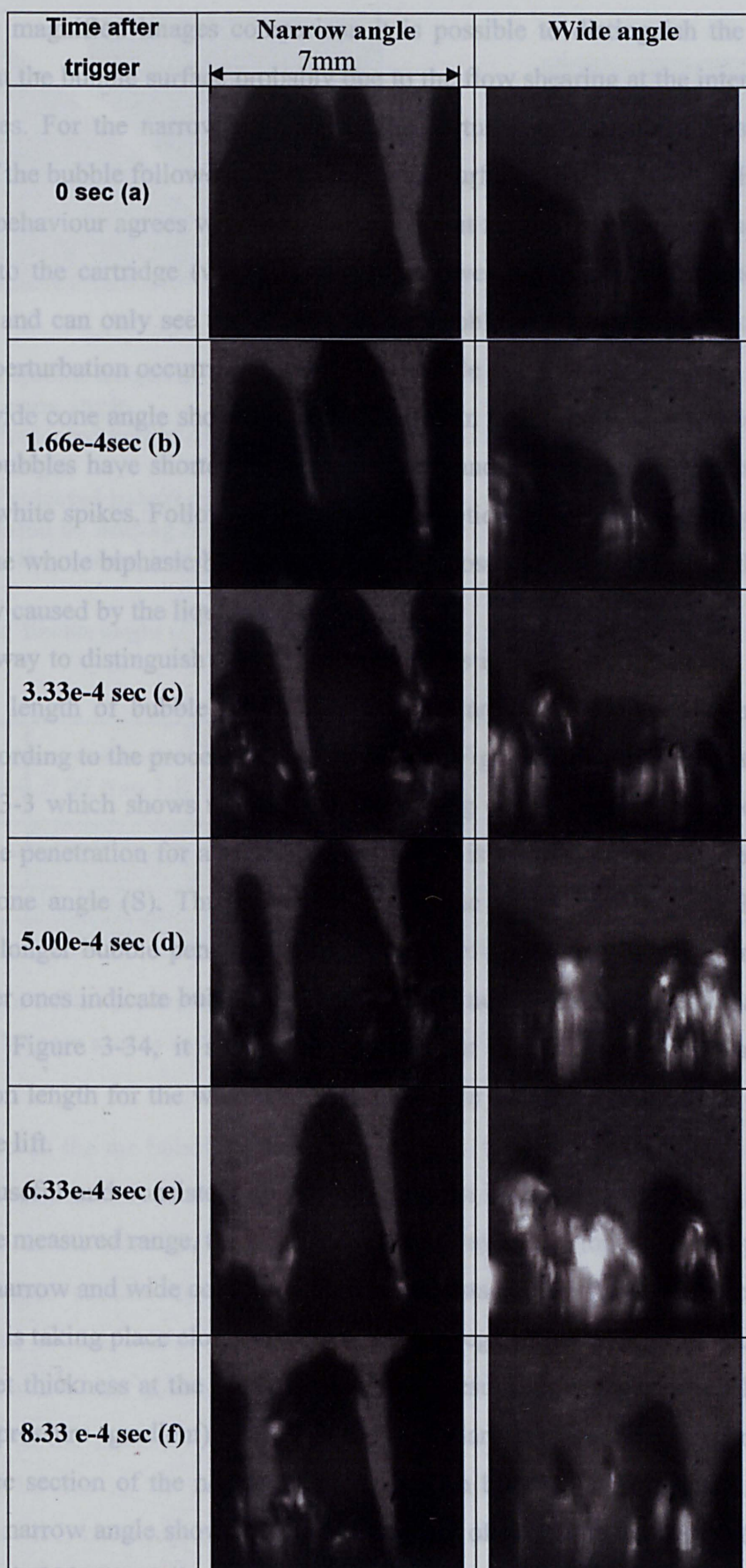
cases would be different. In the case of bubbles attached to the cartridge, the observed shadow of the bubbles viewed from the window was uniformly black, while in the case of bubbles attached to the needle there were some discontinuities in the black shadow in the form of bright spikes, which can be due to internal light deflection/refraction on the unstable liquid/gas interface inside the nozzle seat.



**Figure 3-32 High-speed video images for comparison between the shadows of the air bubbles from the narrow and wide cone angles.**

These effects can be seen in almost all CCD and video recorded images and, as an example, Figure 3-32 provides such comparison. A comparison between wide and narrow angles is also shown in a high-speed video sequence captured at 15000 fps and are shown in Figure 3-33.





**Figure 3-33** Real time images of air entrainment evolution into the nozzle flow passage for a needle lift of 0.55mm and a flow rate is 1.8 l/s; and Injection pressure 2.16 bar.

---

From the magnified images comparison it is possible to distinguish the instability forming at the bubble surface probably due to the flow shearing at the interface of the two phases. For the narrow cone angle, the perturbation is mainly present on the profile of the bubble followed sometimes by the surface burst as shown in Figure 3-33 (f). This behaviour agrees with the assumption that for the narrow angle the bubble is attached to the cartridge (window) thus the viewer is not exposed to the air/water interface and can only see the shadow of the bubble in contact with window seeing only the perturbation occurring behind or at the side of the bubble.

For the wide cone angle shown in the right column of Figure 3-33 it can be observed that the bubbles have shorter penetration length and their surface are rather covered by fizzy white spikes. Following the same assumption, if the bubble is attached to the needle, the whole biphasic bubble interface is exposed to the viewer thus showing the instability caused by the liquid disturbance.

Another way to distinguish between the two cases is by measuring in the images the projected length of bubble penetration into the nozzle. These measurements were made according to the procedure shown below in Figure 3-34 and the results are given in Table 3-3 which shows that for same operating condition the measured height of the bubble penetration for a wide cone angle (M) is always shorter than those for the narrow cone angle (S). Thus, when observing the air bubbles through the viewing window, longer bubble penetration implies bubble attachment to the cartridge while the shorter ones indicate bubble attachment to the needle. From the explanation given below in Figure 3-34, it should be noticed that the true measured value of the penetration length for the wide cone angle given in Table 3-3 is  $W=M+L$  where L is the needle lift.

Another useful and consistent conclusion that can be drawn from Table 3-3 is that, within the measured range, the lower valve lift always gives longer bubble penetration for both narrow and wide cone angles. This suggests that the flow separation on either boundary is taking place closer to the needle seat region; this might be expected as the annular jet thickness at the lower lift is thinner resulting in stronger deceleration (or adverse pressure gradient) close to the boundary as the flow expands in the divergence section of the nozzle. The comparison between the projected heights for wide and narrow angle shows a height difference of about the needle lift (Table 3-3) as if the bubble was displaced from needle to cartridge which agrees with the proposed flow model previously described.



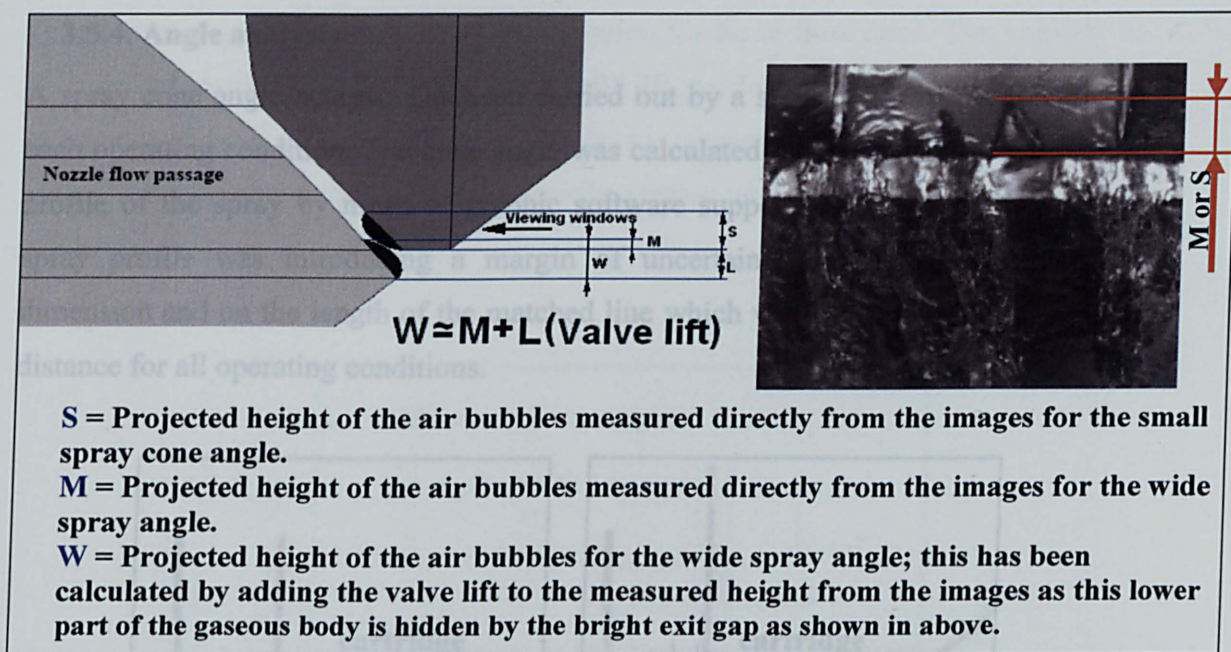


Figure 3-34 Bubble height as projected in a plane parallel to the injector axis. Schematic

	Bubble penetration				Comparison (small -wide)	
Valve lift	0.92 mm	0.57 mm	0.92 mm	0.57 mm	0.92 mm	0.57 mm
flow rate						
0.7 l/s	1.0 mm	1.6 mm	-	1.0 mm	-	0.6 mm
1.2 l/s	1.7 mm	2.0 mm	-	1.4 mm	-	0.6 mm
1.3 l/s	1.7 mm	-	0.9 mm	1.6 mm	0.8 mm	-
	small angle		wide angle			

Table 3-3 Air bubble penetration into the nozzle for different operating conditions. The difference between narrow and wide angle is about equal the valve lift

The height of the air bubble penetration depends also on the needle lift and the exit liquid velocity as will be discussed later. But in the case of velocity, in general it was found that, as the velocity increases, the pressure drop across the nozzle also increases with stronger suction created within the separated flow and, therefore, longer penetration of the bubble into the nozzle. However, beyond a certain threshold, penetration does not increase anymore and a further increase in velocity resulted in reduction of the penetration until the bubbles disappear from the viewing window. This may be due to the fact that the flow of higher momentum will expand more rapidly and it is covering the convergence exit section of the nozzle thus reducing the size of the separated flow.



### 3.5.4. Angle analysis

A spray cone angle analysis has been carried out by a statistic out of 60 images for each operating condition. The cone angle was calculated by overlapping a line on the profile of the spray by mean of graphic software support. The shaded edge of the spray profile was introducing a margin of uncertainty depending on the pixel dimension and on the length of the matched line which was chosen at the same axial distance for all operating conditions.

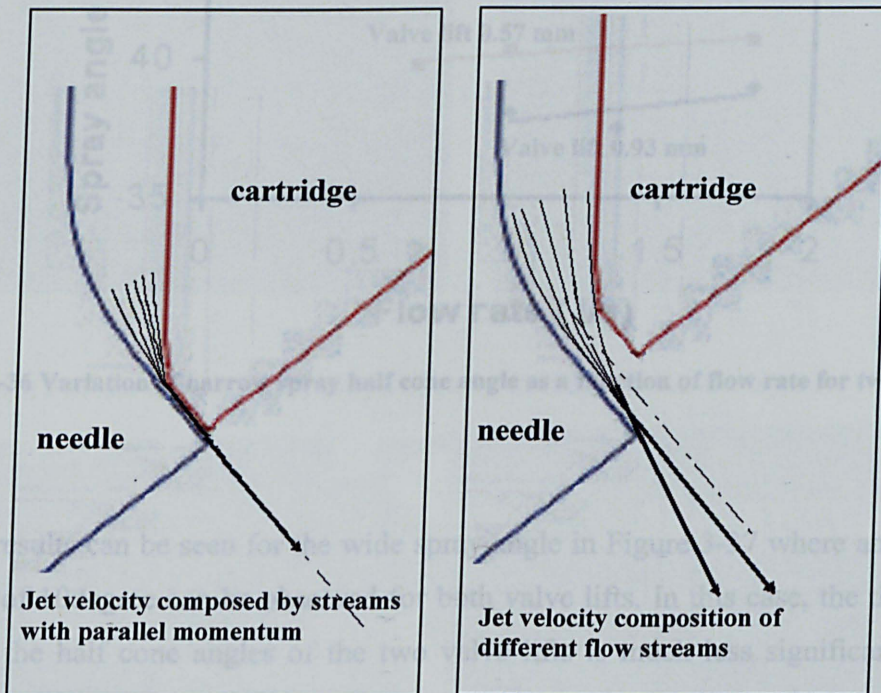


Figure 3-35 Effect of needle lift on the cone angle for narrow angle case.

For the narrow cone angle case, the results are presented in Figure 3-36 which show a slight angle increase with flow rate for both valve lifts. The results show also that at the smaller valve lift, 0.57mm, the cone angle is to some extent larger than that at the full valve lift of 0.93mm by about 2 to 3 degree. This trend can be explained by the flow momentum direction, which might vary as the liquid passes through the small diverging passage of the nozzle exit for the two valve lifts as shown in Figure 3-35. The liquid trajectory can be affected by the presence of flow separation, which, as it will be explained in the next paragraph, increases with the flow velocity. The possibility of flow separation on the needle surface is higher, since in the diverging section of the nozzle the cartridge surface is straight whereas the needle surface boundary deflects towards the injector axis. Another consideration from Figure 3-36



can be drawn by comparing the angle variation for same flow rates. The velocity in the passage restriction is higher at low needle lift, producing a higher momentum per cross-section unit. The liquid thus tends to preserve its momentum direction increasing flow separation from the needle surface and therefore increasing cone angle.

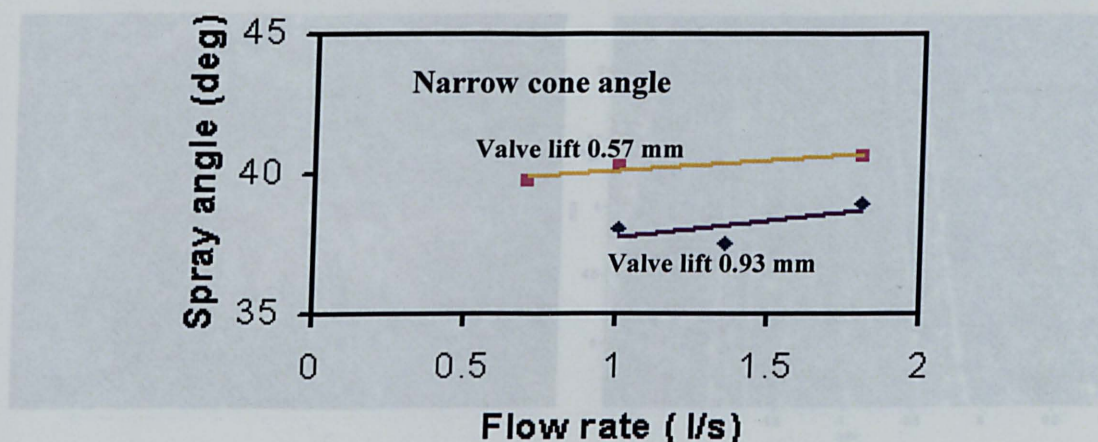


Figure 3-36 Variation of narrow spray half cone angle as a function of flow rate for two valve lifts.

Similar results can be seen for the wide spray angle in Figure 3-37 where an increase of order of 10 degree can be observed for both valve lifts. In this case, the difference between the half cone angles of the two valve lifts is much less significant with a maximum difference of order of  $\pm 1$  degree whereas the gradient of angle increase with flow rate is more significant at lower lift.

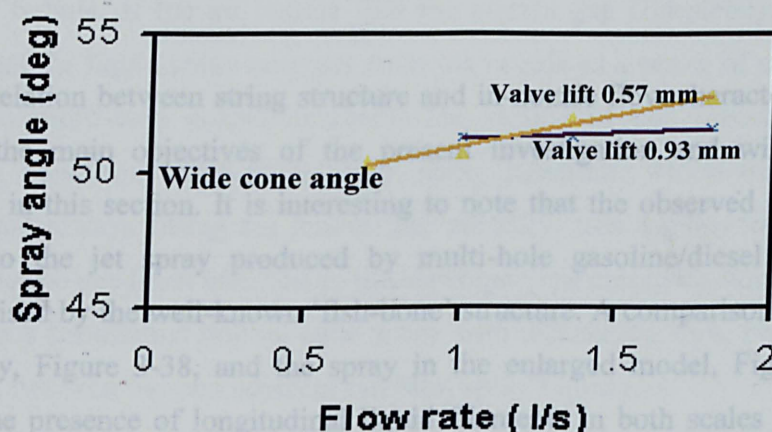


Figure 3-37 Variation of wide spray half cone angle as a function of flow rate for two valve lifts.



### 3.5.5. String structure analysis

As mentioned above, a very important aspect of the spray characteristics with an outwards opening injector is the presence of the string structure which appears in the form of longitudinal filaments and it can be observed in the magnified spray images of real size injector shown in Figure 3-38

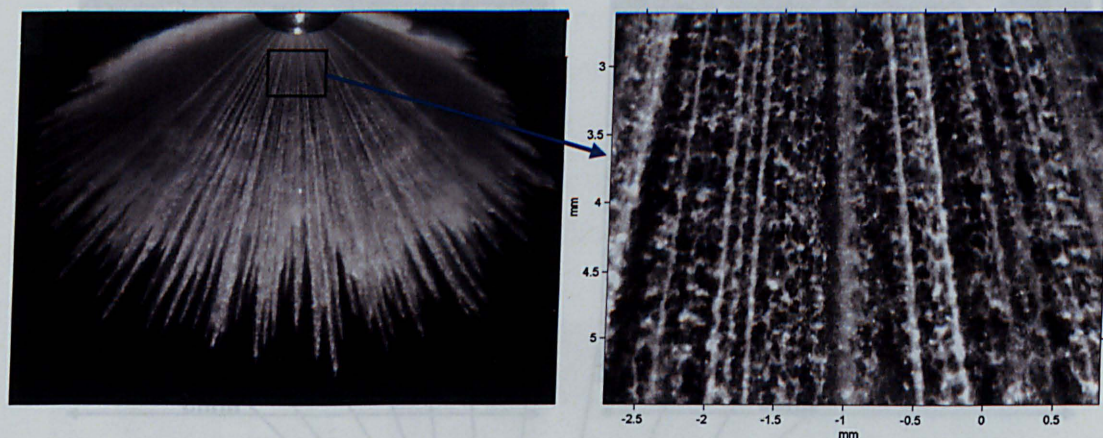


Figure 3-38: Full size and magnified images of string structure of real size injector.

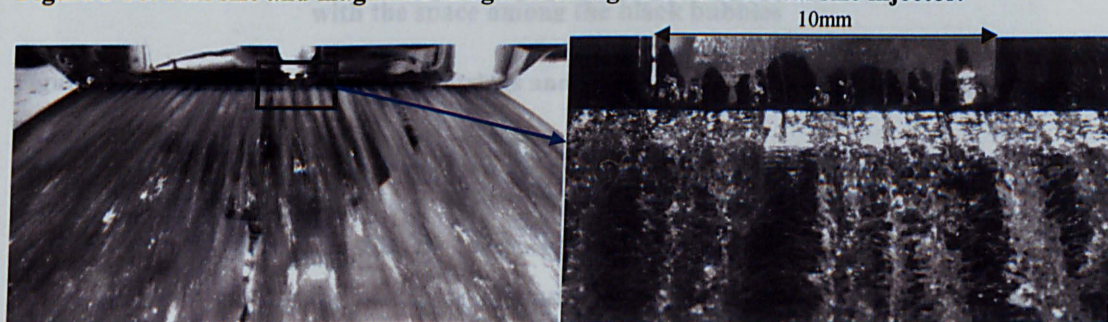
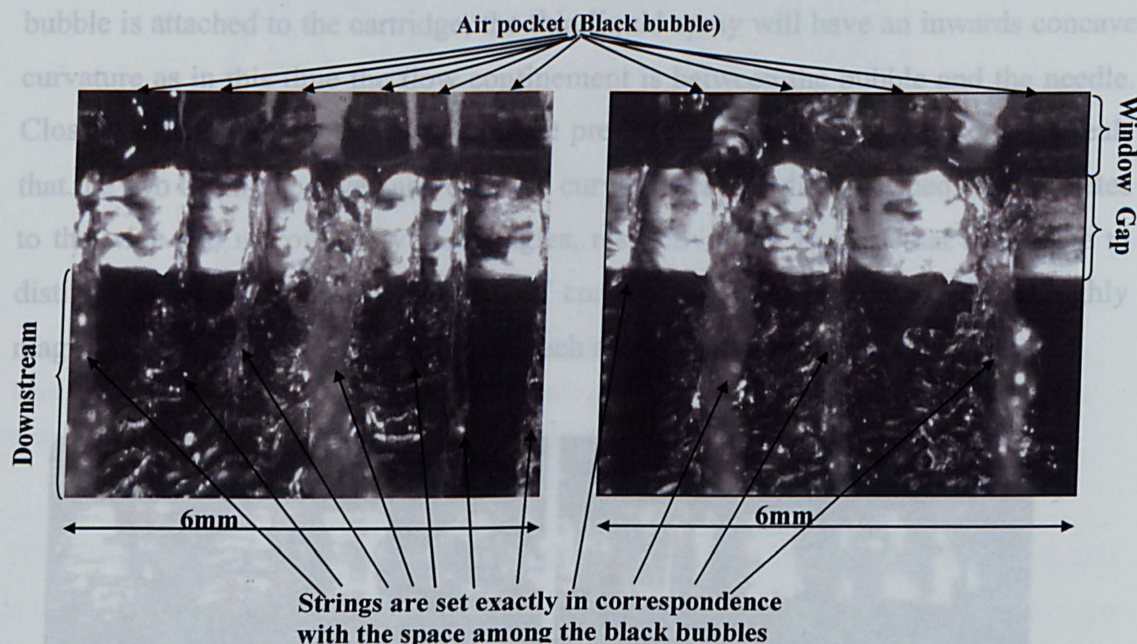


Figure 3-39 Full size and magnified images of string structure of large-scale injector

The correlation between string structure and in-nozzle flow characteristics represents one of the main objectives of the present investigation and will be extensively analysed in this section. It is interesting to note that the observed string structure is similar to the jet spray produced by multi-hole gasoline/diesel injectors and is characterised by the well-known 'fish-bone' structure. A comparison between the real size spray, Figure 3-38, and the spray in the enlarged model, Figure 3-39, shows clearly the presence of longitudinal liquid filaments in both scales which prove the consistency of the phenomenon against scale variation. Therefore, the investigation of the string phenomenon on the large-scale model can be useful to identify the mechanism responsible for the string formation in the real size injector. The two



magnified images of Figure 3-40 shows the string structure in the large-scale model which clearly indicate the existence of a link between the position of the air bubble inside the nozzle and the liquid filament outside the nozzle.



**Figure 3-40: Correlation between the strings and the in-nozzle air bubble in the large-scale model.**

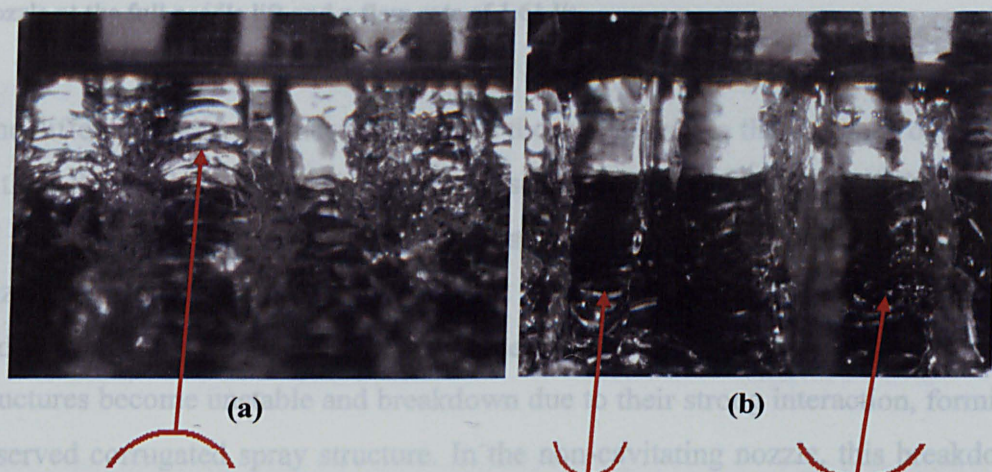
In this case, the liquid is forced to go around the bubbles and forms an emerging liquid filament leaving the nozzle as a liquid string. Immediately below the air bubble, there is a thin liquid stream coming out of the nozzle which is the liquid flow passing over the bubble. If the air bubble fills the nozzle gap completely, then one would expect that the liquid spray emerges from the nozzle as a series of separated jet flows similar to multi-hole nozzle injectors. The results of this investigation under all operating conditions showed no such spray structure, which means that the air bubbles are always filling the nozzle gap partially; this implies that they are either attached to the needle or attached to the cartridge. The emerging liquid spray structure looks like a continuous hollow cone spray with alternating thin, below the bubbles, and thick, between the two adjacent bubbles, spray liquid jets.

Figure 3-41 presents a third way for identifying the position of the air bubble with respect to the needle or cartridge surfaces. Again, as mentioned previously, the location of the air bubbles is important as it explains the mechanism under which the narrow and wide cone angles are initiated. Considering the thin liquid jet flow exiting



the nozzle, if the bubble is attached to the needle then part of the flow that passes over it will take the shape of the new boundaries (the flow is confined between the bubble and the cartridge) and the result to a viewer will be a thin spray jet (or film) with an outwards convex curvature emerging from the nozzle exit. On the other hand, if the bubble is attached to the cartridge, the thin liquid spray will have an inwards concave curvature as in this time the flow confinement is between the bubble and the needle. Close inspection of the images like those presented in Figure 3-41(a) and (b) reveals that the two types of convex and concave curvature can be distinguished which relates to the wide and narrow spray cone angles, respectively. It is clear that to be able to distinguish between these two types of curvature it is necessary to obtain highly magnified images with high resolution, such as those of Figure 3-41.

Figure 3-42 Image of corrugated liquid spray strings when there is an air bubble present in the nozzle



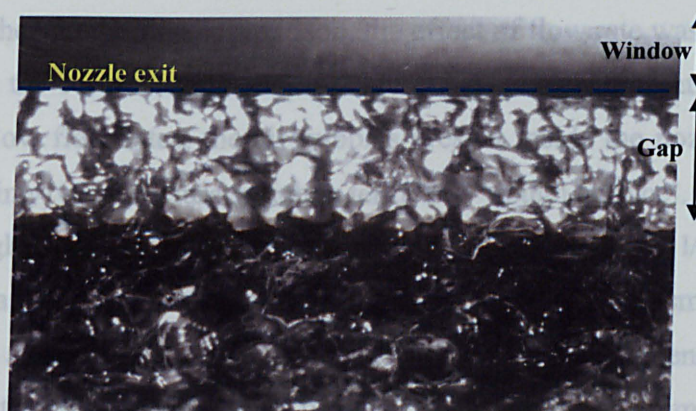
**Figure 3-41 Visual differences in the strings structure observed in the images for the (a) wide and (b) narrow cone angle at a needle lift of 0.57mm and a flow rate of 1 l/s.**

To emphasize the effect of air entrainment on the string structure, it can be observed the spray structure in case there is no air entrainment into the nozzle. The test showed that in the absence of air bubbles the liquid spray structure, downstream of the nozzle exit, was very different with no longitudinal liquid filament. Instead, a complex structure was formed with a corrugated surface as shown in Figure 3-42 for the full valve lift and a flow rate of 1.61 l/s. From the image, it is clear that there is no air bubble trapped inside the nozzle when viewed through the optical window.

It can be argued that there is a possibility of tiny air bubbles being trapped right at the exit of the nozzle, which may not be visible through the window due to the obstruction by the bottom edge of the cartridge. The corrugated liquid spray emerging

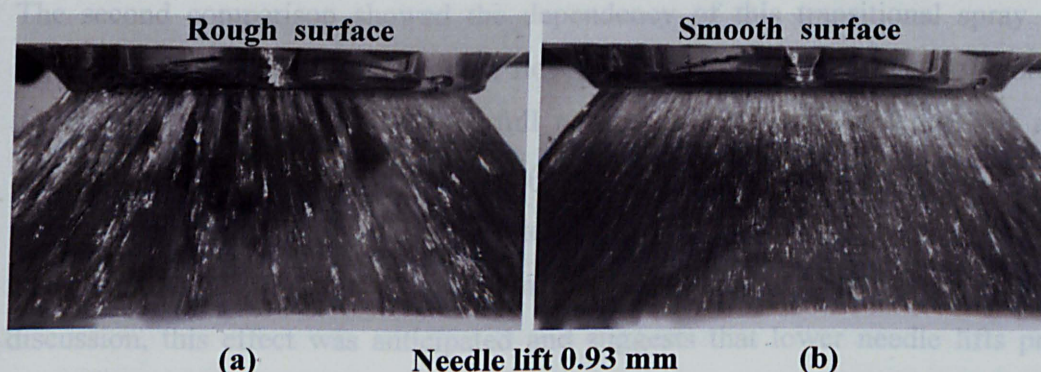


from the nozzle has no defined pattern, but right under the nozzle exit-line a pattern of string-like structures is visible which may support the presence of tiny air bubbles in that region.



**Figure 3-42** Image of corrugated liquid spray strings when there is no air bubble present in the nozzle at the full needle lift and a flow rate of 1.61 l/s.

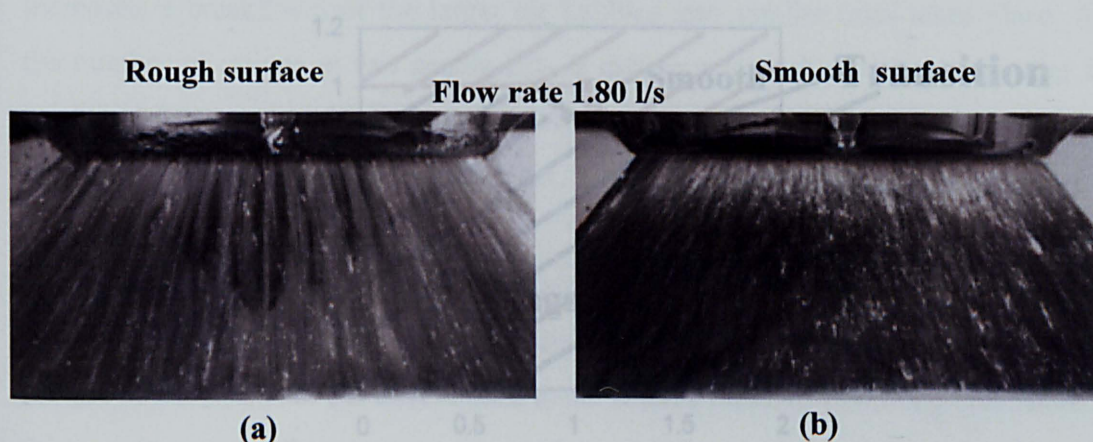
The difference between these strings and those observed in the presence of air bubbles is their Reynolds number, which in the case of no air bubble is much higher. This type of smaller strings is very similar to those observed in the previous non-cavitating nozzle injector model with a parallel exit passage. However, with the present nozzle and over a short distance away from the exit-line (see Figure 3-42) these string-type structures become unstable and breakdown due to their strong interaction, forming the observed corrugated spray structure. In the non-cavitating nozzle, this breakdown of strings does not take place as early as for the cavitating nozzle and the strings preserve their stability, forming longitudinal strings further downstream.



**Figure 3-43** Effect of flow rate on surface quality at full needle lift for flow rates of (a) 1.35l/s with air bubble (string structure) and (b) 1.8l/s without air bubble (smooth or corrugated structure).



The transformation of the spray structure from longitudinal ligaments into a corrugated type depends on two parameters: the flow rate (or Reynolds number) and the needle lift. Both cases were studied by keeping one parameter constant and varying the other. In the first comparison, the effect of flow rate was considered at full valve lift and the results are shown in Figure 3-44 which present the overall spray structure. At low flow rates, the air bubbles present inside the nozzle and the spray cone had a string-type structure which is termed as 'rough surface'. The spray surface remained rough as the flow rate increased until a value of 1.35 l/s after which the transition to a corrugated surface structure (also termed as 'smooth surface' to emphasise the absence of strings) occurred with no air entrainment observed inside the nozzle. As the flow rate increased further, the spray structure remained the same.



**Figure 3-44 Effect of the valve lift on surface quality at a flow rate of 1.8 l/s at valve lift 0.57mm (a) and full lift 0.93mm (b).**

The second comparison showed the dependency of this transitional spray on the variation of the valve lift at the high flow rate of 1.80 l/s, as shown in Figure 3-44. Although at this flow rate for the full needle lift the spray structure has already transformed into the corrugated surface (smooth), it proved possible to obtain a string-type spray (rough surface) for a needle lift of 0.57 mm Figure 3-44(a). Based on measurements of the air bubble penetration presented before and the related discussion, this effect was anticipated and suggests that lower needle lifts produce stronger suction and therefore higher flow separation than larger lifts.

In order to identify more precisely the operating conditions in which the string type or smooth type structures exist, a map was constructed from measured data of the transition points of flow rate against lift as presented in Figure 3-45. The experiment



was carried out by setting a fixed lift and gradually varying the flow rates until the spray structure started presenting sign of instability. By increasing the flow rate for different valve lifts within a range of 1 to 0.67mm, it was found a transition curve from string type to smooth type structure. In the same way, by decreasing the flow rate for a valve lift in the same range another transition curve from smooth to string type structure could be identified. Above 1mm it was not possible to have string type structure for any flow rate as well as it was not possible to observe smooth structure for a valve lift below 0.67mm. Between these two thresholds, two transitional curves define a tiny area of instability where the spray switches between the two structures and presents different spray patterns along the spray cone.

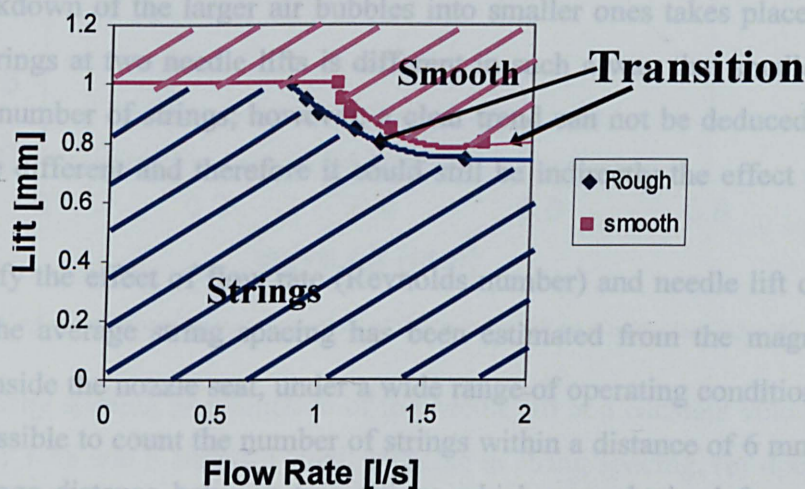


Figure 3-45 Spray structure map

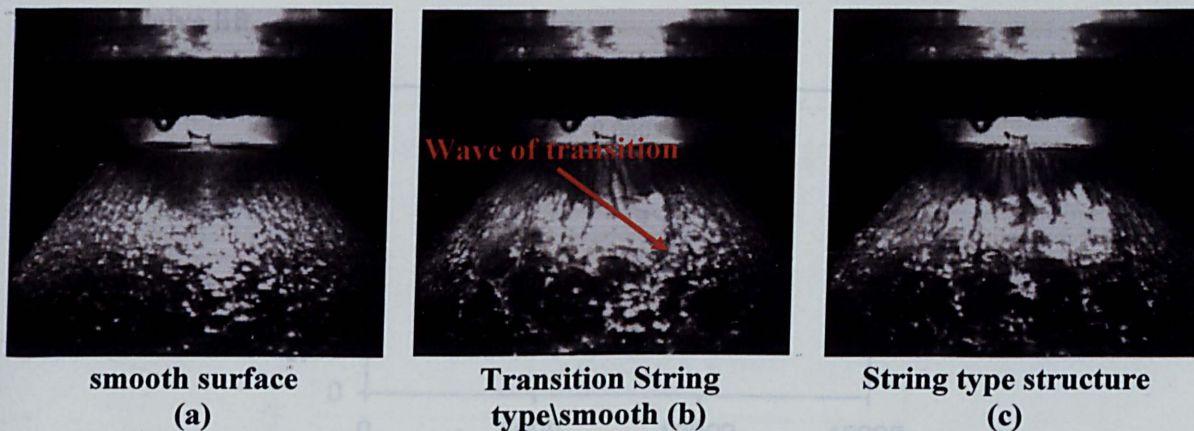


Figure 3-46 Overall snapshots of surface type transition from smooth (or corrugated) to string type (rough)

Figure 3-46 shows 3 snapshots of a transformation between smooth (Figure 3-46(a)) to string type (Figure 3-46 (c)) through a transitional phase (Figure 3-46 (b)) where the string structure advance in anticlockwise development (from left to right of the image) showing the boundary of separation of the two modes.

Another phenomenon characterising the spray of the cavitating model is the dependency of the number of strings on the flow rate and needle lift which was also previously observed for the non-cavitating model. The same effect produced by the flow rate is visible in the cavitating prototype also and it can be observed by comparing images of Figure 3-43(a) with Figure 3-44(a). The comparison clearly show that higher flow rate produces an increase in the number of strings (i.e. smaller space between two adjacent strings) and suggests that, as the velocity of the liquid increases, a breakdown of the larger air bubbles into smaller ones takes place. Also the number of strings at two needle lifts is different in such a way that smaller lifts produce a larger number of strings; however, a clear trend can not be deduced since the flow rates are different and therefore it could still be indirectly the effect of the velocity.

In order to quantify the effect of flow rate (Reynolds number) and needle lift on the string structure, the average string spacing has been estimated from the magnified images obtained inside the nozzle seat, under a wide range of operating conditions. In this way it was possible to count the number of strings within a distance of 6 mm and therefore the average distance between two strings which was obtained from each image and finally averaged over 40 images. The results are presented in Figure 3-47 and show the variation of string spacing as a function of Reynolds number,  $Re$ , for a given valve lift.

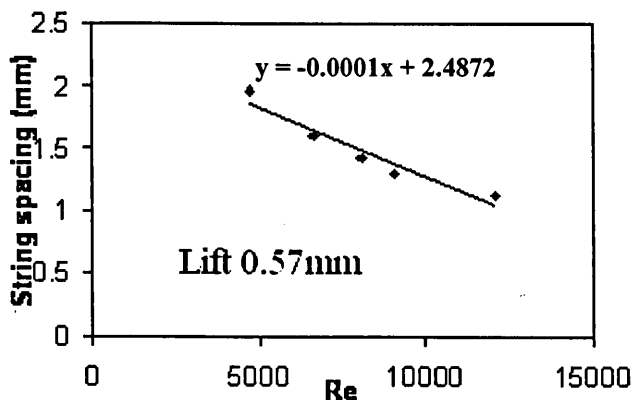
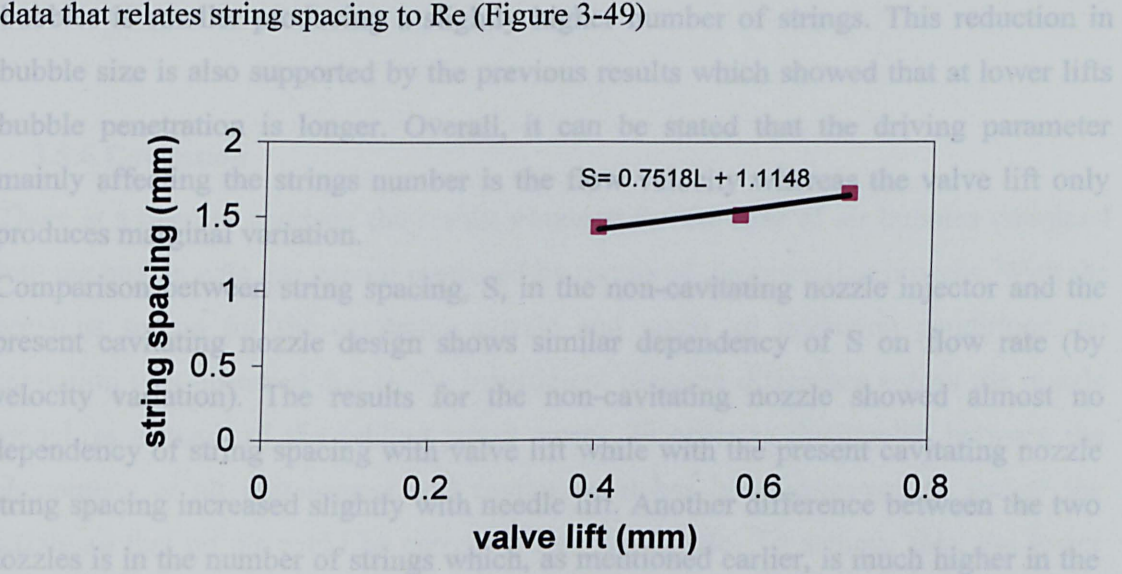


Figure 3-47 Variation of string spacing as a function of Reynolds number at a valve lift of 0.57mm.

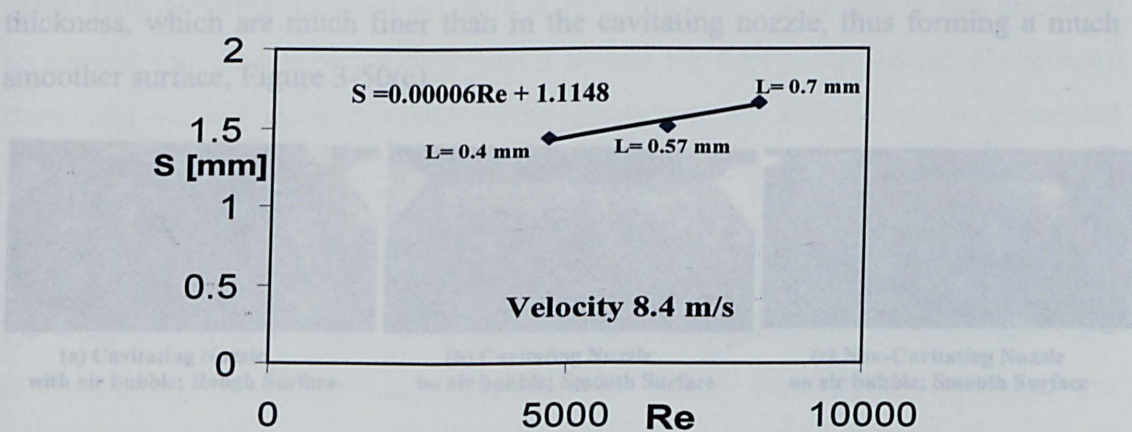


The results reveal that string spacing decreases linearly with Reynolds number so that the string spacing is reduced by about 37% when Re is increased from 5000 to 12000. Since the valve lift has been kept constant, the observed effect should be due to the change of liquid flow rate or velocity. Within the measured range, an empirical relationship can be obtained from the linear trend line interpolation of the measured data that relates string spacing to Re (Figure 3-49)



**Figure 3-48** Variation of string spacing as a function of the needle lift at a constant velocity of 8.4m/s.

The variation of string spacing as a function of the needle lift at a constant velocity is presented in Figure 3-48 and it shows a small increase in string spacing, (or decrease in number of strings) with needle lift. Another representation of the dependence of needle lift on string spacing, S, is shown also in Figure 3-49 where the string spacing variation is presented as a function of Reynolds number at a constant velocity and for different needle lifts.



**Figure 3-49** Variation of string spacing as a function of Reynolds number at a constant velocity for different needle lifts.



It can be observed that the dependence of string spacing on the needle lift (Figure 3-49) is much smaller than the dependence on the velocity as it can be seen also from the order of magnitude of the gradients for lift variation compared with velocity variation in Figure 3-47 (-0.0001 Vs. 0.00006). However this slow growing trend suggests that at lower needle lift the circumferential size (or diameter) of the air bubbles is smaller producing a slightly higher number of strings. This reduction in bubble size is also supported by the previous results which showed that at lower lifts bubble penetration is longer. Overall, it can be stated that the driving parameter mainly affecting the strings number is the flow velocity whereas the valve lift only produces marginal variation.

Comparison between string spacing,  $S$ , in the non-cavitating nozzle injector and the present cavitating nozzle design shows similar dependency of  $S$  on flow rate (by velocity variation). The results for the non-cavitating nozzle showed almost no dependency of string spacing with valve lift while with the present cavitating nozzle string spacing increased slightly with needle lift. Another difference between the two nozzles is in the number of strings which, as mentioned earlier, is much higher in the non-cavitating nozzle by up to 3 times.

As it was previously analysed, the emerging spray structure from the cavitating nozzle looks like a continuous hollow cone spray with alternating thin and thick liquid filaments forming a string-type structure with a rough surface as can be seen in Figure 3-50(a). It was also observed that when the air bubble was pushed out of the nozzle at higher flow rates, the surface became smoother, as shown in Figure 3-50(b). A similar spray structure was observed in the non-cavitating nozzle but with a different string thickness, which are much finer than in the cavitating nozzle, thus forming a much smoother surface, Figure 3-50(c).



**Figure 3-50 Comparison of spray surface quality obtained for cavitating and non-cavitating nozzle models.**

---

The discussed results have shown that the mechanism of string formation in the cavitating nozzle is due to the presence of air trapped inside the nozzle in its diverging section and the link between these air bubbles and the emerging liquid spray was established. With the non-cavitating nozzle a similar mechanism responsible for the formation of strings is expected but with the entrained air bubbles being much smaller in size, penetrating less and trapped towards the exit of the nozzle, which justifies the observed higher number of strings.

### **3.5.6.Cavitation**

There is a need to compare the results obtained for the case of air bubbles entrained into the nozzle with gas vapour produced by means of the cavitation process. With the previous set up for the cavitating nozzle and under all operating conditions, no cavitation was observed due to the insufficient pressure difference across the nozzle model, as a result of the limited pump power. In order to distinguish between the phenomena of air entrainment and cavitation, it has been necessary to isolate the nozzle so that no air could be entrained into the nozzle. To achieve this, the lower chamber was added to the cartridge casing to allow injection of water into water, as shown in Figure 3-2(b).

To initiate cavitation it was necessary to push the operating conditions by increasing the flow rate and reducing the needle lift in order to increase the pressure drop across the nozzle. By lowering the valve lift below 0.5 mm it was possible to identify vapour presence emerging from the injector nozzle, in contrast, the previously observed phenomenon of air entrainment was observed for much higher lift and lower flow rates. To achieve the required pressure difference across the nozzle, it was necessary to connect two pumps in the flow circuit so that the first pump acts as the delivery pump and was connected upstream of the nozzle, and the second one was connected to the exit of the chamber to create suction at the exit of the nozzle. The flow operating conditions included three different needle lifts and it was observed by mean of a high-speed camera at different frame rates as show in Table 3-4.

The onset of cavitation was investigated first and its dependency on parameters such as CN, Re and needle lift was established. To identify the onset of cavitation, the following procedure was carried out since the determination of the occurrence of cavitation was quite subjective. Since at the onset of cavitation, the number of vapour bubbles was very small, it proved very difficult to observe them either by naked eyes



or in the images, despite the sound of pinging noise being audible. It was thus decided to define the onset of cavitation from the identification of the pinging noise rather than from visual observation. The cavitation number, CN, for different operating conditions was calculated from the relationship given earlier on for three needle lifts of 0.35, 0.4 and 0.5mm. The results of CN as a function of the Reynolds number showed that the onset of cavitation occurred at almost the same cavitation number for all valve lifts, independently of the Reynolds number, with an average CN value of 0.53. From a qualitative analysis within the observed range it is possible to conclude that the onset of cavitation mainly depends on the pressure difference across the nozzle which is represented by a unique cavitation number.

valve lift [mm]	Flow rate [l/s]	CN	Camera Speed [fps]
0.3	0.80	3.12	27000
0.3	0.80	3.12	18000
0.4	0.94	1.22	27000
0.4	1.12	1.3	27000
0.4	1.12	1.3	18000
0.5	1.05	1.04	27000
0.5	1.34	1.29	27000

Table 3-4 Flow tests conditions for cavitation.

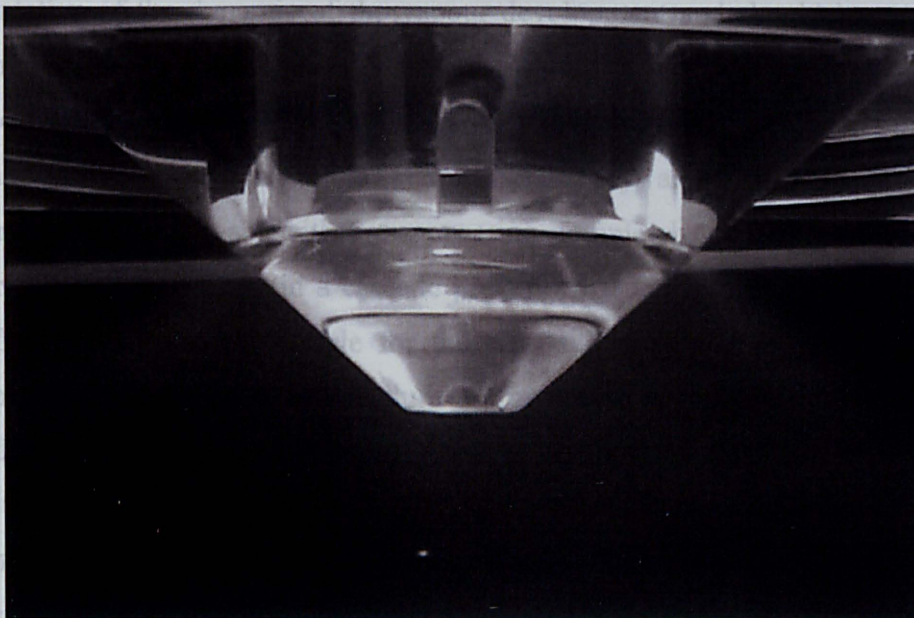


Figure 3-51 Image of a cavitating jet spray emerging from the nozzle at  $L=0.4$  mm,  $Q=1.12$  l/s and  $CN=1.3$ .



---

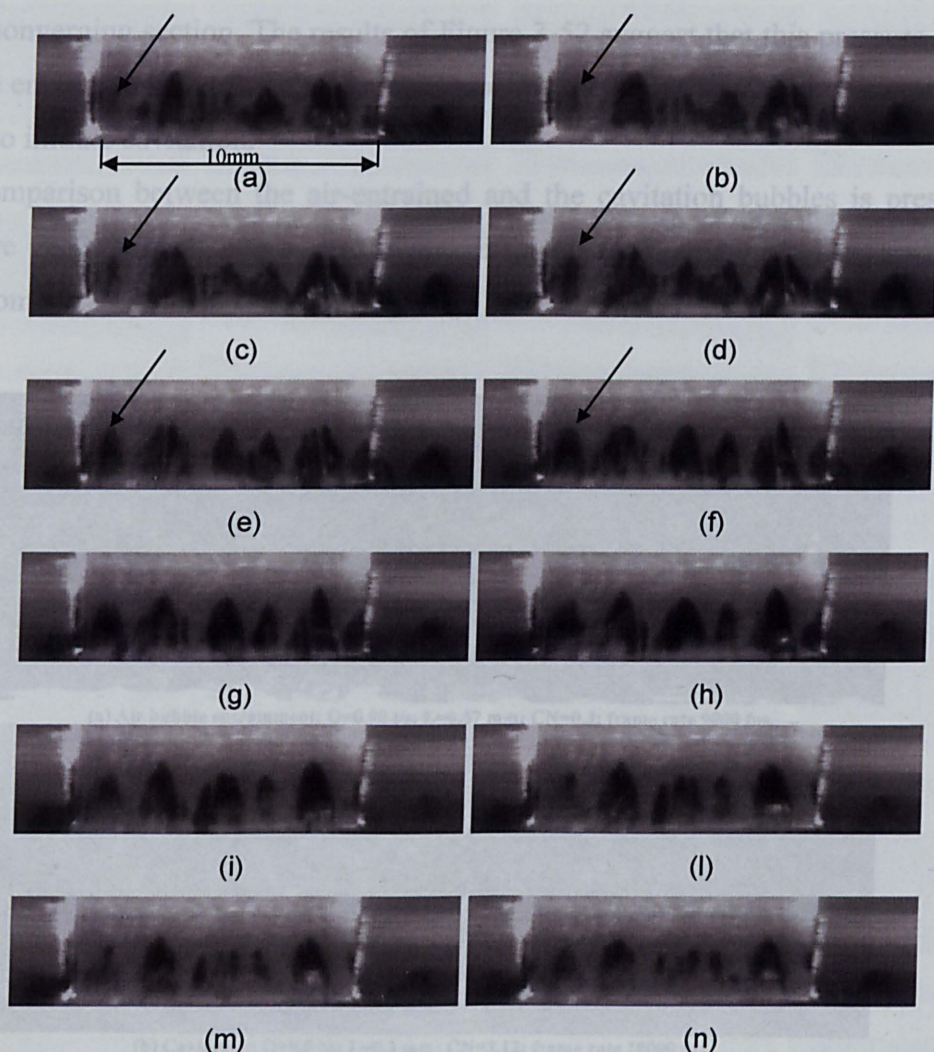
A typical example of cavitation inside the nozzle is presented in Figure 3-51 which shows clearly very small (like mist) vapour bubbles exiting the nozzle into the chamber. This suggests that when the pockets of vapour were initiated inside the nozzle they undergo extensive breakdown within the nozzle passage so that by the time they have reached the exit are fully disintegrated, appearing as mist of vapour at the exit. To gain more insight into vapour initiation and its development, it was decided to obtain highly magnified images inside the nozzle through the viewing window.

Vapour formation and its development were visualized through the viewing window in the cartridge by means of the high-speed video recorder; a sample of the results is presented in Figure 3-52 for a needle lift of 0.4mm, flow rate of 0.94 l/s, a CN value of 3.12 and a framing rate of 18000 fps. The aim of the sequence of Figure 3-52(a)-(n) is to show the location of cavitation and its development inside the nozzle. Even with this high framing rate, it proved very difficult to follow the dynamics of the vapour and a higher framing rate was required; however, at a rate of 27000fps the better dynamic resolution was gained at the expense of lower spatial resolution without considerable result improvement.

From the sequence of images, it was also possible to obtain a typical time scale required by the vapour pockets to emerge and disappear; this time response is useful for the behaviour of isolated pockets of vapour that can be identified, but is not representative of the dynamic of the vapour development and should be considered with care.

The arrow in Figure 3-52(a) indicates the area where cavitation is about to initiate. As soon as vapour pockets reach a certain size, they are quickly broken down and convected downstream, either disappearing completely or disintegrating into a number of smaller pockets (in a cascade process) that tends to move sideways. The mean flow velocity in the nozzle for the case shown in Figure 3-52 is 12.9m/s. Therefore, applying the same procedure as for the air entrainment process, it was found that the mean flow time response was of the order of 0.023ms. This suggests that, to resolve the vapour dynamics, the framing rate has to be more than 44,000 fps. The time response from the emerging pockets of vapour bubbles until their extinction was about 0.66ms (within 12 frames for a camera speed of 18000fps), which is much faster than that of the air entrainment development by about 4 times, and much slower than the flow time response by about 28 times. This suggests that as soon as vapour is

formed it is subjected to a flow at high velocities and strong shear across the nozzle which deforms, breaks up and convects the vapour pockets downstream so fast that they emerge from the nozzle as a monodispersed vapour bubble. The presence of vapour inside the nozzle at this flow condition with a cavitation number of 3.12, (Figure 3-52), was characterised by a continuous plum and thereby the nozzle can be considered to be at full cavitation state.



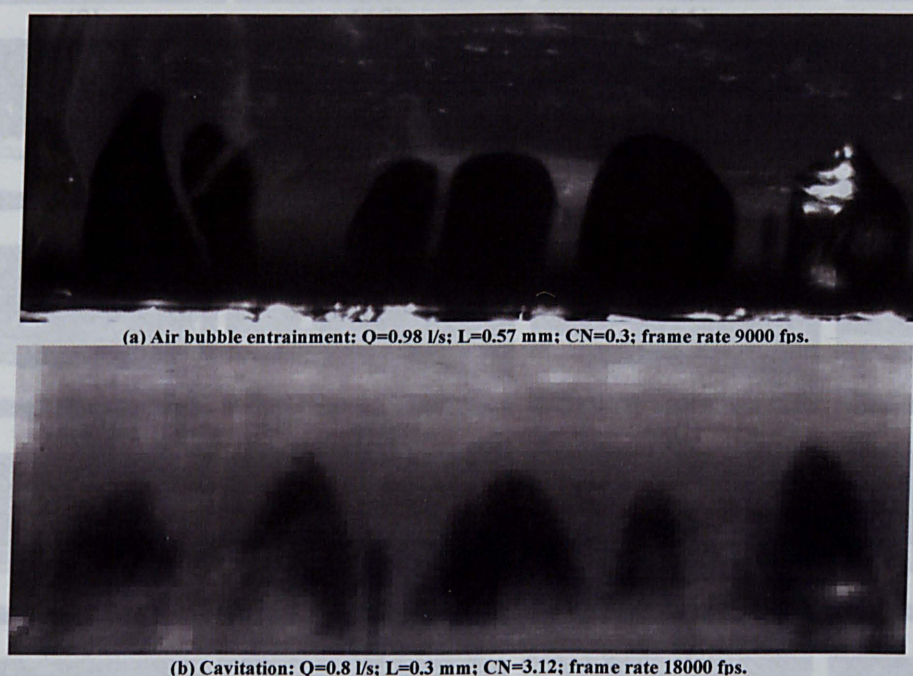
**Figure 3-52 Images of cavitation development inside nozzle seat at  $L=0.3$  mm,  $Q=0.8$  l/s,  $CN=3.12$  and a framing rate of 18000 fps.**

From the images, it is also clear that cavitation (unlike the phenomenon of air entrainment) forms and develops away from the nozzle exit; close to the nozzle seal band where the liquid pressure-drop is highest. It initiates at a point and disperses quickly downstream, forming a triangular shape with its apex being the location of the initiation of cavitation. Dark areas in the flow indicate where the vapor bubbles are forming as a result of the boiling process. Closer inspection of the images revealed clearly shows the presence of vapour pockets forming a triangular shape structure



that the starting point of cavitation was along a horizontal line across the window which coincided with the edge dividing the constant (parallel) nozzle passage and the beginning of the diverging part of the nozzle exit, as shown in Figure 3-52. This was expected because, as the flow undergoes extensive acceleration within the converging section and into the parallel section of the nozzle, the pressure drops progressively with minimum pressure towards the end of the parallel section and just upstream of the converging section. The results of Figure 3-52 suggest that this pressure drop was large enough to lower the liquid pressure below the liquid vapour pressure of the fluid and to initiate cavitation.

A comparison between the air-entrained and the cavitation bubbles is presented in Figure 3-53 which shows clearly the different flow structures between the two phenomena.



**Figure 3-53 Close up Comparison between the air bubbles entrainment and cavitation structure. (image width 6mm)**

The effect of the time scale is obvious with sharp images of the air bubbles, confirming the singularity of the air trapped; this suggests that the framing rate adopted was enough to freeze the bubble movement. However, this is not the case for the vapour bubbles which are very difficult to be distinguished from each other; this highlights the problem mentioned earlier that a much higher framing rate camera is required to capture the dynamics of the vapour bubbles. However, the close-up image clearly shows the presence of vapour pockets forming a triangular shape structure



with the onset of cavitation at its apex. seen in Figure 3-54, which represents another sequence of flow images at a larger needle lift, 0.4mm, than that of Figure 3-52 and a

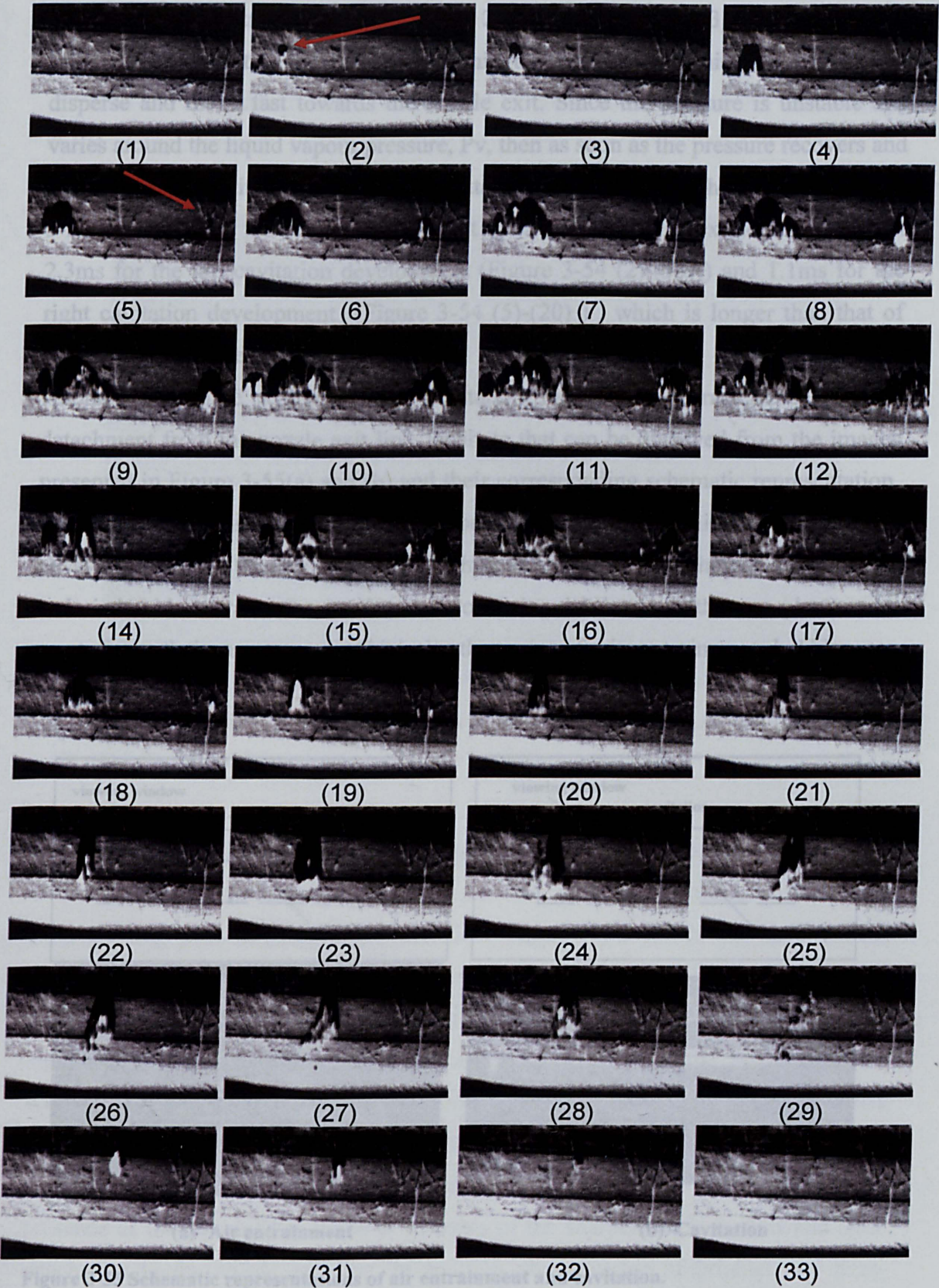


Figure 3-54 Images of cavitation development inside nozzle seat at  $L=0.4\text{mm}$ ,  $Q=1.60\text{l/s}$ ,  $CN=2.1$  and a time step of  $80\text{ }\mu\text{s}$  (25000 fps).



The initiation of cavitation can also be seen in Figure 3-54, which represents another sequence of flow images at a larger needle lift, 0.4mm, than that of Figure 3-52 and a much smaller cavitation number, CN, of 2.1. Figure 3-54(1)-(33) show clearly the initiation of cavitation bubbles well within the nozzle seat which then break up, disperse and move fast towards the nozzle exit. Since the pressure is unstable and varies around the liquid vapour pressure,  $P_v$ , then as soon as the pressure recovers and goes above  $P_v$  cavitation stops causing intermittent cavitation. The results of Figure 3-54 show that the time between the onset of cavitation and its extinction was about 2.3ms for the left cavitation development (Figure 3-54 (2)-(33) ) and 1.1ms for the right cavitation development (Figure 3-54 (5)-(20) ) , which is longer than that of Figure 3-52, as expected.

Another distinctive feature of the cavitation bubbles is characterized by their detachment from the nozzle exit line, attribute that can be observed from the images presented in Figure 3-55(a) and (b) and their corresponding schematic representation. This characteristic is in contrast to the air bubbles entrainment, which was found to be always attached to the nozzle exit line. This difference in the behavior of cavitation and air bubble entrainment can be used to distinguish between the two phenomena apart from their appearance which in the case of air entrainment bubbles are uniformly dark.

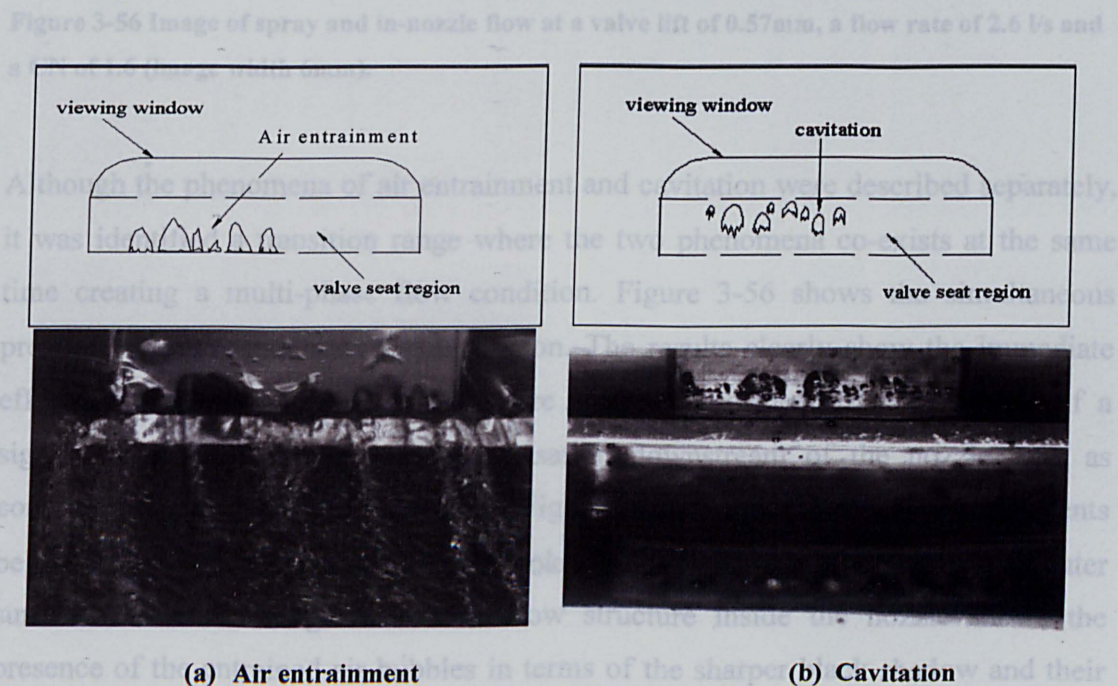
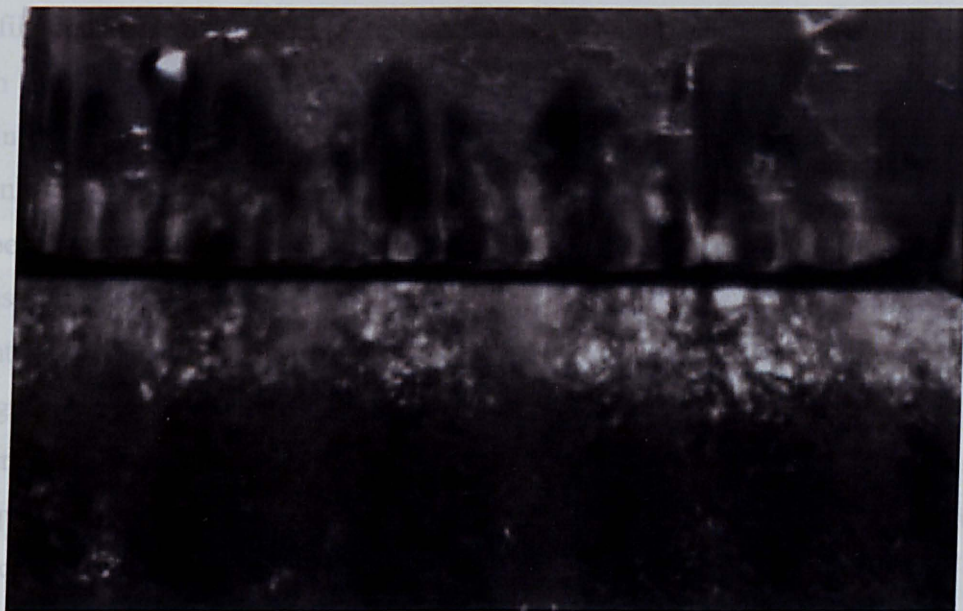


Figure 3-55 Schematic representations of air entrainment and cavitation.



It proved impossible to assess the quality of the spray under cavitation because injection took place into water. Also, as mentioned previously, it was very difficult to initiate cavitation when injecting water into air. However, using the two pumps in series to boost the delivered pressure difference across the nozzle, a condition that satisfied the cavitation criteria, i.e. at  $CN=1.6$ , could be achieved for a needle lift of 0.57mm and the results is presented in Figure 3-56.



**Figure 3-56** Image of spray and in-nozzle flow at a valve lift of 0.57mm, a flow rate of 2.6 l/s and a CN of 1.6 (image width 6mm).

Although the phenomena of air entrainment and cavitation were described separately, it was identified a transition range where the two phenomena co-exists at the same time creating a multi-phase flow condition. Figure 3-56 shows the simultaneous presence of air entrainment and cavitation. The results clearly show the immediate effect of increased velocity and pressure drops across the nozzle by means of a significant increase in the spray atomisation downstream of the nozzle exit, as compared to those of Figure 3-40 and Figure 3-41. Here, the thin liquid ligaments below the air pockets are almost fully broken and the same can be seen on the outer surface of the thick ligaments. The flow structure inside the nozzle shows the presence of the entrained air bubbles in terms of the sharper black shadow and their attachment to the nozzle exit-line. In addition, the presence of brighter and fizzy coloured shadows is evident which resembles those of the cavitation vapour cloud that



---

could rapidly disperse. It can also be observed that although the presence of cavitation seems breaking the flow downstream, it is still possible to distinguish a string type structure which is similar to the previously observed in the real size injector of Figure 3-38.

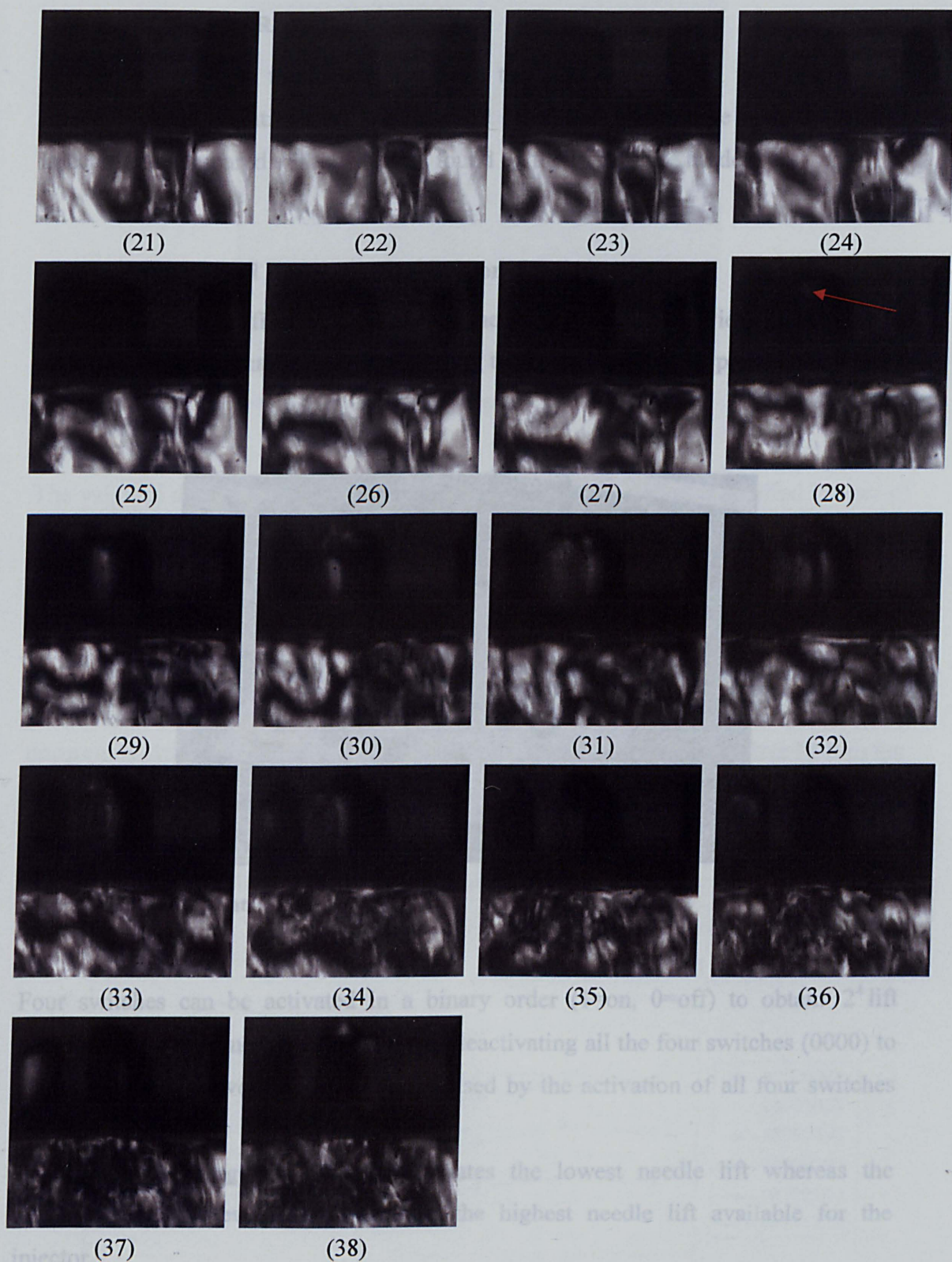
To have a better understanding of the dynamic of this particular operating condition it was captured a high-speed video at 30000fps where a frame out of two was reported in the sequence of Figure 3-57. The images show the presence of three air bubble and two filaments downstream based at the side of the central bubble which slowly fades down until completely disappearing in the dark area immediately before the exit line in Figure 3-57 (11). Subsequently the two air bubble at the side start approaching causing the two strings merging in a single filament. Finally after Figure 3-57 (28) it can be observed the onset of cavitation represented by very fast white spot moving downstream as indicated by the red arrow in Figure 3-57 (28). The impact of the cavitation on the exiting flow breaks the filament type structure causing a completely corrugated surface similar to that seen in Figure 3-56.

The presence of the two phenomena and the increase in the relative velocity between the liquid flow and air outside the injector, gives rise to a higher Weber number which enhances atomisation as evident in the relevant images.



Figure 3-57 Real time images at 30kips of air entrainment and cavitation evolution into the nozzle flow passage for a needle lift of 0.55mm, a flow rate is 1.21% and cavitation number of 0.47. (Image width 7cm)





**Figure 3-57** Real time images at 30kfps of air entrainment and cavitation evolution into the nozzle flow passage for a needle lift of 0.55mm, a flow rate is 1.2l/s and cavitation number of 0.47. (image width 7mm)



### 3.6. REAL SIZE SPRAY CORRELATION

In order to correlate the characteristics of the large-scale model with the real size injector several quantification were carried out on the pintle-type inward seal band injector and compared with the results found on the large-scale model.

#### 3.6.1. Inward Seal Band - needle position

As described in the first chapter, one of the advantages of the Piezo injector is the option to set up the max valve lift according the energy level of its piezo bodies.

Figure 3-59 Magnified image of the needle lift. (Image width 1.12mm)



Figure 3-58 Injector control panel

Four switches can be activated in a binary order (1=on, 0=off) to obtain  $2^4$  lift positions from low energy level set up by deactivating all the four switches (0000) to maximum energy level which is characterised by the activation of all four switches (1111).

The minimum energy level (0000) actuates the lowest needle lift whereas the maximum energy level (1111) actuates the highest needle lift available for the injector.

Figure 3-60 Variation of needle lift as a function of time for different switch positions.



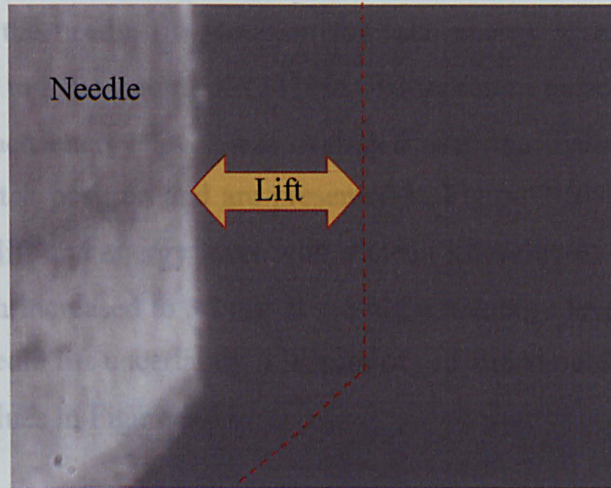


Figure 3-59 Magnified image of the needle lift. (Image width 1.13mm)

The value of the needle lift was determined by cross correlating magnified images of the injector tip when it is open to that magnified images of the injector tip when closed. The analysis was performed automatically by a Matlab code, which was correlating 20 images of the closed injector with 20 images of the open injector, Figure 3-59. In this way the needle lift can be quantified for different energy levels as a function of time and the results are presented in Figure 3-60 with a measurement uncertainty within  $\pm 3 \mu\text{m}$  ( $\sim\text{STD}$ ). The injector holder oscillation is filtered out in the analysis by the large amount of cross image correlation between open and close needle lift however tip bouncing or a discontinuity in the energy level during the open phase could cause a discontinuity in the lift position.

### 3.6.2. Inward Seal Band - Fuel mass rate

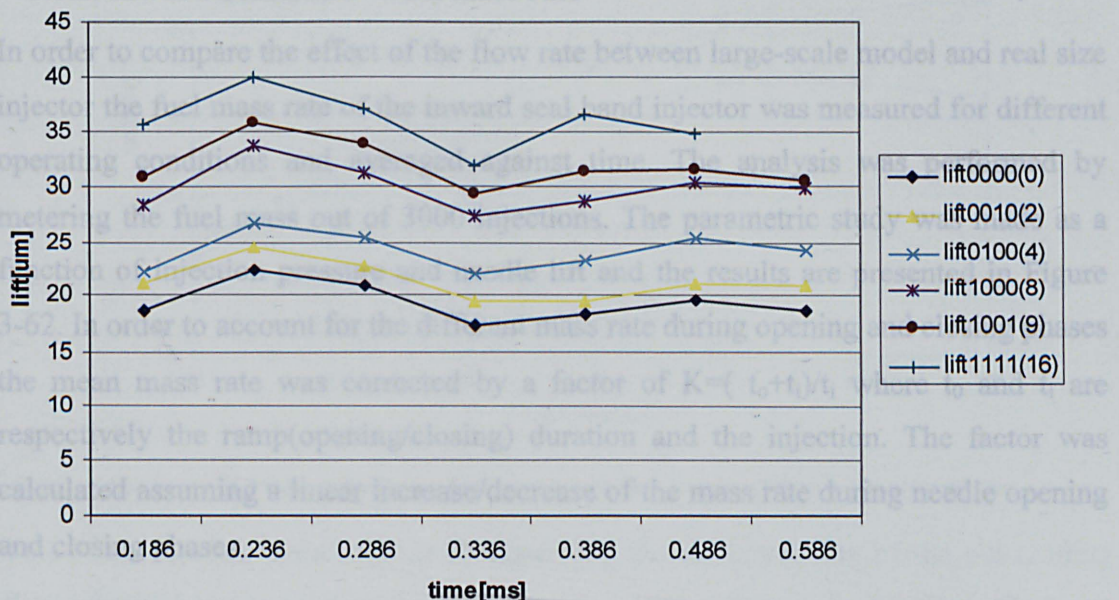


Figure 3-60 Variation of needle lift as a function of time for different switch positions.

The results show the needle lift variation for each energy level, from a minimum value of 0000 bits to a maximum of 1111bits. To represent these results in a simpler way, the lift at each energy level was averaged over the measured time and then plotted versus switch position and are presented in Figure 3-61. The plot shows the linearity between lift and energy level with a mean lift value of 19  $\mu\text{m}$  at minimum energy level which increased to 36  $\mu\text{m}$  at the highest energy level. However, for the above mention needle lift uncertainty a margin of  $\pm 3 \mu\text{m}$  should be accounted when considering the values in Figure 3-61.

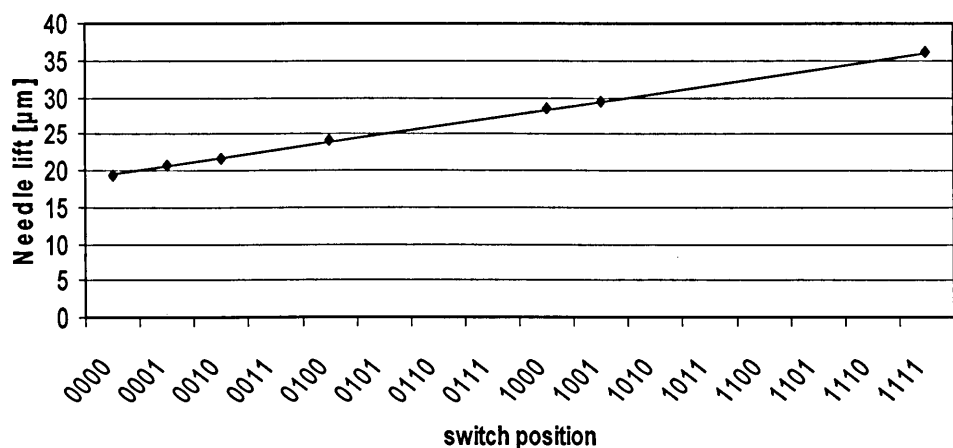
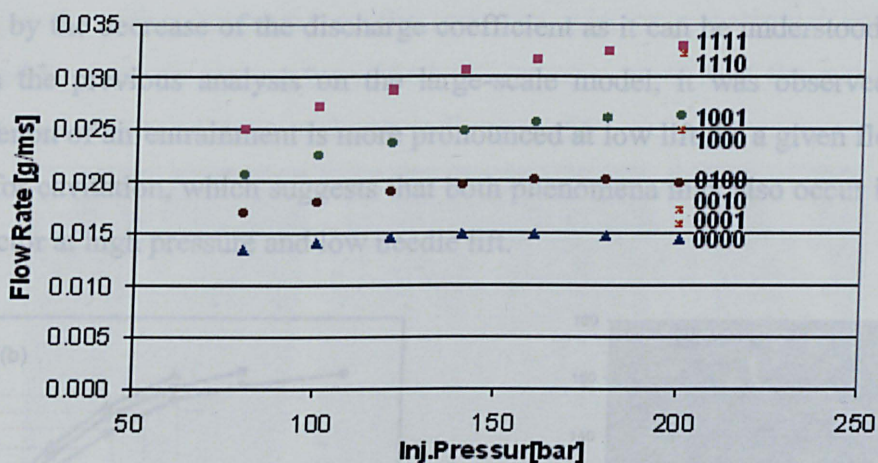


Figure 3-61 Variation of needle lift as a function of switch position calculated from image cross correlation.

### 3.6.2. Inward Seal Band - Fuel mass rate

In order to compare the effect of the flow rate between large-scale model and real size injector the fuel mass rate of the inward seal band injector was measured for different operating conditions and averaged against time. The analysis was performed by metering the fuel mass out of 3000 injections. The parametric study was made as a function of injection pressure and needle lift and the results are presented in Figure 3-62. In order to account for the different mass rate during opening and closing phases the mean mass rate was corrected by a factor of  $K=(t_o+t_i)/t_i$  where  $t_o$  and  $t_i$  are respectively the ramp(opening/closing) duration and the injection. The factor was calculated assuming a linear increase/decrease of the mass rate during needle opening and closing phases.

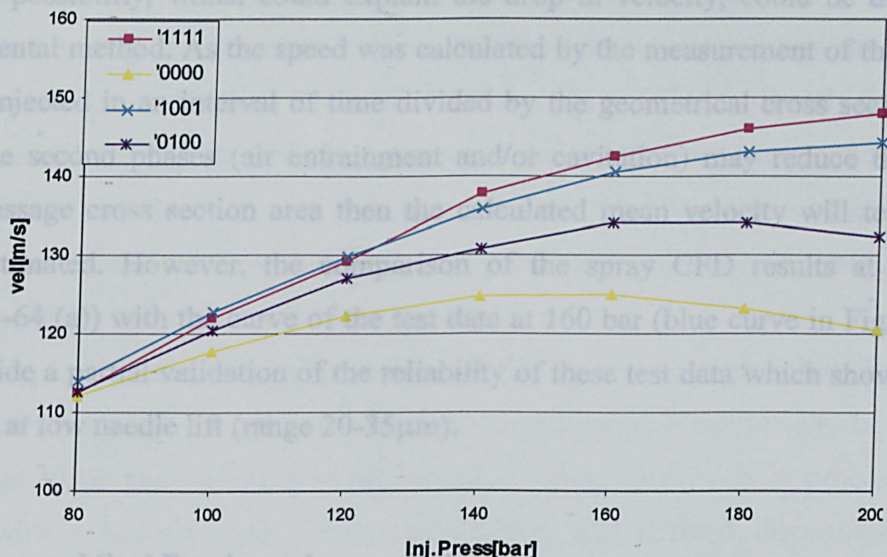




**Figure 3-62** Variation of real size injector mass rate as a function of injection pressure for different needle lift set up.

As it could be expected, (Figure 3-62), the mean mass rate increases with injection pressure and also with the needle lift as a result of the increase in the discharge coefficient. Note that the mass flow rate at 200bar injection pressure includes all eight different lifts which follows the same increasing trend.

What is less evident is the decrease of flow rate at low lift for injection pressures higher than 160bar which may suggest that phenomena affecting the discharge flow coefficient due to the formation of the air entrainment or cavitation occurs.

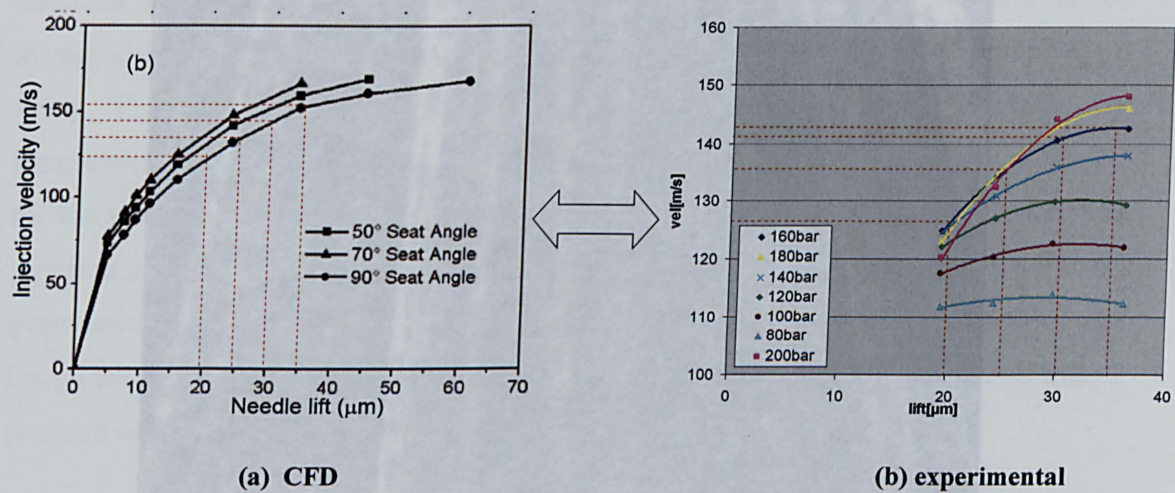


**Figure 3-63** Averaged flow velocity variation through the nozzle with injection pressures.

This effect is even more evident by observing the mean velocity of the out coming flow which shows a decrease in flow rate after 160bar for needle lift 0100 (24.2 $\mu$ m) and 1001 (29.5 $\mu$ m). On the other hand, the velocity at higher needle lift seems less



affected by the decrease of the discharge coefficient as it can be understood in Figure 3-63. In the previous analysis on the large-scale model, it was observed that the phenomenon of air entrainment is more pronounced at low lift for a given flow rate as well as for cavitation, which suggests that both phenomena may also occur in the real size injector at high pressure and low needle lift.



**Figure 3-64** Variation of needle lift as a function of injection velocity: comparison of (a) CFD simulation [78] for injection pressure 160bar and (b) experimental tests at different injection pressures.

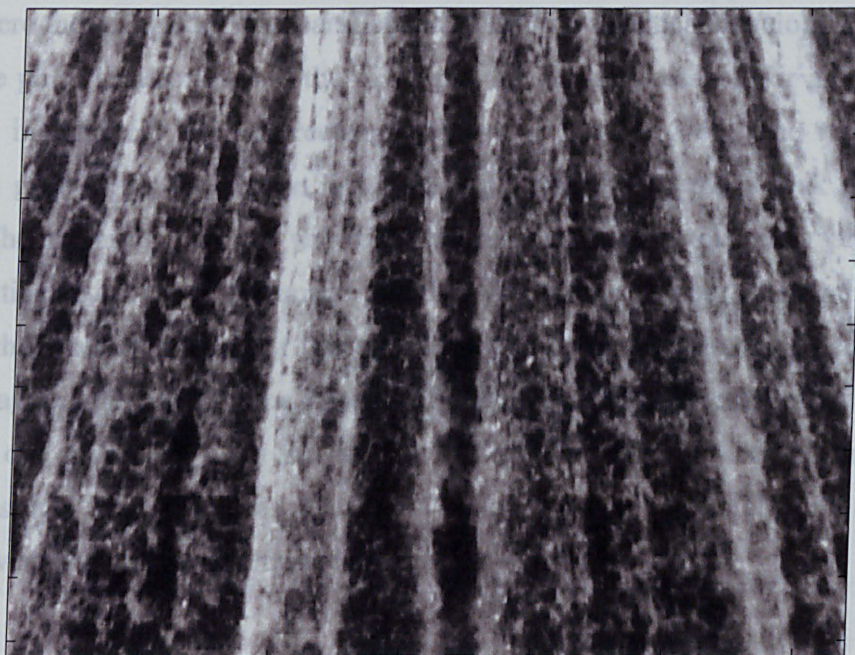
Another possibility, which could explain the drop in velocity, could be due to the experimental method. As the speed was calculated by the measurement of the amount of fuel injected in an interval of time divided by the geometrical cross section area, and since second phases (air entrainment and/or cavitation) may reduce the actual liquid passage cross section area then the calculated mean velocity will tend to be under estimated. However, the comparison of the spray CFD results at 160 bar (Figure 3-64 (a)) with the curve of the test data at 160 bar (blue curve in Figure 3-64 (b)) provide a partial validation of the reliability of these test data which show a good matching at low needle lift (range 20-35μm).

### 3.6.3. Inward Seal Band – string analysis

In the large-scale model, the strings number was previously quantified, as well as their behaviour as a function of velocity, needle lift and Reynolds number. It has been shown that string variation was mainly depending on velocity and nearly independent on the lift position (at constant velocity) in the range of experiment. In order to



investigate the string behaviour in the real size injector a statistical analysis was performed by post processing magnified images of a portion of the spray taken at different operating conditions as shown in Figure 3-65



**Figure 3-65 Real size spray magnification at injection pressure of 200bar and needle lift energy level “1001” (~30 $\mu$ m). (image width 3.5mm)**

Figure 3-65 clearly shows the presence of the filament type structure uniformly distributed and also the well known fish bone structure as seen with jet spray from multihole injectors. In the large-scale model, the parameters defining the operating condition were needle lift and flow rate. As it was not possible to directly fix the flow rate in the real size injector the two parameters defining the operating condition were the maximum needle lift and the injection pressure. From these two parameters and from the previous mass flow analysis it was possible to work out the estimated flow rate and velocity at the different operating conditions.

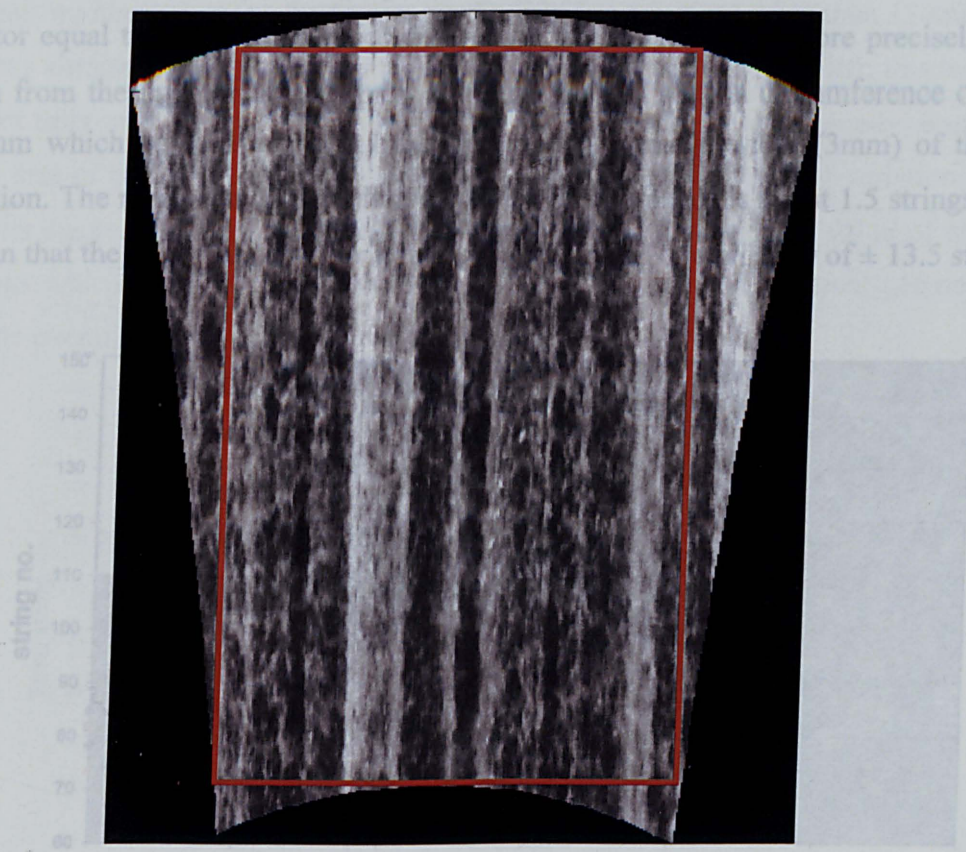
For each operating condition of pressure and lift, 20 images were taken for each of two injector positions. In order to overcome the human eye subjectivity in counting the strings, their calculation was performed automatically by post processing the images with a Matlab code. Given the uniform and defined disposition of the filaments, the idea was to compute the grey level on each row of the image and average it for all the available rows. However, the conical shape of the spray results in an expanding effect of the strings producing a projected image of diverging strings (beams) which would fuse the vertical location of the grey level peaks for each image row. To overcome this problem the image was transformed from a rectangular system



in to a polar system in which the pole was calculated from the projection of the strings upward. The result of the transformation is shown in

Figure 3-66 which shows the transformation in polar system of the image of Figure 3-65 where the strings are now parallel and following a vertical development.

After the polar transformation, the pixel grey level was averaged for all the rows of the area included in the red rectangle shown in Figure 3-66. The results of the averaged grey levels are shown in Figure 3-67 where each main peak represents a string. The counting process was first filtering the irrelevant peaks produced by irregularities and noise in the image and then the strings number was again averaged for the whole set of images for one operating condition. Finally, the calculation was repeated again after rotating the injector of a random angle (approximately 180°) and averaged one more time with the previous result. The final number of string of the image was then extended to the whole spray circumference for which scale and image position were previously determined.



**Figure 3-66 Polar transformation of Figure 3-65 in order to obtain a vertical representation of the string structure.**



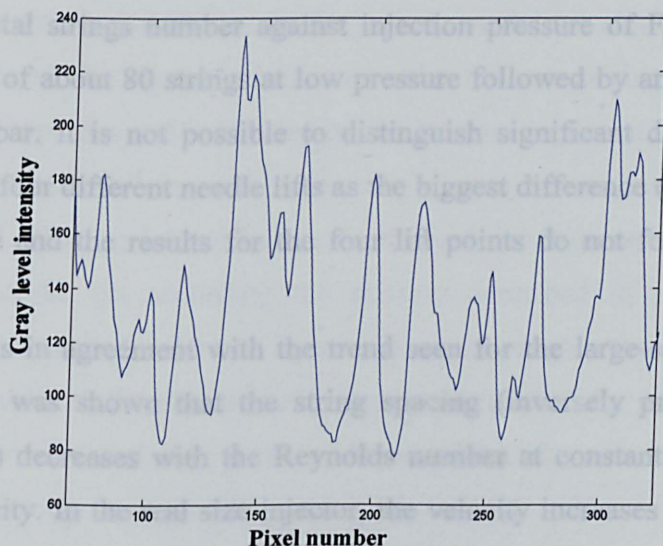


Figure 3-67 Averaged pixel grey level distribution of Figure 3-66.

In this way, the error produced in the calculation is considerably reduced by the several times averaging different feature of the estimation. However as the analysis is applied to a small portion of spray and consequently extended to the whole circumference by simple arc proportion it implies that the error also increases for a factor equal to the circumference divided by the image width. More precisely at 3.5 mm from the injector tip the spray cone has a cross section circumference of about 28mm which contains about 9 times the visualize image width (3mm) of the pray portion. The mean standard deviation for sets of 40 images is about 1.5 strings which mean that the total number of strings is subjected to an overall STD of  $\pm 13.5$  strings.

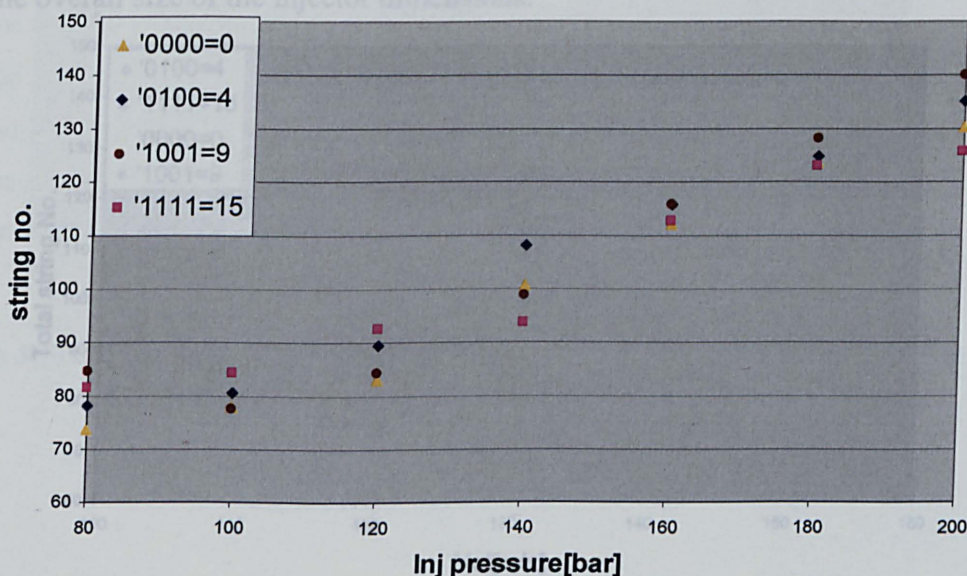


Figure 3-68 Strings number along the whole spray circumference as a function of injection pressure for different needle lift set up.



The plot of total strings number against injection pressure of Figure 3-68 shows a constant trend of about 80 strings at low pressure followed by an increase up to 135 strings at 200bar. It is not possible to distinguish significant differences from the comparison of four different needle lifts as the biggest difference (at 140bar) is within the error range and the results for the four lift points do not follow any particular trend.

This outcome is in agreement with the trend seen for the large-scale model (Figure 3-47) where it was shown that the string spacing (inversely proportional to total strings number) decreases with the Reynolds number at constant needle lift and so with flow velocity. In the real size injector, the velocity increases as consequence of the increase in injection pressure. More precisely from the previous fuel mass analysis it was possible to correlate the injection pressure to the estimated fuel velocity and plot strings number versus velocity and Reynolds number as presented in Figure 3-69 and Figure 3-70.

In general, the trend of the points plotted in Figure 3-69 shows an increase of the total strings number except at the lowest needle lifts for velocity higher than 120m/s which shows similar number of strings or a small reduction at the lowest lift; this behaviour is not fully understood and it needs further investigation. At low velocity, none of the four sets of points seems to be particularly affected by the velocity variation and the results suggest that the strings number tends to have a minimum value of about 80 strings which may depend on the conical configuration of the internal geometry and on the overall size of the injector dimensions.

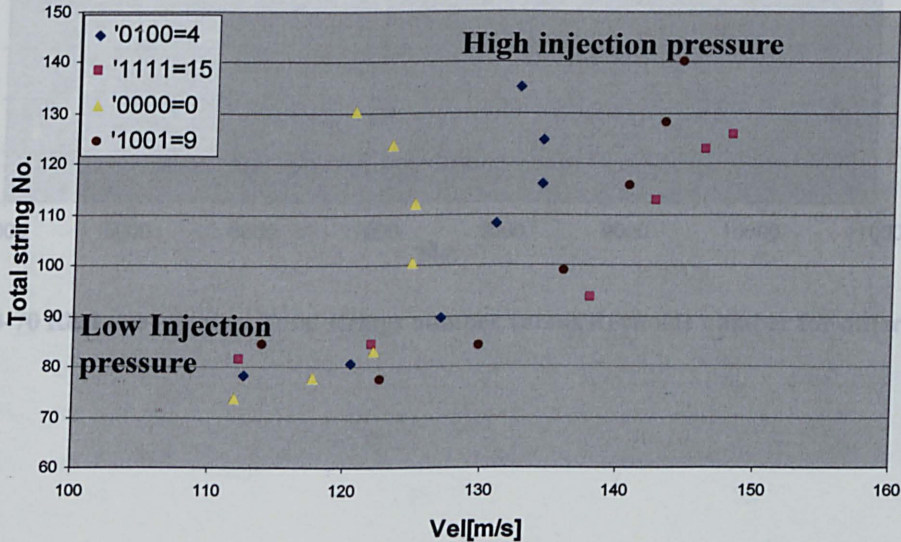


Figure 3-69 Variation of strings number as a function of injection velocity for different needle lift set up.



The number of strings counted on the large-scale model are almost double than those counted on the real size injector which means that the strings number does not respect the similitude properties and is affected by the increase in size of the injector. A direct comparison between real size and large-scale injector can be seen from Figure 3-70 and Figure 3-71. The Reynolds numbers for the real size injector were calculated from velocity and needle lift according the relation described in paragraph 3.4. The Reynolds number range for the two injector sizes are roughly the same however only for the large-scale model the linear growth is extended for the whole range of measurement. For the real size, a resemblance of linearity can be observed only at high Reynolds number corresponding to full needle lift (1111).

It can also be observed that for low needle lift the strings number increases at a constant velocity (Figure 3-69) or Reynolds Number (Figure 3-70). This type of result, as explained for the fuel rate analysis, can be due to presence of cavitation or air entrainment which may cause an under estimation of the actual velocity. In fact such effect is mainly evident at low lift and high injection pressure which are the most favourable conditions for cavitation and air entrainment.

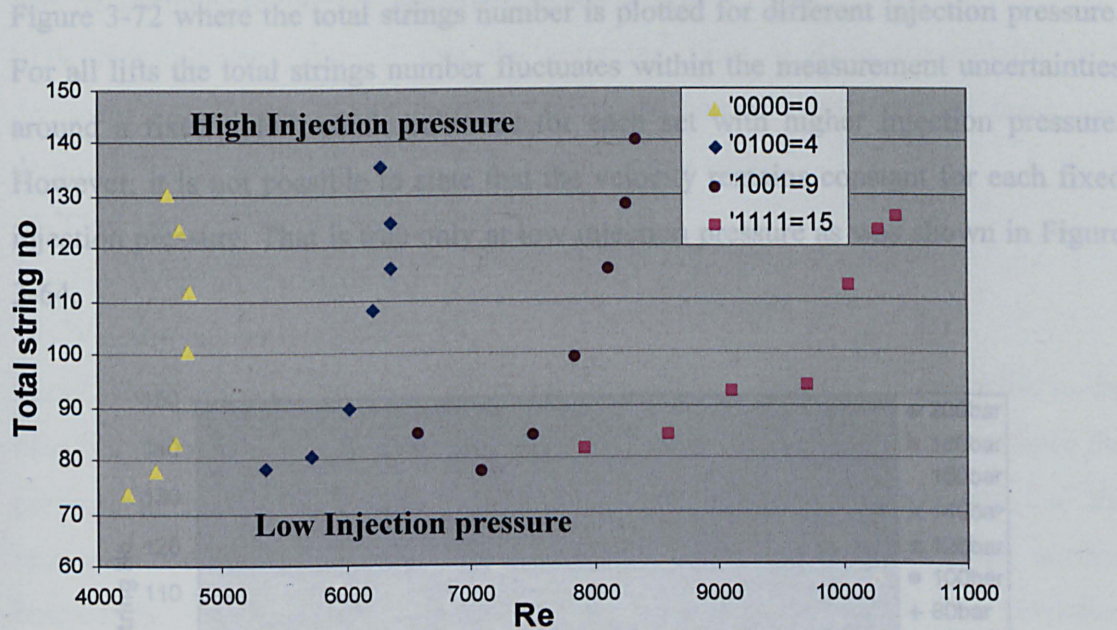
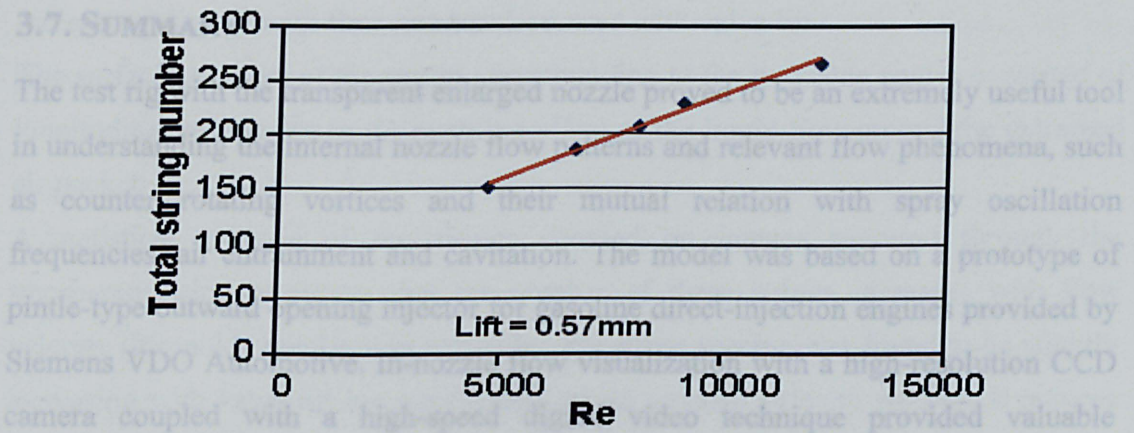


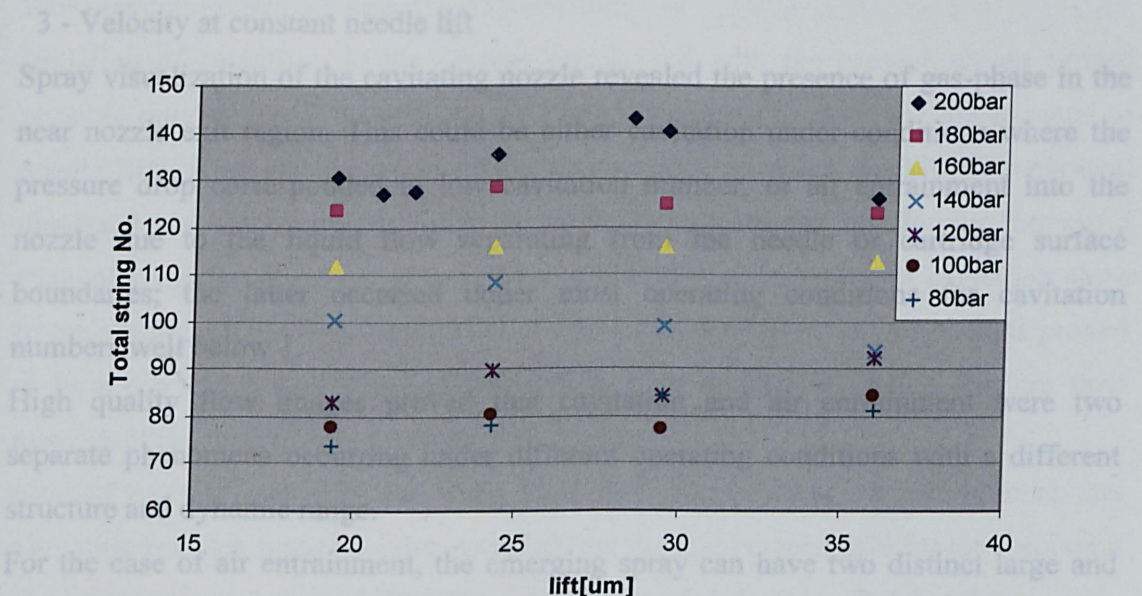
Figure 3-70 Real size injector: Total strings number versus Reynolds number for different needle lifts.





**Figure 3-71 Large-scale injector: Total strings number versus Reynolds number at constant lift of 0.57mm corresponding to 0.025mm lift in the real size injector (0100).**

Another similarity between real size and large-scale injector can be observed by comparing the trend of string spacing versus needle lift in Figure 3-48 and in Figure 3-72. It was previously seen that the large-scale model is not particularly affected by needle lift when the flow velocity is kept constant, a similar result can be observed in Figure 3-72 where the total strings number is plotted for different injection pressure. For all lifts the total strings number fluctuates within the measurement uncertainties around a fixed value which increases for each set with higher injection pressure. However, it is not possible to state that the velocity remains constant for each fixed injection pressure. That is true only at low injection pressure as was shown in Figure 3-64.



**Figure 3-72 Variation of the strings number as a function of needle lift for different injection pressures.**

---

### 3.7. SUMMARY

The test rig with the transparent enlarged nozzle proved to be an extremely useful tool in understanding the internal nozzle flow patterns and relevant flow phenomena, such as counter rotating vortices and their mutual relation with spray oscillation frequencies, air entrainment and cavitation. The model was based on a prototype of pintle-type outward opening injector for gasoline direct-injection engines provided by Siemens VDO Automotive. In-nozzle flow visualization with a high-resolution CCD camera coupled with a high-speed digital video technique provided valuable information about the overall flow patterns, mechanisms of air entrainment and cavitation development and, in particular, the dynamics of the gas-phase inside the nozzle. The following is a summary of the main findings:

The flow between the end of the square needle guide and the nozzle exit is of a complex nature, which consists of four high velocity jets and four pairs of counter-rotating vortices (unstable zone). These four vortices are highly unstable and could break down into more vortices. The images indicate that the instability in the spray may be attributed to the flow upstream the needle seat.

LDV measurements showed that the emerging flow oscillate tangentially with dominant frequencies linked with the upstream vortical structure. All these low dominant frequencies were found to increase linearly with:

- 1- Flow rate (exit bulk velocity)
- 2 - Needle lift at constant velocity
- 3 - Velocity at constant needle lift

Spray visualization of the cavitating nozzle revealed the presence of gas-phase in the near nozzle exit region. This could be either cavitation under conditions where the pressure drop corresponded to low cavitation number, or air entrainment into the nozzle due to the liquid flow separating from the needle or cartridge surface boundaries; the latter occurred under most operating conditions for cavitation numbers well below 1.

High quality flow images proved that cavitation and air entrainment were two separate phenomena occurring under different operating conditions with a different structure and dynamic range.

For the case of air entrainment, the emerging spray can have two distinct large and small cone angles according to the attachment of the air bubbles to the cartridge and needle surfaces, respectively. The large and small spray angles were found to be



---

increasing slightly with flow rate but decreased with valve lift.

The surface structure of the sprays corresponding to the two cone angles consisted of longitudinal strings due to the profiling effect of the liquid flow around the entrained air pocket.

A statistical analysis of the strings counted on images captured through the transparent window shown that the number of these strings increases with flow velocity (Reynolds number). In particular, the string spacing was found to be slightly increasing with valve lift but almost uniform at constant velocity whereas it reduces linearly as the injection velocity increases.

Although a similar spray structure has been observed in the real size injector, it is still risky to speculate that air entrainment is the only mechanism responsible for the string-type structure since a finer string structure has been observed in a non-cavitating nozzle previously tested. However, with the non-cavitating geometry, it can be argued that smaller size bubbles, that are unable to penetrate deeply into the nozzle, can in principle be generated at the exit of the nozzle, due to the geometric restriction, and therefore initiate finer strings.

For the small angle and at full lift, the amount of air bubbles increased with flow rate up to 1.45 l/s then the bubbles suddenly disappear switching the spray structure from string type to a smooth one. A parametric study of flow rate and valve lift variation showed that a flow with high momentum beyond a certain critical flow rate becomes more dominant and it fully expands to occupy the diverging section of the nozzle, thus preventing flow separation in that section.

Initiation of cavitation in the present nozzle and with the present set up proved possible only at low lifts, with full cavitation occurring towards the lower range of needle lifts. After the inception of the vapour pockets, these quickly disintegrated, dispersed and they were convected downstream towards the nozzle exit forming a triangular vapour shape with its apex being the point of inception of cavitation close to the sealing edge of the nozzle. The dynamics of cavitation vapour pockets proved to be much faster than those of the entrained air bubbles so that to capture their movement required a higher framing rate camera.

Limited tests at low lifts and very high flow rates, where air entrainment and cavitation bubbles could co-exist, revealed that the main mechanism for the formation of a string-type structure was still the entrainment of air bubbles, but that the presence of cavitation at high liquid velocities and could create a string-type spray structure

---

which was very similar to that of the real size injector. The high-speed sequence has shown also how the cavitation contributes to liquid flow structure brake up downstream the nozzle exit which enhanced the atomisation considerably and suggests how cavitation could improve atomisation in the real size model.

The analysis on the real size injector has shown that the total number of strings is almost constant for low injection pressure and grows by increasing the injection pressure above 100bar. The total number of strings in the real size injector presents a similar trend to the large-scale model only at high needle lift however, at low velocity the strings number tends asymptotically to a minimum constant number. At constant injection pressure, the total number of string presents small variation with lift, a similar trend was previously observed in the large-scale model for different lift and fixed flow velocity.

For the real size injector it is not possible to state that velocity is the only parameter driving the string phenomenon like for the large-scale model. In fact, such a variable does not necessarily obey to the laws of geometrical and dynamical similitude. However, for several operating condition the behaviour of the two model sizes has proved to be very similar suggesting that similar mechanisms could occur at least partially on both injector sizes. Considering the absence of the needle transient phase in the enlarged model the obtained results are quite satisfactory.

Overall, the presented results suggest that, apart from air entrainment, there may be other mechanisms that might either hinder or enhance the formation of string-type spray structures like the balance between dynamic, surface tension and aerodynamic forces due to the induced air recirculation near the nozzle exit.

---

## Chapter 4.

### *Spray Characterization under atmospheric and high pressure conditions*

#### 4.1. INTRODUCTION

An important operating criterion of a well-designed GDI engine is that the fuel must be sufficiently vaporised before the ignition event occurs in order to minimise UBHC emissions to an acceptable level. Moreover, the complete evaporation of the fuel can make the ignition process more robust. One of the major factors influencing vaporisation of the fuel is the standard of atomisation. Effective atomisation increases the specific surface area of fuel droplets permitting high rates of mixing and evaporation of the fuel.

In the present investigation, the performance of this pintle-type injector was characterized for different operating conditions. The injector was tested in a constant volume pressurized chamber, which has full optical access and is equipped with special control system to adjust chamber ambient temperature and pressure; in case of injection into atmosphere, the injector was mounted on a purposed designed adjustable support, which allowed turning the injector axis with respect of the optical axis.

The first part of the investigation consisted of integral and 2D Mie scattering visualisation to determine spray structure characteristics in terms of shape, penetration and dynamic and also to optimize the second phase of the experiment by helping to locate the best measuring zones for the following laser diagnostics. The spray imaging was also useful to give a qualitative meaning to the quantitative results outcome of the PDA experiment.

The second part of the investigation covers the quantitative study of the spray including simultaneous measurements of droplets diameter and velocity distribution using Phase Doppler Anemometry (PDA). In the same section it is also included some result obtained from PIV measurement which gave an overall view of the velocity field previously quantified by PDA diagnostic.



---

#### 4.1.1. Atomisation

The process of atomisation consists in liquid jet or sheet disintegration by kinetic energy of the liquid itself, either by the interaction with high-velocity air or gas, or, as a result of mechanical energy applied externally through a rotating or vibrating device [93].

The surface tension acting on a liquid suspended freely in space will tend to pull the liquid into a sphere since this geometry has the minimum surface energy. If external aerodynamic forces act on the droplet (as in the case of fuel being injected into a cylinder) exceed the consolidating surface tension force, break up of the droplet occurs. This mechanism can be described as atomisation.

Under equilibrium conditions the internal pressure at any point on the drops surface,  $P_i$ , is just sufficient to balance the external aerodynamic pressure  $P_A$  and the surface pressure  $P_\sigma$  so that,

$$P_i = P_A + P_\sigma = \text{Constant} \quad (4-1)$$

#### 4.1.2. Disintegration of liquid sheets

Multi-hole injectors produce liquid jets, whereas pressure-swirl type atomisers, and outwardly opening pintle-type injectors, aim to form conical liquid sheets. When a sheet of liquid emerges from a nozzle, its subsequent development is mainly influenced by its initial velocity, the physical properties of the fuel, and the thermodynamic conditions of the ambient gas. In order to expand a sheet against the contracting surface tension force, a minimum sheet velocity is required. The initial velocity is determined by the injection pressure and nozzle geometry. Increasing the initial velocity expands and lengthens the sheet until a leading edge is formed where equilibrium exists between surface tension and inertial forces.

In 1953, Fraser and Eisenklam [94] defined three modes of sheet disintegration, they are, rim, perforated, and wave sheet disintegration. It is possible for two different modes to occur simultaneously. In the rim mode, forces created by surface tension cause the free edge of the liquid to contract into a thick rim; the rim is then broken down by a mechanism corresponding to the disintegration of a free jet. The resulting drops continue their trajectory but remain attached to the receding surface by thin threads that also rapidly break up into rows of drops. In perforated sheet disintegration, holes appear in the sheet. The holes grow rapidly in size until the rims

---

of holes coalesce with the rims of adjacent holes, producing ligaments of irregular shape that finally break up into drops.

Wave disintegration occurs in the absence of perforations where a half or full wavelength oscillation is torn away by the aerodynamic forces before the leading edge is reached. Wave-sheet disintegration is highly irregular and consequently the range of drop sizes is larger.

Studies of Dombrowski and Johns (1963), Dombrowski and Fraser (1954) [95] and Crapper and Dombrowski (1984)[96], established that ligaments are caused principally by perforations in the liquid sheet. If the holes are created by other means, such as turbulence in the nozzle, of rough nozzle surfaces, then the ligaments are broken more slowly. From a number of tests on a wide variety of liquids, they concluded that:

1. Liquid sheets with high surface tension and viscosity are most resistant to disruption.
2. The effect of liquid density on sheet disintegration is negligibly small [74].

#### 4.1.3. Drop size distribution

There are a wide range of drop sizes in a typical spray formation. It is beneficial to classify the spread of drop sizes within the spray in order to make comparisons between sprays. The Sauter Mean Diameter (SMD), Mass Median Diameter (MMD) and Arithmetic Mean Diameter (AMD) are terms used to measure the spread of droplet sizes in the spray. The SMD is the diameter of a droplet whose surface-to-volume ratio is equal to that of the entire spray. The symbol describing the SMD is  $D_{32}$ , its application is for mass transfer, and can be expressed as

$$\text{SMD} = \frac{\sum N_i D_i^3}{\sum N_i D_i^2} \quad (4-2)$$

Where  $N_i$  is the number of droplets and  $D_i$  is the droplet diameter.

The Mass Median Diameter is the diameter of a droplet, below or above which, 50% of the total mass (volume) of droplet lies. The Arithmetic Mean Diameter (AMD) is the Arithmetic mean value of a considered group of droplets.

The SMD provides a better representation of the fuel volume than both the Arithmetic Mean Diameter (AMD), and root mean squared (RMS) which is mainly used as a measure of diameter fluctuations, when analysing sprays. For example, if 1,000 droplets are collected, 990 of which are small and 10 are large, then an average

---

diameter value will be biased towards the small droplet diameters and an unrealistic representation of the fuel volume will be given.

No single parameter can completely define a drop size distribution. For example, two sprays are not necessarily similar because they have the same (SMD) or the same (AMD). In many practical applications, it is the smallest drop sizes in a spray or the largest drop sizes that are of paramount importance, and neither SMD nor AMD can provide this information.

The AMD may not in fact be the single best indicator of the spray quality required for the GDI engine, as a very small percentage of large droplets is enough to degrade the engine UBHC emissions even though the AMD may be quite small.

#### **4.1.4. Typical Droplet sizes**

The pressure swirl type atomizer used in wide spaced GDI engines is required to provide a highly atomised fuel spray having a SMD of generally less than  $25\mu\text{m}$  [19]. The close spaced injector on the other hand, is required to produce an even finer spray, and therefore lower SMD values, since the time available for evaporation in its stratified mode is much less.

According to Xu and Markle, experiments conducted in 2000, showed that the outward opening injector was able to produce a spray with an SMD of less than  $15\mu\text{m}$  as measured by laser diffraction at 30 mm downstream from the nozzle and a maximum limiting penetration of 70mm into atmosphere[19]. The pintle-type injector is now expected to produce droplets as small as  $10\mu\text{m}$ , particularly in the vicinity of the spark plug (point of ignition) during standard temperature and pressure tests. (Note, for normal operating temperatures within the engine, they expect only vaporised fuel in this area).

Each  $50\mu\text{m}$  fuel droplet in a spray having an SMD of  $25\mu\text{m}$  not only has eight times the fuel mass of the mean droplet, but also will remain as liquid long after the  $25\mu\text{m}$  droplet has evaporated. In fact, when all of the  $25\mu\text{m}$  droplets have evaporated the original  $50\mu\text{m}$  droplets will still have a diameter of  $47\mu\text{m}$  [19].

For a gasoline droplet with a diameter of  $80\mu\text{m}$ , vaporisation under typical compression conditions takes tens of milliseconds, corresponding to more than 100 crank angle degree at an engine speed of 1500 rpm. By contrast, the vaporisation of a  $25\mu\text{m}$  droplet requires only several milliseconds, corresponding to tens of crank angle degree [19]. This is the essence of the degradation of GDI engine combustion



---

characteristics for sprays in which the droplet mean diameter exceeds  $25\mu\text{m}$  for wide spaced GDI, and  $15\mu\text{m}$  for close spaced GDI.

Generally, the smaller the droplet sizes, the quicker the droplets will vaporise. The rapid vaporisation of very small droplets helps to make the GDI concept feasible. Therefore, many techniques have been proposed for enhancing the spray atomisation of GDI injectors. Fuel injectors used in GDI engines are expected not only to break up the fuel into droplets but also to distribute the drops uniformly into the surrounding gaseous medium at a highly repeatable rate.

## **4.2. EXPERIMENTAL TECHNIQUES AND EQUIPMENT DESCRIPTION**

The following paragraphs describe the experimental procedure and the techniques used in the current experimental phase.

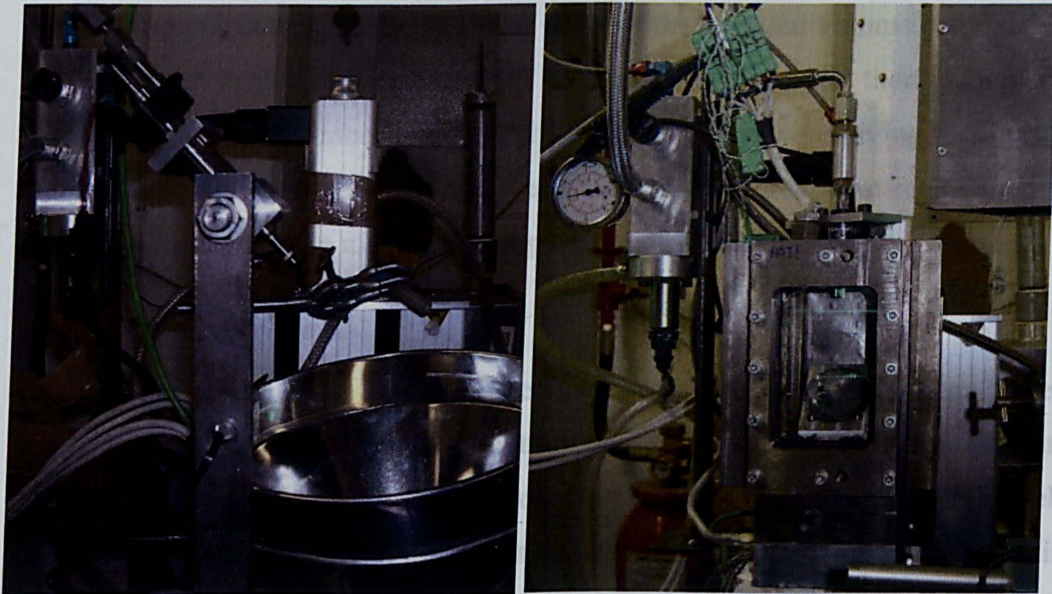
The main experimental system used in this investigational phase was PDA technique, which gave the possibility to identify droplet diameter and at the same time two velocity components. However, its principle is based on single point measurement which does not give an overall view of the whole velocity field.

The PIV system, on the other hand, despite its limitation in dense spray measurement was found to be a useful technique to have a global overview of the instantaneous velocity field of air entrainment and recirculation occurring after the trailing edge of the spray. Spray imaging methods and their explanation were given in the third chapter of this thesis so here only the experimental arrangement will be briefly described.

---

### 4.3. TEST RIG STRATEGIES

Due to its safety and its consistent property Iso-octane is preferable than gasoline for optical studies and therefore it was chosen as fuel flow for the current experiments. Nevertheless, the physical property of the Iso-octane are very similar to those of the gasoline and more specifically it has a density, kinematic viscosity and surface tension of  $692\text{kg/m}^3$ ,  $0.78\text{cSt}$  and  $0.0188\text{N/m}$ , respectively. Spray images were obtained using a 12-bit CCD camera (Sensicam) with a time resolution of  $50\mu\text{s}$ , a spatial resolution of  $512 \times 640$  pixels and minimum exposure time of  $100\text{ns}$ . A strobe light of  $20\mu\text{s}$  duration was used as the light source, which was synchronised to the camera. A high-speed video camera acquiring at a rate up to  $40\text{k fps}$  was used to visualize the dynamics of the phenomena occurring during the spray evolution. To contain the heat rate radiated against the injector a continuous  $200\text{W}$  HMI lamp (ARRI light) with low heat diachronic reflector was employed as light source.



(a) Flexible injector holder

(b) constant volume chamber set up

**Figure 4-1 Experimental set up for variable and ambient backpressure PDA measurement**

As the investigation involved different set of parameters, the experiments required two different injector assembly arrangements. In the first approach, (Figure 4-1a) the spray was studied for different operating conditions at ambient pressure. The mounting set up consisted of a rotating support, which allowed a flexible positioning of the injector. The purpose of the rig was to give full optical access to the laser, scattered light path, and thus perform a complete set of measurement through the

---

spray thickness without facing problem related with light attenuation due to dense spray. With the same rig arrangement, PIV measurements were performed for the determination of the velocity field of air entrainment and spray recirculation by suspending atomised water droplets as seeding samples.

The second approach (Figure 4-1b) focused on the observation of the effect of surrounding temperature and backpressure on the spray, which required a rig capable to artificially modify the surrounding thermodynamic conditions by controlling the ambient parameters. For this purpose, a constant volume chamber with variable ambient pressure and temperature was employed. The chamber was equipped with four quartz windows and connected to a pressurised bottle of nitrogen to maintain the required high pressure inside the chamber up to 25bar by mean of an accurate pressure regulator. The fuel pressure regulator attached to the common rail, the solenoid valve in the exhaust pipe of the chamber and the injector were all controlled electronically. In order to simulate high temperature of the gas inside the chamber, two heating plates were installed in the walls of the constant volume chamber and the nitrogen was heated before entering the chamber. Several thermocouples were installed inside the chamber at different locations, which were giving feedback to the temperature control system to ensure constant temperatures were maintained within  $\pm 1.5^{\circ}\text{C}$ ; with this setup a maximum temperature of  $180^{\circ}\text{C}$  could be achieved.

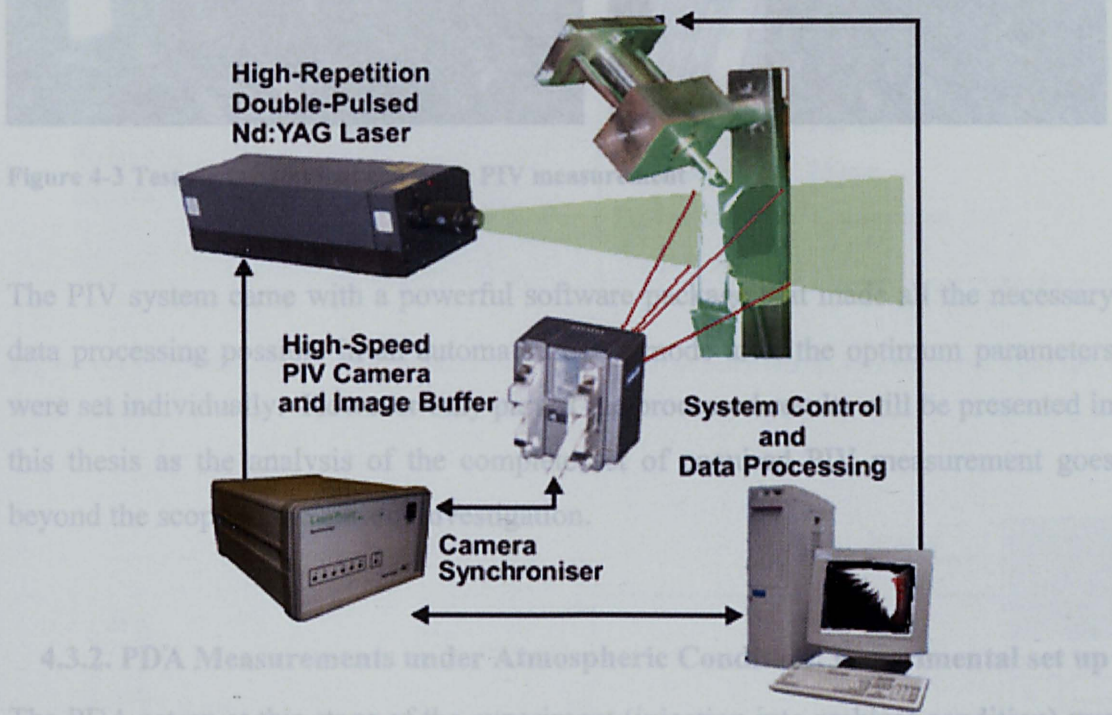
#### **4.3.1.PIV Experimental set up**

The PIV technique was used to investigate two different phenomena. The first experiment aimed to observe the air entrainment behaviour at the near nozzle area of the injector. The second PIV investigation focused on the measurement of the velocity field of the spray recirculation 50mm away from the injector tip and beyond in the final phase of the spray evolution.

In order to measure the air entrainment velocity it was necessary to produce special flow seeding with sizes small enough to follow the flow stream without slipping and large enough to scatter sufficient light that can be captured by the camera. Therefore, a purposed built water atomiser was employed to produce very fine droplets with size of order of  $2\mu\text{m}$ . The water droplets were blown into the region of interest around the nozzle tip with a mean velocity in the absence of spray of about 0.3m/s. These details on the water droplets were assessed by LDV measurement and will be presented later in this chapter. The velocity range of the suspended water droplets is well below the air-entrained motion and far below the spray droplets velocity with no effect on the



dynamics of the spray and therefore this seeding produces reliable results. The second phase of PIV measurements focused on the investigation of the spray recirculation in which the water atomiser was no longer needed as the object of the velocity field was the fuel droplets motion and not the surrounding air. In this setup, the investigation area lies well away from the injector tip and takes place during the final phase of injection when the spray is no longer dense. Consequently, high-speed PIV system can be employed to obtain instantaneous spray velocity field with a sensible resolution in terms of droplet samples per velocity spots (interrogation area). Figure 4-2 shows schematically the PIV system (TSI) setup of the latter configuration incorporating the injector system.

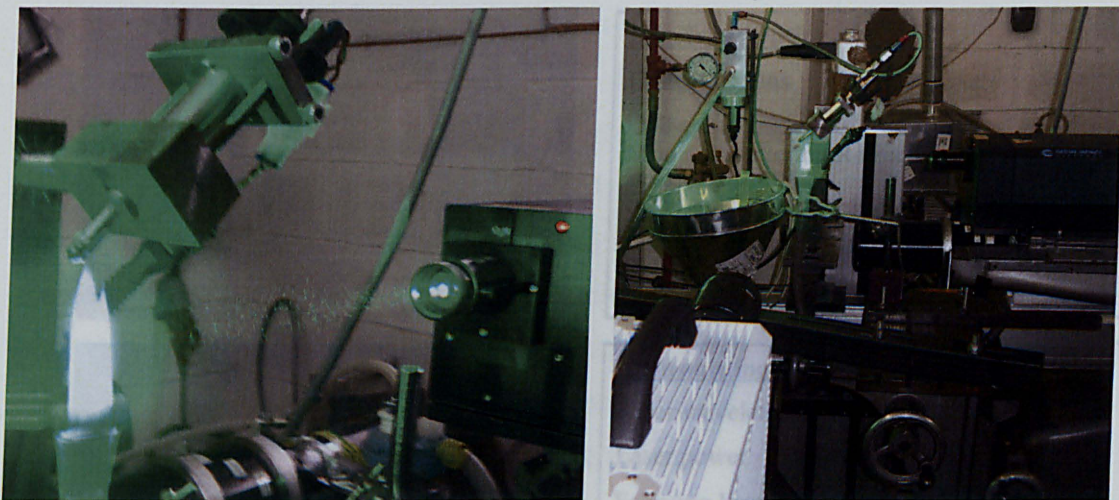


**Figure 4-2 Schematic of experimental setup of the high-speed PIV system with incorporated Injector system**

A pulsed Nd:YAG laser unit illuminated the area of interest with a planar laser sheet corresponding with the symmetry plane of the spray and the camera was oriented with its axis perpendicular to the laser sheet. Due to technical limitation with the processor memory, the recorded frame rate was also limiting the maximum spatial resolution. The pair of images was captured by a high-speed video camera with a relatively long shutter time whereas the time step between the two image of the pair was defined by two laser pulses at a frequency of 50 kHz (time step = 20  $\mu$ s). Laser and shutter are internally synchronized by a synchroniser box in order to shoot a pulse during each exposure interval. The image pairs were recorded with frequency of 3000Hz for high



image resolution and 5000Hz for high time resolution. The images stored in the image buffer memory of the camera had to be downloaded to the PC for further processing after each set of measurements taken for each spray case.



**Figure 4-3 Test rig for ambient condition PIV measurement**

The PIV system came with a powerful software package that made all the necessary data processing possible in an automated batch mode after the optimum parameters were set individually. However only part of the processed results will be presented in this thesis as the analysis of the complete set of acquired PIV measurement goes beyond the scope of the current investigation.

#### **4.3.2. PDA Measurements under Atmospheric Condition: Experimental set up**

The PDA set up at this stage of the experiment (injection into ambient condition) was set according to Figure 4-4 where the characteristics of the transmitting and receiving optics are also given. The transmitting laser beams and the receiving optics were set up to minimize the effect of beam and scattered light attenuation to collect full spray signal near the injector exit where the spray is very dense. The data were collected over a time window of 0.2 ms to 2.4 ms during the injection process and up to 15000 samples were collected over many injection cycles for each measuring location. The measurements were synchronised with needle lift by an external reset pulse and restricted to the first 1ms after the start of the injection (ASOI) up to 2.4ms ASOI at a axial distance of 50 mm from the injector tip. The collected information of time, velocity and the size were resolved over a time interval of 0.1 ms to obtain the ensemble-averages. The number of validated samples in 0.1 ms time interval varied



from 250 to 1500 with maximum statistical uncertainty of  $\sim 2.5\%$  in the mean velocity value.

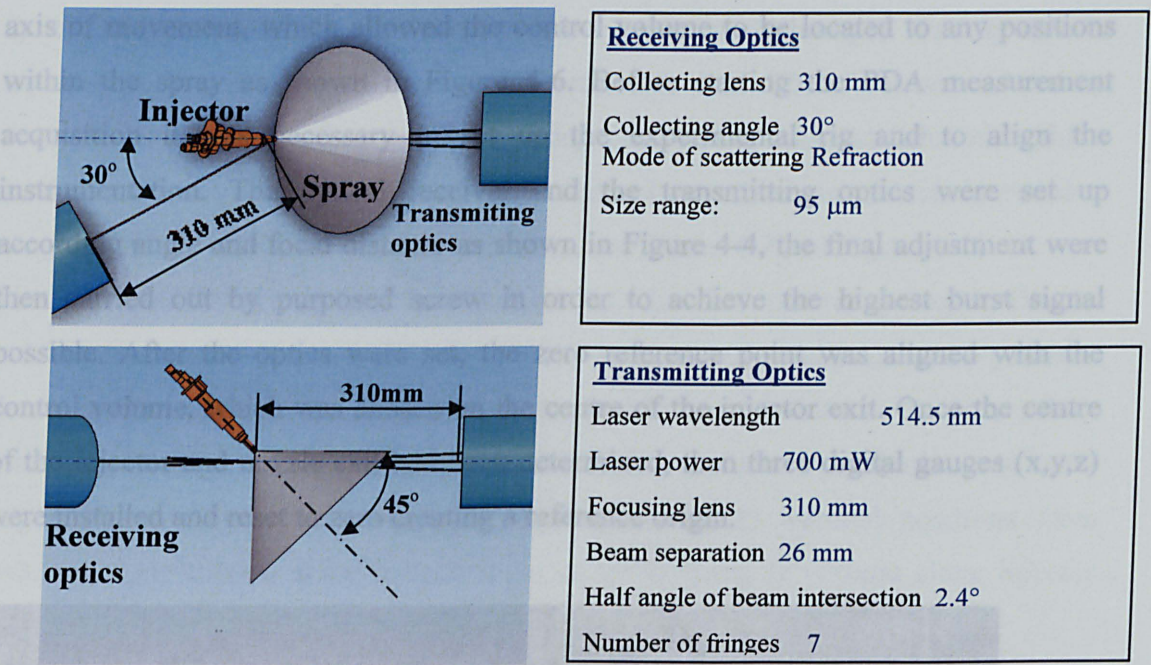


Figure 4-4 Purposed design setup to minimize attenuation of laser beams and scattered light to allow full spray measurements inside the central region of the spray thickness.

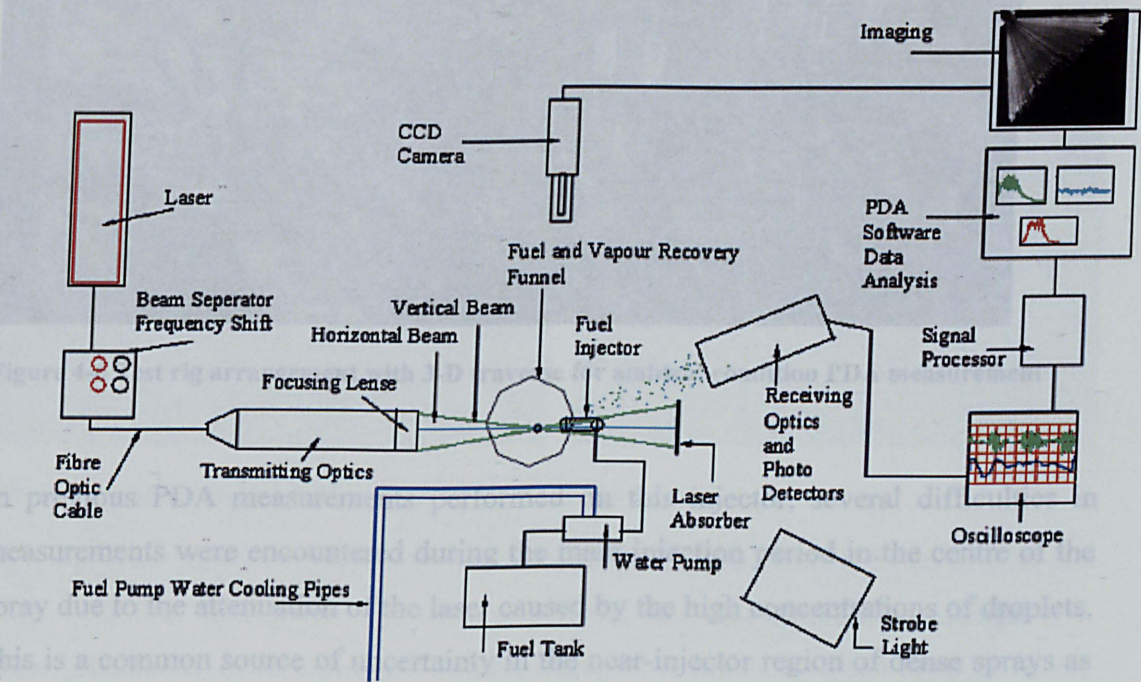
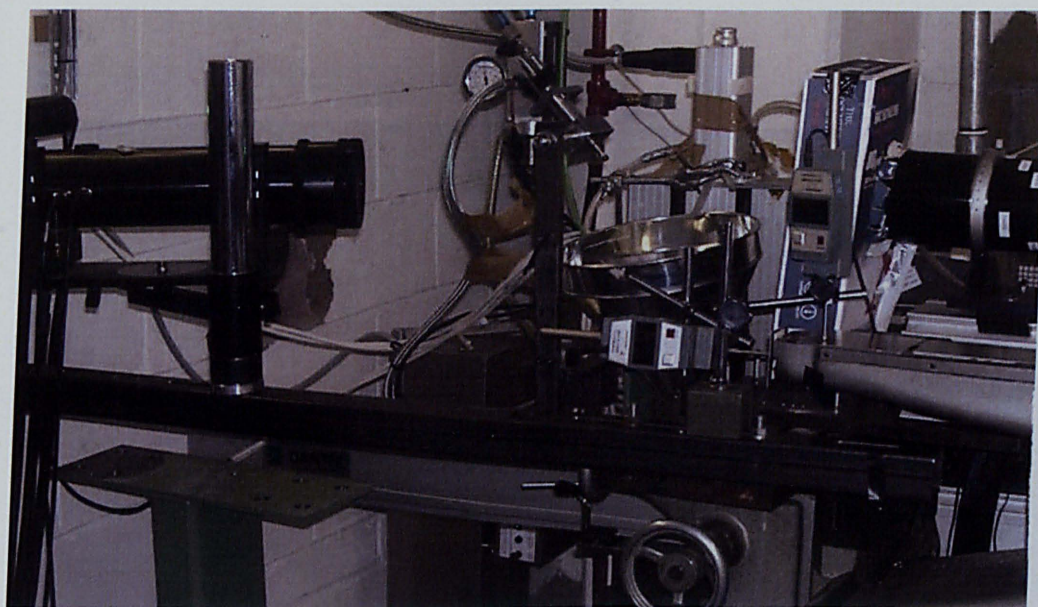


Figure 4-5 Experimental set-up schematic of fuel injection system and optical devices.



The complete PDA experimental set-up is shown schematically in Figure 4-5 including all optics, control systems, processor and instrumentation. The laser transmitting and receiving optics were mounted on an adjustable platform with three axis of movement, which allowed the control volume to be located to any positions within the spray as shown in Figure 4-6. Before starting the PDA measurement acquisition it was necessary to set up the experimental rig and to align the instrumentation. The optical receiver and the transmitting optics were set up according angle and focal distance as shown in Figure 4-4, the final adjustment were then carried out by purposed screw in order to achieve the highest burst signal possible. After the optics were set, the zero reference point was aligned with the control volume, which was chosen on the centre of the injector exit. Once the centre of the injector and nozzle exit had been determined, then three digital gauges (x,y,z) were installed and reset to zero creating a reference origin.

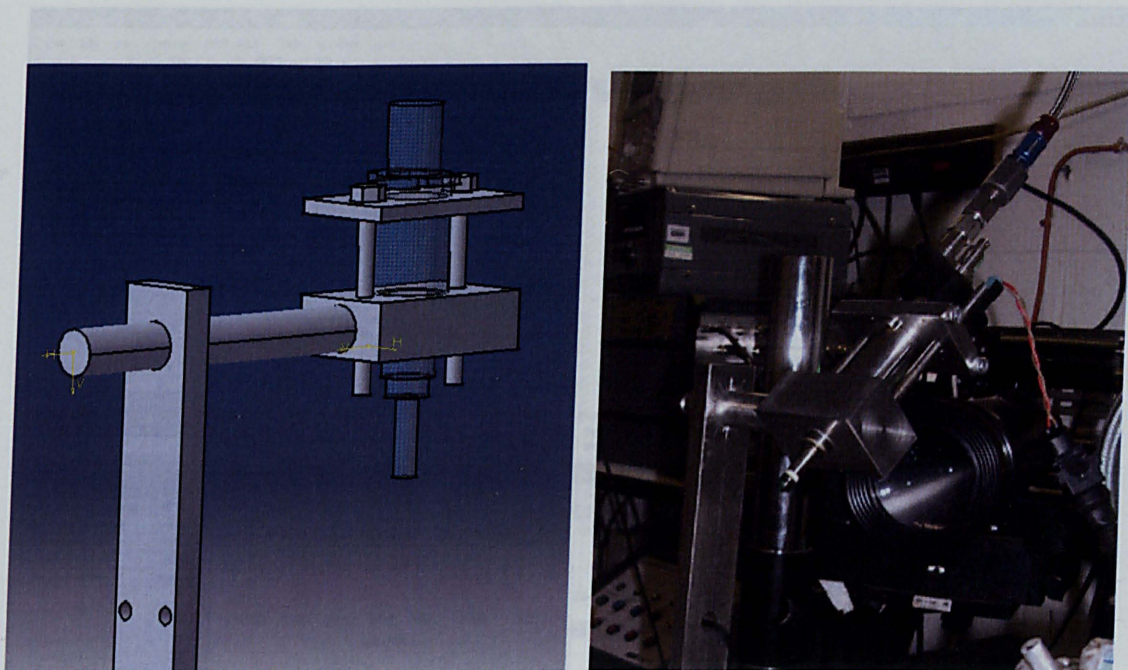


**Figure 4-6 Test rig arrangement with 3-D traverse for ambient condition PDA measurement**

In previous PDA measurements performed on this injector, several difficulties in measurements were encountered during the main injection period in the centre of the spray due to the attenuation of the laser caused by the high concentrations of droplets. This is a common source of uncertainty in the near-injector region of dense sprays as was reported by [97, 98], and although it had no effect on size measurement accuracy [97], the effect of high droplet density can be considerable causing the system to fail



in detecting droplets during the main injection period. In order to achieve good results, it was necessary to minimise attenuation of the laser beam and the most appropriate way of achieving this without using a sharp edge splitter (which opens the spray cone to allow beams pass through), was to turn the injector at  $45^\circ$  angle with respect of the transmitter axis. Therefore, one side of the cone profile described a horizontal trajectory, clear of the beam, and the other side a vertical trajectory where the measurement took place. All measurements were taken along the centre line of the vertical trajectory, see Figure 4-7 and Figure 4-11. Finally, once the set up had been completed, the data recording began. Droplet velocity and size were measured across spray strings, first locally along the y-axis to determine the centre of the string (the centre position was defined as the point where maximum average velocity occurs), and then in the x-plane, from the inner to outer edges. The horizontal scan was then repeated along 13 vertical positions from  $z=3.54\text{mm}$  ( $z'=2.5\text{mm}$  along injector axis), to  $z=70.71\text{mm}$  ( $z'=50\text{mm}$  along injector axis).



**Figure 4-7 Injector holder built and installed into the test rig**

Signal processing by the PDA flow software produces data, such as mean droplet and RMS velocities (horizontal and vertical planes), and droplet diameter distribution, either graphically or in numerical values. Figure 4-8 shows a screen printout of the raw data graphs produced by the PDA software. About 15000 samples are required for each measured location. The green graph represents the droplets vertical



velocities, the blue graph represents the droplets horizontal velocities, and the red graph represents the droplet size distribution. The accuracy of the measurement and the detailed error analysis can be found in the appendix at the end of the thesis.

The text files can then be exported into a Matlab code to obtain a more detailed analysis of the raw data. Post-processing of the acquired data was done by in-house developed software which allowed formatting and plotting the raw data obtained from the PDA acquisition in a more convenient way. Functions were written within a Matlab code to produce histograms, temporal and special graphs for velocity and diameter distributions, to determine mean and RMS velocity values, and other statistical data. The main graphs produced by Matlab and presented in this investigation are temporal variation graphs, (droplet size or velocity vs. time), and spatial graphs (droplet size or velocity vs. control volume position). Spatial graphs are particularly useful to compare spray characteristics across the whole cross-section (profile) of the spray.

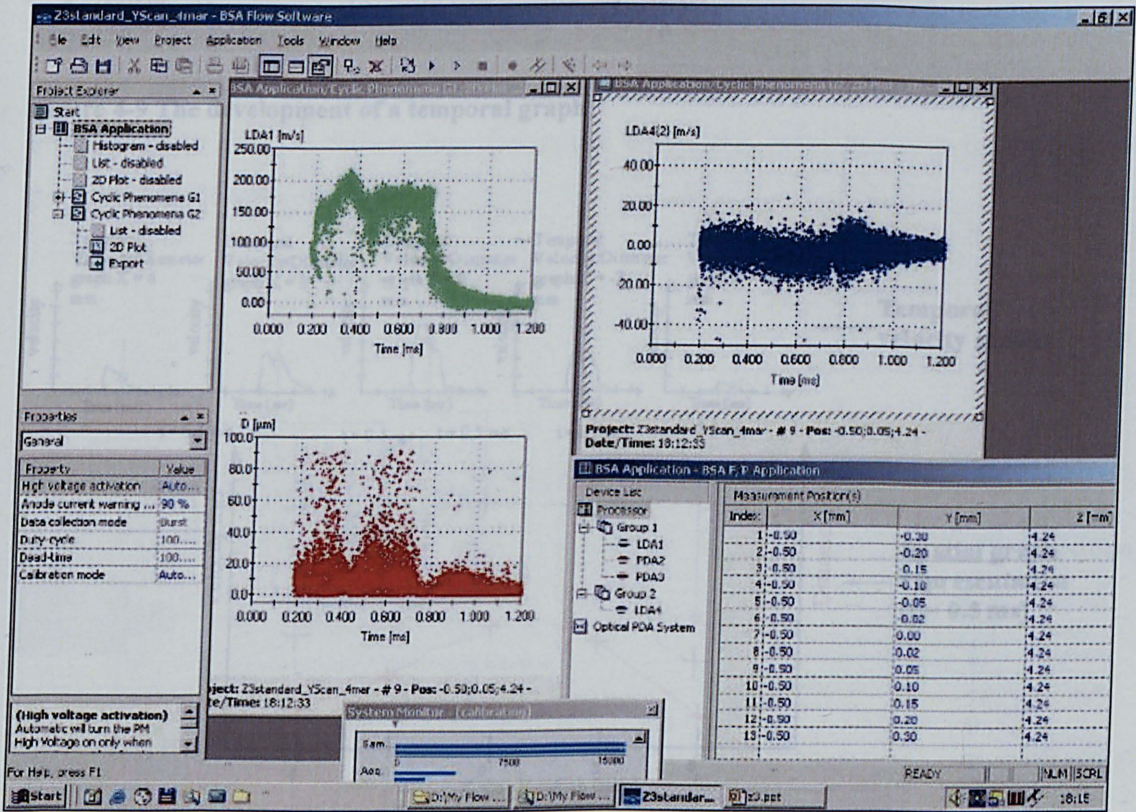


Figure 4-8 Screen print out of the PDA software while acquiring data.

The development of a temporal graph is described graphically in Figure 4-9. Graphs representing spatial distribution are dependent on information provided in



temporal graphs. The relationship between these two graphs is described in Figure 4-10, which represent the spatial distribution at 0.5 ms ASOI.

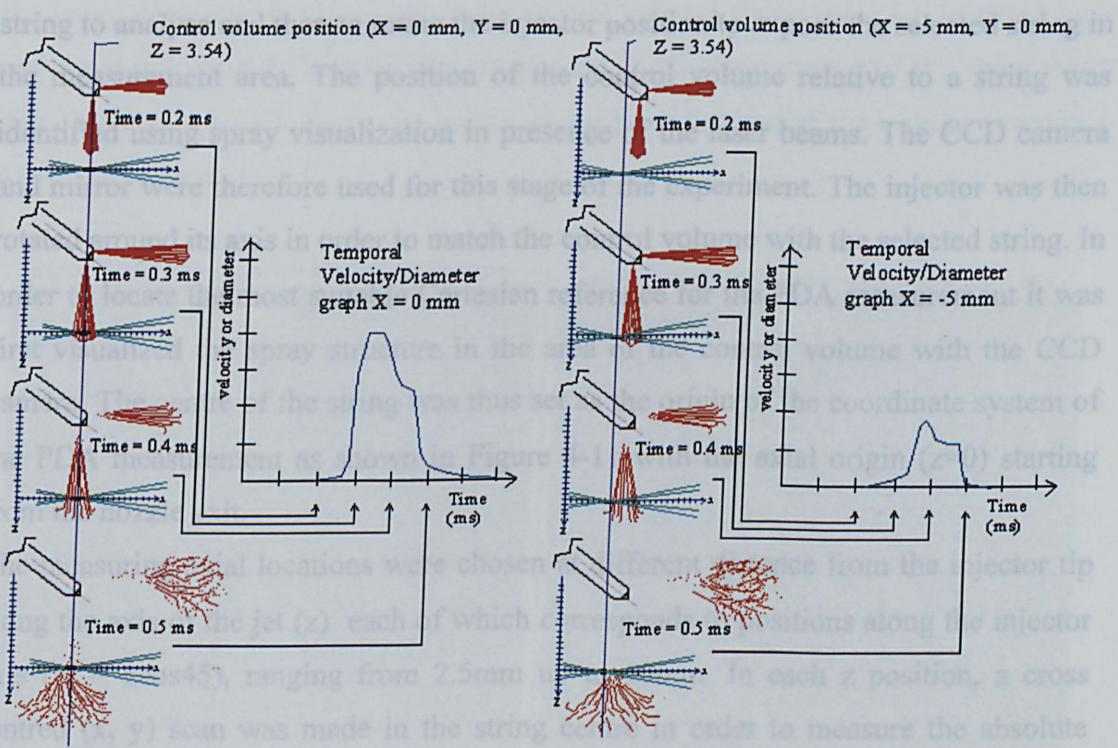


Figure 4-9 The development of a temporal graph

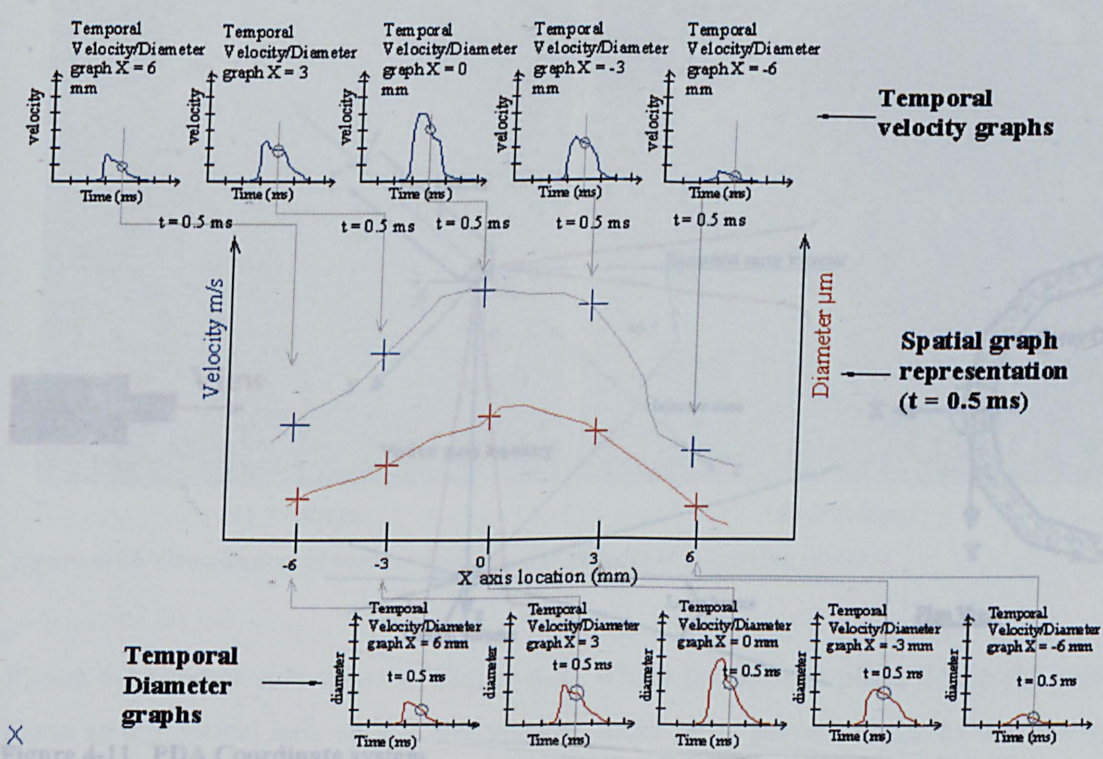


Figure 4-10 Development of a spatial graph.



### 4.3.3. String Identification

Before starting the PDA measurements it was necessary to identify a representative string to analyse and then to rotate the injector position to expose the selected string in the measurement area. The position of the control volume relative to a string was identified using spray visualization in presence of the laser beams. The CCD camera and mirror were therefore used for this stage of the experiment. The injector was then rotated around its axis in order to match the control volume with the selected string. In order to locate the most suitable Cartesian reference for the PDA measurement it was first visualized the spray structure in the area of the control volume with the CCD camera. The centre of the string was thus set as the origin of the coordinate system of the PDA measurement as shown in Figure 4-11 with the axial origin ( $z=0$ ) starting from the nozzle exit.

The measuring axial locations were chosen at different distance from the injector tip along the axis of the jet ( $z$ ) each of which corresponds to positions along the injector axis ( $z' = z \cos 45^\circ$ ), ranging from 2.5mm up to 50mm. In each  $z$  position, a cross centred ( $x, y$ ) scan was made in the string centre in order to measure the absolute velocity and droplet distribution throughout the string. In order to refer the axial coordinate to the jet rather than the spray cone, the axial position in the results presented in this chapter is referred to  $z$

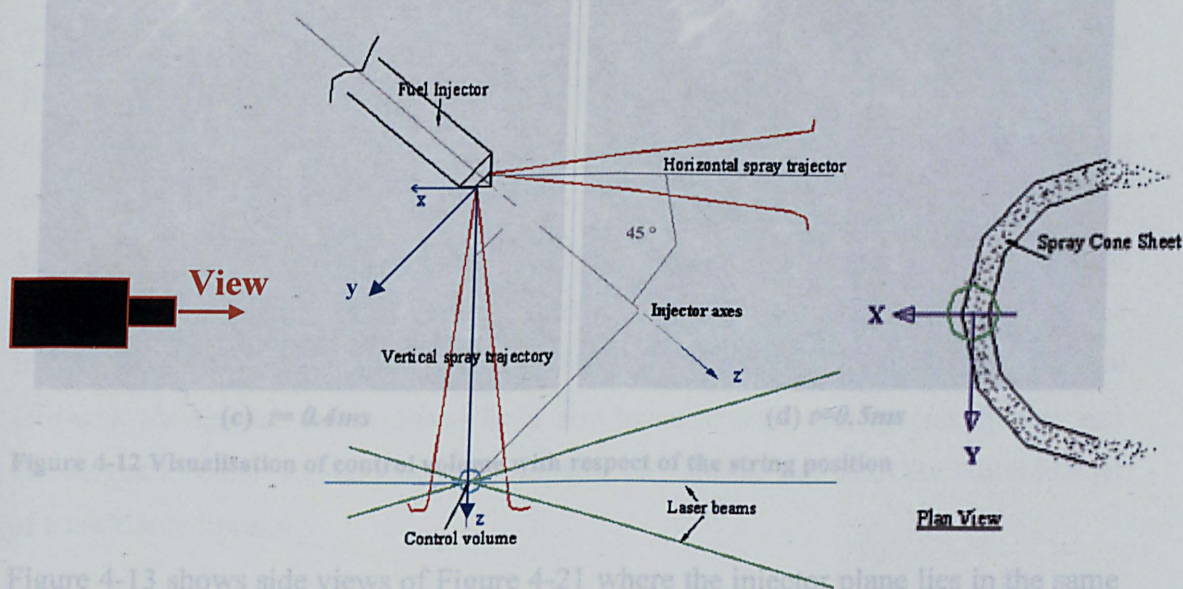


Figure 4-11 PDA Coordinate system



Figure 4-12 (a) to Figure 4-12(d) show the control volume produced by the crossing points of the two laser beams positioned on a particular string within the spray whilst the spray develops; the location of the control volume (laser spot) is identified by a red circle in Figure 4-12 (a-d). The images show the outer surface of the spray taken directing the camera towards the laser coming from the transmitting optics through a 45-degree mirror.

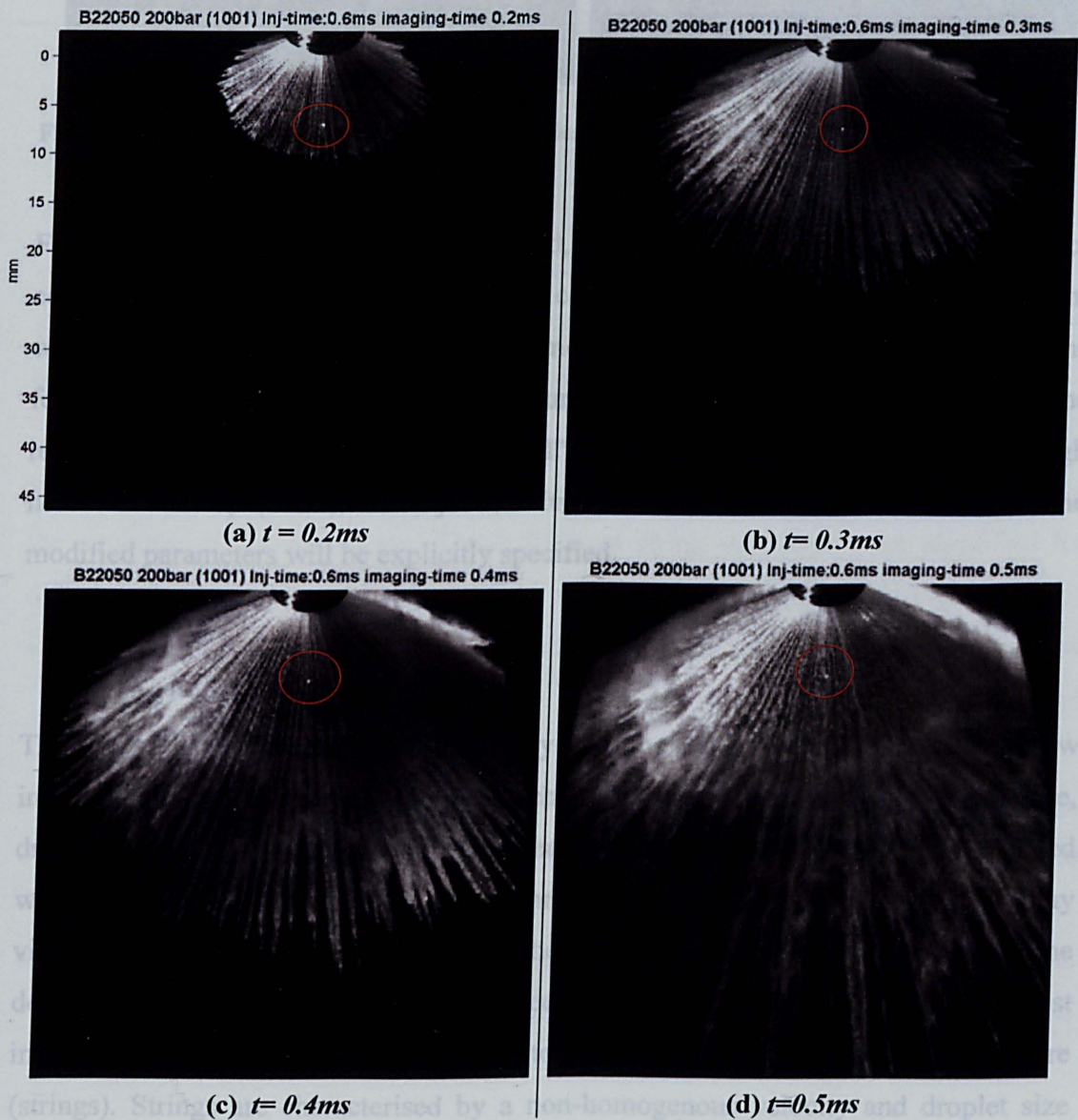


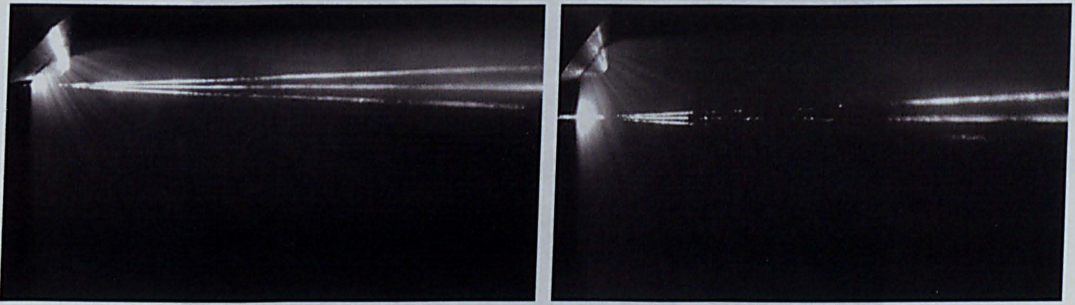
Figure 4-12 Visualisation of control volume with respect of the string position

Figure 4-13 shows side views of Figure 4-21 where the injector plane lies in the same plane as the optical axis so that the vertical spray jet is perpendicular to the beams. The images were taken directly and no mirror was required. The frames show the



---

control volume produced by the converging laser beams, intercepting the vertical spray cone, right below the nozzle exit and at z coordinates 3.56mm.



**Figure 4-13** Laser beams converging in the vertical edge of the spray during PDA measurement

Four operating conditions were analysed, one of which was chosen as reference condition and is referred to as standard condition. The remaining three conditions were obtained by varying one of the parameters with respect to the standard one. The following nomenclature will be adopted during the discussion of the PDA results. The reference condition referred as "Standard" is set at 200bar injection pressure, high needle lift set up (1001), and injection duration 0.6ms. For all the other cases, the modified parameters will be explicitly specified.

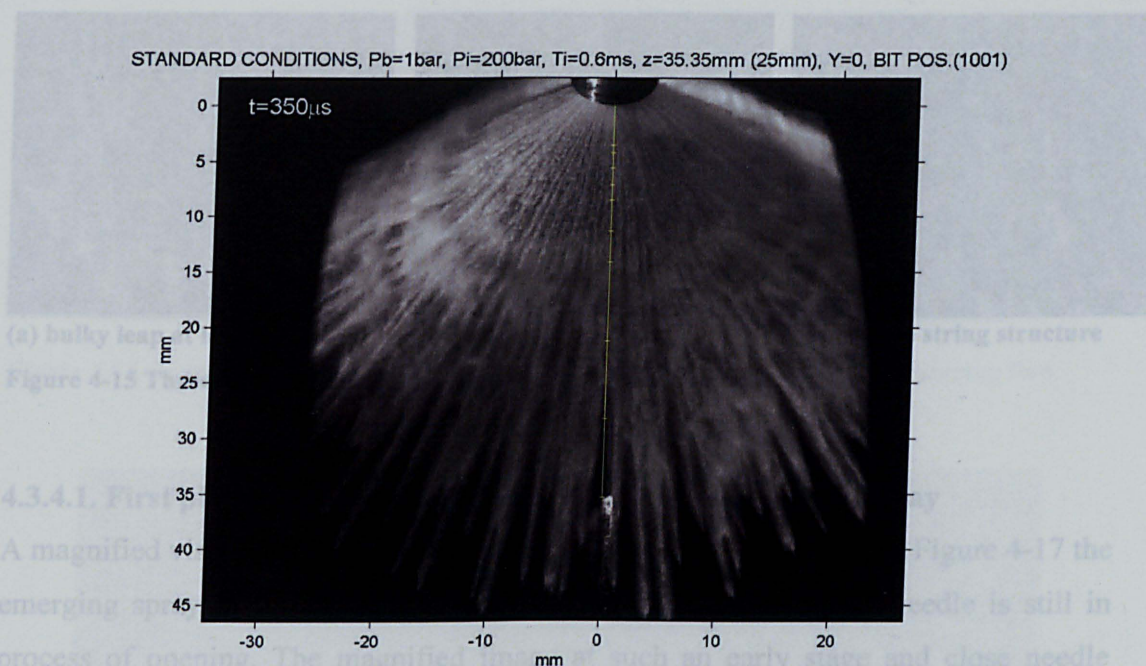
string structures were identified for different phases of the injection during the spray evolution, as shown in Figure 4-15.

• The first phase is described by the leading edge of the spray, which is composed by the shearing action between liquid and

#### **4.3.4. Results and discussion**

The first set of results is based on the analysis of the standard conditions, which show in details several aspects of the spray characteristics in terms of spray structure, droplet diameter and velocity. These three aspects will be analysed and correlated with a special effort in trying to connect qualitative information from spray visualisation and quantitative data from the PDA measurement occurring during the development of a spray event. As it was seen in the previous chapter, one of the most important attribute of the pintle-type injector spray is its typical filamentous structure (strings). Strings are characterised by a non-homogenous velocity and droplet size throughout its cross-section with a distribution very similar to that of the individual jet of a multihole injector.





**Figure 4-14** Front view of the spray turned  $45^\circ$ . The white spot is the reflected laser light of the control volume. The ticks along the yellow line represent the measurement locations.

For this reason a more careful and detailed study was carried out here to characterise the structure of a single string. Three different string structures were identified for different phases of the injection during the spray evolution, as shown in Figure 4-15.

- The first phase is described by the leading edge of the spray, which is composed by the spray front, which is broken by the shearing action between liquid and surrounding gas.
- The second phase is characterised by a steady and well-defined structure of strings. The strings are very straight and defined showing a very clear and nit fishbone structure.
- After a fixed interval of time, the nit and clear strings observed in the second phase lose their individuality and become rapidly distorted to form an amorphous shape which lasts until the end of injection.



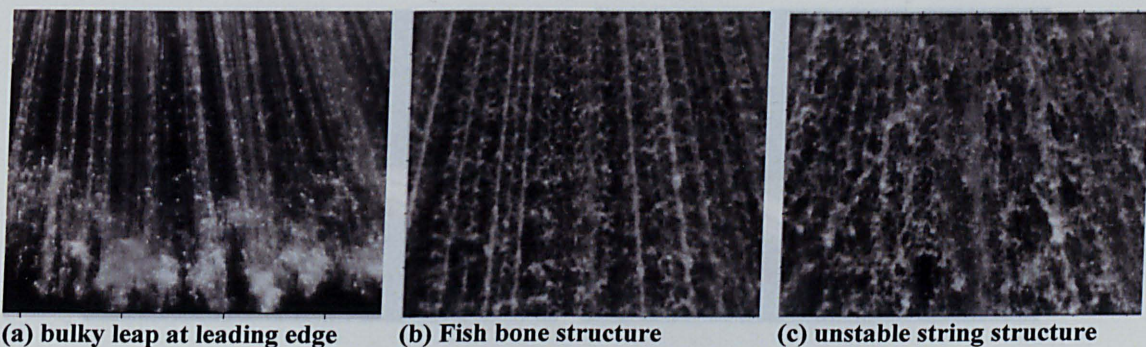


Figure 4-15 Three phases of the spray structure at 3.5mm from the nozzle exit

#### 4.3.4.1. First phase structure. Bulky leap at leading edge of the spray

A magnified visualization of the spray at standard conditions shows in Figure 4-17 the emerging spray at the very early phase of the injection when the needle is still in process of opening. The magnified image at such an early stage and close needle position was achieved by a fortunate lighting set up and by inclining the camera toward the nozzle passage to visualise through a mirror the nozzle exit as shown in Figure 4-16.

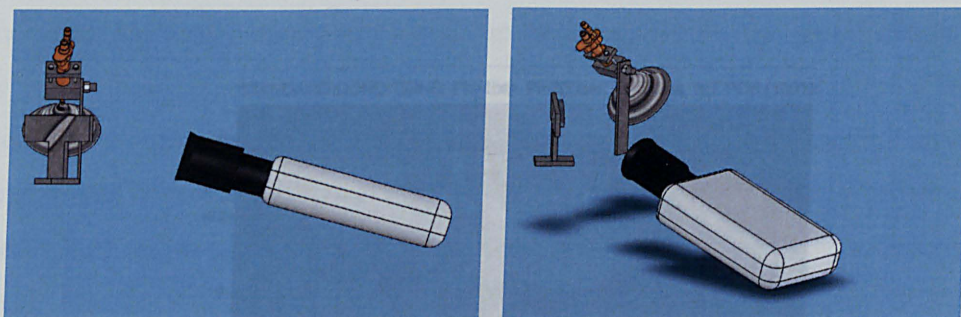
In the first snap shot of Figure 4-17 the flow has just emerged and the rim produced by the shearing action with the air is not formed yet however, a hint pre-announcing the string formation is already visible in both images showing the same profile pattern even though the snap shots do not belong to the same injection. Such a consistency suggests that the string formation is completely unrelated to the upstream turbulence, which has random and chaotic nature.

The second snap shot taken just few  $\mu\text{s}$  after the first one shows the onset formation of the bulky leap where the rim of the liquid sheet start thickening due to the interaction with the surrounding air.

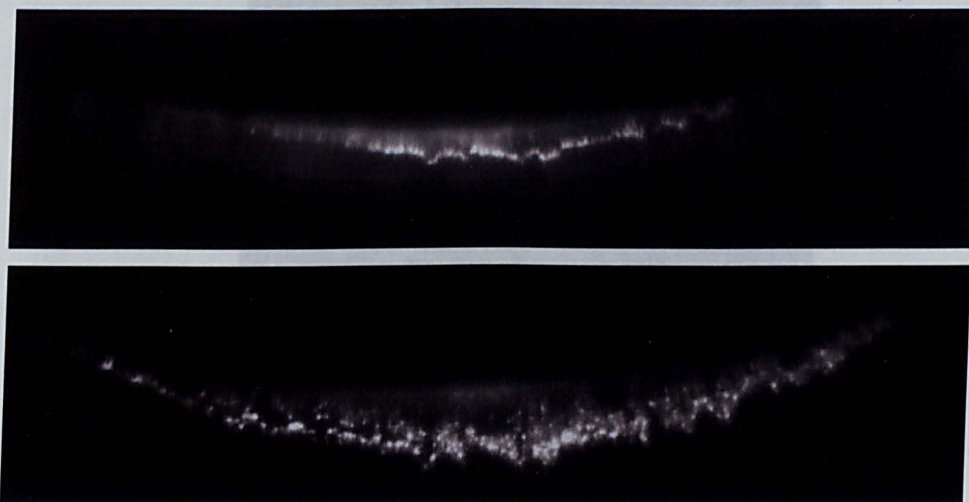
It is also interesting to note that even when the liquid sheet is still intact, the strings already possess their individuality and they are visible immediately after emerging from the injector, which means that they are not the results of liquid sheet break up in ligaments.

15 $\mu\text{s}$  after the start of injection where the spray rim is affected by the impact against the surrounding air and forms a bulky lip. As the leading edge advances downstream (second image  $t=25\mu\text{s}$ ) the preceding liquid catch up the leading sheared front which extends its length backward initiating a tendency for the liquid sheet to breakup mainly in between two adjacent strings.





**Figure 4-16 Camera, mirror and injector layout for the spray visualisation of emerging flow**



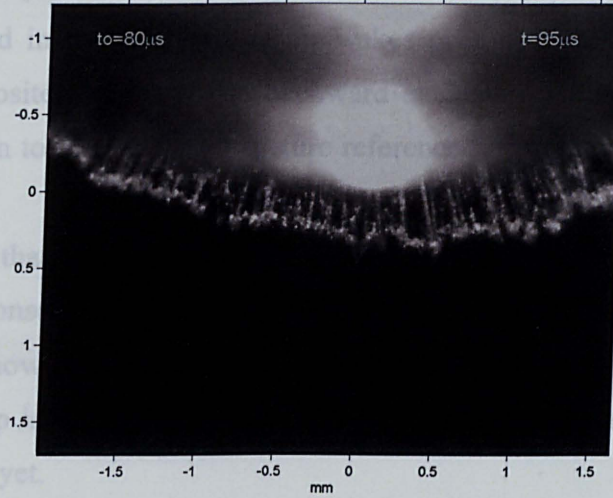
**Figure 4-17 Emerging spray at start of injection:  $P_i=200\text{bar}$ , Needle lift =  $29\mu\text{m}$  (1001 ).**

The following set of images in Figure 4-18 shows the evolution of the spray at the initial stage of the injection when the formation of the first phase structure and the filaments start being more defined. In the three images in Figure 4-18,  $t_0$  represents the start of the injection with respect to the electrical pulse from injector driver whereas the actual injection timing  $t - t_0$  is respectively  $15\mu\text{s}$ ,  $25\mu\text{s}$  and  $35\mu\text{s}$  after start of the injection (ASOI).

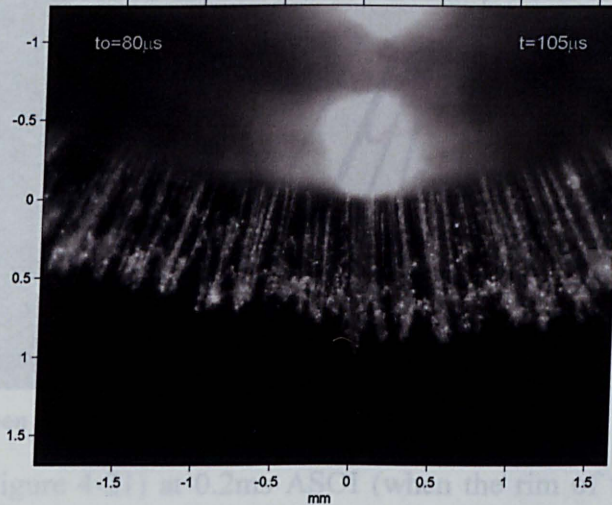
The first picture in Figure 4-18 shows the leading edge as fuel emerging from the injector at  $15\mu\text{s}$  after the start of injection where the spray rim is affected by the impact against the surrounding air and forms a bulky lip. As the leading edge advances downstream (second image  $t=25\mu\text{s}$ ) the preceding liquid catch up the leading sheared front which extends its length backward initiating a tendency for the liquid sheet to breakup mainly in between two adjacent strings.



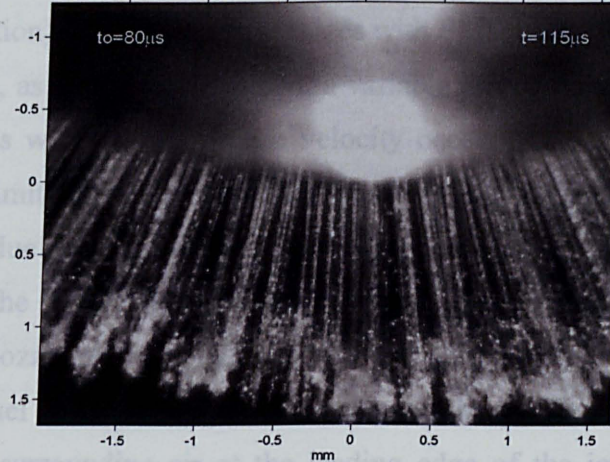
STANDARD CONDITIONS,  $P_b=1\text{bar}$ ,  $P_i=200\text{bar}$ ,  $T_i=0.6\text{ms}$ , BIT POS.(1001)



STANDARD CONDITIONS,  $P_b=1\text{bar}$ ,  $P_i=200\text{bar}$ ,  $T_i=0.6\text{ms}$ , BIT POS.(1001)



cap between  
rings typical of a  
am type liquid  
sheet break up [93]

STANDARD CONDITIONS,  $P_b=1\text{bar}$ ,  $P_i=200\text{bar}$ ,  $T_i=0.6\text{ms}$ , BIT POS.(1001)

**Figure 4-18 Spray structure at start of injection:  $P_i=200\text{bar}$ , Needle lift =  $29\mu\text{m}$  (1001 ) at 15, 25, 35  $\mu\text{s}$  ASOI.**



As the spray develops, secondary break up takes place and the small droplets with lower momentum disperse towards inner and outer surface of the spray jet. These fine droplets are trapped in the surrounding air wakes or simply are slowed by the air moving in the opposite direction. The backward extension of this cloud of sheared droplets gives origin to this starting structure referenced in this chapter as first phase structure.

A particular feature that can be observed in the two first images (15 - 25  $\mu$ s ASOI) are the leap between consecutive strings which looks like a liquid sheet in process of breaking which is shown more clearly in Figure 4-19. That suggests that in this phase the primary break up is occurring and liquid sheet and ligaments are not completely broken into droplets yet.

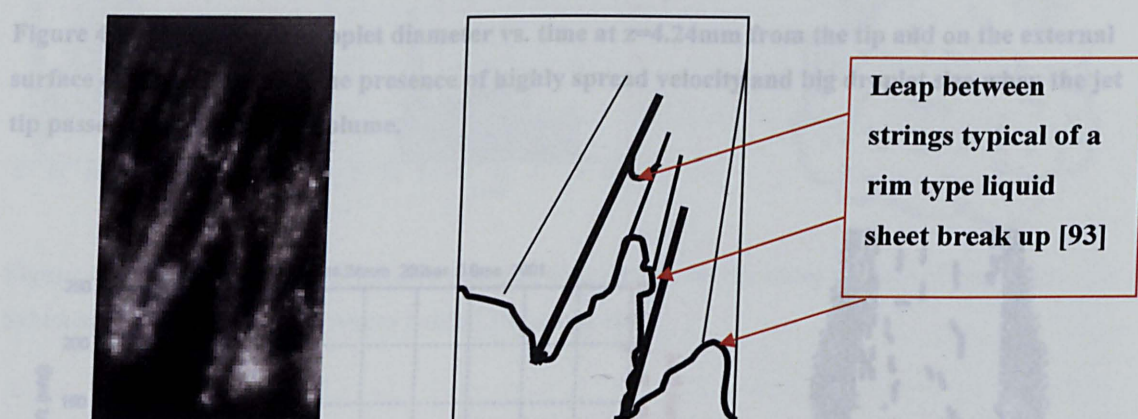
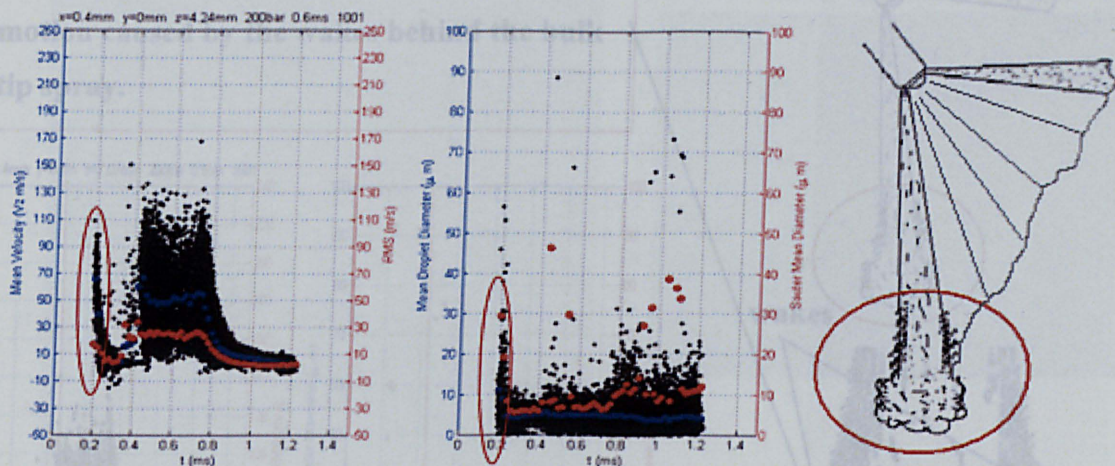


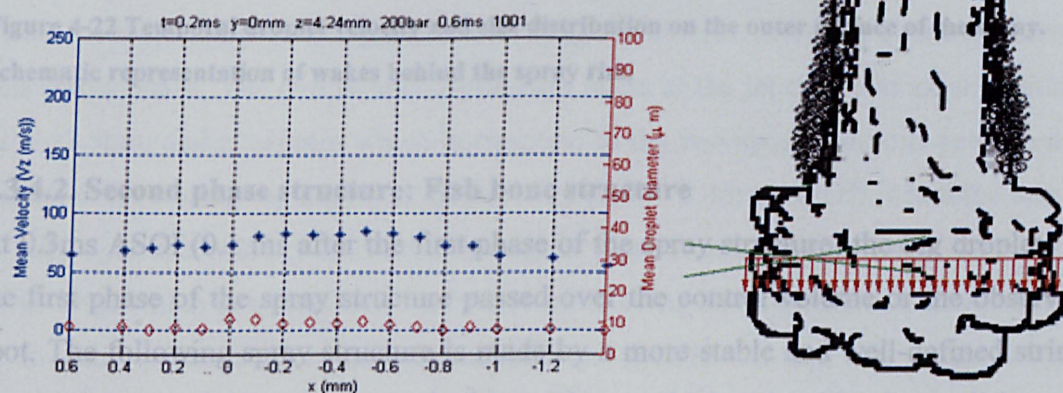
Figure 4-19 Leap between strings (particular of Figure 4-18 at 25  $\mu$ s ASOI).

The PDA results, (Figure 4-21) at 0.2ms ASOI (when the rim of the spray hits the control volume) show a uniform mean velocity distribution through the whole string thickness (x-direction) with large droplet sizes with SMD up to 30  $\mu$ m, (Figure 4-20 at 0.2ms). In general, as it will be described, a variable distribution is expected through the spray thickness with the peak mean velocity occurring at the jet centre and the minimum in proximity of the surface. The uniform mean velocity through the rim thickness can be due to the residual fuel trapped outside the nozzle sealing in the divergent part of the nozzle of the injector sealing (Figure 3-8) which does not go through the same nozzle path and therefore it is not affected by the same wall friction as the following fuel flow. Another reason can also be attributed to initial uniform shearing effect of surrounding air at the leading edge of the jet, which slows the emerging droplet uniformly across the spray thickness. Immediately after the bulky spray rim, the drop size at  $z=4.2$ mm reduces to an SMD between 8-12  $\mu$ m and it remains similar until the end of injection.





**Figure 4-20** Velocity and droplet diameter vs. time at  $z=4.24\text{mm}$  from the tip and on the external surface of the jet. It shows the presence of highly spread velocity and big droplet size when the jet tip passes through control volume.

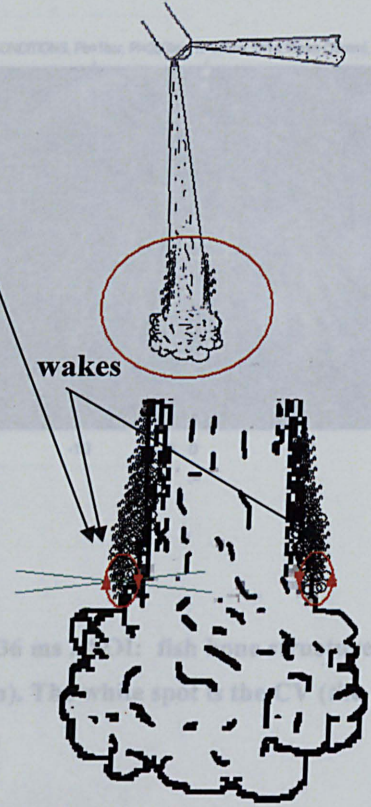
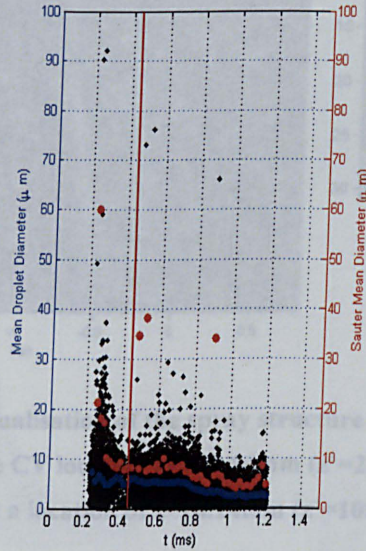
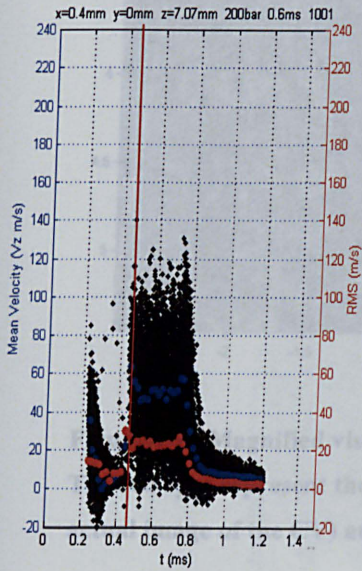


**Figure 4-21** Spatial velocity distributions at the start of the injection across the tip of the spray.

By examining the velocity distribution immediately after the aforementioned spray rim the temporal variation in Figure 4-22 shows a zone with lack of droplets and a certain amount of droplets with negative velocity. These are typical characteristics of a wake region, which can be present behind the bulky leap of the spray with small droplets as shown in Figure 4-22



**Small droplets dragged by recirculation motion caused by the wakes behind the bulk tip spray.**

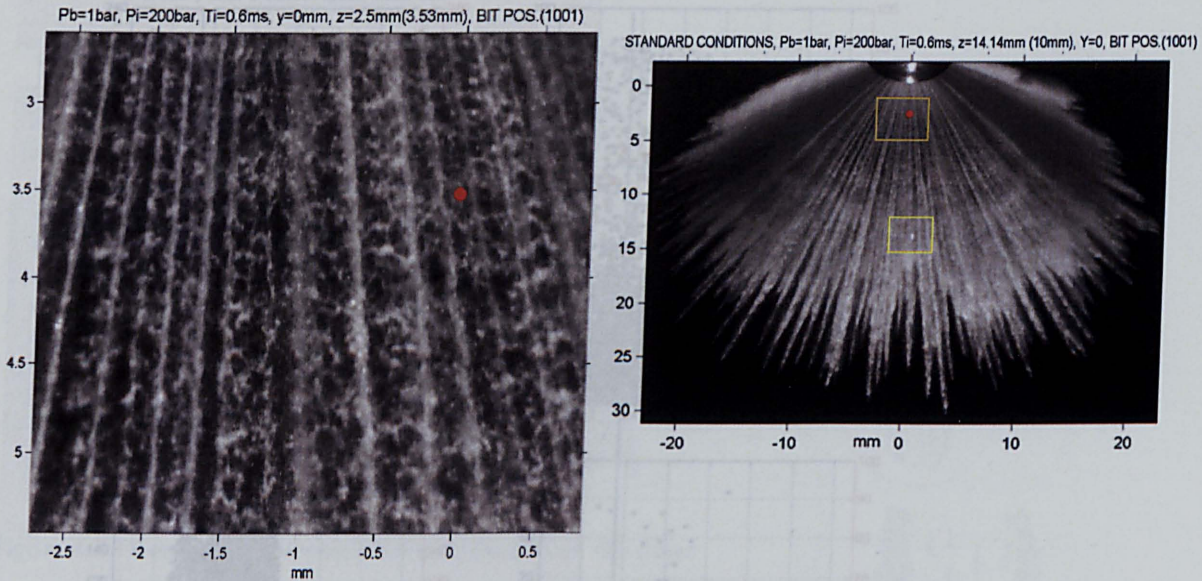


**Figure 4-22 Temporal droplet velocity and size distribution on the outer surface of the spray. Schematic representation of wakes behind the spray rim.**

#### 4.3.4.2. Second phase structure: Fish bone structure

At 0.3ms ASOI (0.1 ms after the first phase of the spray structure) the big droplets of the first phase of the spray structure passed over the control volume or the observed spot. The following spray structure is made by a more stable and well-defined string pattern composed by straight and clear strings, which resemble the well-known fishbone structure, observed with the jet sprays produced by multi-hole injectors. (Figure 4-23); this stable pattern persists up to an axial location of  $z = 21.2\text{mm}$  ( $z' = 15\text{mm}$ ).



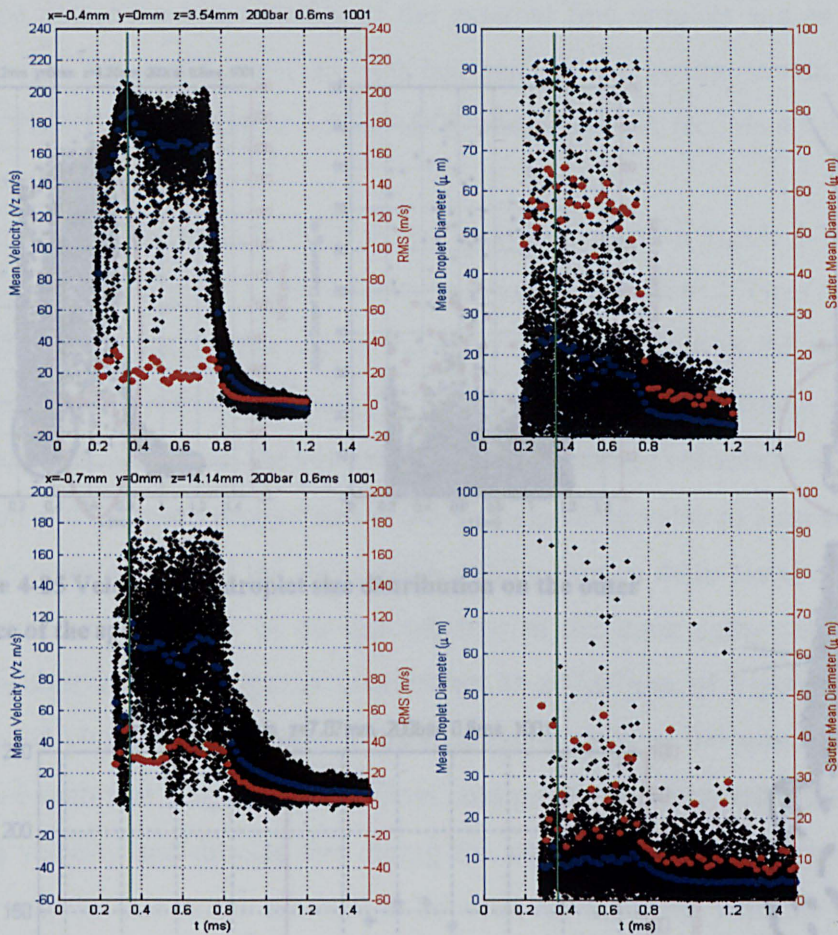


**Figure 4-23 Magnified visualisation of the spray structure at 0.36 ms ASOI: fish bone structure. The red spot represent the CV location at  $z=3.54\text{mm}$  ( $z'=2.5\text{mm}$ ). The white spot is the CV (the actual image of the CV) at a location of  $z=14.14\text{mm}$  ( $z'=10\text{mm}$ ).**

From the temporal plot of Figure 4-24, it is possible to describe the characteristics of this stable phase. The two temporal plots are taken at the jet centre at axial positions of  $z'=2.5\text{mm}$  and  $z'=10\text{mm}$  which correspond to the two spots positions presented in Figure 4-23. During the main part of injection (0.3 to 0.45ms ASOI), when the needle is fully open the velocity fluctuates through a very narrow velocity range with a low RMS level which is an indication of the level of string stability. Further downstream, at an axial position of 10mm, the stability is slightly reduced due to the higher fluctuation in the jet direction and to the stronger interaction of the air entrainment with the spray droplets (Figure 4-48). The PDA plots during the same interval considered at  $z'=2.5\text{mm}$  exhibit a higher velocity fluctuation which is also reflected in high level of RMS velocity.

could be produced by the pressure wave associated with the hammer effect occurring during the needle-opening event. That would explain why it is particularly pronounced at an axial location very close to the nozzle exit and why such an effect is barely observable further downstream at  $z'=10\text{mm}$  ( $z=14.14\text{mm}$ ). It is also evident that droplet sizes at 10mm from injector are considerably lower than that those at 2.5mm, especially during the main injection period. This indicates that at 2.5mm, secondary breakup has not fully started yet and it certainly takes place within 2.5mm and 10mm.

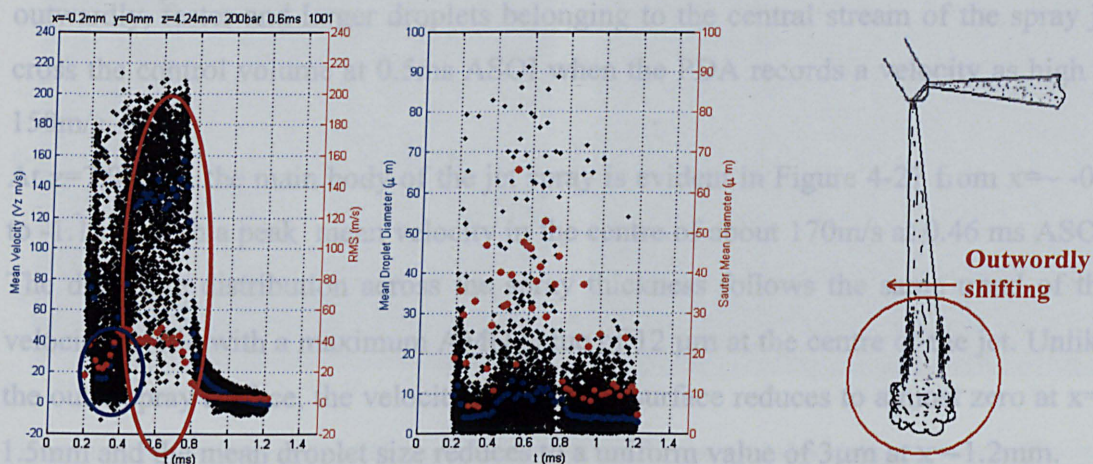




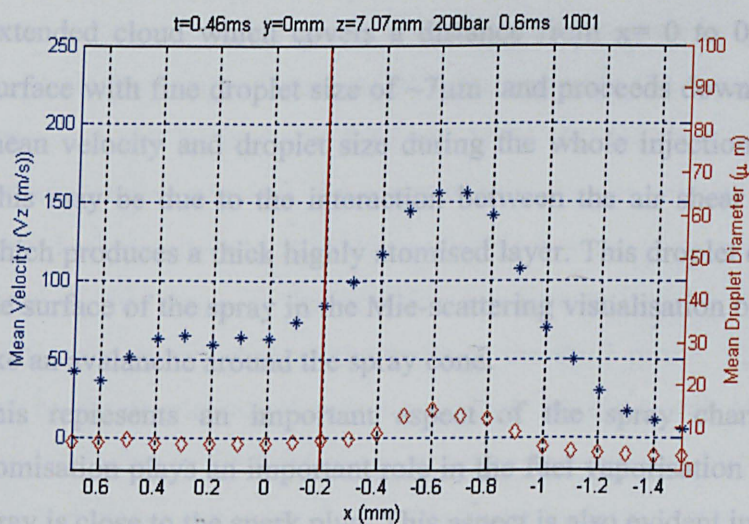
**Figure 4-24** Temporal variation of droplets mean velocity and AMD diameter at the string centre for  $z = 3.54\text{mm}$  ( $z' = 2.5\text{mm}$ ) and  $z = 14.14\text{mm}$  ( $z' = 10\text{mm}$ ) from injector nozzle. The magenta line corresponds to the time of the snap shot of Figure 4-23.

Another characteristic that can be observed at the centre of the string in this phase of the spray structure (Figure 4-24) is the peak velocity occurring at 0.36ms (needle fully open) which is also associated to an AMD peak at the same instant. The peak matching between velocity and diameter can be explained by the higher momentum possessed by the larger droplets which tend to loose their velocity more slowly. The velocity peak formation could be produced by the pressure wave associated with the hammer effect occurring during the needle-opening event. That would explain why it is particularly pronounced at an axial location very close to the nozzle exit and why such an effect is barely observable further downstream at  $z' = 10\text{mm}$  ( $z = 14.14\text{mm}$ ). It is also evident that droplet sizes at 10mm from injector are considerably lower than that those at 2.5mm, especially during the main injection period. This indicates that at 2.5mm, secondary breakup has not fully started yet and it certainly takes place within 2.5mm and 10mm.

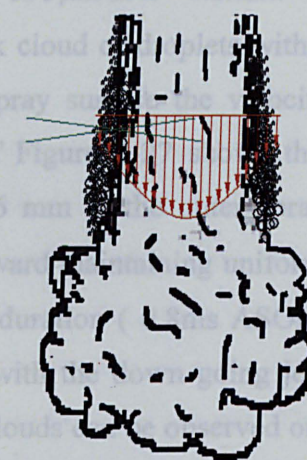




**Figure 4-25** Velocity and droplet size distribution on the outer surface of the spray.



**Figure 4-27** X distribution of Mean droplet velocity and size at 0.46ms ASOI, immediately after the spray leading edge.



**Figure 4-26** Scheme showing the velocity distribution through the spray thickness after the leading edge

At 0.45 ms ASOI the spray flaps outwardly (the spray cone opens) and this can be observed from the analysis of Figure 4-25 where the CV is positioned just at the outer surface of the spray jet ( $x=-0.2\text{mm}$ ). A variation in the velocity distribution can be observed between the droplets at the outer spray surface (in the wake of the spray rim) composed by small slow-moving droplets and the main jet (centre of the jet thickness) composed by large droplets with higher momentum (Figure 4-26).

Therefore, during the injection event the control volume initially fixed at the outer



surface detect the low velocity of the external fine droplets and as the spray flaps outwardly, faster and larger droplets belonging to the central stream of the spray jet cross the control volume at 0.5ms ASOI when the PDA records a velocity as high as 150m/s.

At  $z=7.07\text{mm}$ , the main body of the jet spray is evident in Figure 4-27 from  $x \sim -0.2$  to  $-1.1\text{mm}$  with a peak mean velocity in the centre of about 170m/s at 0.46 ms ASOI. The drop size distribution across the spray thickness follows the same trend of the velocity profile with a maximum AMD value of  $12\text{ }\mu\text{m}$  at the centre of the jet. Unlike the outer spray surface, the velocity at the inner surface reduces to almost zero at  $x=-1.5\text{mm}$  and the mean droplet size reduces to a uniform value of  $3\text{ }\mu\text{m}$  at  $x=-1.2\text{mm}$ .

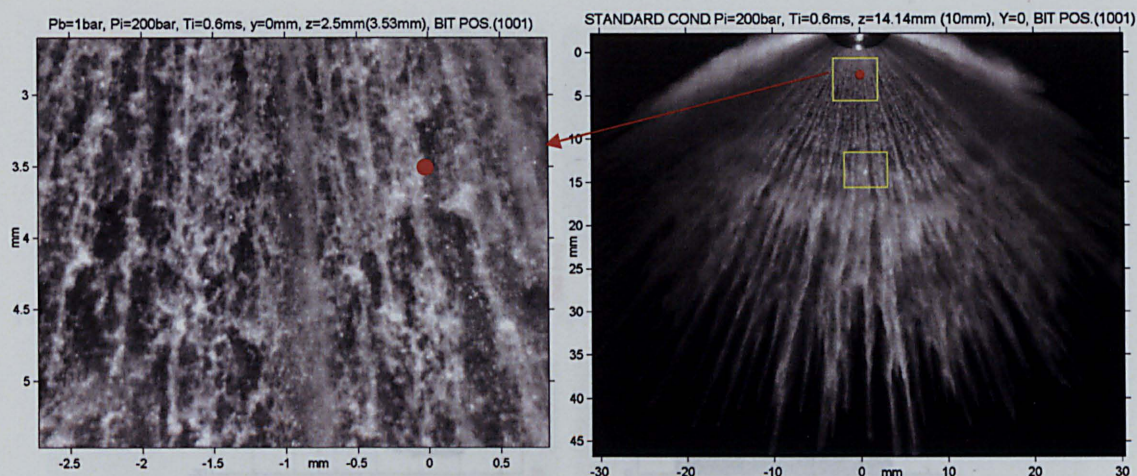
At the outer surface of the spray, PDA results show a thick cloud of droplets with a uniform mean velocity of 60 m/s whereas at the inner spray surface the velocity approaches zero. The spatial distribution at  $z=7.07\text{mm}$  of Figure 4-27 shows this extended cloud which covers a distance from  $x=0$  to  $0.6\text{ mm}$  at the outer spray surface with fine droplet size of  $\sim 7\text{ }\mu\text{m}$  and proceeds downward maintaining uniform mean velocity and droplet size during the whole injection duration ( 0.8ms ASOI). This may be due to the interaction between the air shear with the down going jet, which produces a thick highly atomised layer. This droplet clouds can be observed on the surface of the spray in the Mie-scattering visualisation of Figure 4-28 which looks like an avalanche around the spray cone.

This represents an important aspect of the spray characteristics where a fine atomisation plays an important role in the fuel vaporisation as the outer region of the spray is close to the spark plug. This aspect is also evident in Figure 4-33 where it can be observed the full velocity distribution at different  $z$ -locations and the downward propagation of the above-mentioned cloud.

#### 4.3.4.3. Third phase structure: unstable string structure

The peculiarity of this structure derives from the sudden string distortion, which comes from the alteration of straight and stable filaments to irregular and shapeless flow as shown in Figure 4-28. The followings PDA results, Figure 4-29 and Figure 4-30, show the velocity and droplet distribution for this spray phase as represented in Figure 4-28 by the red spot.



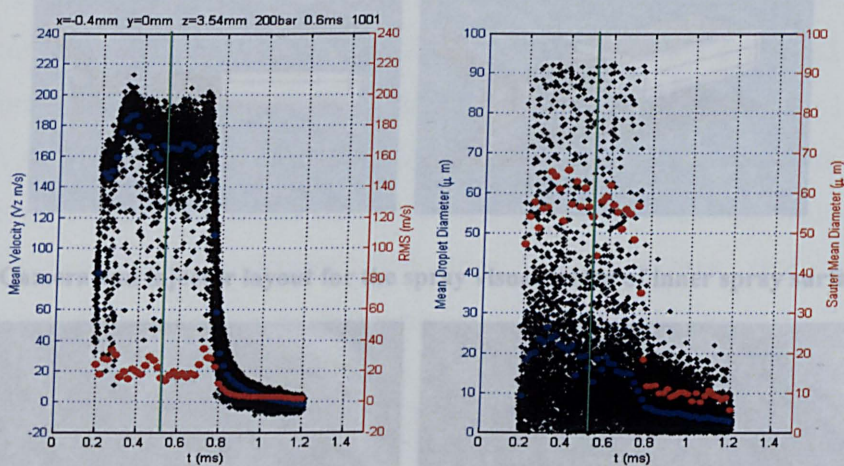


**Figure 4-28 Magnified image of the spray structure at 0.53 ms: unstable string structure. The red spot represent the CV location at  $z'=3.54$  ( $z=2.5\text{mm}$ ).**

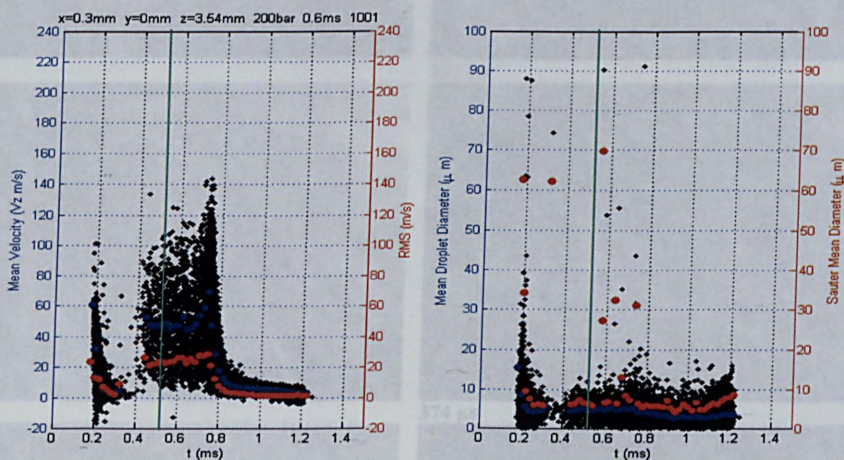
At the centre of the jet ( $x=-0.4\text{mm}$ ,  $z=3.54\text{mm}$ ), it was previously observed the fish bone structure (second phase structure) characterised by well-defined filaments and low velocity range (Figure 4-29) occurring after the spray leading edge (first phase structure) and lasting until 0.53 ms ASOI. At this time, although the mean velocity remains almost constant, the instantaneous droplet velocity distribution shows a wide spread of velocity which is also a good indication of secondary breakup process. The spray at this stage of the injection is characterised by different droplet sizes and trajectories, which defines the starts to the third phase. The same trend is followed also by the droplet size distribution, which reveals a peak of higher AMD of about  $28\text{ }\mu\text{m}$  decreasing in the third phase structure to a value of just above  $15\text{ }\mu\text{m}$ . The higher flow turbulence occurring during this unstable phase promotes probably the secondary break up with consequent decrease in droplet size. However, the change in phase structure is not evident for the SMD trend, which appears quite high (up to about  $65\text{ }\mu\text{m}$ ) and in general relatively scattered during the whole injection event.

At the inner surface of the spray ( $x=0.3\text{mm}$ ), the three phase are well defined and can be observed in Figure 4-30. Higher velocity and large droplet diameter for the spray front (first phase), RMS velocity reduction (0.2 to 0.3ms ASOI) characterises the narrow velocity band of the compact fish bone structure (second phase). Just before the beginning of the third phase the high spray density causes a lack of signal which right away recovers showing the highly spread velocity observed for the third phase structure. It can be noticed that at the inner edge, the secondary break up is almost completed as the SMD for second and third phase is as low as  $8\text{ }\mu\text{m}$ .





**Figure 4-29 Temporal velocity and droplet size distribution at the spray centre ( $x=0.4\text{mm}$ ) at standard condition**



**Figure 4-30 Temporal velocity and droplet size distribution at the inner edge of the spray ( $x=0.3\text{mm}$ ) at standard condition**

The inner surface of the spray was visualised by the camera arrangement shown in Figure 4-31 and the sequence of the images is presented in Figure 4-32. The following spray visualisation shows the string development during the spray evolution and in particular, it can be observed the transition between the second and the third spray structure, which occurs between  $374\mu\text{s}$  and  $415\mu\text{s}$  in agreement with the PDA results. If the set of images of Figure 4-32 could be viewed in continuous sequences then the start of instability could be observed revealing a gradual shifting of strings in tangential direction which lose their individual fixed angular position. This outcome could also be explained by the results seen in Chapter3 in the large-scale model where it was observed the tangential shifting caused by the turbulent oscillation of the eight counter rotating vortices forming downstream of the needle guide.



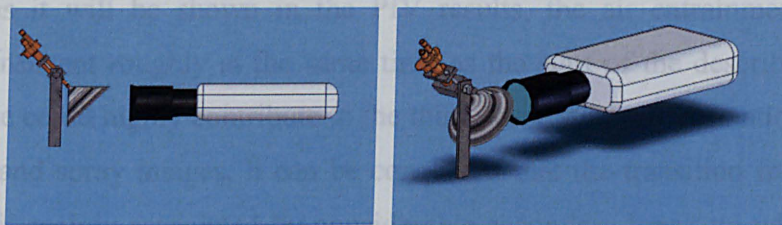


Figure 4-31 Camera and injector layout for the spray visualisation of inner spray surface.

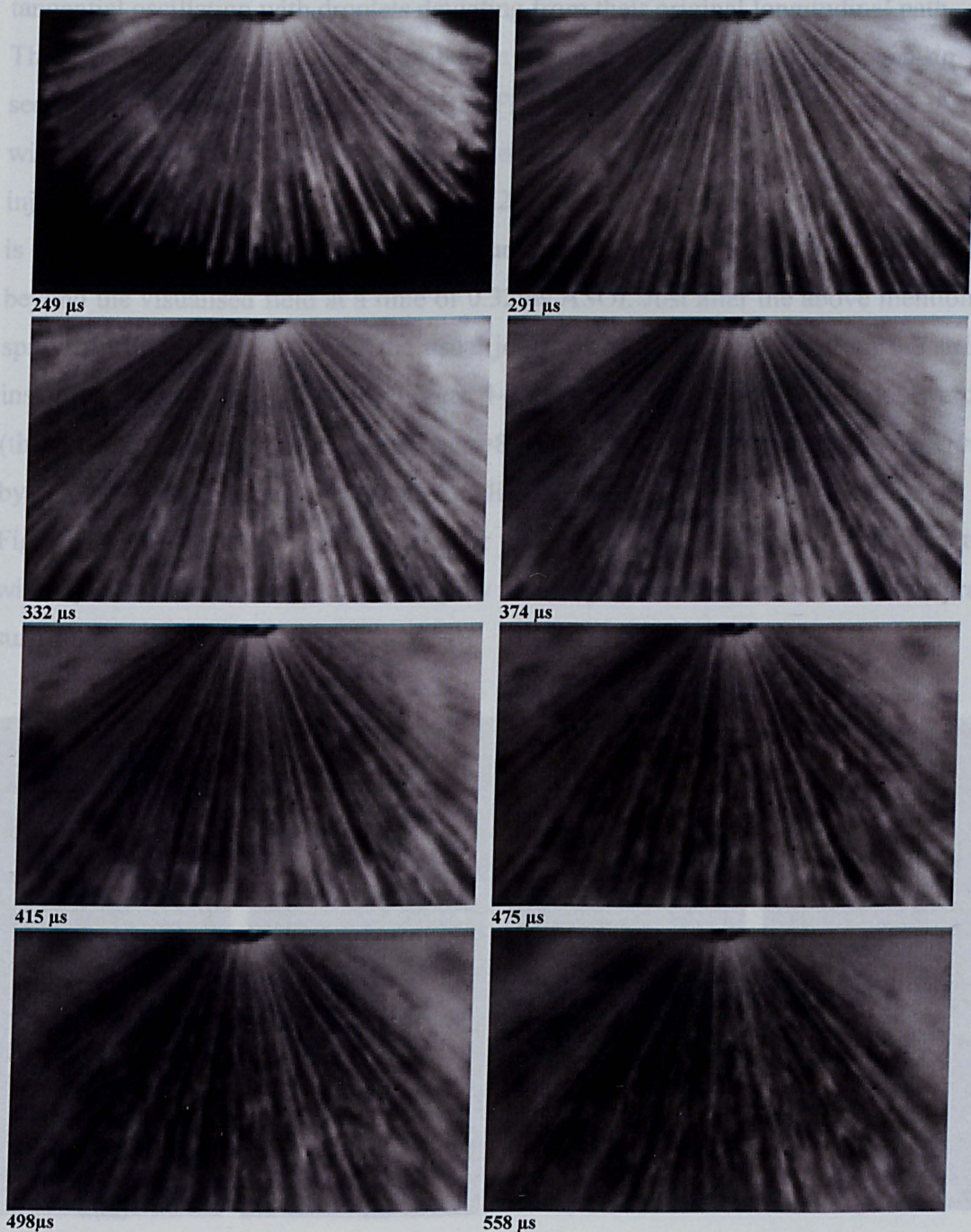


Figure 4-32 High-speed video of inner spray surface. Standard conditions: Injection duration 1ms, Pi 200bar, Needle lift (1001)



However, as it will be shown in the PIV results, the air entrainment interaction becomes consistent roughly at the same time as the start of the described instability and therefore could highly contribute to the third phase structure formation.

From PDA and spray images, it can be concluded that the transition from second to third phase is mainly associated by considerable secondary break up which generate new smaller droplets with different velocities and trajectories that can initiate tangential oscillation with droplets deviating from their original longitudinal path.

The overall droplet velocity distribution (temporal and spatial) is given in the sequence of velocity field presented in Figure 4-33 from 0.2ms to 0.84ms ASOI, within a radial range from  $x=-3.5$  mm to  $x=11.2$  mm and an axial distance from injector tip from 2.5mm to 8mm. From 0.2ms to 0.32ms, ASOI the front of the spray is propagating downward with almost a uniform profile of about 50m/s which goes beyond the visualised field at a time of 0.32ms ASOI. Just after the above mentioned spray rim the velocity assumes the usual jet-like profile until 0.4ms when the string instability takes place (according Figure 4-32) and the peak velocity flaps outwardly (the spray cone opens) up to 0.50ms at  $z=8.5$ mm. The displacement can be observed by comparing the peak against the dashed line of the sequence from 0.4ms to 0.5ms in Figure 4-33. The jet like profile is similar to those observed with multi-hole injector with a peak value in the centre of the spray reducing towards the inner and outer spray surface.

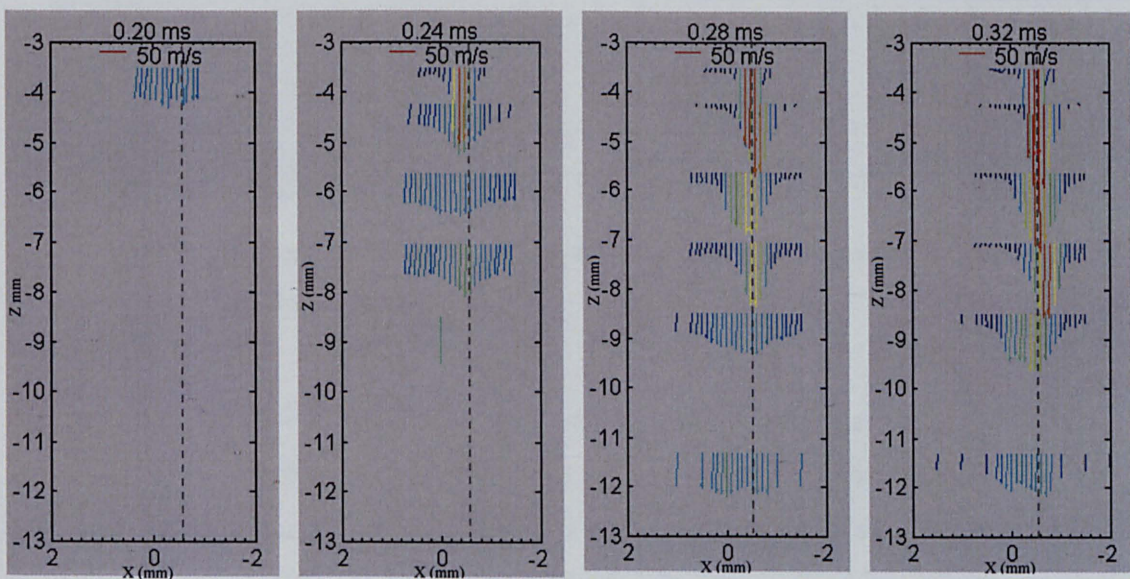


Figure 4-33 Vector velocity distribution for standard condition from 0.2ms to 0.84ms ASOI



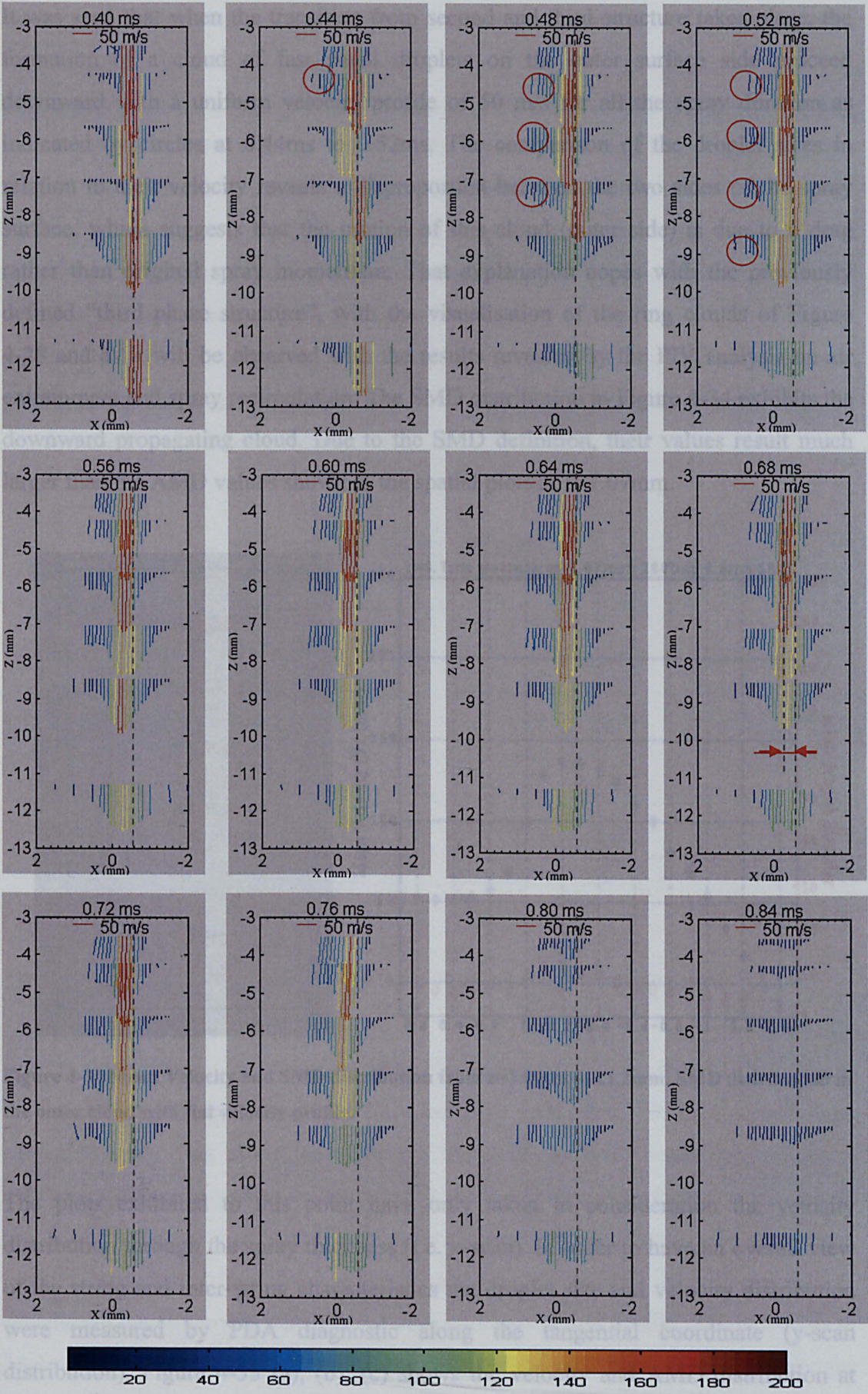
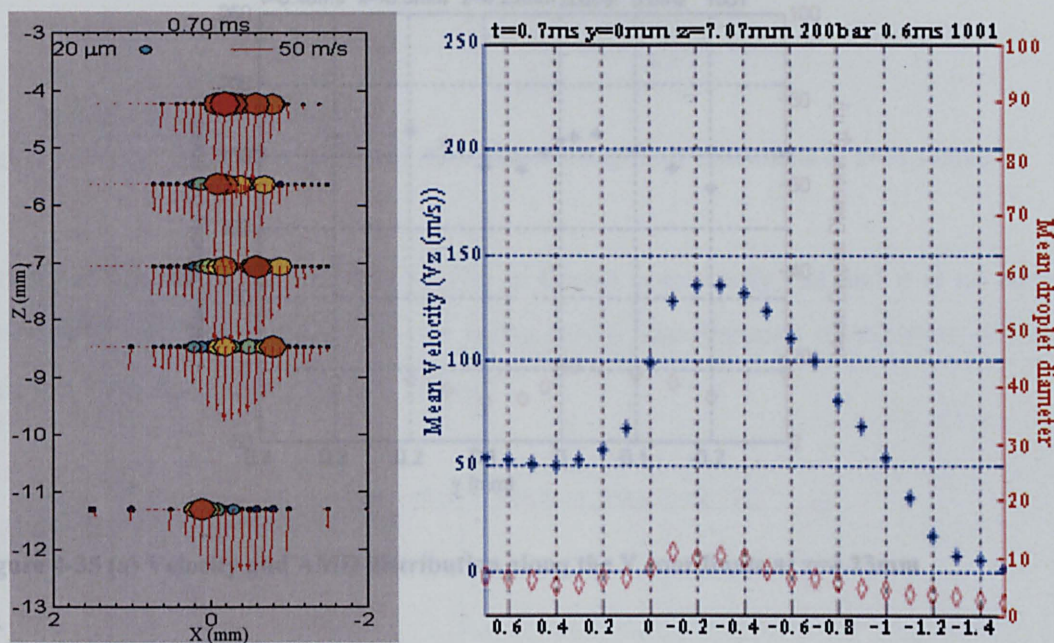


Figure 4-33 Vector velocity distribution for standard condition from 0.2ms to 0.84ms ASOI



It was seen that when the transition from second and third structure takes place, the formation of a cloud of fast small droplets on the outer surface side proceed downward with a uniform velocity profile of 50 m/s for all the spray duration as indicated by circles at 0.44ms to 0.52ms. The comparison of the droplet sizes in relation to their velocity reveals a disproportion between the two sides of the spray surface, which suggests that the motion of this cloud (outer side) is due to a drag rather than original spray momentum. That explanation copes with the previously defined “third phase structure”, with the visualisation of the ring clouds of Figure 4-28 and as it will be observed with the results revealed by the PIV analysis on air entrainment and spray recirculation. The SMD distribution in Figure 4-34 exhibits the downward propagating cloud. Due to the SMD definition, their values result much larger than the AMD values shown in the spatial plots at  $z=7.07\text{mm}$ .



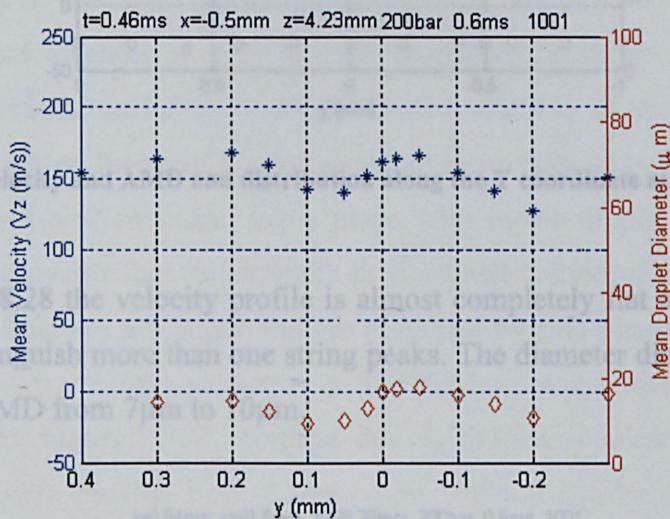
**Figure 4-34 Mean Velocity and SMD distribution from  $z=3.0\text{mm}$  to  $11.2\text{mm}$ . SMD distribution in the outer cloud with flat velocity profile.**

The plots exhibited to this point have only taken in consideration the velocity distribution through the spray thickness (i.e. x-scan). In order to have an overall view of the string and inter-string characteristics the droplet size and velocity distribution were measured by PDA diagnostic along the tangential coordinate (y-scan distribution). Figure 4-35 (a), (b), (c) shows the velocity and AMD distribution at three different axial (vertical) locations along the tangential coordinate. The



measurement trace was chosen at the x location corresponding to maximum peak velocity, which was defined as spray centre.

The graph of velocity and diameter in Figure 4-35 (a) at  $z=4.23\text{mm}$  shows a wavy profile which evidences the presence of two peaks correspondent to two adjacent strings. At this axial location, the string distribution around the spray cone is very packed and the two adjacent peaks representing the string centre are about  $0.2\text{mm}$  distant apart. The droplet diameter varies from  $20\mu\text{m}$  in the middle to  $10\mu\text{m}$  in the trough with a fluctuation of about 50%, which follows perfectly that of the velocity profile. Such a trend confirms as previously observed that the higher momentum is possessed by the larger droplets at the string centre while around the periphery the droplets are finer with lower momentum.



**Figure 4-35 (a) Velocity and AMD distribution along the Y coordinate at  $z=4.23\text{mm}$**

Further downstream,  $14.14\text{mm}$  far from the injector tip, (Figure 1 37 (b)), due to secondary breakup the split droplet have lost their momentum. Droplet Area/volume ratio decreases, drag effect increases and therefore the split droplets at the centre decrease their velocity. The velocity profile tends to become uniform and as a result, the peak to trough velocity ratio decreases. Furthermore, downstream the spray cone expands and the strings diverge from each other however it is still possible to distinguish the trend observed at  $z=4.23\text{mm}$  with two strings profile. The PDA data at  $14.14\text{mm}$  only show one peak within the measured range of  $2\text{mm}$ , but the two troughs around the periphery at  $y=0.6$  and  $-0.4$  are evident suggesting a distance between the



two string of about 1mm which is five time larger than that at  $z=4.23\text{mm}$ . Alternatively, the next peak can be extrapolated from the plot to be at  $y=1.2\text{mm}$  suggesting a distance of 1.2mm between two adjacent strings. From the previous and the current string distance, it is then possible to estimate the angle between the two filaments, which was found to be  $5.7^\circ$ .

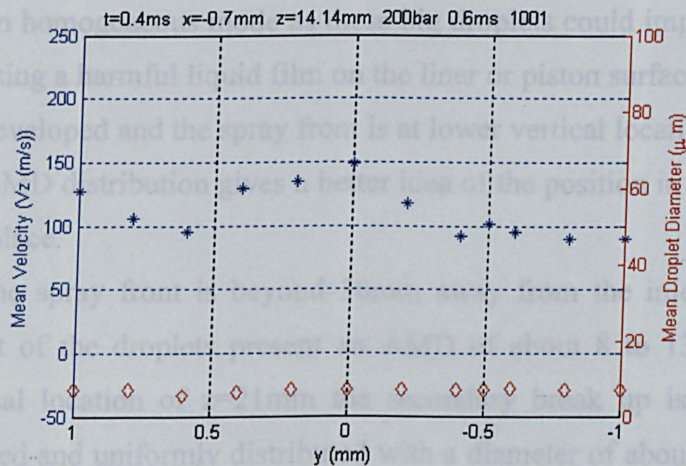


Figure 4-35 (b) Velocity and AMD and distribution along the Y coordinate at  $z=14.14\text{mm}$ .

Finally at  $z = 28.28$  the velocity profile is almost completely flat and it is no longer possible to distinguish more than one string peaks. The diameter distribution it is also uniform with AMD from  $7\mu\text{m}$  to  $10\mu\text{m}$ .

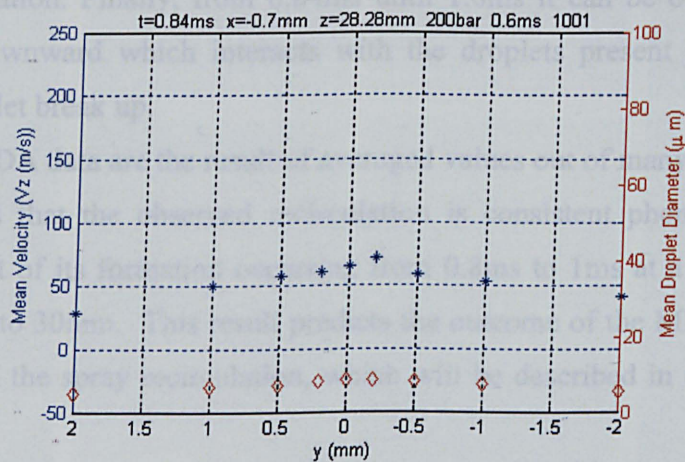


Figure 4-35 (c) Velocity and AMD distribution along the Y coordinate at  $z=28.28\text{mm}$ .

---

#### 4.3.4.4. Analysis of droplet diameter distribution

A wider view of the diameter distribution (temporal and spatial) is displayed from the PDA results as a series of image sequences in Figure 4-36 where velocity and AMD are shown up to 70mm away from the injector exit. Following the image sequence from 0.24ms, the presence of large droplets can be seen in the spray rim propagating downward up to the last z location of the measured data. This could represent a problem even in homogeneous mode as these big droplets could impinge the cylinder boundaries causing a harmful liquid film on the liner or piston surface. After the spray is completely developed and the spray front is at lower vertical location a clear picture of the droplet AMD distribution gives a better idea of the position in which secondary break up takes place.

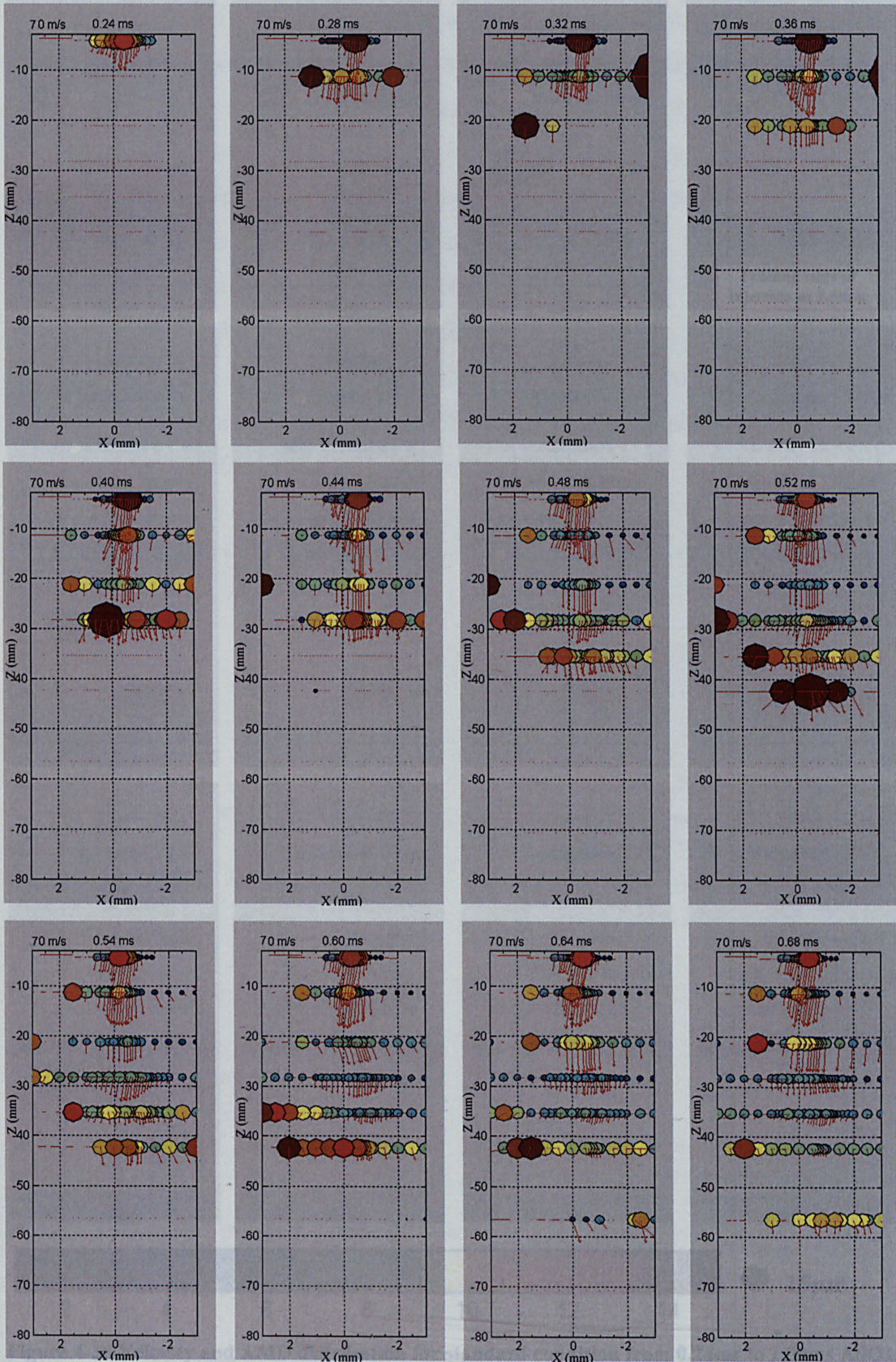
From 0.52ms the spray front is beyond 30mm away from the injector exit and at  $z=10.4\text{mm}$  most of the droplets present an AMD of about 8 to  $13\mu\text{m}$ . Just at the following vertical location of  $z=21\text{mm}$  the secondary break up is completed, the AMD is decreased and uniformly distributed with a diameter of about 5 to  $7\mu\text{m}$ . This situation occurs during the second string structure and it lasts up to 0.6ms and then the instability phase (third structure) takes place with larger droplets. This is clearly evident from the results that the droplets in front and behind of these fine droplets (second phase structure) are larger and are produced by first phase (spray front) and third phase (spray instability), respectively. The third unstable structure is propagating downstream with higher AMD, perhaps due to droplets coalescence or injection pressure fluctuation. Finally, from 0.84ms until 1.0ms it can be observed a tumble propagating downward which interacts with the droplets present in its centre and producing droplet break up.

The analysed PDA data are the result of averaged values out of many injection events, which indicates that the observed recirculation is consistent phenomenon at least during the onset of its formation occurring from 0.8ms to 1ms at a vertical location between 20mm to 30mm. This result predicts the outcome of the MIE scattering and PIV findings on the spray recirculation, which will be described in detail later on in this chapter.

Far from the injector exit, beyond 70mm, the mean droplets diameter remains quite large with an AMD of about  $15\mu\text{m}$ . These big droplets could be the residual of the spray front which have lost their momentum and are unable to break up further.



However, the strong presence of recirculation can also suggests the possibility of coalescence occurrence due to droplet collision.





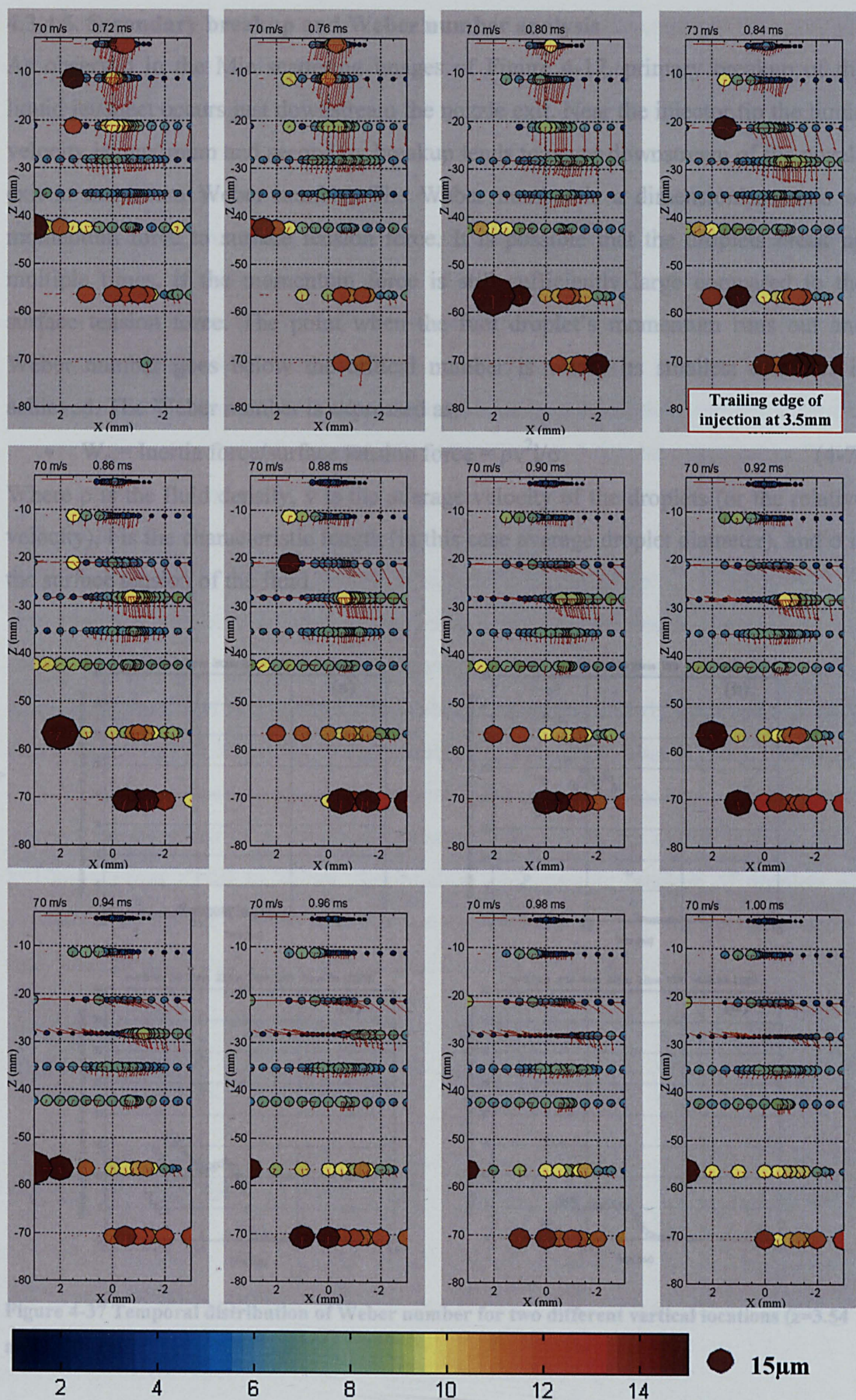


Figure 4-36 Velocity and AMD distribution for standard condition from 0.24ms to 1.00ms ASOI.



4.3.4.5. Secondary breakup and Weber number analysis

As observed in the Mie scattering images of Figure 4-17, primary breakup of the liquid jet/sheet occurs just downstream the nozzle exit. Near the injector tip the liquid velocity is maximum and secondary breakup tends to occur downstream of the nozzle exit at maximum Weber number. The Weber number is a dimensionless ratio of momentum force to surface tension force. It is possible that the droplets break up multiple times, if the momentum force is still sufficiently large compared to the surface tension force. The point when the fuel droplet’s momentum runs out and Weber number goes below the critical number is where its smallest diameter is achieved. The Weber number is expressed as:

•  $We = \text{Inertia force} / \text{surface tension force} = \rho v^2 l / \sigma$  (4-7)

Where  $\rho$  is the fluid density,  $v$  is the average velocity of the droplets (or the relative velocity),  $l$  is the characteristic length (in this case average droplet diameter), and  $\sigma$  is the surface tension of the fluid.

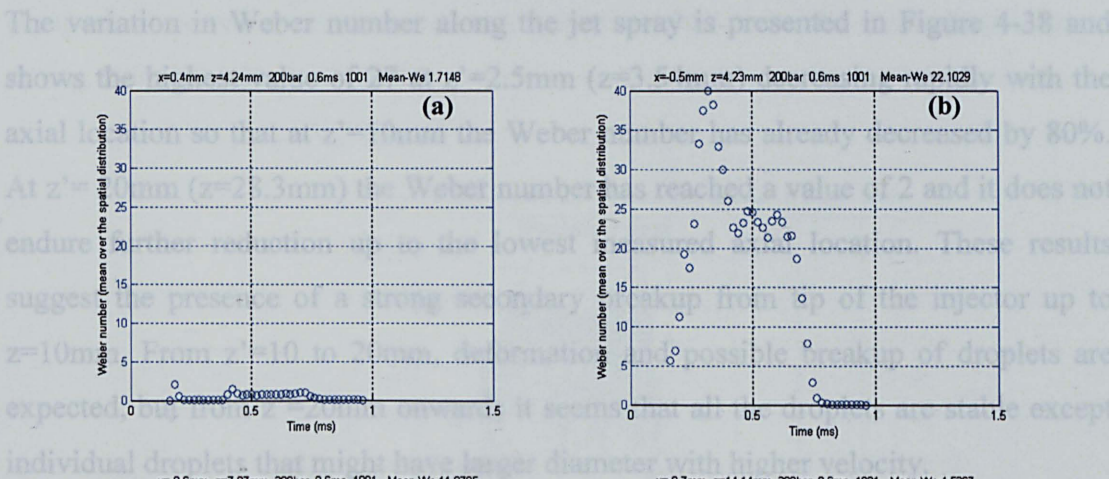


Figure 4-37 Temporal distribution of Weber number for two different vertical locations ( $z=3.54$  and  $z=14.14$ ).

Figure 4-37 presents the temporal distribution of Weber at different x-locations

(Figures (a) and (b)) and z-locations (Figures (b) to (d)) at the centre of the spray jet. The top two graphs of Figure 4-37 exhibits the Weber number at the outer spray surface (Figures (a)) and at the centre of the spray thickness (Figures (b)) near the injector at  $z=4.23\text{mm}$ . The Weber number distribution at the centre of the spray thickness follows the trend of mean velocity variation (Figure 4-29) with a maximum value of 40 at 0.3ms ASOI. Just at the outer spray surface ( $x=0.4\text{mm}$ ) the Weber number,  $We$ , is very low along the whole time range and drops to values lower than 1 which suggests stable droplets with no possibility for further break up. However, the high values of the Weber number in the core region suggest that the droplets are breaking up and dispersing towards the string boundary. In all three vertical locations at core region (Figures (b), (c) and (d)), a similar trend can be observed in Weber number but with magnitude progressively reducing moving away from the injector exit so that the maximum value decreases from  $We=40$  at  $z=3.54\text{mm}$  to  $We=7$  at  $z=14.14\text{mm}$  which is still high enough to initiate further breakup.

The variation in Weber number along the jet spray is presented in Figure 4-38 and shows the highest value of 27 at  $z'=2.5\text{mm}$  ( $z=3.54\text{mm}$ ) decreasing rapidly with the axial location so that at  $z'=10\text{mm}$  the Weber number has already decreased by 80%. At  $z'=20\text{mm}$  ( $z=28.3\text{mm}$ ) the Weber number has reached a value of 2 and it does not endure further reduction up to the lowest measured axial location. These results suggest the presence of a strong secondary breakup from tip of the injector up to  $z=10\text{mm}$ . From  $z'=10$  to  $20\text{mm}$ , deformation and possible breakup of droplets are expected, but from  $z'=20\text{mm}$  onwards it seems that all the droplets are stable except individual droplets that might have larger diameter with higher velocity.

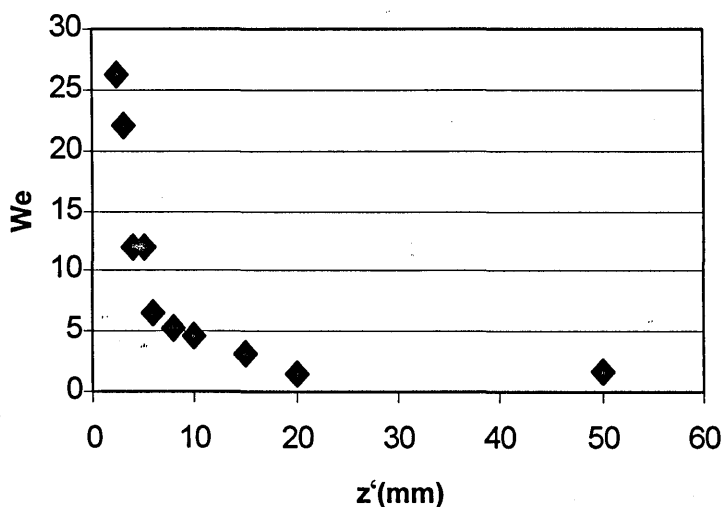


Figure 4-38 Weber Number distribution along the axial location

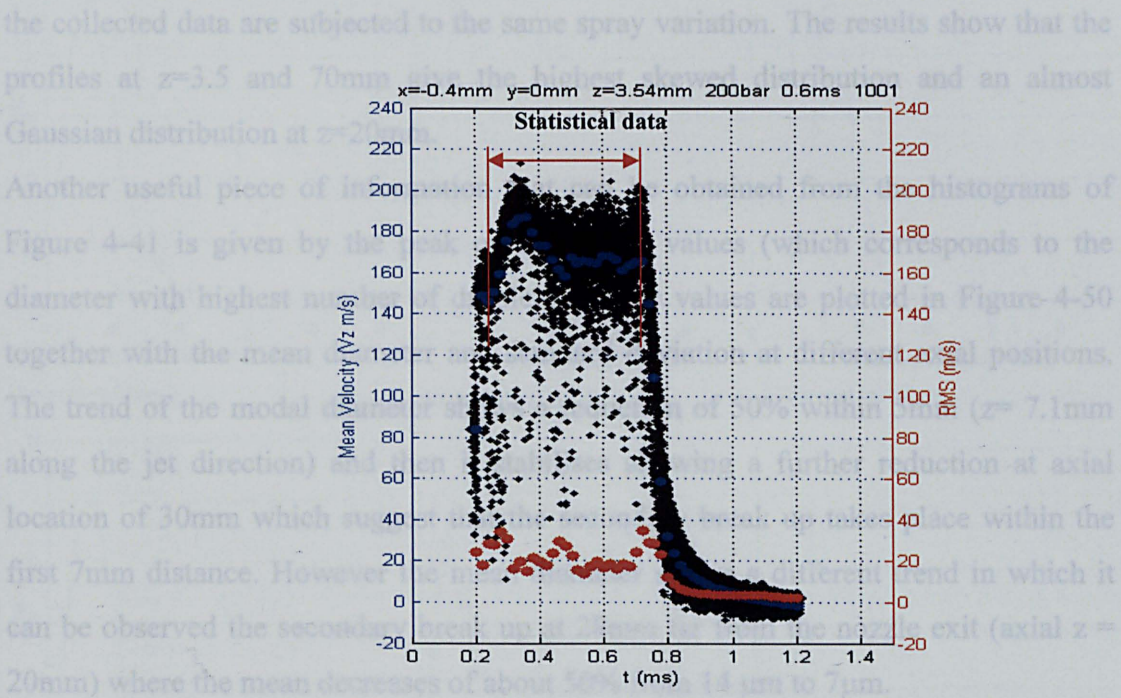


Therefore, the following We distribution can be summarised:

The Weber number at the outer spray surface is much lower than that at the spray centre and it decreases with the axial location away from injector. Since the droplets are more likely to break up for Weber number greater than 10, then it is expected that the droplets in these regions of the spray will not undergo any further break up; the Weber numbers at the outer spray surface for  $z=14.14\text{mm}$  and  $z=35.36\text{mm}$  is lower than 5 which confirms no further break up occurrence.

#### 4.3.4.6. Average Mean Diameter distribution along the axial direction.

In order to have a statistical view of the droplet diameter the normalized probability density function (pdf) distribution of the diameter was analysed in the core region of the spray, when the needle is fully lifted and cutting the data at the leading and trailing edges of the spray as shown in Figure 4-48. In this way, a better representation and understanding of the phenomenon is therefore achieved when the comparison is based on the number of droplets that cross the measuring location during the main injection event.



**Figure 4-39** Time range considered in the droplet size statistical analysis which excludes the leading and trailing edge of the spray.

The comparison of the pdf histograms in Figure 4-40 shows differences in shape at different  $z$  locations. For instance, near the nozzle exit a jagged shape histogram can

---

be observed which gradually gets smoother and smoother moving away from the injector tip until an axial position of 40mm where the histograms again start showing an irregular profile. This behaviour can be due to the presence of more spray patterns in the same collected data group. In the near nozzle area, where the spray thickness is very thin, multiple peak profiles could be produced by the spray-to-spray variation, which would lead different flow streams through the control volume. Another reason could also be explained by the massive secondary break up which occurs within 15mm from injector. As the spray develops downstream, the streams expand and the droplet size pattern is less affected by spray angle variation. Far from the injector, other phenomena like droplets coalescence and spray recirculation take place which makes the spray transient and therefore the collected data from CV is exposed to different spray stream types and these are evident in the last two histograms where the superimposition of more size distribution patterns can be observed.

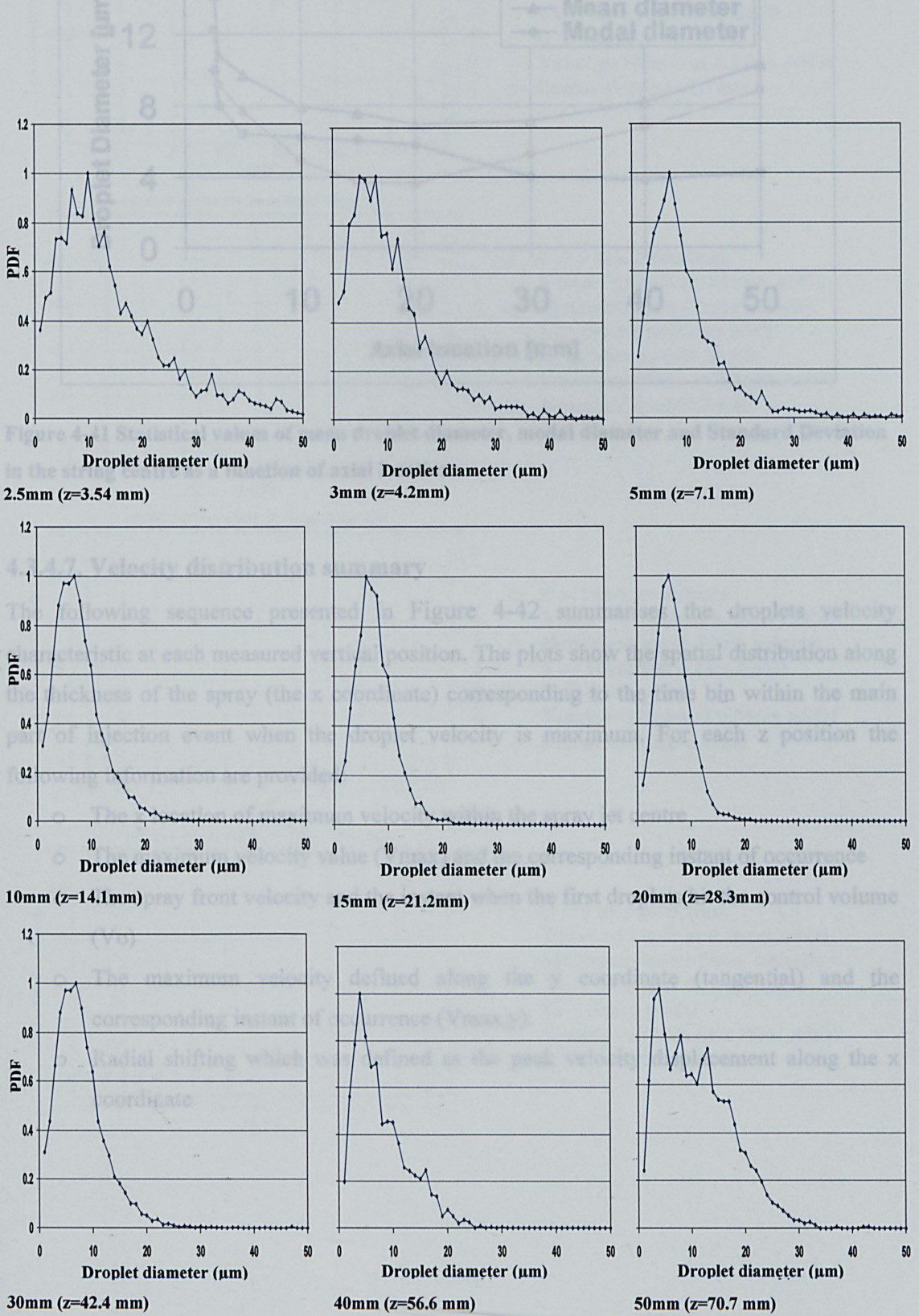
Another effect that can be clearly seen from the results of Figure 4-49 is the skewness of the histogram profiles towards the higher droplets size. The degree of skewness varies at different axial distances and follows the same pattern as mention above as the collected data are subjected to the same spray variation. The results show that the profiles at  $z=3.5$  and 70mm give the highest skewed distribution and an almost Gaussian distribution at  $z=20$ mm.

Another useful piece of information that can be obtained from the histograms of Figure 4-41 is given by the peak or the modal values (which corresponds to the diameter with highest number of droplets). These values are plotted in Figure 4-50 together with the mean diameter and standard deviation at different axial positions. The trend of the modal diameter shows a reduction of 50% within 5mm ( $z= 7.1$ mm along the jet direction) and then it stabilises showing a further reduction at axial location of 30mm which suggest that the secondary break up takes place within the first 7mm distance. However the mean diameter shows a different trend in which it can be observed the secondary break up at 28mm far from the nozzle exit (axial  $z = 20$ mm) where the mean decreases of about 50% from  $14\ \mu\text{m}$  to  $7\ \mu\text{m}$ .

The divergence between mean and modal diameter can be explained by the trend of the standard deviation, which show that when the modal value is about constant the STD and so the width of the histogram distribution reduces toward the lower diameters. At 56mm away from the injector tip the droplet diameter starts to increase again which means that the effect of the coalescence get more relevant probably due



to the higher effect of the spray recirculation at the far nozzle area. At this stage, the standard deviation also grows and in fact, the saw shape is extended further toward the higher diameters as it can be observed in the last two histograms of Figure 4-41.



**Figure 4-40 Probability density function of droplet diameters at the centre of the string for different  $z$  locations .**



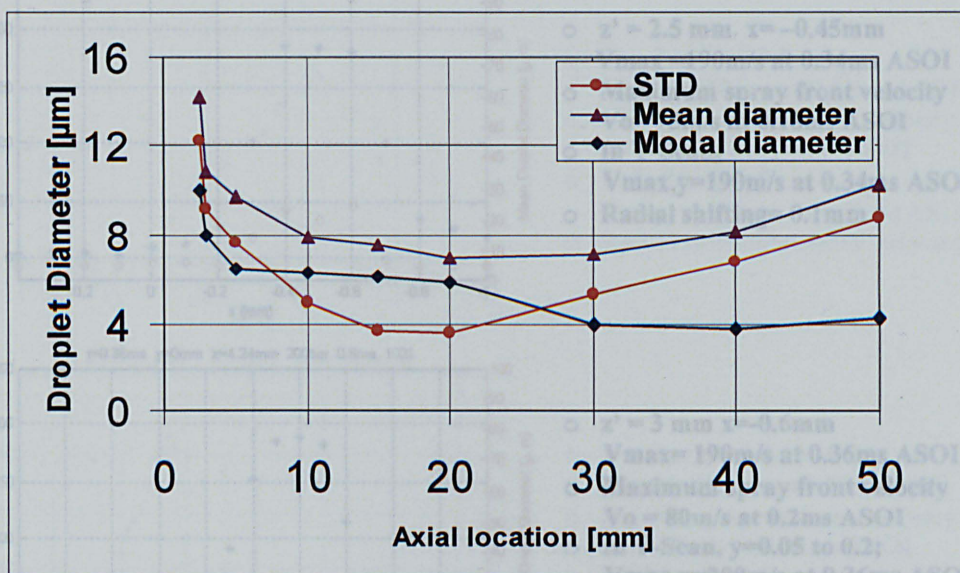


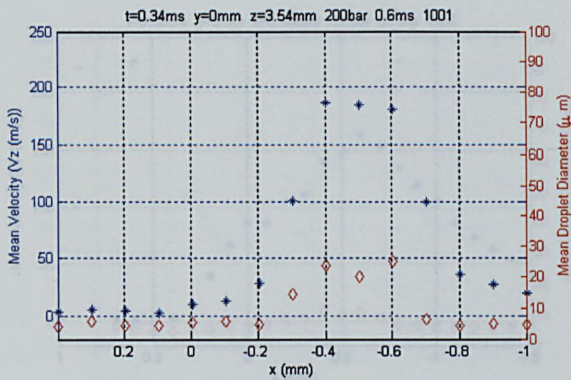
Figure 4-41 Statistical values of mean droplet diameter, modal diameter and Standard Deviation in the string centre as a function of axial locations.

#### 4.3.4.7. Velocity distribution summary

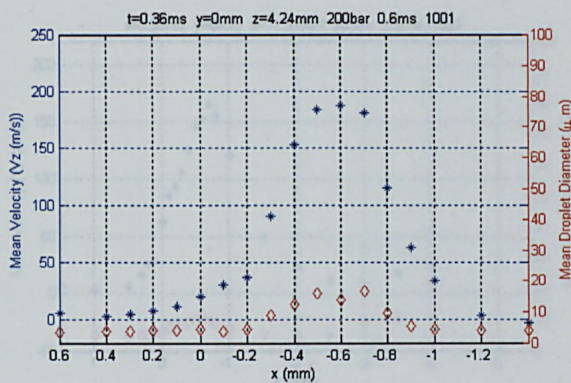
The following sequence presented in Figure 4-42 summarises the droplets velocity characteristic at each measured vertical position. The plots show the spatial distribution along the thickness of the spray (the x coordinate) corresponding to the time bin within the main part of injection event when the droplet velocity is maximum. For each z position the following information are provided:

- The x location of maximum velocity within the spray jet centre
- The maximum velocity value ( $V_{max}$ ) and the corresponding instant of occurrence
- The spray front velocity and the instant when the first droplets hit the control volume ( $V_o$ )
- The maximum velocity defined along the y coordinate (tangential) and the corresponding instant of occurrence ( $V_{max,y}$ ).
- Radial shifting which was defined as the peak velocity displacement along the x coordinate

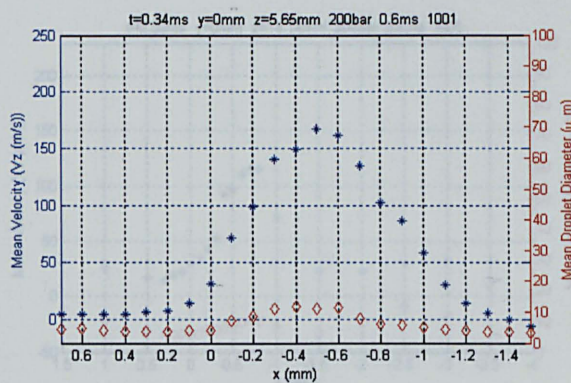




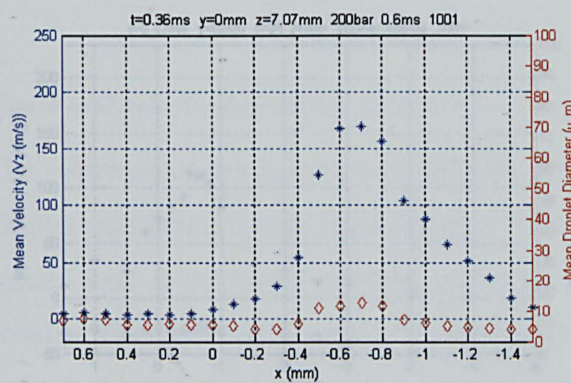
- $z' = 2.5 \text{ mm}$   $x = -0.45 \text{ mm}$   
 $V_{\text{max}} = 190 \text{ m/s}$  at 0.34ms ASOI
- Maximum spray front velocity  
 $V_o = 75 \text{ m/s}$  at 0.18ms ASOI
- In Y-Scan,  
 $V_{\text{max},y} = 190 \text{ m/s}$  at 0.34ms ASOI
- Radial shifting = 0.1mm



- $z' = 3 \text{ mm}$   $x = -0.6 \text{ mm}$   
 $V_{\text{max}} = 190 \text{ m/s}$  at 0.36ms ASOI
- Maximum spray front velocity  
 $V_o = 80 \text{ m/s}$  at 0.2ms ASOI
- In Y-Scan,  $y = 0.05$  to  $0.2$ ;  
 $V_{\text{max},y} = 200 \text{ m/s}$  at 0.36ms ASOI
- Radial shifting = 0.3mm

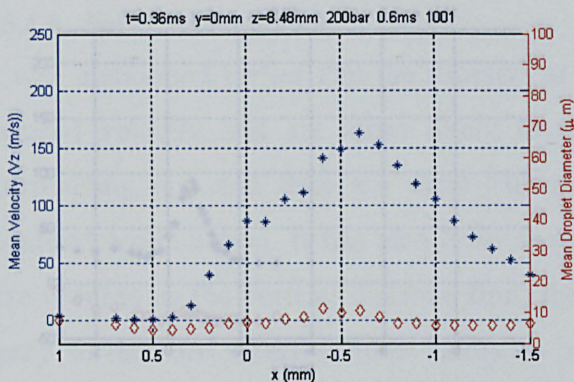


- $z' = 4 \text{ mm}$   $x = -0.5 \text{ mm}$   
 $V_{\text{max}} = 170 \text{ m/s}$  at 0.34ms ASOI
- Maximum spray front velocity  
 $V_o = 100 \text{ m/s}$  at 0.2ms ASOI
- In Y-Scan,  $y = 0.1$   
 $V_{\text{max},y} = 175 \text{ m/s}$  at 0.36ms ASOI
- Radial shifting = 0.4mm

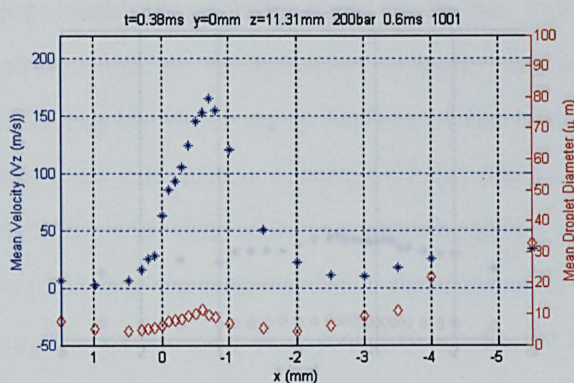


- $z' = 5 \text{ mm}$   $x = -0.7 \text{ mm}$   
 $V_{\text{max}} = 175 \text{ m/s}$  at 0.36ms ASOI
- Maximum spray front velocity  
 $V_o = 100 \text{ m/s}$  at 0.22ms ASOI
- In Y-Scan,  $y = -0.1$   
 $V_{\text{max},y} = 180 \text{ m/s}$  at 0.38ms ASOI
- Radial shifting = 0.4mm

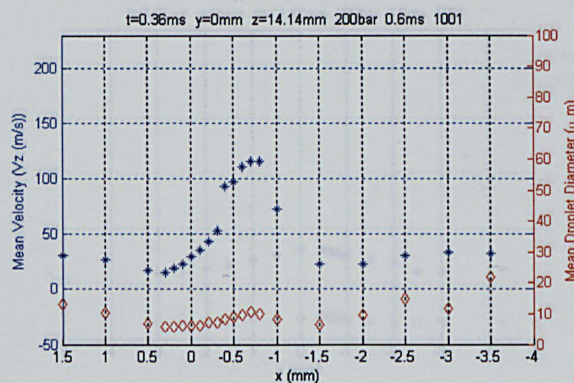




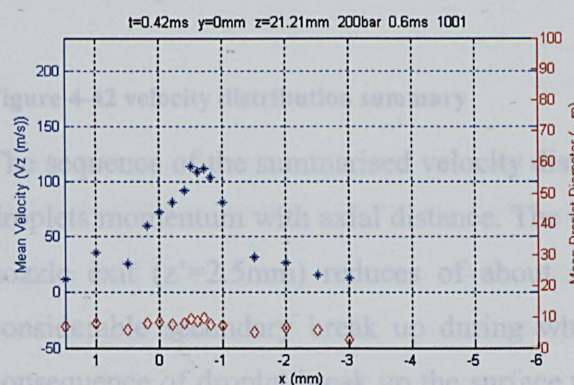
- $z' = 6\text{ mm}$   $x=-0.6\text{mm}$   
 $V_{\text{max}}=170\text{m/s}$  at 0.36ms ASOI
- Maximum spray front velocity  
 $V_o=80\text{m/s}$  at 0.24ms ASOI
- In Y-Scan,  $y=0$   
 $V_{\text{max},y}=170\text{m/s}$  at 0.36ms ASOI
- Radial shifting=0.4mm outwardly



- $z' = 8\text{ mm}$   $x=-0.8\text{mm}$   
 $V_{\text{max}}=165\text{m/s}$  at 0.38ms ASOI
- Maximum spray front velocity  
 $V_o=90\text{m/s}$  at 0.26ms ASOI
- In Y-Scan,  $y=0$   
 $V_{\text{max},y}=165\text{m/s}$  at 0.38ms ASOI
- Radial shifting=0.5mm outwardly

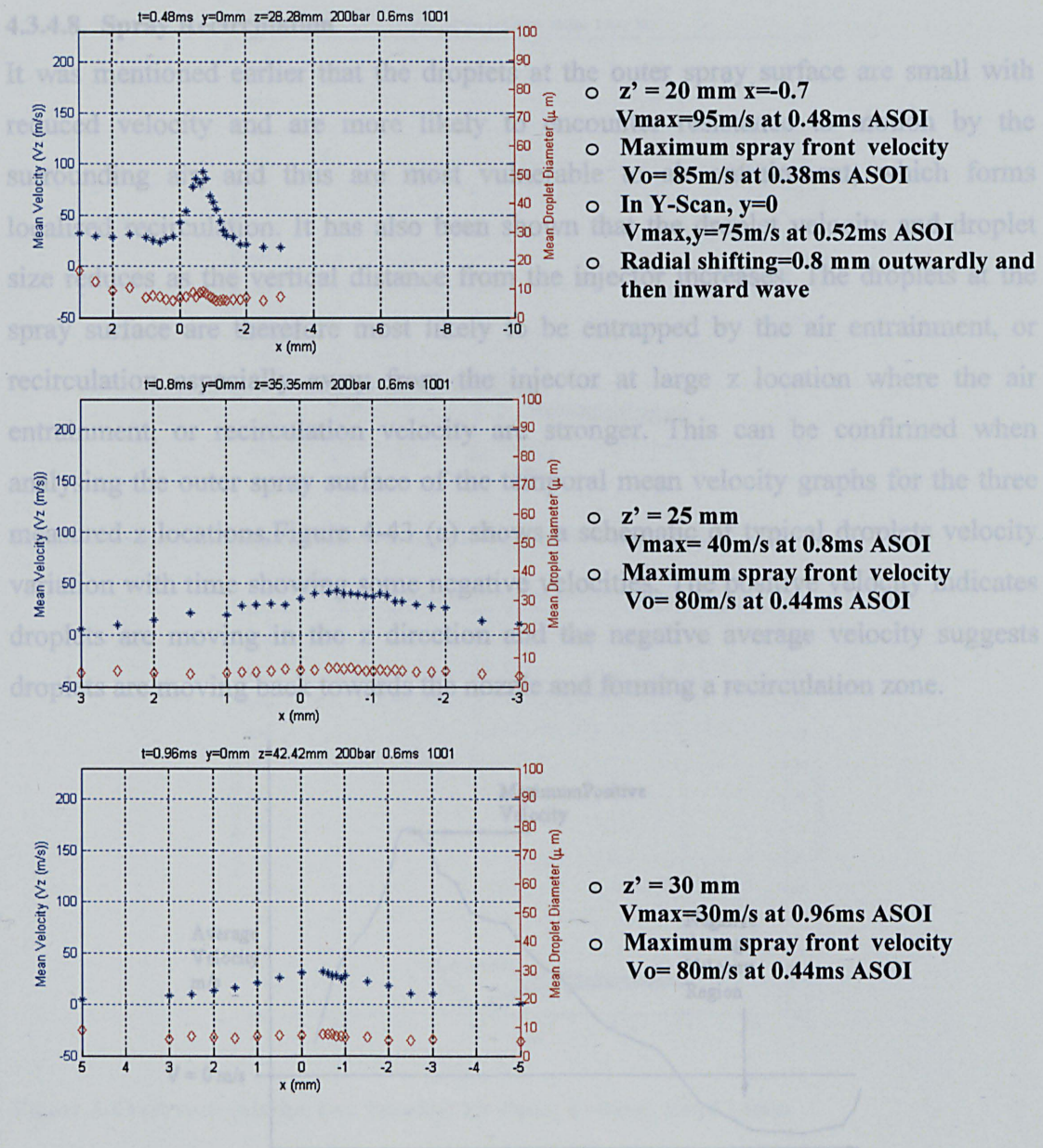


- $z' = 10\text{ mm}$   $x=-0.7\text{mm}$   
 $V_{\text{max}}=120\text{m/s}$  at 0.36ms ASOI
- Maximum spray front velocity  
 $V_o=75\text{m/s}$  at 0.28ms ASOI
- In Y-Scan,  $y=0$   
 $V_{\text{max},y}=150\text{m/s}$  at 0.4ms ASOI
- Radial shifting=0.5mm inwardly



- $z' = 15\text{ mm}$   $x=-0.7$   
 $V_{\text{max}}=115\text{m/s}$  at 0.42ms ASOI
- Maximum spray front velocity  
 $V_o=95\text{m/s}$  at 0.58ms ASOI
- In Y-Scan,  $y=0.4$   
 $V_{\text{max},y}=130\text{m/s}$  at 0.52ms ASOI
- Radial shifting=0.7 mm outwardly and then inward wave





**Figure 4-42 velocity distribution summary**

The sequence of the summarised velocity distribution reveals the considerable loss of droplets momentum with axial distance. The maximum velocity of 200m/s around the nozzle exit ( $z'=2.5$ mm) reduces of about 30m/s at  $z'=30$ mm mainly due to the considerable secondary break up during which the droplets split their mass. As a consequence of droplet break up the surface to volume ratio increases and drag force imposed by the surrounding gas increases with respect of the droplet momentum. The corresponding values of the droplets diameter over the same axial distance are 27 $\mu m$  and 8 $\mu m$ , which corresponds to a reduction of about 19  $\mu m$ .



4.3.4.8. Spray Recirculation

It was mentioned earlier that the droplets at the outer spray surface are small with reduced velocity and are more likely to encounter resistance to motion by the surrounding air, and thus are most vulnerable to air entrainment, which forms localised recirculation. It has also been shown that the droplet velocity and droplet size reduces as the vertical distance from the injector increases. The droplets at the spray surface are therefore most likely to be entrapped by the air entrainment, or recirculation especially away from the injector at large  $z$  location where the air entrainment, or recirculation velocity are stronger. This can be confirmed when analysing the outer spray surface of the temporal mean velocity graphs for the three measured  $z$  locations. Figure 4-43 (a) shows a schematic of typical droplets velocity variation with time showing some negative velocities. The positive velocity indicates droplets are moving in the  $z$  direction and the negative average velocity suggests droplets are moving back towards the nozzle and forming a recirculation zone.

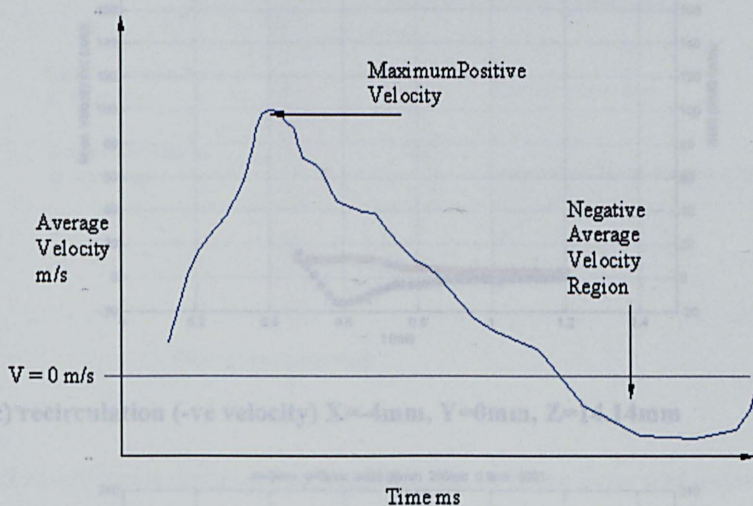


Figure 4-43 (a) Schematic of a typical temporal velocity variation showing negative velocities indicative of the presence of a recirculation zone.

Figure 4-43 (b), (c) and (d) show similar characteristics to the above schematic plot, and suggest that recirculation zones are present at the outer side of the spray. Although the data capture duration is not sufficiently long enough to record the extent of the recirculation in Figure 4-43 (d), it is assumed from the trend that the recirculation zone at  $z = 35.36\text{mm}$  will be the most severe. This supports the argument that the recirculation phenomenon becomes more enhanced as vertical distance from the injector exit increases. This is supported by results when comparing the magnitude of the negative velocity in Figures (b) and (c).



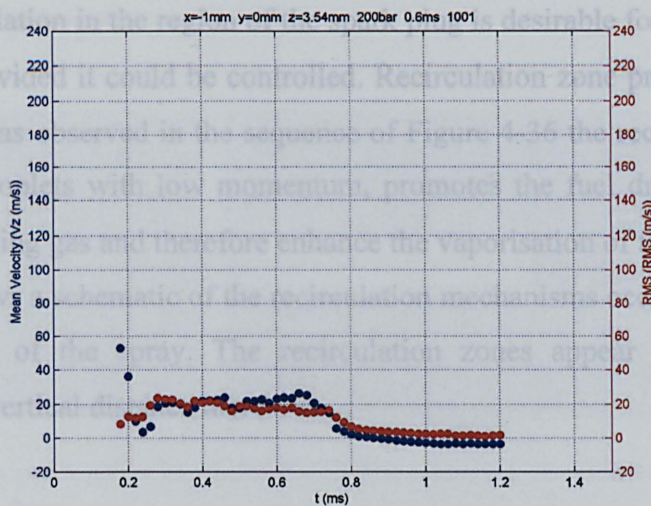


Figure 4-43 (b) recirculation (-ve velocity) X=-1mm, Y=0mm, Z=3.54mm

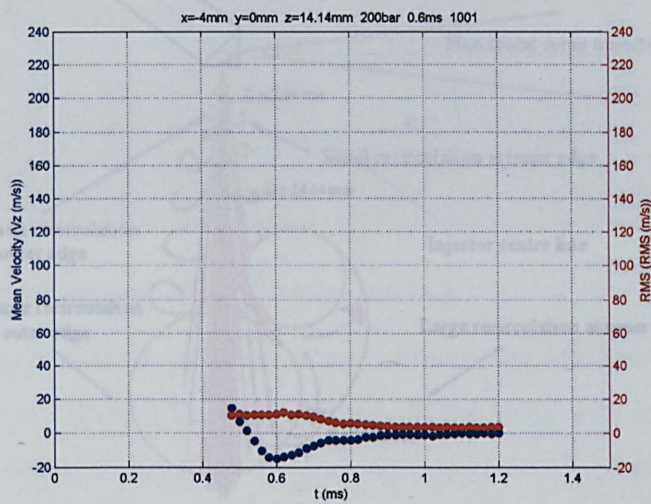


Figure 4-43 (c) recirculation (-ve velocity) X=-4mm, Y=0mm, Z=14.14mm

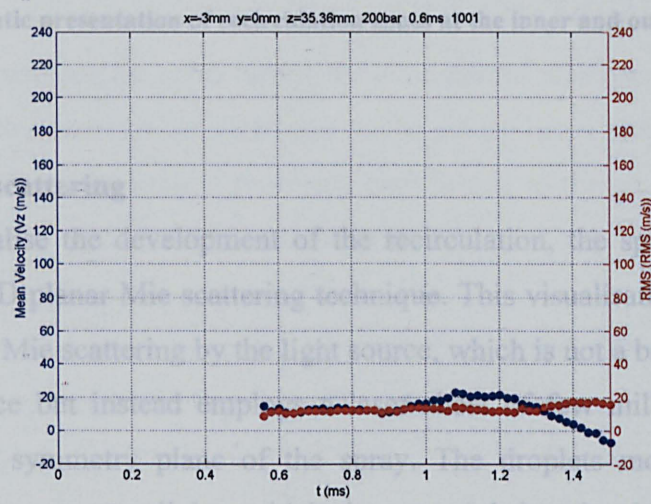


Figure 4-43 (d) recirculation (-ve velocity) X=-3mm, Y=0mm, Z=35.36mm



Localised recirculation in the region of the spark plug is desirable for the close spaced SIDI engines provided it could be controlled. Recirculation zone produces high rates of mixing as it was observed in the sequence of Figure 4-36 the recirculation entraps the broken up droplets with low momentum, promotes the fuel droplets interaction with the surrounding gas and therefore enhance the vaporisation of the fuel. Figure 4-44 shows a schematic of the recirculation mechanisms occurring at the inner and outer edges of the spray. The recirculation zones appear to become more enhanced as the vertical distance increases.

Figure 4-43 Camera and injector layout for the 2D Mie scattering visualisation.

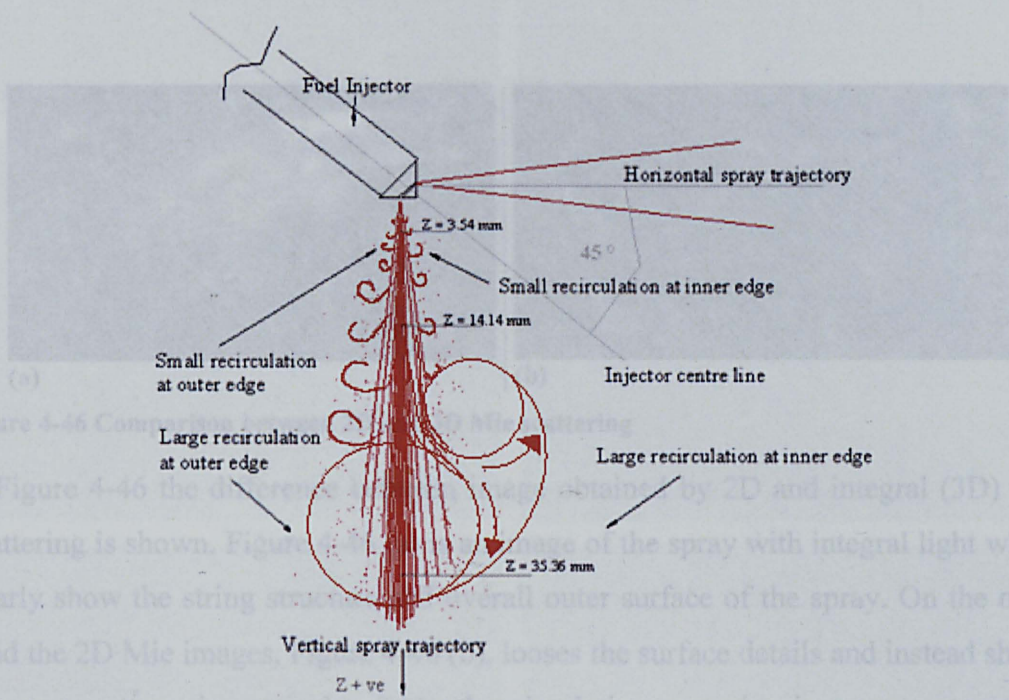


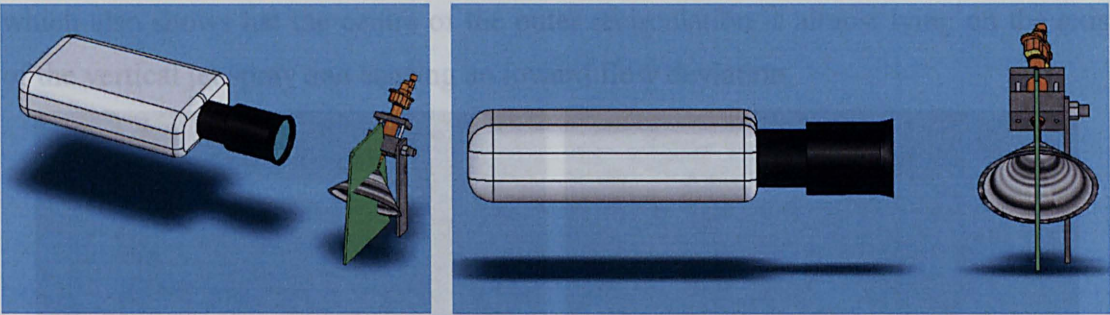
Figure 4-44 Schematic presentation of recirculation zones at the inner and outer edges of the spray

#### 4.3.4.9. 2D Mie scattering

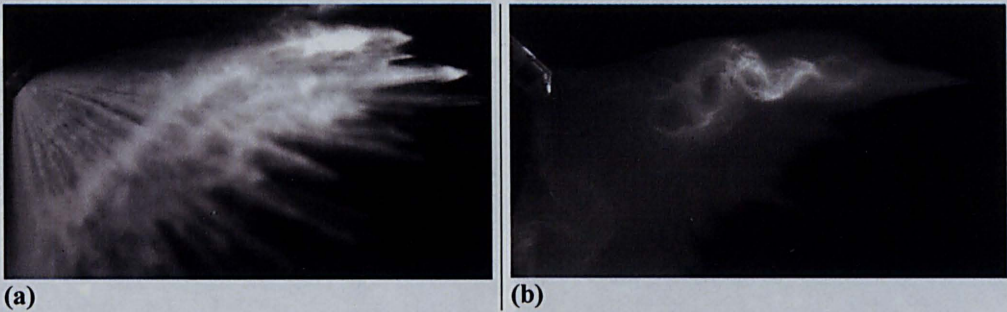
In order to visualise the development of the recirculation, the spray evolution was recorded using 2D planar Mie scattering technique. This visualisation method differs from the integral Mie scattering by the light source, which is not a based on traditional white light source but instead employs a laser sheet of few millimetres thickness projected to the symmetry plane of the spray. The droplets moving in this thin intersection region scatter light, which is captured by the high-speed camera producing the image of the spray cone cross section. The schematic shown in Figure 4-45 depicts the camera arrangement with respect of the spray and laser sheet in



axonomic and side view. while the spray jet before this point near the injector appears to be undisturbed. This recirculation can be seen more clearly at 1.5ms ASOI.



**Figure 4-45** Camera and injector layout for the 2D Mie scattering visualisation.



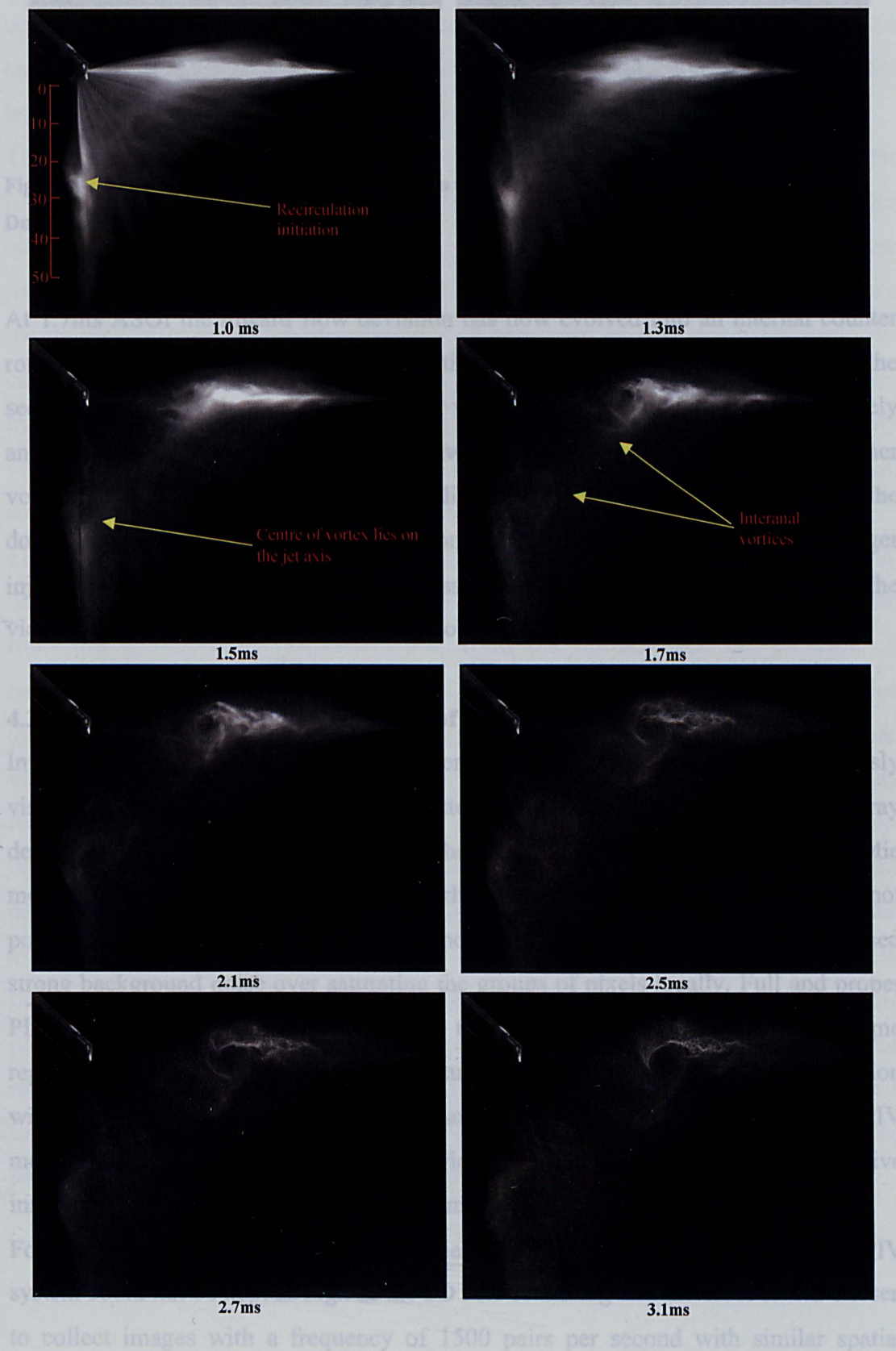
**Figure 4-46** Comparison between 2D and 3D Mie scattering

In Figure 4-46 the difference between image obtained by 2D and integral (3D) Mie Scattering is shown. Figure 4-46 (a) is an image of the spray with integral light which clearly show the string structure and overall outer surface of the spray. On the other hand the 2D Mie images, Figure 4-46 (b), loses the surface details and instead shows the spray pattern, in particular, internal recirculation occurring in a symmetry plane illuminated by the laser sheet. It should be noted that 2D Mie method was not that successful for visualising the spray during the main part of injection, as the laser beam was not able to pass through the spray due to the severe beam attenuation caused by the dense spray. Thus, the images presented here belong to the phase close to end of injection (EOI) and beyond (in the wake of the spray) where the spray density is much lower.

A sequence of 2D Mie scattering captured with a high-speed video recorder at frame rate of 7200fps is shown in the Figure 4-47. The spray is injected for 1ms in ambient environment with an injection pressure of 200bar and needle lift set to a bit position of 1001. For shortness, only the most relevant shots from 1.0ms to 5ms ASOI will be shown in the sequence which covers the EOI and the wake of the spray. The image at 1.0ms shows the first clear sign of recirculation formation, which occurs at about



20mm from the injector tip while the spray jet before this point near the injector appears to be undisturbed. This recirculation can be seen more clearly at 1.5ms ASOI, which also shows that the centre of the outer recirculation is almost lying on the axis of the vertical jet spray and causing an inward flow deviation.







**Figure 4-47 2D Mie scattering: High-speed video of spray recirculation  $P_i=200\text{bar}$ , 1ms Inj. Duration, Bit pos.1001**

At 1.7ms ASOI the inward flow deviation has now evolved into an internal counter rotating vortex of smaller diameter than the external one. Following the rest of the sequence, it can be observed that the outer vortex propagates downward progressively and increases its diameter. A similar downward progression can be seen with the inner vortex but, at the same time, its centre is displaced toward the injector axis due to the dominating action of the outer recirculation. Similar effects were observed for longer injection duration and higher injection pressure but the aforementioned outcome at the vicinity of the injector axis was more pronounced.

#### **4.3.4.10. Particle Imaging Velocimetry of the spray recirculation area**

In order to have a better view and understanding of the velocity field previously visualised (Figure 4-47) by 2D Mie scattering method the end phase of the spray development was analysed with PIV technique. As mentioned before for 2-D Mie method, the application of PIV for the earlier phase of the spray (main part) was not possible as the spray was very dense and apart from beam attenuation, it caused strong background noise over saturating the groups of pixels locally. Full and proper PIV analysis is beyond the scope of this thesis and therefore the reported outcome represent only the initial phase of the result processing whereas the full description will be completed in future PIV publications. Thus, the aim of the present PIV measurements is to provide an overview of the quantitative and qualitative instantaneous velocity field and flow stream patterns.

For the sake of image resolution, the frequency of pair of images acquisition with PIV system could not be kept as high as the 2D Mie scattering and therefore it was chosen to collect images with a frequency of 1500 pairs per second with similar spatial

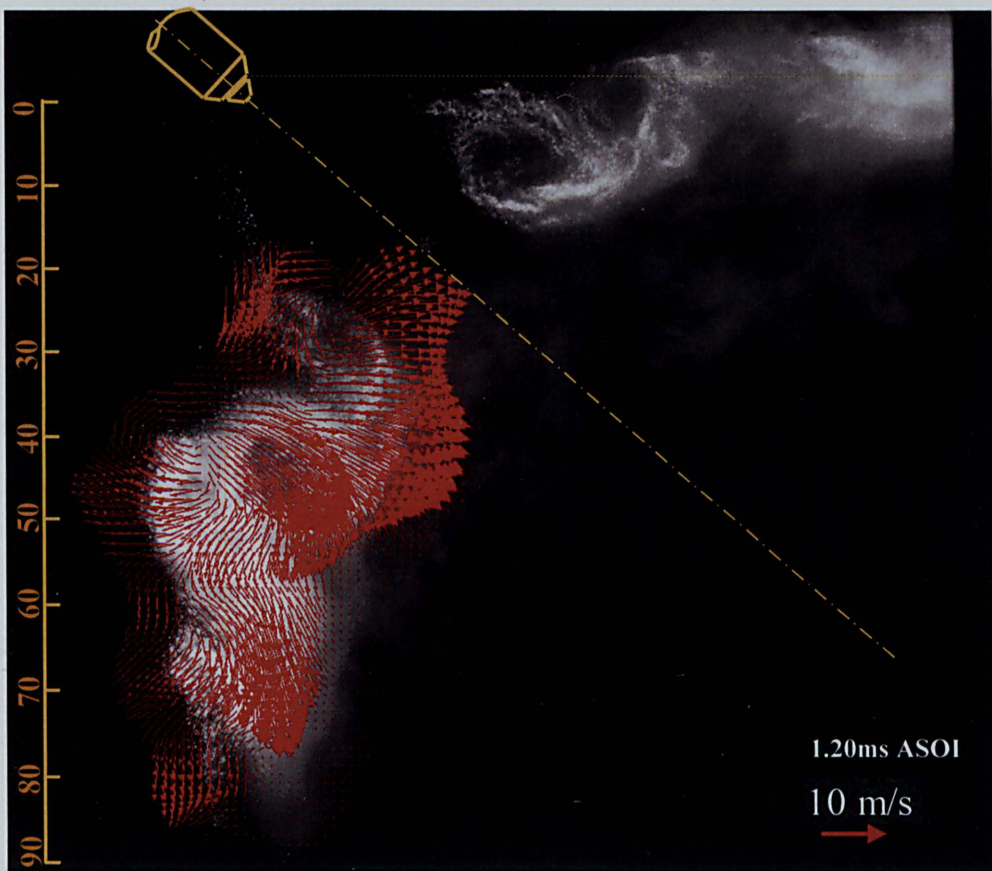
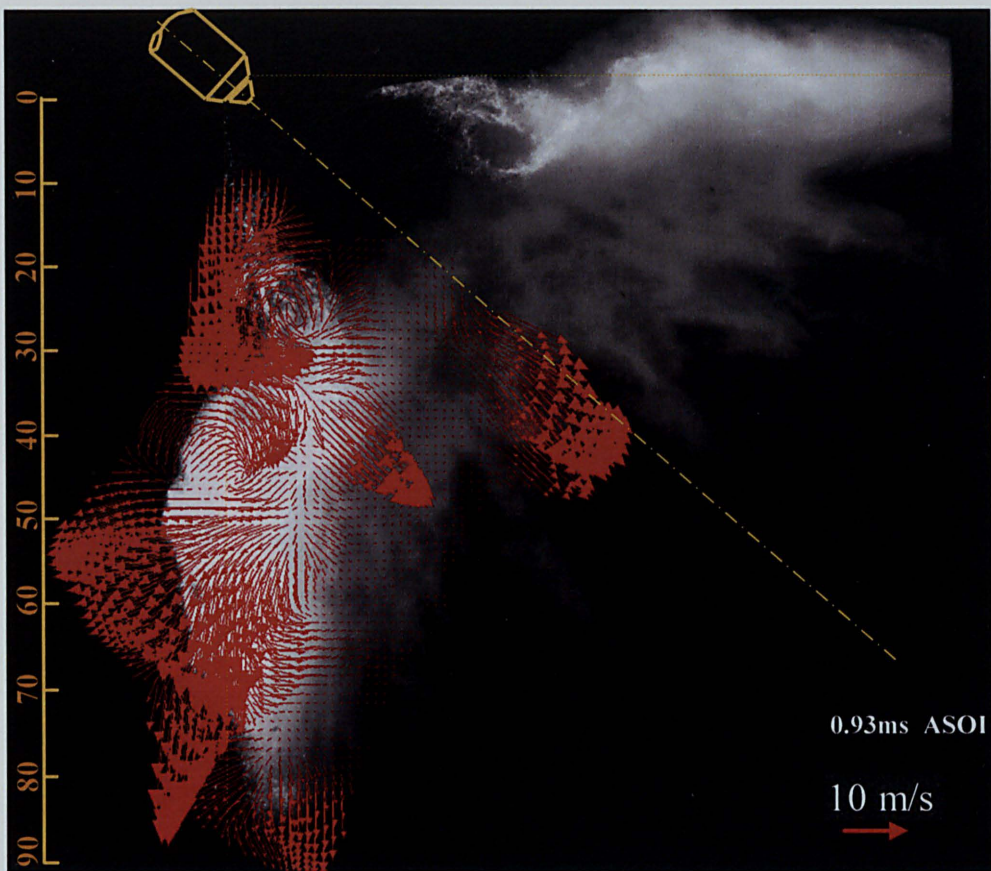
---

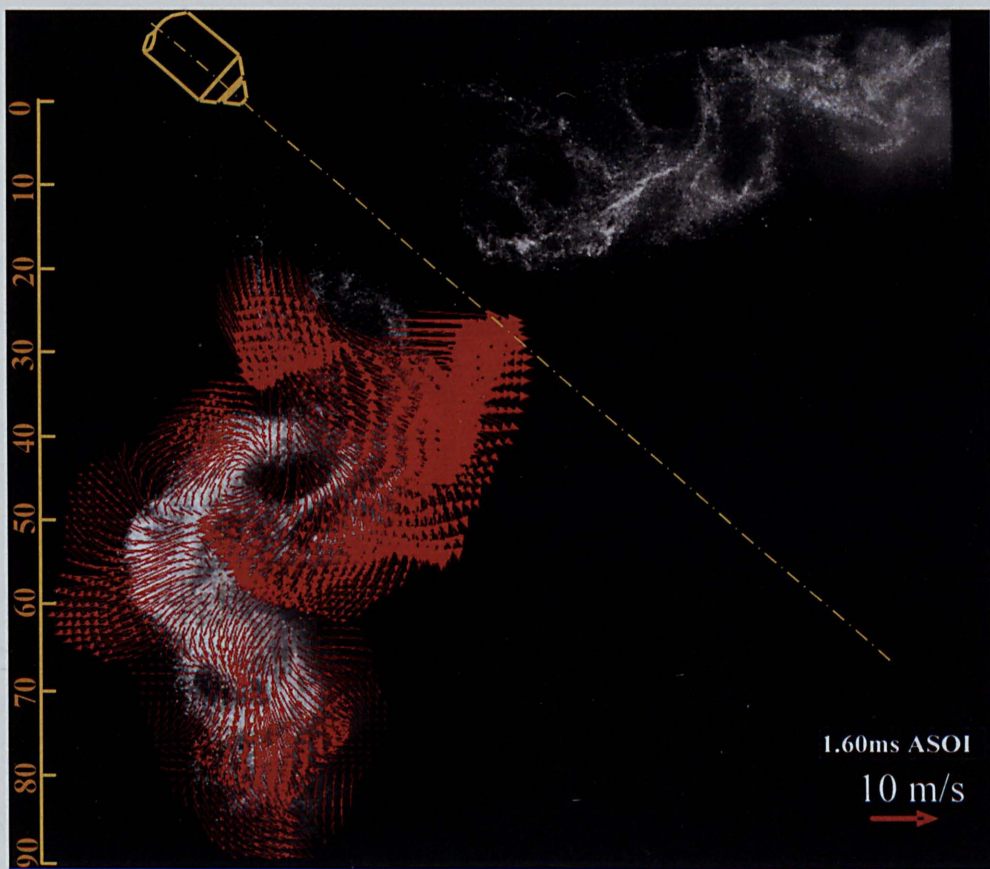
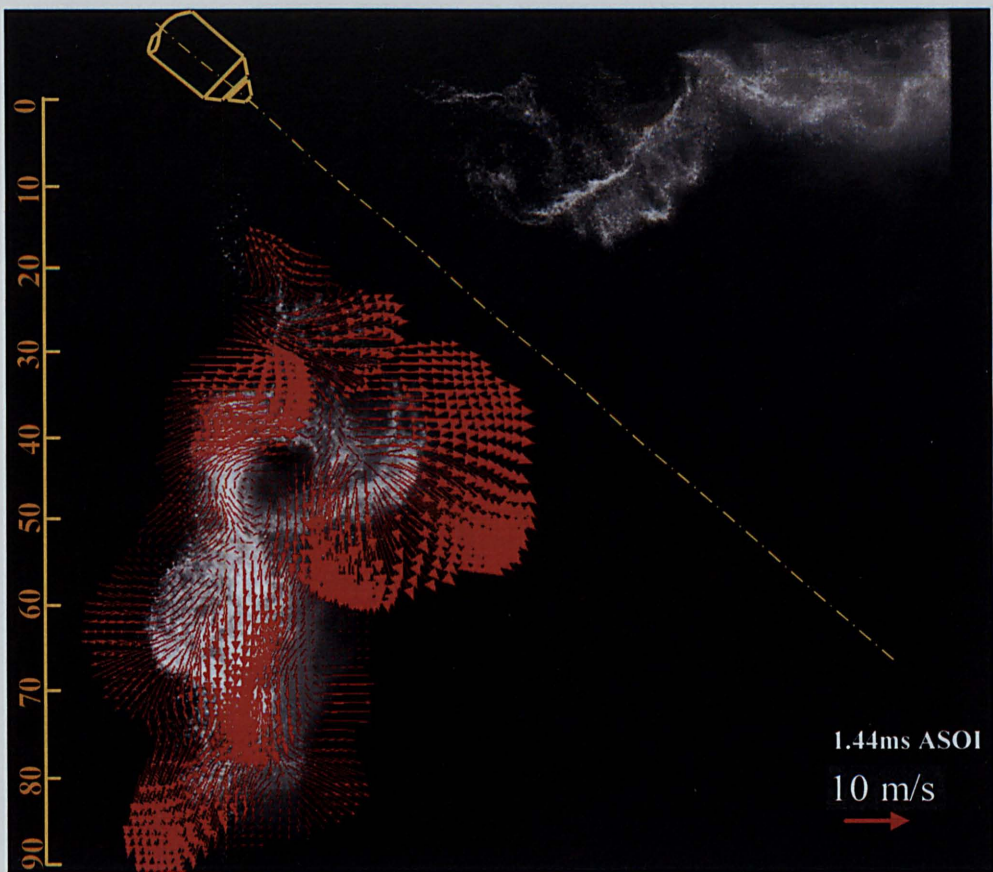
resolution as that of 2D Mie. A sample of such images is presented in Figure 4-48 and it shows the development of the spray wake velocity, which are superimposed on the processed images. Since the laser sheet was projected through the spray from left to right in a vertical plane (in reference to Figure 4-48) then some portion of the spray cone was less bright due to the insufficient scattered light for the PIV measurement and therefore those areas were not processed; only the lower half of the spray on the left hand side had sufficient data for PIV processing as presented in Figure 4-48.

The image sequence shown in Figure 4-48 confirms the existence of two counter rotating vortices not symmetrical with respect to the jet axis and composed of a larger outer wake (in the figure rotating clock-wise) and a smaller inner wake (in the figure rotating anti-clock-wise). The sequence of velocity fields reveals that the outer wake moves downward along the spray trajectory whereas the smaller internal wake forms closer to the injector tip than the outer wake and it is pushed toward the injector axis by the action of the outer wake. This inward motion is evident from the velocity vector direction in the images of Figure 4-48. It should be mentioned that the overall structure of the external and internal wakes are in the form of ring vortices.

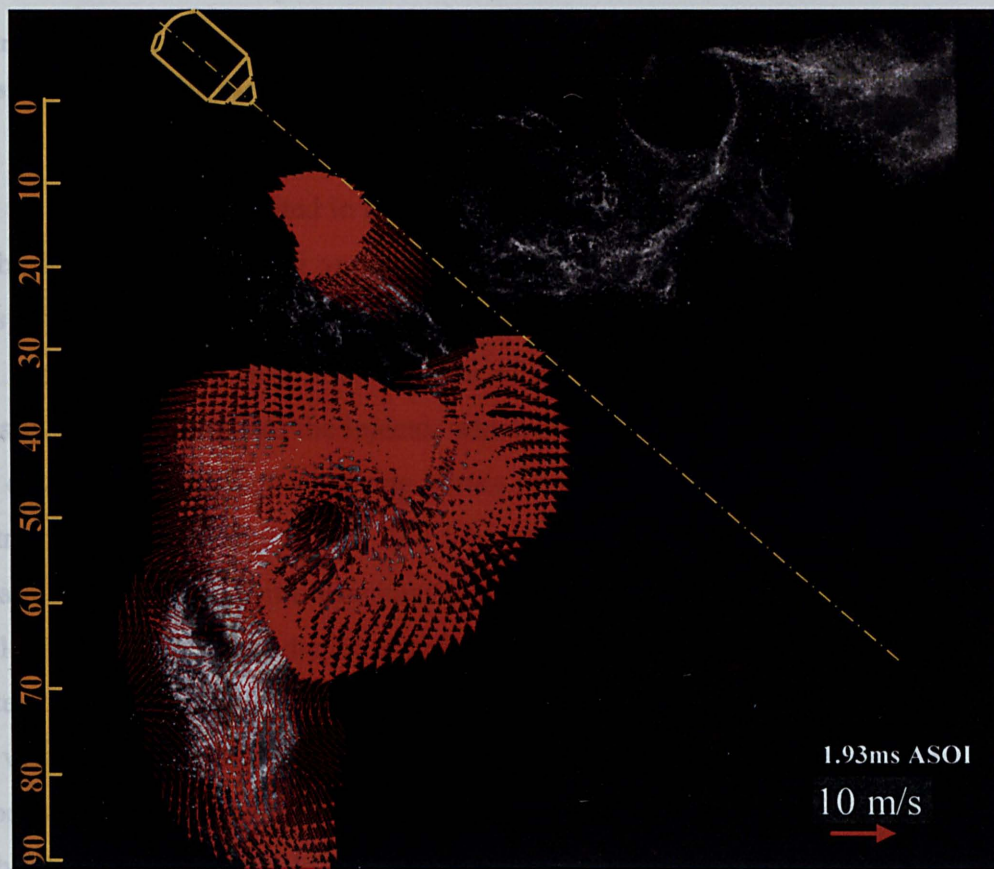
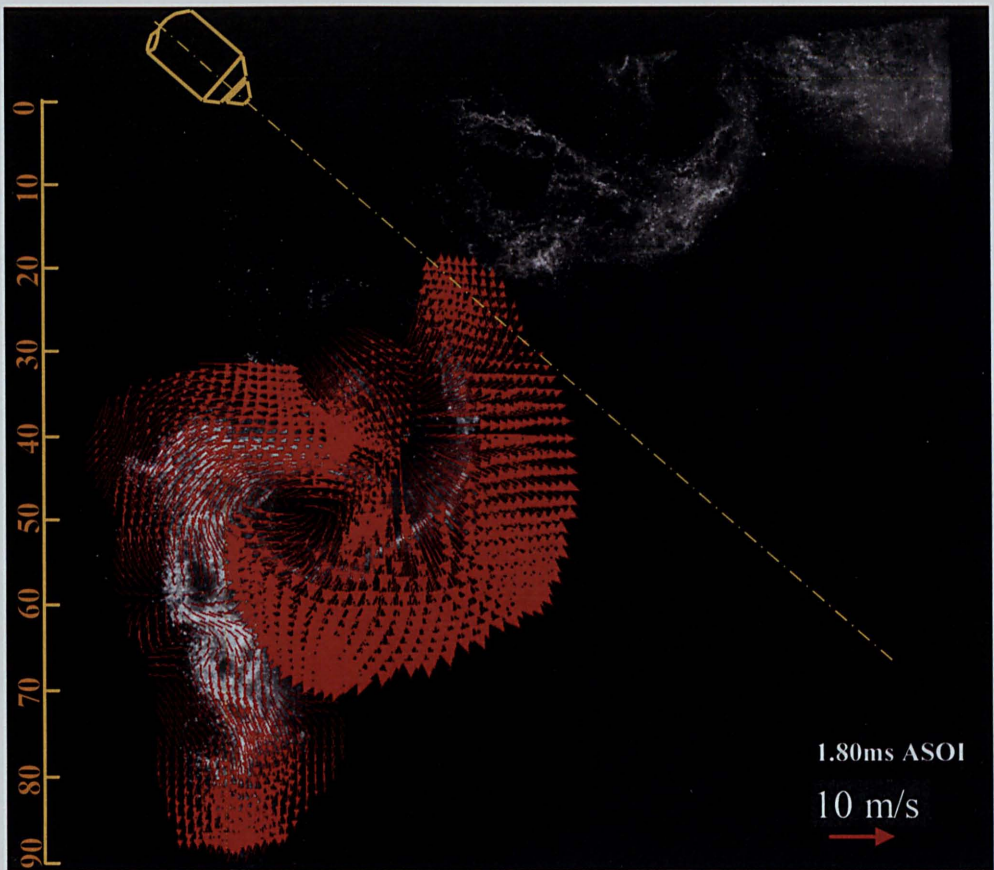
The formation of the external wake is in agreement with the PDA results in the spatial map of Figure 4-36 at 0.9 ms, which reveal the presence of a vortex at about 20 mm from the tip. However, beyond 30mm from the injector exit the presence of recirculation is no longer visible in the PDA averaged velocity field suggesting that the recirculation near the nozzle-exit is highly repeatable thus appearing in the mean velocity measurement over many injections. On the other hand, the recirculation further downstream becomes much more unstable varying its position injection-by-injection, causing the smearing of PDA mean velocity measurement. Therefore, the presence of the late recirculation is revealed only in the instantaneous field presented in the PIV image. The instability of the external vortex could be related to the well-known issue of the spray-to-spray variation (flapping) as well as the unstable “third phase structure” as was previously described. In fact, the turbulent nature of the recirculation could produce radial expansion or contraction according to the vortex diameter variation, and at the same time, it could affect the continuity of the string propagation causing the unstable string structure.

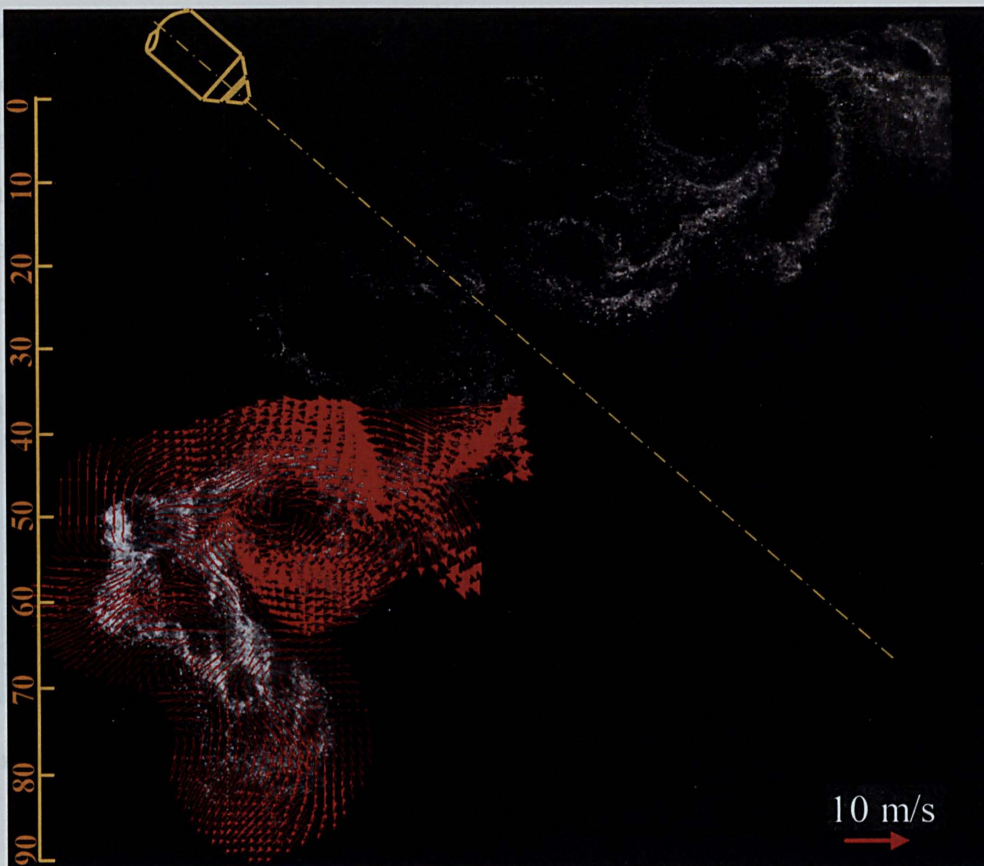












**Figure 4-48 Recirculation velocity field of spray injected in atmospheric condition with injection pressure of 200bar and needle set to 1001 bit position.**

The velocity fields presented in Figure 4-48 shows the effect of the mutual interaction of the two counter rotating vortices, generating a flow directed into the spray cone (this is particularly evident in the image at 0.93ms ASOI). Another interesting feature that can be observed from the sequence of images is the expansion of the vortices radially toward the axis of the injector which can be observed clearly at 1.20ms ASOI and onwards. Because of inner ring vortex rotation an upward flow is built up in the central region of the spray cone. At 1.93ms ASOI, this ascending flow sucks droplets toward the injector tip with velocities of about 15 m/s.

At 1.60ms, ASOI it can be observed that the centre of velocity field of the outer vortex does not coincide with the centre of the background image which suggests that the vortex is not static and its centre translates with a sliding velocity. This sliding velocity is graphically described in Figure 4-49 and it shows the vectorial composition of the absolute velocity field as the summation of relative velocity (static) and rotating velocity (sliding). More specifically the schematic wants to show how the sliding velocity is always normal to the displacement between centre of the velocity field and



centre of the wake eye. Therefore, assuming the background image of the wake as static representation of the rotating field it can be stated that up to 1.60ms ASOI the outer wake moves toward the jet direction with a sliding velocity of about 10m/s. Finally, at 2.27ms ASOI the centre of the velocity field is almost overlapped to the centre of the wake image, which means that the vortex at this stage does not move any further.

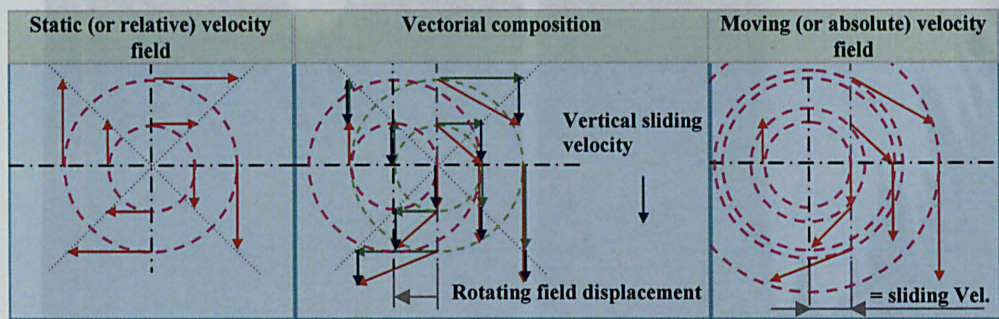


Figure 4-49 Vectorial composition: Relative field + Sliding velocity = absolute rotating field

#### 4.3.4.11. Particle Imaging Velocimetry of the near nozzle area

In the previous paragraph it was explained the development of the spray recirculation area by mean of visualisation of the wakes and analysis of the velocity field at the latest stage (EOI and wake) of the injection evolution. However, from the PIV analysis of the near nozzle air entrained motions it is possible to identify, in part, the mechanism of formation of the outer recirculation that was described in previous section. Besides, it should be added that in the direct-injection engines, the cylinder air motion plays a primary role in the dynamic of the spray evolution. Thus, it would be of great interest to observe how the air entrainment is acting and influencing the out coming spray.

The airflow was seeded with fine atomised water droplets with sizes of the order of 2µm and a mean settling velocity of 0.3 m/s ± 1.3m/s suspended around the spray jet toward the injector exit by a commercial purposed built atomiser; when injection occurs these fine water droplets were used to trace the induced air motion. The PIV images presented in Figure 4-50 shows a sequence of the air entrainment velocity with a time step resolution of 0.1ms on the left hand side of the spray evolution.



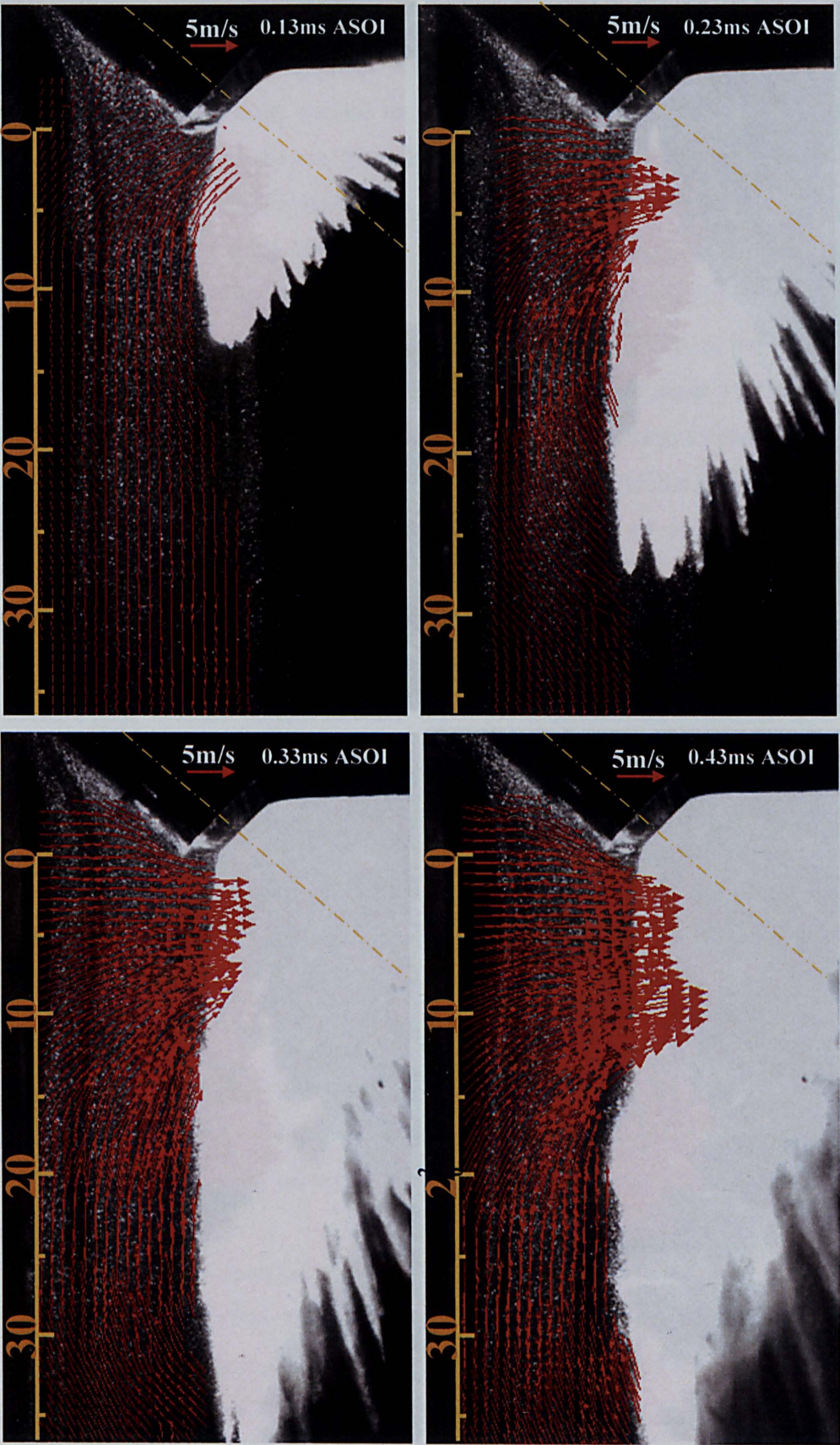
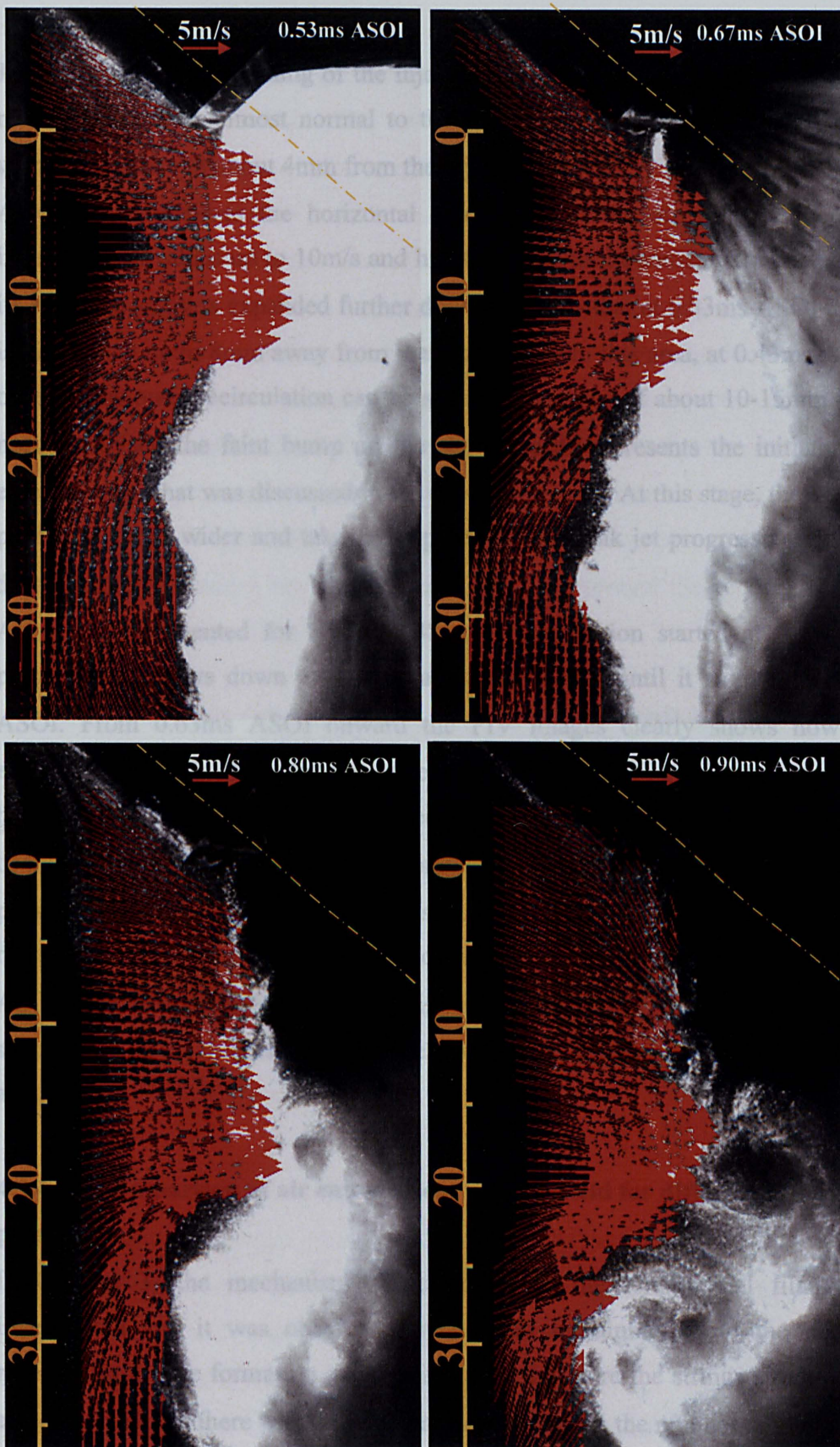


Figure 4-50 Air entrainment velocity field around spray when injected into air at ambient condition with injection pressure of 200bar and needle set to 1001 bit position.





**Figure 4-50** Air entrainment velocity field around spray when injected into air at ambient condition with injection pressure of 200bar and needle set to 1001 bit position.

---

Just from the very beginning of the injection, the direction of air entrainment clearly reveals a direction almost normal to the spray flow and exhibits a jet like profile within a distance of about 4mm from the injector exit.

As the spray evolves the horizontal component of the air velocity increases in intensity with values up to 10m/s and hits the spray in the same near nozzle area, but its effect on spray is expanded further downstream so that at 0.33ms ASOI the air jet is distributed up to 8mm away from the nozzle exit. In this area, at 0.43ms ASOI, the onset of the outer recirculation can be seen at a distance of about 10-15mm from the nozzle; in fact, the faint bump on the spray profile represents the initiation of the external wake that was discussed in the previous section. At this stage, the air velocity profile becomes wider and takes a shape of double peak jet progressively extending downstream.

As it was commented for Figure 4-48, the recirculation started at 0.43ms ASOI progressively slows down to 10 m/s at 1.60ms ASOI until it stops within 2.27ms ASOI. From 0.63ms ASOI onward the PIV images clearly shows how the air entrainment wraps the evolving external wake promoting its formation with a horizontal velocity of about 10m/s preceding its motion. Finally, 0.30ms after the end of the injection (0.90 ms ASOI), the spray starts losing its density and therefore it is possible to visualise the internal cross-section of the spray and the full set of counter rotating vortices as was previously shown in Figure 4-48. The last image at 0.9ms ASOI, also reveals how the air entrainment is interacting on the wakes and more specifically on the internal vortex, which explains its displacement toward the injector axis.

#### **4.3.4.12. Comparison of air entrainment velocity field for different injection pressure**

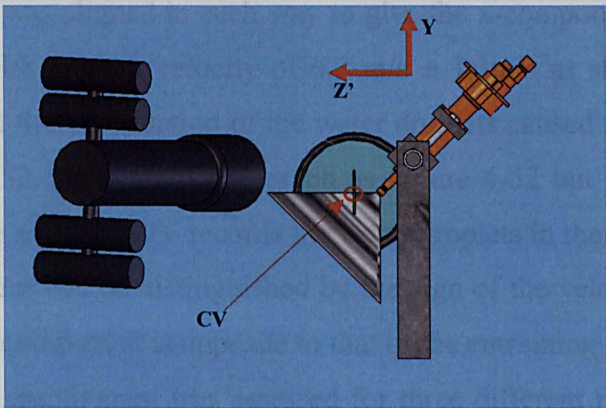
In Chapter 3, the mechanism of formation of the longitudinal filaments was investigated and it was observed how the air entrainment into the nozzle was responsible for the formation of air pocket and therefore the strings structure. It was also observed that there was a direct correlation between the number of strings and the injection pressure. However, the mechanism linking cause and the effect is still unclear and it could be related either to the flow momentum variation which causes flow detachment or phenomena related with the dynamics of the liquid inside the



nozzle.

It can be also speculated that the air entrainment may also play a role in the formation of the in-nozzle air bubble. The intensity of the velocity component hitting the proximity of the emerging spray could be associated with the amount of air pocket and therefore enhancing the breakdown of the bubbles into smaller sizes when the air velocity is increased with the effect of increasing the number of strings. As a increase in injection pressure results in a greater air entrainment velocity and this, in turn, is responsible for the breakdown of the air entrainment bubbles inside the nozzle it is then possible to associate the increase in strings number with injection pressure.

To support this analysis, it is of interest to observe whether the increase in rail pressure actually causes an increase of the air entrainment velocity normal to the spray surface in the proximity of the injector exit. This was assessed in the following experiments with which the air entrainment velocity around the spray was measured at different injection pressures.

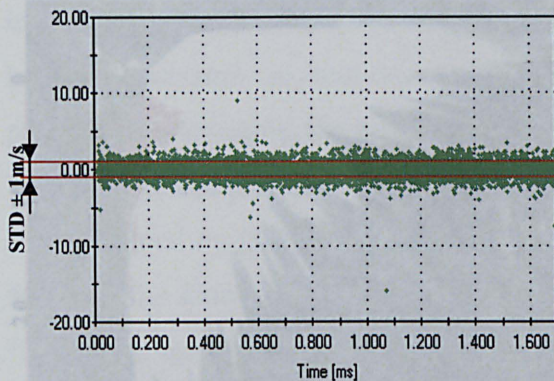


**Figure 4-51 LDV Set up for air entrainment investigation**

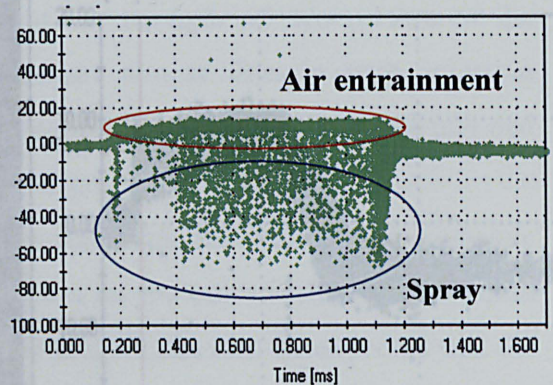
In order to assess the velocity of the air entrainment both PIV and LDV methods (as shown in Figure 4-51) were used to measure air velocity in the proximity of the injector exit; the LDV measurements were made at the same axial location as that of the opening edge of injector.

The LDV set up was aligned in such a way to give the same velocity component as that of the PIV system with the only difference was that the measurement point was chosen above the horizontal edge of the spray profile in order to measure both normal and longitudinal velocity components as shown in Figure 4-51





**Figure 4-52 LDV assessment of the seeding dispersion velocity during idle**



**Figure 4-53 LDV air motion and spray droplet areas in the normal velocity component ( $V_y$ )**

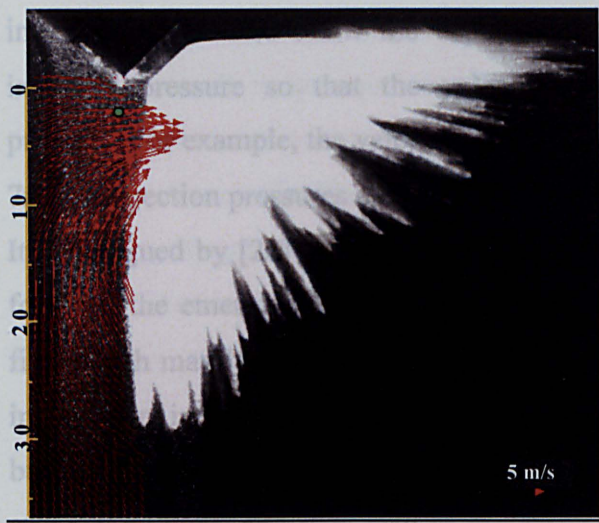
Figure 4-52 shows the LDV measurement when only the seeding (fine water droplets) flow is active (in the absence of the spray) and passing through the control volume area. As for the PDA plots, each sample represents the normal component of a droplet crossing the CV which was aligned in such way to give the x-component (the normal component) velocity with a mean velocity of  $0.3 \text{ m/s} \pm 1.3\text{m/s}$  as shown in Figure 4-52. This suggests that the introduction of the water droplets caused no predominate flow motion. Figure 4-53 shows the same graph as Figure 4-52 but in this case the injection is taking place and the LDV records the water droplets in the presence of the spray. The two flow areas can be distinguished by the sign of the velocity as the fuel jet expands its velocity component is opposite to that of the entraining air.

The velocity of the air entrainment was assessed for three different rail pressures of 200bar, 100bar and 50bar and the results are presented in Figure 4-55. Each of the three different image rows in this Figure 4-55 corresponds to an injection pressure. The left images represent the PIV velocity field measurements and the right hand graphs show the temporal variation of LDV measurements for normal velocity components; LDV measurement is taken at a point which is identified in the PIV image (lhs plot) as a green dot. A comparison between PIV and LDV measurement is made first and the results at 0.23ms ASOI show good agreement between the normal velocity component measured by the two methods with maximum difference of up to 5%.

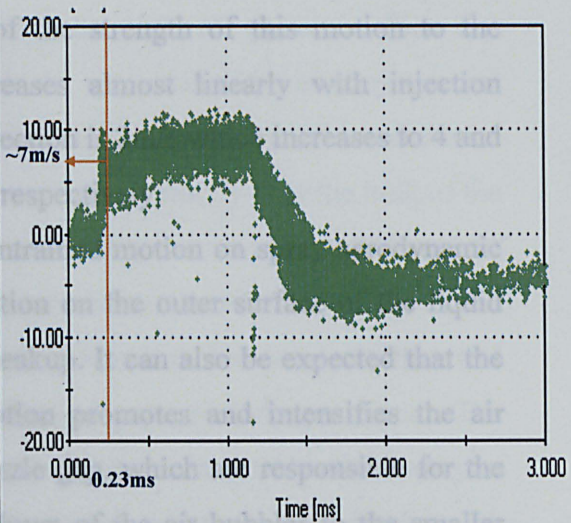
The air entrained flow motion show a uniform and relatively strong velocity field near the nozzle exit, which is set up as soon as the injection process starts and remains active with almost the same strength during the entire injection period.



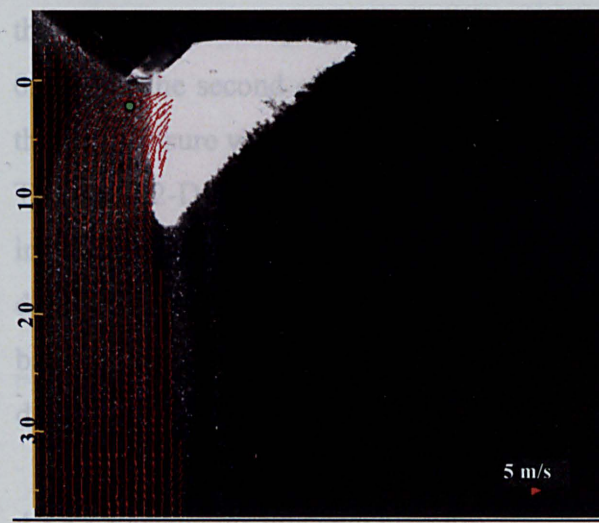
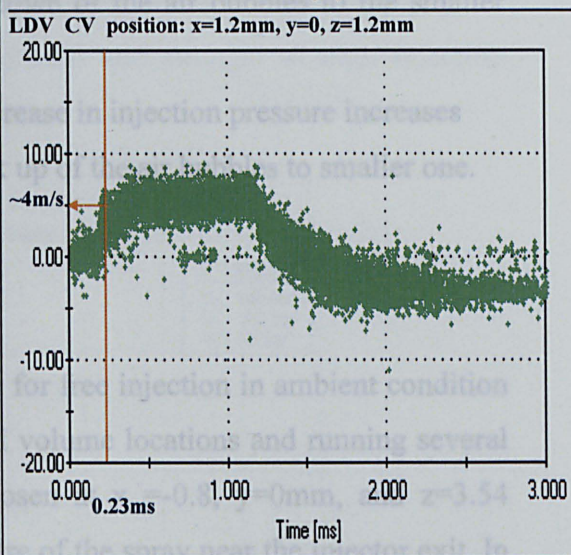
The LDV results show clearly the uniformity of the entrained motion during the



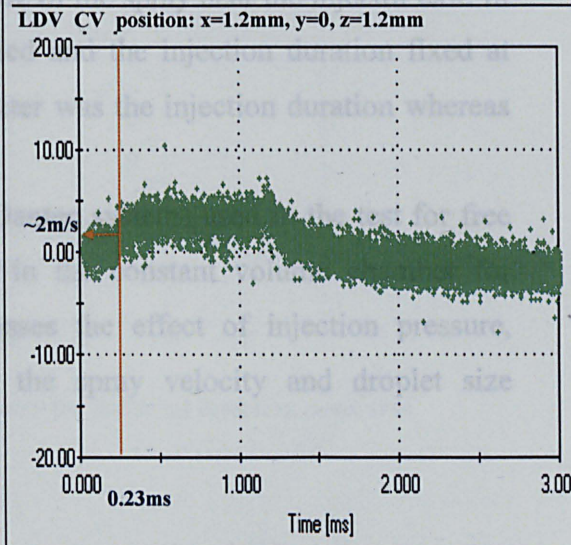
0.23ms ASOI Pi.200bar



0.23ms ASOI Pi.100bar



0.23ms ASOI Pi.50bar



**Figure 4-54 Air entrainment investigations: PIV velocity field, LDV normal velocity component.**  
 (The green dots in the PIV images represent the CV position for the LDV experiments)

---

The LDV results show clearly the uniformity of the entrained motion during the injection which also show the dependency of the strength of this motion to the injection pressure so that the velocity increases almost linearly with injection pressure. For example, the velocity at 50bar injection is 2m/s which increases to 4 and 7m/s at injection pressures of 100 and 200 bar, respectively.

It was argued by [26] that the impact of the entrained motion on spray aerodynamic force on the emerging liquid initiates a distortion on the outer surface of the liquid film which may lead to instability and then breakup. It can also be expected that the increase in intensity of the entrained air motion promotes and intensifies the air bubble trapped (or entrainment) inside the nozzle gap, which are responsible for the string formation, and may lead in the break down of the air bubbles to the smaller sizes and therefore more strings.

The results of previous chapter showed that increase in injection pressure increases the number of strings, which supports the break up of the air bubbles to smaller one.

#### **4.3.5. Parametric investigation**

A parametric study of the spray characteristics for free injection in ambient condition was performed by selecting a common control volume locations and running several test cases; the fixed control volume was chosen at  $x = -0.8$ ,  $y = 0\text{mm}$ , and  $z = 3.54$  ( $z' = 2.5\text{mm}$ ) which is a location within the centre of the spray near the injector exit. In the first case, the injection pressure was varied and the injection duration fixed at 0.6ms. In the second case, the varying parameter was the injection duration whereas the rail pressure was fixed at 200bar.

The same 2-D Phase-Doppler Anemometer (Dantec system) used in the test for free injection in ambient environment was used in the constant volume chamber for different operating conditions in order to assess the effect of injection pressure, backpressure, and chamber temperature on the spray velocity and droplet size distribution.

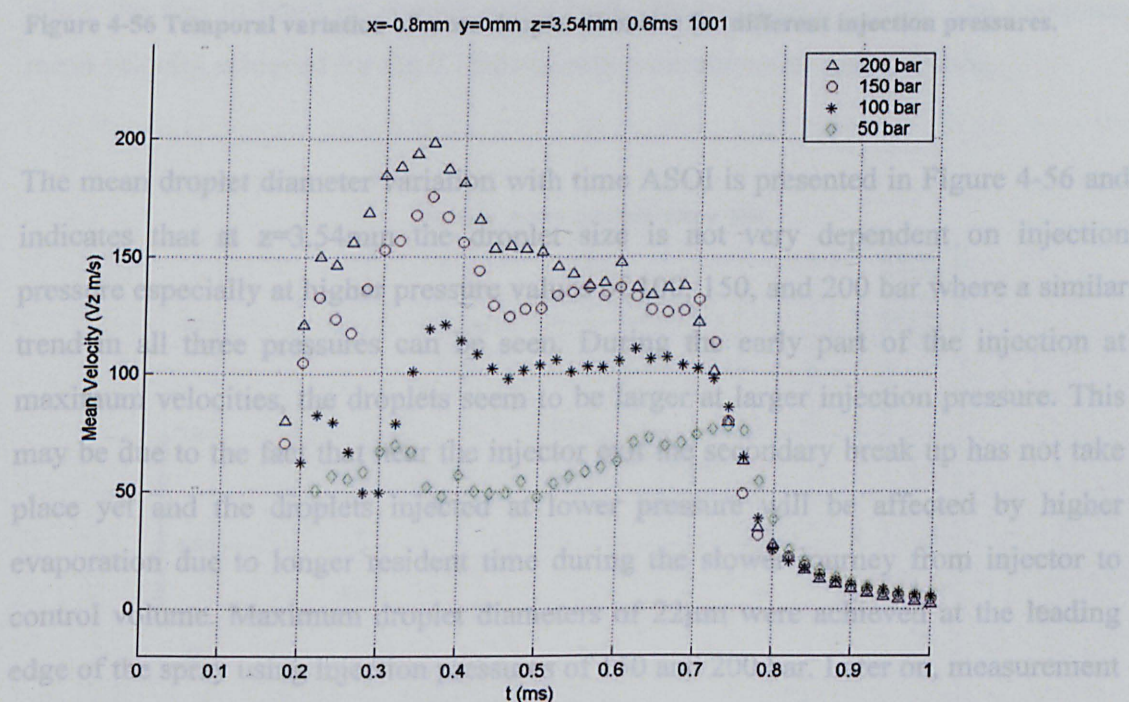
##### **4.3.5.1. Varying the injection pressure**

The results of temporal variation of mean droplet velocity for four injection pressures of 50, 100, 150 and 200 bar are presented in Figure 4-55. The first most obvious observation that can be deduced from Figure 4-55 is that an increase in injection



pressure produces higher mean spray velocity especially during the main part of injection event. However, an equal increment increase of pressure does not necessarily result in an equal incremental gain in spray velocity, as they are not directly proportional to one another. The maximum mean velocity achieved for an injection pressure of 200bar was 200m/s, with an average velocity over the bulk of the spray event of approximately 145m/s. The corresponding values at 150, 100 and 50 bar were 175m/s-138m/s, 120m/s-105m/s and 80m/s- 60m/s, respectively.

The velocity variation is much greater for higher injection pressures (200bar and 150bar) with the initial peak of the leading edge being particularly prominent. The lowest injection pressure has a relatively uniform velocity variation over the main part of injection event, suggesting that pressure fluctuations, perhaps caused by the peak overshoot of the injector valve, are more apparent and stronger at high injection pressures.

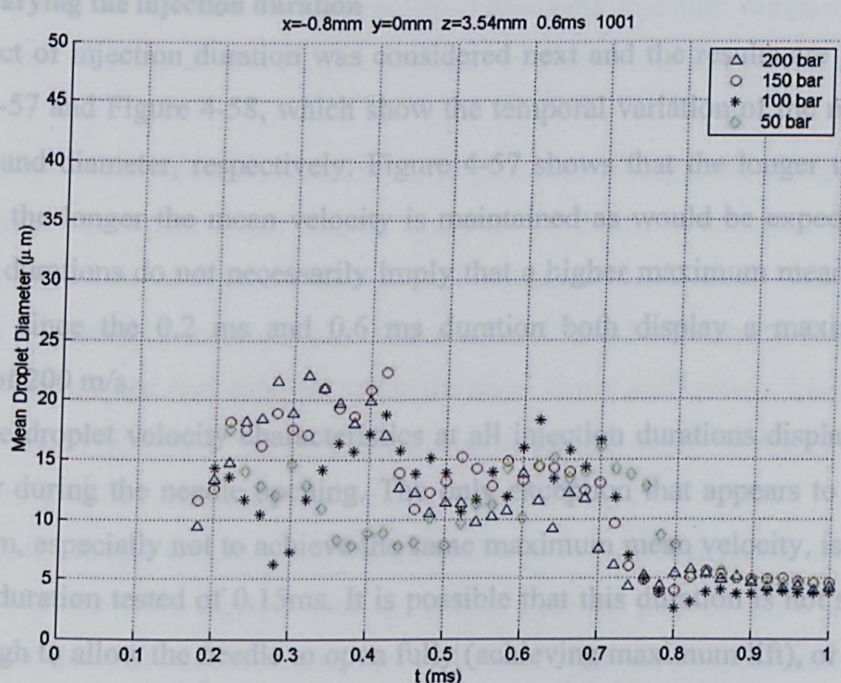


**Figure 4-55 Temporal variation of mean droplet velocity for different injection pressures.**

There is no sign of a negative velocity, hence no recirculation of the droplets, for any of the pressures tested. This result was expected, since the control volume was positioned at a point in the spray very near to the centre of the jet, and as shown earlier, recirculation zones take place further downstream and visible to the PDA only



at the outer edge.



**Figure 4-56** Temporal variation of mean droplet diameter for different injection pressures.

The mean droplet diameter variation with time ASOI is presented in Figure 4-56 and indicates that at  $z=3.54mm$  the droplet size is not very dependent on injection pressure especially at higher pressure values of 100, 150, and 200 bar where a similar trend in all three pressures can be seen. During the early part of the injection at maximum velocities, the droplets seem to be larger at larger injection pressure. This may be due to the fact that near the injector exit the secondary break up has not take place yet and the droplets injected at lower pressure will be affected by higher evaporation due to longer resident time during the slower journey from injector to control volume. Maximum droplet diameters of  $22\mu m$  were achieved at the leading edge of the spray using injection pressures of 150 and 200 bar. Later on, measurement carried out in the constant volume chamber will show different trend for the mean droplet diameter with injection pressure at a location  $z=14.1mm$  ( $z'=10mm$ ).

For all the injection pressure, it can be observed that the mean droplet diameters reduce in size within the main part of the injection event showing a similar size distribution with an average value of around  $12.5 \pm 3\mu m$ . The droplet sizes also appear to be sensitive to the pressure fluctuations, which seem to be occurring within the injector and follow similar behaviour to the velocity distributions.



4.3.5.2.Varying the injection duration

The effect of injection duration was considered next and the results are presented in Figure 4-57 and Figure 4-58, which show the temporal variation of the mean droplet velocity and diameter, respectively. Figure 4-57 shows that the longer the injection duration, the longer the mean velocity is maintained as would be expected. Longer injection durations do not necessarily imply that a higher maximum mean velocity is achieved, since the 0.2 ms and 0.6 ms duration both display a maximum mean velocity of 200 m/s.

In fact the droplet velocity characteristics at all injection durations display the same behaviour during the needle opening. The only exception that appears to not follow this pattern, especially not to achieve the same maximum mean velocity, is the lowest injection duration tested of 0.15ms. It is possible that this duration is not sufficiently long enough to allow the needle to open fully (achieving maximum lift), or perhaps to allow the fuel to build up enough momentum due to its own inertia. The maximum mean velocity achieved for the 0.15ms injection duration was only 165m/s.

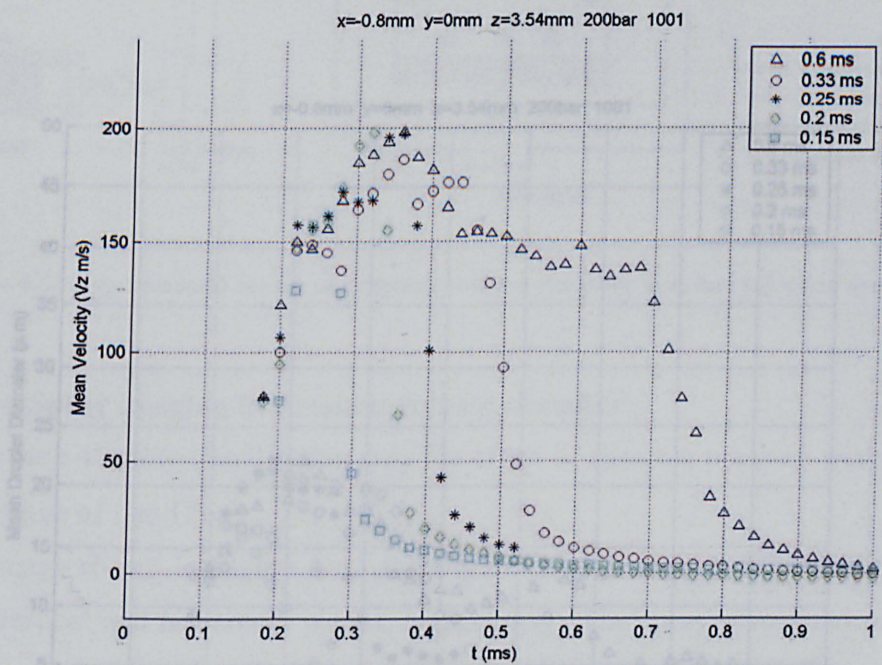


Figure 4-57 Temporal variation of mean droplet velocity for different injection durations.

The profile produced using the 0.6ms injection duration appears to be the most stable, possibly because there is sufficient time to allow the pressure fluctuations to dampen



down, following the suspected peak over shoot of the valve. The 0.33ms injection duration produced the most erratic profile. The 0.6ms injection duration is the only duration that displays an almost flat, uniform velocity variation during the injection period.

The influence of the injection duration on droplets size is displayed in Figure 4-58 and shows that a maximum mean droplet diameter of 24μm is achieved for injection durations of 0.2ms and more. The lowest injection duration (0.15ms), however, produced a maximum mean droplet diameter of 17μm lower than other durations. Again it is suspected that this particular duration is not sufficiently long enough to allow maximum flow rate to take place due to the valve being unable to achieve its full lift, and therefore, resulting in a smaller cross sectional.

In general, the longer the injection duration, the less fluctuation in the mean droplet diameters become. This suggests that the longer injection periods allow the pressure fluctuation to dampen out before the injector closes. This can be seen when observing the 0.6ms duration results as it features the most stable behaviour, i.e., least variation in droplet diameters. The results also show that the variation in droplet diameter with time follow the same pattern as that of mean droplet velocity profile. In all cases the final droplet sizes at the end of injection are 4μm ± 1μm.

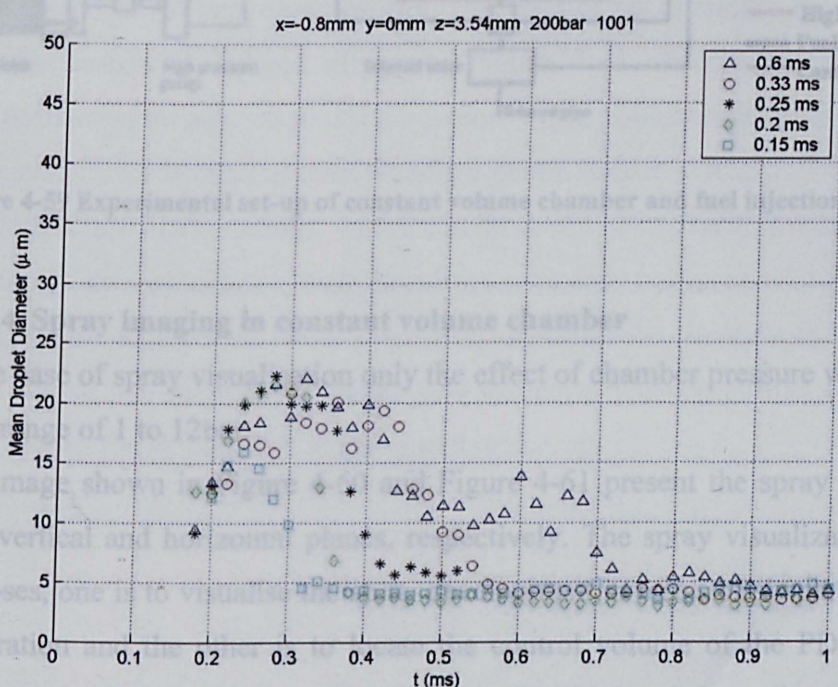


Figure 4-58 Temporal variation of mean droplet diameter for different injection durations



#### 4.3.5.3. PDA Measurements in constant volume chamber: - Experimental Set-up

The transmitting and receiving optics were installed in the same 3-D traverse mechanism with a resolution of  $12.5\mu\text{m}$  in x, y-axis and  $6.25\mu\text{m}$  in z-axis relative to the injector position. The same wall mounted Argon-Ion laser was used with a maximum power of around 1.5W and the output beam was aligned with the fibre optic unit. The transmitting and collecting optics and instrumentations are the same as those described in the early part of this chapter. Figure 4-59 shows the fuel injection system connected to the constant volume chamber, which is equipped with a heating control system capable of maintaining temperatures up to  $180\pm 3^\circ\text{C}$

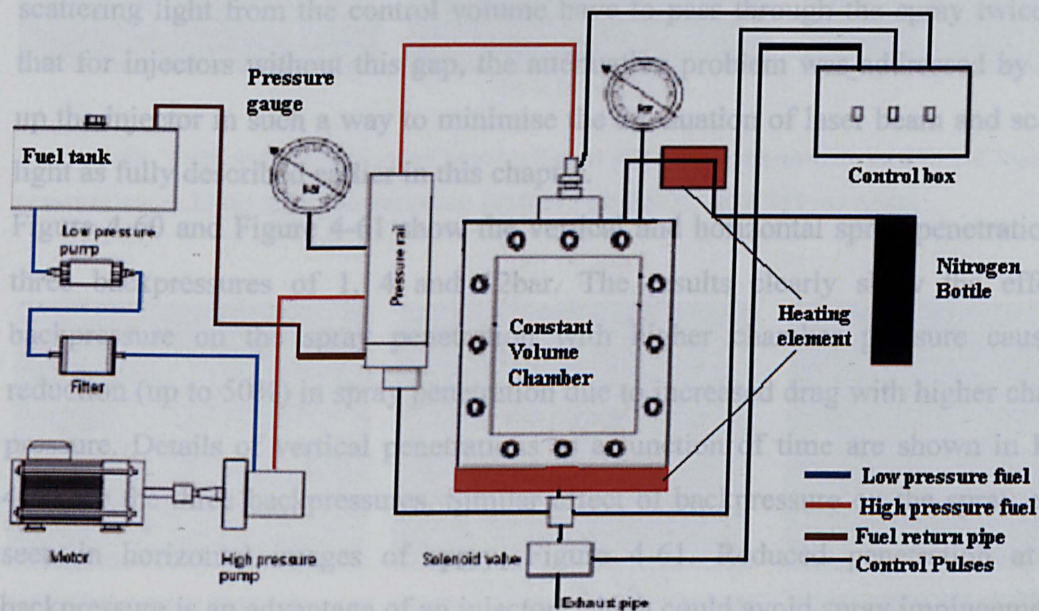


Figure 4-59 Experimental set-up of constant volume chamber and fuel injection system

#### 4.3.5.4. Spray imaging in constant volume chamber

In the case of spray visualisation only the effect of chamber pressure were considered for a range of 1 to 12bar.

The image shown in Figure 4-60 and Figure 4-61 present the spray visualization in both vertical and horizontal planes, respectively. The spray visualization serves two purposes, one is to visualise the spray development in terms of shape, cone angle and penetration and the other is to locate the control volume of the PDA system on a chosen string as was discussed earlier on. Combining information from the spray visualization with that of the PDA measurement results will be used for studying the spray characteristics.

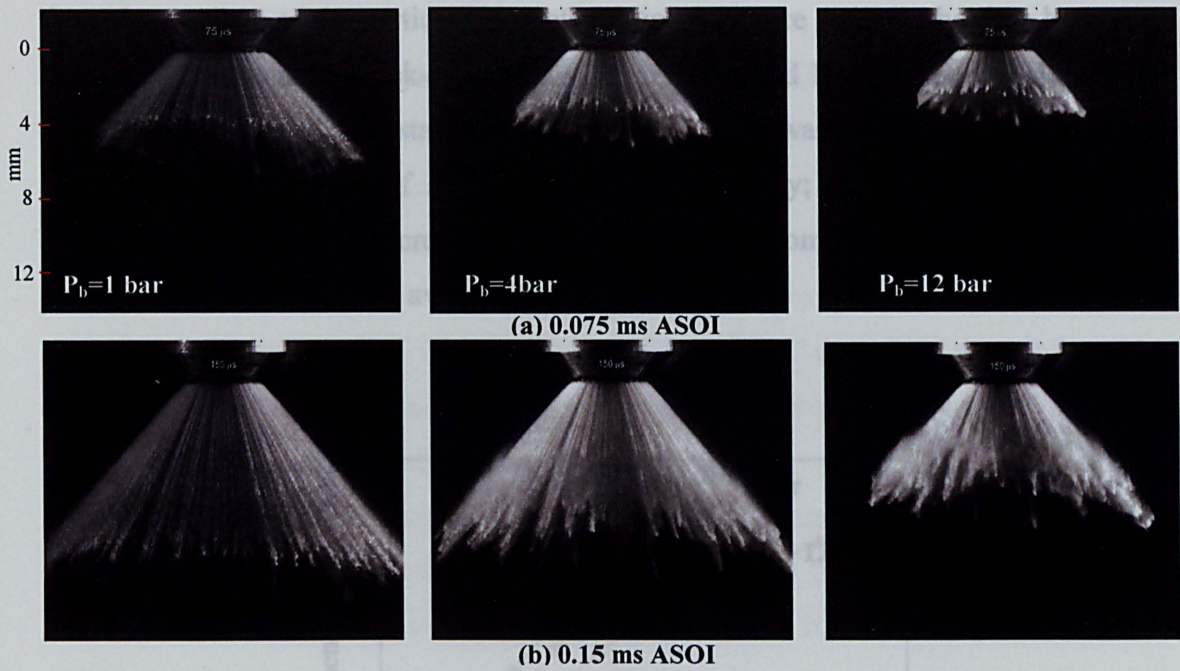
---

By observing the images, the first noticeable feature was the presence of a natural gap in the spray, which can be clearly seen from the horizontal images of spray in Figure 4-61. The existence of such a gap is not a designed feature of the injector and it could be caused by a local surface condition inside the injector nozzle. This gap as a part of the string structure was very stable so that its location did not change at all; this was found to be very useful in the PDA measurement. It provided an opening passage for the incident laser beams to reach the other side of the spray cone surface without any attenuation of the laser beams by the spray. The dense feature of the spray caused so much laser beam attenuation that the PDA measurement was not possible to be achieved, especially in the centre of the spray, if either the incident laser beams or the scattering light from the control volume have to pass through the spray twice. Note that for injectors without this gap, the attenuation problem was addressed by setting up the injector in such a way to minimise the attenuation of laser beam and scattered light as fully described earlier in this chapter.

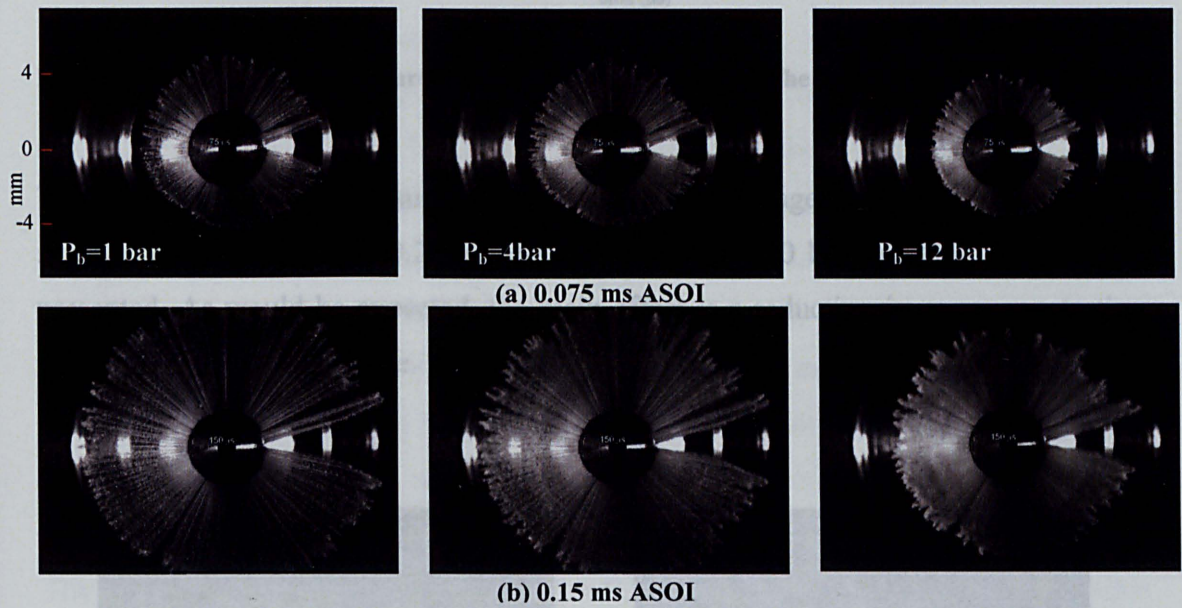
Figure 4-60 and Figure 4-61 show the vertical and horizontal spray penetrations for three backpressures of 1, 4 and 12bar. The results clearly show the effect of backpressure on the spray penetration with higher chamber pressure causing a reduction (up to 50%) in spray penetration due to increased drag with higher chamber pressure. Details of vertical penetrations as a function of time are shown in Figure 4-62 for the three backpressures. Similar effect of backpressure on the spray can be seen in horizontal images of spray, Figure 4-61. Reduced penetration at high backpressure is an advantage of an injector, which could avoid spray impingement on the piston crown at late injection when the piston is near TDC.

The locations of large strings, which can be easily identified in the string structure of the spray, do not change their locations with the backpressure. As backpressure increases, the ambient air density increases causing a deceleration of the droplets, as a result the strings seem to be denser and the gaps between strings are less clear, in other words, the strings look cloudier and joined up.





**Figure 4-60** Vertical images of spray penetration at different back-pressures, 200 bar injection pressure and 0.33 ms injection duration: (a) 0.075 ms ASOI; (b) 0.150 ms ASOI.

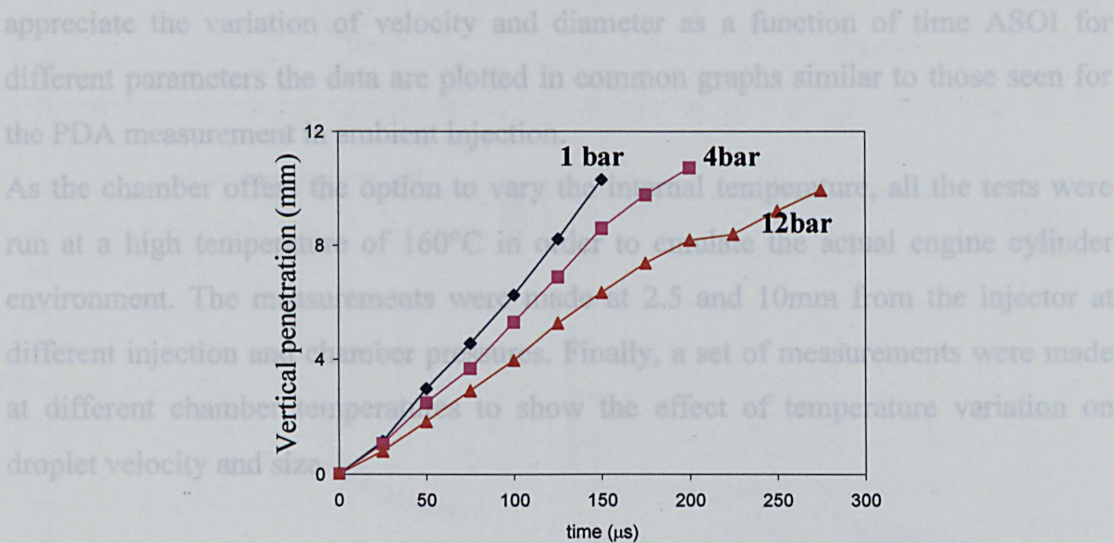


**Figure 4-61** Horizontal images of spray penetration at different back-pressures, 200 bar injection pressure and 0.33 ms injection duration: (a) 0.075 ms ASOI; (b) 0.150 ms ASOI.

According to the gradients of the penetration graphs in Figure 4-62, the vertical spray tip velocity accelerates after leaving the injector nozzle as the injector needle opens up and then it starts to decelerate as the droplets loose their momentum further downstream. Averaged vertical tip velocities of 73 m/s, 62 m/s and 46m/s are found



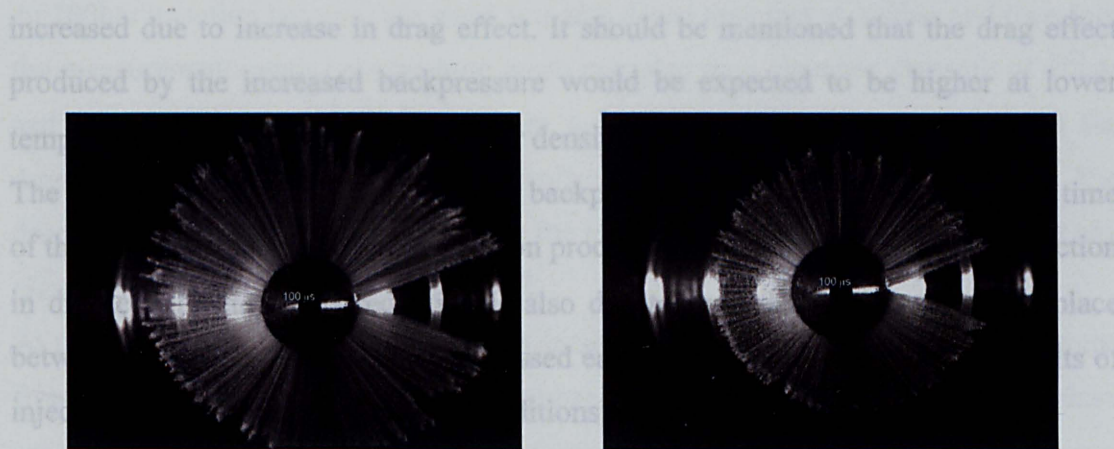
from the gradient of the vertical penetration curves (Figure 4-62) at the time between 50  $\mu$ s and 150  $\mu$ s under back-pressures of 1 bar, 4 bar and 12 bar, respectively. From Figure 4-62, the vertical distance penetration at 150  $\mu$ s was found to be 10, 8.5 and 6.2 mm for backpressure of 1, 4 and 12 bar, respectively; a maximum reduction of 37% in penetration by increasing the backpressure from 1 to 12bar. The same reduction can be seen in the average tip velocity.



#### 4.3.5.6. Effect of Backpressure at $P_i = 200$ bar

**Figure 4-62 Effect of backpressure on the vertical penetration of the spray.**

The effect of injection pressure can be seen from the images of Figure 4-63 where a sample of spray image at 0.2 ms ASOI for 100 and 200 bar injection pressure are presented. As would be expected, the main effect is a reduction in spray penetration with lower injection pressure.



**(a) 200 bar Injection pressure**

**(b) 100 bar injection pressure**

**Figure 4-63 Horizontal images of spray penetration at 100ms after SOI, ambient back-pressure and 0.33ms injection duration: (a) 200bar Injection pressure; (b) 100bar injection pressure.**



---

#### **4.3.5.5. PDA measurement in the constant volume chamber - Introduction**

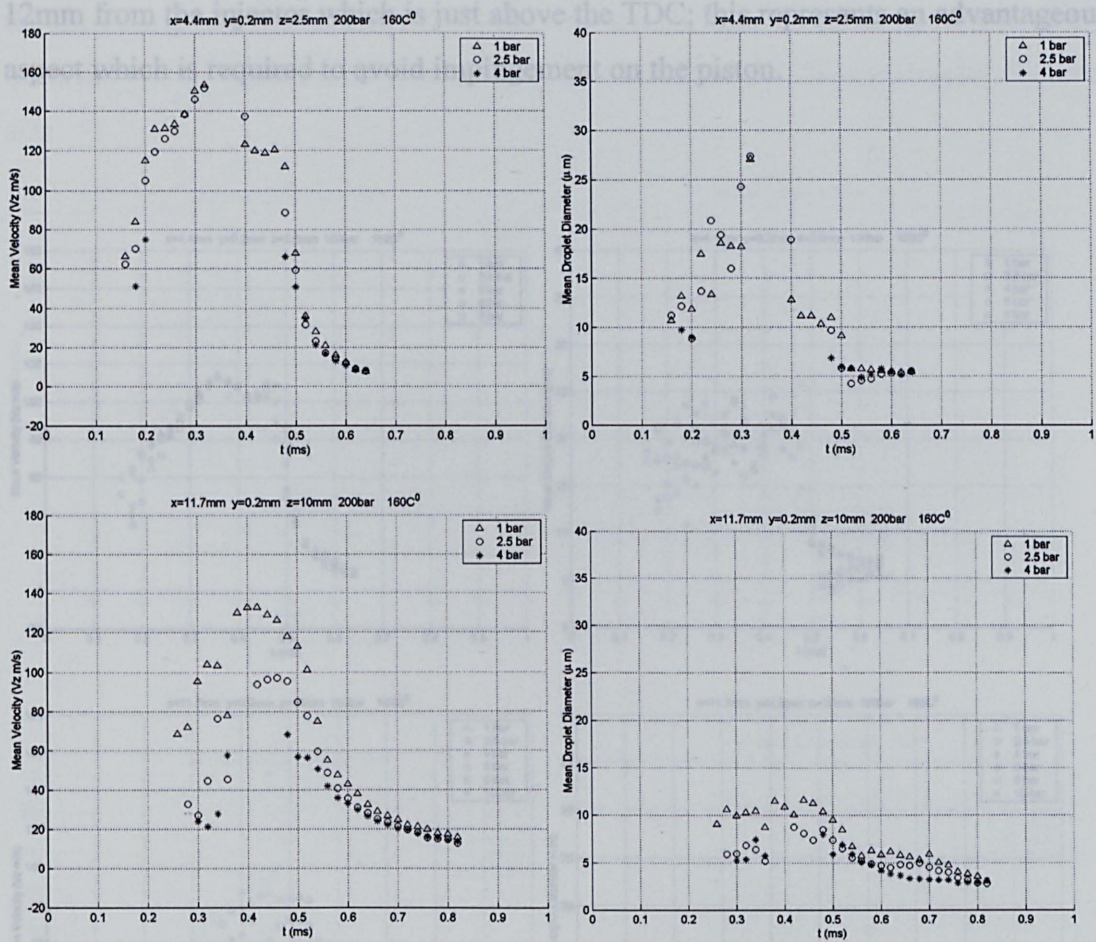
After establishing the correct control volume location according to the previous spray visualisation, it was then possible to proceed to the PDA measurement. As it was observed in the spray imaging, the string position is quite insensitive to the several operating parameters therefore, it was possible to compare several series of data. To appreciate the variation of velocity and diameter as a function of time ASOI for different parameters the data are plotted in common graphs similar to those seen for the PDA measurement in ambient injection.

As the chamber offers the option to vary the internal temperature, all the tests were run at a high temperature of 160°C in order to emulate the actual engine cylinder environment. The measurements were made at 2.5 and 10mm from the injector at different injection and chamber pressures. Finally, a set of measurements were made at different chamber temperatures to show the effect of temperature variation on droplet velocity and size.

#### **4.3.5.6. Effect of Backpressure at $P_i = 200$ bar**

The results are shown in Figure 4-64 for both  $z=2.5$  and 10mm from the injector and for chamber pressure 1, 2.5 and 4bar; measurements above 4bar at this injection pressure were not possible as the spray was too dense. Within the measured range and at  $z=2.5$  mm, close to injector exit, the overall effect of chamber pressure on droplets velocity and size is small with no clear trend. At  $z=10$ , the effect of backpressure on droplets velocity is evident with a reduction in velocity as the chamber pressure is increased due to increase in drag effect. It should be mentioned that the drag effect produced by the increased backpressure would be expected to be higher at lower temperature because of the increased air density.

The reduction in droplets velocity with backpressure will increase the residence time of the droplets enhancing the evaporation process, which is evident from the reduction in droplet diameter. This reduction is also due to secondary break up taking place between  $z=2.5$  and 10mm as was discussed earlier on this chapter when the results of injection into atmosphere (ambient conditions) were presented.



**Figure 4-64 PDA measurement at different Pb: Temporal variation of droplet mean velocity and diameter at  $P_i = 200$  bar,  $T = 160$  °C,  $z=2.5$ mm (upper row) and  $z=10$ mm (lower row).**

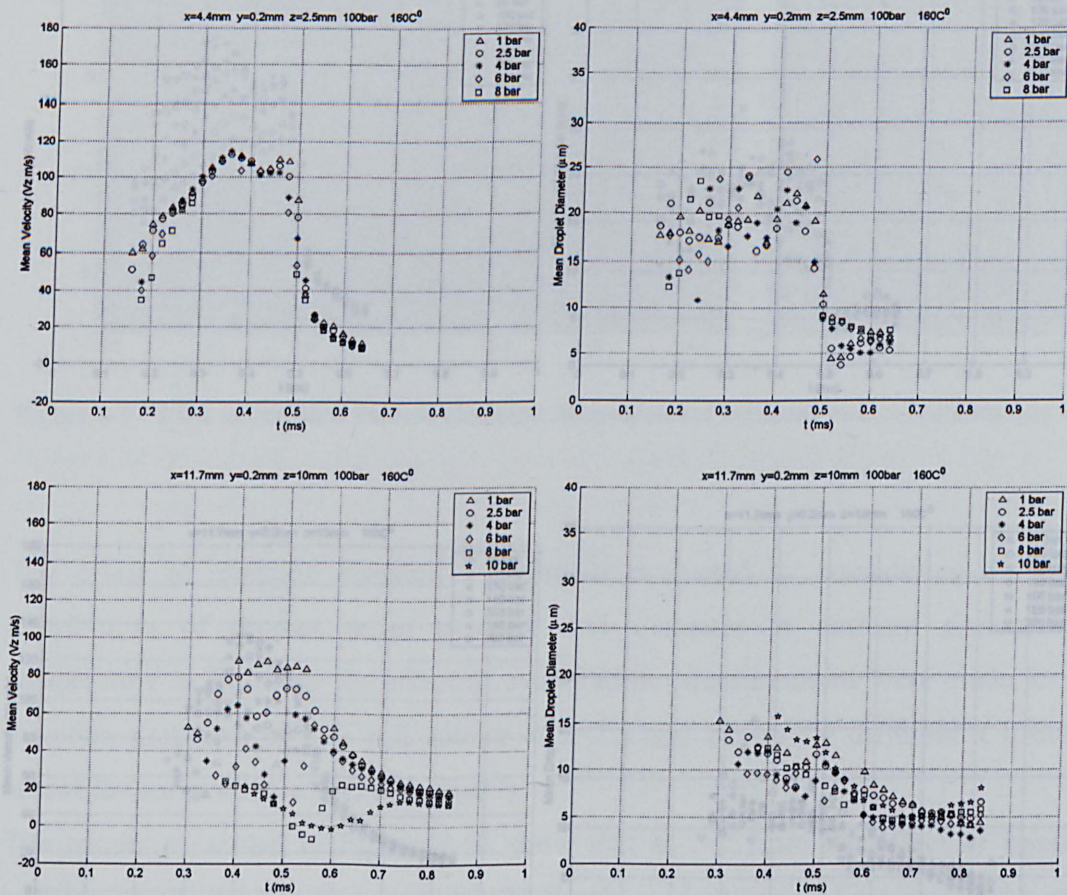
#### 4.3.5.7. Effect of Backpressure at $P_i = 100$ bar

At 100bar injection pressure the spray was less dense than that at 200bar and therefore the measurements with backpressure were extended to a chamber pressure of 10bar and the results are presented in Figure 4-65. The effect of backpressure on the droplets velocity is small at  $z=2.5$ mm similar to that at 200bar injection pressure. The droplet size varies from 16 to 24  $\mu\text{m}$  in the main part of spray without following any clear trend.

At  $z=10$ mm, the velocity decreases with increase in backpressure with the same trend from 1 bar to 4 bar, but from 6 bar to 10 bar the droplet velocity reduces everywhere especially in the middle of spray and onwards where it decreases rapidly even reaching negative value due to the presence of recirculation area. It was also observed from spray visualisation in optical engine that at these high backpressure (injection around the end of compression stroke) that the spray do not penetrate more than



12mm from the injector which is just above the TDC; this represents an advantageous aspect which is required to avoid impingement on the piston.



**Figure 4-65 PDA measurement at different  $P_b$ : Temporal variation of droplet mean velocity and diameter at  $P_i = 100\text{ bar}$ ,  $T = 160^\circ\text{C}$ ,  $z=2.5\text{mm}$  (upper row) and  $z=10\text{mm}$  (lower row).**

#### 4.3.5.8. Effect of Injection Pressure

The results for seven injection pressures ranging from 80 to 200 bar are displayed in Figure 4-66 at a chamber pressure of 1 bar and temperature of  $160^\circ\text{C}$ .

At  $z=2.5\text{mm}$ , the trend shown in Figure 4-66 reveals that the velocity increases with injection pressure as it would be expected. However, as observed in the ambient spray analysis at  $z=2.5\text{mm}$  ( $z=3.54$  along jet), the expected reduction in droplet diameter with increase in injection pressure is not so evident at location near the injector. The reason can be explained by the trade off between lower droplets evaporation caused by the decreasing droplet residence time against the higher break up level induced by



the increasing relative velocity. As in the near nozzle area the break up may not have occurred yet the evaporation effect may play a dominant role on the droplet diameter size.

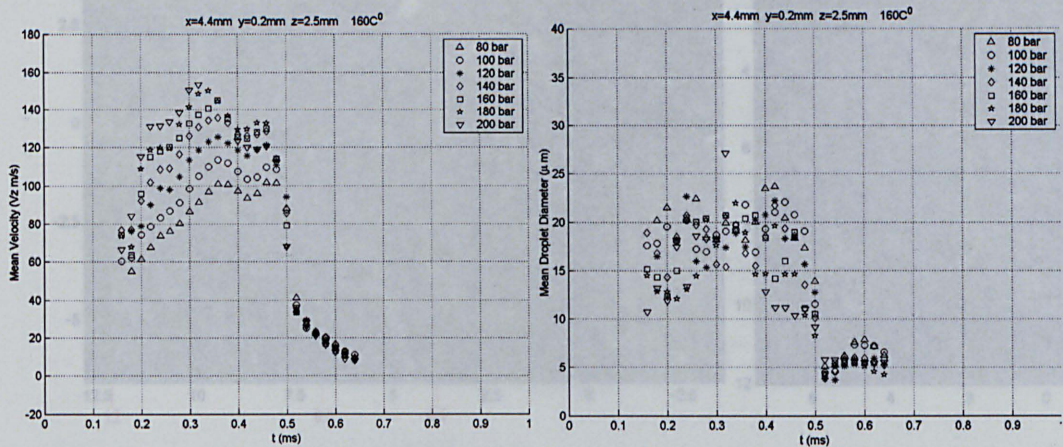


Figure 4-67 PDA in constant volume chamber measurement locations and coordinate system.

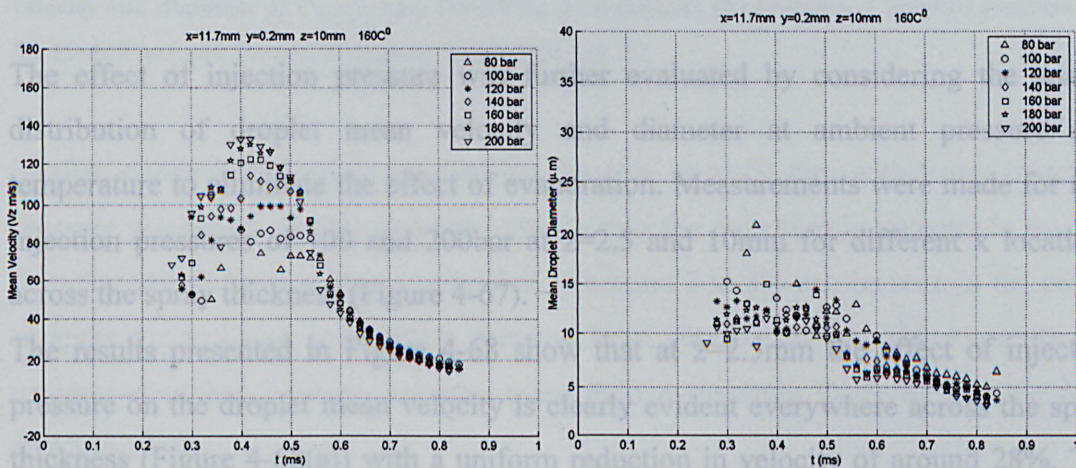
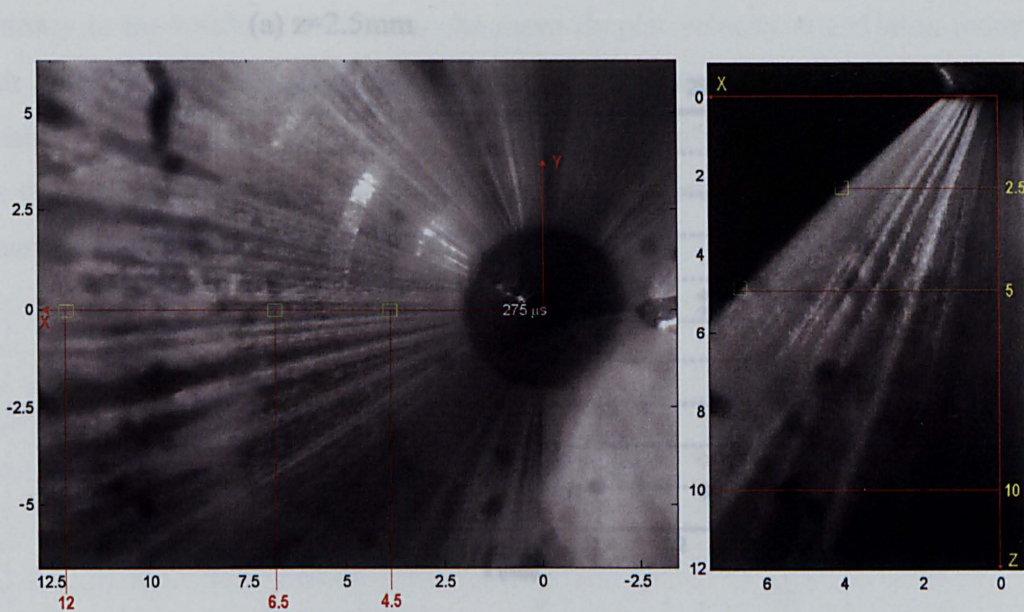


Figure 4-66 PDA measurement at different injection pressures: Temporal variation of droplet mean velocity and diameter at  $P_b = 1$  bar,  $T = 160^\circ\text{C}$ ,  $z = 2.5\text{mm}$  (upper row) and  $z = 10\text{mm}$  (lower row).

At  $z = 10\text{mm}$ , the effect of the injection pressure is more effective on the secondary break up and this is also evident from the graphs in Figure 4-66 which show that the velocity increases with increase in injection pressure and droplets diameter decreases as the injection pressure increases. In comparison with the previous experiment at room temperature (ambient injection), at  $160^\circ\text{C}$  the drag effect is lower as the gas is less dense which means higher relative velocity and therefore better atomisation. This, in turn, leads to a higher loss of momentum due to the enhanced droplet break up and therefore an increase in residence time or more effective evaporation.



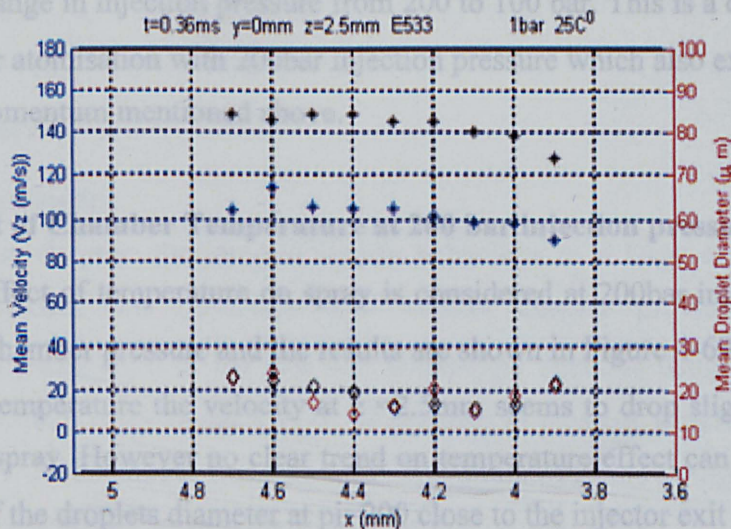


**Figure 4-67 PDA in constant volume chamber; measurement locations and coordinate system.**

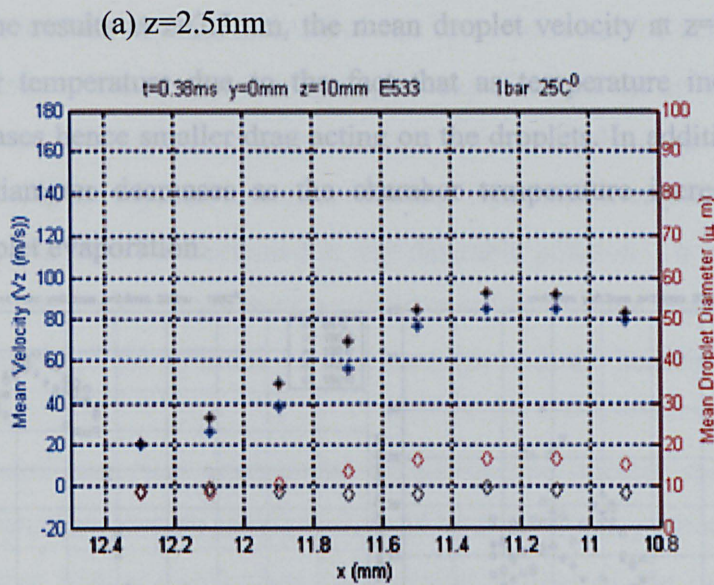
Figure 4-68 PDA measurement at different injection pressures: Spatial variation of droplet mean velocity and diameter at  $P_b = 1$  bar,  $T = 25^\circ\text{C}$ ; (a)  $z=2.5\text{mm}$ , (b)  $z=10\text{mm}$ . Coloured symbols are for  $P_i=100$  bar and the black symbols for  $P_i=200$  bar.

The effect of injection pressure was further evaluated by considering the spatial distribution of droplet mean velocity and diameter at ambient pressure and temperature to eliminate the effect of evaporation. Measurements were made for two injection pressures of 100 and 200bar at  $z=2.5$  and 10mm for different  $x$  locations across the spray thickness (Figure 4-67).

The results presented in Figure 4-68 show that at  $z=2.5\text{mm}$  the effect of injection pressure on the droplet mean velocity is clearly evident everywhere across the spray thickness (Figure 4-68(a)) with a uniform reduction in velocity of around 28%. The effect of injection pressure on droplets size is however very small at this axial location.







**Figure 4-68 PDA measurement at different injection pressures: Spatial variation of droplet mean velocity and diameter at  $P_b = 1$  bar,  $T = 25^\circ\text{C}$ ; (a)  $z=2.5\text{mm}$ , (b)  $z=10\text{mm}$ . Coloured symbols are for  $P_i=100$  bar and the black symbols for  $P_i=200$  bar**

Similar effect on the mean velocity can be seen at  $z=10$  mm with lower injection pressure producing smaller droplets velocity, but the reduction in velocity is smaller than that at  $z=2.5\text{mm}$  so that a reduction of around 7 to 8% can be seen in the centre of spray for a change in injection pressure from 200 to 100 bar. This suggests that droplets at higher injection pressure loose their momentum faster by moving from  $z=2.5$  to 10mm.

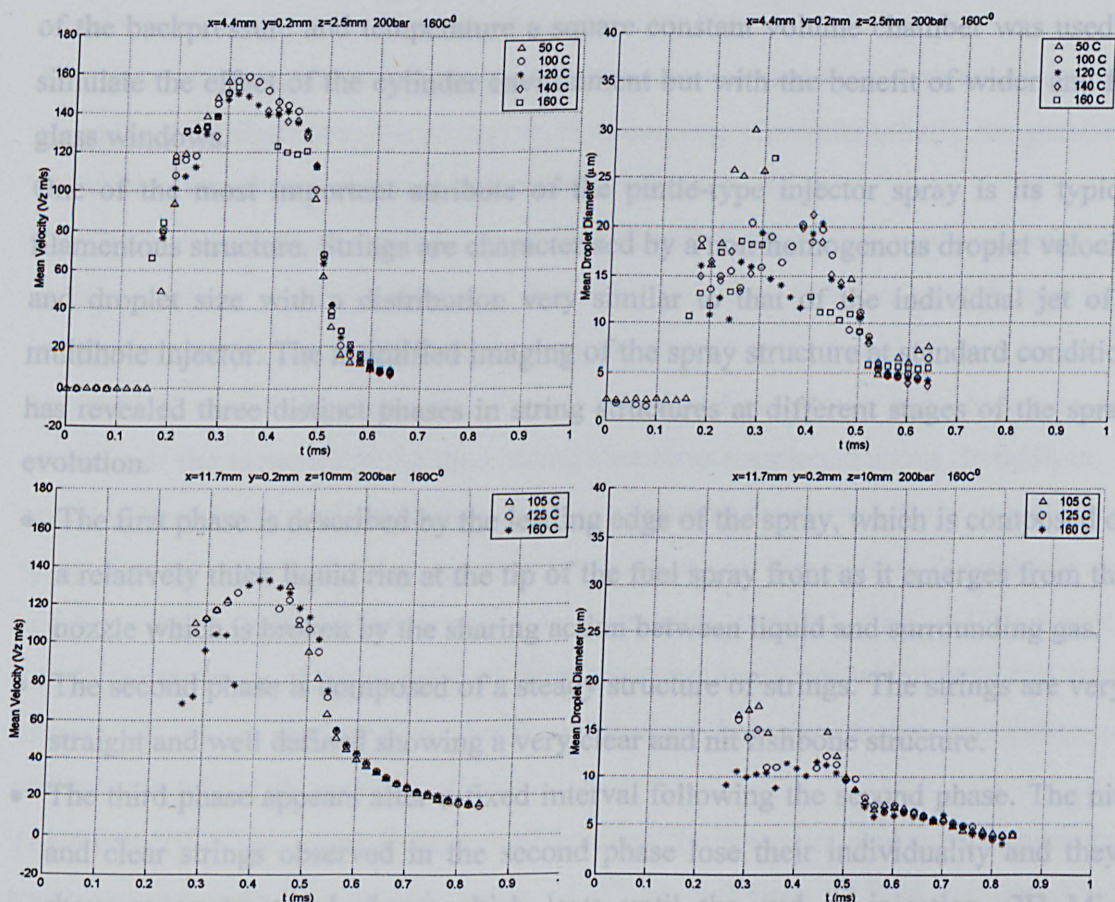
Unlike at  $z=2.5\text{mm}$ , the effect of injection pressure on droplets size occurring at  $z=10\text{mm}$  is considerable so that an increase of twofold can be seen in the centre of the spray for a change in injection pressure from 200 to 100 bar. This is a clear indication of much better atomisation with 200bar injection pressure which also explains the loss of droplets momentum mentioned above.

#### 4.3.5.9. Effect of Chamber Temperature at 200 bar injection pressure

Finally, the effect of temperature on spray is considered at 200bar injection pressure and ambient chamber pressure and the results are shown in Figure 4-69. By increasing the chamber temperature the velocity at  $z = 2.5\text{mm}$  seems to drop slightly within the centre of the spray. However no clear trend on temperature effect can be seen on the distribution of the droplets diameter at  $p_i=200$  close to the injector exit



Contrary to the results at  $z=2.5\text{mm}$ , the mean droplet velocity at  $z=10\text{mm}$  increases with chamber temperature due to the fact that as temperature increases, the gas density decreases hence smaller drag acting on the droplets. In addition, as expected, the droplet diameter decreases as the chamber temperature increases due to the enhanced droplet evaporation.



**Figure 4-69 PDA measurement at different chamber temperature: Temporal variation of droplet mean velocity and diameter at  $P_b = 1$  bar,  $P_i = 200\text{bar}$ ,  $z=2.5\text{mm}$  (upper row) and  $z=10\text{mm}$  (lower row).**

## 4.4. SUMMARY

### Spray Characteristics

In the previous chapter, the internal nozzle behaviour in a large-scale model of a pintle-type injector was observed. The current chapter provides a thorough experimental investigation of the real size pintle-type injectors using Mie scattering techniques to obtain spray images, PDA diagnostics to measure droplets velocity and size, LDV, PIV diagnostics to measure spray and entraining air velocity field.

The following is a summary of main finding of this investigation.

---

In order to achieve full optical access into the spray cone and be able to measure the full characteristic of the near nozzle spray, the experimental set up was rearranged to ensure minimum interference between the laser beams and the dense spray. This was achieved by using an adjustable support for free injection in atmosphere with which the injector could have been oriented at any desirable position. To observe the effect of the backpressure and temperature a square constant volume chamber was used to simulate the effect of the cylinder environment but with the benefit of wider and flat glass windows.

One of the most important attribute of the pintle-type injector spray is its typical filamentous structure. Strings are characterised by a non-homogenous droplet velocity and droplet size with a distribution very similar to that of the individual jet of a multihole injector. The magnified imaging of the spray structure at standard condition has revealed three distinct phases in string structures at different stages of the spray evolution.

- The first phase is described by the leading edge of the spray, which is composed of a relatively thick liquid rim at the tip of the fuel spray front as it emerges from the nozzle which is broken by the shearing action between liquid and surrounding gas.
- The second phase is composed of a steady structure of strings. The strings are very straight and well defined showing a very clear and nit fishbone structure.
- The third phase appears after a fixed interval following the second phase. The nit and clear strings observed in the second phase lose their individuality and they show an unstructured shape which lasts until the end of injection. 2D Mie scattering and PIV investigation have shown this phase taking place after the occurrence of the secondary break up and it is possibly induced by the interference of the air-entrained recirculation with the string filaments.

The magnified images of the first structure revealed that the emerging spray presents a liquid sheet between two consecutive strings, which is in process of braking up. The PDA measurement showed the presence of large droplet belonging to this initial structure with SMD up to  $30\mu\text{m}$  and uniform velocity across the whole jet thickness. After a duration of about 0.1ms (at 0.3ms ASOI) the big droplets of the first phase of the spray structure turn into a more stable and sharp pattern composed by straight and clear strings resembling the well-known fishbone structure.

Finally, the last phase of the spray structure is characterised by the sudden string distortion which comes from the alteration of straight and stable filaments to irregular



---

and rather shapeless spray. At the centre of the spray thickness, the change from the second to the third structure is described by a sudden increase in the RMS velocity and decrease in AMD values. Decrease in droplets velocity and diameter and an increase in RMS velocity are clear indication of secondary break up occurrence. When these effects are accompanied with high flow turbulence and recirculation/air entrainment, the spray development becomes unstable.

The spray visualisation with high-speed video also shows that as soon as the unstable structure is initiated then the strings tend to oscillate circumferentially (tangentially) and start to lose their individual well-defined angular position.

The PDA measurement scan in tangential direction showed a wavy velocity and droplet diameter profile, which confirms the presence of more strings and their uneven velocity/diameter distribution along the measurement path.

The overall spatial droplet size and velocity distribution map has confirmed the presence of the sequence of the three string structures mentioned above. In addition, it revealed the presence of a tumble motion propagating downward in the wake of the spray. Finally at the end of the injection at  $z$  locations of 70mm, from the injector exit and beyond, the droplet diameters become larger with an AMD of about  $15\text{ }\mu\text{m}$  partly due to the presence of spray residual from the spray front rim which have lost their momentum and it is unable to break up further, but also to the possibility of coalescence caused by droplets collision.

The summary of the mean Weber number along the spray jet shows an hyperbolic trend starting from the highest value of 27 at  $z=2.5\text{mm}$  (3.5 in jet direction) decreasing rapidly with the axial location so that at  $z=20\text{mm}$  (27mm in jet direction) the  $We$  has reached a value of 2 and it does not endure further reduction up to the lowest measured axial location. These results suggest the presence of a strong secondary breakup from tip of the injector up to  $z=10\text{mm}$ , break up and deformation between 10 to 20mm and then stabilisation of the droplets beyond 20mm.

### **Spray Recirculation and Air Entrained Motion**

The second part of this section focused on the analysis of the effect of surrounding air on the spray. More specifically, the same injector set up was employed to investigate the recirculation area and air entrainment by using PIV and 2D Mie scattering techniques. The 2D visualisation has revealed the presence of a pair of counter rotating vortices forming two recirculating spray rings at the inner and outer sides of

---

the spray cone. For the free injection at ambient condition and injection pressure 200 bar, the formation of the external wake is first observed at 1.0ms ASOI which occurs at about 20mm from the injector tip whereas upstream the spray jet seems undisturbed. For the rest of the sequence it can be observed that the outer vortex propagates along the jet direction progressively increasing in diameter whereas the inner vortex also grows progressively but its centre is also displaced toward the injector axis due to the dominating action of the outer recirculation.

The recirculation mechanism was then confirmed by PIV diagnostic on the same spray operating conditions. The formation of the external wake is in agreement with the PDA results in the spatial map at 0.9 ms ASOI which shows the presence of a vortex at about 20 mm from the tip. The PDA results also suggest that the recirculation near the nozzle exit is highly repeatable because it was consistently appearing in the mean velocity data over many injections.

Downstream, the recirculation becomes more unstable and transient varying its position injection by injection and therefore it becomes invisible (or averaged) to the mean velocity measurement obtained from PDA mapping. This instability could be related to the well-known issue of the spray-to-spray variation (flapping) as well as the observed unstable third type of string structure explained above.

The air entrained velocity field was analysed using PIV and LDV methods by seeding fine water droplets in quasi-still motion around near nozzle area. As the spray evolves a jet-like air motion with the horizontal component of the air velocity increases in intensity to about 10m/s and hits the spray near nozzle area. As the spray evolves further, the air motion expands so that at 0.33ms ASOI it is extended up to 8mm away from the nozzle exit. Finally at 0.63ms ASOI and onward, when the droplet velocity are reduced, the PIV images shows clearly how the air entrainment penetrates into the spray, wrapping the evolving external wake and initiating its formation with a horizontal velocity of 10m/s. The PIV sequence also showed how the air entrainment acts on the internal wake forcing it to be displaced toward the injector axis.

Comparison between PIV and LDV measurements at the same point showed reasonable agreement, which provided more confidence in the presented results. The LDV results of air entrainment at different injection pressures have shown a linear variation of the air velocity component normal to the spray surface in proportion to injection pressure. These, in turn, may influence the size of the air pockets inside the nozzle and thus the number of strings. It is expected that as the air entrainment



---

velocity increases the possibility of a break up in the air pockets become higher and therefore higher number of strings. This trend is also in agreement with the results seen in chapter 3 which show how the number of strings increases with the injection pressure

### **Parametric Study**

From PDA parametric study, it was found that an increase in injection pressure results in a higher maximum mean spray velocity being achieved. However, an equal increment increase of pressure did not necessarily result in an equal incremental gain in spray velocity due to the non-linear variation of the discharge coefficient with the injection pressure.

The mean droplet diameter graph showed that a part from the lowest pressure (50bar) the droplet size was less dependent on injection pressure, since the trends were similar. The graphs also suggested that higher injection pressures produce smaller droplet size only far from the injection exit whereas at the near nozzle region the effect of the longer droplet resident time which increases the evaporation has higher effect on the droplet size than the enhanced secondary break up produced by the increased relative velocity. All injection pressures showed a similar size distribution in the main body of the spray, being  $12.5\mu\text{m} \pm 3\mu\text{m}$ .

The longer the injection duration, the longer the mean velocity is maintained. Longer injection durations do not necessarily imply that a higher maximum mean velocity will be achieved, since 0.2 ms and 0.6 ms duration both displayed a maximum mean velocity of 200 m/s. It was found that perhaps the 0.15ms duration is not sufficiently long enough to allow the needle to open fully (achieve maximum lift), since its maximum spray velocity achieved was 25% less than all the other durations tested.

The last experiment described in this section was carried out in a constant volume chamber in order to simulate the operating condition of temperature and backpressure occurring in the real engine. PDA has been applied successfully to the measurement of piezo injectors to obtain axial velocity and fuel droplet size. The effects of injection pressure, backpressure and ambient temperature on fuel spray penetration, velocity distribution and droplet size were also determined.

In general, the velocity distribution shows a rapid increase in droplets velocity during the needle opening to a maximum value, which remains high during the main part of

---

injection, and then dropping fast during the closing of the needle.

The effect of backpressure at  $z'=2.5$  mm is not clear due the closeness of measuring point to the exit but at  $z'=10$  mm, the effect of backpressure is evident, as the backpressure increases the velocity of the droplet decreases. This lead to longer residence time of droplet hence evaporation taking place, which is evident from the decrease in droplets diameter. It was also noted from spray visualisation that the penetration of the spray decreases with increase in backpressure.

The effect of the injection pressure showed as the pressure increases the velocity of the droplet increases and the droplet diameter decreases due to the increase in drag hence resulting in enhanced secondary break up.

The increase in chamber temperature increases the velocity of the droplet due to decrease in gas density, which also leads to a decrease in droplets diameter for the enhanced evaporation rate.



---

## Chapter 5.

### *Spray characteristics in the Optical Engine*

#### 5.1. INTRODUCTION

This chapter describes the investigation of the spray characteristics of the pintle type injector mounted in an optical engine equipped with direct injection system and in particular, the analysis of the behaviour of different prototype of piezo injector under different operating conditions. The piezo type outwardly opening has the potential to overcome many of the typical problems related to spray-guided injection. The outwardly sealing has definitely solved the problems caused by the sac-volume present in the inward opening injector. The conical shape of the nozzle passage prevents from carbon deposit formation, which is a typical problem of the multihole injector. Furthermore, the hollow cone presents a better air utilization than the multi-hole with good performance of penetration during early injection and a negligible dependence of the spray angle from the backpressure; the latter is essential for spray-guided approach to be successful as it fully depends on spray stability. For this reason, during the evolution and development of the piezo type injector it was put big effort on preventing flapping and on enhancing spray stability.

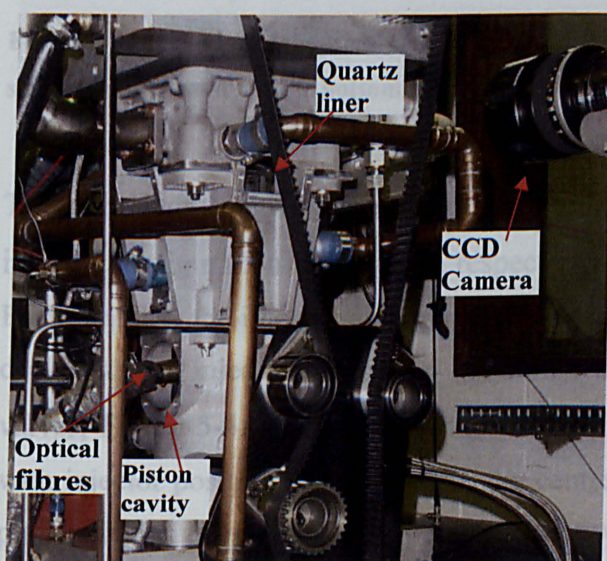
In this chapter, comparison between three Siemens piezo injector prototypes was analysed by visualising the spray injections through the transparent cylinder wall of the optical engine. The injectors have been investigated under different operating condition of injection pressures, injector needle lift and backpressure. Double injections were also tested under similar injection conditions as in the single injection test cases. The analysis aimed to compare the spray characteristics in terms of spray penetration, spray angle and stability. The post processing was based on the statistic computation of many set of images under different operating conditions. The object of the assessment consisted of the comparison of average and standard deviation images obtained from automated graphic processing.

#### 5.2. EXPERIMENTAL SET UP

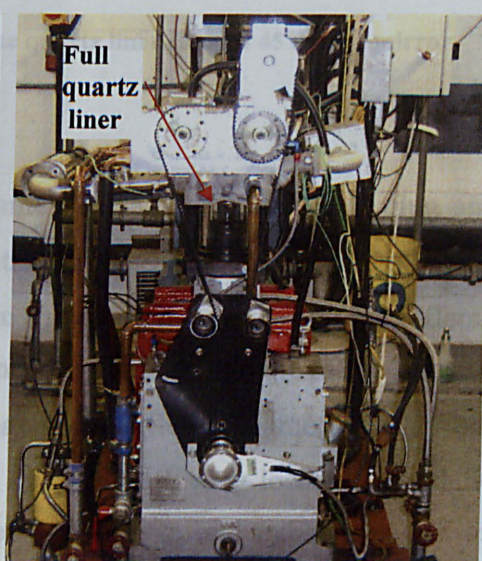
The Spray visualization has been performed using two Ricardo-Hydra optical engines supplied by BMW. The first model shown in Figure 5-1 was used in the first phase of

the investigation. The cylinder was characterised by a short portion of transparent cylinder liner (25 mm) made in quartz with full optical access from all four sides of the cylinder but with only front and back sides exposing the pentroof through an extension of the transparent window above the gasket. The partial optical access of this model resulted in a restricted internal visibility and a limited freedom of illumination.

A relevant improvement was achieved in the second Hydra model shown in Figure 5-2 and Figure 5-3 where the mono cylindrical engine is provided with a full stroke transparent liner in quartz, which allowed the internal visualization through the cylinder around the four sides of the engine head along the whole stroke.



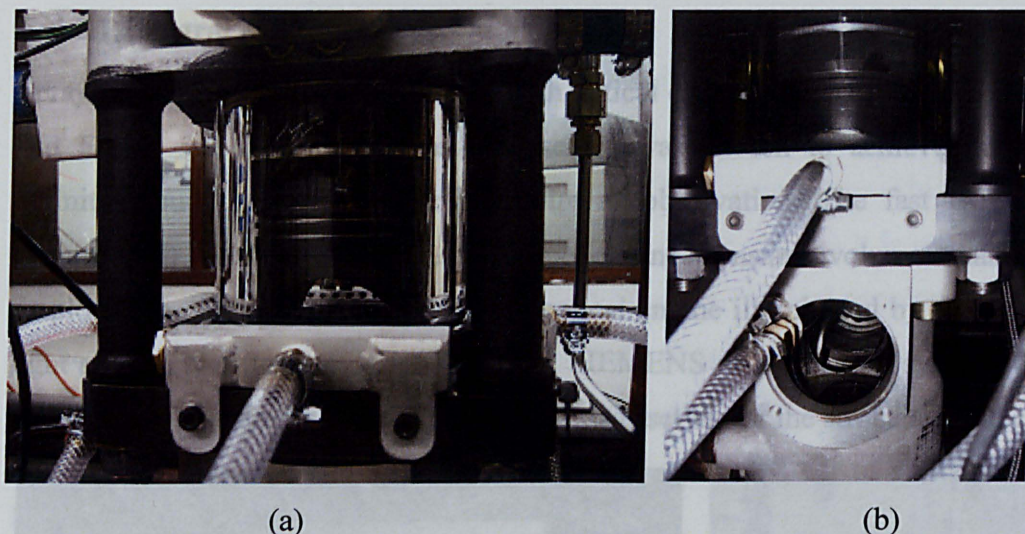
**Figure 5-1** First model optical engine with limited quartz window.



**Figure 5-2** Second model optical engine with full quartz liner.

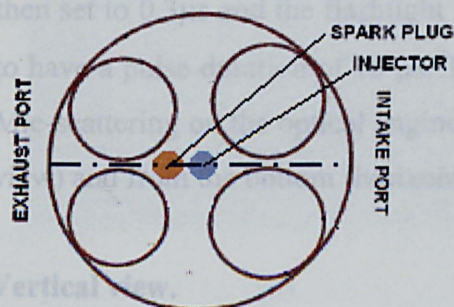
As a drawback, the full quartz liner solution had the effect of a decreased heat rejection capacity due to removal of the engine cooling system around the cylinder and as a result the friction generated between piston and quartz liner increased the liner temperature considerably, which was tackled using appropriate cooling systems of compressed air cooled by liquid nitrogen or ice. In both model the piston is equipped with head in quartz, which gives an additional optical way for visualization or lighting. In order to direct the optical path toward the combustion chamber through the piston window, a mirror is placed at the bottom of the piston inclined 45deg with respect of the light beam as shown in Figure 5-3 (b).



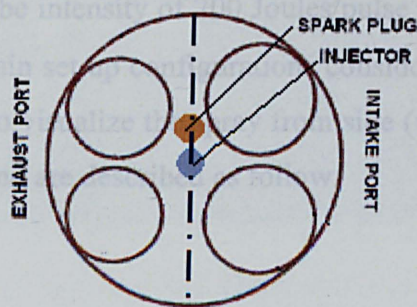


**Figure 5-3: Second model optical engine: (a) full stroke quartz liner (b) and 45 degree mirror situated in the cavity at the bottom of the piston.**

The two Hydra engines present a different flame deck layout with spark plug and injector configuration rotated with respect of intake and exhaust valves. In the former Hydra model, the injector and spark plug lay in the plane of symmetry of the flame deck with the injector located on the centre and the spark plug next to the exhaust valves, Figure 5-4. The latter Hydra version has got a different flame deck lay out with injector position still located in the centre but the spark plug located in a plane perpendicular to the symmetry plane in between the intake and exhaust valves as shown in Figure 5-5. As no firing test were carried out in the course of this investigation, the only consequence of a different lay out would be a slight change on the in-cylinder air motion produced by the spark plug protrusion which, as will be shown, has negligible effect on spray angle and stability.



**Figure 5-4 Flame deck configuration for first model Hydra engine.**



**Figure 5-5 Flame deck configuration for second model Hydra engine.**



### 5.2.1. Integral Mie scattering

Spray visualization was performed in both optical engine models shown in Figure 5-1 and Figure 5-2 and the best test rig set-up was chosen to achieve good image definition and the most meaningful point of observation. The fast CCD camera (Figure 5-6) used in the large-scale model and constant volume chamber was employed to obtain spray images in the optical engine illuminated by the same flash light and the two flexible optical fibres. A SIEMENS driver control system was used to trigger the injector and signal process unit was set up for the strobe and the camera.



Figure 5-6 Fast CCD camera in front of the engine cylinder.

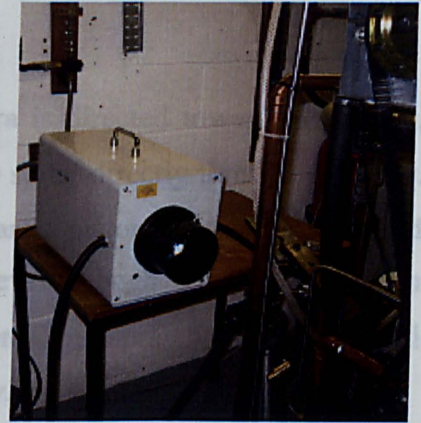


Figure 5-7 Flash light device on the left of the engine.

Due to the fast evolution of the spray, to obtain a satisfactory clear image the exposure time had to be very small. However, a too reduced exposure time could cause lack of light photons emission onto the cells of the CCD camera. Therefore, it was necessary to set an exposure time short enough to freeze the dynamics of the spray but long enough to obtain satisfactory bright images. The camera exposure was then set to  $0.3\mu\text{s}$  and the flashlight with a strobe intensity of 200 Joules/pulse was set to have a pulse duration of  $10\mu\text{s}$ . The two main set up configurations considered for Mie-scattering on the optical engine allowed to visualize the spray from side (vertical view) and from the bottom (horizontal view) and are described as follow.

#### Vertical view.

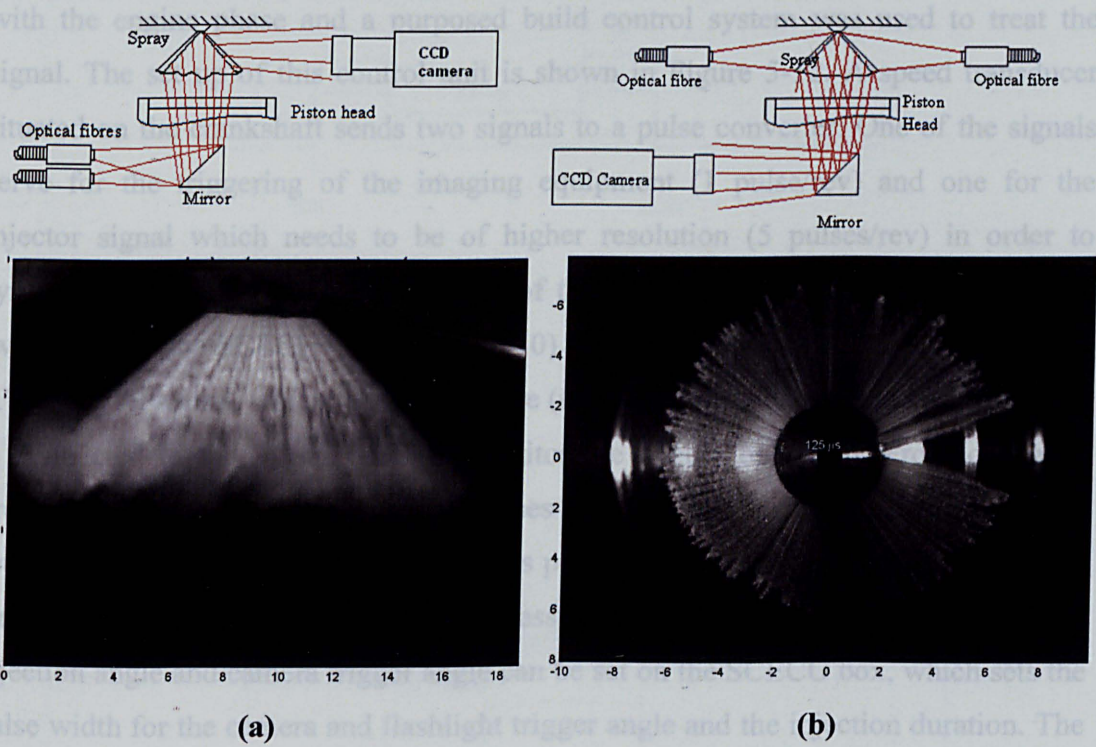
The camera is placed in front of the cylinder liner and viewing the spray motion along the cylinder axis as shown in Figure 5-8(a). In order to have more flexibility on the light arrangement, two optical fibres connected to the main flash light are used as light source. For the vertical view, the optimum light set up is achieved by directing



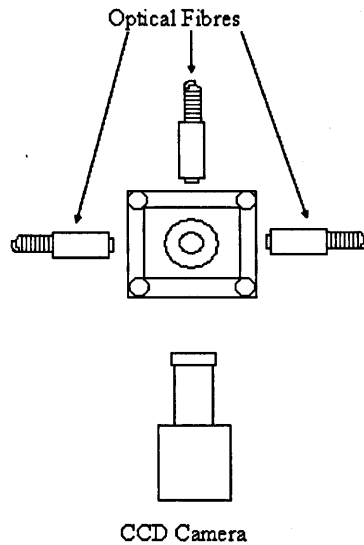
the fibres toward a mirror placed inside the cavity of the piston. The light reflected by this mirror inclined 45 degree is directed vertically through the quartz of the piston head. Once the beams reach the spray cone, the light is spread horizontally exiting through the quartz liner and reaching finally the CCD camera lens. This set up allows the frontal view of the spray of the outer surface of the cone as it is shown in Figure 5-8 and it will be employed to analyse the spray angle, vertical penetration and spray stability. A different illumination set up might be adopted by directing light from one fibre or both of them through other three free sides of the liner as shown in Figure 5-9.

**Horizontal view.**

To capture the bottom view of the spray the camera is directed toward the mirror, Figure 5-8(b). The optical fibres are illuminating the spray directly through the liner. The light is scattered by the spray through the transparent piston head and is reflected by the mirror toward the CCD camera. However, even though this view gives an overall image of the spray, it did not give information about spray angle and vertical penetration, which are the main objective of this study.



**Figure 5-8 Mie scattering Set up in the optical engine: (a) Vertical view set up (b) Horizontal view set up.**



**Figure 5-9 Available Positions of the optical fibres around the liner.**

### 5.3. SIGNAL CONTROL SET-UP

In order to obtain double injection Mie-scattering images, a sophisticated signal control unit was required. The imaging triggering equipment needs to be synchronised with the engine phase and a purposed build control system was used to treat the signal. The set up of this control unit is shown in Figure 5-12. A speed transducer situated on the crankshaft sends two signals to a pulse converter. One of the signals serve for the triggering of the imaging equipment (1 pulse/rev) and one for the injector signal which needs to be of higher resolution (5 pulses/rev) in order to synchronise the injector with the speed of the engine. The pulse converter delivers two signals to the SCECU box (Figure 5-10) and two signals to the AVL Indyset. The AVL Indyset signal, which provides engine (manifold, cylinder and exhaust) pressure, is connected to the PC in order to monitor the engine operation. From displayed pressure data on the PC, the software uses this information to calibrate the device setting zero at TDC. As the software reads pressure in the cylinder, the value of zero was then aligned with peak cylinder pressure at TDC. After that, the values for injection angle and camera trigger angle can be set on the SCECU box, which sets the pulse width for the camera and flashlight trigger angle and the injection duration. The high-resolution signal sent to the SCECU box for injection duration, is converted from 5pulses/rev to 1pulse/deg.

For the double injection, (Figure 5-11) the first injection duration ( $t_1$ ) was set on the SCECU box with respect to the start of the first injection (SOI1). As the injection



driver presents a certain lag between injection pulses due to the electronic response, the CCD camera was triggered with a delay of 0.08ms in order to capture the spray at end of injection (EOI).

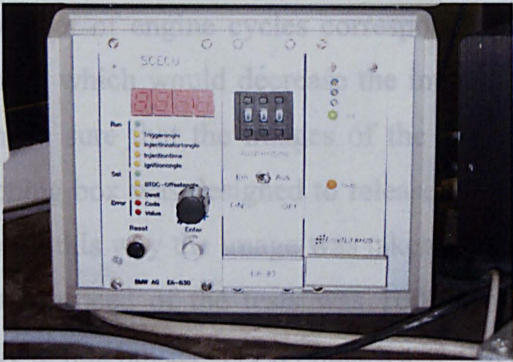


Figure 5-10 Control SCECU box.

The injector signal was being inverted in the SCECU box and the output signal was then sent to the double injection box (double injection box uses negative pulse). An additional pulse was produced and the delay and second injection duration ( $t_2$ ) were set with respect to the end of the second injection (EOI2), Figure 5-12, on the double injection box. From this box the two pulses had to be inverted again and be sent to the injector driver, which eventually feeds the injector at a predefined needle lift.

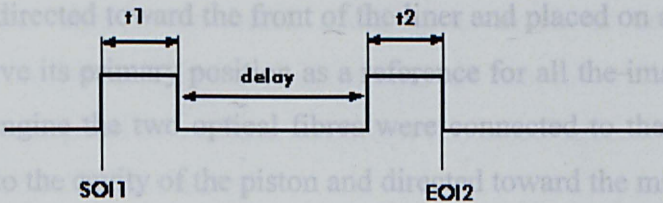


Figure 5-11 Square signal set for double injection.

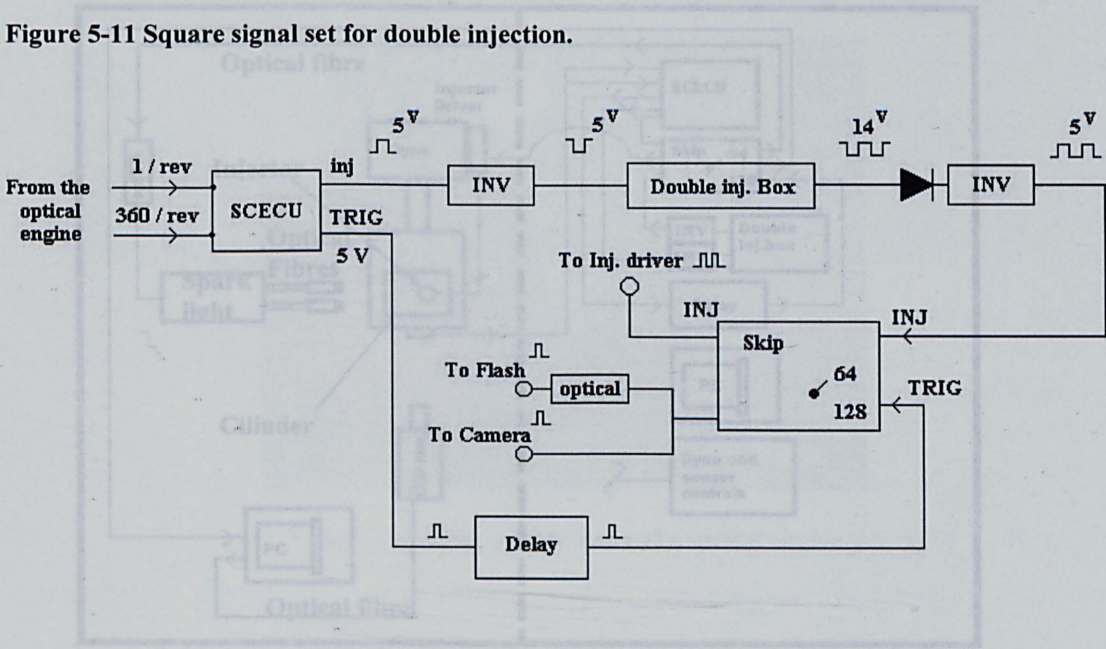


Figure 5-12 Synchronization System for Double Injection.

The other signal coming from the SCECU box was fed to the skip processor in order to treat it and send it to the imaging equipment. Since the spark light needs almost 8 seconds to recharge its capacitor, the skip processor set the control system to give an output every certain number of engine cycles corresponding to 8 seconds therefore avoiding useless injection, which would decrease the interval between liner cleaning events. However, to make sure that the images of the spray, were a representative steady sample, the skipping box was designed to release three pulses before enabling the pulse to the camera, in this way the image was taken just after having injected for four times. The operating speed of the tests was 1000 rpm and 2000 rpm, which corresponds respectively to one pulse every 64 pulses and 128 pulses.

### 5.4. TEST CELL LAY OUT

The test layout was arranged in two rooms as shown in Figure 5-13. In the main room, the optical engine and its auxiliary devices are placed in the centre of the cell whereas for safety reason the control system devices are placed in the adjacent cell separated by a wide glass window.

The camera was directed toward the front of the liner and placed on a stable basement in order to preserve its primary position as a reference for all the images obtained. At one side of the engine the two optical fibres were connected to the spark light unit, positioned close to the cavity of the piston and directed toward the mirror

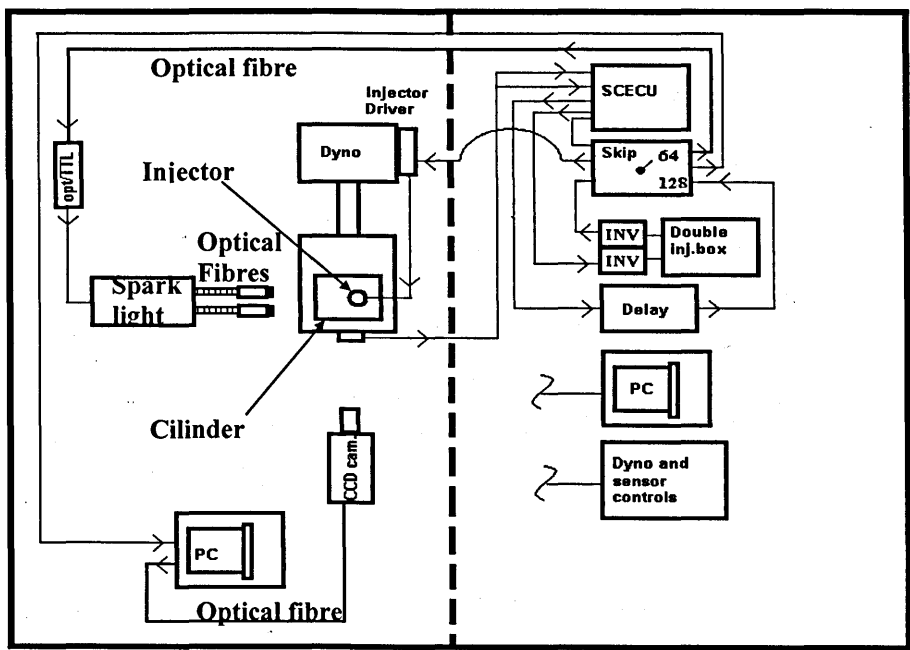
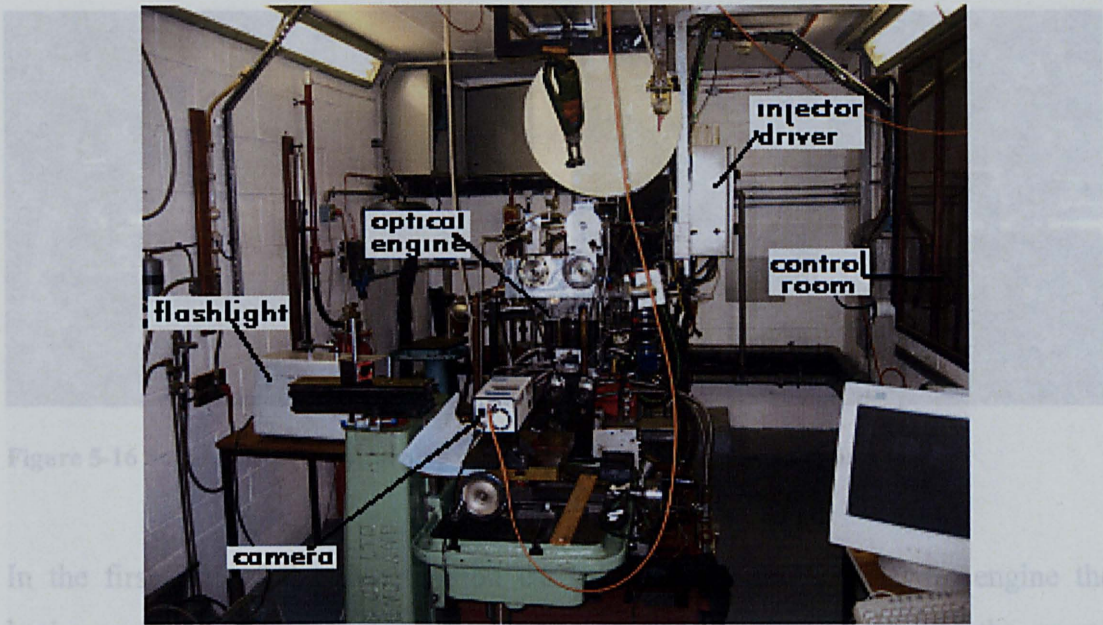


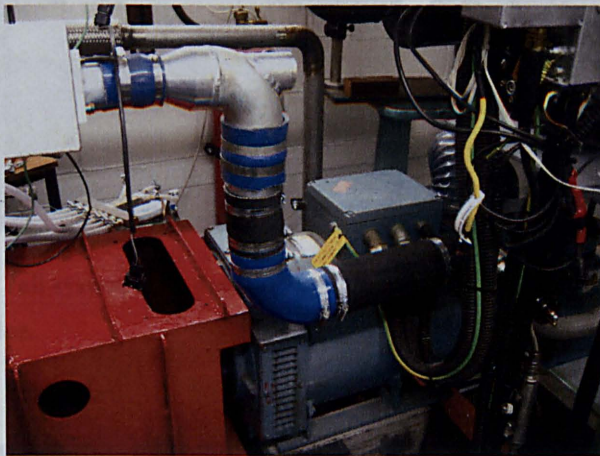
Figure 5-13 Test cell lay out and system and signal arrangement.





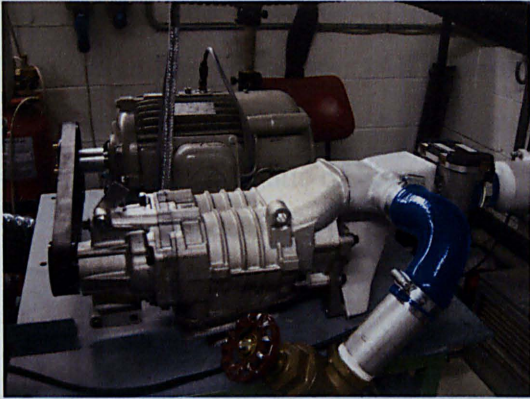
**Figure 5-14 Optical engine test cell lay out.**

The camera was positioned with a small inclination of 4 degree upwards, in such a way that the injector tip was displayed in the centre of the image and also to capture a better view of the injector tip itself, avoiding as much as possible any view interference with the gasket. Since the engine does not fire, the driving power moving the engine shaft is supplied by an electrical motor (Dyno), (Figure 5-15) placed on the same bed as that of the engine unit.

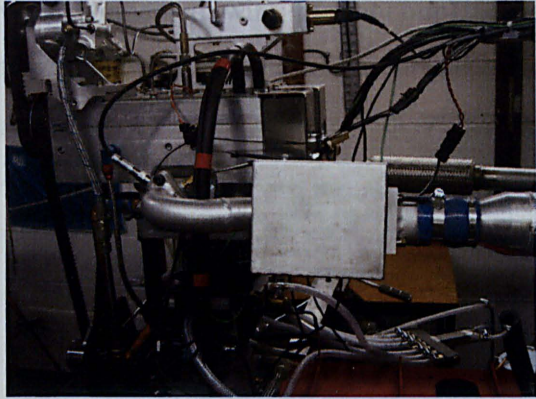


**Figure 5-15 Dyno used to drive the optical engine**



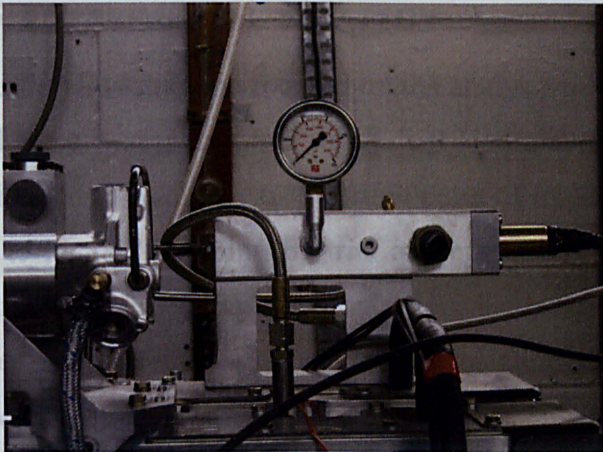


**Figure 5-16 Supercharger with turning vane**

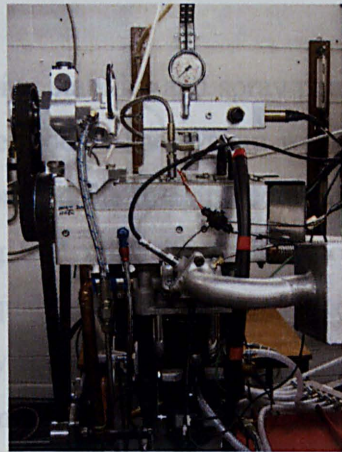


**Figure 5-17 Plenum chamber**

In the first part of the investigation carried out with the first Hydra engine the backpressure was uniquely depending on the crank angle position whereas the second engine model was provided with a supercharger, Figure 5-16, which allowed a more flexible cylinder pressure set up. This was located behind the engine and was driven by a motor driven by a belt. A by-pass intake system was introduced in order to enable or disable the supercharged air, as required, with the use of a turning vane.



**Figure 5-18 Common rail system with pressure gauge on top of the optical engine.**



**Figure 5-19 Right hand side view of optical engine.**

The air was then driven into the engine through the plenum chamber (Figure 5-17) in to the manifold, where a pressure transducer was fitted in order to give manifold pressure readings to the control unit. The rail pressure was set at 100bar and 200bar, by means of the high-pressure common rail system (Figure 5-18, Figure 5-19). In the



control room where the engine and signal controls are located, (Figure 5-21), pressure and temperature indicators, Figure 5-20, were connected with thermocouples and pressure transducer sensors. All control units were interconnected to synchronize and treat the signals from engine crank angle enabling injection and camera triggering according the schematic of Figure 5-12



**Figure 5-20** Engine temperature and pressure display unit.



**Figure 5-21** Engine and signal control unit.

## 5.5. EXPERIMENTAL STRATEGY

The first investigation focused on the analysis of spray stability and spray penetration and these were performed in the first Hydra engine model. The system was visually calibrated to find the exact starting point of injection and the imaging equipment was set to match this point, by trial and error, varying SOI until the desired point was found. After injection synchronisation, the image quality was adjusted and tested by capturing a set of images using single injection early at the end of injection and finally it was possible to proceed with the image acquisition at the actual operating condition. The main part of the investigation consisted of 31 single injection cases and 31 double injection cases each of which comprised of a set of 64 images. For double injection at high cylinder pressure a set of 64 images were taken for both EOI, for the other double injection cases only images at EOI of first injection.

The 64 images were then processed with a Matlab code, which produces a mean an RMS image for each operating condition. The statistical images were obtained respectively averaging and calculating the RMS of the level value of each pixel out of all 64 images. The mean image gives a representative view of the spray general



behaviour and shows the location of the main strings from which the repeatability of spray-to-spray behaviour can be deduced. The RMS image shows the variability of the spray pattern and it can be used to identify the degree of the spray satability. More specifically the RMS graphic operation produces an image with brighter areas where the gray level is more variable and therefore where there is a phisical light variation induced by object displacement (spray-to-spray variation). Since one of the aims of this investigation is the analysis of the flapping behaviour of the spray, the RMS image gives a good qualitative measure of the repeatability of the spray shape and thus of the entity of the spray flapping.

The parameters defining the operating condition of each case are:

- Injector model.** Three injector prototypes with different needle geometry were tested to establish the effect of the step between cartridge internal diameter and needle external diameter. The step is evident when the injector is closed which consists in a positive or negative edge between needle and cartridge rims. The injector with diameter of the needle which is larger than the cartridge will be called positive step Inward Seal Band injector (+ISB) while vice versa, negative step Inward Seal Band injector (-ISB) as can be seen in Figure 5-22. The third injector presents needle diameter of the same size as the cartridge and therefore with no step when the injector is close. This prototype is named standard inward seal bend (SSB) which is also the real size injector correspondent to the large-scale model described in the third chapter.

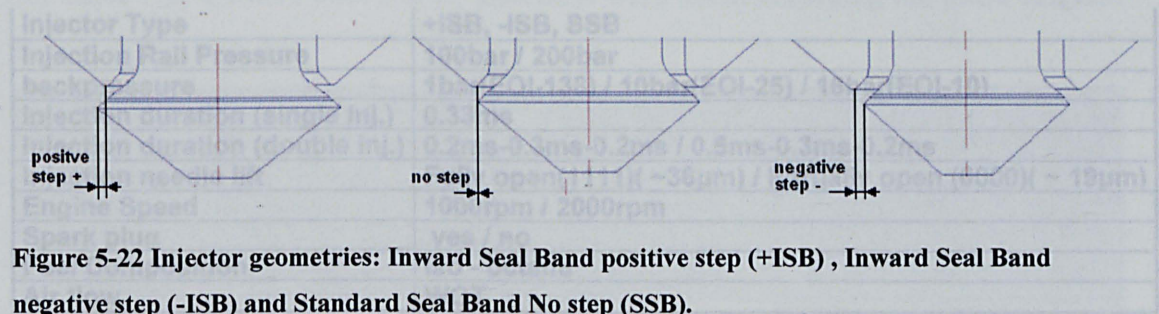


Figure 5-22 Injector geometries: Inward Seal Band positive step (+ISB) , Inward Seal Band negative step (-ISB) and Standard Seal Band No step (SSB).

- Backpressure.** Three different in-cylinder backpressures were considered. As the spray behaviour at homogenous condition (full load) is of much interest as well as late injection (part load) the three most representative conditions were chosen at the early intake stroke phase (~180degBTDC), 10deg BTDC and 25deg BTDC
- Injection rail pressure.** Two injection pressures (100bar and 200bar) were considered to investigate the effect of rail pressure on the spray stability and on the



penetration.

- **Needle lift.** As described in the previous chapters the piezo injector presents the characteristic of a variable maximum lift, which can be adjusted by the activation of the injector piezo bodies. To investigate the effect of the lift on the penetration and spray angle two lifts were analysed: maximum lift (full piezo body activation:1111) and minimum lift (minimum piezo body activation:0000).
- **Engine speed.** The engine speed has a strong effect on the in-cylinder air motion. Tumble and swirl are strongly affecting the spray stability and therefore it was decided to observe the spray behaviour for two engine speeds: 1000 rpm and 2000 rpm. Due to vibrational problem on the engine, it was not possible to push the engine to higher speeds than 2000 rpm.
- **Spark plug.** The effect of the spark plug on the spray stability was observed by assessing wheater in-cylinder air motion is affected by cylinder head protrusions. For same operating conditions, the spray stability was compared with and without sparkplug.
- **First/second injection duration.** For double injection, the effect of the first injection duration may influence the intensity of the wakes and the in-cylinder air motion, which could consequently affect the stability of the second injection. Two injection durations ( $t_1 = 0.2\text{ms}, 0.5\text{ms}$ ) were chosen and compared at different operating conditions.

All the aforementioned operating conditions are summarised in Table 5-1 below.

<b>Injector Type</b>	<b>+ISB, -ISB, SSB</b>
<b>Injection Rail Pressure</b>	<b>100bar / 200bar</b>
<b>backpressure</b>	<b>1bar(EOI-138) / 10bar(EOI-25) / 16bar(EOI-10)</b>
<b>Injection duration (single inj.)</b>	<b>0.33ms</b>
<b>Injection duration (double inj.)</b>	<b>0.2ms-0.3ms-0.2ms / 0.5ms-0.3ms-0.2ms</b>
<b>Injection needle lift</b>	<b>Fully open(1111)( ~36<math>\mu\text{m}</math>) / Partially open (0000)( ~ 19<math>\mu\text{m}</math>)</b>
<b>Engine Speed</b>	<b>1000rpm / 2000rpm</b>
<b>Spark plug</b>	<b>yes / no</b>
<b>Fuel Composition</b>	<b>Iso - octane</b>
<b>Air flow</b>	<b>WOT</b>

Table 5-1 Operating parameters and Engine set up.

For single injection the duration was fixed at 0.33 ms for all the 31 cases whereas the remaining parameters were varied case by case according Table 5-2.

Rail pressure		200 bar					100 bar		
Injector	RPM Spark Plug	1000 -	1000 -	1000 -	1000 X	2000 -	1000 -	1000 -	1000 -
	Bitposition	intake stroke	(EOI-25) 10bar	EOI-10 (16bar)	EOI-10 (16bar)	EOI-10 (16bar)	intake stroke	(EOI-25) 10bar	EOI-10 (16bar)
-ISB (step: -) ti=0.33ms	0000	6	12	4	4K	-	10	14	8
	1111	5	11	3	3K	-	9	13	7
+ISB (step: +) ti=0.33ms	0000	16	22	2	2K	2_2000	20	24	18
	1111	15	21	1 (25)	1K	1_2000	19	23	17
SSB (No step) ti=0.33ms	0000	29	31	27	-	-	-	-	-
	1111	28	30	26	-	-	-	-	-

**Table 5-2 Operating conditions under which the images were obtained for single injection investigation. (First set of results)**

In order to test the repeatability of the tests after long periods and following parameter variation the 25th case was set equal to the first case and compared as case reference.

The comparison between spray image with and without spark plug was carried out only for the first four cases whereas the effect of engine speed was observed only for case1 and 2. For cases1 to 4 a series of 55 spray evolution images were acquired. The camera was triggered to get an image every 0.025ms for the whole cycle so that the spray development could be visualised as a function of time including first and second injection. After defining the penetration distance, the tip velocity could then be calculated and compared for the two cases.

After the single injection imaging was completed, all the cases were repeated for the double injection mode by triggering the camera at the end of the first injection except for cases 1 to 4 where both end-of-injections were taken according the pulse diagram shown in Figure 5-24.

Rail pressure		200 bar						100 bar		
Injector	Imaging Time	EOI 1	EOI 2	EOI 1	EOI 2	EOI 1	EOI 2	EOI 2	EOI 2	EOI 2
	Bit-position	intake stroke	(EOI-25) 10bar	EOI-10 (16bar)	EOI-10 (16bar)	intake stroke	(EOI-25) 10bar	EOI-10 (16bar)	EOI-10 (16bar)	EOI-10 (16bar)
-ISB (step: -)	0000		6-2		12-2	4-1	4-2	10-2	14-2	8-2
	1111		5-2		11-2	3-1	3-2	9-2	13-2	7-2
+ISB (step: +)	0000		16-2		22-2	2-1	2-2	20-2	24-2	18-2
	1111		15-2		21-2	1-1 (25-1)	1-2 (25-2)	19-2	23-2	17-2
SSB (No step)	0000		29-2		31-2	27-1	27-2			
	1111		28-2		30-2	26-1	26-2			

**Figure 5-23 Test conditions for double injection investigation. (case No – injection No)**



The imaging signal (which corresponds to the visualisation of the spray phase on the screen) follows the same pattern of the injection signal; however, the timing of EOI1 and EOI2, SOI1 and SOI2 are delayed due to the difference in lag response between imaging and injection apparatus.

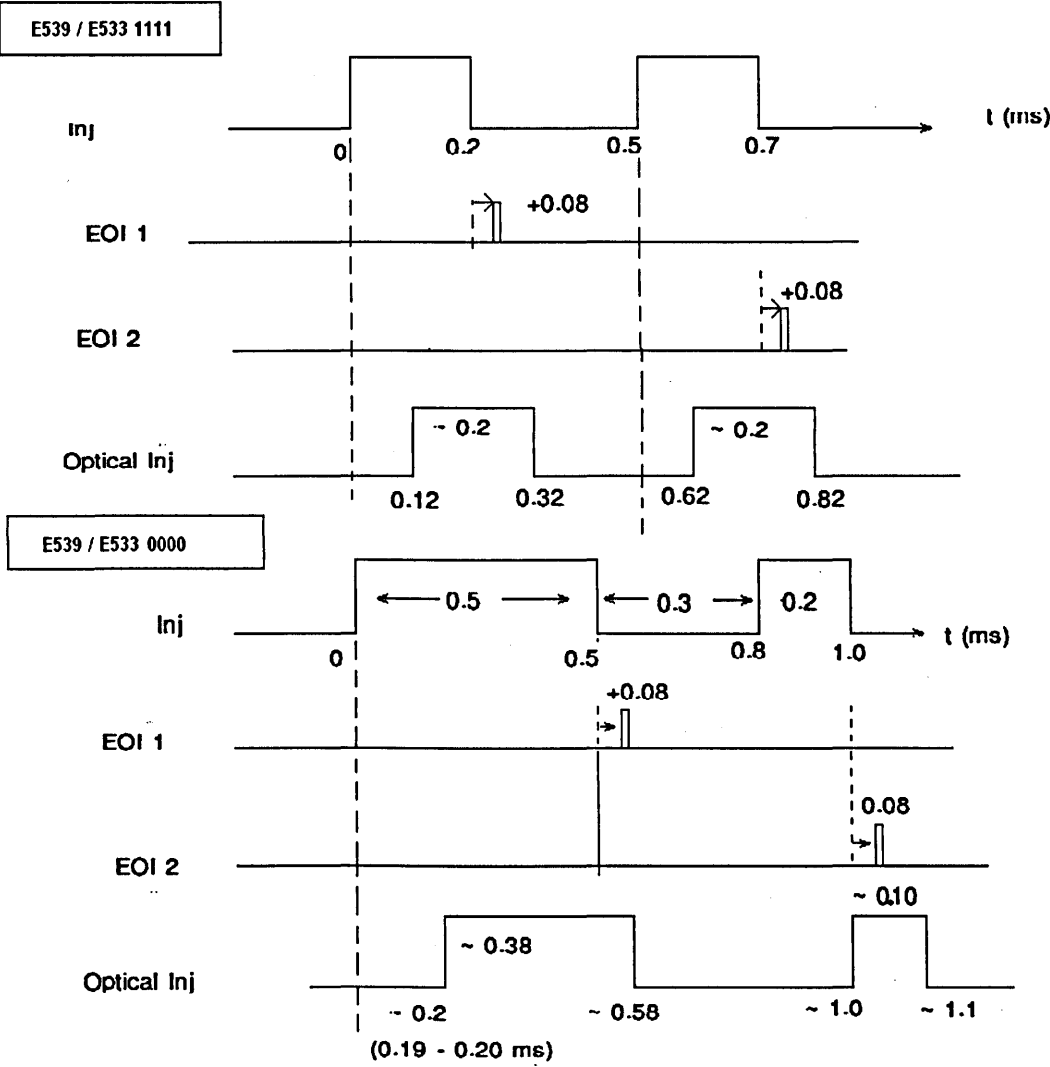


Figure 5-24 Synchronization System for Double Injection.

The black and white images obtained from the CCD camera were converted from 16-bit to JPEG for visualisation purpose only. For statistical processing (Mean, RMS), spray angle and penetration, the images were processed in b16 format by automated codes. All the spray images reported in this angle analysis are marked by rows of red crosses distant 10mm from each other to represent the reference scale.

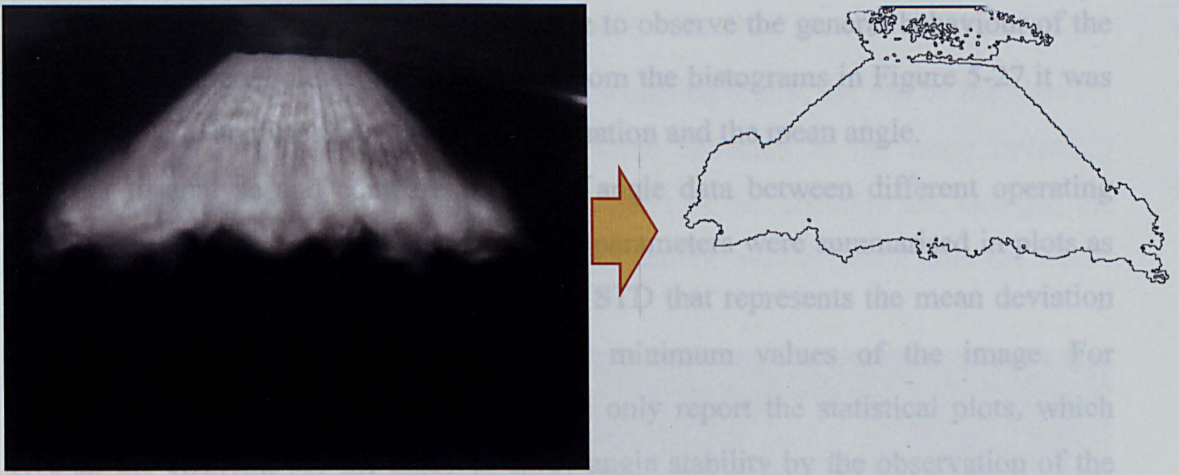


Figure 5-25 Image Processing procedure.

### 5.5.1. Spray Angle Analysis

For the spray angle analysis, the contour was first determined by fixing a threshold to the pixel level variation as depicted in Figure 5-25. The spray angle determination was performed automatically enclosed between injector tip and a fixed axial distance. For each individual spray image the angle between the axis and a segment was measured starting from the injector exit and laid on the spray contour.

The overall spray angle was defined as twice the angle between that segment and the spray axis. Both sides and the overall angle were performed for all the images for each case; an example is shown in Figure 5-26.

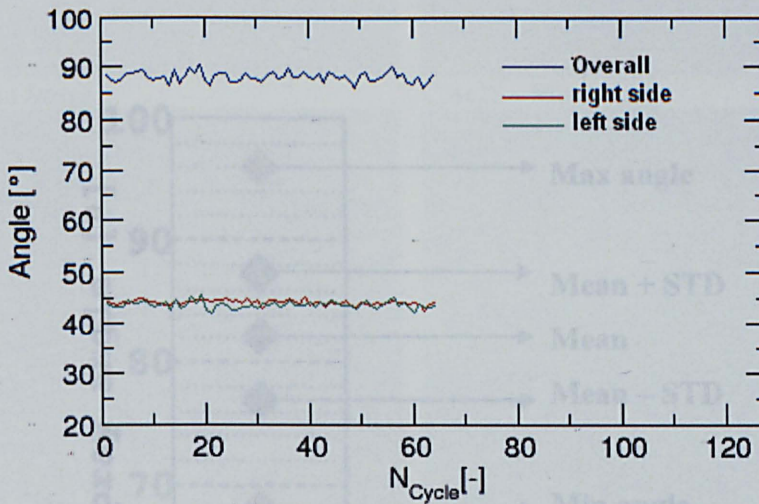


Figure 5-26 Spray angle for each image cycle.



From plot in Figure 5-26 it was then possible to observe the general behaviour of the spray through the whole set of images and from the histograms in Figure 5-27 it was then possible to analyse the spray angle fluctuation and the mean angle.

In order to analyse and compare the spray angle data between different operating conditions the more representative statistical parameters were summarised in plots as shown in Figure 5-28 reporting the mean,  $\pm$  STD that represents the mean deviation from the mean value and maximum and minimum values of the image. For conciseness, the following comparisons will only report the statistical plots, which give all the elements for the study of spray angle stability by the observation of the STD and of the range of spray angle variation given by maximum and minimum angles.

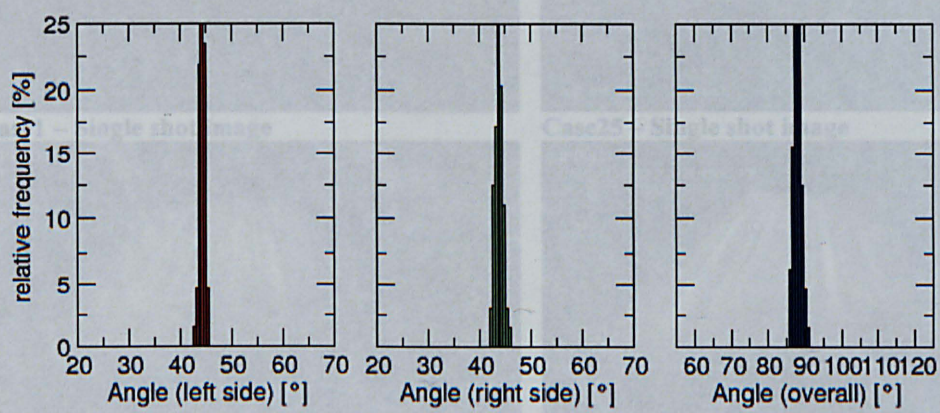


Figure 5-27 Histograms for left side angle, right side angle and overall angle.

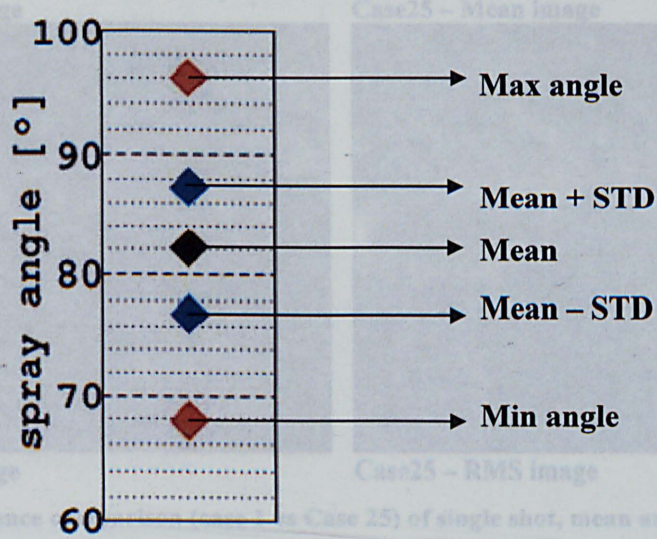


Figure 5-28 Statistical spray angle value for a set of 64 images.



5.6. SINGLE INJECTION: RESULT AND DISCUSSION , mean and RMS images.

As mentioned in the previous session, at the beginning and at the end of the tests for injectors +ISB and -ISB, sets of images were collected at the same operating condition in order to see whether some disturbance or modification had changed the original equipment setting or whether the spray pattern were different after the whole set of image acquisitions. fact, in the mean image the strings appear as straight

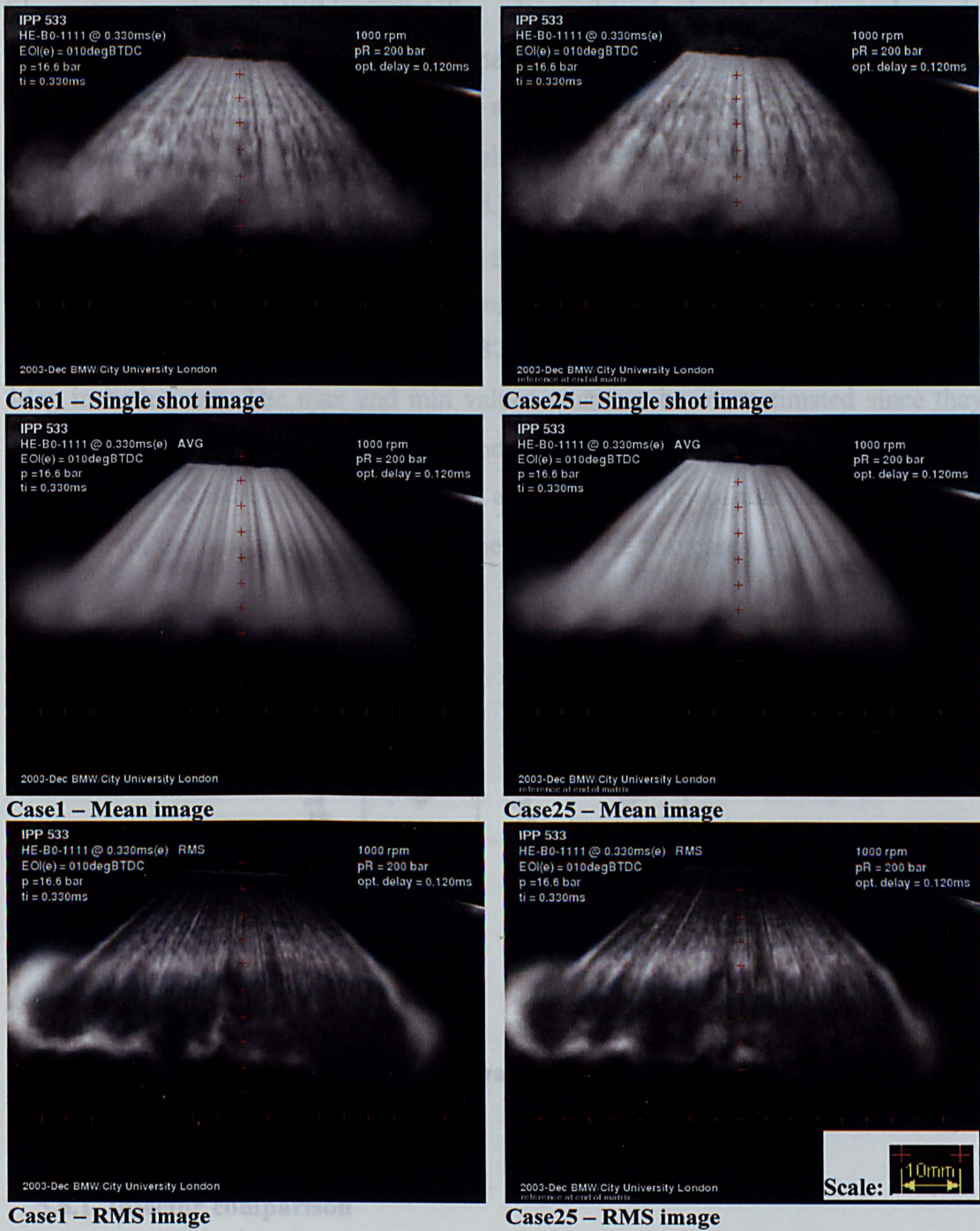


Figure 5-29 Reference comparison (case 1 vs Case 25) of single shot, mean and RMS spray images for same operating condition.

Figure 5-29 presents such comparison between cases 1 and 25 which show good



degree of similarity between the single shot (instantaneous), mean and RMS images. It can be seen from the mean images that the strings are very well defined even over an average out of 64 images thus showing a strong repeatability of the string pattern. It is not the same for the circumferential undulations conferring a curly aspect to the strings visible in the spray sample of the first case which resemble a Kelvin-Helmholtz instability. In fact, in the mean image the strings appear as straight filaments meaning that this instability along the single string is a dynamic phenomenon which does not occupy the same position in every image. In the comparison, it is possible to recognize the same spray pattern, only rotated around the spray axis due to the imprecision in replicating the same identical position when mounting the injector on the cylinder head. The RMS images show white areas in the recirculation zone for both cases and in general, the bright contour seems equally distributed in both images. Finally, the angles statistic in Figure 5-30 shows a very nice match of the mean angles which is 87deg for both cases and the RMS is about 1deg in both cases. The max and min values must not be overestimated since they represent the picks of the set of images and they may be due to isolated events. Such results give a measure of the repeatability and comparability of this study and a good reference for the image acquisition taken between these two cases.

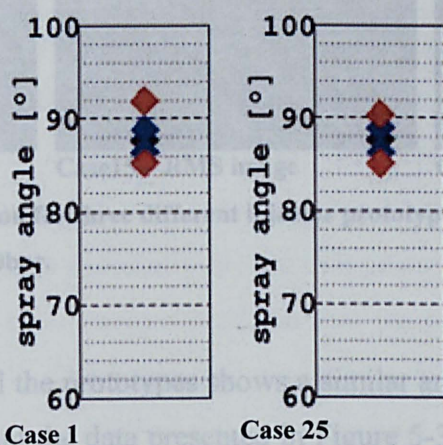


Figure 5-30 Angle comparison for the same operating condition. (Case 1 and Case 25)

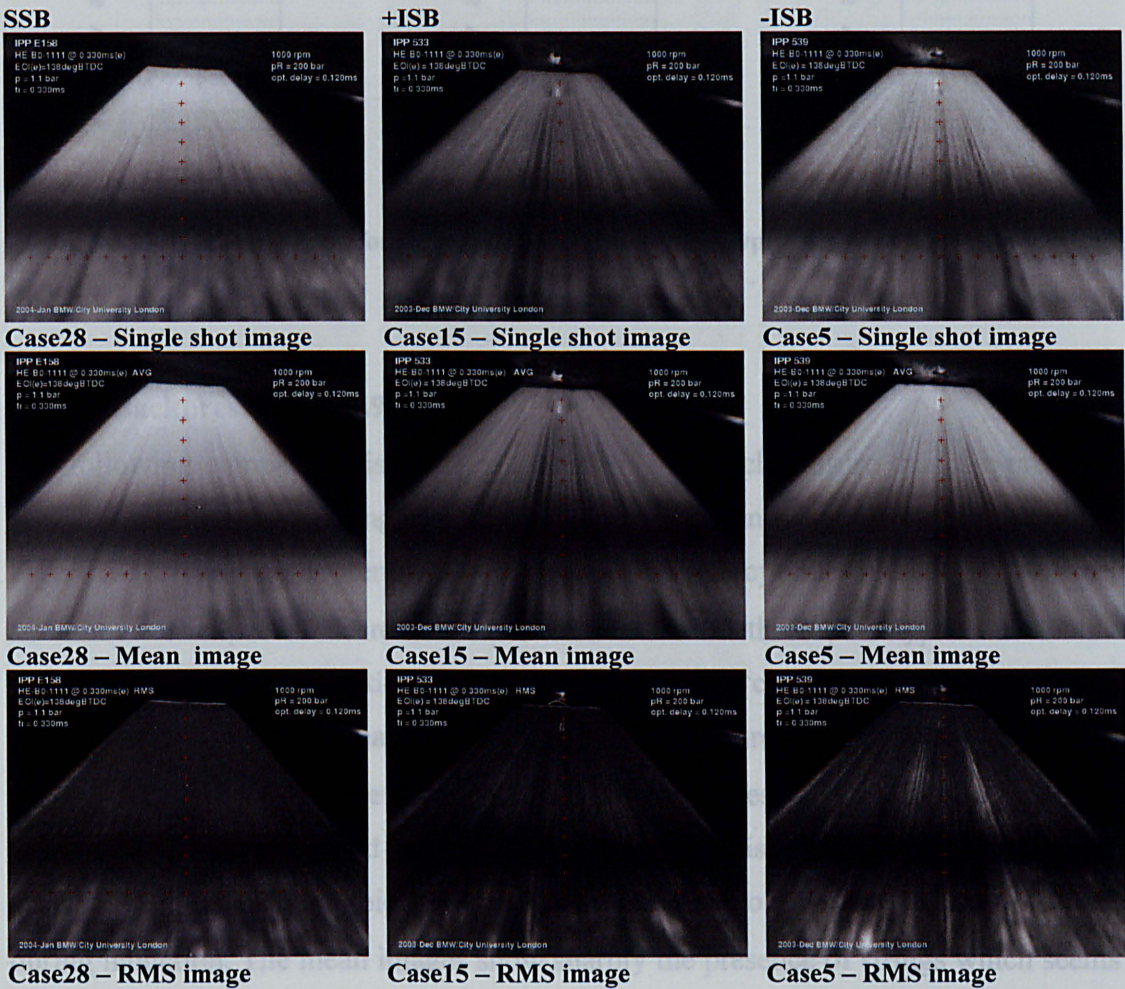
5.6.1. Injector comparison

5.6.1.1. Backpressure: ambient condition

The first comparison takes in consideration the three prototypes described in the previous section at the same operating conditions of full lift (Bit position 1111),



engine speed 1000 rpm and injection pressure of 200 bar. The images were taken at intake stroke phase and therefore at ambient cylinder pressure. The string pattern of the SSB seems to be less defined than for the other prototypes; however even the RMS images do not show significant differences in the image deviation.



**Figure 5-31 Image comparison for three different injector prototypes. Bit position 1111, 1000rpm, Pb=1.1bar, Pi=200bar.**

The angle analysis for all the prototypes shows a similar angle varying from 87deg to 90deg as it is evident from the data presented in Figure 5-32. The RMS is very small (~1deg) which means that this operating condition is very stable for all the three injector geometries.



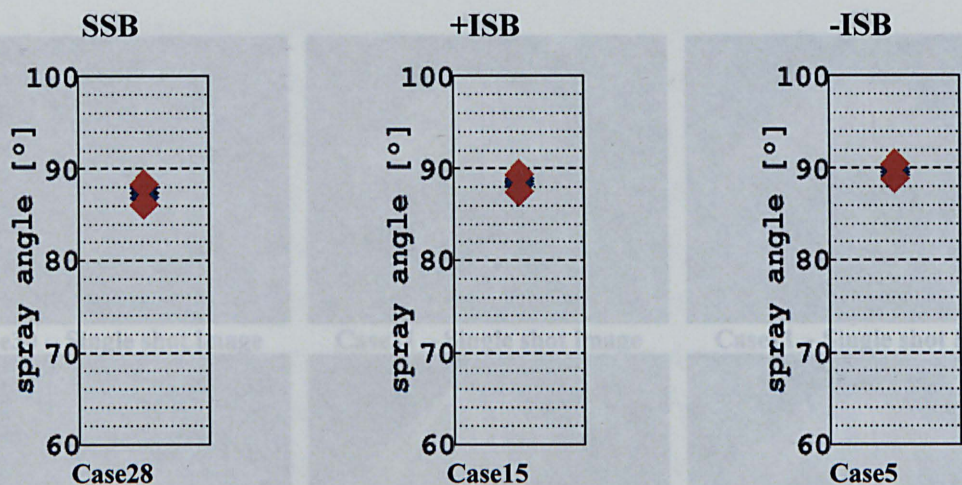


Figure 5-32 Angle comparison for three different injector prototypes. Bit position 1111, 1000rpm,  $P_b=1.1\text{bar}$ ,  $P_i=200\text{bar}$ .

#### 5.6.1.2. Backpressure: 10.9bar

The following comparison is made at a much higher backpressure than the previous case by injecting fuel during late compression stroke and the results are shown in Figure 5-33. The images were taken at 25deg BTDC (in-cylinder pressure of 10.9bar) and show an expected decrease in penetration for all three prototypes due to the increased in drag. In addition, the strings pattern is “curlier” than the strings at ambient condition, which may be due to an increase in circumferential instability that causes undulation along the strings. The SSB prototypes on the left seem slightly asymmetrical and projected toward the sparkplug. This effect was absent in the previous comparison at ambient condition probably due to the milder effect of tumble during induction. The mean images show sharply the presence of strings which seems very repeatable although a variation in curvature may be suggested by the bright area revealed by the RMS images especially for the ISB prototypes. As the bottom bright rim is equally thick for each injector it seems that the penetration deviation is the same for the three models. The angle analysis, Figure 5-34, also confirms a higher angle variation for the SSB, which has also a smaller angle than positive and negative step injectors.



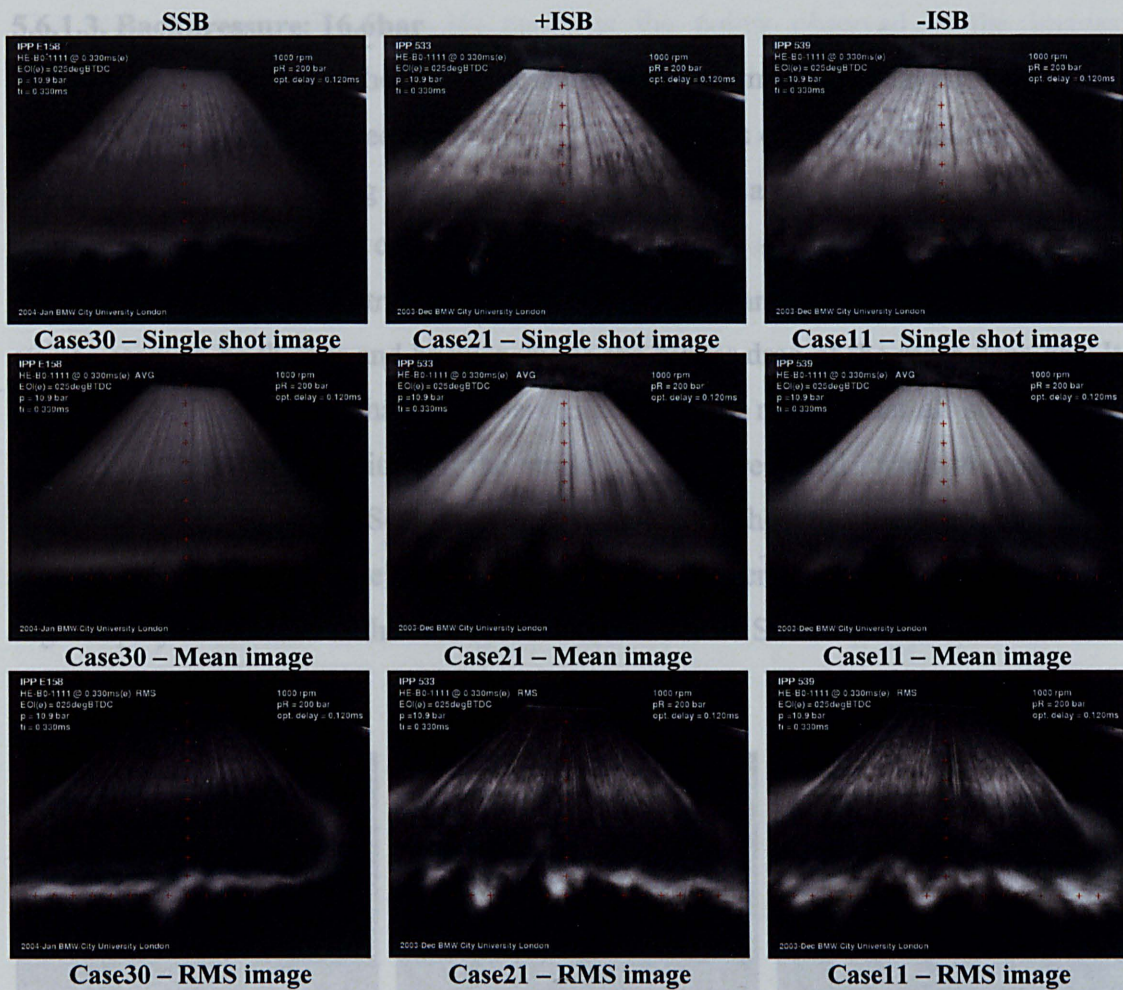


Figure 5-33 Image comparison for the three different injector prototypes. Bit position 1111, 1000rpm, Pb=10.9bar, Pi=200bar.

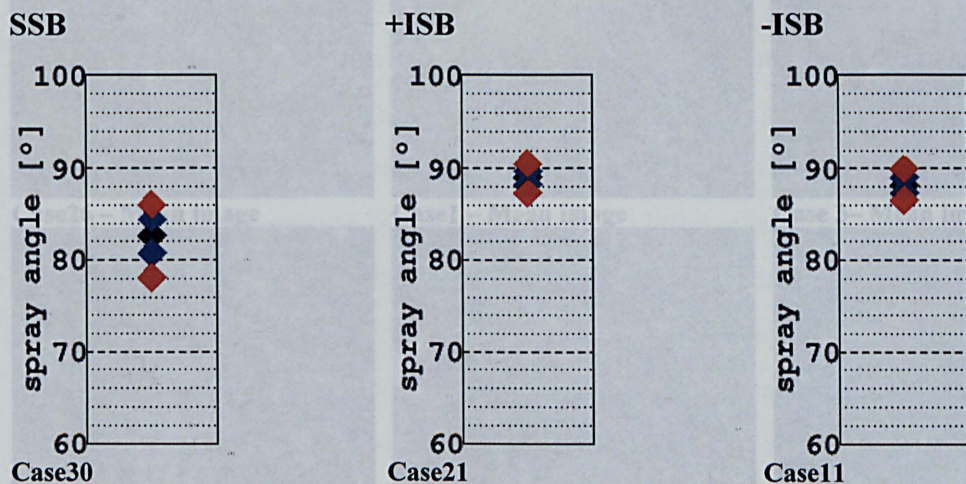


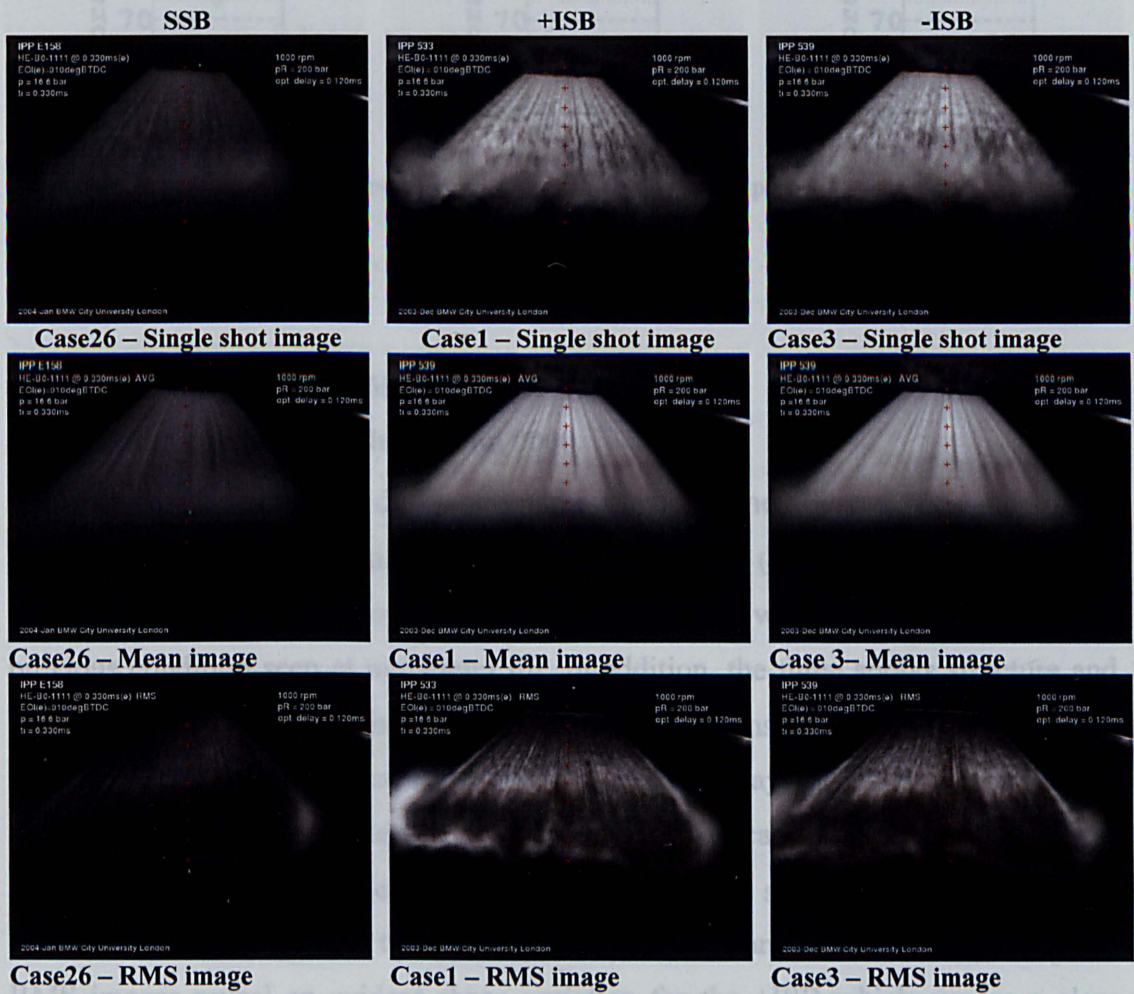
Figure 5-34 Angle comparison for the three different injector prototypes. Bit position 1111, 1000rpm, Pb=10.9bar, Pi=200bar.



**5.6.1.3. Backpressure: 16.6bar**

The comparison at the highest backpressure was performed by delaying the end of injection (EOI) just 10degree before TDC. This phase is extremely important as it is adopted at part load during stratified charge operation and it represents one of the main challenges of the GDI concept.

A further decrease in penetration is noticeable for all three prototypes and even the strings seem to be thicker and bushier due to the higher drag of the more dens gas. It must also be emphasised that the observed comparison reveals that all strings have maintained their individuality and the string pattern is repeated for all the operating conditions. The Standard Seal Band still seems stretched toward left and with a smaller cone angle than the two ISB injectors. However the RMS images shows a higher spray fluctuation in the recirculation area with the Standard Seal Band



**Figure 5-35 Image comparison for the three different injector prototypes. Bit position 1111, 1000rpm, Pb=16.6bar, Pi=200bar.**



The angle analysis, (Figure 5-36) confirms the points observed in the images especially for SSB injector, showing a much lower angle (78deg) than for the ISB, which is almost 10 degree larger.

For all three tested backpressures, the higher standard deviation of the SSB is associated with the higher backpressures, which has also shown to cause higher angle instability.

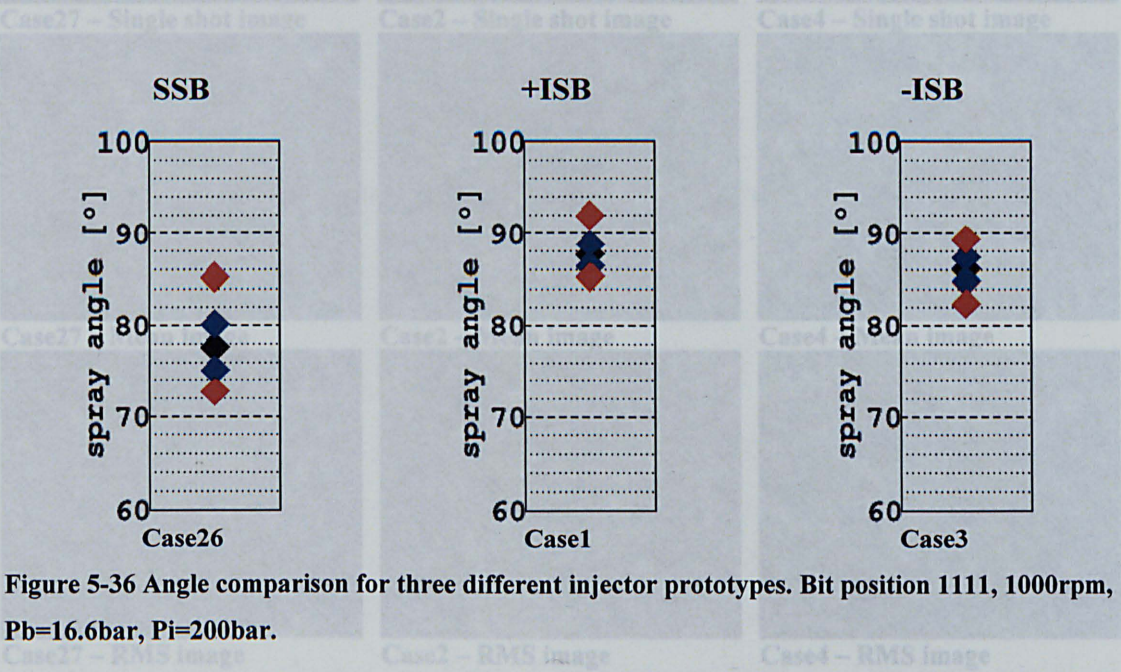


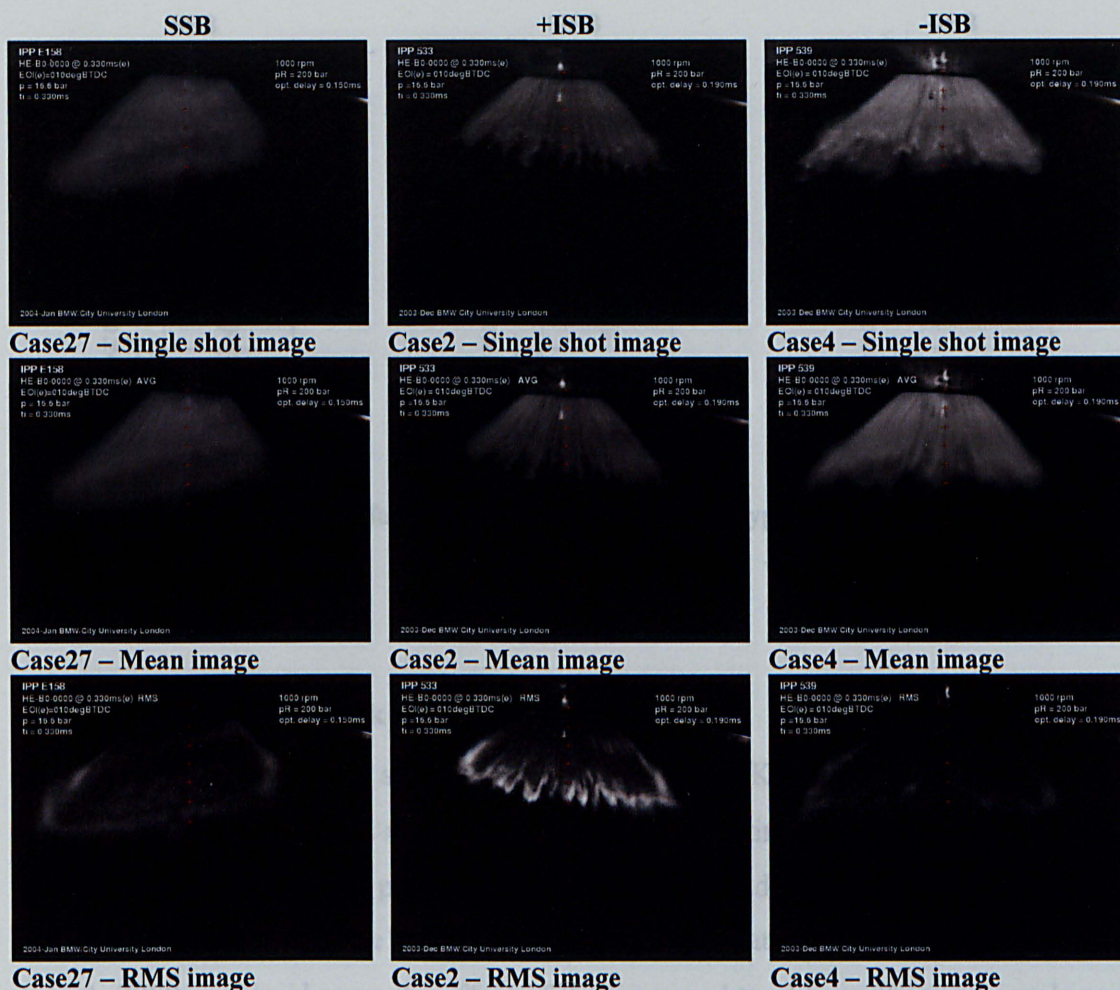
Figure 5-36 Angle comparison for three different injector prototypes. Bit position 1111, 1000rpm, Pb=16.6bar, Pi=200bar.

### 5.6.2. Backpressure: 16.6bar,

#### Minimum needle Lift: bit position 0000.

The following comparison differs from the previous one (Figure 5-35 and Figure 5-36) by the needle lift which is now set to minimum (0000) (~19µm). The most evident variation appears to be the spray penetration, which is about half of the previous condition seen at maximum lift. In addition, the three sprays structure and shape look now more different to one another. For instance, the -ISB in case4 presents the most symmetrical shape and a more dens spray, the +ISB in case2 shows the most sharper string pattern and finally the SSB in case27 is characterised by a blurry structure with an accented asymmetry which here seems to be mainly caused by lack of homogeneity in the needle sealing rather than for air flow motion. The RMS images reveal an evident shape variation for the +ISB which expose a clear bright rim all around the spray profile.





**Figure 5-37 Image comparison for three different injector prototypes. Bit position 0000, 1000rpm, Pb=16.6bar, Pi=200bar.**

The comparison of the angles within the three injectors does not show significant differences in terms of STD, which is similar for the three prototypes. However, the comparisons with the previous maximum lift conditions show an increased angle variation for both ISB injectors while almost unvaried for the SSB injector. Both -ISB and SSB present the same mean angle observed in the previous comparison whereas the +ISB shows a drop of about 10degree.

Overall it seems that the needle lift reduction produces a detrimental effect on the spray stability which is specially felt by SSB and + ISB whereas the negative step Standard Seal Band is more robust and insensitive to the needle lift set up.



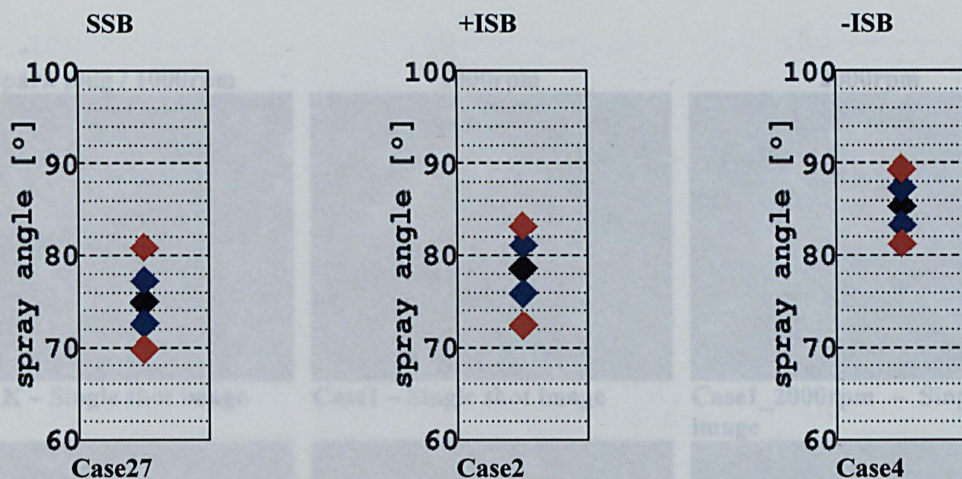


Figure 5-38 Angle comparison for three different injector prototypes. Bit position 0000, 1000rpm, Pb=16.6bar, Pi=200bar.

### 5.6.3. Influence of Spark Plug and Engine speed

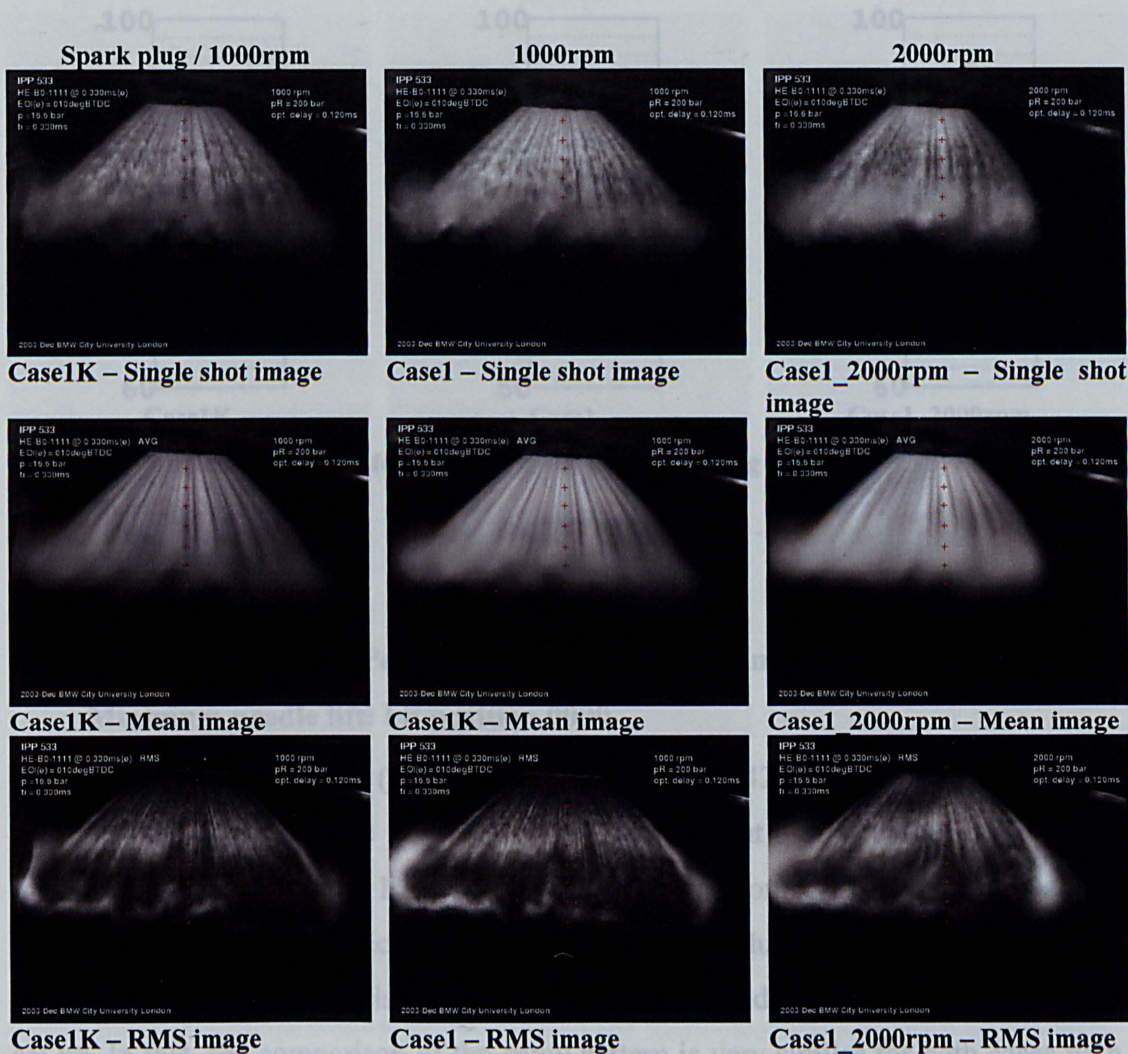
This comparison between spray structure with (case1K) and without (case1) the presence of spark plug was made under the same operating conditions of in cylinder and rail pressures, injector prototype and maximum needle lift set up. However, the reference condition (case1) is being compared at different engine speed (case1\_2000rpm) to observe the effect of the increased tumble on the spray angle and its stability. It was also observed whether the presence of the spark plug affects the spray and the in-cylinder air motion.

#### 5.6.3.1. Injector prototype: Positive step Inward Seal Band (+ISB).

##### Minimum needle lift: bit position 1111

The comparison of Case1K (K stands for Kerze which is the German translation for spark plug) with spark plug presence and reference Case1, Figure 5-39, shows no difference between single shot, mean and RMS images. That, it is not the case in the comparison between 1000rpm and 2000rpm engine speed which shows that the spray is pushed by the tumble towards the sparkplug. The RMS image of Case1\_2000rpm evidences also a higher variation in the recirculation area which suggests an increase of instability with engine speed. As it will be described at the end of this chapter, the increase in engine speed results in a better recirculation, which was observed in the 2D Mie scattering associated to an extended and non-uniform recirculation area.





**Figure 5-39 Spray comparisons for different speed and spark plug presence: +ISB, Bit pos. 1111, Pb=16.6bar, Pi=200bar.**

As mentioned for the full lift, the increase of speed showed a tendency of the spray to move toward the spark plug, but in this case (minimum lift) it is less evident probably because of the low lift. The spray pattern is very similar for all three cases. As expected from the observation of the processed images, although the mean angle is equal in all three cases at high engine speed an increase of STD can be observed as affect of the increased air motion and turbulence.

On the other hand, the presence of spark plug does not produce any variation or difference in mean angle, which means that the effect of the spark plug protrusion on the in-cylinder air motion is irrelevant. The comparison between case1 and case1k also confirms the consistency and repeatability of cases running with similar operating condition.



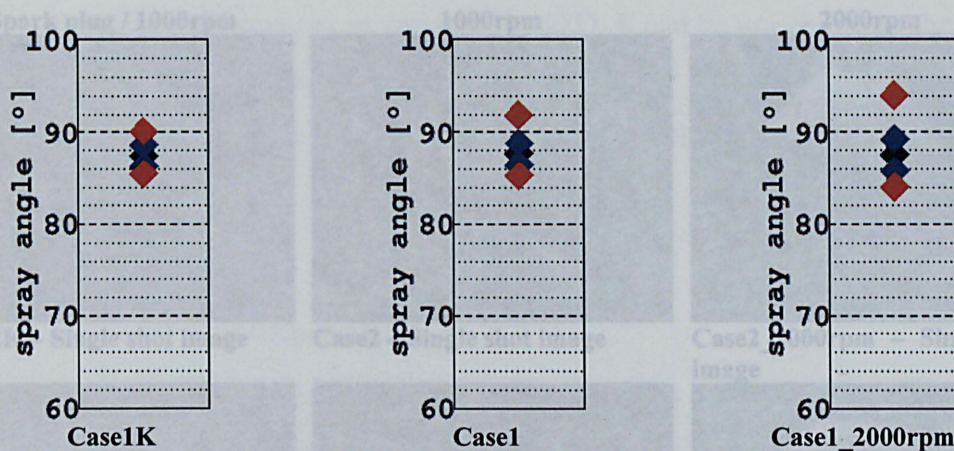


Figure 5-40 Angle comparisons for different speed and spark plug presence: +ISB, Bit pos. 1111, Pb=16.6bar, Pi=200bar.

#### 5.6.4. Injector prototype: Positive step Inward Seal Band (+ISB).

##### Minimum needle lift: bit position 0000

The following comparison (Figure 5-41 and Figure 5-42) is similar to that of the previous case study (Figure 5-39 and Figure 5-40) but at a different needle position that is now set to minimum lift (0000). In the previous comparison, the results at full lift did not show any significant influence of the spark plug and also at minimum lift the difference in brightness is probably caused by an accidental change in the lighting set up. In fact, the comparison of the spray pattern is very similar for both cases with and without spark plug, for the single shot, mean and RMS images.

As mentioned for the full lift, the increase of speed showed a tendency of the spray to move toward the spark plug, but in this case (minimum lift) it is less evident probably due to the smaller penetration of the spray. The RMS image at 2000rpm engine speed presents a very bright boundary not only in the recirculation areas but also at the bottom profile which is even more accentuated than for maximum full lift suggesting higher penetration variability.

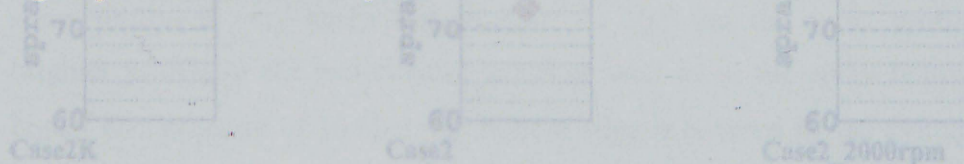


Figure 5-42 Angle comparisons for different speed and spark plug presence: +ISB, Bit pos. 0000, Pb=16.6bar, Pi=200bar

The mean angle appears higher for the operating condition with spark plug, while



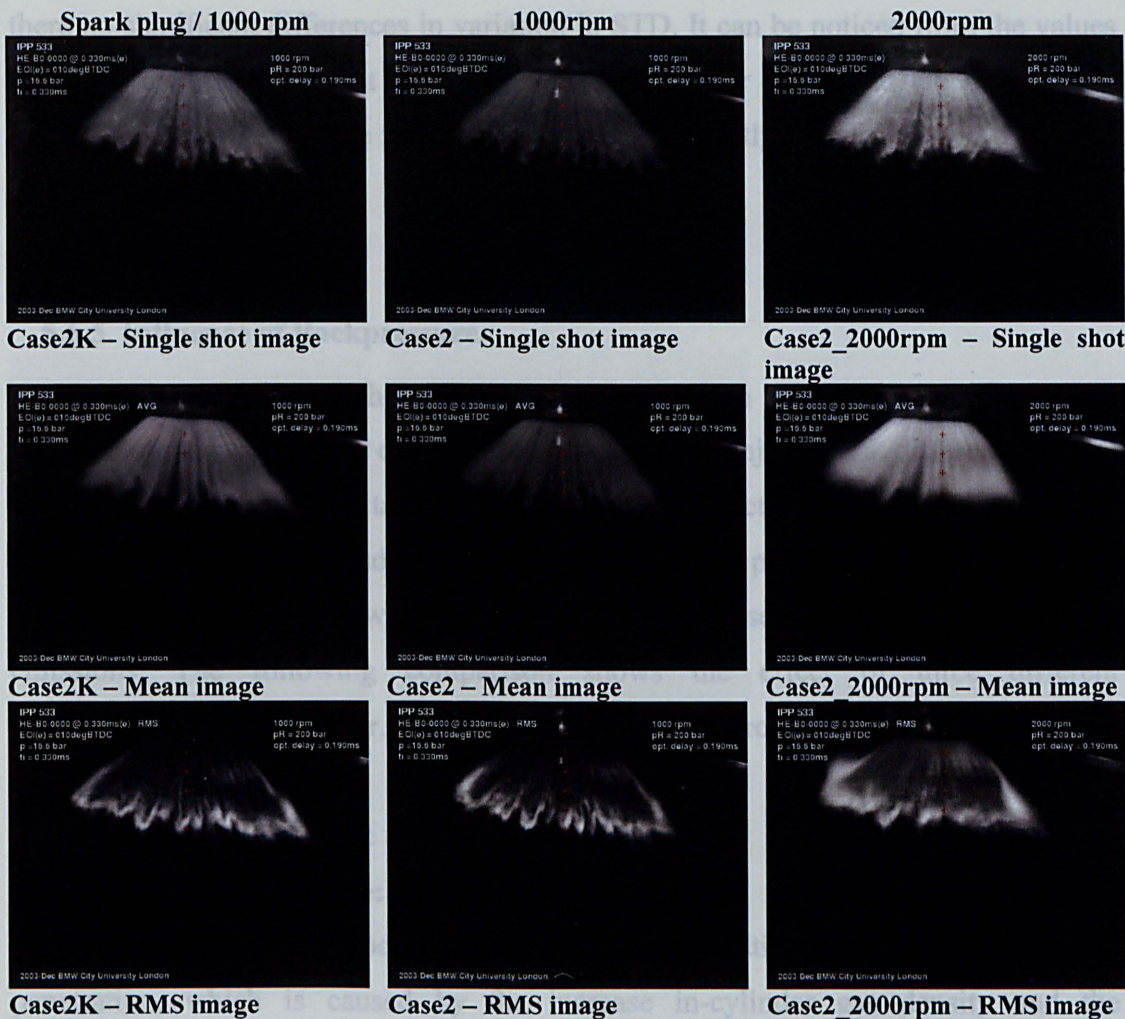


Figure 5-41 Spray comparisons for different speed and spark plug presence: +ISB, Bit pos. 0000, Pb=16.6bar, Pi=200bar.

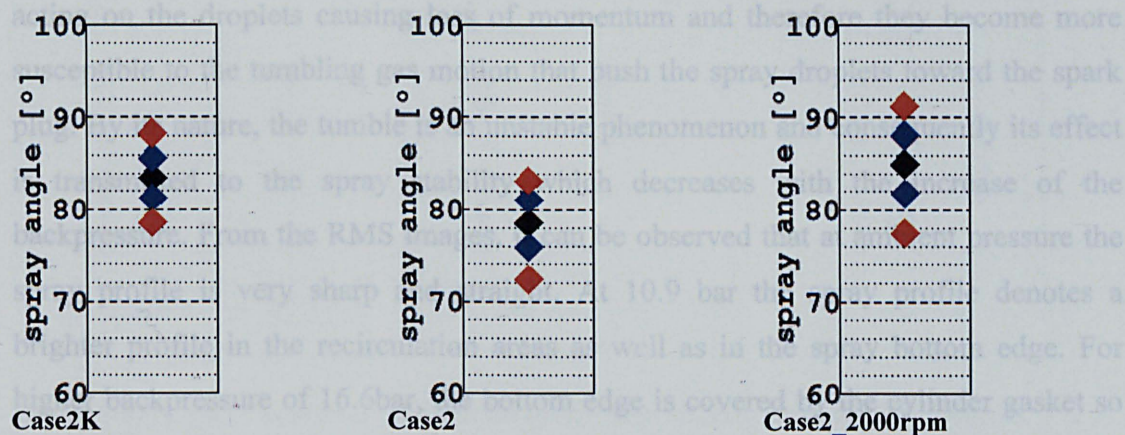


Figure 5-42 Angle comparisons for different speed and spark plug presence: +ISB, Bit pos. 0000, Pb=16.6bar, Pi=200bar'

The mean angle appears higher for the operating condition with spark plug, while

---

there no significant differences in variation in STD. It can be noticed from the values at higher engine speed that the spray tends to become wider and the mean angle results higher as well as the flapping which results slightly higher than the other two cases.

#### **5.6.5. Influence of Backpressure.**

As previously mentioned the GDI concept is based on the possibility to vary the injection mode based on the engine load, which implies injections at different cylinder pressures. It becomes important the capability of the injector to provide a stable spray with the potential to self adjust the penetration as the piston advances in order to avoid wall impingement which otherwise would cause unburned and increased emissions. The following comparison shows the effect of three different backpressures (1bar, 10.9bar, 16.6bar) for each injector prototype.

##### **5.6.5.1. Injector prototype: Standard Seal band (SSB)**

###### **Injection pressure: 200bar**

One of the main effects produced by backpressure elevation is evidently the drop in penetration, which is caused by the increase in-cylinder gas density and the consequent raise of drag. The spray shape seems to be also affected by the backpressure that affects the spray axial-symmetry by the enhanced effect of the air motion. In fact, the raise of density of the surrounding gas amplifies the drag forces acting on the droplets causing loss of momentum and therefore they become more susceptible to the tumbling gas motion that push the spray droplets toward the spark plug. By its nature, the tumble is an unstable phenomenon and consequently its effect is transmitted to the spray stability which decreases with the increase of the backpressure. From the RMS images, it can be observed that at ambient pressure the spray profile is very sharp and straight. At 10.9 bar the spray profile denotes a brighter profile in the recirculation areas as well as in the spray bottom edge. For higher backpressure of 16.6bar, the bottom edge is covered by the cylinder gasket so that a clear evaluation of the spray instability is not possible.



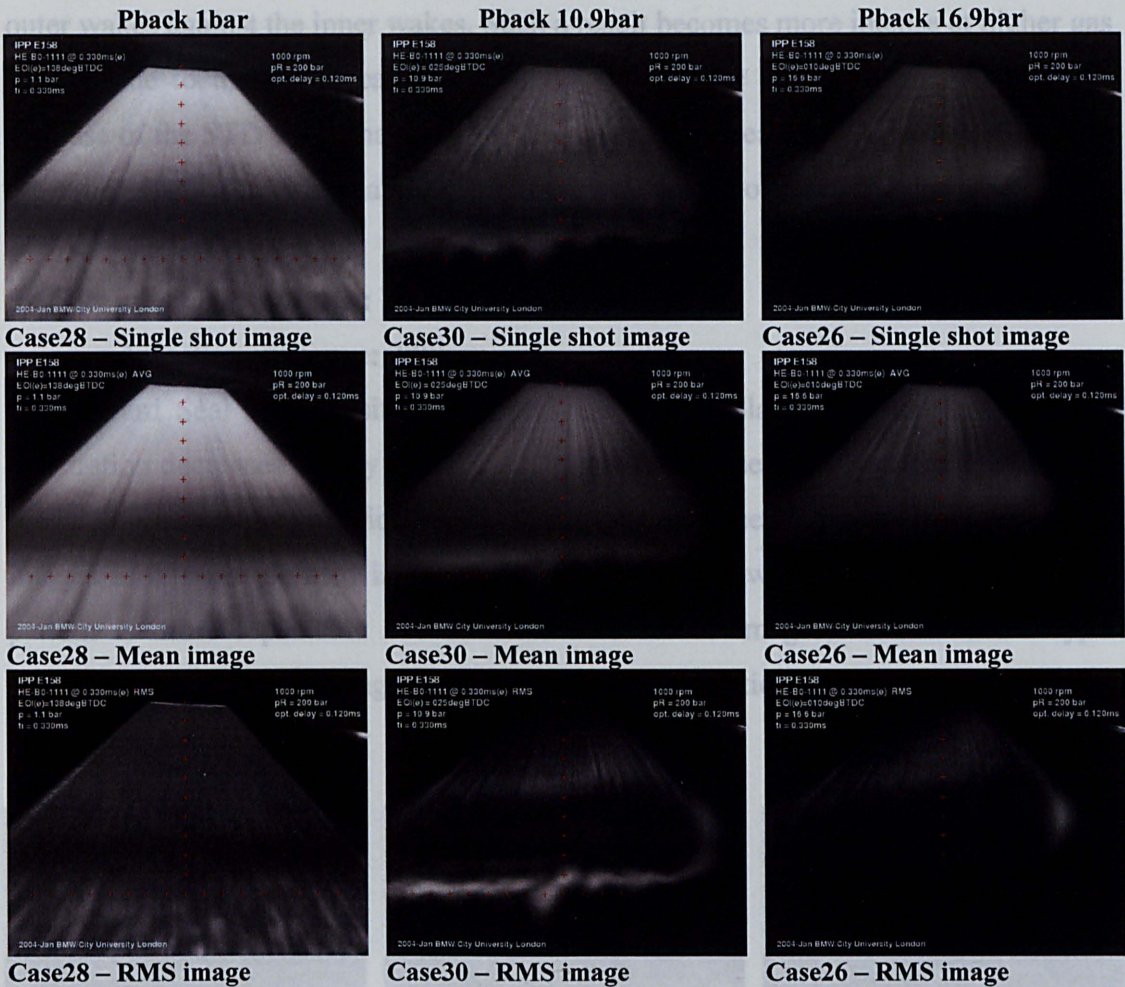


Figure 5-43 Spray comparisons for different backpressures: SSB, Bit pos. 1111, 1000rpm,  $P_i=200\text{bar}$ .

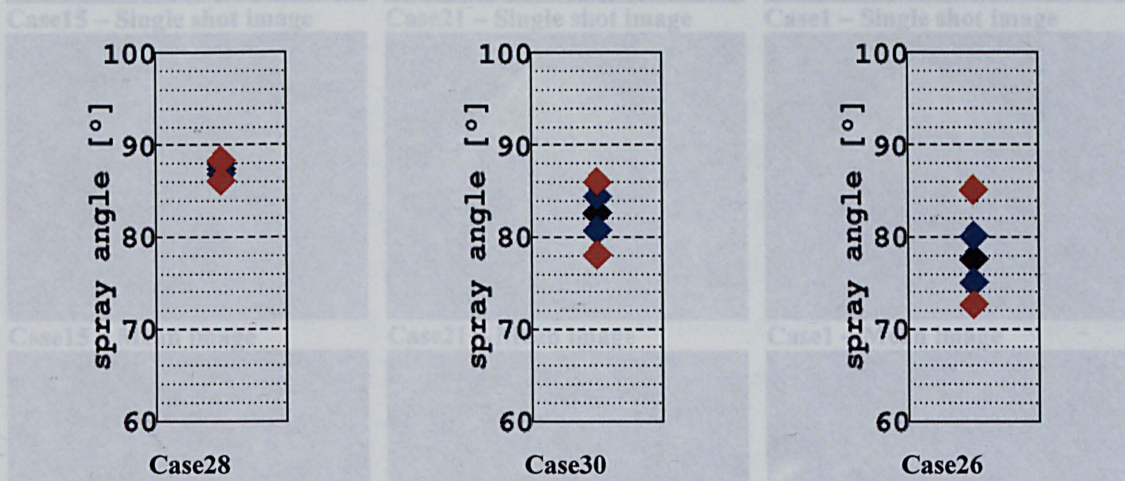


Figure 5-44 Angle comparisons for different backpressures: SSB, Bit pos. 1111, 1000rpm,  $P_i=200\text{bar}$ .

A very clear trend showing the effect of the backpressure is shown in the following angle analysis, Figure 5-44. The mean angle collapses with higher backpressure (from 87deg at 1bar Pb to 78deg at 16.6bar) which may be due to the stronger effect of the



outer wakes against the inner wakes. Such a result becomes more intense at higher gas density due to the amplification of the drag. It can be also observed a consistent increase of the STD value that indicates an objective increase of spray instability with the cylinder pressure which agrees with the visual results of the RMS images.

### 5.6.5.2. Injector prototype: Inward Seal Band (+ISB)

#### Injection pressure: 200bar

The Inward Seal Band positive step presents also similar results as the SSB. The penetration decreases visibly as the cylinder pressure raises however, the spray seems preserving a more symmetrical shape despite the increase in density. Even the mean images look more defined in terms of string structure which means that the spray pattern is more repeatable out of the whole set of images, than the SSB type. However, still the RMS images reveal a high spray variation in both recirculation and leading edge area.

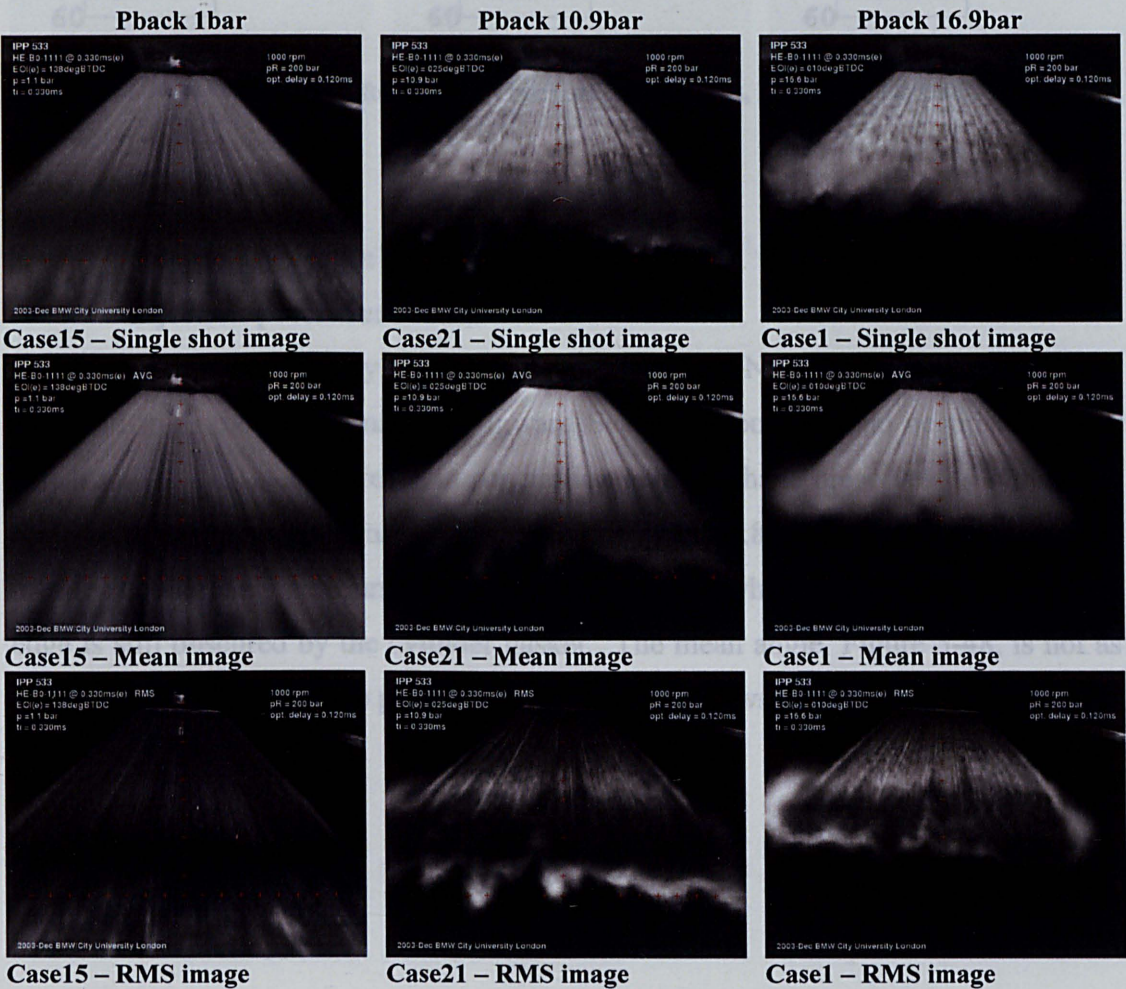


Figure 5-45 Spray comparisons for different backpressures: +ISB, Bit pos. 1111, 1000rpm, Pi=200bar.



The improvement in this prototype injector can be observed even in the following angle analysis of Figure 5-46. For all backpressures, the mean angle is almost invariable with a value of 88deg for all three cases. The STD still increases with the backpressure but the variation in STD is much more contained than the variation seen in the SSB injector.

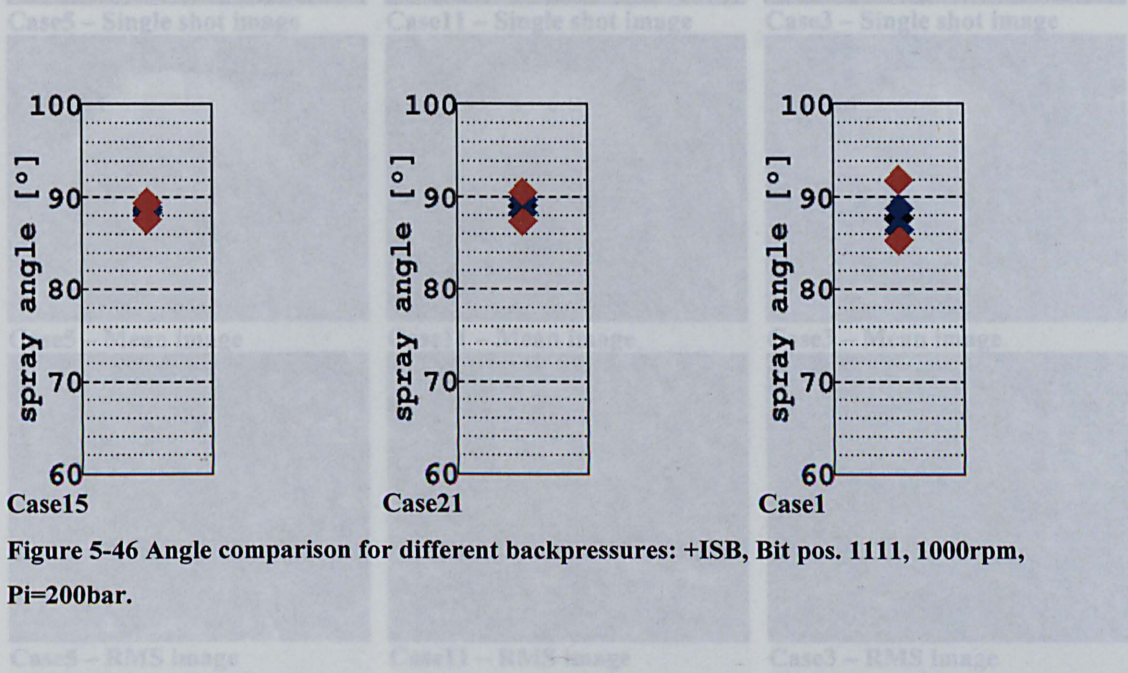


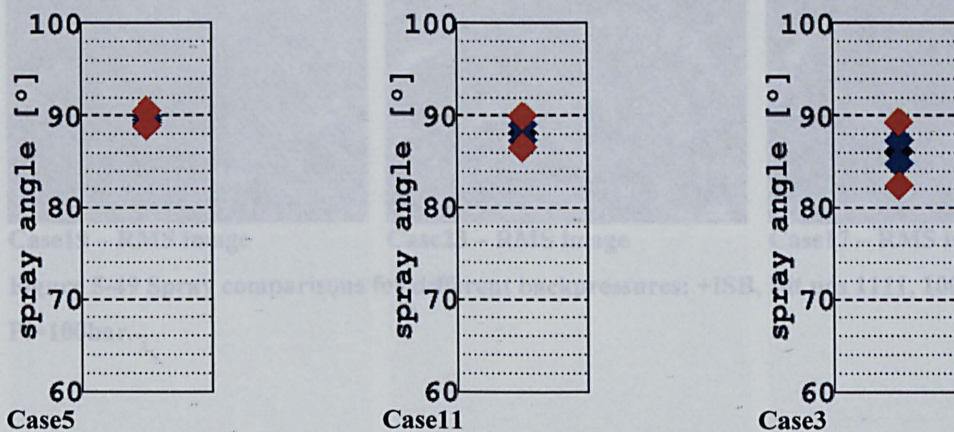
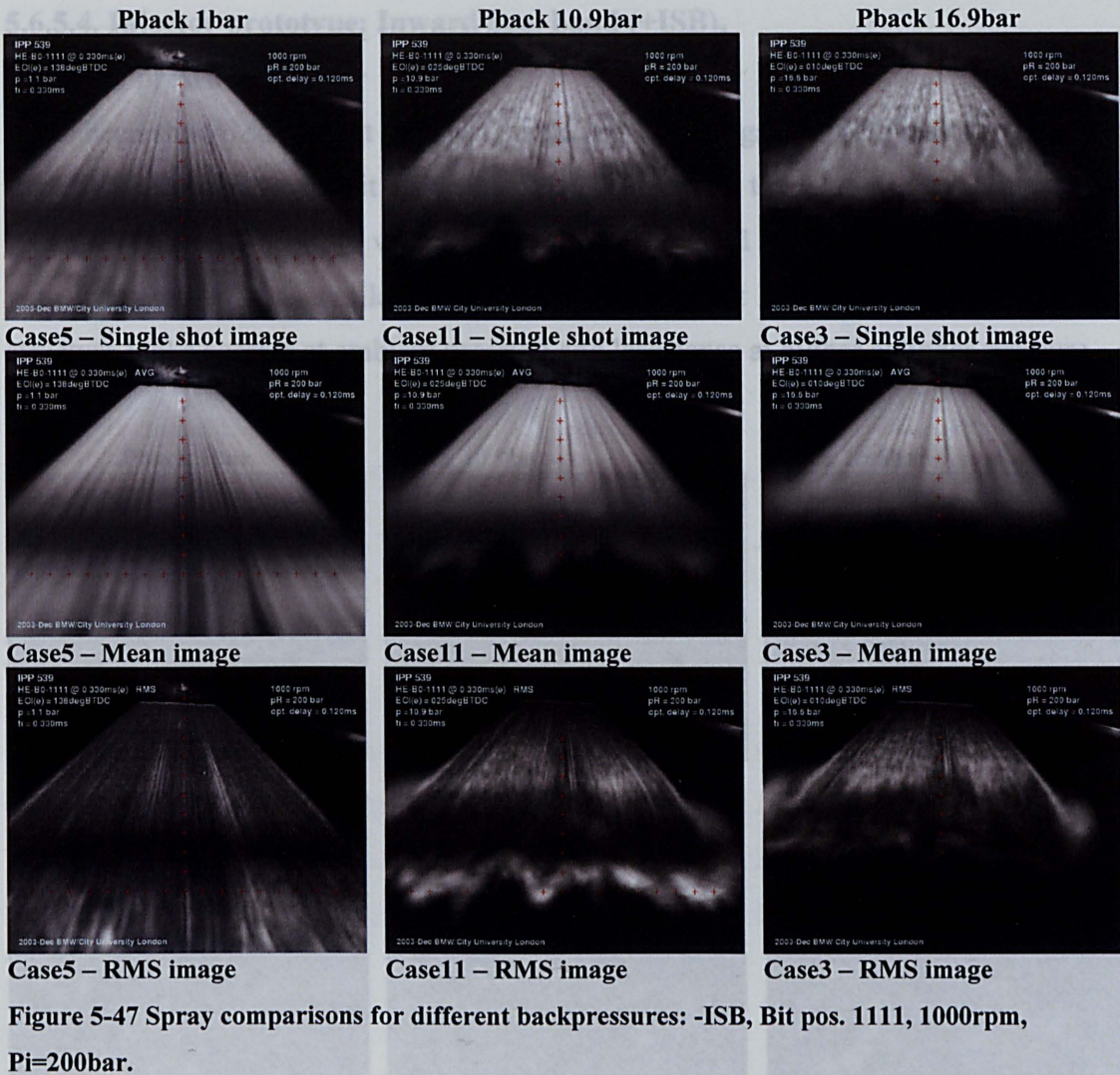
Figure 5-46 Angle comparison for different backpressures: +ISB, Bit pos. 1111, 1000rpm,  $P_i=200\text{bar}$ .

### 5.6.5.3. Injector prototype: Inward Seal Band (-ISB)

**Injection pressure: 200bar**

Figure 5-47 shows the spray images with -ISB injector. No evident difference can be observed from the spray images of Inward Seal Band positive and negative step. A part from the expected decrease in penetration still the shape preserves its symmetry. RMS images shows an intense variation especially at 10.8bar backpressure where the profile is completely surrounded by a thick bright area whereas at 16.6bar the leading edge is still obscured by the cylinder gasket. The mean angle, Figure 5-48, is not as constant as the positive step prototype but the STD follows the same trend.







5.6.5.4. Injector prototype: Inward Seal band (+ISB),

Injection pressure: 100bar

It has been shown so far that the most stable prototypes against backpressure were the two ISB prototypes, and it is worth now to analyse them at different injection pressures. The rail pressure was decreased to 100bar and the decrease in penetration with backpressure was similar as previously observed at 200bar however, the string structure looks coarser at ambient pressure and less dense at higher cylinder pressure.

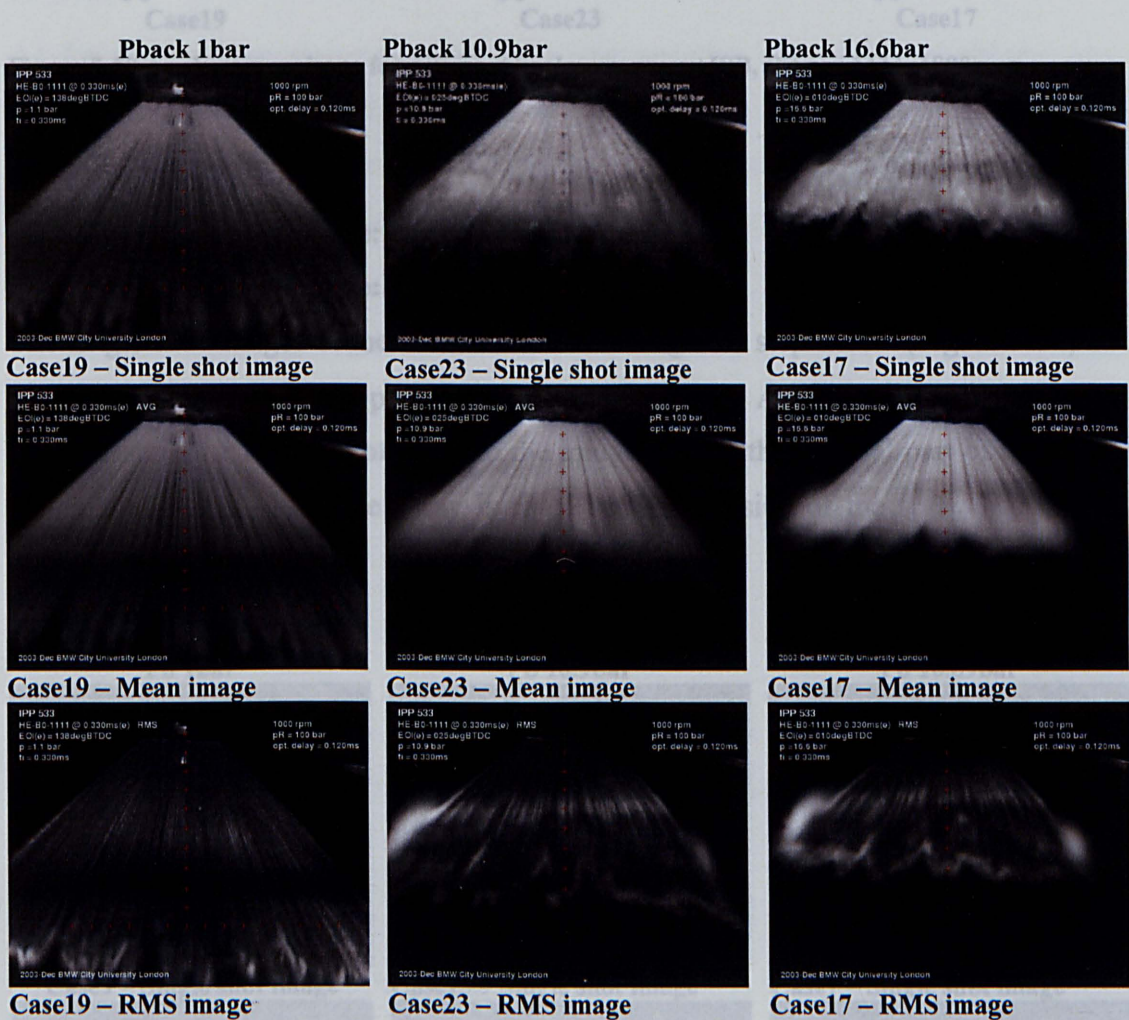


Figure 5-49 Spray comparisons for different backpressures: +ISB, Bit pos 1111, 1000rpm, Pi=100bar.

The effect of backpressure on mean spray angle is negligible (Figure 5-50), but STD of spray angle increases with backpressure slightly more than the case at 200bar rail pressure. This minor increase of spray variability may be due to the weaker momentum possessed by the spray at lower injection pressure which is easily affected by the in-cylinder air motion;



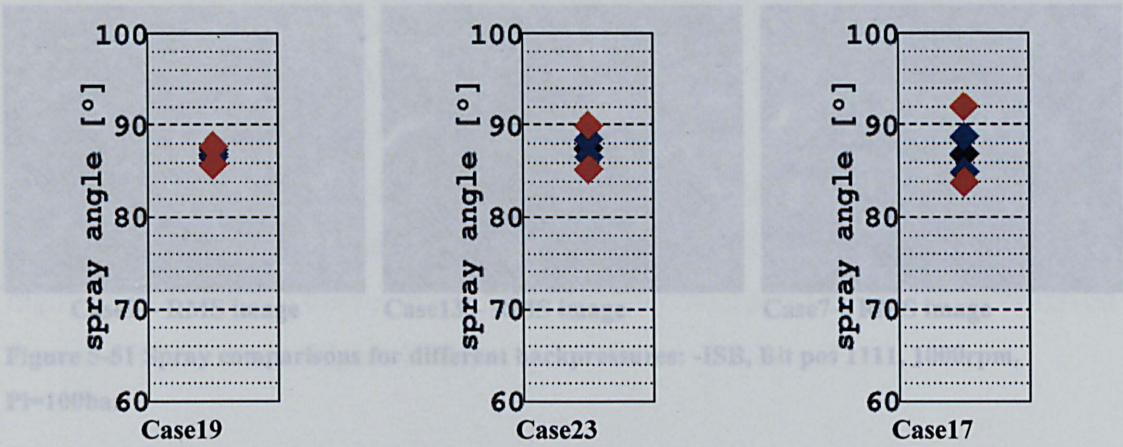
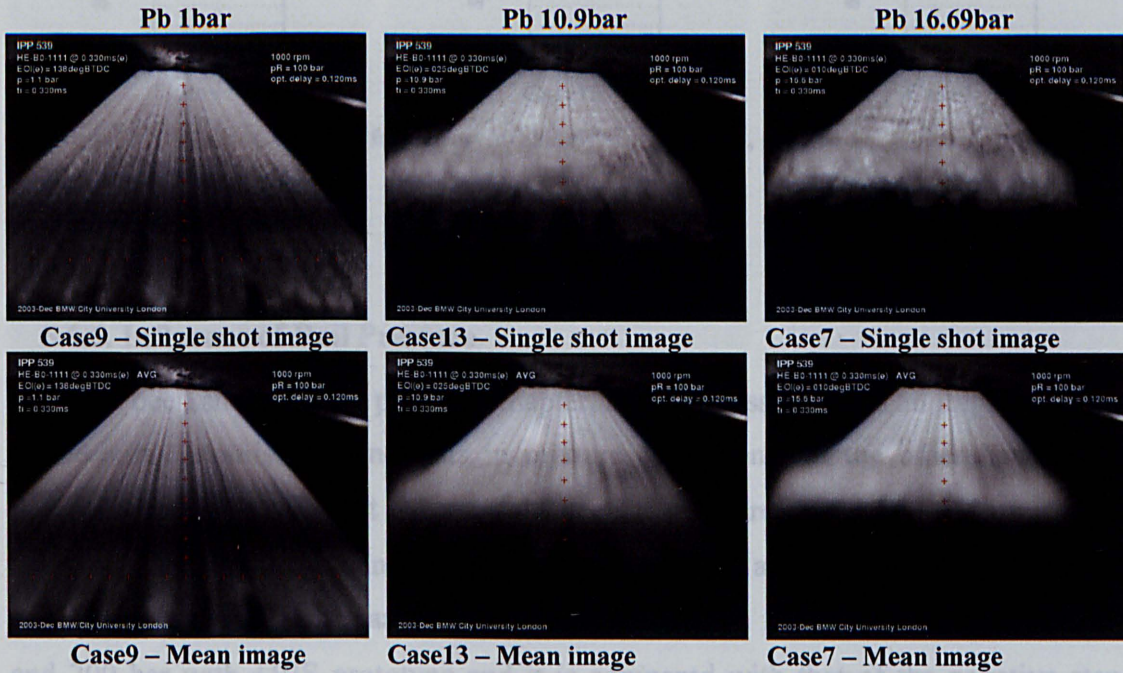


Figure 5-50 Angle comparisons for different backpressures: +ISB, Bit pos 1111, 1000rpm, Pi=100bar.

### 5.6.5.5. Injector prototype: Inward Seal band (-ISB),

Injection pressure: 100bar

The single shot images of the Inward Seal Band negative step shows (Figure 5-51) an irregular distribution of the penetration around the spray. As it can be seen at 10.9bar backpressure, the rear part of spray in the image reveals the internal part of the cone, which means that either the spray is tilted or the backside of the spray has higher penetration.







Case9 – RMS image

Case13 – RMS image

Case7 – RMS image

Figure 5-51 Spray comparisons for different backpressures: -ISB, Bit pos 1111, 1000rpm,  $P_i=100\text{bar}$ .

As for the positive step prototype, even the negative step does not present any significant mean angle variation with the backpressure and yet the spray-to-spray variation increases at higher cylinder pressure and injection pressure. That supports the previous hypothesis for which lower injection pressure produces less stable injections.

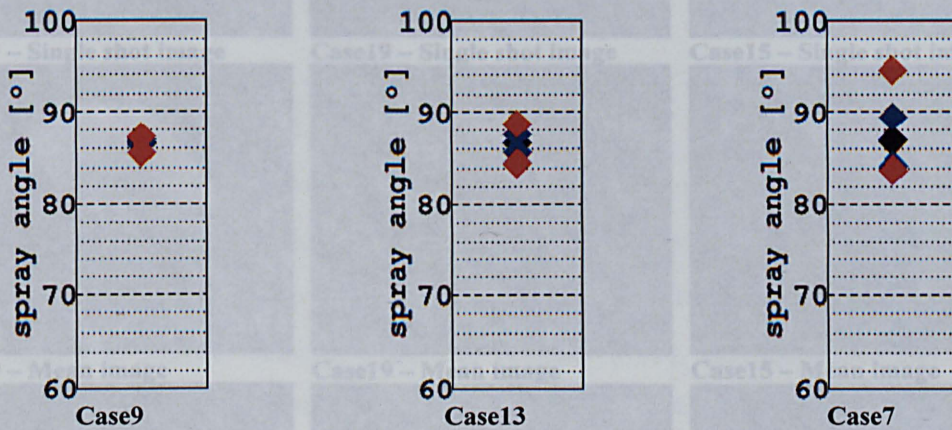


Figure 5-52 Angle comparisons for different backpressures: -ISB, Bit pos 1111, 1000rpm,  $P_i=100\text{bar}$ .

### 5.6.6. Influence of Rail Pressure

As it has been shown in the previous chapter, the rail pressure plays an important role in the spray atomisation and thus in mixture formation. On the other hand, it is important to make sure that the needed injection pressure does not compromise the spray stability. The following comparison, Figure 5-53 and Figure 5-54, shows the spray structure differences and the spray angle variation for rail pressure of 100 bar and 200 bar with +IBS prototype and it is compared with that of the negative step prototype at 100bar.



5.6.6.1. Comparison at ambient pressure:

-ISB 100bar; +ISB 100bar / 200bar.

The +ISB shows a very similar spray pattern to that of the -ISB at 100bar injection pressure whereas the comparison with the spray at 200bar rail pressure presents a higher penetration and thicker string structure. No obvious difference can be observed from the RMS images (Figure 5-53).

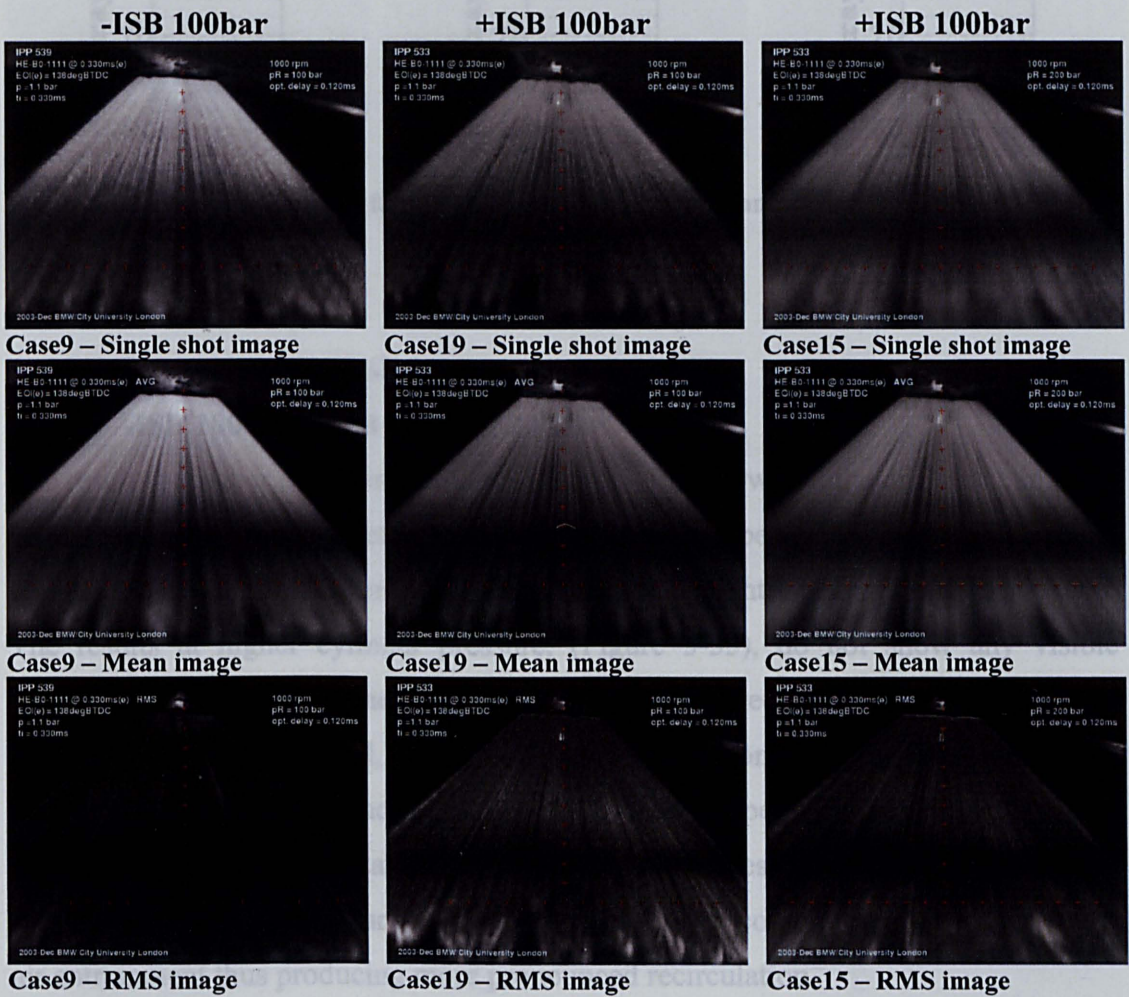


Figure 5-53 Spray comparisons for different Injection pressures and Injector prototypes: Bit pos 1111, 1000rpm, Pb=1.1bar.





At ambient pressure, the rail pressure variation for both +ISB and -ISB does not influence the STD, Figure 5-54, resulting in a very stable sprays whereas the mean angle slightly increases at 200bar injection pressure.

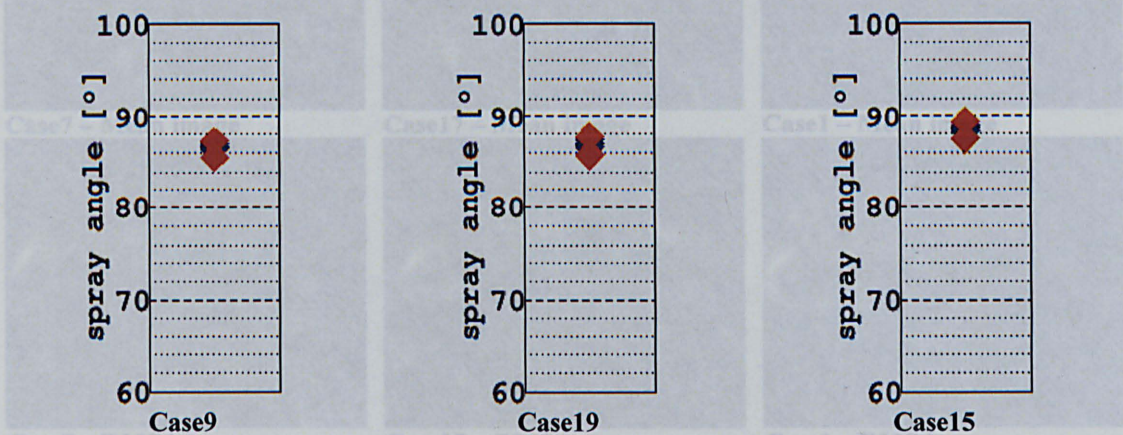


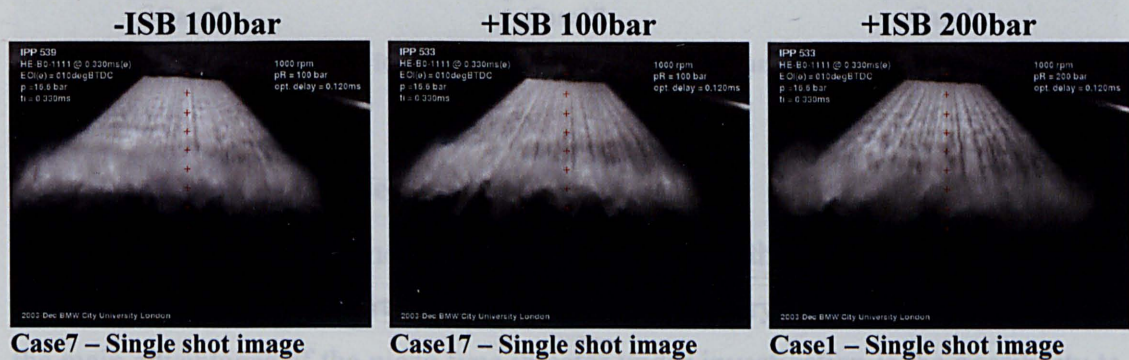
Figure 5-54 Angle comparisons for different Injection pressures and Injector prototypes: Bit pos 1111, 1000rpm, Pb=1.1bar.

### 5.6.6.2. Comparison at 16.6bar backpressure:

**-ISB 100bar; +ISB 100bar / 200bar.**

The results at higher cylinder pressure, (Figure 5-55), show that the difference in penetration is less evident between the two injectors and between the two injection pressures although the higher pressure tend to have a slightly penetration

The results at higher cylinder pressure, (Figure 5-55), do not show any visible difference in penetration neither between the two injector nor between the two injection pressures. Instead, a much larger recirculation area can be observed at 200bar injection pressure and also the string structure appears curlier. This may be an indication of better atomisation at higher injection pressure in which the smaller droplets lose their momentum more rapidly and thus become more susceptible to the air entrainment thus producing more pronounced recirculation.





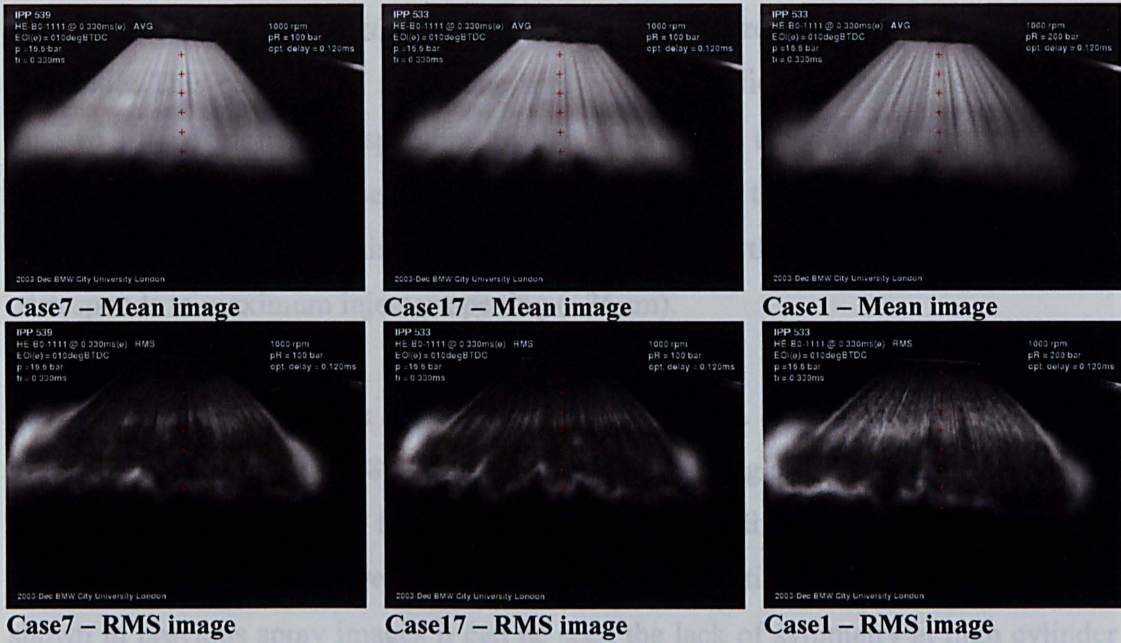


Figure 5-55 Spray comparisons for different Injection pressures and Injector prototypes: Bit pos 1111, 1000rpm, Pb=16.6bar.

From the spray angle analysis, Figure 5-56, it seems that the injection pressure has a stabilizing effect on the spray that presents a lower STD at 200bar. This conclusion had already been identified in the previous comparison of the individual injector prototype. However, no significant mean angle difference can be observed for any of the three cases.

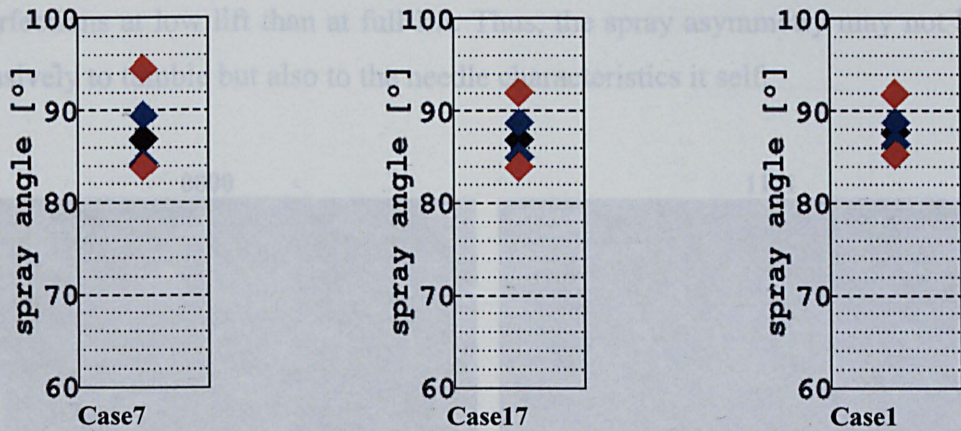


Figure 5-56 Angle comparisons for different Injection pressures and Injector prototypes: Bit pos 1111, 1000rpm, Pb=16.6bar.

### 5.6.7. Influence of Needle Lift.

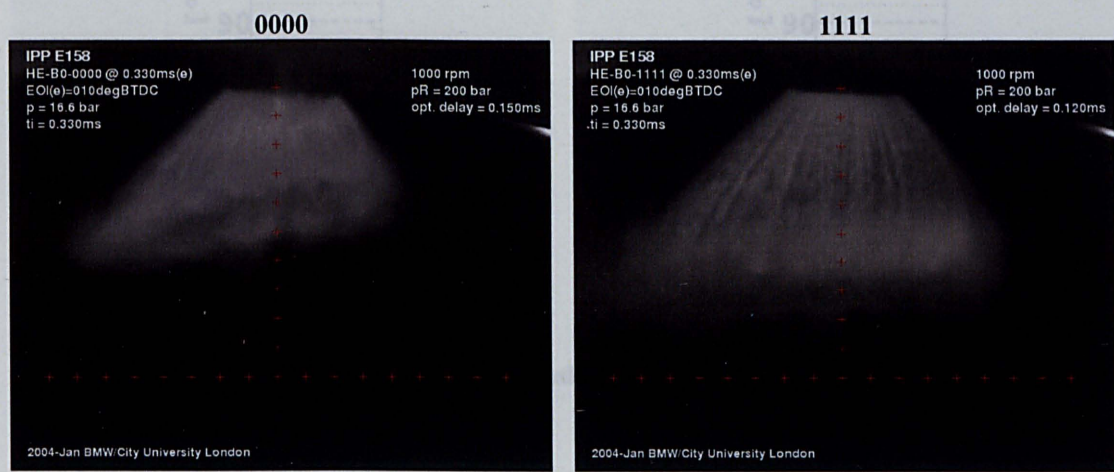
In order to avoid impingement it is necessary to have the full control of the spray penetration especially at part load when the piston is very close to the TDC. One of the main advantages of the piezo type injector under investigation is the possibility to



vary the maximum lift according the activation of the piezo body, which set in motion the pintle. This comparison shows the spray characteristics in terms of stability and for two lift positions corresponding to the extremes of the possible lift set up. As mentioned in the previous section, when the switches in the injector driver are set to “0000” the lift is the minimum ( $\sim 19\mu\text{m}$ ) whereas the full activation “1111” corresponds to maximum injector opening ( $\sim 36\mu\text{m}$ ).

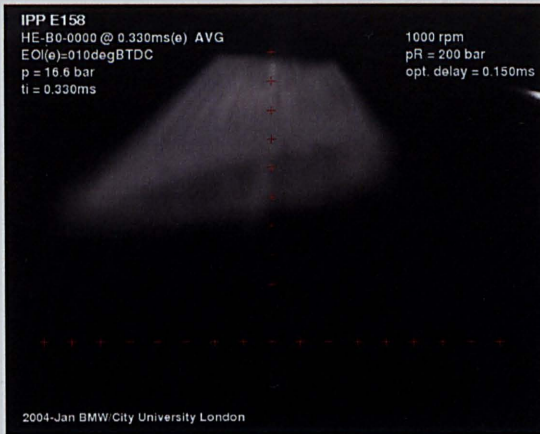
**5.6.7.1. Injector prototype: Standard Seal Band (SSB).**

Figure 5-57 and Figure 5-58 compare the sprays and angles for SSB injector at two extreme needle lifts. The first and most important difference is the significant penetration difference between the two needle lift positions. In addition, as it was shown in previous spray images it can be seen the lack of symmetry at high cylinder pressure due to the increase of drag effect at higher gas density. For lower needle lift, this effect seems to be amplified and in Case27, the penetration at the two sides of the spray cone is very different. The spray symmetry difference between high and low lift may be also due to the fact that the emerging flow is more sensitive to cross section area variation at lower lift. Needle imperfections or non-uniformity in the opening phase create an uneven cross section exit and the relative geometrical error is much higher when the exit cross section area is smaller and more comparable with the error it self. Therefore, the emerging flow will be more sensitive to geometrical exit imperfections at low lift than at full lift. Thus, the spray asymmetry may not be due exclusively to tumble but also to the needle characteristics it self.



**5.6.7.2. Injector prototype: positive step Inward Seal Band (+ISB).**  
The results for +ISB, (Figure 5-59), show a massive increase in penetration at full lift





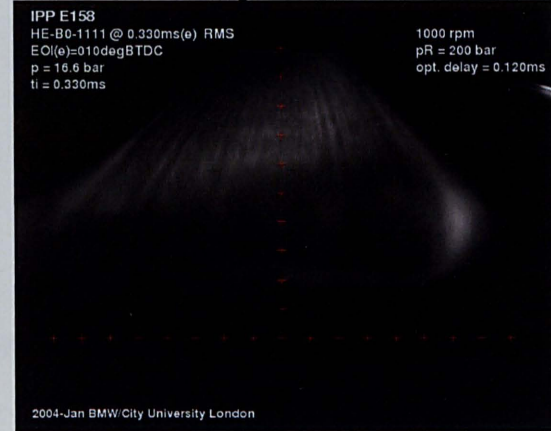
Case27 – Mean image



Case27 – RMS image



Case26 – Mean image



Case26 – RMS image

Figure 5-57 Spray comparisons for different needle lifts: SSB, 1111, 1000rpm, Pi=200bar, Pb=16.6bar.

The angle comparison shows that the mean angle decreases at low need lift even though no difference in spray variation can be seen from the STD.

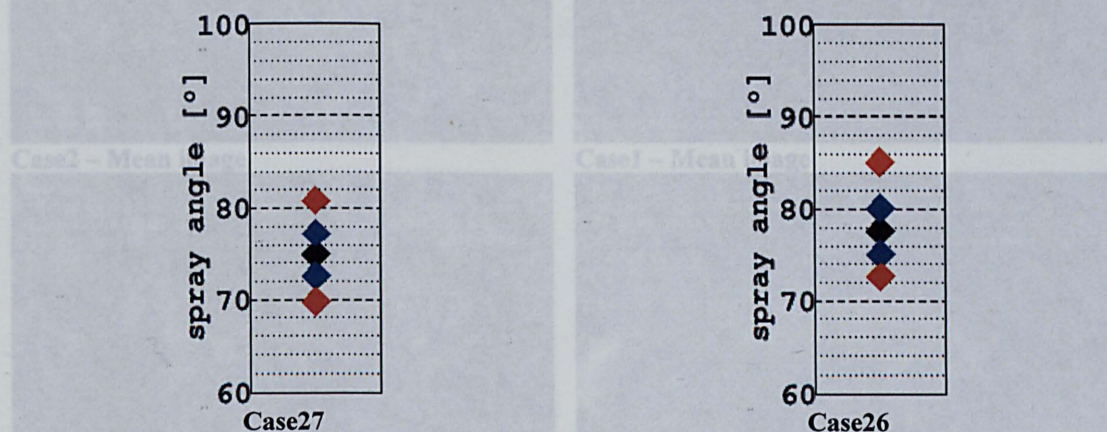


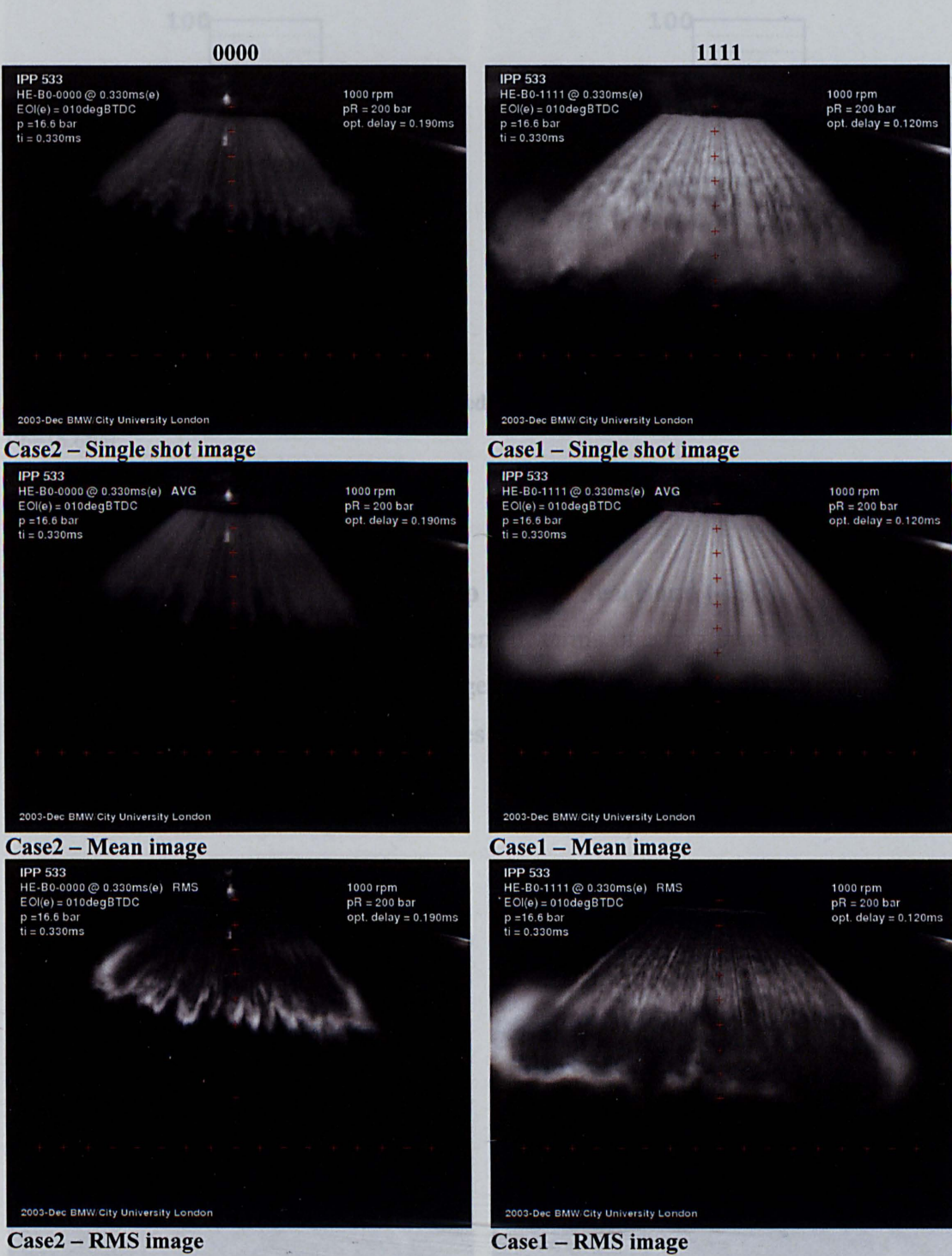
Figure 5-58 Angle comparisons for different needle lifts: SSB, 1111, 1000rpm, Pi=200bar, Pb=16.6bar.

### 5.6.7.2. Injector prototype: positive step Inward Seal Band (+ISB).

The results for +ISB, (Figure 5-59), show a massive increase in penetration at full lift



with a good degree of spray symmetry which is absent at the lower lift. This phenomenon support the previous hypothesis about the effect of the needle lift characteristics at low needle lift (paragraph 5.6.7.1). It must also be noticed that the spray recirculation area is much more pronounced at full lift whereas at low lift it is almost absent. That may represent a draw back during of the penetration control, which implies smaller ignitable areas at lower lift.





Consistently with the results observed in the previous prototype, at full lift, the +ISB injector presents a mean angle increase of about 10deg. The STD at low lift is similar for both SSB and +ISB whereas at full lift the STD suggests that the current injector is more stable.

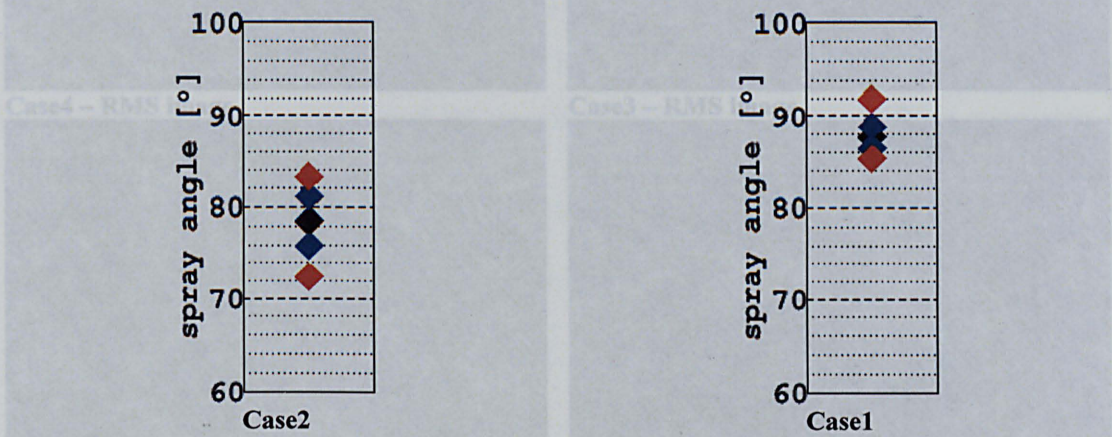
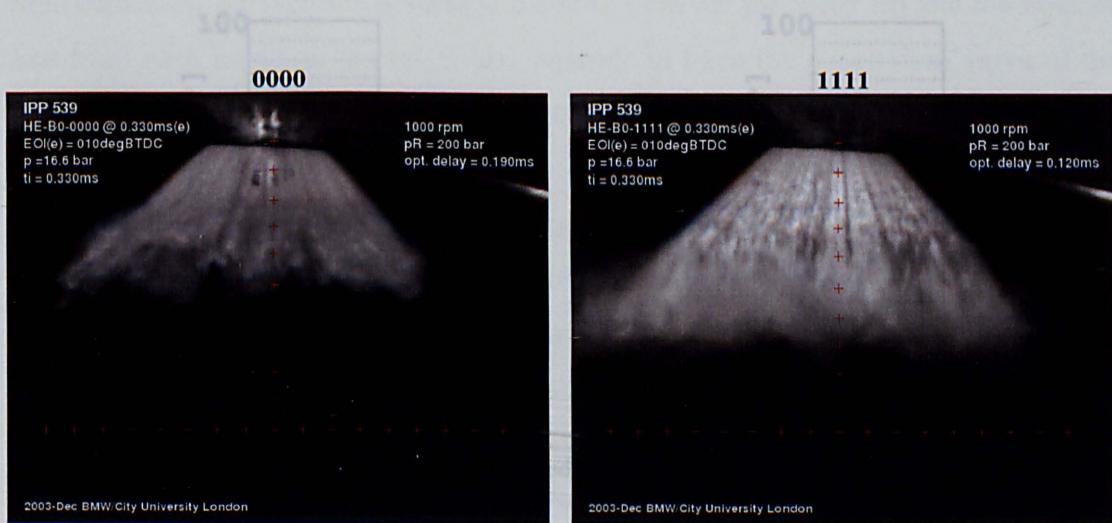


Figure 5-60 Angle comparisons for different needle lifts: +ISB, 1111, 1000rpm, Pi=200bar, Pb=16.6bar.

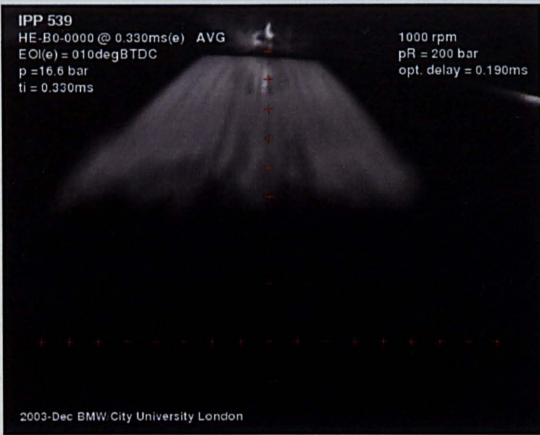
Figure 5-61 Spray comparisons for different needle lifts: -ISB, 1111, 1000rpm, Pi=200bar, Pb=16.6bar.

### 5.6.7.3. Injector prototype: negative step Inward Seal Band (-ISB).

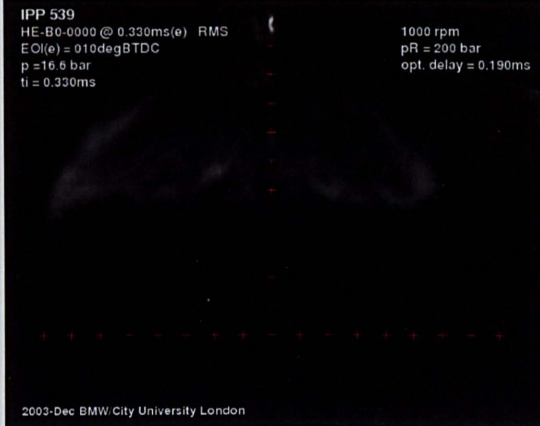
The -ISB prototype shows an improvement in terms of spray symmetry at low lift. Even if not completely, the leading edge of the spray at low lift shows a better regularity than the other injector prototypes previously observed.







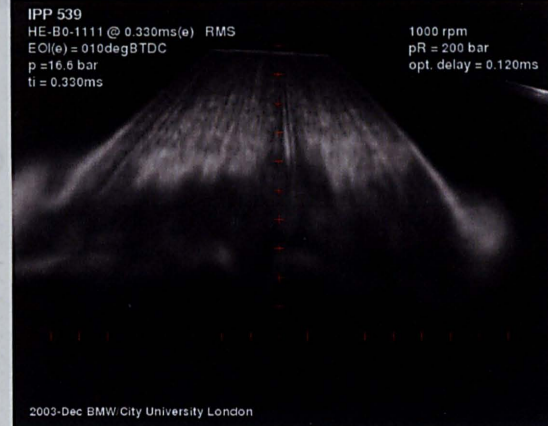
Case4 – RMS image



Case4 – RMS image



Case3 – RMS image



Case3 – RMS image

Figure 5-61 Spray comparisons for different needle lifts: -ISB, 1111, 1000rpm,  $P_i=200\text{bar}$ ,  $P_b=16.6\text{bar}$ .

Beside the spray shape regularity it seems that this prototype preserve quite well its angle characteristics as well as the spray-to-spray variation which is quite similar for both lifts.

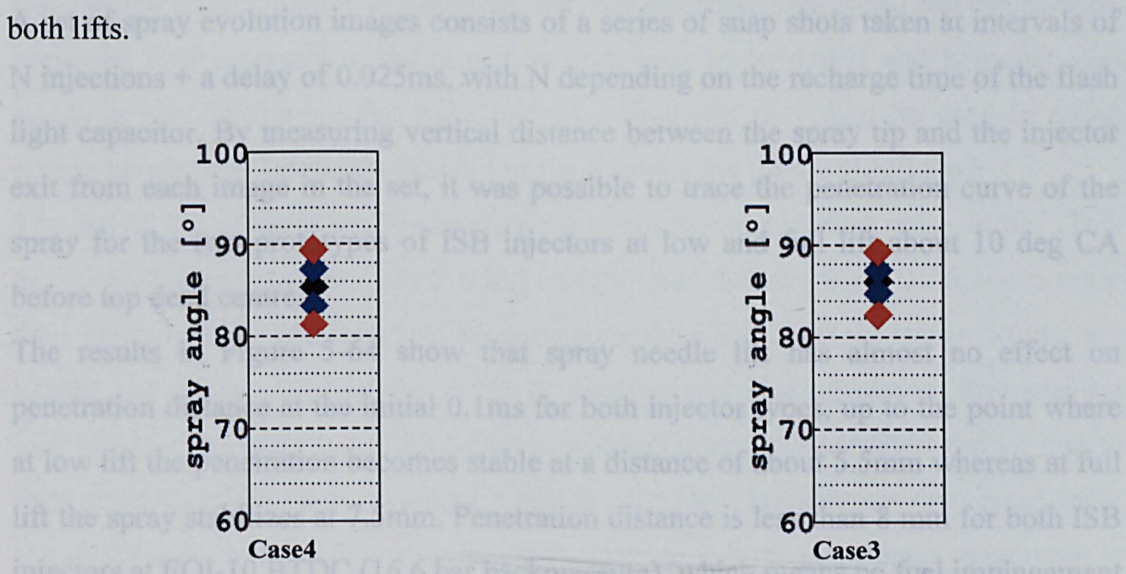


Figure 5-62 Angle comparisons for different needle lifts: -ISB, 1111, 1000rpm,  $P_i=200\text{bar}$ ,  $P_b=16.6\text{bar}$ .



5.6.7.4. Influence of Needle Lift: angle analysis summary

The summary of the needle lift analysis on the three prototypes can be observed on the following series of plots in Figure 5-63. The SSB has performed the poorest characteristics in terms of STD and thus of spray stability and in general it presents a relatively low mean angle which slightly increases at full lift. The -ISB presents a much higher mean angle than the SSB and the STD is much reduced at both lifts with a slight improvement at full lift. The +ISB injector exhibits an intermediate behaviour between SSB and -ISB. At low lift the mean angle is as low as for the SSB with similar STD whereas at full lift the mean angle raise of about 10deg comparable to that of -ISB with a similar STD.

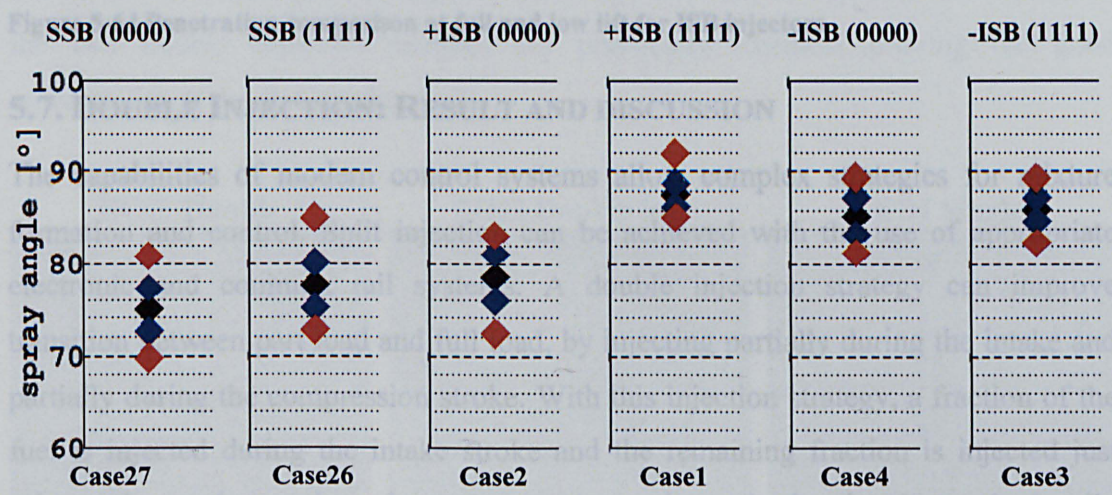


Figure 5-63 Angle comparisons for different needle lifts for the three injector prototypes: 1000rpm,  $P_i=200\text{bar}$ ,  $P_b=16.6\text{bar}$ .

A set of spray evolution images consists of a series of snap shots taken at intervals of  $N$  injections + a delay of  $0.025\text{ms}$ , with  $N$  depending on the recharge time of the flash light capacitor. By measuring vertical distance between the spray tip and the injector exit from each image in the set, it was possible to trace the penetration curve of the spray for the two prototypes of ISB injectors at low and full lift about  $10\text{ deg CA}$  before top dead centre.

The results in Figure 5-64 show that spray needle lift has almost no effect on penetration distance at the initial  $0.1\text{ms}$  for both injector types, up to the point where at low lift the penetration becomes stable at a distance of about  $5.5\text{mm}$  whereas at full lift the spray stabilizes at  $7.5\text{mm}$ . Penetration distance is less than  $8\text{ mm}$  for both ISB injectors at EOI-10 BTDC ( $16.6\text{ bar}$  backpressure), which means no fuel impingement on the piston top surface. The maximum difference in penetration has shown to be of



order of 36% between the two lift settings, which gives a high flexibility for the penetration control at part load.

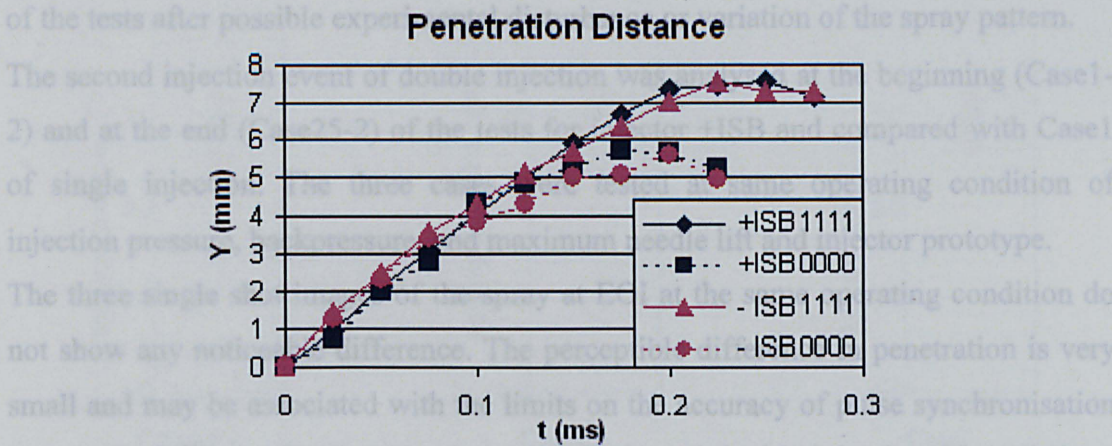


Figure 5-64 Penetration comparison at full and low lift for ISB injectors.

### 5.7. DOUBLE INJECTION: RESULT AND DISCUSSION

The capabilities of modern control systems allow complex strategies for mixture formation and control. Split injection can be achieved with the use of appropriate electronic and common rail systems. A double injection strategy can improve transition between part load and full load, by injecting partially during the intake and partially during the compression stroke. With this injection strategy, a fraction of the fuel is injected during the intake stroke and the remaining fraction is injected just prior to the spark, creating a homogeneous lean mixture in the chamber and a locally rich mixture at the area around the spark gap. The use of double injection during part load, steady state operation is beneficial for soot emissions reduction, and can provide improved fuel economy at the transition area between stratified and homogeneous mode, at low engine speeds. Split injection strategies may also be used to avoid engine knock or to extend the knock limit and enhancing torque at full load.

The use of two or more injection pulses per cycle requires smaller pulse widths. This may decrease spray quality and causing unstable fuel delivery for GDI injectors other than piezoelectric. This happens because common GDI injectors' pulse widths are longer and devote most of the pulse to opening and closing ramps. Piezoelectric injectors, on the other hand, can operate with accuracy in such short pulses due to their rapid actuation. Incorporating tip designs that have sac volumes may cause spray instability even with piezoelectric injectors. The sac volume contributes to increase in HC emissions in many applications.



5.7.1. Comparison of Reference.

With reference to Figure 5-65, the following set of images assesses the repeatability of the tests after possible experimental disturbance or variation of the spray pattern. The second injection event of double injection was analysed at the beginning (Case1-2) and at the end (Case25-2) of the tests for injector +ISB and compared with Case1 of single injection. The three cases were tested at same operating condition of injection pressure, backpressure, and maximum needle lift and injector prototype. The three single shot images of the spray at EOI at the same operating condition do not show any noticeable difference. The perceptible difference in penetration is very small and may be associated with the limits on the accuracy of pulse synchronisation due to the different signal setting between single and double injection. Nevertheless, the two double injection samples are practically identical proving the good repeatability of the test condition.

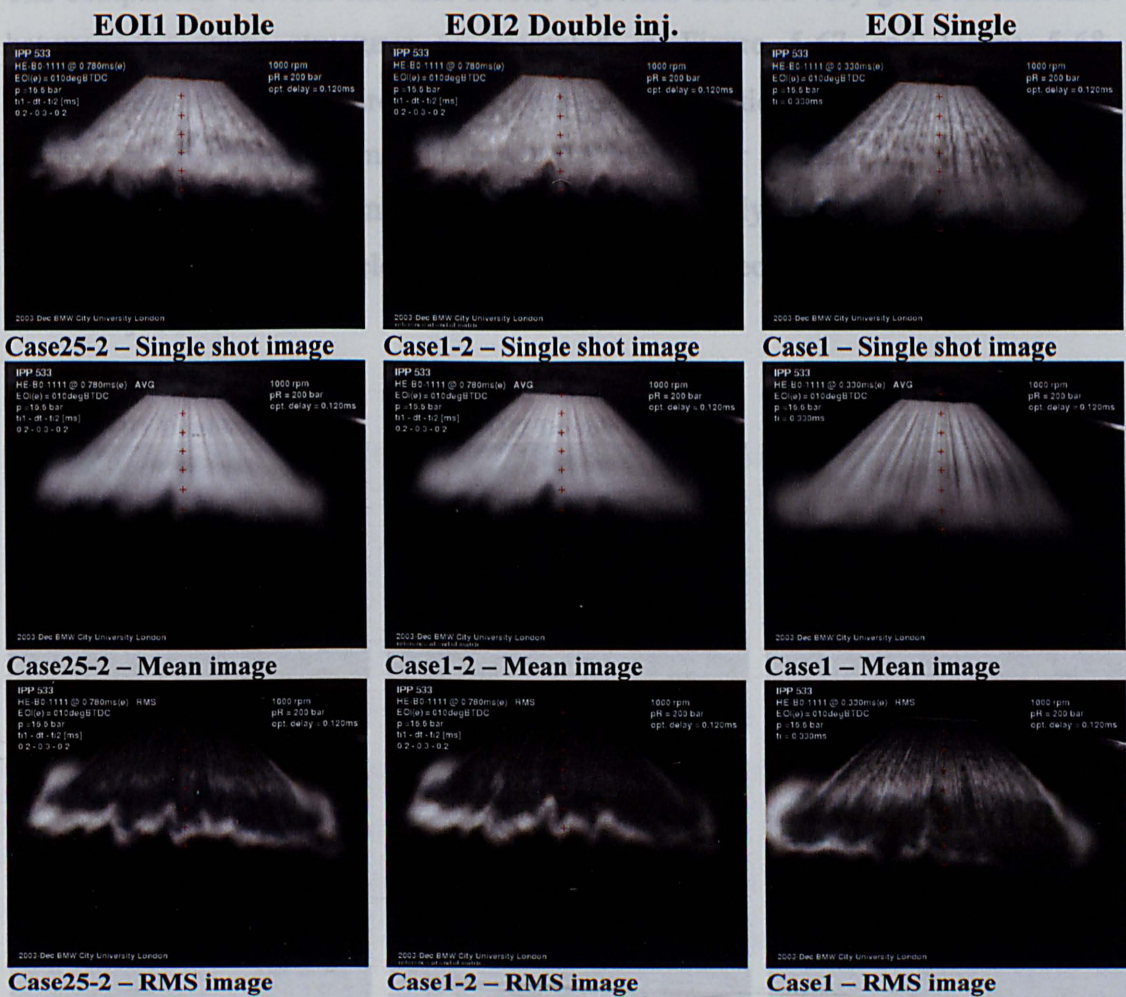


Figure 5-65 Reference comparison (Case 1, Case 1-2, Case 25-2) at same operating conditions.



The angle analysis does not show differences in STD for all of the cases and even the mean angle do not reveal any significant difference.

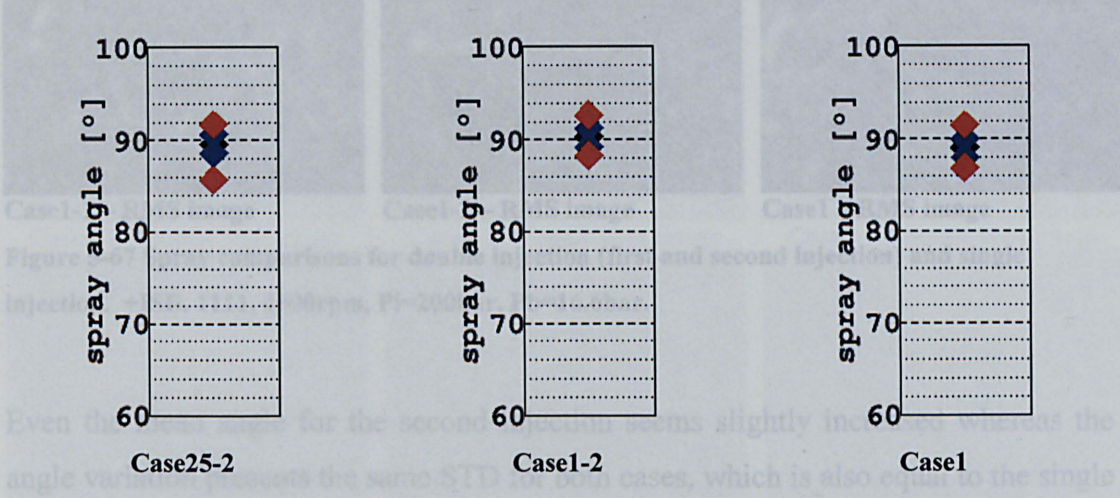
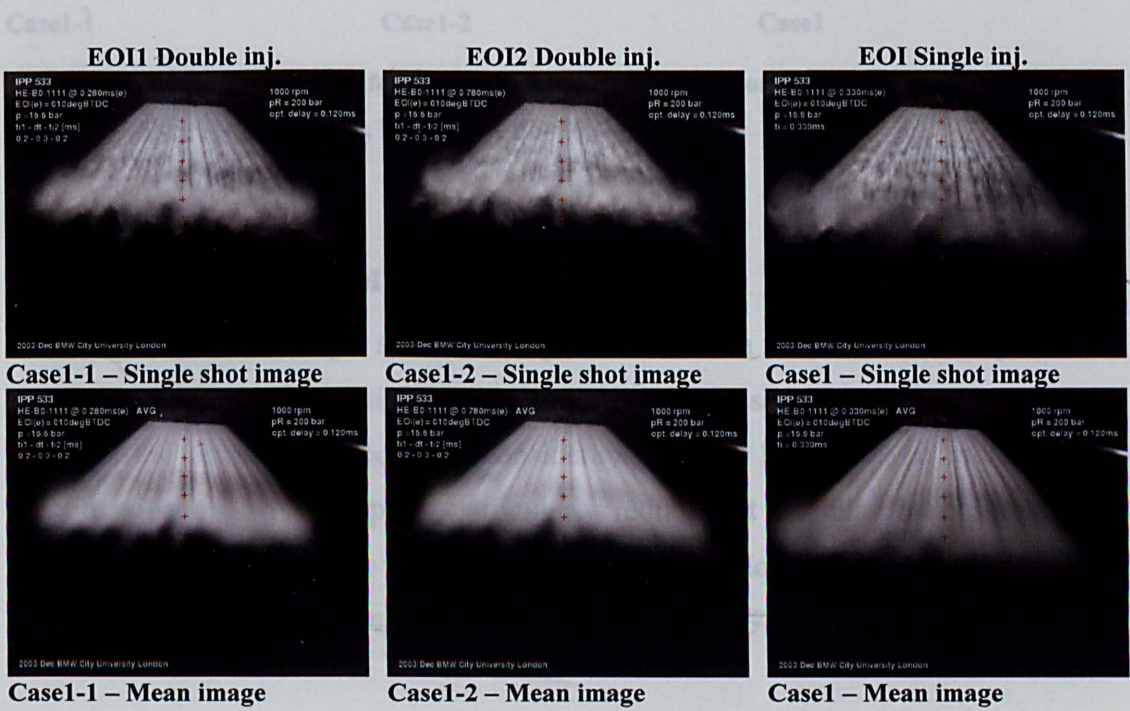


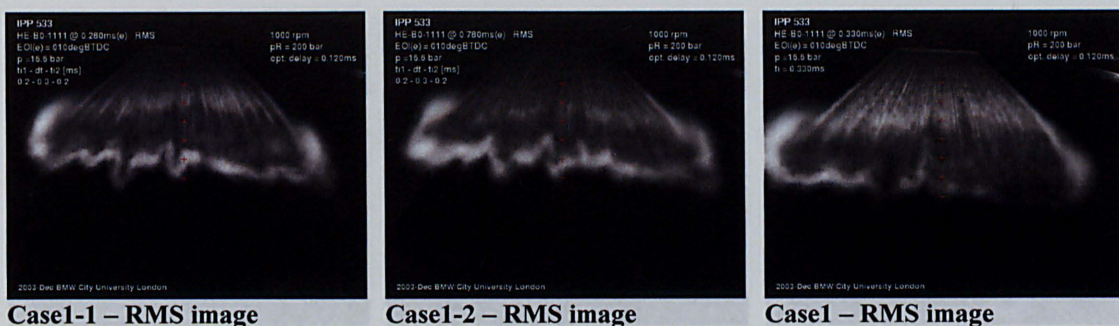
Figure 5-66 Angle Comparisons for same operating conditions (Case 1, Case 1-2, Case 25-2) .

### 5.7.2.Comparison between EOI1 and EOI2.

The comparison between first and second injection shows a very good resemblance between the spray structures as presented in Figure 5-67 and Figure 5-68. Nevertheless, the spray recirculation in the second injection looks slightly disturbed. In fact, the first injection may influence the in-cylinder air motion, which in turns affects the out coming second injection. More specifically, the recirculating ring and surrounding air velocity field produced by the first injection may interact with the second injection.

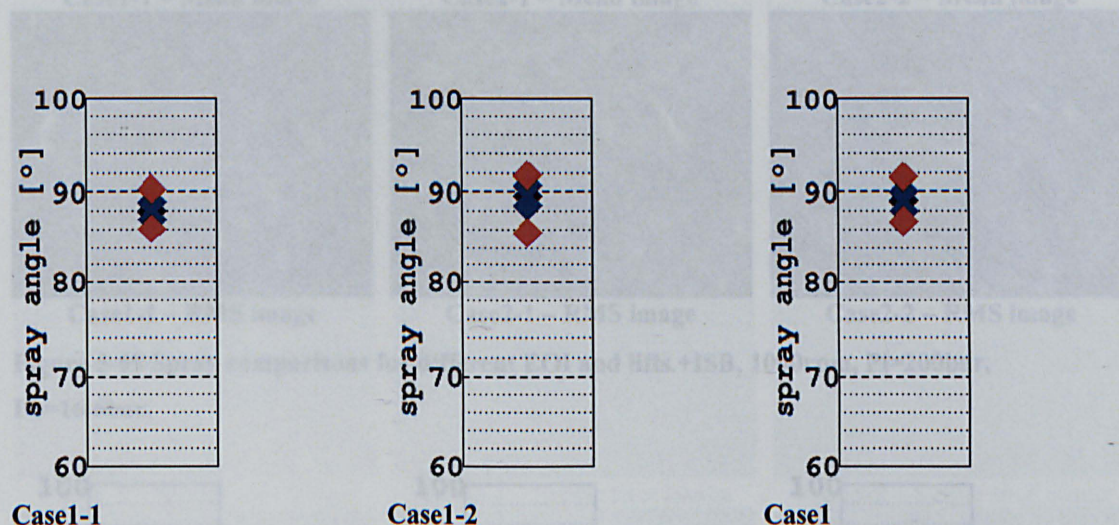






**Figure 5-67 Spray comparisons for double injection (first and second injection) and single injection. +ISB, 1111, 1000rpm, Pi=200bar, Pb=16.6bar.**

Even the mean angle for the second injection seems slightly increased whereas the angle variation presents the same STD for both cases, which is also equal to the single injection reference case.



**Figure 5-68 Angle comparisons for double injection (first and second injection) and single injection. +ISB, 1111, 1000rpm, Pi=200bar, Pb=16.6bar.**

### 5.7.3.Comparison of EOI1, EOI2 and Lift.

The following set of images shows a comparison between first and second injection at low lift and first injection at full lift as a reference. As seen for the single injection analysis, the penetration decreases considerably at low lift and even more for the second injection, which appears particularly reduced. It can also be observed that there is no trace of visible recirculation ring in both low lifts spray and that the leading edge of the second injection appears extremely asymmetrical.



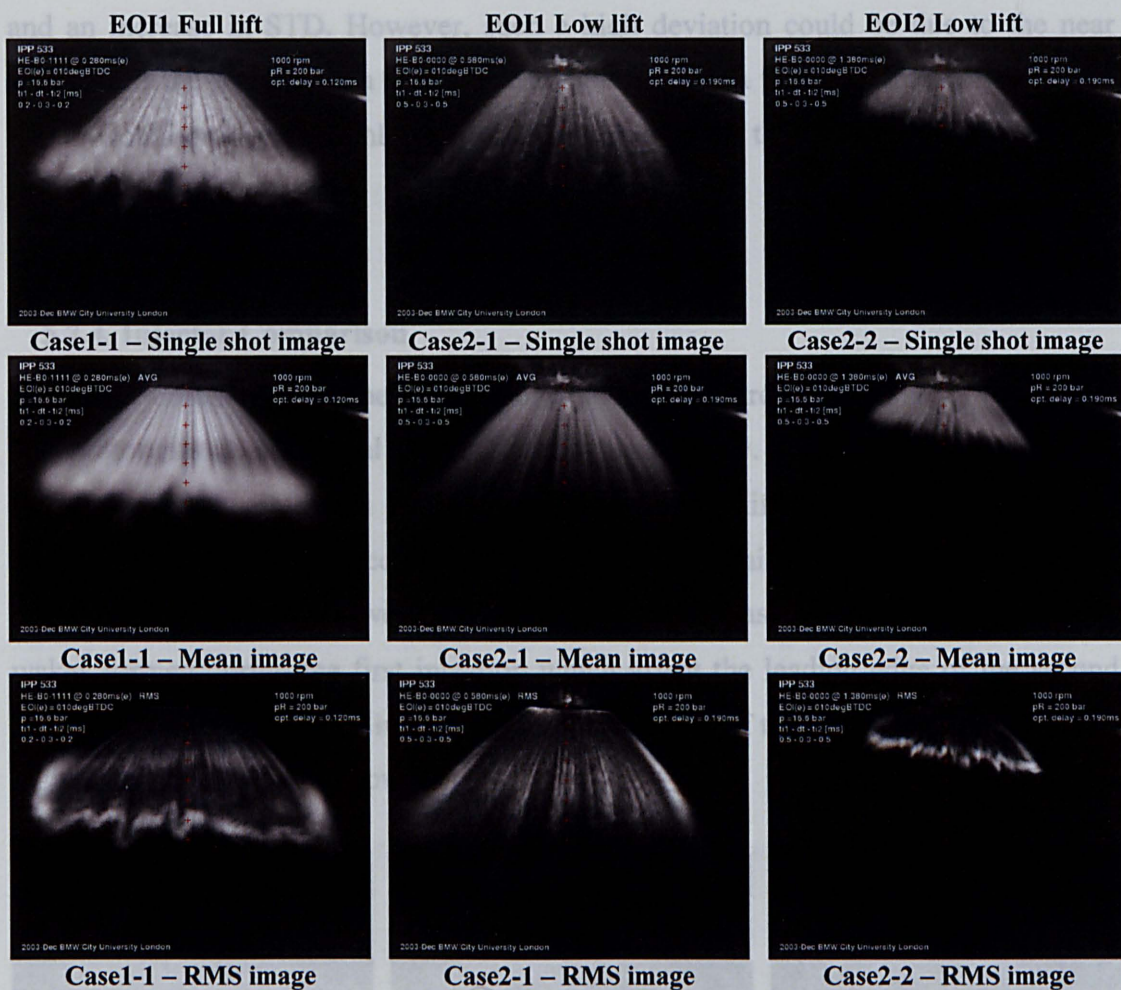


Figure 5-69 Spray comparisons for different EOI and lifts.+ISB, 1000rpm,  $P_i=200\text{bar}$ ,  $P_b=16.6\text{bar}$ .

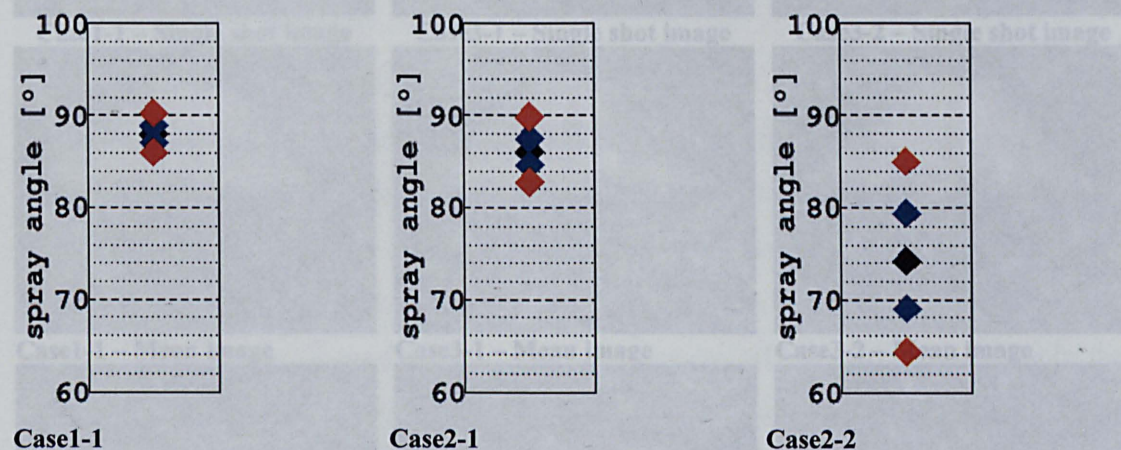


Figure 5-70 Angle comparisons for different EOI and lifts. +ISB, 1000rpm,  $P_i=200\text{bar}$ ,  $P_b=16.6\text{bar}$ .

At low lift, the injection seems considerably degraded presenting lower mean angle and higher angle variation. The second injection presents a massive mean angle drop



and an increase in STD. However, such a high deviation could be due to the near distance of the recirculation area (or leading edge) from the angle measuring points which would produce a highly inconsistent evaluation of the angle statistic for such a short penetration.

### 5.7.4. Injector Comparison.

As can be observed from the single shot images of Figure 5-71 the spray of the two ISB prototypes do not reveal any significant dissimilarity. In the comparison between first and second injection for the -ISB, a slight difference is visible in the recirculation area for the second injection which seems faintly extended upward. This effect already observed between Case1-1 and Case1-2 was said to be produced by the wakes formed during the first injection which affect the leading edge of the second injection. Even in the RMS images, a slight projection of the bright border (typical of recirculation area) further upward can be noticed.

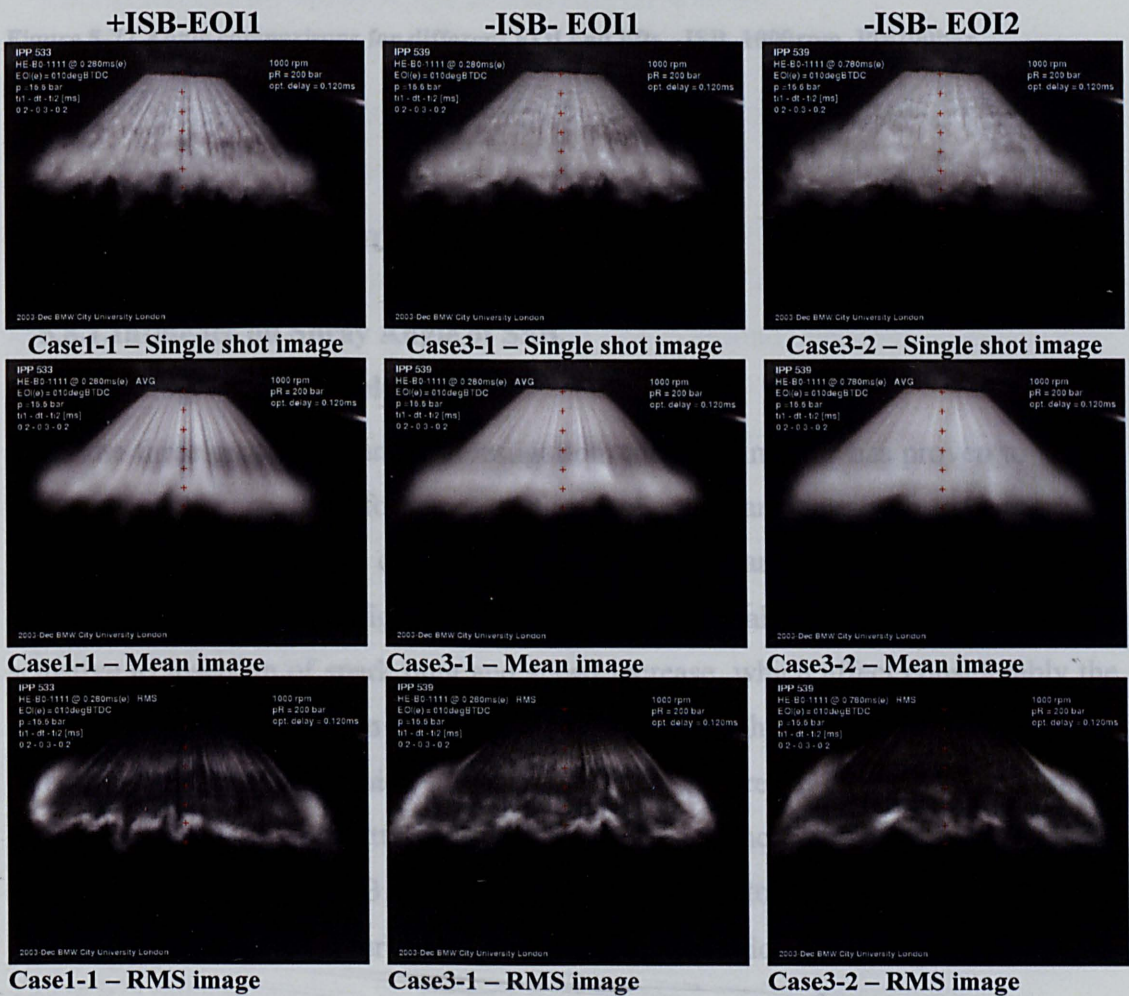


Figure 5-71 Spray comparisons for different EOI and lifts. -ISB, 1000rpm, Pi=200bar, Pb=16.6bar.



No difference in mean angle can be observed between the ISB injectors nor any visible difference in the STD. The second injection instead, still present a higher mean angle which may well be the result of the extended recirculation area previously mentioned.

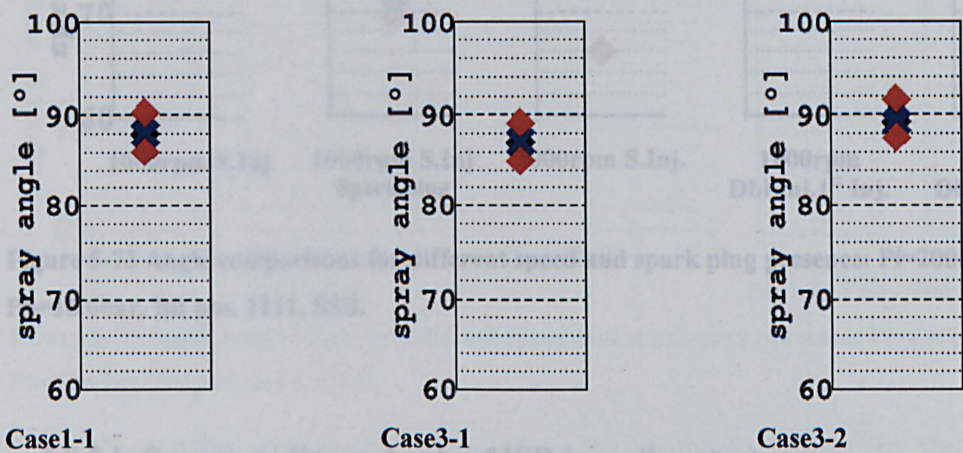


Figure 5-72 Angle comparisons for different EOI and lifts. -ISB, 1000rpm, Pi=200bar, Pb=16.6bar.

## 5.8. SUMMARY OF RESULTS

### 5.8.1.Influence on Spray Angle of SSB.

#### Spark Plug, RPM, Double Injection.

From the three prototypes under investigation, the SSB injector has proven to be the prototype with poorest performance in terms of mean angle stability and spray-to-spray variation. The effects of Spark Plug, engine RPM and double injection for SSB injector is summarised in Figure 5-73. The statistical analysis shows that the SSB is sensitive to insertion of spark plug and speed increase, which affect considerably the spray-to-spray variation. In double injection mode, the second injection seems affected by the first one, which shows a significant difference in both STD and mean angle, in particular, the latter one which shows an increase by approximately 5 degrees. In general, the SSB seems to be very sensitive to any variation of operating condition that causes a perturbation of in-cylinder air motion.



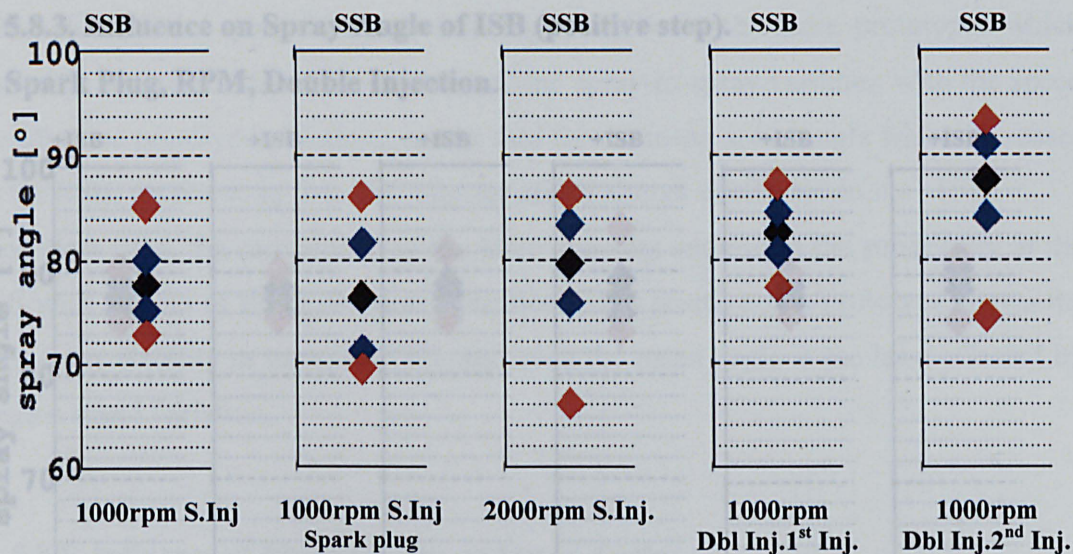


Figure 5-73 Angle comparisons for different speed and spark plug presence:  $P_i=200\text{bar}$ ,  $P_b=16.6\text{bar}$ , Bit pos. 1111, SSB.

### 5.8.2. Influence on Spray Angle of ISB (negative step).

#### Spark Plug, RPM, Double Injection.

The -ISB presents a substantial improvement with respect the SSB, as can be seen in Figure 5-74. It is particularly affected by the spark plug presence; however, at 2000rpm it shows a drop in mean angle and an increase in spray angle STD. The double injection seems performing quite well presenting a stable and contained STD and only a slight increase in mean angle from first to second injections.

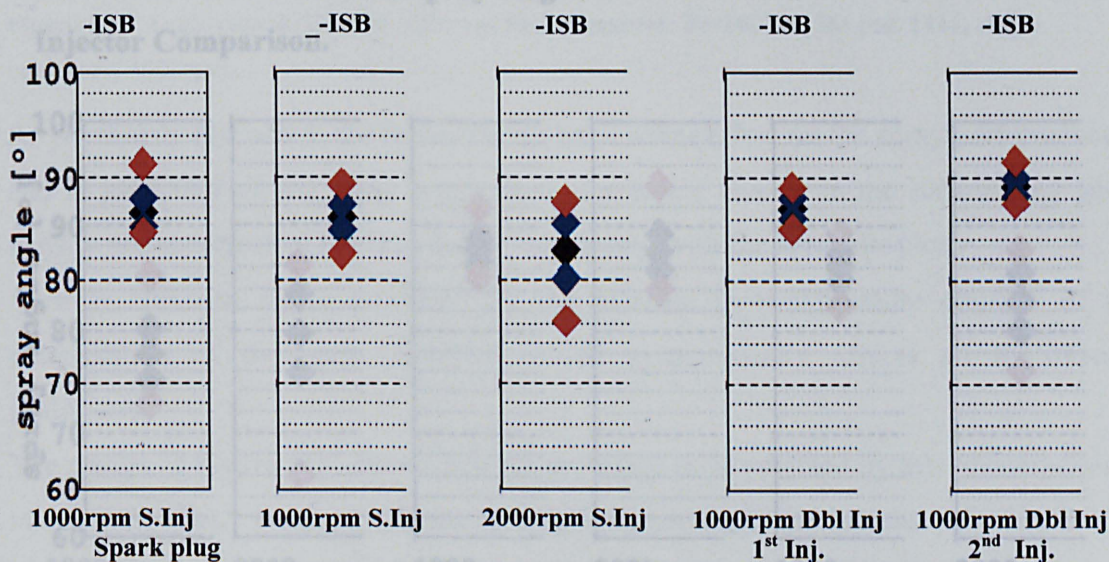


Figure 5-74 Angle comparisons for different speed and spark plug presence:  $P_i=200\text{bar}$ ,  $P_b=16.6\text{bar}$ , Bit pos. 1111, -ISB.



5.8.3. Influence on Spray Angle of ISB (positive step).

Spark Plug, RPM, Double Injection.

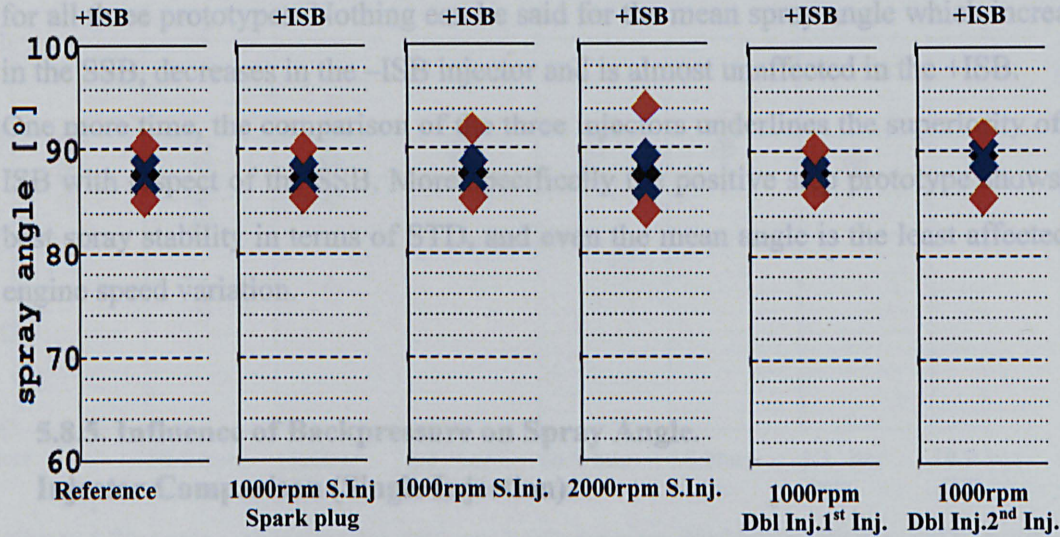


Figure 5-75 Angle comparison for different speed and spark plug presence:  $P_i=200\text{bar}$ ,  $P_b=16.6\text{bar}$ , Bit pos. 1111, +ISB.

The ISB positive step is the best performing prototype within the three injectors, (Figure 5-75). The mean angle is insensitive to spark plug and engine speed variation as well as the STD which is also quite contained. The double injection does not show relevant difference between first and second injection revealing a low spray variation and just a slightly increased mean angle like observed for the negative step prototype.

5.8.4. Influence of RPM on Spray Angle.

Injector Comparison.

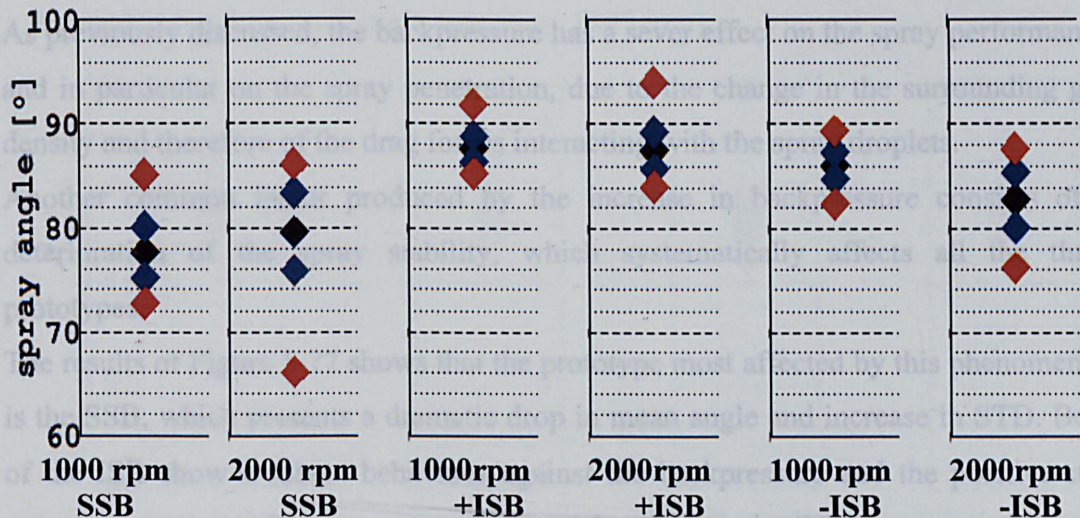


Figure 5-76 Angle comparison for different speeds and injector prototypes:  $P_i=200\text{bar}$ ,  $P_b=16.6\text{bar}$ , Bit pos. 1111, single injection.



The effect of the speed is reported in Figure 5-76 for the three prototypes which shows as a common trend the increase of the spray-to-spray variation with the speed for all three prototypes. Nothing can be said for the mean spray angle which increases in the SSB, decreases in the -ISB injector and is almost unaffected in the +ISB.

One more time, the comparison of the three injectors underlines the superiority of the ISB with respect of the SSB. More specifically the positive step prototype shows the best spray stability in terms of STD, and even the mean angle is the least affected by engine speed variation.

### 5.8.5. Influence of Backpressure on Spray Angle.

#### Injector Comparison (Single Injection).

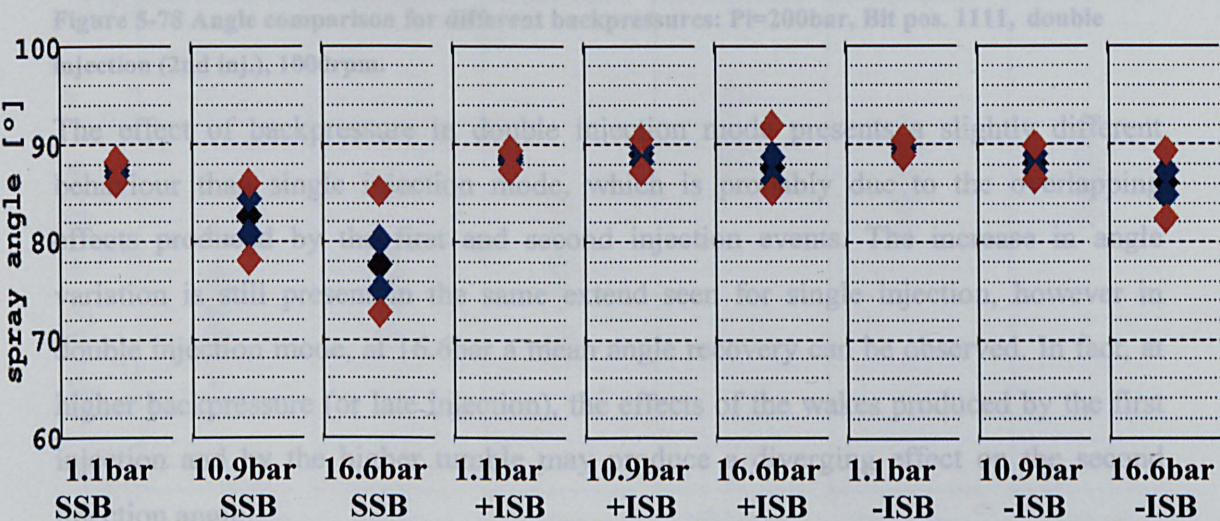


Figure 5-77 Angle comparison for different backpressures:  $P_i=200\text{bar}$ , Bit pos. 1111, single injection), 1000rpm.

As previously discussed, the backpressure has a sever effect on the spray performance and in particular on the spray penetration, due to the change in the surrounding gas density and therefore of the drag forces interacting with the spray droplets.

Another common factor produced by the increase in backpressure consists of a deterioration of the spray stability, which systematically affects all the three prototypes.

The results of Figure 5-77 shows that the prototype most affected by this phenomenon is the SSB, which presents a dramatic drop in mean angle and increase in STD. Both of the ISB show a robust behaviour against the backpressure and the positive-step prototype presents almost constant mean angle whereas the STD is comparable with negative-step prototype.



### 5.8.6. Influence of Backpressure on Spray Angle.

#### Injector Comparison (Second Injection).

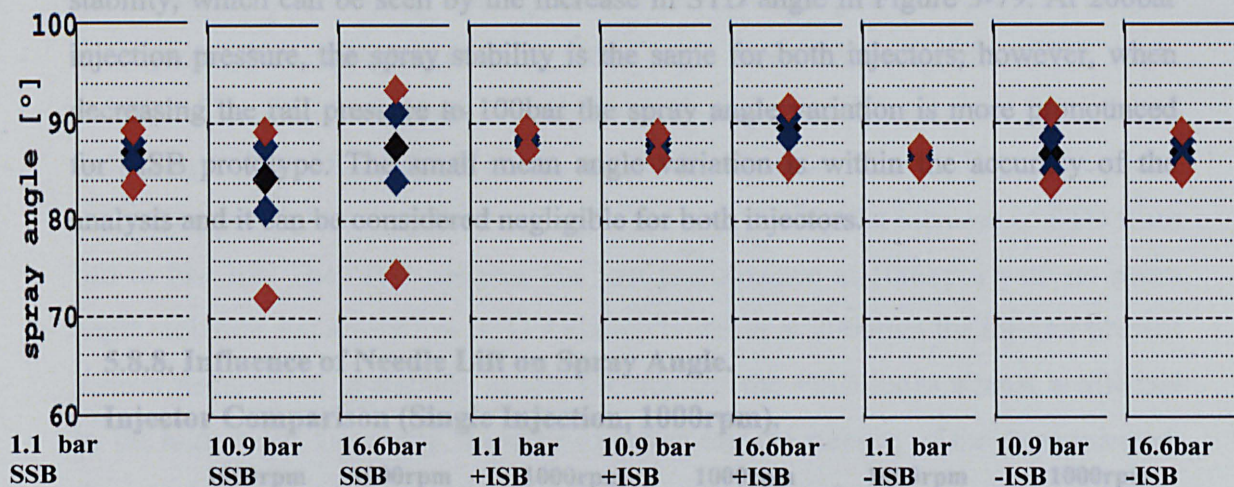


Figure 5-78 Angle comparison for different backpressures:  $P_i=200\text{bar}$ , Bit pos. 1111, double injection (2nd inj.), 1000rpm.

The effect of backpressure in double injection mode presents a slightly different behaviour than single injection mode, which is probably due to the overlapping effects produced by the first and second injection events. The increase in angle variation is still present in the same extend seen for single injection, however in double injection mode, at 16.6bar a mean angle recovery can be observed. In fact, at higher backpressure (or late injection), the effects of the wakes produced by the first injection and by the higher tumble may produce a diverging effect on the second injection angle.

### 5.8.7. Influence of Injection pressure on Spray Angle.

#### Injector Comparison (Single Injection, 1000rpm).

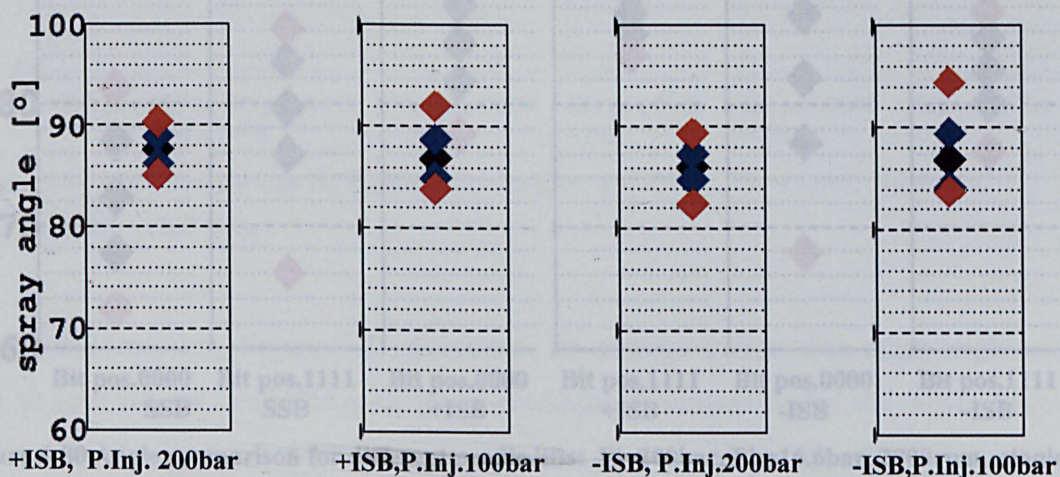


Figure 5-79 Angle comparison for different needle lifts:  $P_i=200\text{bar}$ ,  $P_b=16.6\text{bar}$ , 1000rpm, double injection (2nd inj.).



The comparison of injection pressure was performed only for the two ISB prototypes. With both injectors, the decrease of spray momentum was resulting in loss of stability, which can be seen by the increase in STD angle in Figure 5-79. At 200bar injection pressure, the spray stability is the same for both injectors; however, when decreasing the rail pressure to 100bar the spray angle variation is more pronounced for -ISB prototype. The small mean angle variation is within the accuracy of the analysis and it can be considered negligible for both injectors.

### 5.8.8. Influence of Needle Lift on Spray Angle.

#### Injector Comparison (Single Injection, 1000rpm).

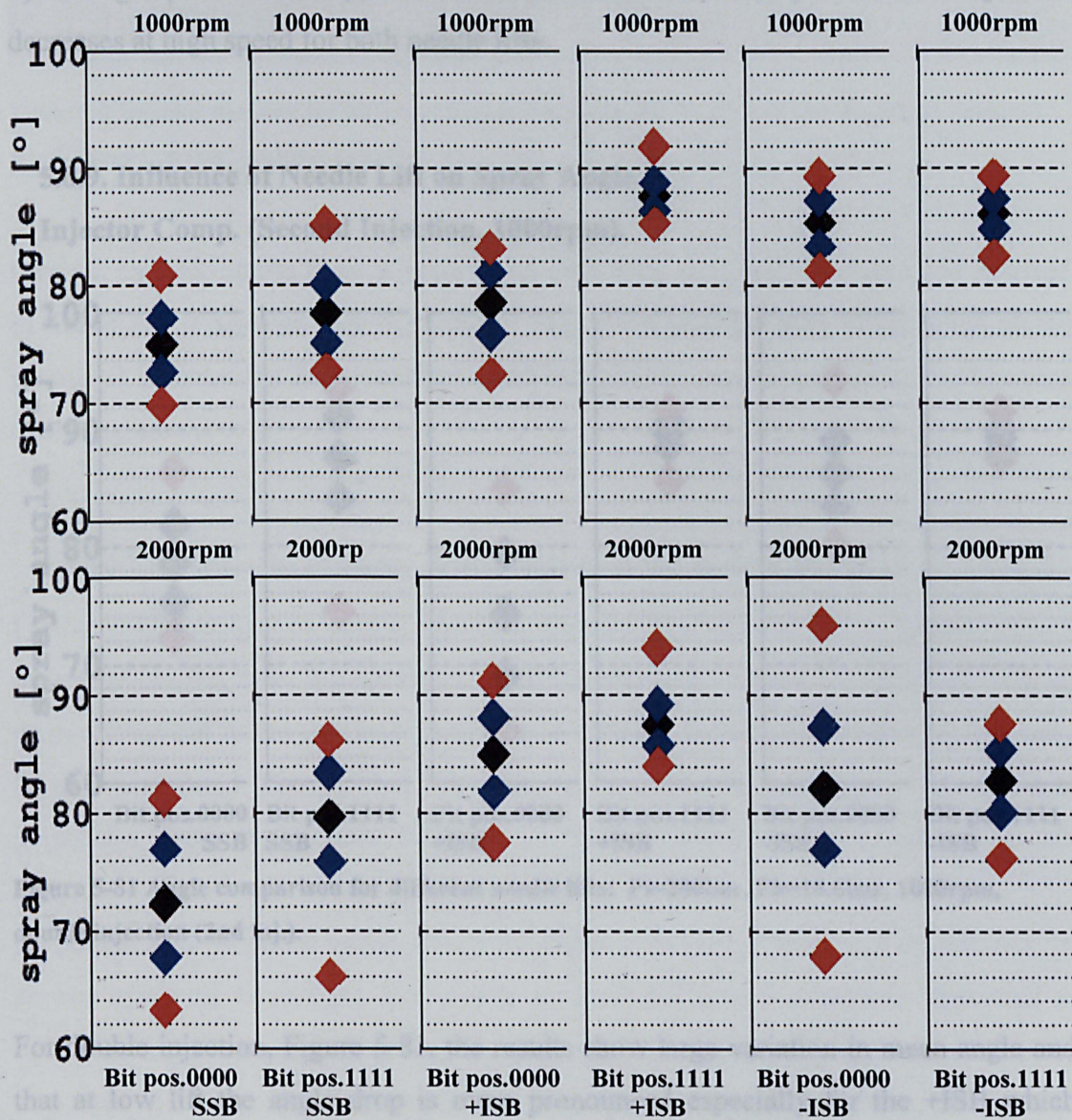


Figure 5-80 Angle comparison for different needle lifts:  $P_i=200\text{bar}$ ,  $P_b=16.6\text{bar}$ , 2000rpm, single injection.



In general, when considering the needles lift as a parameter of analysis, the injector

The needle lift plays an important role in the control of the penetration; however, it has an impact on the spray stability, as can be seen in Figure 5-80. At low lift, the three prototypes present a drop in mean angle and a deterioration of the angle stability. The SSB in general already presents a high STD even at full lift and switching to low lift does not change much the situation. The +ISB is the injector presenting the highest drop in mean angle and also the highest increase of STD from full to low lift. The -ISB presents the best performance at 1000rpm with no mean angle variation and a very low STD variation however at 2000rpm the injector present a sever degradation in stability at low lift whereas the +ISB looks almost unaffected by the high speed. Generally, it can be observed that the stability of the three injectors decreases at high speed for both needle lifts.

Table 5-3 Injector ranking for different parameter variation. (1,2,3) injector prototype ranking.

### 5.8.9. Influence of Needle Lift on Spray Angle.

Injector Comp. (Second Injection, 1000rpm).

Overall, by ranking the three injector types over each analysed parameter summarised

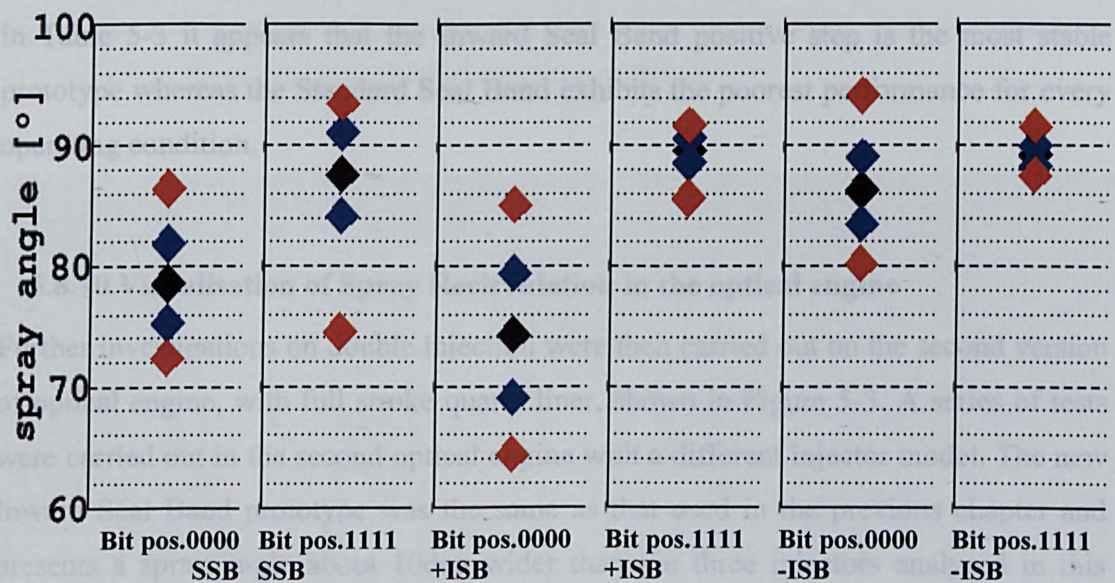


Figure 5-81 Angle comparison for different needle lifts: Pi=200bar, Pb=16.6bar, 1000rpm, double injection (2nd inj.).

For double injection, Figure 5-81, the results show large variation in mean angle and that at low lift the angle drop is more pronounced especially for the +ISB which shows the highest STD angle. The -ISB is the most stable of the three prototypes against the needle lift variation and even the mean angle does not suffer a sever drop.



In general, when considering the needles lift as a parameter of analysis, the injector showing the best performance in terms of stability is the Inward Seal Band negative step. However, for all the other parameters considered so far the the Inward Seal Band positive step has exposed the best performance of mean angle variation and of spray stability.

	Performance	spark plug presence	Engine speed variation	Single vs. 2nd Inj.	Back pressure single inj.	Back pressure 2nd Inj.	Needle lift variation (single Inj.)	Needle lift variation 2000rpm	Needle lift variation (2 Inj)	rail pressure variation
SSB	mean angle variation	+	+	-	-	-	+	+	--	\
	Angle stability	3	3	2	2	3	3	3	3	\
+ISB	mean angle variation	+	++	+	++	++	-	+	--	+
	Angle stability	1	1	1	1	1	2	1	2	1
-ISB	mean angle variation	+	+	+	+	++	+	++	+	+
	Angle stability	2	2	1	1	2	1	2	1	2

Table 5-3 Injector ranking for different parameter variation. (1,2,3 injector prototype ranking. ++,+,- very positive, positive, negative)

Overall, by ranking the three injector types over each analysed parameter summarised in Table 5-3 it appears that the Inward Seal Band positive step is the most stable prototype whereas the Standard Seal Band exhibits the poorest performance for every operating condition.

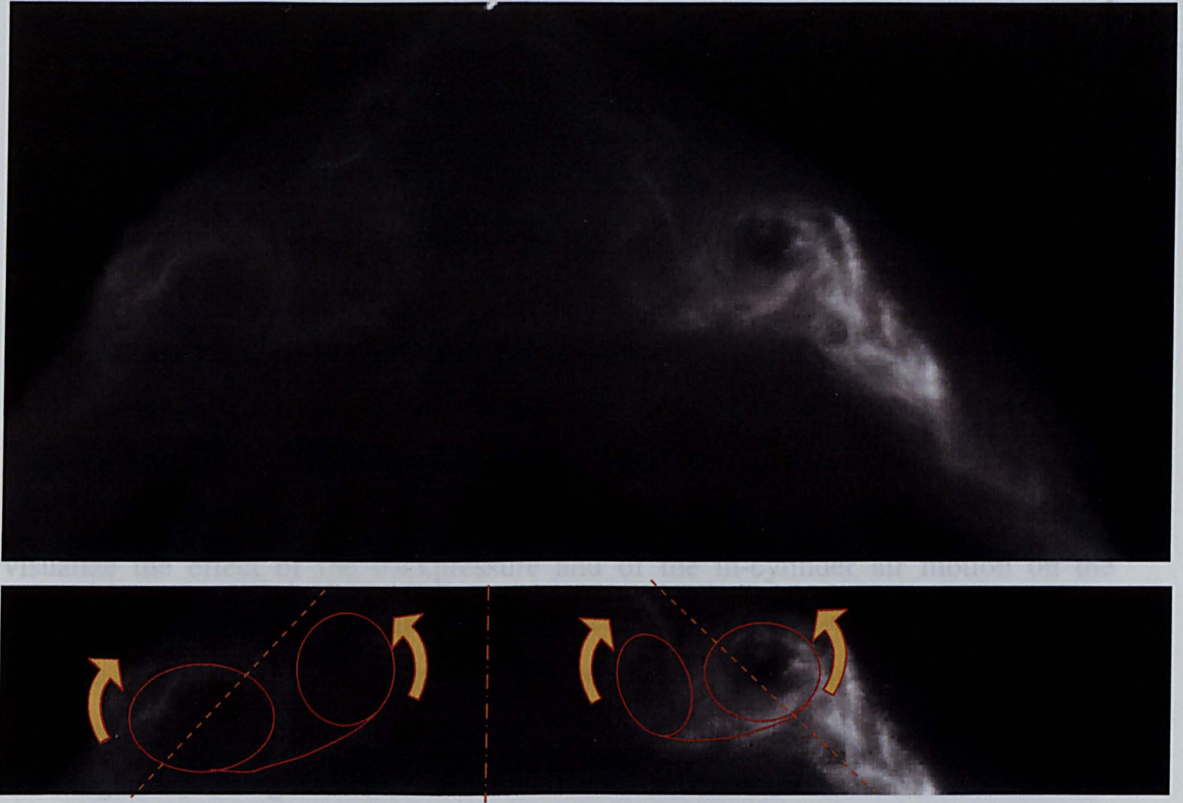
### 5.8.10. Visualisation of Spray Recirculation in the optical engine

Further investigations on double injection were then carried out on the second version of optical engine, with full stroke quartz liner, shown in Figure 5-3. A series of tests were carried out in the second optical engine with a different injector model. The new Inward Seal Band prototype was the same as that used in the previous chapter and presents a spray angle about 10deg wider than the three injectors analysed in this chapter.

In the previous section it was analysed the effect of the spray angle and its stability for several operating conditions. It was said that such outcome is extremely important as it determine if the spray injection evolves toward the spark plug area or instead impinges against in-cylinder components (valve, spark plug, liner, piston, etc.) or also if the spray presents a repeatable pattern rather than spray-to-spray variation which could lead to misfiring events.

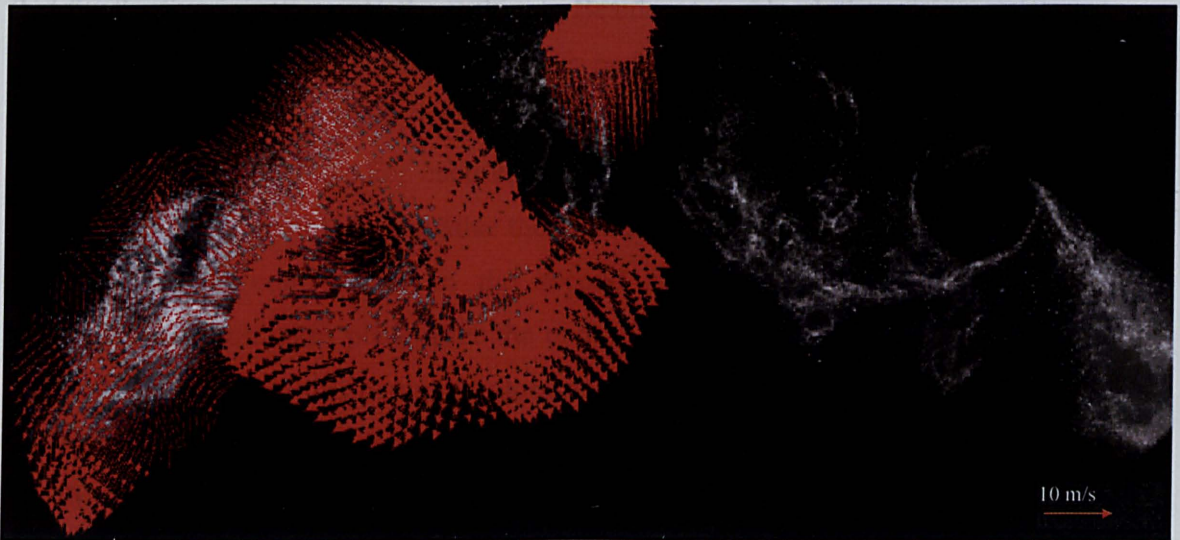


spray development. In Chapter4, it was shown the typical structure of the wake



**Figure 5-82 Mie scattering images: High-speed video of spray injected under ambient condition at 2.1ms ASOI,  $P_i=200\text{bar}$ , 1ms Inj. Duration, Bit pos.1001.**

a source of distortion and it was not possible to visualise the recirculation as clear as



**Figure 5-83 Recirculation velocity field of spray (using PIV) injected in ambient condition at 1.93ms ASOI Injection pressure of 200bar and needle set to 1001 bit position.**

However there are other aspects playing an important role in the flow propagation, in the space utilisation, and in particular the spray recirculation as it was observed in the previous chapter can be consider as a driving phenomenon of the final stage of the

spray development. In Chapter4, it was shown the typical structure of the wake evolution for an injection under ambient pressure.

Figure 5-82 reports a rotated snap shot of the image shown in the previous chapter for an injection under ambient condition which clearly illustrates the two pairs of counter rotating vortices. The confirmation of the way these vortices rotated and the order of magnitude of their velocities are shown in the velocity field in Figure 5-83.

However, the PIV post processing was unable to capture completely the velocity field for the internal wake and only a small group of vectors near the injector axis which show the upward direction of the flow agrees with the order of rotation schematised in Figure 5-82.

The same 2D Mie scattering investigation was then applied on the Hydra engine to visualize the effect of the backpressure and of the in-cylinder air motion on the reticulating flow. In order to relate the recirculation to the in-cylinder air motion it must be kept in consideration the fact that both intake valves are on the right of the image and therefore according the crank angle position the tumble intensity is likely to be higher on the right side.

By mean of an optical fibre, it was possible to adjust the laser sheet to split the spray through its symmetry plane. However, the presence of the cylindrical liner introduced a source of distortion and it was not possible to visualise the recirculation as clear as that for the free injection into the ambient. Beside, at part load, the raising piston near the top dead centre was also cutting the laser path creating large areas of shadow.

The test conditions, at which it was possible to visualise the recirculation area, are listed in Table 5-4 below. For each case, it is shown an image during the injection event in which is possible to visualise the formation of the external vortex and have a reference of the cone angle. In the second snap shot it is shown the actual recirculation which takes place after the end of the injection. As the static nature of the images reported in this paragraph does not give the feeling of the flow motion the same image is repeated tracing the recirculation areas with respect to the injector axis and of the cone profile traces.

Cylinder pressure		1bar		2.7bar	4bar
Engine speed		2000rpm	1000rpm	1000rpm	1000rpm
Injection duration	0.6ms		Case5	Case6	Case7
	1ms	Case4	Case3	Case1, Case2	

Table 5-4 Test conditions for spray recirculation visualisation (for all cases full lift 1001).

The first two cases show the recirculation for same injection conditions which gives a



reference of the nature of the recirculation repeatability for different spray events. In Figure 5-84 (case1), the top image of the spray at 0.56ms ASOI shows a visualisation in which is possible to observe the formation of the external wake. At this stage, the spray is too dense to allow the laser light passing through the spray cone and therefore no information of recirculation formation inside the cone spray.

In the second image the visualisation shows a snapshot taken after the end of the injection at 1.28ms ASOI. At this point of the spray evolution the plume is less dense and the laser light is no longer trapped by the spray cone and therefore it is possible to visualise the full section of the reticulating area which gives a better view of the late development of both inner and outer wakes.

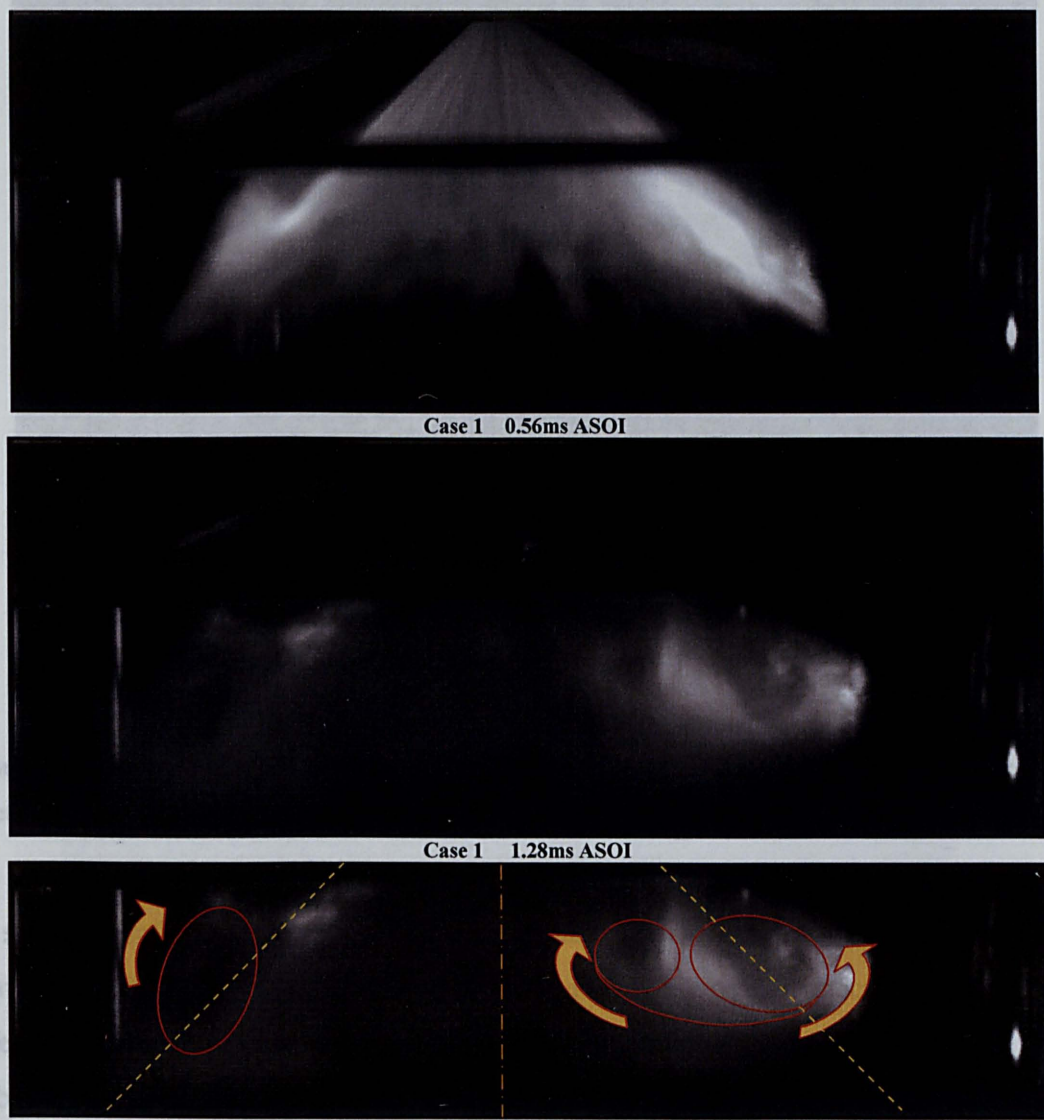


Figure 5-84 Mie scattering images of spray recirculation. N/A 70 BTDC, 1000rpm, Pb=2.7bar, injection duration  $T_i=1.0$  ms,  $P_i=200$ bar, Needle lift set up. Bit. 1001

The recirculation image of Figure 5-84 is similar as the visualisation proposed in



Figure 5-85 in which it can be observed the counter rotating vortices. However in the left side of the spray only the external wake is visible with no information about the inner recirculation which is either missing or is simply hidden by the shadow due to the lighting arrangement.

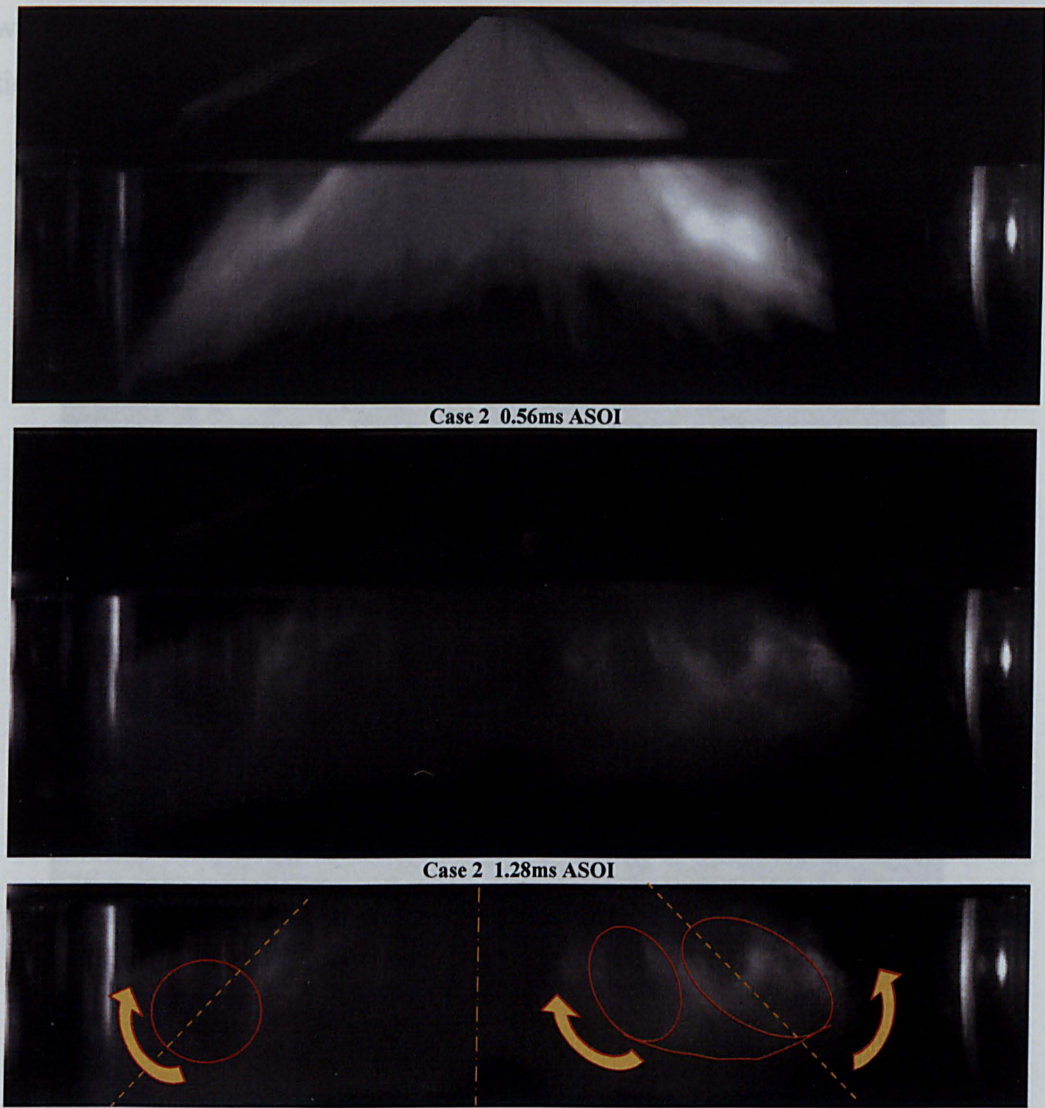


Figure 5-85 Mie scattering images of spray recirculation. N/A 70 BTDC, 1000rpm, Pb=2.7bar, injection duration  $T_i=1.0$  ms,  $P_i=200$ bar, Needle lift set up. Bit pos 1001.

The recirculation areas in Figure 5-85 are very similar to the previously observed for the same operating conditions and even the wakes present similar relative distance from axis and cone traces. In both cases, the two sides of the injection look quite different and overall the recirculation areas seem very asymmetric that could be probably due to the disturbing effect of the cylinder tumble.

However, in all recirculation images observed under ambient condition or in the hydra engine, the external wake was always found to lay on the spray cone trace direction whereas the internal wake was displaced toward the injector axis.



**5.8.10.1.Effect of Engine speed on the spray recirculation**

Figure 5-86 and Figure 5-87 compare the recirculation images obtained at 1000 and 2000 rpm, respectively. The snap shot of the spray recirculation at ambient cylinder pressure at 1000 rpm presents an image of the wakes quite blurry and undefined. However, from the video of the spray evolution it could be possible to trace the wake motion for both side of the spray.



Case 3 0.66ms ASOI



Case 3 2.0ms ASOI

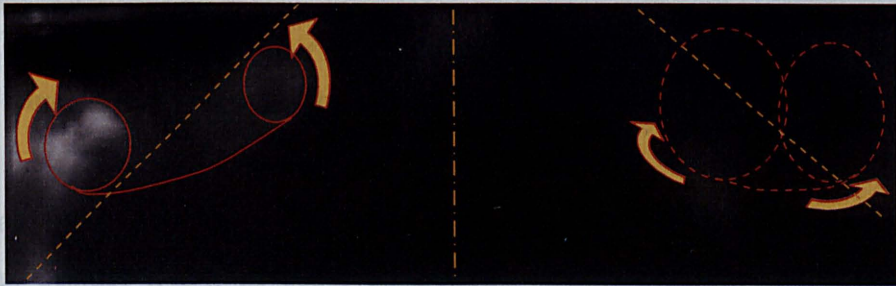


Figure 5-86 Mie scattering images of spray recirculation. N/A 120 BTDC, 1000rpm, Pb=1bar, injection duration Ti=1.0 ms, Pi=200bar, Needle lift set up. Bit pos 1001.





Case 4 0.66ms ASOI



Case 4 2.0ms ASOI

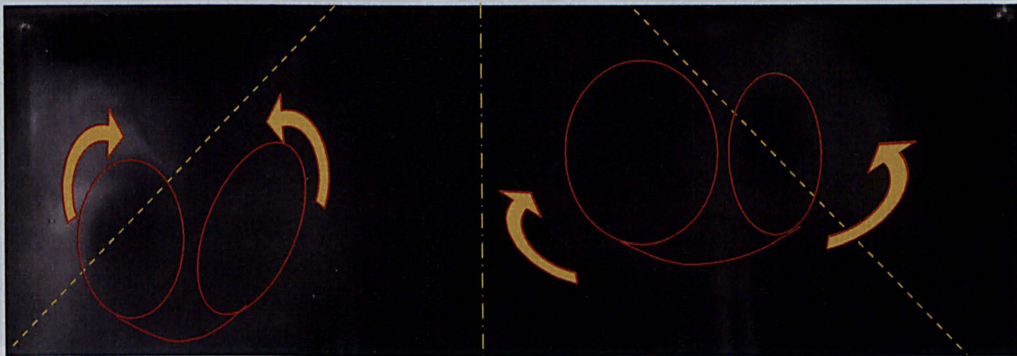


Figure 5-87 Mie scattering images of spray recirculation. N/A 120 BTDC, 2000rpm,  $P_b=1\text{bar}$ , injection duration  $T_i=1.0\text{ ms}$ ,  $P_i=200\text{bar}$ , Needle lift set up. Bit pos 1001.

The spray recirculation at 2000rpm produces larger wakes than those seen at 1000rpm, besides it can be observed a higher degree of asymmetry of the vortex levels which could be due to the effect of the higher tumble motion caused by the higher engine speed.

For the case at 0.6ms injection duration, the snap shot for the recirculation are



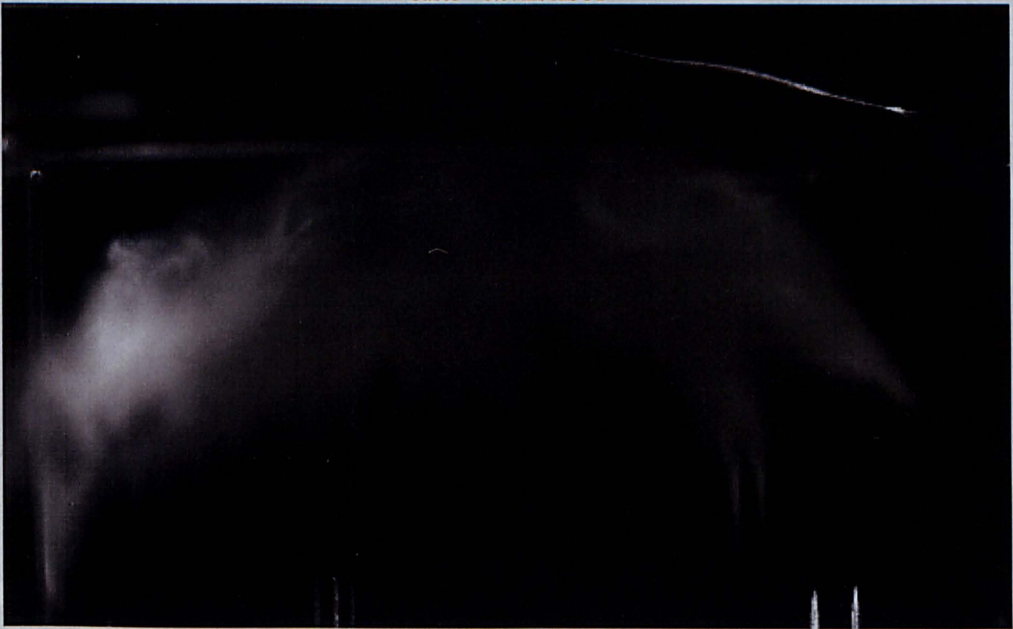
**5.8.10.2.Effect of backpressure on the spray recirculation**

Next, a comparison between different crank angle phases and therefore different backpressure will be shown in Figure 5-88, Figure 5-89 and Figure 5-90

is at a lower level position compared to the right recirculation area. In this case the strong recirculation has been observed. The spray is more symmetrical and both side vortex pairs are visible. A common point of comparison between the



Case5 0.67ms ASOI



Case 5 1ms ASOI

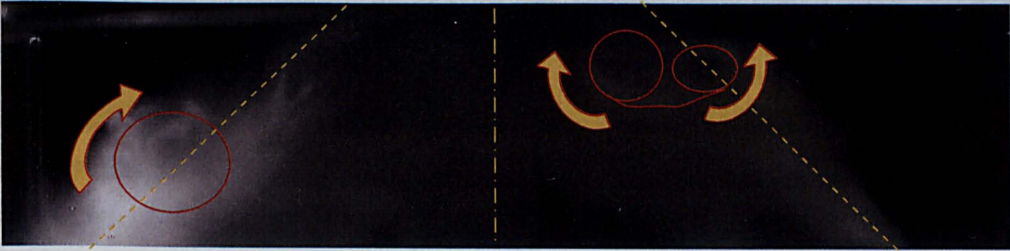
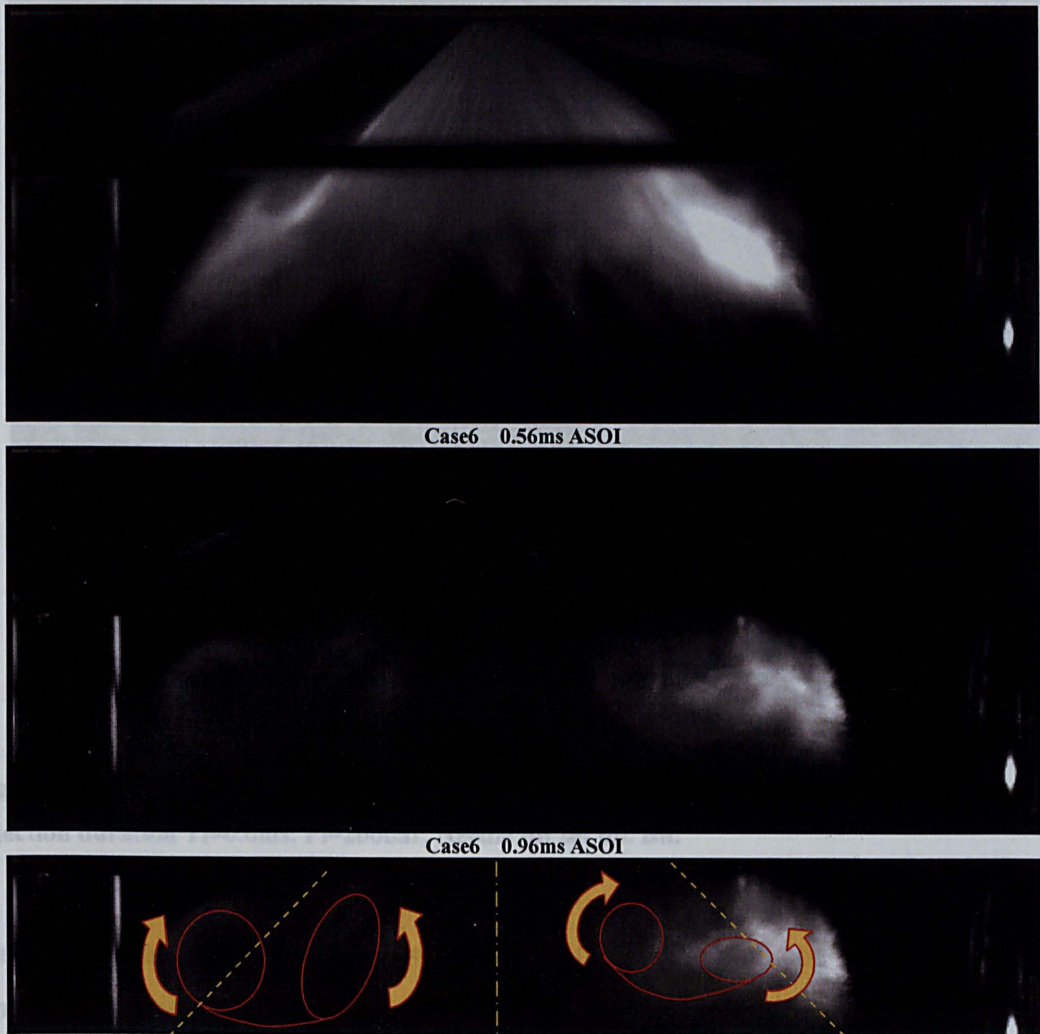


Figure 5-88 Mie scattering images of spray recirculation. N/A 120 BTDC, 1000rpm, Pb=1 bar, injection duration  $T_i=0.6\text{ms}$ ,  $P_i=200\text{bar}$ , Needle lift set p. Bit 1001.

For the case at 0.6ms injection duration, the snap shot for the recirculation are

compared to that of 1ms ASOI. The recirculation area at ambient condition in Figure 5-88 again shows only the two counter rotating wakes on the intake side. However, the exhaust side shows the presence of a large external vortex which is at a lower level position compared to the right recirculation area. In this case the strong recirculation asymmetry could be due to the early injection when still the intake phase has not completely finished and the tumble (or air wakes) caused by the closing valve are relatively strong and they could introduce a drag resistance to the propagating spray vortices.



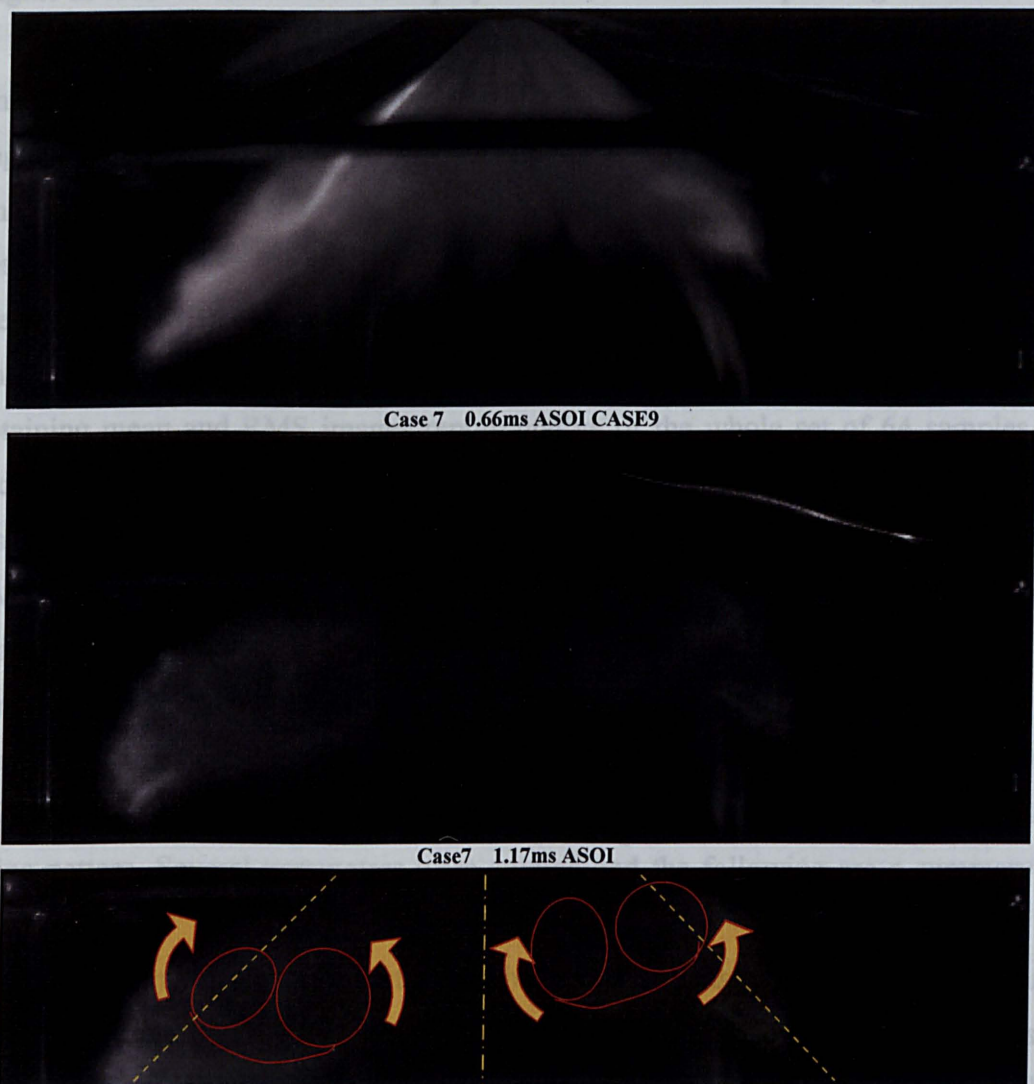
**Figure 5-89** 2D Mie scattering images of spray recirculation. N/A 70 BTDC, 1000rpm, the higher  
**Pb=2.7bar**, injection duration  $T_i=0.6\text{ms}$ ,  $P_i=200\text{bar}$ , Needle lift set up. Bit pos.1001. air motion.

Therefore, it seems that for this engine setup and for this injector prototype there is an

At 2.7 bar backpressure (Figure 5-89) the wake pattern seems more symmetrical and both side vortex pairs are visible. A common point of comparison between the recirculation at 1000rpm ambient vs. high cylinder pressure is the position of the



wakes with respect of the spray leading edge. At low backpressure the wakes does not drag the whole spray flow and the spray propagate further. On the contrary, the higher is the cylinder pressure the more compact are recirculation and the spray leading edge.



**Figure 5-90** Mie scattering images of spray recirculation. SC 70 BTDC, 1000rpm, Pb=4bar, injection duration  $T_i=0.6\text{ms}$ ,  $P_i=200\text{bar}$ , Needle lift set up. Bit.

Finally, at 4bar backpressure it is still possible to observe both counter rotating wakes. The recirculation pattern looks again very asymmetrical with the exhaust pair of wakes at a lower level with respect of the intake side wakes. In this case, the higher pressure could amplify the effect of the drag forces due to the in-cylinder air motion. Therefore, it seems that for this engine setup and for this injector prototype there is an optimal backpressure ( $\sim 2.7\text{bar}$ ) in which air motion from induction phase and drag effect from the increased air density do not affect the symmetry of the recirculation pattern.

---

## 5.9.SUMMARY

The present chapter exposed the experimental work performed in the hydra optical engine in order to characterise the spray structure at different operating conditions and to identify the effect of the internal air flow on the spray angle and its stability.

The investigation strategy was based on the comparison of the spray images and angles for different injector prototypes and for three different operating conditions. The injector prototypes differs from each other according to the relative position between the needle and cartridge sealing area so called “step” and are referred to as the positive (+ISB), neutral (SSB) or negative (-ISB) step.

The images of the spray at the end of the injection were post processed in order to obtaining mean and RMS images representative of the whole set of 64 samples for each operating condition. For the purposes of presentation, comparison and discussion, the spray images are grouped by single shoot (instantaneous), mean and RMS images at a common operating parameter and are followed by the statistical analyses of the spray angle which revealed useful information of the sensitivity of the variables on the mean cone angle and stability.

For all the injector types the mean images showed, in general, very well defined strings even over an average out of 64 images thus showing a strong and repeatable string pattern. Several parameters were studied and the following are a summary of each effect.

In the first comparison, the effect of the backpressure was investigated for the three different injector types. No obvious difference was observed between the injectors at ambient cylinder pressure whereas at 10.9 bar the Standard Seal Band (SSB) prototypes showed slight asymmetrical shape tilted toward the sparkplug which suggests higher sensitivity to the tumble motion at higher backpressure. Similar results were confirmed at 16.6bar where the SSB spray seems to be stretched toward the sparkplug and it presents a smaller mean spray angle (78deg) than those of the Inward Seal Band injectors (both steps) by 10 degree. For all three tested backpressures, the SSB revealed the highest standard deviation which also suggests highest angle instability.

The previous comparison at 16.6bar was then repeated at lower needle lift (bit position 0000) for the three injectors and showed a significant decrease in penetration due to the drop in discharge coefficient. The negative step prototype presents the most symmetrical shape while both neutral and positive steps describe a non-uniform



---

penetration along the spray circumference.

It was then tested how the increase of engine speed and the presence of the spark plug affect the spray by modifying the in-cylinder air motion. As expected, the increase of speed produced an increase in angle variability (higher STD) due to the increase of air motion for all three prototypes whereas no relevant differences were identified by adding the sparkplug.

Each injector was then separately analysed according a parametric comparison of the operating condition. It was observed that the penetration reduces considerably by increasing the cylinder pressure due to the resulting raise of the gas density which in turn intensifies the drag effect against the spray propagation. The spray shape also seemed to be affected by the backpressure and as the pressure rose the spray lost its symmetry progressively and stretched toward the spark plug. In fact, as for the spray penetration, the increase in the surrounding gas density amplifies the drag forces and therefore reduces the fuel droplets velocities (penetration) so that they become more vulnerable to the tumble motion directing the spray towards the sparkplug. Since the tumbling, by its nature, is an unstable phenomenon then its effect is transmitted to the spray stability which damps down with the increase of the backpressure.

First, the Standard Seal Band injector was analysed against the backpressure variation and the results revealed a significant sensitivity of the spray penetration. The angle reduction is accompanied by an increase in STD as the backpressure increases indicating also an increase of spray-to-spray variation which could introduce problems such as misfiring during the part load mode.

The Inward Seal Band injectors present similar trend as the Standard Seal Band but are less sensitive in terms of mean angle variation and STD revealing a higher resistance against the in-cylinder pressure conditions. More specifically both step-type injectors seem preserving their symmetrical shape despite the increase in gas density and the mean images seem more defined in terms of string structure which suggests that the spray pattern is more repeatable.

The same backpressure analysis was then repeated for the step-type injectors for lower rail pressure of 100 bar showing the similar decrease in penetration and the mean spray angle variation against the backpressure as seen at 200bar injection pressure. It can be concluded that the rail pressure may be a driving parameter for the mechanism concerning the spray atomisation however; it does not seem to affect appreciably the spray shape and its stability.

---

As one of the main advantages of the Piezo Injector is the possibility to vary the needle lift at different levels according the activation of the piezo body which set the maximum lift position of the pintle. Therefore, it was of interest to see the comparison of the angle and penetration characteristics between the maximum needle lift (Switches @ 1111) and minimum needle lift (Switches @ 0000). The most noticeable difference after decreasing the needle was the well defined decrease in spray penetration which provides a possible mechanism to control the penetration with this type of injectors and therefore to prevent wall/piston impingement. By switching the needle lift from minimum to maximum, at 200bar injection pressure and 1bar backpressure, both step-type injectors present an increase in axial penetration of 36% from 5.5mm to 7.5mm which can give a high flexibility for the penetration control at part load.

In terms of angle comparison, the SSB has shown the highest STD and therefore the highest spray angle variability. The ISB negative step presents a much higher mean angle than the SSB but the STD is much reduced for both lifts with a slight improvement at full lift. The Positive step injector prototype presents an intermediate behaviour between SSB and -ISB. At low lift, the mean angle is as low as for SSB with similar STD whereas at full lift the mean angle rises of about 10deg comparable with the negative step injector. Thus, the results indicate that increasing the valve lift causes an increase in the spray cone angle and improves its stability. Among the three prototypes, still the no-step type presents the worst performance in terms of angle variability for both lifts whereas the negative step ISB seems to be the most robust against needle lift change.

Another important potential with the DISI technology is the ability to perform the double injection strategy which can improve transition between part load and full load, by injecting partially during the intake phase and partially during the compression stroke and at part load can be beneficial for soot emissions reduction, and can provide improved fuel economy at the transition area between stratified and homogeneous mode.

For this strategic potential a limited comparative angle analysis at different operating conditions was performed. The results have shown that the wake of the first injection was strong enough to influence the in-cylinder air motion a head of the second injection, affecting its spray characteristics with an increase in spray cone angle and a deterioration of its stability.



---

The effect of backpressure in double injection mode presents a slightly different behaviour from the single mode due to the overlapping effect produced by the first injection and tumble. The increase of angle variation is still present in the same extend seen for single injection, however, at 16.6bar it can be observed a mean angle recovery which may suggest that at higher backpressure, the combination effects of the wakes caused by the first injection and by the higher tumble can produce a diverging effect on the second injection angle.

In the comparison of second injection for the three Seal Band types the SSB has revealed the poorest performance in terms of mean cone angle variation and spray stability. The second injection of the +/-step-type injectors showed better performance and overall the positive step Inward Seal Band has shown to be the most robust prototype in terms of stability and mean angle variability at different operating conditions. In Table 5-3, the three injector prototypes were ranked for each individual parameter and it appeared that the Inward Seal Band positive step is the most stable prototype. whereas the Standard Seal Band presented the poorest performance for every operating condition.

Further investigation on spray recirculation was then carried out on a second version of optical engine with full stroke quartz liner and the tests were carried out with the same injector model used in chapter 4

The spray recirculation, as explained above, has been considered as the driving phenomenon of the final stage of the spray development. 2D Mie scattering investigation was applied on the Hydra engine in order to visualize the effect of the backpressure and of the in-cylinder air motion on the reticulating flow for different operating conditions. The recirculation area showed the presence of two pairs of counter rotating vortices as previously observed (Chapter 4) in the visualisation for free injection under ambient condition.

The results of spray images showed that for different cylinder pressure the counter rotating wakes present an asymmetric pattern with respect of the injector axis with the recirculation on the intake side having a lower penetration which may be due to the intake air stream or the in-cylinder tumble. However, it seems that for this engine setup and for this injector prototype there is an optimal backpressure (~2.7bar) in which air motion from induction phase and drag effect from the increased air density do not affect the symmetry of the recirculation pattern. The spray recirculation at 2000rpm exposed more expanded wakes than those observed at 1000rpm, in addition,

---

the spray images showed a higher degree of asymmetry of the vortex levels which could be due to the effect of the higher tumble motion caused by the higher engine speed.



---

## Chapter 6.

### *Conclusion and recommendations for future work*

The experimental investigation of the internal flow and spray characteristics from outwards opening gasoline pintle injectors has been carried out at different operating conditions using a range of optical techniques. In the present research programme measurements were obtained in large-scale transparent models of pintle-type injectors and several real size prototypes within a constant volume chamber and optical engines.

A summary of the main findings obtained from the results of this research programme are presented in the following sections:

#### **6.1. LARGE-SCALE MODEL**

The investigation on the large-scale nozzle model has provided additional benefits in understanding the internal flow structures and their dynamics between the injector needle guide and nozzle seat and the complex two-phase in-nozzle flow between the nozzle seat and the nozzle exit. More specifically, the results revealed the presence of four counter-rotating vortices inside the injector and their effect on the tangential oscillation of the resulting spray. Furthermore, the magnified image of the spray and of the internal flow pattern obtained with the CCD camera and the high-speed video camera have identified the presence of air entrainment, cavitation at the nozzle exit and their combined effects on the spray structure and surface. A summary of the main findings observed in the large-scale model is reported below:

- Between the end of the square guide on the needle and upstream of the nozzle seat the flow exhibits a complex nature, consisting of four jet flows which after interaction created four pairs of unstable counter-rotating vortices with a predominant circumferential oscillation as was observed from high-speed videos. Simultaneous visualisation between the upstream flow and the spray showed that the source of the observed tangential flow oscillations was actually the upper vortical structure.

---

Parametric analysis of the measured LDV data has revealed a linear increase of these tangential flow frequencies with flow rate, needle lift and velocity at constant needle lift.

- Spray visualisation of the in-nozzle cavitating flow in convergent-divergent nozzle seat area has shown the presence of gas phase downstream of the nozzle seat region. These bubbles could be either air entrainment (hydraulic flip) due to the separation of the liquid stream from the internal surfaces at operating conditions with low to moderate flow rates where the cavitation number was below 1, or purely cavitation when the operating conditions correspond to a cavitation number equal or higher than 1.1.
- From several optical and quantitative considerations, it was established that cavitation and air entrainment are two different phenomena possessing different structures and dynamic evolutions and occurring at different operating conditions.
- The study of the air entrainment phenomenon has shown that the emerging spray could have two distinct cone angles according to the location of the air entrainment in the nozzle, which was attached either to the needle or to the cartridge wall surfaces. In the former case the air bubble attached to the needle forced the flow to be deflected away forming a large spray cone angle whereas in the latter case the liquid flow was deflected inwards as it passed over the air bubble attached to the cartridge surface, thus producing a smaller spray angle.
- The internal flow and spray visualisation images revealed that the string-type spray structure with both cone angles was formed by longitudinal filaments due to the profiling effect of the liquid passing around the trapped air bubbles. These images showed the presence of alternating thin and thick filaments, with the latter positioned downstream of the air bubbles and the former located between two adjacent bubbles.
- A quantitative analysis of the strings number at different operating conditions showed an increasing trend of the strings number with flow rate (or Reynolds number), more specifically, the spray velocity was identified as the main driving parameter promoting the strings number increase.
- With the cavitating model, although the obtained string-type structures were similar to the spray structures observed in real-size injectors, it can not be stated that the only mechanism driving the filament formation was air entrainment since a finer string structure has been observed in an injector design not having a convergent-divergent nozzle seat, i.e. with parallel nozzle seat, where no air entrainment was observed. However, it can be argued that in the parallel nozzle seat injector, also called non-cavitating design, the strings are formed by much smaller size bubbles right at the



---

nozzle exit which are unable to penetrate into the nozzle but they can still produce the profiling effect responsible for the finer string formation.

- Inception of cavitation in the convergent-divergent nozzle was observed only for needle lifts of 0.57 and below, with full cavitation occurring at the lower range of needle lifts. Visualisation of the cavitation bubbles at all conditions showed that cavitation initiated at the edge (seat region) formed by the converging-diverging passage, followed by a quick disintegration and dispersion as it was convected downstream towards the nozzle exit. The flow dynamics of this phenomenon proved to be much faster than those observed for the air entrainment bubbles so that a higher frame rating was required to capture the sequential motion of the cavitation evolution.
- In order to discern the two phenomena, the in-nozzle flow was visualised for certain operating conditions where the air entrainment and cavitation bubbles were occurring simultaneously, which showed clearly the difference between the bubble and vapour dynamics. The results also revealed that the mechanism driving string formation was still air entrainment; however, the presence of cavitation at high liquid velocities was creating a spray structure resembling that of the real size injector.
- Flow visualisation also revealed how the presence of cavitation contributes to the enhancement of the break up of the liquid surface structure downstream of the nozzle exit, which confirms the beneficial effect of cavitation on fuel atomisation.
- The statistical analysis of the strings number in the real size injector showed good correlation with the large-scale model but only at high needle lifts and Reynolds numbers. In the large-scale model the observed linear growth is valid across the whole range of measurements whereas in the real size of linearity can be observed only at high Reynolds numbers which correspond to full needle lift.

Overall, in the real size nozzle it can be argued that the flow velocity is not the only parameter driving the strings number formation as in the large-scale model; in fact this phenomenon does not necessary obey the laws of dynamic and geometric similarities.

However, qualitative information could still be derived from the enlarged model and for instance, it was observed that both injector sizes exhibited the same trend of increasing strings number with injection pressure.

---

## 6.2. REAL SIZE INJECTOR

### 6.2.1. Spray Characteristics

Following the large-scale model, the investigation of the inward seal band injector focused on the characterisation of the real size injector. Mie imaging, PDA and PIV were used to evaluate the spray development, droplet size and velocity distribution, as well as the air entrained motion near the nozzle exit. However due to difficulties with the instrumentation in the optical engine, like optical accessibility, distortion and signal attenuation, the real-size nozzle investigation was first carried out in more detail in a special by designed constant-volume chamber followed by some limited measurements inside the optical engine. Here is the summary of the main findings:

- Spray visualisation of the pintle-type injector flow showed the filament-like nature of the emerging spray in the form of longitudinal strings which were characterised by a non-homogenous droplet velocity and droplet size distribution, similar to that of the individual spray of a multihole injector. The magnified images of the emerging spray flow at standard conditions revealed the presence of three spray structures at different phases of its development.
  - The first type of structure occurred in the early phase of the spray, during the needle opening period, as the fuel emerged from the nozzle and was characterised by a group of large droplets and a liquid sheet moving at uniform velocity against the shearing action of the air.
  - The second spray structure, which followed in time the first type, and was characterised by a stable set of well-defined straight strings and a fishbone structure.
  - After a fixed period, the third spray structure appeared when the well-defined string pattern started oscillating transversally. The PDA results at the centre of the string showed sharply the change between the two phases associated with an increase in the velocity range of the droplet sample and a decrease in AMD probably due to flow turbulence, which promoted the secondary break up. Subsequent investigation with 2D Mie scattering, PDA and PIV diagnostic measurements revealed that the possible cause of this instability was the strong secondary break up and the formation of a recirculation zone, which disturbed the straight propagation of the strings.
- The overall droplet size and velocity distributions have confirmed the sequential



---

presence of the three string structures mentioned above. In addition, the results revealed the presence of a tumble motion propagating downwards in the wake of the spray.

- According to the Weber number trend, the secondary breakup takes place up to an axial location of 20mm (27mm in jet direction). This result was in agreement with the mean diameter distribution which shows a reduction from 14 $\mu$ m to 7 $\mu$ m (50%) within 27mm from the injector tip.
- At axial location beyond 40mm, phenomena such as turbulence and recirculation could promote droplet collision and, therefore, coalescence represented in PDA plots by bimodal distribution corresponding to a group of very fine droplets and a group of agglomerated droplets.

#### **6.2.2. Spray Recirculation and Air Entrainment**

- The qualitative analysis of the spray image obtained by 2D visualisation, PIV and LDV diagnostics, along the symmetry plane has revealed the presence of two counter-rotating rings forming internally and externally to the spray cone trajectory. It was interesting to note that the spray structure within 20mm from the nozzle exit looked completely undisturbed. The images sequences also showed that the propagation of the external wake was in the direction of the jet whereas the internal vortex was pushed towards the injector axis through expansion of the outer vortex and the action of air entrainment.
- The PIV technique was also used to quantify the air entrainment process by seeding the surrounding air with fine quasi-static water droplets and injecting fuel at 200bar towards ambient backpressure. The results showed the formation of a jet like air motion almost in the normal to the spray direction as soon as the spray emerged from the nozzle. The velocity field of the air increased progressively with time after the start of injection as the spray evolved. The area of air entrainment interacting with the spray surface gradually increases with time.
- Towards the end of injection at 0.63ms ASOI and beyond, when the droplet velocities were reduced, the PIV images showed clearly how the entrained air penetrated into the spray contributing to the formation of recirculation zones. The results also showed how air entrainment acted on the internal recirculation zone forcing it to be displaced toward the injector axis.
- Comparison between the PIV and the LDV measurements showed good

---

agreement, which provided added confidence to the presented results. The LDV data of air entrainment at different injection pressures have shown the variation of the air velocity component normal to the spray surface and its proportionality to any changes of the injection pressure.

- This outcome could link the current results with the previous findings in the large-scale model where it was seen how the air bubbles entrained up stream at the nozzle exit were responsible for the string formation. It was also quantified in the real size injector how the increase in rail pressure (i.e. the injection velocity) affected the increase in the number of strings. Therefore, from the PIV outcome, it could be deduced that the link between strings number and injection pressure is due to the increase in the air entrainment velocity at the nozzle exit which affects the size of the entrained air bubbles into the nozzle and, thus, the strings number.

### 6.2.3. Parametric Studies

- Further parametric analysis was carried out in a constant-volume chamber in order to simulate the actual cylinder backpressure and temperature. The effects of these parameters together with injection pressure were quantified by considering the spray development and the droplet velocity and size distribution obtained from 2D Mie images and PDA measurements at an axial position of 10mm. The following is a summary of the main findings:
  - At a chamber temperature of 160°C, an increase in backpressure caused an immediate decrease in the average droplet velocities due to the increased drag motion as a result of the increase in gas density. The consequence of this is droplets deceleration resulting in a smaller Weber number and reduced probability of secondary breakup. Another consequence could be an increase in droplet penetration time and therefore the longer time available for evaporation. The latter effect was evident in the droplet size trend, which decreased as the backpressure increased due to the loss of droplet mass during the evaporation process.
  - The parametric analysis revealed a droplet velocity increasing as the rail pressure increased and a droplet diameter decrease due to the increase in the droplet relative velocity and, therefore, the Weber number which enhanced the droplet secondary break up.
  - Finally, the increase of chamber temperature gave rise to an increase of the



---

droplet velocity and a decrease of the droplet diameter. The former effect is probably linked to the decrease in gas density and, therefore, a decrease in the drag force from the surrounding gas, whereas the latter effect is caused by the enhanced evaporation resulting from the increase in temperature.

### **6.3. REAL SIZE INJECTOR IN THE OPTICAL ENGINE**

To complete the characterisation process it has been necessary to observe the injector performance under actual operating conditions. The spray visualisation was thus carried out in an optical engine in order to observe the effects of the in-cylinder airflow and thermodynamic conditions on the spray stability and spray cone angle. This study was based on the comparison of three different injector prototypes varying in terms of their exit geometry; more specifically, in the presence of a positive (+ISB), neutral (SSB) or negative (-ISB) steps between cartridge and needle in the cross-sectional profile. Different operating conditions were considered and at each condition the spray visualisation results were post-processed in order to obtain spray cone angle data and statistical images of the mean and RMS from a representative set of images.

- The first important observation for all injector types was the spray structure and, in particular, the string structure. The results showed a spray pattern with a well-defined string structure and a repeatable string pattern.
- For all three injector prototypes, it was observed that spray penetration was reduced considerably with increasing chamber pressure due to the resulting increase of gas density, which enhances the drag forces against the propagating spray; an increase from 1bar to 10bar produces a reduction in penetration of ~30%.
- The effect of engine speed on the spray characteristics was considered next; as expected, the increase in engine speed caused an increase of spray instability due to the augment action of the in-cylinder turbulence.

One of the advantages of the piezo injector is its adjustable needle lift through control of the piezo body activation. Therefore, the injector's response was compared at full lift and at minimum needle with the following conclusion:

- A strong decrease in spray penetration was observed when the needle lift was reduced which can be used for controlling the injection process and preventing wall impingement during part load operation.
- The comparison of the three prototypes revealed that the SSB exhibits the worst performance in terms of spray angle stability for both lifts and is not suitable for the

---

spray-guided configuration during part load operation, while the Inward Seal band negative step (-ISB) has proved to be the most robust and stable configuration against needle lift variation.

Another important flexibility offered by the piezo injector is its multiple injection operation due to its very fast response time, which can enhance the transition between part load and full load by fractioning the total fuel mass, injected during the intake and compression strokes. The main findings are listed below:

- In general, the first of a multiple injection was found to be similar to that of single injection but the second injection was affected by the residual flow field persisting from the first injection. More precisely, 200bar injection and low lift during the induction stroke the spray angle of the second injection was reduced and the angle instability increased. However, at the higher cylinder pressures during the compression stroke a good recovery in the mean cone angle of the second injection was observed which might be due to the fact that the residual flow field from the first injection was suppressed by the higher backpressure, being much less influential to the second injection spray.
- The comparison of the three injector prototypes identified the Standard Seal Band as the injector with the poorest performance in terms of spray stability and mean angle whereas both step-type injectors exhibited better performance; in particular, the positive step seemed to produce the most robust spray in stability with less spray flapping over the different operating conditions.
- Overall, the classification of the three prototypes has shown that the Inward Seal band positive step produces the most robust spray angle, which is appropriate for use in stratified fuel mixtures based on the spray-guided configuration, whereas the Standard Seal band injector (no step) has shown the poorest performance for almost each parameter analysis.

#### **6.4. SPRAY RECIRCULATION IN THE HYDRA ENGINE**

In order to investigate the spray recirculation phenomena under actual engine operating conditions, 2D Mie scattering imaging was carried out in the optical engine with the same procedure adopted for the free spray imaging presented in Chapter 4. The following effects of the backpressure and in-cylinder air motion on the spray reticulating flow were observed:

- At the late stage of injection, at about 1.0ms ASOI, has two toroidal counter rotating vortices similar to those identified with the free spray were observed, at the inner and



---

outer side of the spray jet. The cross sectional image of the recirculation zones showed an asymmetric pattern of the pairs of vortices with respect to the injector axis and that this pattern became more asymmetric with increasing cylinder pressure.

- The cause of this asymmetry was attributed to the disturbance from the air entrained during the induction phase, from the strong tumbling air motion and the increased drag effect at the higher cylinder pressure.
- The observation of spray recirculation at 2000rpm showed larger zones than those seen at 1000rpm.; at this speed the recirculation pattern revealed a higher degree of asymmetry probably attributed to the stronger in-cylinder charge motion and higher turbulence intensities at higher engine speeds.

## **6.5. RECOMMENDATION FOR FURTHER WORK**

### **6.5.1. Large-scale Injector Model**

The experiment in the large-scale injector model has proved to be a powerful tool in the effort to understand the mechanism responsible for the string formation in the generated sprays. Nevertheless, certain aspects of this phenomenon remain unexplained and require further investigation. For instance, the mechanism driving the formation of fine strings in the non-cavitating nozzle, where no air entrainment bubbles in the nozzle passage are detected, is still unresolved. However, it can be argued that the presence of tiny air bubbles near the nozzle exit, which were not visible through the optical window, are responsible for the string formation.

To address this problem the following experiments can be performed:

- The presence of these small air pockets could be assessed by testing different models with intermediate geometry between the parallel type (non-cavitating) and the convergent-divergent type (cavitating) nozzle. This approach could also provide a view of how the observed phenomena are related to the nozzle geometry and the way the angle of the convergent divergent nozzle seat influences cavitation.
- The observation of models of intermediate scale would help to assess how the scale affects the phenomena of cavitation and air entrainment, as well as the limits of the criteria of similitude. Therefore, it could be possible to obtain validation of the previous results and also to deduce results for the real size injector from the extrapolation of the outcome of the scaled models.

- 
- Further enhancement to the visualisation and the optical diagnostic techniques adopted for the large-scale model could be achieved by application of the refractive index matching method [35, 38, 99] in which the present working fluid (water) will be replaced by a mixture of liquids having a refractive index equal to that of Perspex. With this technique, the internal edges of the enlarged model would disappear when the model is filled up with this liquid mixture, thus preventing the light path from optical distortion. A previous PIV experiment in a large-scale model had shown some limitations due to the strong distortion of the image in the proximity of the internal edges. The use of refractive index matched liquid would allow capturing the velocity field of the exit jet spray, the in-nozzle flow in the proximity of the wall and around the exit edges where often phenomena of turbulence and flow separation are more important. However, the toxic nature of the refractive index matched liquid would require the model to run completely sealed (close loop) and thus, necessitating injection into liquid. This will make impossible the investigation of air entrainment with the refractive matching technique unless non-irritant liquids will be identified with a mixture refractive index matching that of Perspex.

### **6.5.2. Spray Characterisation of the Real Size Injector.**

The experiment carried out on the adjustable injector holder has proved to be extremely useful to overcome the problem of light attenuation in the PDA and visualisation tests. The results obtained in such an accessible test rig have been useful to identify the spray mechanism occurring under real engine operation. Similar advantages were obtained in the transparent large-scale model and were reported in Chapter 3 due to the larger dimensions and the full optical access, which allowed observation of the in-nozzle flow. Unfortunately for several phenomena occurring in the large-scale model the criteria of similitude were not working. In addition, in the large-scale model the effect of flow transient due to needle movement was absent since it was operating under steady-state conditions. In order to overcome this difficulty several compromise solutions can be proposed which could provide additional information on the internal flow phenomena like air entrainment, initiation of cavitation and counter rotating vortices; for example:

- To manufacture a small radial portion of needle and cartridge in transparent material to allow inlet and outlet light paths for improved visualisation of the in-nozzle (seat passage) flow. This portion could be machined from a real prototype and embedded by means of adhesive resin.



- 
- An alternative could also be the complete replacement of the nozzle injector tip with a transparent one but in that case the sealing capability and resistance of the needle against the metal injector body would need to be assessed.
  - Further investigation could also be carried out on the air entrainment according to the investigation performed by Siebers et al. [66]. In fact, as it was observed, the strong resemblance between the string behaviour and that of an individual jet from a multihole injector may also suggest that the scaling law applied by [66] on the multihole jet could also be applied on a single string of the pintle-type spray. Therefore, more detailed information on the spray mass rate in the real size injector would allow analysis of the correlation between the amount of air entrainment and the emerging spray. Besides, further PIV experiments on the air entrainment velocity field could provide additional validation for the previously analysed flux calculation.
  - The application of PIV diagnostics could also be extended to the constant volume chamber in order to perform a more detailed parametric study on the effects of chamber pressure and temperature on the spray structure.

### **6.5.3. Optical Engine.**

The present results have allowed classification of the performance of three different pintle nozzle geometries but without providing a precise understanding of the mechanism related to each different type of step. This can be achieved by the following investigations:

- Use the large-scale model of the injector, which proved to be a powerful method to observe the internal flow and the spray behaviour in the near nozzle region, to perform a parametric study with LDV on nozzle models with different step dimensions. This would allow improved understanding of the way the emerging flow is affected by the geometry of the nozzle and how this influences the spray angle stability by studying the spectral analysis of the velocity distribution.
- In addition, further investigations on the three real size injectors could be done in order to study their performance in terms of spray atomisation using PDA in a constant-volume chamber. This may require a more manageable and accessible test rig with improved optical access.

### **6.5.4. Optical Engine: Spray Recirculation**

The spray visualisation has successfully shown the presence of recirculation zones at different operating conditions, which are candidate locations for mixture ignition. It was possible to speculate several theories relating the recirculating pattern with the in-cylinder

---

air motion. To understand the suggested points better, the following experimental works may be performed:

- In order to assess these phenomena, a more detailed understanding of the mechanism driving the recirculation zones is needed and therefore a further study with PDA, LDV and PIV diagnostics in optical engine could help to quantify the spray velocity field and to assess the air motion and turbulence through introduction of external seeders into the intake system.
- However, due to the distortion of the laser path through the engine's cylinder wall and its attenuation due to the piston partially interrupting the light path, an alternative approach is needed such as the insertion of the laser fibre from the flame deck in place of the spark plug. Although not a straightforward approach, it deserves further attention.

### Concluding Remarks

The successful introduction into the market of the second-generation direct-injection gasoline engines has raised expectations about their ability to compete directly with advanced diesels in terms of fuel efficiency and CO<sub>2</sub> emissions. Since then two major issues are complicating their further development and market penetration: the fluctuations in the oil price and the financial crisis, which has paralysed the automotive industry. Nobody can predict the impact of the crisis on the different car markets and, in particular, on the gasoline-to-diesel market share as well as on the measures to be taken to address the threat of global warming.



## Appendix A

### 7. MEASURING TECHNIQUES AND ERROR ANALYSIS

#### 7.1. PHASE-DOPPLER ANEMOMETRY –MEASURING PRINCIPLES

Phase Doppler anemometry (PDA) is a non-intrusive optical technique that allows the simultaneous measurement of droplet velocity and size. It is a more complete version of laser Doppler anemometry (LDA) first described by Durst *et al* (1976). A typical PDA set-up consists of a laser tube, a light frequency phase shifter (Bragg-cell), a laser-beam splitter, a transmitting optical unit, a receiving optical unit and a signal processor [100-102].

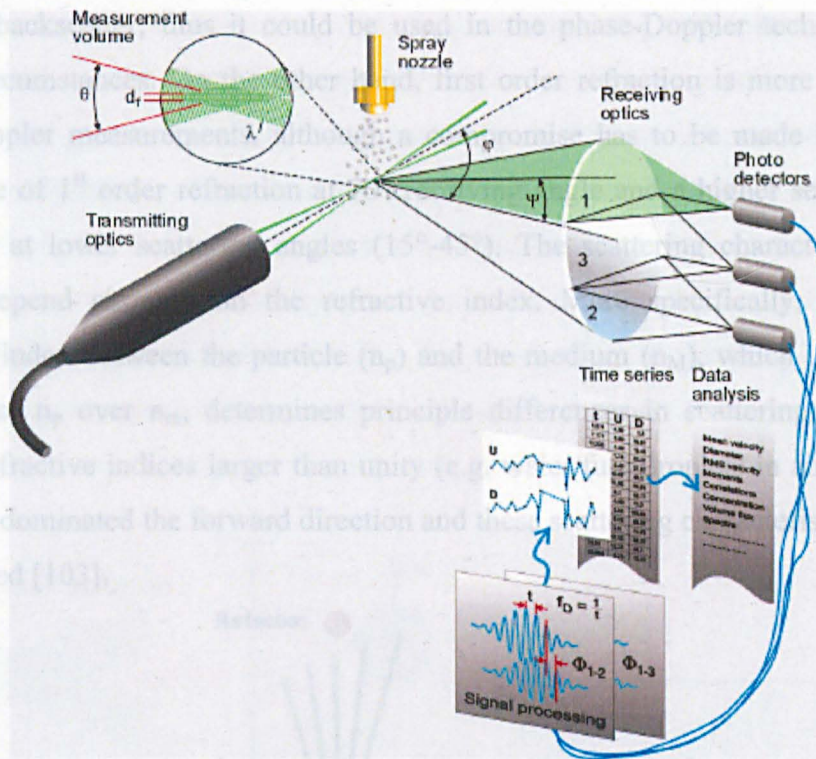


Figure 7- 1 Schematic of the measurements principle of PDA (Source: Dantec Dynamics).

When a droplet passes through the measuring volume, it scatters light at all directions. Receiving optics is placed at an off-axis location and projects a portion of the scattered light onto multiple photo-detectors. Due to the structure of the measuring volume (it is made of fringes created by the intersection of two individual laser beams) and the photo-multipliers position, scattered light is converted into Doppler bursts. The frequency of the Doppler bursts is linearly proportional to the particle



velocity. Each photo-detector captures the same burst signal although, due to their relative positions, there is a phase shift in signals acquired by each detector. This phase shift has been shown to be directly proportional to the droplet diameter. More specifically, the principal of the phase-Doppler anemometry technique is based on light scattering theory. Visualised ray tracing can provide better understanding of how light is scattered by a spherical transparent droplet, as illustrated in Figure 7- 1, where it shows different mode of light scattering. The incident light beam is partially reflected at the surface of the particle and partially refracted into the particle. Upon exiting the particle without any further internal reflection, the scattered beam is known as 1<sup>st</sup> order of refraction. Higher order of refraction (2<sup>nd</sup> order of refraction) also arises after internal reflections and subsequent refraction out of the particle into the surrounding medium. Second order of refraction is responsible for the rainbow effect in backscatter, thus it could be used in the phase-Doppler technique under special circumstances. On the other hand, first order refraction is more suitable for phase-Doppler measurements, although a compromise has to be made between the dominance of 1<sup>st</sup> order refraction at 70° receiving angle and a higher scattered light amplitude at lower scattering angles (15°-45°). The scattering characteristics of a particle depend strongly on the refractive index. More specifically, the relative refractive index between the particle ( $n_p$ ) and the medium ( $n_M$ ), which is effectively the ratio of  $n_p$  over  $n_m$ , determines principle differences in scattering modes. For relative refractive indices larger than unity (e.g. water/fuel droplets in air) first order refraction dominated the forward direction and these scattering characteristics are well documented [103].

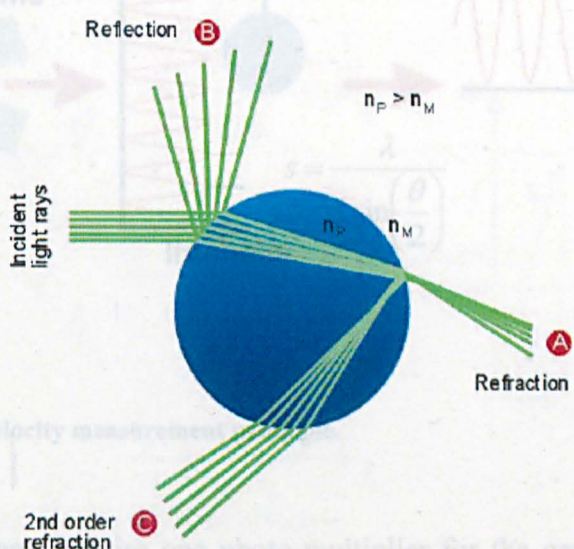


Figure 7- 2 Scattered light from a spherical particle (Source: Dantec Dynamics).



As illustrated in the top left corner of Figure 7- 2, the measurement volume of a PDA system is formed by the intersection of two laser beams. The focused laser beams intersect and form an ellipsoid shaped pattern of bright and dark stripes, so called fringes. The spacing of these fringes is determined by the light wavelength and the angle between the two laser beams that is set by the transmitting optics. The laser-tube output beam features a multi-colour wavelength that ranges from 420 to 520nm. A optical laser beam splitter separates the output beam into green (514nm) and blue (488nm) wavelengths. Both of these laser beams are further split into two green and two blue beams by another set of beam splitters. The majority of PDA/LDA systems feature a frequency shift between the two laser beams of same wavelength generated by means of a Bragg-cell. This frequency shift makes the fringe pattern of the control volume move at a constant velocity. Stagnant particles will generate a signal corresponding to the shift frequency. Particles moving at positive or negative velocities will generate positive and negative signal frequencies relative to the shift frequency, respectively. Thus, it is essential to use the frequency shift based systems that can effectively distinguish positive and negative particle velocities and provide a zero velocity measurement. Finally, when a particle traverses the control volume, the scattered light fluctuates in intensity at a frequency equal to the velocity (U) of the particle, divided by the fringe separation distance (s), as shown in Figure 7- 3.

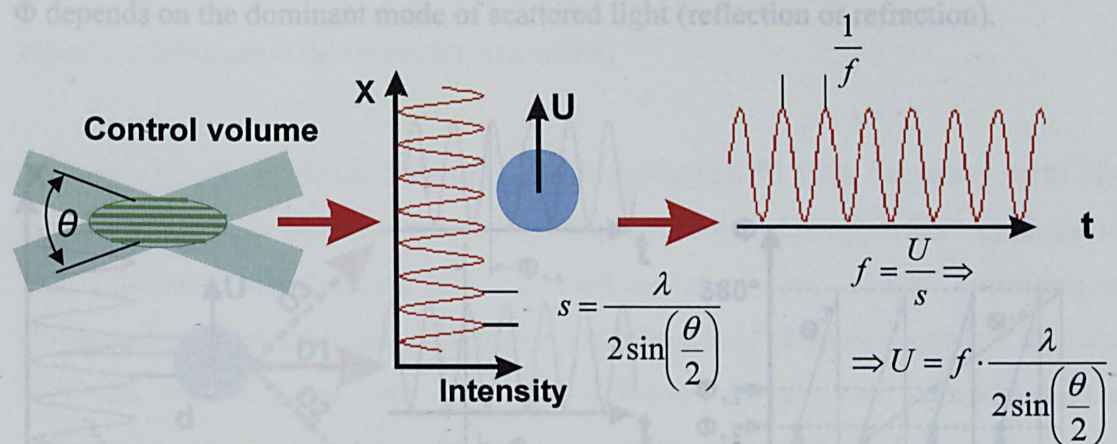


Figure 7- 3 Doppler Velocity measurement principle.

Velocity measurements require one photo-multiplier for the generation of the time-based signal and the velocity value calculation. The same principle does apply to size



measurements though, but for accurate particle sizing information, more than one photo-multiplier is needed. In the case of two photodiodes, particle size measurement is achieved by measuring the time delay of the scattered light signal that is captured by the first detector at time (t) and the second detector at time (t+Δt), as shown in the following Equation , where T is the period of one cycle of the signal.

$$\Delta\phi = 2\pi \frac{\Delta t}{T} \quad (7-1)$$

The phase difference ( $\Delta\phi$ ), calculated by the above equation, increases with increasing particle size. Since phase is a module of  $2\pi$  function, it cannot exceed this value, i.e.  $360^\circ$ . Therefore, if a particle is large enough and causes the phase to go beyond a  $2\pi$  jump, a two-detector PDA system could not discriminate between this size and a much smaller particle that has the similar phase shift. Hence, three-detector systems are used, where two independent phase differences are obtained from two detector-pairs having different relative positions. Three-detector PDA systems (D1-2 and D1-3 in Figure 7- 4) provides certain advantages and apart from overcoming the  $2\pi$  ambiguity, the measurable size range is increased (D1-3) by adding the third detector and at the same time high measurement resolution is maintained (D1-3). A processor attached to the system measures the phase shift between the two signals, which is proportional to the droplet radius of curvature, thus allowing determination of the droplet diameter, according to the calculation illustrated in Figure 7- 4, where  $\Phi$  depends on the dominant mode of scattered light (reflection or refraction).

Figure 7- 5 Schematic of the Daniec 2D PDA system.

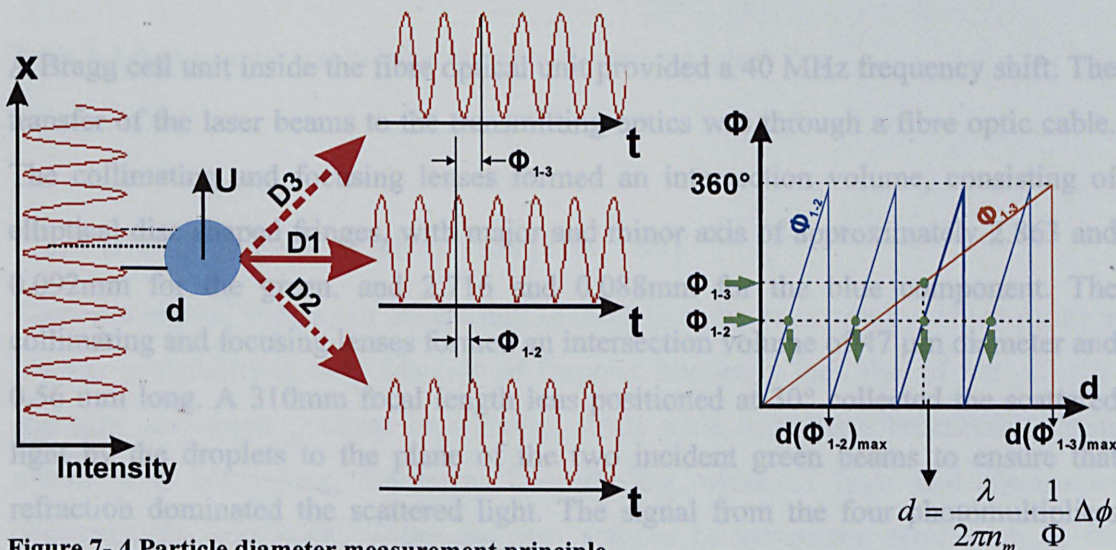


Figure 7- 4 Particle diameter measurement principle.



In the present study, a 2-D PDA system (Dantec) was used to allow simultaneous measurement of the two velocity components and diameter of a particle as illustrated in Figure 7- 4. A wall mounted Argon-Ion laser with a maximum power of around 1.5W was used and output beam was aligned with fibre optic unit; this unit was responsible for the splitting of the laser beam into two pairs of different wavelengths and each pair had two beams of equal intensity. The first pair was green light with wavelength of 514.5nm, responsible for axial velocity component and droplet sizing, while the second pair was blue light with 488nm wavelength providing the radial velocity component.

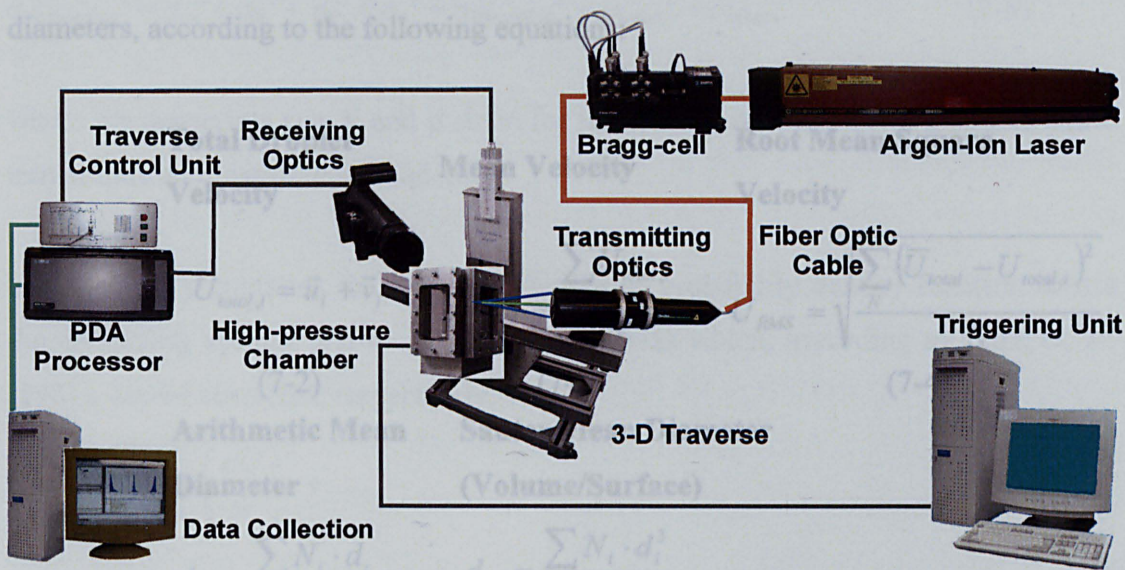


Figure 7- 5 Schematic of the Dantec 2D PDA system.

A Bragg cell unit inside the fibre optical unit provided a 40 MHz frequency shift. The transfer of the laser beams to the transmitting optics was through a fibre optic cable. The collimating and focusing lenses formed an intersection volume, consisting of elliptical disc shaped fringes, with major and minor axis of approximately 2.863 and 0.092mm for the green, and 2.716 and 0.088mm for the blue component. The collimating and focusing lenses formed an intersection volume of 47  $\mu\text{m}$  diameter and 0.56 mm long. A 310mm focal length lens positioned at 30° collected the scattered light by the droplets to the plane of the two incident green beams to ensure that refraction dominated the scattered light. The signal from the four photomultipliers was transmitted to the processor unit where all the data processing was carried out. The processor was connected to a desktop computer via an Ethernet adopter, where all

the data were saved.

The measurement period was defined by the injection duration for each test case. This period varied from 1 – 3ms (for 0.33 –1ms injection duration), so did the total number of samples collected each time that were of the order of 10,000 samples per millisecond of measurement. The total number of samples was collected over many injection cycles. The measurement period was divided in narrow time windows of 0.02ms for further post-processing of the collected data. These data consisted of time, and two velocity components as well as droplet size information. Post-processing involved calculation of ensemble-averaged values of droplet mean and root mean square (RMS) velocities and arithmetic mean (AMD) and Sauter mean (SMD) droplet diameters, according to the following equations:

<b>Total Droplet Velocity</b>	<b>Mean Velocity</b>	<b>Root Mean Square Velocity</b>
$U_{total,i} = \vec{u}_i + \vec{v}_i$	$\bar{U}_{total} = \frac{\sum_N U_{total,i}}{N}$	$U_{RMS} = \sqrt{\frac{\sum_N (\bar{U}_{total} - U_{total,i})^2}{N}}$
(7-2)	(7-3)	(7-4)
<b>Arithmetic Mean Diameter</b>	<b>Sauter Mean Diameter (Volume/Surface)</b>	
$d_{10} = \frac{\sum N_i \cdot d_i}{\sum N_{total}}$	$d_{32} = \frac{\sum N_i \cdot d_i^3}{\sum N_i \cdot d_i^2}$	
(7-5)	(7-6)	

Table 7- 1 Post-processing calculation of ensemble-averaged values

### 7.2. PDA/LDA ERROR ANALYSIS [104, 109]

There are several sources of uncertainty in laser-Doppler anemometry which result in a wider probability density function of Doppler frequency than that of the velocity, and they are: mean gradient broadening, small scale turbulence broadening, finite transit time broadening, Brownian motion, line width of laser and electronics characteristics and noise. There are also sources of systematic error such as the velocity biasing error and the mean gradient effect. Finally, there are the uncertainties of the orientation of the laser beams relative to the geometry and, the positional errors



of measurement volume introduced by the milling table and by the visual procedure of locating the measuring volume at a given reference point.

### 7.2.1 Error and Uncertainties

The total Doppler variance  $\sigma_T^2$  equals the sum of the velocity variance and broadening effects and, assuming total independence and randomness of its constitutive terms, is given by:

$$\sigma_T^2 = \sigma_{\text{velocity}}^2 + \sigma_{\text{broadening}}^2 \quad (7-7)$$

And

$$\sigma_{\text{broadening}}^2 = \sigma_t^2 + \sigma_g^2 + \sigma_F^2 + \sigma_p^2 + \sigma_{\text{Brownian}}^2 + \sigma_{\text{Laser}}^2 + \sigma_{\text{others}}^2 \quad (7-8)$$

where the subscripts t, g, F and p stand for turbulence, mean velocity gradient, finite transit time and instrument broadening.

Mean velocity gradients lead to a broadening of probability density function across the measuring volume and to a mean velocity bias which, according to Durst et. al. (1981), can be corrected, respectively, via

$$\sigma_g^2 = \left(\frac{l_m}{4}\right)^2 \left(\frac{dU}{dr}\right)^2 + \dots \quad (7-9)$$

$$U_{\text{true}} - U_{\text{measured}} = \left(\frac{l_m}{4}\right)^2 \frac{d^2U}{dr^2} + \dots \quad (7-10)$$

where the higher order terms of the expansions are negligible. As it is evident, these broadenings are important in the region where the velocity gradient is strongest like near the wall regions. In the current investigation, these effects were negligible as the measurements inside the large scale were mainly within the centre of the jet and with the air entrainment measurements within a uniform air jet stream near the nozzle.

Turbulence intensifies the finite transit time broadening in frequency domain instruments. A second turbulent effect results from the small-scale turbulent fluctuations in velocity within the scattering volume and can be accounted by:

$$\sigma_t^2 = \frac{2}{15} \left(\frac{l_m}{4}\right)^2 \left(\frac{4\pi \sin \phi}{\lambda}\right)^2 \frac{\varepsilon}{\nu} \quad (7-11)$$

where  $\varepsilon$  is the dissipation rate, for a small angle  $\phi$ , and assuming local and a scattering volume size of the order of the Kolmogoroff length scale. For larger measuring volumes the correction becomes more complicated but always dependent on the dissipation rate and is difficult to apply especially for bidimensional and tridimensional flows. According to Melling (1975) and based on experiments and corrections of Berman and Dunning (1973) on their pipe flow experiments at different Reynolds numbers,  $\sigma_t^2$  has the same order of magnitude as the combined gradient and finite transit time broadening, except for a very small scattering when the previous equation can be used therefore in the case of spray droplet velocity measurement is negligible and also in the in-nozzle flow measurement except near the wall where it accounts for an uncertainty of 4%.

Broadening introduced by the deviation of the laser light from monochromatic is negligible as is that of Brownian motion, except for very slow laminar flows. Finite transit time broadening occurs when more than one particle is within the measuring volume but is limited in frequency counting system. A combination of a slit of 100 $\mu$ m in the receiving optics and an appropriate validation circuitry used in the current system to ensure that only one particle is within the scattering volume. Instrument broadening,  $\sigma_p^2$ , takes into account all

Finally, under the broadening due to other effects ( $\sigma_{others}^2$ ), is included a diffraction grating disc jitter of 0.2% for long period of time and according to the manufacturers specifications. For flows, which are strongly unidirectional, the accuracy in positioning the laser beams in a plane parallel to the flow can affect the measurement of transverse components. This effect had little influence on current velocity measurements inside the large-scale model and within the air entrainment region near the nozzle.

In addition to above, velocity bias effects can be significant in turbulent flow measurement when the mean velocity is calculated via an ensemble averaging of data obtained from individual realizations. With more particles of higher velocity crossing the measuring volume than of low velocity, the calculated velocity becomes biased toward higher values and, as shown by McLaughlin and Tiederman (1973), a one directional correction shows negligible error for turbulence intensities up to 15% but an error of 10% for a turbulence intensity of around 40%. Therefore, bias corrections have to take into account the duration of the burst, the particle arrival rate and its relation to turbulence time scale (Durst et al (1981)). Ensemble averaging is an



accurate estimate of time averaging whenever the time scale of the particle arrival rate is less than the turbulent integral time scale if sampling technique and velocity are uncorrelated or if the sampling time scale is much greater than the turbulent integral scale. Under other conditions an appropriate sampling technique will be necessary to remove the correlation between velocity time consuming an alternative is the use of a time weighting approach such as that one proposed by Dimotakis (1976)

$$\overline{U} = \frac{\sum_{K=1}^{N_s} (U_K \Delta t_K)}{\sum_{K=1}^n (\Delta t_K)} \quad (7-12)$$

Where  $\Delta t_K$  is the duration of the Doppler signal when its amplitude varies from maximum to half maximum.

Another source of bias, but in the opposite direction, is introduced by the existence of a correlation between Doppler frequency (velocity) measured by the photomultiplier and the particles residence time inside the measuring volume. That is to say that the fast moving droplets with small residence time produce low Doppler signal amplitudes, while the slow moving droplets with large residence time produce large signal amplitudes, and therefore biasing velocities towards lower values, as shown by Durão and Whitelaw (1979). Both effects are opposite and become negligible when taken together for a wide range of flows and relationships between particle, sampling and turbulent time scales, as illustrated in Durão et al (1980). Vafidis (1985) used the above equation and reported a mean velocity bias of +2% and a 5% broadening of the rms velocities in regions of high turbulence when comparing with non-corrected data. For the measurement of in nozzle flow and spray droplet velocity measurement, the uncertainties of both biasing effects are small and negligible because the estimated turbulent intensities were lower than 20%.

The gradual definition of cut-off frequencies in band pass filters means that its misuse is another source of bias because signal that might lie outside bandwidth or very close to the edges will not be considered. In the present systems, passive band pass filters were used with sharp cut-off edges and therefore this biasing effect was negligible. At the same time, the signals pdf distributions were monitored all the time to ensure all the Doppler frequencies are detected.

The relative statistical error of a sample of finite size on both mean and rms velocities can be estimated by Gaussian velocity probability function by

$$Error_{mean} = Z_C \frac{u'}{\sqrt{N_s}} \quad (7-13)$$

$$Error_{rms} = Z_C \frac{1}{\sqrt{2N_s}} \quad (7-14)$$

Where  $N_s$  and  $u'$  are the sample size and turbulence intensity with  $Z_C=1.98$  for 95% confidence level, Yanta and Smith (1973). In the present measurements (both in the enlarge model and air entrained region near the injector) the number of samples per measuring point were of order 3000 to 5000 giving a maximum statistical error of 0.73% in the ensembled mean and 2.5% in the rms of the velocity fluctuations for a 20% turbulence intensity.

There are positional errors due to the method used to locate the control volume inside measuring region. This relies on visual observation of the beam crossing at a reference point, which can lead to an uncertainty of about half the measuring volume length, i.e. 200 $\mu$ m; here the interface gap between the needle and the cartridge was used as the reference point both for enlarge model and the real size injector. The movement of traversing table was monitored in all three directions with digital gauges with a resolution of  $\pm 0.05$ mm.

### 7.2.2. PDA, size accuracy

Size and time, information were collected continuously over many injection cycles. From which ensemble-averages were obtained over a time window of 0.1 ms which was found to be sufficient to describe temporal characteristics of the spray. The total number of samples ranged from 30,000 to 50,000, and the number of validated samples in the 0.1 ms time interval varied from 250 to 1500 samples with maximum statistical uncertainties of around 2.5% in the ensembled mean and 8.8% in the rms of the velocity fluctuations, based on 95% confidence and 20% turbulence intensity, Yanta et al.(1973)

Detailed accounts of the uncertainties and limitation associated with the PDA measurements are given by, for example, Wigley (1993) and Hardalupas et al (1994). An important source of uncertainty in the near-injector region was the attenuation of the laser beams and the scattered light due to high concentrations of droplets. The extent of the turbidity of the spray with the present injector was evident up to 60 mm from the injector as shown by Nouri et al. (1999). The phase-Doppler results presume



---

spherical droplets and, since sprays are known to include ligaments in the near field, this is a potential source of uncertainty very close to the injector. The photographic investigation suggested that there were very few, if any, ligaments in the regions of present measurements and the verification system of the counter should have rejected non-spherical droplets. In order to minimize the beam and scattered light attenuation, a special injector holder was design to set up the injector orientation accurately to avoid any unnecessary beam/spray and scattered light/spray contact; this arrangement made great improvement in data collection in the core spray near the exit nozzle as demonstrated in the results section.

In the present study a three Photomultipliers (PM) system (Dantec dynamics) was used to maintain a high measurement resolution and to remove measurements ambiguity. With this system, the same droplet size was measured twice with two different pairs of PMs positioned at two different locations. One PM pair (1 and 2) was positioned with relatively large separation from each other to provide very high sensitivity (resolution) and smaller size range, while the other pair (1 and 3) had a shorter separation with larger size range and lower resolution. With this arrangement, two independent size measurements, the  $2\pi$ -jump uncertainty (an inherent problem with PDA system) is fully removed and the ambiguity of the droplets sphericity will be minimised. The later depended on the validation level which can be set by the user; in this experiment a tolerance of about 5 to 10% was used between the two set of size measurements and implies the level of ambiguity in droplets sphericity.

There are other minor sources of uncertainties like oscillations in phase-diameter curve, low signal-to-noise ratio due to low intensity or extinction which can introduce biasing towards larger droplet size, Gaussian intensity profile in the measurement volume and phase changes which can be due to droplet surface distortions and multiple scattering effects. All these effects can be minimise by proper set up of the transmitting and receiving optics as descript in PDA setup in Chapter 4.

### **7.3 PARTICLE IMAGING VELOCIMETRY - MEASUREMENT PRINCIPLE**

Planar Particle Image Velocimetry (PIV) with digital image processing is nowadays one of the most powerful experimental techniques to measure two-dimensional velocity fields of fluid flows with excellent spatial resolution[105, 106]. This technique can also deliver velocity and acceleration data of transient flows when

The diagram illustrates the PIV system components and data processing flow:

- Double-pulsed laser:** Emits two light pulses separated by a time interval  $\Delta t$ .
- Cylindrical lens:** Focuses the laser light into a **Light sheet**.
- Measurement volume:** The region where the light sheet intersects the **Flow with seeding particles**.
- Target area:** A specific region within the measurement volume.
- Imaging optics:** Collects light from the target area and focuses it onto the **CCD** camera.
- CCD:** Captures two image frames, **Image frame from pulse 1** and **Image frame 2**.
- Particle images:** Individual particle images are extracted from the frames, labeled  $I_1$  and  $I_2$ , with a displacement  $\Delta X$  between them.
- Correlation:** A process that correlates the two image frames to determine the displacement of particles.
- Data:** A table showing the resulting velocity field with columns for X, Y, U, and V.
- Data analysis:** A list of analysis techniques including Streamlines, Vorticity, Averages, RMS velocity, Spatial correlation, and Flow scales.

given below:

1. Seed the fluid flow of interest with tracer particles
2. Assure that the particles are able to follow the flow and scatter light
3. Illuminate the measuring plane with a sufficiently short laser pulse to “freeze”



4. Take a digital image of that frozen flow field
5. Repeat steps 3 & 4 after a predetermined delay time  $\Delta t$  during which the tracer particles moved with the flow
6. Determine the displacement  $\Delta \vec{s}$  of the particles during  $\Delta t$  in a given area of the imaged flow field with the PIV correlation algorithm
7. Calculate the “raw” velocity vector field from the known  $\Delta t$ , the obtained  $\Delta \vec{s}$  and the definition of velocity

$$\vec{v} = \frac{\Delta \vec{s}}{\Delta t} \quad (7-15)$$

8. Further process the velocity data as required and plot results

Following this guide, the basic aspects of PIV are described in more detail below. Since PIV is based on a visual representation of the fluid motion in the form of consecutive flow images, it is necessary to seed the single-phase fluid with suitable particles (tracers), which can scatter the incident light efficiently. The requirements for the seeding particles in the case of PIV are more stringent than those for LDV and, depending on the individual flow applications, the particles must be chosen carefully following these criteria:

- Particles must be able to follow the flow without significant slip
- Sufficient light for the camera must be scattered by the particle when illuminated
- All particles should be of similar size  $d_p$  (monodisperse)
- Particles must be uniformly distributed within the flow
- Particles should not be poisonous, corrosive or abrasive
- Particles should not (or only very slowly) evaporate
- Particles must not react chemically with the working fluid or the materials of the flow rig

The first two criteria are particularly important and must be considered together. Smaller particles follow the flow easily since their inertia is small, but they might not scatter enough light for a high imaging signal-to-noise ratio. When there is sufficient scattered light by means of using larger seeding particles, the ‘low slip-velocity’

criterion might be violated significantly. This trade-off concerning the particle size was investigated in [109] and the following general recommendations were given:

- Use oil droplets with  $d_p \cong 5\mu m$  for PIV measurements in gaseous flows
- Use solid spherical particles with  $d_p \geq 10\mu m$  for PIV measurements in liquid flows

For all PIV systems, it is essential to have a stable and repeatable quality of the light pulses, since image exposure is solely determined by illumination. Therefore, double-pulsed Nd:YAG laser units equipped with highly accurate quality-switches are most commonly used to illuminate the flow area of interest. These lasers are capable of emitting very short light pulses (order of ns) with relatively high energies (order of mJ) and with short interval times between the pulses (order of  $\mu s$ ).

The laser light sheet with a typical thickness of 0.5-1mm is created by a set of cylindrical and spherical lenses. Thicker light sheets would diminish the PIV's distinctive character as a planar measurement technique.

A double-shutter camera will take the two successive flow field images in the case of the standard two-dimensional PIV system. For the time resolved (high-speed) PIV it is necessary to utilise high-speed pulsed Nd:YAG lasers together with very fast CCD cameras capable of recording high resolution images with frame rates of the order of kHz and more.

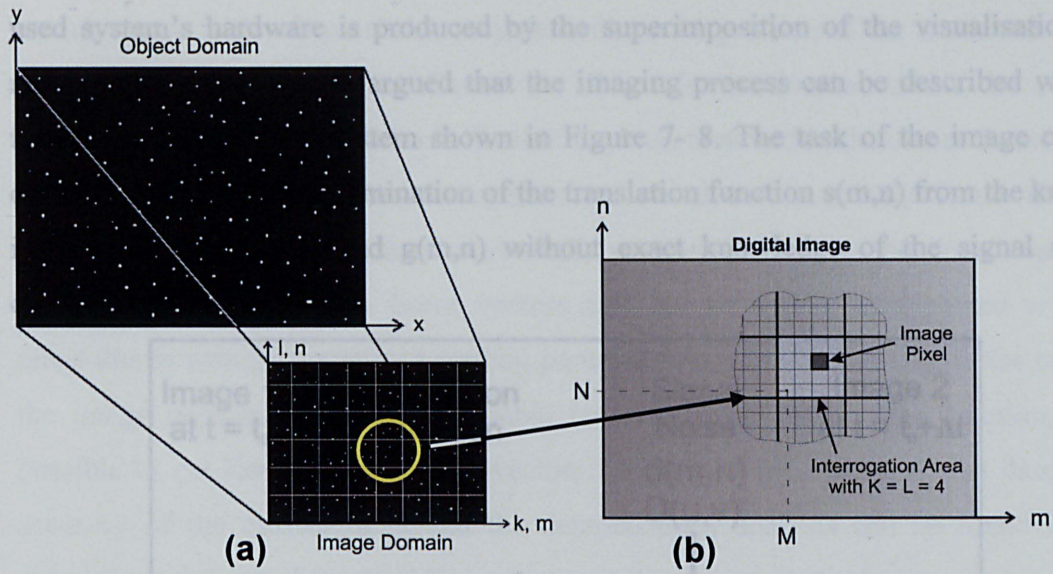
The recorded digital images (image domain) are based on the grey level intensity maps of the visualised particle-laden flow (object domain). This is shown schematically on the l-h-s of Figure 7- 7. The first step of processing the images is now the determination of the scale factor SF between object and image. For this purpose, a known dimension O length of the object domain is related to its corresponding projection I (Pixel) in the image domain. Thus:

$$SF = \frac{O}{I} \left[ \frac{\text{mm}}{\text{pixel}} \right] \quad (7-16)$$

The image therefore scales completely with SF. After dividing the pixel domains of one image pair into the so-called interrogation areas, i.e. rectangular regions of fixed size (K x L pixel) with local origins (M,N), as shown on the r-h-s of Figure 7- 7, it is possible to apply the core of the PIV technique, namely the image correlation



algorithm (see details below).



**Figure 7- 7 (a) Representation of the particle-laden flow on the CCD chip; (b) and discretisation of image domain into interrogation areas.**

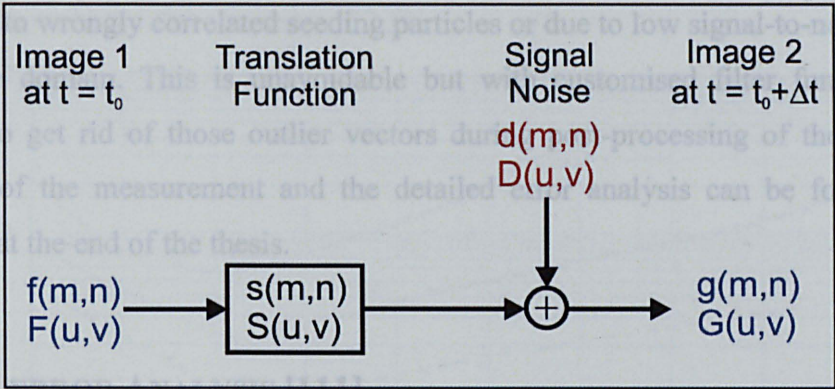
The size of the interrogation area and the image interval time  $\Delta t$  can be chosen arbitrarily, but the following has to be considered. The main assumption for the image correlation procedure is that all particles belonging to one interrogation area have travelled the same distance in the same direction along a straight line during  $\Delta t$  (uniform translational motion/displacement). Therefore, only one velocity vector will be assigned per interrogation area, thus the resolution of the vector field is in principle determined by the size of the interrogation area. For this reason, it is necessary to adapt closely the size of the interrogation areas and  $\Delta t$  to the general flow conditions, e.g. velocity magnitude. Care must be taken to resolve the flow structures with sufficient spatial resolution, but without having too many particles moving from one interrogation area into another in-between the image recordings. An additional important aspect is the fact that the most commonly used Fast-Fourier Transform (FFT) based correlation algorithms work only with square interrogation areas of size  $K = L = 2^n$  ( $n \in \mathbb{N}$ ). With the considerations mentioned above and  $V_{\max}$  as the estimated maximum velocity of the flow field of interest, the following recommendation can be given with  $d_{IA} = SF \cdot K$  :

$$\left| \Delta \vec{s} \right| < \frac{1}{4} \cdot d_{IA} \Rightarrow \Delta t < \frac{1}{4} \cdot \frac{d_{IA}}{V_{\max}} \quad (7-17)$$

The grey level distribution of the images can be regarded as two-dimensional functions in the spatial  $(m, n)$  pixel-coordinate system. With this in mind and the fact

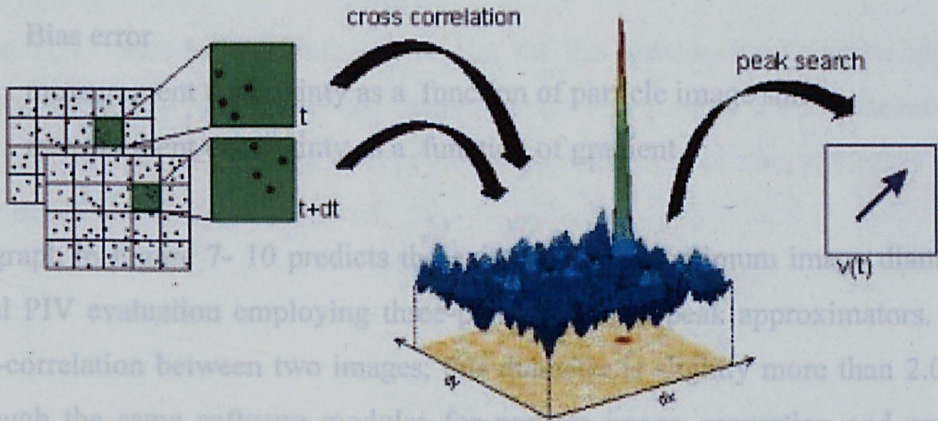


that signal noise as a systematic error (representing the image displacement) of the used system's hardware is produced by the superimposition of the visualisation of moving particles it can be argued that the imaging process can be described with a transfer function of the system shown in Figure 7- 8. The task of the image cross-correlation is now the determination of the translation function  $s(m,n)$  from the known image functions  $f(m,n)$  and  $g(m,n)$  without exact knowledge of the signal noise  $d(m,n)$ .



**Figure 7- 8 Schematic of imaging transfer function for one image pair**

The two-dimensional cross-correlation method compares the grey level values of the interrogation area of image 1 with the values of the corresponding interrogation area and its close neighbourhood of image 2 (Figure 7- 8). This must be repeated for all interrogation areas. A fast way to do this is the transformation of all functions from the spatial pixel domain (m, n) to the spatial frequency domain (u, v) with FFT. The PIV algorithm is then carried out more efficiently in the frequency domain and the obtained results are transformed back into the pixel domain, thus reducing the number of arithmetic operations by two orders of magnitude.



**Figure 7- 9 Cross-correlation, correlation array and peak search [110]**



---

The so-called correlation array in the pixel domain is obtained with this procedure and a peak search with sub-pixel accuracy determines the position of the maximum value within that array. Employing Equation (7.16) this position represents the overall displacement of all the particles in the interrogation area within the object domain and the velocity vector of that interrogation area is therefore readily found through Equation (7.17). When reiterated over all interrogation areas, the “raw” velocity vector field can be plotted. Some vectors may not lie within the expected velocity range due to wrongly correlated seeding particles or due to low signal-to-noise ratio in the image domain. This is unavoidable but with customised filter function, it is possible to get rid of those outlier vectors during post-processing of the data. The accuracy of the measurement and the detailed error analysis can be found in the appendix at the end of the thesis.

## **7.4. PIV ERROR ANALYSIS [111]**

### **7.4.1. Particle image diameter**

Even though the current PIV study aimed to give qualitative information or at the most just magnitude values, it is still possible to calculate an estimate of the accuracy for this case limit. In the present study, the highest velocity observed was about 15m/s, which corresponds to a displacement of 0.3mm or 3.8pixel.

Based on the image displacement (3.8pixel) and on the simulations data reported on the graphs presented in this section it is possible to estimate the following accuracy:

- measurement uncertainty as a function of particle size
- measurement uncertainty as a function of particle displacement
- Bias error
- measurement uncertainty as a function of particle image shift
- measurement uncertainty as a function of gradient

The graph in Figure 7- 10 predicts the existence of an optimum image diameter for digital PIV evaluation employing three-point Gaussian peak approximators. For the cross-correlation between two images, this diameter is slightly more than 2.0 pixels. Although the same software modules for particle image generation and evaluation (FFTs, peak finder, etc.) were used for Monte Carlo simulations, there is a

discrepancy in the optimum particle image diameter for which no plausible explanation is known.

When the particle images become too small, another effect arises which can also be observed towards integral values. The effect increases as the particle image diameter is reduced which is a clear indication that the chosen sub-pixel peak estimator. For the current PIV analysis it was used a interrogation spot of  $32^2$  pixels size and the particle image size was within 4-8 pixel resulting in a maximum RMS uncertainty of  $\sim 0.1$  pixel corresponding to an accuracy of 2.5%

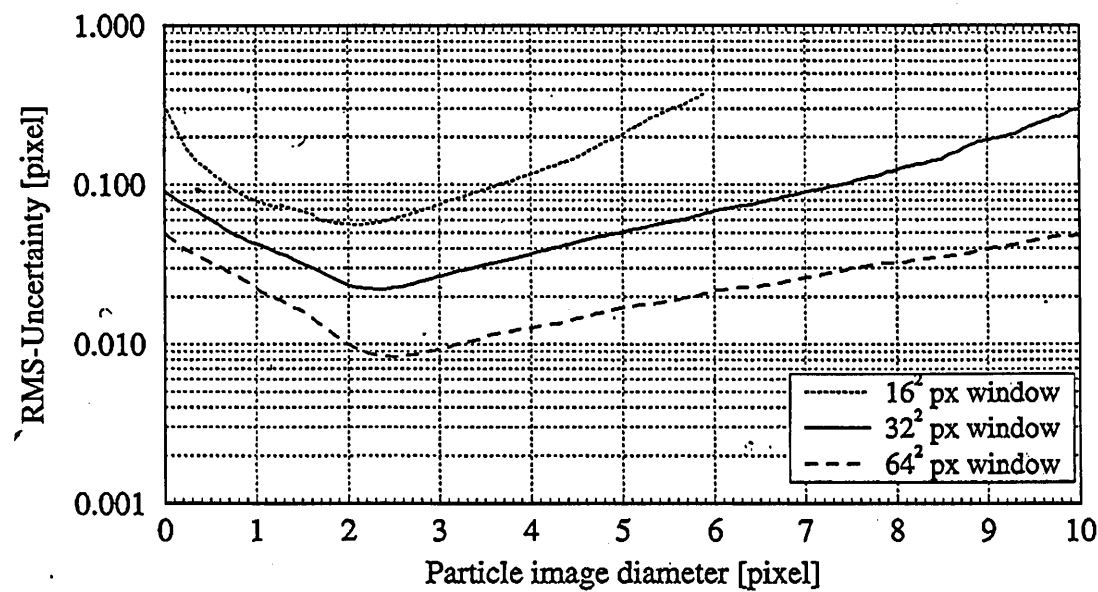


Figure 7- 10 Measurement uncertainty (RMS random error) in digital cross correlation PIV evaluation with respect to varying particle image diameter for single exposure/double frame PIV imaging.

### 7.4.2. Particle image shift

Figure 7- 11 shows the simulation results for the measurement uncertainty (RMS random error) as a function of the displacement. For most of the displacements, the uncertainty is nearly constant except for displacements less than 0.5 pixel where a linear dependency can be observed.



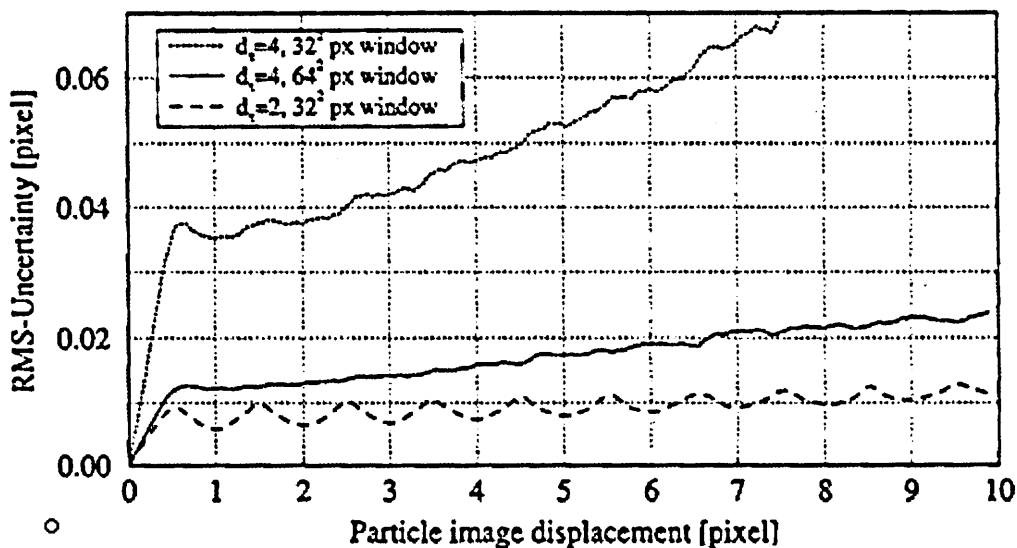


Figure 7- 11 Monte Carlo simulation results for the measurement uncertainty in digital PIV cross correlation PIV evaluation as a function of particle image displacement.

The drastic reduction in the measurement uncertainty for  $|d| < 0.5$  pixel may be exploited by offsetting the interrogation windows with respect to each other according to the mean displacement vector within the interrogation window. This offset has the additional side-effect of increasing the detectability of the correlation peak by increasing the number of particle matches.

The displacement bias arising due to the in-plane loss of pairs is shown in Figure 7- 11. By dividing out the appropriate weighting function from the correlation values prior to applying the three point fit, this displacement bias can be nearly completely removed which is also shown in Figure 7- 11.

For the above max speed case and 3.8 pixel displacement the RMS uncertainty results  $\sim 0.05$  pixel corresponding to an accuracy of 1.3%

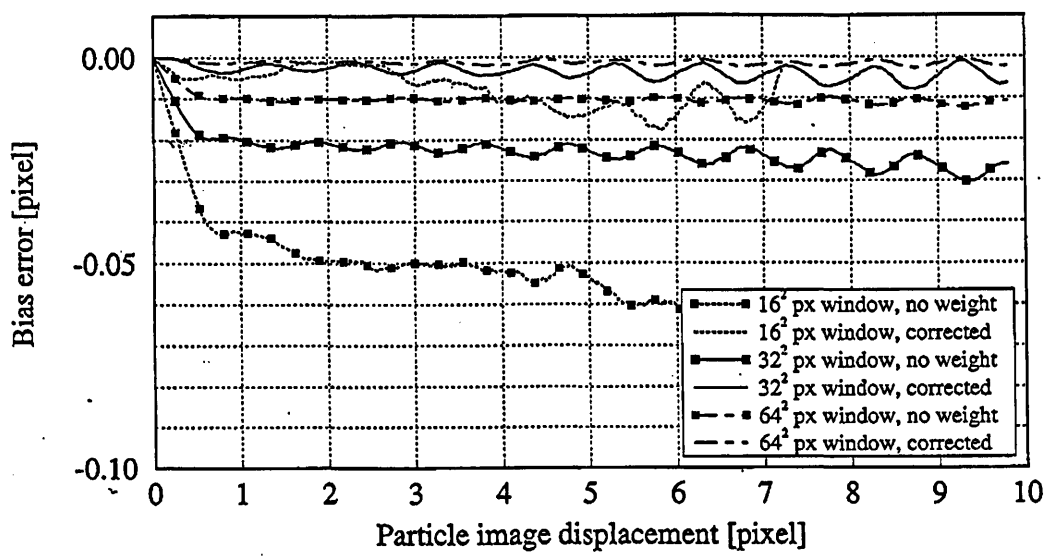
#### 7.4.3. Effect of Particle Image Density

The particle image density has two primary effects in the evaluation of PIV images. First, the probability of valid displacement detection increases when more particle image pairs enter in the correlation calculation. The number of image pairs captured in an interrogation area itself depends on three factors, namely, the overall particle image density,  $N_I$ , the amount of in-plane displacement and the amount of out-plane displacement. It has been defined these three quantities as the effective particle image pair density within the interrogation spot,  $N_I$ , a factor expressing the in-plane loss-of-

pairs,  $F_I$  and a factor expressing the out-of-plane loss-of-pairs,  $F_0$ . When no in-plane or out-of-plane loss is present, the later two are unity.

For the above max speed case and 3.8 pixel displacement the bias error results  $\sim 0.02$  pixel corresponding to an accuracy of 0.5%.

The second effect the particle image density has for the evaluation of PIV images is its direct influence on the measurement uncertainty. In Figure 7- 12 the measurement uncertainty is plotted as a function of particle image displacement for various particle image densities,  $N_I$ . The displacement range was limited to the one pixel range, which can be ensured by an interrogation window offset. For displacement less than  $\frac{1}{2}$  pixel the same linear trend as in Figure 7- 12 can be observed for all  $N_I$ . For  $|d| > 0.5$  pixel the uncertainty remains approximately constant. The principle effect of the particle image density,  $N_I$ , is that the measurement uncertainty substantially, which can be explained by the simple fact that more particle image pairs increase the signal strength of the correlation peak.



**Figure 7- 12 Simulation results showing the difference between actual and measured displacement as a function of the particle image displacement. Bias correction removes the displacement bias**

Together the effects described above indicate that if a flow can be densely seeded then both a high valid detection rate as well as a low measurement uncertainty can be achieved using small interrogation windows, which in turn allows for a high spatial resolution.



In the air entrainment PIV experiments the seeding was maintained by the water atomiser at a satisfying level which we can assume being in the range of 20-30 per interrogation area whereas for the spray recirculation assessment the particle density depended on the spray phase and on the position of interrogation area. However, it can be assumed a particle density below 10 droplets per interrogation area. Based on these density assumptions and on the above max speed case and 3.8 pixel displacement the RMS uncertainty results  $<0.03$  pixel corresponding to an accuracy of 0.8%.

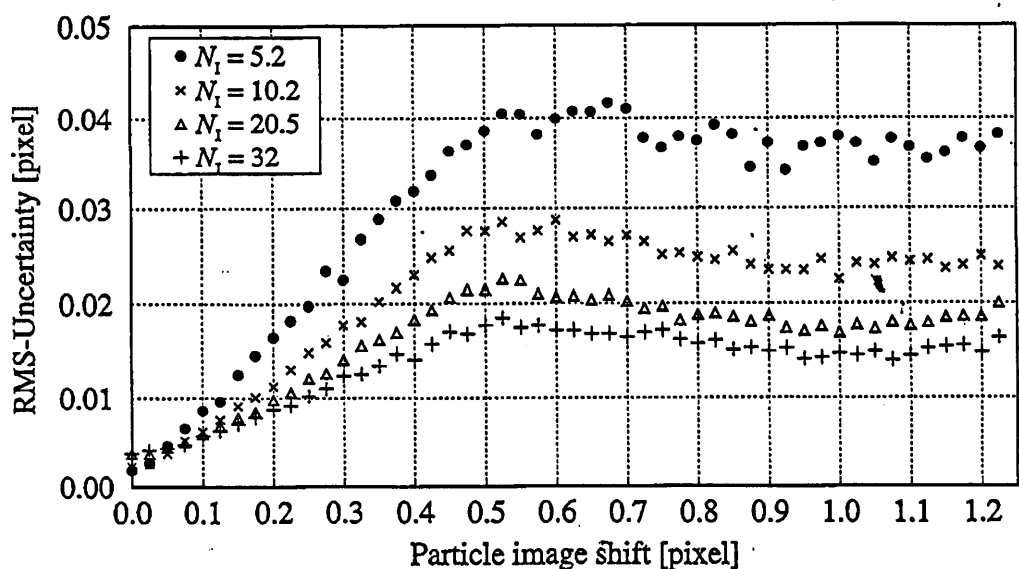


Figure 7- 13 Measurement uncertainty for single exposure/double frame PIV as a function of particle image shift for various particle image densities  $N_I$ .

---

## References

1. Nieuwenhuis, P.M.A., *Car CO2 Reduction Feasibility Assessment; Is 130g/km Possible?*, The Centre for Business Relationships, Accountability, Sustainability and Society, 2007.
2. Wirth, M., D. Zimmermann, R. Friedfeldt, J. Caine, A. Schamel, M. Davies, G. Peirce, A. Storch, K. Ries-Müller, K.P. Gansert, G. Pilgram, R. Ortmann, G. Würfel, J. Gerhardt, *A Cost Optimised Gasoline Spray Guided Direct Injection System for Improved Fuel Economy*, IMechE Seminar on Fuel Economy and Engine Downsizing, 2004.
3. Spichel, D.C., Bardasz, E. A., Schifererl, E. A., and Fisher, D. W., *A Comparison of Gasoline Direct Injection Part 1- Fuel System Deposits and Vehicle performanc*, Society of Automotive Engineers, 1999-01-01498, 1999.
4. Hentschel, W., *Gasoline Direct Injection-A Promising Engine Concept for Future Demands*. SAE, 2000(2000-01-0248).
5. <http://www.dieselnets.com/standards/eu/hd.php>.
6. Helmut Eichseder, E.B., Peter Müller and Stephan Rubbert, *Gasoline Direct Injection – A Promising Engine Concept for Future Demands*. SAE 2000-01-0248, 2000.
7. Nouri, N.M., Y. Yan and C. Arcoumanis, *Internal Flow and Cavitation in a Multi-hole Injector for Gasoline Direct-Injection Engines*. SAE 2007-01-1405, 2007.
8. Mitsubishi-Motors, w., *Latest MMC technologies and near-future goals: GDI - The pursuit of a high-efficiency engine*.
9. *European Launch for GDI CARISMA*. Mitsubishi Motors press release, August 29, 1997.
10. Mark Wan, A.T.S., *Direct Injection Petrol engine - Mitsubishi GDI*.
11. *GDI engine production tops 1,000,000 unit mark*. Mitsubishi Motors press release, September 11, 2001
12. *Mitsubishi Motors and PSA Peugeot Citroen Reach Agreement on GDI Engine Technical Cooperation*. Mitsubishi Motors press release, January 12, 1999
13. *GDI-ASG Pistachio*. Mitsubishi Motors press release, September 28, 1999
14. Edmunds.com, *Inside BMW's Latest Powertrain Technologies*. Retrieved on May 12- 2006.
15. Papoulias D., G.E., Mitroglou N., Gavaises M., and Theodorakakos A., *Cavitation in Fuel Injection Systems for Spray-guided Direct Injection Gasoline Engines*. SAE 01-1418, 2007.
16. Tait, N.P., *Development of Planar Laser Diagnostic Techniques for Fuel and Soot Imaging in Combustion Applications, in Mechanical Engineering Department*. Cranfield University, Bedfordshire, 1994.
17. Fuquan Zhao, D.H., Ming Chia Lai, *Automotive Gasoline Direct-Injection Engines*. SAE publishing,, 2002.
18. Arcoumanis, C., Niouri, J., Xu, H.M., and Stone, R. , *Analysis of the Steady Flow Characteristics of Tumble-Generating Four-Valve Cylinder Heads*. Optical Diagnostics in Engineering, Vol 2(2) 1997.
19. F. Zhao, M.-C.L., D.L. Harrington, , *Automotive spark-ignited direct-injection gasoline engines*, . 1999.



20. Mansour, A.a.C.N., *Dynamic behavior of liquid sheets*. Phys. Fluids A, , 3, 12, pp. 2971-2980, 1991.
21. M. Wirth; D. Zimmermann; R. Friedfeldt; J. Caine; A. Schamel, M.D., G Peirce IMechE, *A Cost Optimised Gasoline Spray Guided Direct Injection System for Improved Fuel Economy*. IMechE, 2004.
22. Davies, M., *A Cost Optimised Gasoline Spray Guided Direct Injection System for Improved Fuel Economy*. IMechE, 2004.
23. Al, N.T.e., *Stability improvement of direct fuel injection system under lean combustion operation*. SAE technical paper No 982703.
24. Preussner, *GDI : Interaction Between Mixture Preparation, Combustion System and Injector Performance*. SAE 980498, 1998.
25. Sczomak, D.P., Patterson, *Overview of Central-Injection Air-Assisted SIDI Technology Emissions and Fuel Consumption*. SAE 2003-01-0545, 2003.
26. Nouri, J.M., et al., *Internal and near nozzle flow characteristics from an enlarged model of an outward opening gasoline direct injector*. International Conference on Optical and Laser Diagnostics, 2005.
27. Matsumura, E., Tomita, T., Takeda, K., Furuno, S., Senda, J., *Analysis of Visualized Fuel Flow inside the Slit Nozzle of Direct Injection SI Gasoline Engine*. SAE 2003-01-0060., 2003.
28. I.S. Carvalho a, M.V. Heitoyr b, D. Santos c, *Liquid film disintegration regimes and proposed correlations*. International Journal of Multiphase Flow 28 2002.
29. Roth, H., et al., *Effect of Multi-injection Strategy on Cavitation Development in Diesel Injector Nozzle Holes*. SAE 05P-330, 2005.
30. Soteriou, C., et al., *The Flow Patterns and Sprays of Variable Orifice Nozzle Geometries for Diesel Injection*. SAE Paper 2000-01-0943, 2000.
31. Schmidt, D.P., et al., *Cavitation in Two-Dimensional Asymmetric Nozzles*. SAE Technical Paper, 1999: p. 01-0518.
32. Afzal, H., et al., *Internal Flow in Diesel Injector Nozzles: Modelling and Experiments*. IMechE Paper S492/S2/99, 1999.
33. Yule, A.J., A.M. Dalli, and K.B. Yeong. *Transient Cavitation and Separation in a Scaled-Up Model of a VCO Orifice*. in *Proc. ILASS-EUROPE*. 1998, July 6-8. Manchester, UK.
34. Soteriou, C., M. Smith, and R.J. Andrews, *Diesel Injection - Laser Light Sheet Illumination of the Development of Cavitation in Orifices*. IMechE Paper C529/018/98, 1998.
35. Arcoumanis, C., et al., *Analysis of the Flow in the Nozzle of a Vertical Multi Hole Diesel Engine Injector*. SAE Paper 980811, 1998.
36. He, L. and F. Ruiz, *Effect of Cavitation on Flow and Turbulence in Plain Orifice for High-Speed Atomization*. Atomization and Sprays, 1995. 5(6): p. 569-584.
37. Soteriou, C.C.E., M. Smith, and R.J. Andrews, *Cavitation Hydraulic Flip and Atomization in Direct Injection Diesel Sprays*. IMechE Paper C465/051/93, 1993.
38. Arcoumanis, C., J.M. Nouri, and R.J. Andrews. *Application of Refractive Index Matching to a Diesel Nozzle Internal Flow*. in *Proc. IMechE Seminar on Diesel Fuel Injection Systems*. 1992, April 14-15. London, UK.
39. Pouvreau, L., *Characterization of the Internal Flow of a Nozzle Hole and Its Effect on the Issued Liquid Jet Spray and Combustion* Laboratory Faculty of Mechanical Engineering Hiroshima University.
40. Roland Domann, Y.H., *Quantitative Measurement of planar Droplet Sauter*

---

*Mean Diameter in sprays using Planar Droplet Sizing*. Eleventh International Symposium on Application of Laser Techniques to Fluid Mechanics, Lisbon, Portugal, 2002.

41. Hyeonseok Koh, K.J.a.Y.Y., *Quantitative Measurement of Spray Characteristics Using Planar Imaging Techniques*. School of Mechanical and Aerospace Engineering, Seoul National University,, 2002.
42. Z. Dai, G.M.F., *Temporal properties of secondary drop breakup in the multimode breakup regime*. International Journal of Multiphase Flow 27, 2001.
43. Nouri, J.M., Brehm, C., Whitelaw, J.H., *The Spray form a Gasoline Direct Injector*. ILASS-Europe 1999, 1999.
44. Kashdan, J.T., Shrimpton, J.S., Arcoumanis, C. , *Dynamic Structure of Direct-Injection Gasoline Engine Sprays: Airflow and Density Effects*. Journal of the International Institutes of Liquid Atomization and SpraySystems, Vol.12., 2002.
45. Abo-Serie, E., Arcoumanis, C., and Gavaises, M., *Structure of Sprays Generated by Pressure Swirl Injectors for Direct-Injection Gasoline Engines*. ILASS-Europe, Toulouse, France., 1999.
46. Miyajima, A., Okamoto, Y., Kadomukai, Y., Togashi, S., Kashiwaya, M., *A Study on Fuel Pattern Control of Fuel Injector of Gasoline Direct Injection Engines*, . SAE 2000-01-1045, 2000.
47. Shelby, M., VanDerWege, B., and Hochgreb, S. , *Early Spray Development in Gasoline Direct - Injected Spark Ignition Engines*. SAE 980160., 1998.
48. Nouri, J.M., Whitelaw, J.H., *Effect of Chamber Pressure on the Spray Structure for a Swirl Pressure Atomiser for Direct Injection Gasoline Engines*. ICOLAD 2002 pp 121-130, 2002.
49. Mitroglou, N., Nouri, J.M., and Arcoumanis, C., *Spray Characteristics of a Multihole Injector for Direct Injection Gasoline Engines*. International Journal of Engine Research., 2001.
50. Miyajima, A., Okamoto, Y., Kadomukai, Y., Kashiwaya, M., Kubo, H., Fujii, , *H.Experimental Characterization of Flat-Spray Injector in a Gasoline Direct Injection Engines*. SAE 2003-01-0061., 2003.
51. Tanaka, Y., et al., *Analysis on behaviors of swirl nozzle spray and slit nozzle spray in relation to DI gasoline combustion*. 2003, Society of Automotive Engineers. p. 218-237.
52. Pontoppidan, M., et al., *Optimisation by CFD Simulation of Spray Formation Parameters to Adapt Direct Injection High-Pressure Fuel Injectors to High-Speed SI-Engines*. SAE 2004-01-0539, 2004.
53. Choi, K.H., J. H. Park, et al, *A Research on Fuel Spray and Air Flow Fields for Sprak Ignitied Direct Injection using Laser Mesurement Technology*. SAE 1999-01-0503., 1999.
54. Hung, L.S.D., Chmiel, D.M., Markle, L.E., *Application of an Imaging-based Diagnostic technique to Quantify the Fuel Spray Variations in Direct-Injection Spark-Ignition Engine*. SAE 2003-01-0062., 2003.
55. Abe, M., Okamoto, Y., Kadomukai, Y., Tanabe, Y., Ishikawa, T., *Fuel Spray Pattern Control using L-Step Nozzle for Swirl-Type Injector*, . SAE 2004-01-0540., 2004.
56. Kubo, M., Sakakida, A., Iiyama, A. , *Technique for Analyzing Swirl Injectors of Direct-Injection Gasoline Engines*. SAE 2001-01-0964, 2001.
57. Seoksu Moon, J.C., Essam Abo Serie and Choongsik Bae, *The Effects of Injector Temperature on Spray and Combustion Characteristics in a Single*



- 
- Cylinder DISI Engine*. SAE 2005-01-0101, 2005.
58. Eriko Matumura, T.S., Mutsumumi Kanda *Analysis of Fuel and Spray Atomization in Slit Nozzle for Direct Injection SI Gasoline Engines*. sae 2006-01-1000, 2006.
  59. Yan-jun Wang, J.-X., Shi-Jin, Xiao-Hu Lei and Xin-Liang An, *Study of Injection Strategies of Two-stage Gasoline Direct Injection (TSGDI) Combustion System*. SAE 2005-01-0107 2005.
  60. Anand H. Gandhi, C.E.W., Eric W. Curtis, Terrence F. Alger, Carl L. Anderson, Duane L. Abata *Spray Characterization in a DISI Engine During Cold Start: (1) Imaging Investigation*. SAE 2006-01-1004, 2006.
  61. Anand H. Gandhi, C.E.W., Eric W. Curtis, Terrence F. Alger, Carl L. Anderson, Duane L. Abata *Spray Characterization in a DISI Engine During Cold Start: (2) Imaging Investigation*. SAE 2006-01-1003, 2006.
  62. Cossali, G.E., et al., *Effect of gas density and temeperature on air entrainmnet in a transinet diesel spray*. SAE transactions, 1996. **105**(3): p. 1293-1303.
  63. Andriani, R., A. Coghe, and G. Cossali, *Near-Field Entrainment in Unsteady Gas Jets and Diesel Sprays: A Comparative Study*. Proceedings of the Combustion Institute, 1996. **26**: p. 2549–2556.
  64. Cossali, G.E., A. Coghe, and G. Brunello, *Effect of Spray-wall Interaction on Air Entrainment in a Transient Diesel Spray*. 1993: Society of Automotive Engineers.
  65. Cossali, G.E., G. Brunello, and A. Coghe, *LDV characterization of air entrainment in transient diesel sprays*. S A E Technical Papers, 1991: p. 13.
  66. Siebers, D.L., *Scaling liquid-phase fuel penetration in diesel sprays based on mixing-limited vaporization*. SAE transactions, 1999. **108**(3): p. 703-728.
  67. Grünefeld, S.K.a.G., *Planar velocity measurements of the gas and liquid phase in dense sprays by flow tagging*. University of Bielefeld, Faculty of Physics, 1999.
  68. K.D. Driscoll, V.S., C. Gray, *Simultaneous air/fuel-phase PIV measurements in a dense fuel spray*. Experiments in Fluids, 2003.
  69. Nauwerck, A., et al., *A basic experimental study of gasoline direct injection at significantly high injection pressures*. SAE transactions, 2005. **114**(3): p. 218-226.
  70. Cossali, G.E., *An integral model for gas entrainment into full cone sprays*. J. Fluid Mech., vol. 439, 2001.
  71. Y Yan, S.G., J M Nouri, R D Lockett and C Arcoumanis, *Investigation of spray characteristics in a spray guided DISI engine using PLIF and LDV ICOLAD*, 2005.
  72. Himes, M., Farrell, P.V. , *Intake Air Velocity Measurements for a Motored Direct Injection Spark Ignited Engine*, SAE 1999-01-0499. 1999.
  73. Takagi, Y., Itoh, T., Muranaka, S., Iiyama, A., Iwakiri, Y., Urushihara, T., Naitoh, K. , *Simultaneous Attainment of Low Fuel Consumption, High Output Power Low Exhaust Emissions in Direct injection SI Engines*, . SAE 980149, 1998.
  74. Befrui, B., R. Kneer, et al. , *Investigation of a DISI Fuel Injector for a Close-Arranged Spray-Guided Combustion System*. SAE 2002-01-1133, 2002.
  75. Salters, D., P. Williams, et al., *Fuel Spray Characteristics within an Optically Accessed Gasoline Direct Injection Engine using a CCD Imaging System*. SAE 961149, 1996.
  76. Julian T. Kashdan, J.C.a.b.T., *A study of Combustion Structure and Implications on Post-Oxidation Under Homogeneous and Stratified Operation*
-

- 
- in a DISI Engine*. SAE 2006-01-1262, 2006.
77. Brad A. VanDerWege, Z.H., Claudia O. Iyer, Rubén H. Muñoz and Jianwen Yi, *Development and Analysis of a Spray-Guided DISI Combustion System Concept*. SAE International, 2003.
  78. M. Gavaises, S.T.a.A.M., *Modeling of internal and near-nozzle flow of a pintle-type outwards opening gasoline piezo-injector*. JER US/RR 63-5/25/05, 2006.
  79. VanBrocklin, S.D.a.P.G., *Effect of Design and Operating Parameters on the Spray Characteristics of an Outward Opening Injector*. Thirteenth International Multidimensional Engine Modeling User's Group Meeting, 2003.
  80. Ch.Schwarz, E.S., B. Durst, J. Fisher and A. Witt, *Potential of Spray-guided BMW DI Combustion System*. SAE International, 2006.
  81. Stan, C., Troeger, R., Stanciu, A., *Correlation Concept Between Mixture Formation and Ignition Applied to a GDI High Speed Engine*,. SAE 2002-01-0833, 2002.
  82. J M Nouri, M.A.H., Y Yan and C Arcoumanis, *Spray characterization of a piezo pintle-type injector for gasoline direct injection engines*. ICOLAD, 2005.
  83. A. Marchi, J.M.N., Y. Yan and C. Arcoumanis, *Internal Flow and Spray Characteristics of Pintle-type Outwards Opening Piezo Injectors for Gasoline Direct-Injection Engines*. S A E 2007-01-1406, 2007.
  84. B.Befrui, G.C., D. Robart and W. Reckers, *LES Simulation of the Internal Flow and Near-Field Spray Structure of an Outward-Opening GDi Injector and Comparison with Imaging Data*. SAE 01-0137, 2008.
  85. Henning Kleeberg , D.T., Oliver Lang ,Knut Habermann, *Future Potential and Development Methods for High Output Turbocharged Direct Injected Gasoline Engines*. S A E 2006-01-0046, 2006.
  86. Alasdair Cairns, H.B.a.G.I., *Exhaust gas recirculation for improved part and full load fuel economy in a turbocharged gasoline engine*. SAE 2006-01-0047, 2006.
  87. Philip Price, R.S., Tony Collier, Marcus Davies, *Particulate Matter and Hydrocarbon Emissions Measurements: Comparing First and Second Generation DISI with PFI in Sinlge Cylinder Optical Engines*. SAE 2006-01-1263, 2006.
  88. Yang, J., Anderson, R.W., *Fuel Injection Strategies to increase Full-Load Torque Output of a Direct-Injection SI Engine*. SAE 980495, 1998.
  89. Roth, H., *Experimental and Computational Investigation of Cavitation in Diesel Injector Nozzles*. PH.D Thesis, 2007.
  90. L.Liverani, *Simultaneous Observation of Cavitation in a Real Size Transparent Six Holes DENSO Diesel Nozzle and Generated Spray*. Transfer Report, 2006.
  91. Nouri, R.M.H.a.J.M., *Turbulent flow in a baffled vessel stirred by a 60° pitched blade impeller*. 1996.
  92. I.S. Carvalho a, M.V. Heitoyr b, D. Santos c, *Liquid film disintegration regimes and proposed correlations*. International Journal of Multiphase Flow 28, 2002.
  93. Lefebvre, A.H., *Atomisation and Sprays*. Hemisphere publishing, 1989
  94. Fraser, R.P.E., P., *Research into the performance of atomizers of liquids*. Imp. Colloid Chem. Eng. Soc. J., 1953(7): p. 52-68.
  95. Dombrowski and Fraser R.P, *A photographic Investigation into th*
-



- 
- Disintegration of liquid sheets*,. London Ser. ,, September 1954,. A. Vol 247. No. 924, pp. 101-130.,.
96. Crapper, G.D., and Dombrowski, N., *A Note on the effect of Forced Disturbances on the Stability of Thin Liquid Sheets and on the Resulting Drop Size*,. Int. J. Multiphase Flow,, 1984,. vol. 10, No. 6, pp. 731-736.,
  97. Hardalupas, Y., Taylor, A. M. K. P, and Whitelaw, J. H. , 1992. "Int. J. Multiphase Flow,, Characteristics of the spray from a Diesel injector, . vol. 18, pp. 159-179, .
  98. Nouri, J.M.a.W., J. H., *Spray characteristics of a gasoline direct injector with short durations of injection*". Exp. Fluids, vol. 31, pp. 377-383, 2001.
  99. Nouri, J.M., Whitelaw, J.H., & Yianneskis, M. , *A refractive index matching technique for solid/liquid flows*. Laser Anemometry in Fluid Mechanics. , 1988. 3: p. pp. 335-340.
  100. Mitschke, M., et al., *Reconstruction of velocity-diameter relations obtained from PDA measurements during atomisation of inhomogeneous liquids*. ILASS Europe, 1999.
  101. Wigley, G., G.K. Hargrave, and J. Heath, *A high power, high resolution LDA/PDA system applied to dense gasoline direct injection sprays*. 9th International Symposium of Applied Laser Techniques to Fluid Mechanics - Lisbon, 1998. 1.
  102. Wigley, G., et al., *Experimental Analysis of the Response of a Laser/Phase Doppler Anemometer System to a Partially Atomised Spray*. Part. Part. Syst. Charact., 2001. 18: p. 169-178.
  103. Tropea, C. and N. Damaschke, *Phase Doppler Measurements in Ultra-Dense Sprays*. Short Course - TU Darmstadt, 2005.
  104. Pinho, *PhD Thesis (LDV Error analysis)*. 1990.
  105. Adrian, R.J., *Particle-Imaging Techniques for Experimental Fluid-Mechanics*. Annual Review of Fluid Mechanics, 1991. 23: p. 261-304.
  106. Raffel, M., C. Willert, and J. Kompenhans, *Particle Image Velocimetry*. 1998, Berlin: Springer-Verlag.
  107. Eisenberg, S., W. Reckers, and B. Wieneke. *Visualization and PIV Measurements of High-Speed Flows and other Phenomena with Novel Ultra-High-Speed CCD Camera*. in *Proc. West East High Speed Flow Fields*. 2002. Barcelona, Spain.
  108. Dantec, *Online Internet Resources*, in [www.dantecdynamics.com](http://www.dantecdynamics.com). 2004, Dantec Dynamics A/S, Skovlunde, Denmark.
  109. Adrian, R.J. and C.S. Yao, *Pulsed Laser Technique Application to Liquid and Gaseous Flows and the Scattering Power of Seed Material*. Applied Optics, 1985. 24(1): p. 44-52.
  110. LaVision, *Online Internet Resources*, in [www.lavision.de](http://www.lavision.de). 2004, LaVision GmbH, Göttingen, Germany.
  111. Kompenhans, M.R.C.W.S.W.J., *Particle image velocity (a practical guide)*. (2nd edition).
-